Transactions of the ASME®

Journal of Heat Transfer

Published Bimonthly by The American Society of Mechanical Engineers

VOLUME 123 • NUMBER 6 • DECEMBER 2001

Transactions of the ASME, Journal of Heat Transfer (ISSN 0022-1481) is published bi-monthly (Feb., Apr., June, Aug., Oct., Dec.) by The American Society of Mechanical Engineers, Three Park Avenue, New York, NY 10016. Periodicals postage paid at New York, NY and additional mailing offices. POSTMASTER: Send address changes to Transactions of the ASME, Journal of Heat Transfer, c/o THE AMERICAN SOCIETY OF MECHANICAL ENGINEERS, 22 Law Drive, Box 2300, Fairfield, NJ 07007-2300. **CHANGES OF ADDRESS** must be received at Society headquarters seven weeks before they are to be effective. Please send old label and new address. **STATEMENT from By-Laws.** The Society shall not be responsible for statements or opinions advanced in papers or ... printed in its publications (B7.1, Para. 3), **COPYRIGHT © 2001** by The American Society of Mechanical Engineers. For authorization to photocopy material for internal or personal use under those circumstances not falling within the fair use provisions of the Copyright Act, contact the Copyright Clearance Center (CCC), 222 Rosewood Drive, Danvers, MA 01923, tel: 978-750-8400, *www.copyright.com*. Request for special permission or bulk copying should be addressed to Reprints/Permission Department. **INDEXED** by Applied Mechanics Reviews and Engineering Information, Inc. Canadian Goods & Services Tax Registration #126148048.

TECHNICAL PAPERS

(Contents continued on inside back cover)

This journal is printed on acid-free paper, which exceeds the ANSI Z39.48-1992 specification for permanence of paper and library materials. ♾™
♻ 85% recycled content, including 10% post-consumer fibers.

Journal of Heat Transfer Volume 123, Number 6 DECEMBER 2001

On the Solution of Multidimensional Inverse Heat Conduction Problems Using an Efficient Sequential Method

H. M. Park

W. S. Jung

Department of Chemical Engineering,
Sogang University,
Seoul, Korea

An efficient real-time scheme is developed to estimate the unsteady, spatially varying wall heat flux in a two-dimensional heat conduction system from the temperature measurement inside the domain. The algorithm is based on the Kalman filtering and the Karhunen-Loève Galerkin procedure. Although the employment of the Kalman filtering technique allows the derivation of a set of sequential estimation equations, the real-time implementation of these equations is never feasible due to the tremendous requirement of computer time and memory. In the present scheme, this difficulty is circumvented by means of the Karhunen-Loève Galerkin procedure that reduces the governing partial differential equation to a minimal set of ordinary differential equations. The performance of the present technique of inverse heat conduction problems is evaluated by several numerical experiments, and it is found to be very accurate as well as efficient. [DOI: 10.1115/1.1409260]

Keywords: Computational, Heat Transfer, Inverse, Numerical Methods

1 Introduction

There are many industrial processes where one has to adjust the thermal state of the system by manipulating heat flux through the system boundary. Some examples are the vulcanization of complex rubber moldings, the heat treatment of ingots in the soaking pit of steel mill [1] and the baking of ceramic wafers for annealing, oxidation and chemical vapor deposition [2]. In these cases, the amount of heat flux imposed on the boundary determines the temperature distribution in the system and, therefore, the accurate determination of heat flux is a crucial step in the operation of the processes. One may determine the heat flux at the boundary of the domain by exploiting temperature measurements within the domain. This is one of the typical inverse heat conduction problems [3]. The determination of temperature distribution in the domain from the knowledge of heat flux at the boundary is a direct problem, and the determination of heat flux at the boundary based on the temperature measurements in the domain is an inverse problem. Contrary to the direct problem which consists of computing the consequences of given causes, the inverse problem is associated with the reversal of the cause-effect sequence and consists of finding the unknown causes of known consequences. In many situations, the direct measurement of the cause is not practical and one is forced to estimate the cause from the observation of the effect. The solution of inverse problems requires special numerical techniques to stabilize the result of calculations since the inverse problems are ill-posed in the sense of Hadamard; small perturbations in the observed functions may result in large changes in the corresponding solutions. Commonly adopted techniques for the solution of inverse heat conduction problems are the least-square method modified by the addition of regularization terms that impose additional restrictions on admissible solutions [3] and the conjugate gradient method where the regularization is inherently built in the iterative procedure [4]. These algorithms for the inverse problems are iterative ones and therefore require repeated computation of governing equations before obtaining estimations. They also require a complete data base before computation begins and thus nonsequential. But in many situations, it is necessary to estimate the history of unknown properties in real time. For this purpose, we have to adopt a sequential algorithm where initial a priori estimation is continually updated based on current experimental measurements.

In the present investigation we employ the Kalman filtering technique that is a typical sequential estimation method consisting of repeatedly updating the estimates and a covariance matrix to indicate the reliability of the estimates [5–7]. There have been some attempts at applying the Kalman filtering technique to solve one-dimensional inverse heat transfer problems [8,9]. But the straightforward implementation of a Kalman filter to the multidimensional heat conduction equation is never feasible due to the tremendous amount of computer time and memory required to solve the covariance equation. For a two-dimensional heat conduction equation, the covariance equation is a four-dimensional unsteady partial differential equation. It becomes a six-dimensional partial differential equation if we consider a three-dimensional heat conduction. Therefore, one of the most important prerequisites for the successful implementation of a Kalman filter for the purpose of real-time estimation is the development of a reliable low dimensional model that predicts the system behaviors accurately. An appropriate technique for this purpose is the Karhunen-Loève Galerkin procedure [10–12] which is a Galerkin method employing the empirical eigenfunctions of the Karhunen-Loève decomposition as basis functions. Through the Karhunen-Loève Galerkin procedure, one can a priori limit the function space considered to the smallest linear subspace that is sufficient to describe the observed phenomena and consequently reduce the governing partial differential equation to a minimal set of ordinary differential equations. Originally, the Karhunen-Loève decomposition had been devised as a rational technique enabling a stochastic field to be represented with a minimum degree of freedom [13]. If the Karhunen-Loève decomposition is applied to a given stochastic field, we get a set of empirical eigenfunctions. The same stochastic field can be represented with a minimum degree of freedom when employing these empirical eigenfunctions. But recent works [10–12] have extended the applicability of the Karhunen-Loève decomposition to the analysis of nonstationary, nonhomogeneous deterministic as well as stochastic fields and allowed the derivation of rigorous low dimensional dynamic mod-

Contributed by the Heat Transfer Division for publication in the JOURNAL OF HEAT TRANSFER. Manuscript received by the Heat Transfer Division October 13, 2000; revision received April 19, 2001. Associate Editor: R. L. Mahajan.

els that simulate the given systems almost exactly even when the boundary conditions vary. This extension of the original Karhunen-Loève decomposition is called the Karhunen-Loève Galerkin procedure. The Karhunen-Loève Galerkin procedure is not restricted by geometric complexities and can treat irregular geometries as easily as the regular ones. In the present investigation, we reduce the heat conduction equation to a low dimensional dynamic model through the Karhunen-Loève Galerkin procedure, and develop a sequential method of solving inverse heat conduction problems by applying the Kalman filtering technique to the resulting low dimensional model. In the context of inverse problems, the Karhunen-Loève Galerkin procedure filters out the high frequency responses of the system and better conditions the corresponding inverse problem. The present algorithm is found to solve the inverse heat conduction problem accurately in a sequential manner with a meager requirement of computer time and memory.

2 System Governing Equations

As shown in Fig. 1 the domain of the system is a square with a quarter removed to make it non-separable. For non-separable domains like this, it is impossible to obtain analytic eigenfunctions, thus making the traditional Galerkin methods not applicable. But the Karhunen-Loève Galerkin procedure can be applied efficiently to this kind of systems with complicated boundaries. The boundary of the domain, Γ, is splitted into two parts; $\Gamma=\Gamma_N\cup\Gamma_D$. The heat flux $q(x,t)$ is imposed on Γ_N and the homogeneous Dirichlet boundary condition on Γ_D. Also shown in Fig. 1 are the locations of sensors to measure the temperature variations. The purpose of these measurements is to estimate the wall heat flux function $q(x,t)$ by means of an inverse analysis. We define the space-time quantities.

$$\Sigma_D=\Gamma_D\times(0,t_f) \quad \text{and} \quad \Sigma_N=\Gamma_N\times(0,t_f). \tag{1}$$

After these preliminaries, we write down the heat conduction equation,

$$\rho C_p\frac{\partial T}{\partial t}=k\left(\frac{\partial^2}{\partial x^2}+\frac{\partial^2}{\partial y^2}\right)T \tag{2}$$

with the boundary conditions

$$T=0 \ \text{ on } \ \Sigma_D \tag{3}$$

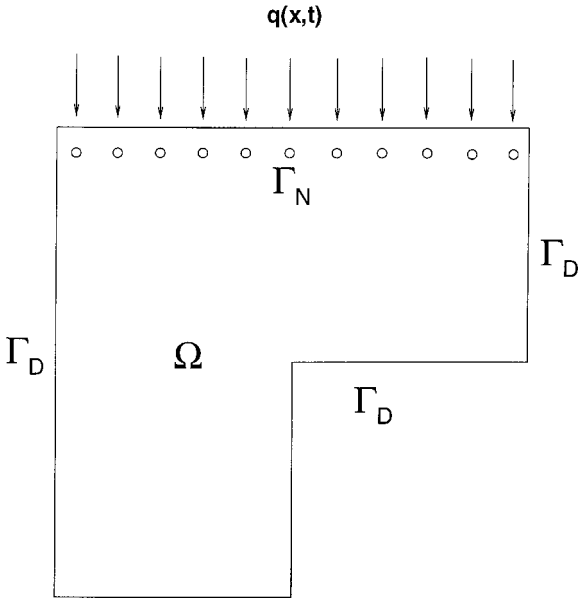

Fig. 1 The system and relevant boundary conditions

$$k\frac{\partial T}{\partial y}=q(x,t) \ \text{ on } \ \Sigma_N \tag{4}$$

and the initial condition

$$T(x,y,0)=0 \ \text{ in } \ \Omega \tag{5}$$

Here T is the temperature field, q is the heat flux into the domain, k is the thermal conductivity, ρ the density and C_p the heat capacity. We nondimensionalize the system such that $k=1.0$, $\rho=1.0$, $C_p=1.0$, $0\leqslant x\leqslant 1$ and $0\leqslant y\leqslant 1$. The set of Eqs. (2)–(5) is solved by a finite difference method employing (40×40) grids, which is found to be sufficient to resolve the temperature fields considered in the present work. The inverse heat conduction problem under consideration is the estimation of spatially and temporally varying heat flux $q(x,t)$ imposed on Γ_N from the temperature recordings of thermocouples positioned inside the domain.

3 The Karhunen-Loève Decomposition

To make this paper self-contained, we introduce the essence of the Karhunen-Loève decomposition. The Karhunen-Loève decomposition, expressed briefly, is a method of representing a stochastic field with a minimum degree of freedom. As a means of explaining the Karhunen-Loève decomposition we select N arbitrary irregularly shaped functions with $n=1,2,\cdots,N$. From now on, we call the irregular shapes of these functions $\{T_n\}$ "snapshots." In Park and Cho [10], it is shown that the most typical or characteristic structure $\phi(\mathbf{x})$ among these snapshots $\{T_n\}$ is given by solving the following eigenvalue problem of the integral Eq. (6):

$$\int_\Omega K(\mathbf{x},\mathbf{x}')\Phi(\mathbf{x}')d\mathbf{x}'=\lambda\phi(\mathbf{x}), \tag{6}$$

where the kernel of the integral equation $K(\mathbf{x},\mathbf{x}')$ is defined as

$$K(\mathbf{x},\mathbf{x}')=\frac{1}{N}\sum_{n=1}^{N}T_n(\mathbf{x})T_n^T(\mathbf{x}'). \tag{7}$$

Usually this kind of integral equation can be solved by means of the Schmidt-Hilbert technique [14].

Let's express the eigenvalues $\lambda_1>\lambda_2>\cdots>\lambda_N$ and the corresponding eigenfunctions $\phi_1,\phi_2,\cdots,\phi_N$ in the order of magnitude of eigenvalues. The eigenfunction ϕ_1 corresponding to the largest eigenvalue λ_1 is the most typical structure of the members of the snapshots $\{T_n\}$ and the eigenfunction ϕ_2 with the next largest eigenvalue λ_2 is the next typical structure, and so forth. Since the kernel $K(\mathbf{x},\mathbf{x}')$ is symmetric, these empirical eigenfunctions $\{\phi_n\}$ are mutually orthogonal. These empirical eigenfunctions $\{\phi_n\}$ can represent the system in the most efficient way. The span of these eigenfunctions is exactly the span of all the realization of snapshots. Thus, any feasible solution can be represented as a linear combination of these eigenfunctions. The set of these empirical eigenfunctions can be made complete in L^2 by including all eigenfunctions with zero eigenvalues. But the eigenfunctions with zero eigenvalue denote solution structures which are impossible for the range of heat flux function $q(x,t)$ under consideration. Therefore, the set of empirical eigenfunctions has no difficulties in spanning the whole realizable solution space. The Karhunen-Loève Galerkin procedure, employing these empirical eigenfunctions as trial functions of a Galerkin method, reduces the original system to a low dimensional model with a minimum degree of freedom.

4 The Low Dimensional Dynamic Model

According to the Schmidt-Hilbert theory [14], the empirical eigenfunctions are expressed linearly in terms of snapshots. Therefore, an appropriate set of empirical eigenfunctions can be obtained only from an ensemble of snapshots which are representative of the system characteristics [10,11]. An ensemble of snap-

shots characterizing the system dynamics is obtained in the following way. We transform the continuous control function $q(x,t)$ into discrete variables as follows:

$$q(x,t)=\sum_{m=1}^{M}\sum_{n=1}^{N}\alpha_{mn}\Psi_m(t)\Psi_n(x), \tag{8}$$

where $\Psi_m(t)$ is the m^{th} time shape function employed to discretize the time variable and $\Psi_n(x)$ is the n^{th} space shape function employed to discretize the space variable x, and M is the number of time shape functions, and N is the number of space shape functions employed. In the present work, we adopt $M=11$, and $N=11$. The values of M and N are determined based on the desired degree of the temporal and spatial resolution of the heat flux function. The function specification by means of Eq. (8) regularizes the problem by restricting the solution space of the inverse problem. Figure 2 depicts these shape functions. Next, we solve the system, Eq. (2)~(5), with $q(x,t)=\Psi_n(x)$ and record the temperature field at an appropriate time intervals until a steady state is reached. These recordings of the temperature field are used as snapshots in the Karhunen-Loève decomposition. If the heat flux $q(x,t)=\Psi_n(x)$ is imposed initially, a thermal boundary layer with a steep temperature gradient appears near Γ_N, and the temperature gradient becomes less steep as time goes on. Thus, the frequency to take snapshots should be high initially and it may be decreased as time elapses to obtain a set of 100 snapshots that fully characterize the thermal boundary layer formed during the process. The Karhunen-Loève decomposition is then applied to this set of snapshots to yield empirical eigenfunctions $\{\varphi_k^{(n)}\}$. The superscript n in the set $\{\varphi_k^{(n)}\}$ designates the fact that these empirical eigenfunctions are obtained from the system with $q(x,t)=\Psi_n(x)$. We repeat the above procedure for $n=1,2,\cdots,N$ to obtain N sets of empirical eigenfunctions, i.e., $\{\varphi_k^{(1)}\},\{\varphi_k^{(2)}\},\cdots,\{\varphi_k^{(N)}\}$. Each set $\{\varphi_k^{(n)}\}$ consists of 100 empirical eigenfunctions. Finally, we choose 10 dominant eigenfunctions from each of these N sets to make an ensemble of $(10\times N)$ snapshots. To this set of $(10\times N)$ snapshots, we apply the Karhunen-Loève decomposition to obtain the final set of empirical eigenfunctions $\{\phi_k\}$ to be employed in the construction of the low dimensional dynamic model. Figure 3(a–d) shows the first, the second, the third and the fourth empirical eigenfunctions with the corresponding normalized eigenvalues $\lambda_1=0.741$, $\lambda_2=0.156$, $\lambda_3=4.969\times10^{-2}$, and $\lambda_4=2.127\times10^{-2}$, respectively. Also shown in Fig. 3(e–h) are some typical eigenfunctions with smaller eigenvalues, i.e, the 17th, the 18th, the 19th, and the 20th eigenfunctions with the corresponding normalized eigenvalues, $\lambda_{17}=2.351\times10^{-4}$, $\lambda_{18}=1.787\times10^{-4}$, $\lambda_{19}=1.391\times10^{-4}$, and $\lambda_{20}=1.127\times10^{-4}$. Figure 3 reveals that the dominant empirical eigenfunctions represent the large scale structures of the temperature field, while the eigenfunctions with small eigenvalues represent the small scale structures. Using these empirical eigenfunctions, we can reduce the heat conduction equation to a set of small number of ordinary differential equations. We represent the temperature field $T(x,y,t)$ as a linear combination of empirical eigenfunctions as follows:

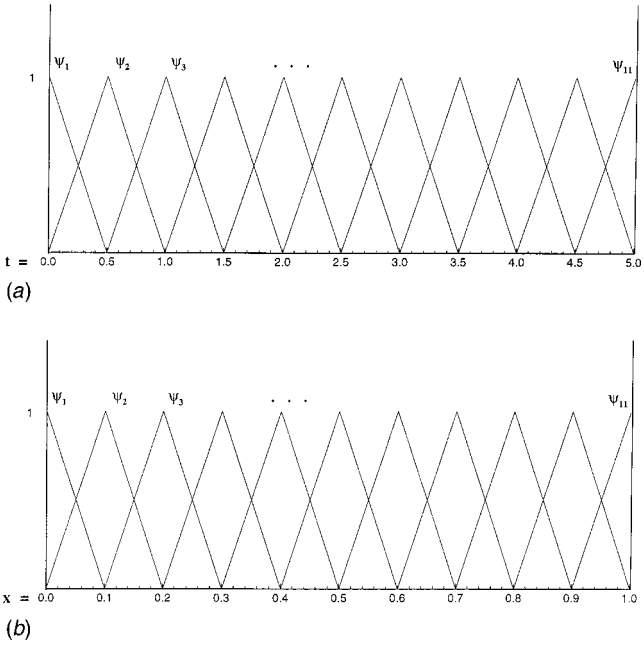

Fig. 2 Definition of shape functions: (*a*) temporal shape functions; and (*b*) spatial shape functions.

$$T(x,y,t)=\sum_{i=1}^{NT}a_i(t)\phi_i(x,y), \tag{9}$$

where ϕ_i is the i^{th} empirical eigenfunction, $a_i(t)$ is the corresponding spectral coefficient and NT is the total number of the empirical eigenfunctions employed in the Karhunen-Loève Galerkin procedure. The residual is expressed as

$$R\equiv\rho C_p\frac{\partial T}{\partial t}-k\left(\frac{\partial^2}{\partial x^2}+\frac{\partial^2}{\partial y^2}\right)T. \tag{10}$$

Applying the Galerkin principle which enforces the residual to be orthogonal to each of the trial functions and exploiting the boundary conditions we find that

$$\rho C_p M_j\frac{da_j}{dt}+k\sum_{i=1}^{NT}H_{ji}a_i=\int_{x=0}^{1}q(x,t)\phi_j(x,1)dx \qquad (j=1,2,\cdots,NT), \tag{11}$$

where

$$M_j\equiv\int\phi_j^2 d\Omega \tag{12}$$

$$H_{ji}\equiv\int\nabla\phi_i\cdot\nabla\phi_j d\Omega. \tag{13}$$

The relevant initial conditions for the system of ordinary differential equations, Eq. (11), are the following:

$$a_j(t=0)=\frac{\int_\Omega\phi_j T(x,y,t=0)d\Omega}{\int_\Omega\phi_j^2 d\Omega} \quad (j=1,2,\cdots,NT). \tag{14}$$

The accuracy of the low dimensional dynamic model, Eq. (11), is corroborated by solving it for various heat flux functions $q(x,t)$ and comparing the resulting temperature field with those obtained by the finite difference method. Usually the error of the low dimensional dynamic model decreases as the number of empirical eigenfunctions employed increases up to an optimal number. But further increase of the number of empirical eigenfunctions beyond the optimal number does not always improve the accuracy because the empirical eigenfunctions with very small eigenvalues are contaminated with round-off errors. A convenient guideline for the selection of optimal number is to balance the intrinsic numerical errors, i.e., the sum of the truncation and round-off error, and the sum of the normalized eigenvalues corresponding to the neglected modes. The optimal number of eigenfunctions for the set of Eq. (11) is found to be 20 after trials with several heat flux $q(x,t)$. With this number of eigenfunctions, the relative error of the low dimensional dynamic model with respect to the finite difference solution is less than 0.3 percent. All the results to be presented in the sequel are obtained by using the low dimensional dynamic model employing 20 empirical eigenfunctions.

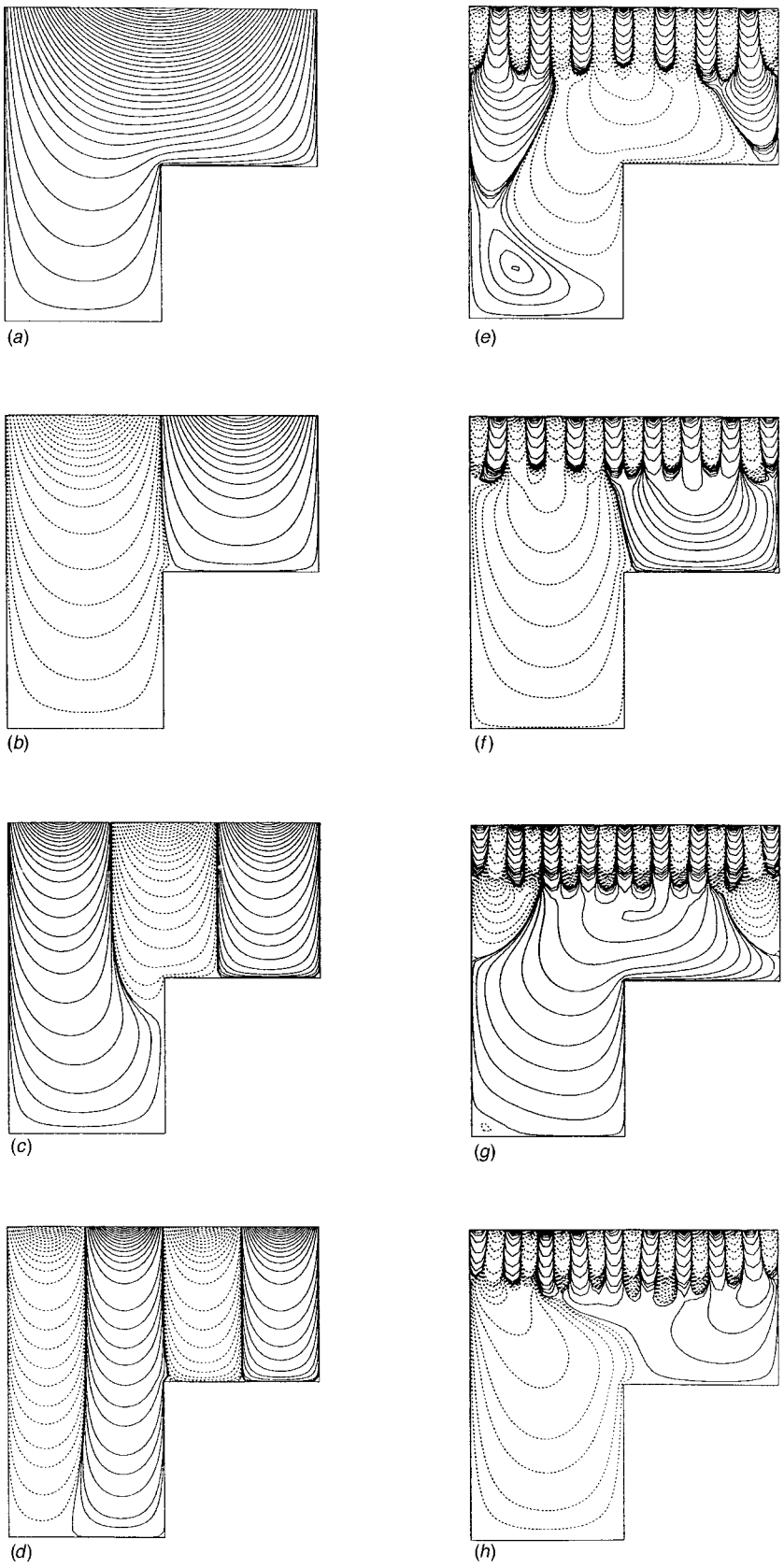

Fig. 3 Empirical eigenfunctions: (*a*) the first eigenfunction ($\lambda_1 = 0.741$); (*b*) the second eigenfunction ($\lambda_2 = 0.156$); (*c*) the third eigenfunction ($\lambda_3 = 4.969 \times 10^{-2}$); (*d*) the fourth eigenfunction ($\lambda_4 = 2.127 \times 10^{-2}$); (*e*) the 17th eigenfunction ($\lambda_{17} = 2.351 \times 10^{-4}$); (*f*) the 18th eigenfunction ($\lambda_{18} = 1.787 \times 10^{-4}$); (*g*) the 19th eigenfunction ($\lambda_{19} = 1.391 \times 10^{-4}$); and (*h*) the 20th eigenfunction ($\lambda_{20} = 1.127 \times 10^{-4}$).

5 Sequential Estimation Technique

Applying the Kalman filtering technique to the low dimensional dynamic model, one can derive a practical sequential algorithm for the estimation of wall heat flux that varies temporally as well as spatially. At the beginning, the temporal domain $t \in (0,t_f)$ and the spatial domain $x \in (0,1)$ are divided into M and N segments, respectively, and $q(x,t)$ is approximated linearly in each segment using linear temporal shape functions $\Psi_m(t)$ and linear spatial shape functions $\Psi_n(x)$ as given by Eq. (8). As shown in Fig. 2, the shape function $\Psi_m(t)$ has a triangular shape with a linear variation and has a unit value at $t=t_m$ and is zero at all other nodes. The spatial shape function $\Psi_n(x)$ can also be given similar description. Thus, α_{mn} in Eq. (8) is the value of heat flux at $t=t_m$ and $x=x_n$. Then for the duration $t \in (t_{m-1},t_m)$, the heat flux function $q(x,t)$ is given by

$$q(x,t)=\sum_{n=1}^{N} \alpha_{m-1,n}\Psi_{m-1}(t)\Psi_n(x)+\sum_{n=1}^{N} \alpha_{m,n}\Psi_m(t)\Psi_n(x), \tag{15}$$

where $\alpha_{m-1,n}$ $(n=1,2,\cdots,N)$ have been estimated during the previous time segment $t \in (t_{m-2},t_{m-1})$ and α_{mn} $(n=1,2,\cdots,N)$ are the N parameters to be estimated based on the temperature measurements during the present time segment $t \in (t_{m-1},t_m)$. Now, the low dimensional dynamic model, Eq. (11), may be rewritten as

$$\frac{da_j}{dt}=-\frac{k}{\rho C_p}\sum_{i=1}^{NT}\frac{H_{ji}}{M_j}a_i+\sum_{n=1}^{N} a_{NT+n}\frac{\Psi_m(t)B_{nj}}{\rho C_p M_j}+\sum_{n=1}^{N}\frac{\alpha_{m-1,n}\Psi_{m-1}(t)B_{nj}}{\rho C_p M_j} \quad (j=1,2,\cdots,NT) \tag{16}$$

$$\frac{d}{dt}a_{NT+n}=0 \quad (n=1,2,\cdots,N), \tag{17}$$

where

$$B_{nj}=\int_{x=0}^{1}\Psi_n(x)\phi_j(x,1)dx, \tag{18}$$

and new variables a_{NT+n} are assigned to the parameters α_{mn} to be estimated, i.e.,

$$a_{NT+n}=\alpha_{mn} \quad (n=1,2,\cdots,N). \tag{19}$$

Since $\alpha_{mn}(n=1,2,\cdots,N)$ are constants during $t \in (t_{m-1},t_m)$, Eq. (17) follows. If the heat flux $q(x,t)$ is known during t

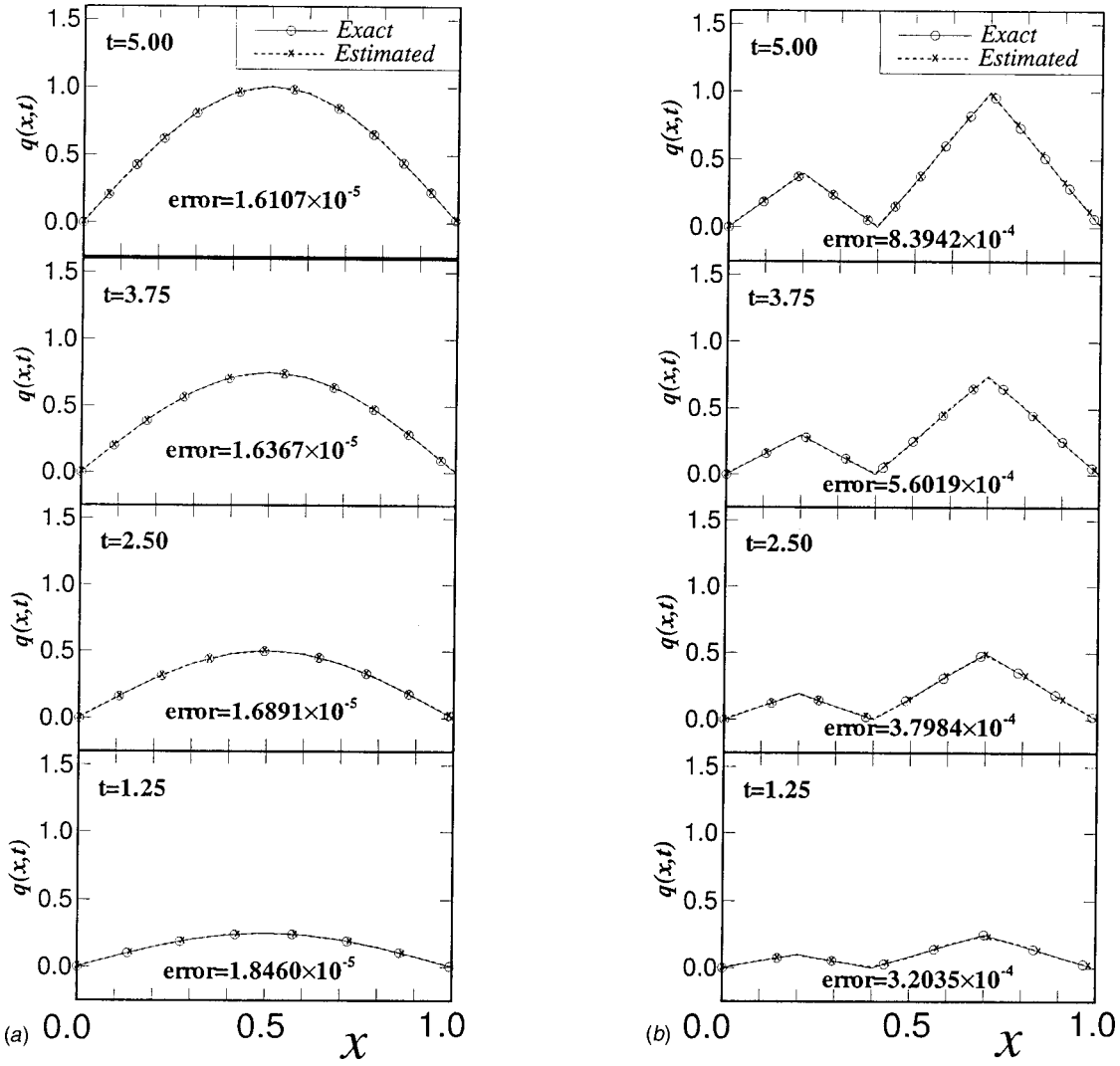

Fig. 4 The estimated profiles of wall heat flux: (*a*) $q(x,t)$ for the case *a* (Eq. 27); and (*b*) $q(x,t)$ for the case *b* (Eq. 28).

$\in(t_{m-1},t_m)$, $\alpha_{mn}(n=1,2,\cdots,N)$ are obtained from Eq. (8). Then Eqs. (16)–(17), in conjunction with Eq. (9), may be used to yield temperature field in the domain. Therefore, $q(x,t)$ or $\alpha_{mn}(n=1,2,\cdots,N)$ can be estimated using the measured values of temperature field at certain locations during $t\in(t_{m-1},t_m)$. The temperature measurements at *MO* locations may be represented as follows:

$$T^*(x_m,y_m,t)=\sum_{j=1}^{NT} a_j(t)\phi_j(x_m,y_m) \quad (m=1,2,\cdots,MO). \tag{20}$$

Equations (16), (17), and (20) may be summarized in the following standard form:

$$\frac{d\mathbf{a}}{dt}=\mathbf{A}\mathbf{a}+\mathbf{b}+\boldsymbol{\xi}(t) \tag{21}$$

$$\mathbf{y}=\mathbf{C}\mathbf{a}+\boldsymbol{\eta}(t), \tag{22}$$

where

$$\mathbf{a}=(a_1,a_2,\cdots,a_{NT},a_{NT+1},\cdots,a_{NT+N})^T \tag{23}$$

$$\mathbf{y}=(T^*(x_1,y_1,t),T^*(x_2,y_2,t),\cdots,T^*(x_{MO},y_{MO},t))^T \tag{24}$$

In the above equations, $\mathbf{A}$ is a $(NT+N,NT+N)$ matrix, $\boldsymbol{\xi}(t)$ is the Gaussian white modeling noise and $\boldsymbol{\eta}(t)$ is the Gaussian white measurement noise. Employing the standard procedure [6,7], we can derive the sequential estimation equation for the heat flux function $q(x,t)$ as follows:

$$\frac{d\mathbf{a}}{dt}=\mathbf{A}\mathbf{a}+\mathbf{b}+\mathbf{P}\mathbf{C}^T\mathbf{Q}[\mathbf{y}-\mathbf{C}\mathbf{a}] \tag{25}$$

$$\frac{d}{dt}\mathbf{P}=\mathbf{P}\mathbf{A}^T+\mathbf{A}\mathbf{P}^T+\mathbf{R}^{-1}-\mathbf{P}\mathbf{C}^T\mathbf{Q}\mathbf{C}\mathbf{P}, \tag{26}$$

where $\mathbf{R}$ and $\mathbf{Q}$ reflect the errors in the model and measurement device, and $\mathbf{P}$ is the error covariance matrix. Because the length of the vector $\mathbf{a}$ is $(NT+N)$, the covariance matrix $\mathbf{P}$ is of the size $(NT+N,NT+N)$ and symmetric. Thus the number of equations to be solved to obtain $\mathbf{P}$ is $(NT+N)(NT+N+1)/2$.

The procedure for the sequential estimation of $q(x,t)$ is as follows: at the outset we assume initial values of $a_i(i=1,2,\cdots,NT)$, and a_{NT+n} $(n=1,2,\cdots,N)$, i.e., $\alpha_{1n}(n=1,2,\cdots,N)$. The initial values of $\mathbf{P}$ and $\mathbf{Q}$ are assumed to be $\mathbf{P}=28.0\mathbf{I}$ and $\mathbf{Q}=(1./0.0025)\mathbf{I}$, respectively. The larger the magnitude of the diagonal components of $\mathbf{P}$, the faster the estimation error is reduced. But larger values of $\mathbf{P}$ tends to incur numerical instability. The model error covariance $\mathbf{R}^{-1}$ is neglected in the present computation since the relative error of the low dimensional dynamic model is less than 0.3 percent. Solving Eqs. (25)–(26) during the first time segment, $t\in(t_1,t_2)$, we obtain $a_{NT+n}(n=1,2,\cdots,N)$, i.e., $\alpha_{2n}(n=1,2,\cdots,N)$. During the next time segment, $t\in(t_2,t_3)$, we solve Eqs. (25)–(26) to find α_{3n} using the results of previous time segment as initial conditions except setting $P(NT+n,NT+n)=28.0$ $(n=1,2,\cdots,N)$ at $t=t_2$. The above procedure is repeated until the final time $t=t_f$ is reached. Although the preparation of low dimensional model requires a nontrivial amount of computer time, it is never significant when compared to the computer time required in the recursive estimation of heat flux using the original partial differential equation. The CPU time required to prepare a low dimensional model is usually less than 1/50 of that needed in the recursive solution

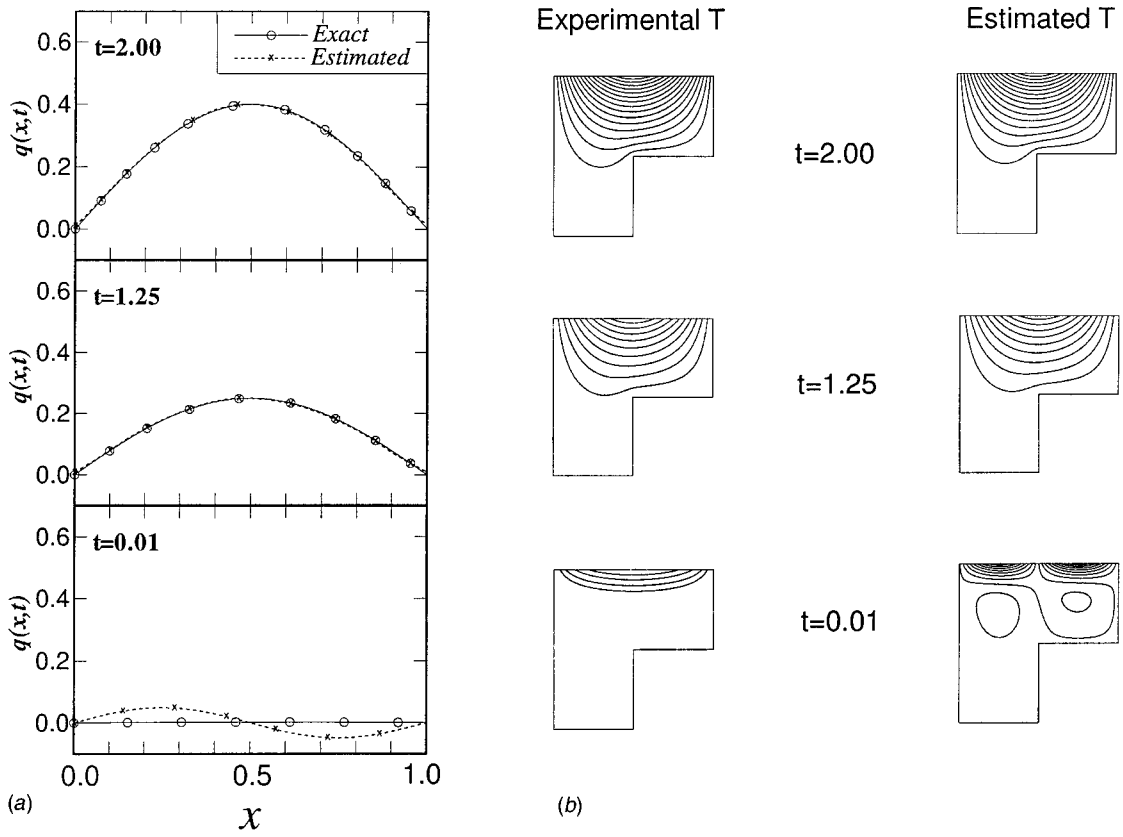

Fig. 5 The effect of initially assumed values of $a_i(t=0)$ and $q(x,t=0)$ on the accuracy of the estimation: (*a*) wall heat flux; and (*b*) temperature field.

procedure using the original heat conduction equation. Moreover, once the low dimensional model is prepared, it can be used repeatedly to solve similar problems [12].

6 Results

The following two wall heat flux functions are considered to assess the efficiency and accuracy of the present algorithm for solving the inverse heat conduction problem sequentially.

$$\text{(case a)} \qquad q(x,t)=(\sin \pi x)\cdot\left(\frac{1}{5}t\right) \tag{27}$$

$$\text{(case b)} \qquad q(x,t)=f(x)\cdot\left(\frac{1}{5}t\right),$$

$$\text{where} \quad f(x)=2x \quad \text{for } 0\leqslant x\leqslant 0.2$$

$$=-2(x-0.4) \quad \text{for } 0.2\leqslant x\leqslant 0.4$$

$$=\frac{1}{0.3}(x-0.4) \quad \text{for } 0.4\leqslant x\leqslant 0.7$$

$$=-\frac{1}{0.3}(x-0.4) \quad \text{for } 0.7\leqslant x\leqslant 1.0 \tag{28}$$

Temperature measurements are taken with 25 sensors located at $(x_m,0.96)$ with $x_m=6.67\times10^{-3}+0.04(m-1)$ $(m=1,2,\cdots,25)$. Equation (2) is solved by using a finite difference method and we adopt these numerical solutions as experimental measurements after adding small random noises. These noises are adjusted such that they are Gaussian distributed. The estimation error is given by the following equation.

$$\text{Error}=\frac{\|q_{\text{estimated}}-q_{\text{exact}}\|_{L_2}^2}{\|q_{\text{exact}}\|_{L_2}^2}, \tag{29}$$

where $\|\cdot\|_{L_2}$ is the usual L_2-norm. In all the computations presented in this work, exact values are taken for the estimated values of $a_i(t=0)$ $(i=1,2,\cdots,NT)$ and $q(x,t=0)$, if not specified otherwise. A simple confirmation of the accuracy of the present algorithm can be made by considering an idealized situation where the measurements are not corrupted by noises. Figures 4(*a–b*) show the estimated $q(x,t)$ for case *a* and case *b* with corresponding errors. They show that the present method yields very accurate estimates for the two cases investigated. The present algorithm requires solving $(NT+N)$ state equations (cf. Eq. (25)) and $(NT+N)(NT+N+1)/2$ covariance equations (cf. Eq. (26)) without any iterations, which allows real-time estimation using a modern computer system. Figures 5(*a–b*) show the effect of incorrectly assumed initial values, $a_i(t=0)$ $(i=1,2,\cdots,NT)$ and $q(x,t=0)$, on the accuracy of the estimation. As the estimated initial, we take $a_i(t=0)=0.01$ and $q(x,t=0)=0.05\sin(2\pi x)$. Figures 5(*a–b*) show that the present algorithm allows very accurate tracking of wall heat flux and temperature field after a short transient period even when the incorrect values of $a_i(t=0)$ $(i=1,2,\cdots,NT)$ and $q(x,t=0)$ are employed. Next consideration is the effect of measurement noises on the accuracy of estimation. Since the experimental errors are unavoidable, a practical algo-

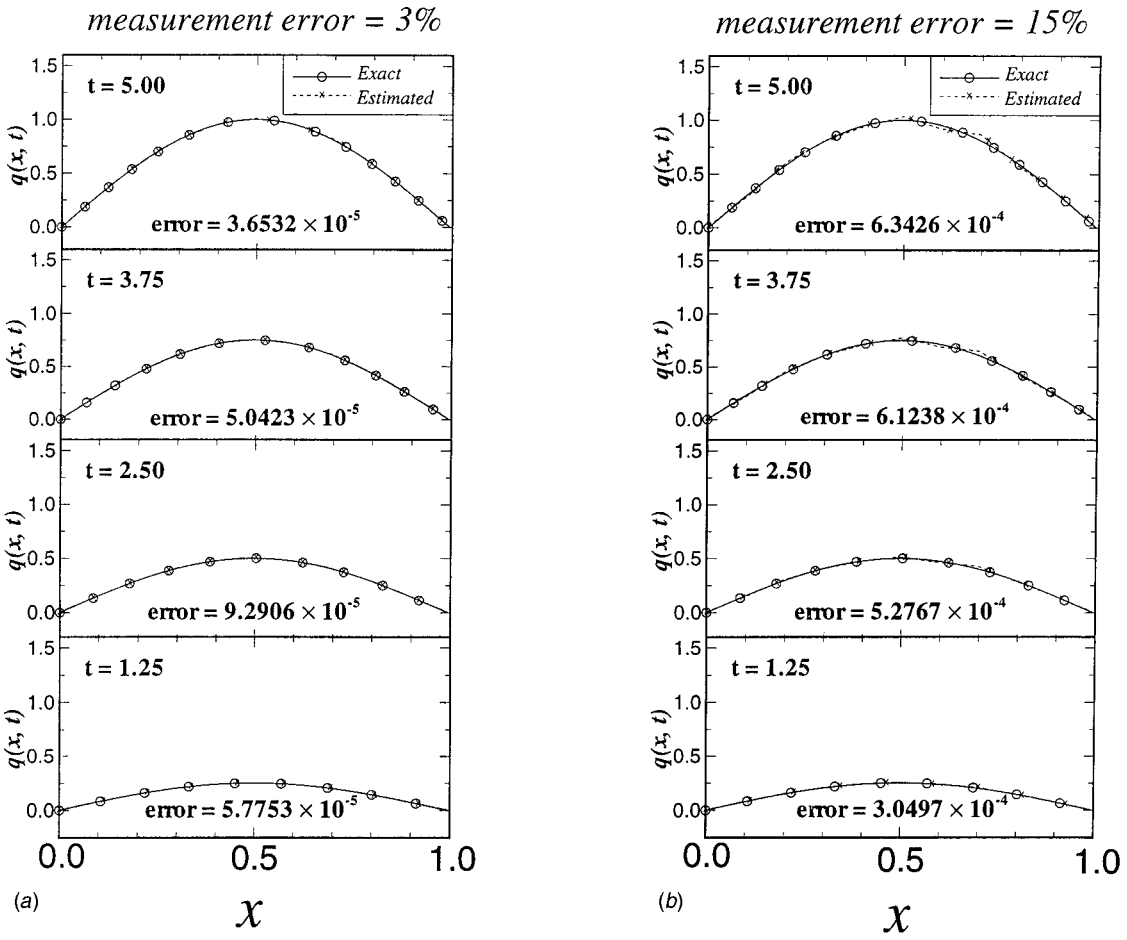

Fig. 6 Estimated $q(x,t)$ from the corrupted temperature measurements: (*a*) 3 percent relative measurement error; and (*b*) 15 percent relative measurement error.

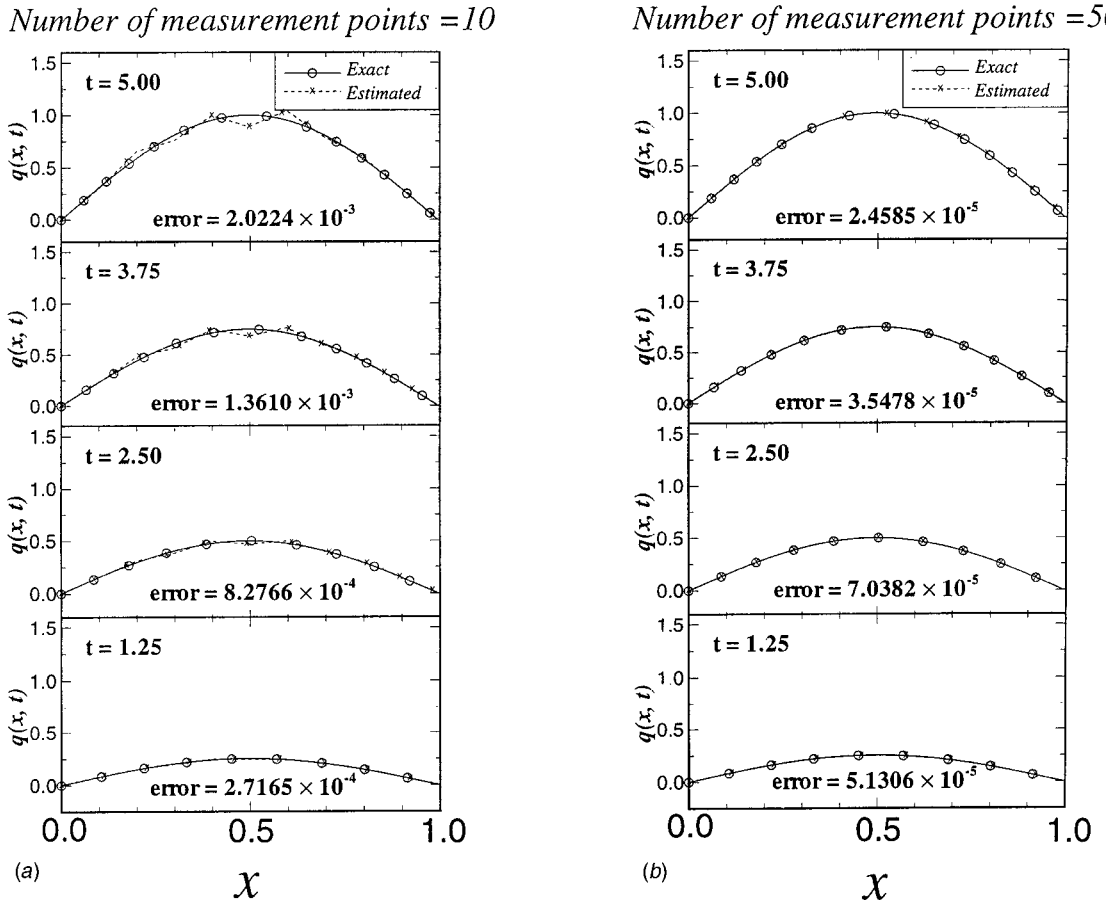

Fig. 7 The effect of the number of measurement points on the accuracy of estimation: (*a*) 10 measurement points; and (*b*) 50 measurement points.

rithm must be able to yield reasonably accurate estimates even with the corrupted measurements. Figures 6(*a*–*b*) show the estimated $q(x,t)$ when the relative measurement errors are 3 percent (Fig. 6(*a*)) and 15 percent (Fig. 6(*b*)), respectively. Comparing these results with the estimate obtained from the exact temperature measurements (Fig. 4(*a*)), it is found that the accuracy of the estimation deteriorates as the measurement noise increases.

The effect of number of measurement points on the accuracy of estimation is shown in Fig. 7. It is expected that the degree of resolution of $q(x,t)$ depends on the number of measurement points that are appropriately arranged in the domain. The default number of measurement points is 25. Now, we employ two different sets of measurement locations; one set consists of 10 sensors and the other set 50 sensors at regular intervals, which are placed at the same vertical distance from the upper wall as the default set. Figure 7(*a*) shows the estimated $q(x,t)$ when employing 10 sensors and Fig. 7(*b*) is the corresponding result obtained with the 50 sensors. It is shown that the accuracy of the estimation improves with the number of sensors, but the improvement obtained with the 50 sensors is not significant compared to the default result (Fig. 4(*a*)) obtained with the 25 sensors. Final consideration is the effect of measurement location on the accuracy of estimation. Instead of the default locations (x_m,0.96), we locate the 25 sensors at (x_m,0.92) and estimate $q(x,t)$, which is shown in Fig. 8. Since the new sensor locations are farther from the boundary than the default ones, the results shown in Fig. 8 have larger estimation error than the default results plotted in Fig. 4(*b*).

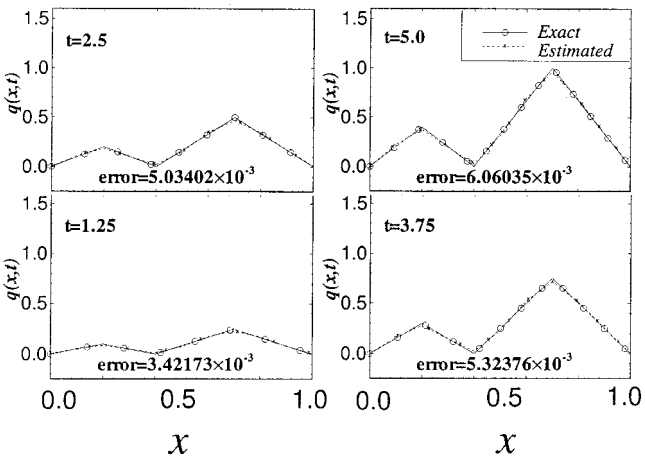

Fig. 8 The effect of measurement location on the accuracy of estimation

7 Conclusion

A practical sequential algorithm for solving multidimensional inverse heat conduction problems is devised by exploiting the Karhunen-Loève Galerkin procedure and the Kalman filtering technique. The Karhunen-Loève Galerkin procedure reduces the multidimensional heat conduction equation to a minimal set of ordinary differential equations, and by applying the Kalman filtering technique to these ordinary differential equations, a set of equations for the sequential estimation of the unknown wall heat flux is obtained. The present technique is shown to yield accurate estimation of wall heat flux from the temperature measurements in

the domain. Since the number of equations to be solved is decent, the real-time implementation of the present algorithm is possible with a modern computer system.

Nomenclature

$\mathbf{A}$ = matrix defined in Eq. (21)
a_i = spectral coefficient premultiplying the ith empirical eigenfunction
$\mathbf{b}$ = vector defined in Eq. (21)
B_{nj} = matrix defined in Eq. (18)
$\mathbf{C}$ = matrix defined in Eq. (22)
C_p = heat capacity
H_{ji} = matrix defined in Eq. (13)
$\mathbf{I}$ = unit matrix
J = performance function
$\mathbf{K}(x,x')$ = two-point correlation function of the Karhunen-Loève decomposition
M = number of temporal shape function in the discretization of heat flux
M_j = vector defined in Eq. (12)
N = number of spatial shape function in the discretization of heat flux
NT = number of empirical eigenfunctions employed in the Karhunen-Loève Galerkin procedure
$\mathbf{P}$ = error covariance matrix
$\mathbf{Q}$ = measurement error covariance matrix
$q(x,t)$ = wall heat flux
R = residual
$\mathbf{R}^{-1}$ = model error covariance matrix
T = temperature field
t = time
$\mathbf{y}$ = measurement vector (cf. Eq. (24))

Greek Symbols

α_{mn} = coefficient in the discretization of heat flux (Eq. (8))
Γ = system boundary
$\boldsymbol{\eta}(t)$ = Gaussian white noise in the measurement
λ_k = the kth eigenvalue
$\boldsymbol{\xi}(t)$ = Gaussian white noise in the model
ρ = density
Σ = space-time system domain
ϕ_i = the ith empirical eigenfunction
$\varphi_k^{(n)}$ = the kth empirical eigenfunction for the nth set of snapshots
$\Psi_m(t)$ = temporal shape function
$\Psi_n(x)$ = spatial shape function
Ω = system domain

Superscripts

$*$ = measurement
T = transpose

Subscripts

N = Neumann boundary condition
D = Dirichlet boundary condition

References

[1] Lausterer, G. K., and Ray, W. H., 1979, "Distributed Parameter State Estimation and Optimal Feedback Control—An Experimental Study in Two Space Dimensions," IEEE Trans. Autom. Control, **AC-24**, pp. 179.
[2] Nulman, J., Krusius, J. P., and Gat, A., 1985, "Rapid Thermal Processing of Thin Gate Dielectrics-Oxidation of Silicon," IEEE Electron Device Lett., **EDL-6**, pp. 205.
[3] Beck, J. V., Blackwell, B., and St. Clair, Jr., C. R., 1985, *Inverse Heat Conduction: Ill-Posed Problems*, Wiley-Interscience, New York.
[4] Jarney, Y., Özisik, M. N., and Bardon, J. P., 1991, "A General Optimization Method Using Adjoint Equation for Solving Multidimensional Inverse Heat Conduction," Int. J. Heat Mass Transf., **34**, pp. 2911–2919.
[5] Kalman, R. E., and Bucy, R. S., 1961, "New Results in Linear Filtering and Prediction Theory," ASME J. Basic Eng., **38D**, pp. 95–108.
[6] Grewal, M. S., and Andrews, A. P., 1993, *Kalman Filtering*, Prentice Hall, Englewood Cliffs, New Jersey.
[7] Jazwinski, A. H., 1970, *Stochastic Processes and Filtering Theory*, Academic Press, New York.
[8] Scarpa, F., and Milano, G., 1995, "Kalman Smoothing Technique Applied to the Inverse Heat Conduction Problem," Numer. Heat Transfer, Part B, **28**, pp. 79–96.
[9] Kaipio, J., and Somersalo, E., 1999, "Nonstationary Inverse Problems and State Estimation," J. Inverse and Ill-Posed Problems, **7**, pp. 273–282.
[10] Park, H. M., and Cho, D. H., 1996, "Low Dimensional Modeling of Flow Reactors," Int. J. Heat Mass Transf., **39**, pp. 3311–3323.
[11] Park, H. M., and Lee, M. W., 1998, "An Efficient Method of Solving the Navier-Stokes Equations for Flow Control," Int. J. Numer. Methods Eng., **41**, pp. 1131–1151.
[12] Park, H. M., Chung, O. Y., and Lee, J. H., 1999, "On the Solution of Inverse Heat Transfer Problem Using the Karhunen-Loève Galerkin Method," Int. J. Heat Mass Transf., **42**, pp. 127–142.
[13] Loève, M., 1977, *Probability Theory*, Fourth ed., Springer, New York.
[14] Courant, R., and Hilbert, D., 1962, *Methods of Mathematical Physics*, Vol. 1, Wiley-Interscience, New York.

Laminar Heat Transfer in the Entrance Region of Internally Finned Square Ducts

V. D. Sakalis

P. M. Hatzikonstantinou

Department of Engineering Science,
University of Patras,
GR 26110 Patras, Greece

The laminar, incompressible, hydrodynamically fully developed and thermally developing flow is studied in straight ducts of square cross section, containing four equal, symmetrical, straight, thin and with 100 percent efficiency internal fins. Both the duct wall and the fins are subjected successively to constant temperature boundary condition. Numerical results are obtained using an iterative ADI scheme for the friction number, the temperature distribution and the Nusselt number for the thermally developing and developed regions as functions of axial distance and fin height. Results obtained are in good agreement with the corresponding literature values. In the thermally developing region a high heat transfer coefficient is obtained. Friction number and Nusselt number in the thermally developed limit increase as the fin height increases until they reach their critical values at fin heights near 0.85 and 0.73 respectively. [DOI: 10.1115/1.1404118]

Keywords: Computational, Finite Difference, Heat Pipes, Laminar

Introduction

Ducts of various cross sections containing inside fins are widely used in modern engineering heat transfer applications, such as compact heat exchangers, nuclear reactors, jet engines, etc. The main advantage of finned tubes than that of finnles tubes is the increase of the heat transfer coefficient by 4. Also the production of single straight finned tubes in manufacturing engineering is easier than other techniques used to enhance heat transfer in ducts, such as the twisted tape inserts, coil spring, helical ribs, spiral fins, etc. The only disadvantage of using finned tubes is the increase of flow pattern and hence of the flow friction and the pumping power.

For the study of straight circular finned ducts many analytical and numerical procedures have been proposed in the literature. Those procedures analyze the hydrodynamically fully developed flow (Nandakumar and Maslyiah [1], Soliman and Feingold [2]), the thermally developed flow (Soliman et al. [3], Masliyah and Nandakumar [4], Hu and Chang [5]) or the thermally developing flow (Rustum and Soliman [6], Prakash and Liu [7]). Several thermal boundary conditions have been studied, like $H1$ (axial uniform wall heat flux with peripherally uniform wall temperature) and T (constant wall temperature) and several radial fin types, like straight fins (Hu and Chang [5], Prakash and Patankar [8], Prakash and Liu [7], Rustum and Soliman [6]), triangular fins (Nandakumar and Maslyiah [1], Maslyiah and Nandakumar [4]) and trapezoidal fins (Soliman and Feingold [2], Soliman et al. [3]). Particular attention has been given to study the influence of buoyancy forces and internal heat generation by Prakash and Liu [7] and Hu and Chang [5], respectively. Recently, Dong and Ebadian [9] and [10] have studied the problem of the flow in a straight duct of elliptic cross section, containing four-straight, thin symmetrical fins. For a complete description about finned tubes see Rohsenow et al. [11].

For straight ducts of rectangular cross sections, Aggarwala and Gangal [12] study analytically the fully developed hydrodynamically and thermally flow and heat transfer, considering four straight, thin fins, equal by two, which are based in two opposite walls of the duct cross section. The effects of buoyancy forces are also studied while the $H1$ thermal boundary condition is employed. Gangal and Aggarwala [13] study the same problem in the case of square cross section using four equal, straight, symmetrical and with 100 percent efficiency fins.

Generally, to the author's knowledge, no results have been reported in the literature for the problem of flow in finned square ducts, with thermal boundary condition T for both the duct wall and the fins as well as for the heat transfer in the entrance region of finned tubes. The last boundary condition has great practical relevance in electrical heating with thin, high conducting wall material.

The present paper analyzes the problem of laminar, incompressible, hydrodynamically fully developed and thermally developing flow into straight square ducts, containing four equal, straight, thin, symmetrical and with 100 percent efficiency fins, which is not a bad assumption except for large numbers of long fins (Soliman et al. [3]). Both the duct wall and the fins are subjected to the constant temperature boundary condition. The effects of axial conduction and buoyancy forces are neglected. Fluid properties assume to be constant and independent of temperature.

Analysis

We consider the laminar flow of incompressible fluid entering a straight duct of square cross section containing four equal, straight, symmetrical, thin fins, shown in Figure 1 and we study the hydrodynamically fully developed and thermally developing flow neglecting the momentum diffusion in the axial direction and the body forces. The nondimensionalized equations of motion and energy in the cartesian coordinate system take the following form.

Axial Momentum Equation.

$$\frac{\partial \overline{w}}{\partial t} = \frac{\partial^2 \overline{w}}{\partial \overline{x}^2} + \frac{\partial^2 \overline{w}}{\partial \overline{y}^2} + 1 \tag{1}$$

Energy Equation.

$$\frac{\overline{w}}{4\overline{w}_m}\left(\frac{\partial \overline{T}}{\partial \overline{s}}\right) = \frac{\partial^2 \overline{T}}{\partial \overline{x}^2} + \frac{\partial^2 \overline{T}}{\partial \overline{y}^2} \tag{2}$$

The mean axial velocity of the flow w_m is given by

$$\overline{w}_m = \int_0^1 \int_0^1 \overline{w}\, d\overline{x}\, d\overline{y}. \tag{3}$$

Contributed by the Heat Transfer Division for publication in the JOURNAL OF HEAT TRANSFER. Manuscript received by the Heat Transfer Division July 24, 2000; revision received May 15, 2001. Associate Editor: M. Faghri.

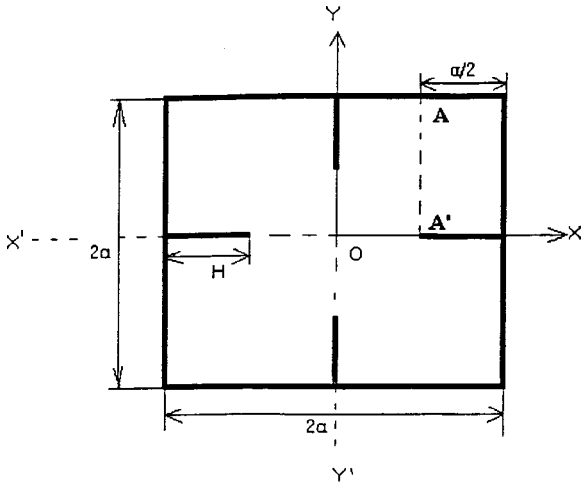

Fig. 1 Duct of square cross section containing four equal thin symmetrical fins

The parabolic equations of momentum and energy are subjected to the following boundary conditions

$$\overline{w}=0, \quad \overline{T}=0 \quad \text{at } \overline{x}=1 \quad \text{and} \quad \overline{x}=-1 \tag{4a}$$

$$\overline{w}=0, \quad \overline{T}=0 \quad \text{at } \overline{y}=1 \quad \text{and} \quad \overline{y}=-1 \tag{4b}$$

$$\overline{w}=0, \quad \overline{T}=0 \quad \text{at } 1-H\leqslant\overline{x}\leqslant 1 \quad \text{and} \quad \overline{y}=0 \tag{4c}$$

$$\overline{w}=0, \quad \overline{T}=0 \quad \text{at } 1-H\leqslant\overline{y}\leqslant 1 \quad \text{and} \quad \overline{x}=0 \tag{4d}$$

$$\overline{w}=0, \quad \overline{T}=0 \quad \text{at } -1\leqslant\overline{x}\leqslant -(1-H) \quad \text{and} \quad \overline{y}=0 \tag{4e}$$

$$\overline{w}=0, \quad \overline{T}=0 \quad \text{at } -1\leqslant\overline{y}\leqslant -(1-H) \quad \text{and} \quad \overline{x}=0 \tag{4f}$$

Owing to the symmetry of the flow, only a quarter of square cross section is used in the numerical procedure. Accordingly, the following symmetry boundary conditions are needed

$$\frac{\partial\overline{w}}{\partial\overline{x}}=0, \quad \frac{\partial\overline{T}}{\partial\overline{x}}=0, \quad \text{at } \overline{x}=0 \quad \text{and} \quad 0\leqslant\overline{y}\leqslant 1-H, \tag{5a}$$

$$\frac{\partial\overline{w}}{\partial\overline{y}}=0, \quad \frac{\partial\overline{T}}{\partial\overline{y}}=0, \quad \text{at } \overline{y}=0 \quad \text{and} \quad 0\leqslant\overline{x}\leqslant 1-H. \tag{5b}$$

Physical quantities of primary interest are the local friction factor and the local Nusselt number, which are defined, respectively, by

$$f=\frac{-\dfrac{dp}{ds}D_h}{2\rho w_m^2}, \tag{6}$$

$$\mathrm{Nu}=\frac{hD_h}{k}, \tag{7}$$

where h the local heat transfer coefficient, and D_h is the hydraulic diameter of the square duct without fin ($D_h=4E/\Pi$).

The characteristic quantity of fluid flow f Re expressed in terms of hydraulic diameter and non-dimensional quantities takes the form

$$f\,\mathrm{Re}=\frac{2}{\overline{w}_m}, \tag{8}$$

where Re is the Reynolds number of the flow.

Considering that the mean bulk fluid temperature of the flow is given by

$$\overline{T}_m=\frac{\int_0^1\int_0^1\overline{w}\,\overline{T}\,d\overline{x}\,d\overline{y}}{\int_0^1\int_0^1\overline{w}\,d\overline{x}\,d\overline{y}}. \tag{9}$$

The expression for the mean Nusselt number obtained from the consideration of the energy balance over the entire cross section takes the final form

$$\overline{\mathrm{Nu}}=\frac{1}{4\overline{T}_m}\frac{d\overline{T}_m}{d\overline{s}}. \tag{10}$$

Solution

The set of uncoupled Eqs. (1)–(2) subjected to the boundary conditions (4), (5) are solved numerically employing the iterative finite difference pseudotransient alternating direction implicit method (ADI). For the discretization of these equations three point central differences are used for the second order derivatives and two points forward differences for the first order derivatives. So an algebraic system of equations is obtained for each variable which is solved by the well-known Tridiagonal Matrix Algorithm (TDMA).

The friction factor product f Re and the local mean Nusselt number are calculated using the Eqs. (8) and (10), respectively. In Eq. (10), the derivative was approximated by three point forward differences. The required integrals are calculated employing Simpson's rule.

Convergence of the iteration procedure for both the momentum and energy equations achieved when the following criterion is satisfied:

$$\left|\frac{B(\overline{x},\overline{y})^{m+1}-B(\overline{x},\overline{y})^{m}}{B(\overline{x},\overline{y})^{m+1}}\right|\leqslant\varepsilon, \tag{11}$$

where $B(\overline{x},\overline{y})$ represents the variable $\overline{w}$ or $\overline{T}$, respectively, m is the iteration number, and $\varepsilon=10^{-5}$.

Considering the symmetry of the flow, as we said before, only a quarter of the whole cross section is used in the numerical computation.

A uniform grid pattern of 151×151 points is employed for the square cross section and all the fin heights. To assure accuracy and the effect of grid size, numerical tests have been made with 101×101 and 201×201 grid points. The maximum deviation in the numerical results of Nusselt number and friction product f Re using grids of 101×101 and 51×151 points is less than 1.2 percent and 1.5 percent respectively. Similarly, the maximum deviation of the results of the same quantities using grids of 151×151 and 201×201 points is less than 0.65 percent and 0.35 percent respectively. Hence the choice of a uniform 151×151 points grid is enough satisfactory to ensure accuracy.

In the momentum equation a time step $\Delta t=0.0002$ was chosen for each fin height. Along the axial direction, a fine grid of size $\Delta s=10^{-6}$ was used near the duct entrance, to avoid numerical fluctuations. As the flow becomes gradually thermally fully developed, in a quite long axial position from the entrance of the duct, an axial step size Δs of about 10^{-4} is considered as satisfactory.

In order to validate the accuracy of the numerical results we perform computations on the well studied problem of thermally developing flow in straight finless square duct ($H=0$), with both wall and fins subjected to constant temperature. The obtained results for the Nusselt number and the corresponding numerical results of Rohsenow et al. [11], are shown in Table 1. The results of both methods are in close agreement. The maximum deviation in the value of Nusselt number is 2.53 percent at $\overline{s}=0.1$ and the mean deviation along the axial coordinate is less than 1,1 percent. The deviation of 2.53 percent between our predicted Nusselt number and that in Rohsenow et al. is due to different numerical techniques. Their solutions are obtained by using the iterative extrapolated Liebmann method.

Table 2 represents the variation of mean Nusselt number Nu, friction product f Re and thermal entrance length Lth against the

Table 1 Variation of the Nusselt number $\overline{Nu}$ in the entrance region as a function of axial length s for square ducts without fins ($H=0$)

$\bar{s}$	Nu (Rohsenow et al (1998))	$\overline{Nu}$ (present)	% deviation
0.005	5.412	5.404	0.148
0.0075	4.755	4.739	0.336
0.01	4.357	4.3430	0.321
0.0125	4.084	4.087	0.0906
0.02	3.611	3.630	0.521
0.025	3.432	3.462	0.874
0.04	3.157	3.208	1.628
0.05	3.074	3.135	1.978
0.1	2.976	3.051	2.53
∞	2.975	3.047	2.423

Table 2 Variation of friction factor fRe, mean Nusselt Number $\overline{Nu}$ and thermal entrance length Lth, as functions of fin height H in the developed region ([*] refer to Rohsenow et al. [11])

H	fRe[*]	fRe (pres)	% DEV	Nu[*]	$\overline{Nu}$ (pres)	%DEV	Lth[*]	Lth (pres)	% DEV
0	14.261	14.277	0.112	2.975	3.047	2.4	0.041	0.0409	0.25
0.125	15.285	15.181	0.68	-	3.068	-	-	0.04125	-
0.25	18.281	18.085	1.072	-	3.268	-	-	0.04251	-
0.375	23.630	23.361	1.138	-	3.840	-	-	0.04538	-
0.5	31.877	31.564	0.982	-	5.195	-	-	0.04983	-
0.625	42.527	42.219	0.701	-	8.540	-	-	0.03888	-
0.7	-	48.330	-	-	11.228	-	-	0.00998	-
0.75	52.341	52.011	0.63	-	11.992	-	-	0.01061	-
0.8	-	54.429	-	-	12.067	-	-	0.01155	-
1	56.919	57.267	0.611	-	11.913	-	-	0.01103	-

fin height H, along with the numerical results of Rohsenow et al. [11]. Comparing our results for fRe with those obtained by Rohsenow (Table 2, $H=0$), it is obtained very close agreement with maximum deviation 1,138 percent and mean deviation 0.75 percent. For the thermal entrance length, the deviation is less than 1 percent.

To the authors knowledge, results for the Nusselt number of square finned duct with (T) thermal boundary condition, do not appear in the corresponding literature till now.

Results and Discussion

Figure 2 represents the axial velocity w of the fluid flow along the length $A'A$ positioned at $x=0.5$, as it is shown in Fig. 1. For the fin heights $H=0$, 0.25, 0.625, and 0.75, it is obvious that the maximum value of axial velocity decreases as fin height H increases, owing to additional surface area provided by the fins with no slip velocity boundary condition.

Figure 3 represents the friction factor product fRe against the fin height H, together with the results of Rohsenow et al. [11]. It is observed that from $H=0$ to 0.4, fRe increases at about 75 percent, from $H=0.4$ to 0.75 about 200 percent and from $H=0.75$ to 1 only about 10 percent reaching its maximum value as H tends to unity. This is due to the fact that fins with heights between 0.25 and 0.8 introduce substantial surface area into the duct, reducing strongly the bulk velocity distribution because of the imposed no slip condition. On the contrary, fins with smaller heights than 0.25, or even larger heights than 0.8, do not affect strongly any further the corresponding velocity distributions and consequently the variation of the values of friction factor. The following expression is proposed for the friction factor product fRe as a function of the fin height H:

$$f\,\mathrm{Re}=13.6345+44.551\cdot e^{-4.85(-0.935+H)^2}. \qquad (12)$$

The maximum deviation between the values of the above equation and the results of Rohsenow et al. [11], is about 2.8 percent at fin height $H=0.625$.

In the region of fully developed hydrodynamic and thermal flow with $\bar{s}\gg 0.1$ the values of the friction product fRe, mean Nusselt number Nu and of the thermal entrance length Lth against the fin height H, together with the results of Rohsenow et al. [11], are presented in Table 2. It is observed that the mean Nusselt number from $H=0$ to 0.4 increases about 40 percent, from $H=0.4$ to 0.75 about 186 percent and from $H=0.75$ to 1 about 0.67 percent reaching its maximum.

Figure 4 represents the variation of mean local Nusselt number $\overline{Nu}(\bar{s})$ in the developing region for the values of the fin hight $H=0$, 0.125, 0.25, 0.375, 0.5, 0.625, 0.75, and 1. For each fin height H, the mean Nusselt number Nu takes higher values in the en-

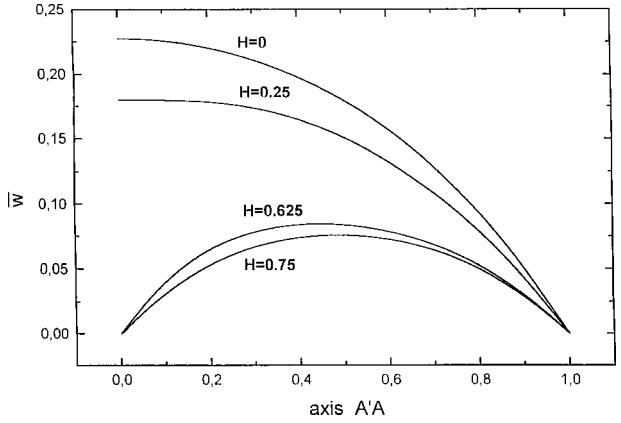

Fig. 2 Variation of the axial velocity along $A'A$ axis for fin height $H=0$, 0.25, 0.625, and 0.75

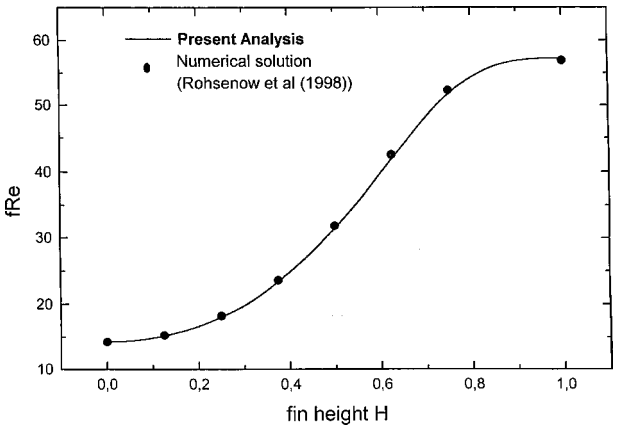

Fig. 3 Variation of the friction factor product as a function of fin height H

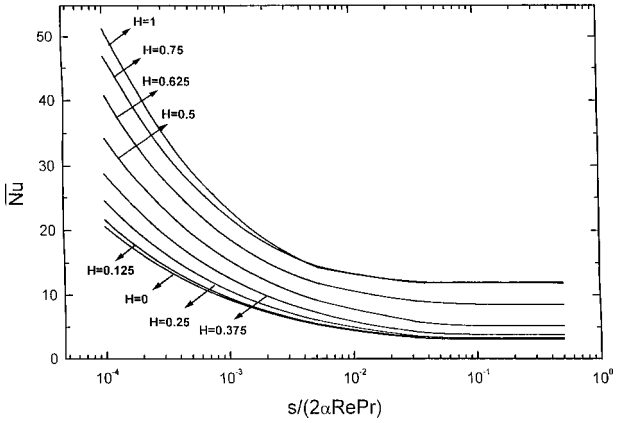

Fig. 4 Mean Nusselt number variation in the entrance region, at each fin height

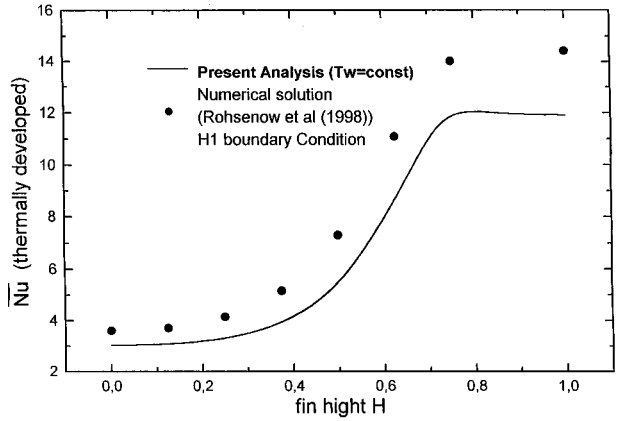

Fig. 5 Variation of mean Nusselt number in the developed region as a function of fin height *H*

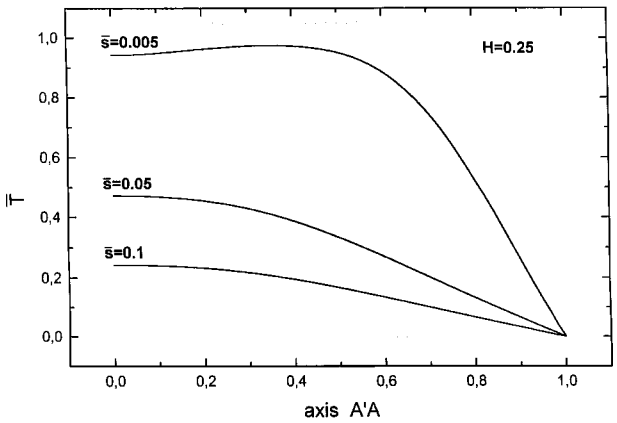

Fig. 7 Temperature distribution along *A′A* axis for axial distances $\bar{s}$=0.005, 0.05, 0.1 and *H*=0.25

trance region than in the fully developed region. This is due to the much larger velocity and temperature gradients which take place in the entrance region with respect to the corresponding ones in the fully developed region. As the fin height H varies from $H=0$ to 1, the mean Nusselt number Nu profiles along the axial distance $\bar{s}$ increase in both the entrance and the developed region. Obviously, the increase of the fin height H introduces surface area yelding the increase of the heat transfer coefficient which is measured by the Nusselt number.

Figure 5 represents the variation of the fully developed mean Nusselt number values Nu (for T boundary condition) as a function of fin height H, together with the results of Rohsenow et al. [11] for the $H1$ boundary condition. As we saw before in the case of friction factor product f Re (Fig. 3), the same situation occurs: the fully developed values of mean Nusselt number increase gradually as fin height H increases from $H=0$ to about $H\approx 0.73$. From this critical value and more, the mean Nusselt number yields almost constant. It is observed that the profile of $\overline{\mathrm{Nu}}$ under the T boundary condition takes lower values than the corresponding one obtained under the $H1$ boundary condition for all values of the fin height H. The reason is that the axial uniform wall heat flux, in the case of $H1$ boundary condition, generates additional heat transfer in the fluid along the axial surface wall of the duct, which is added to the explicit heat transfer which takes place, in the case of T condition, between the wall and the bulk of the fluid along the cross section of the duct.

The following expression is proposed for the Nusselt number of fully developed flow as a function of fin height H:

$$\overline{\mathrm{Nu}} = 12.20175 - \frac{8{,}96497}{1+e^{(H-0.58805)/0.06252}}. \qquad (13)$$

The maximum deviation between the profiles of the above expression and those of Fig. 4 is about 4 percent.

Very interesting for engineering applications is Fig. 6, which represents the ratio of Nusselt number $\overline{\mathrm{Nu}}$ to the friction product f Re, in the thermally fully developed region, against the fin hight H. It is observed that this ratio takes its maximum value at about $H=0.73$. The last fin height 0.73, practically leads to the maximum heat transfer coefficient with respect to the local value of the friction factor. At the fin height 0.43 the ratio $\overline{\mathrm{Nu}}/f$ Re reaches its minimum value. Fig. 7 represents the variation of the temperature of the flow, along the $A'A$ length, for the axial distances $\bar{s}=0.005$, 0.05, 0.1 and fin height $H=0.25$.

Figure 8 represents the variation of the thermal entrance length Lth (the axial position where the local mean Nusselt number becomes 1.05 times the value of the mean Nusselt number in the thermally fully developed flow) against fin height H. It is observed that Lth increases slightly from $H=0$ to $H=0.45$ (about 22 percent) and decreases gradually from $H=0.45$ to about $H=0.73$ (about 75 percent) while for $H\geqslant 0.73$, Lth yields almost constant.

From Figs. 5 and 8, it is observed that the most dramatic reduction of thermal entrance length, in the region of fin heights between 0.45 and 0.75, follows the increase of the Nusselt number in the same region. As the fin height increases providing addi-

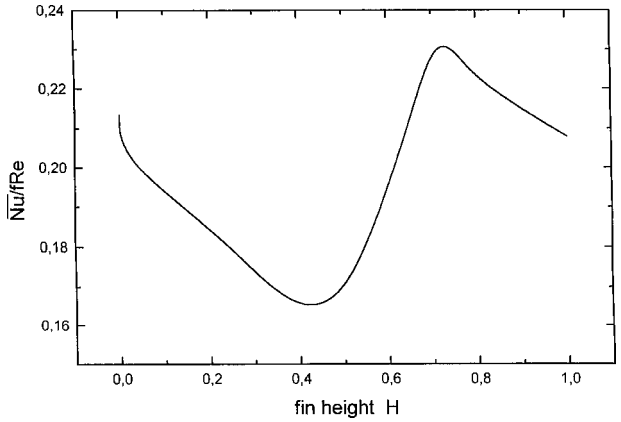

Fig. 6 Variation of the ratio Nu/*f* Re in the developed region, as a function of fin height *H*

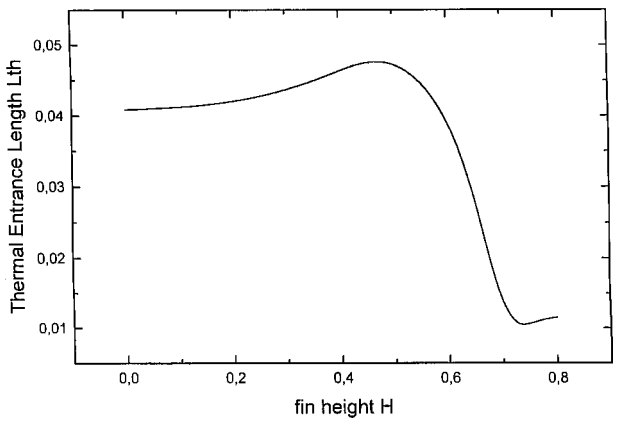

Fig. 8 The thermal entrance length *Lth* variation as a function of fin height *H*

tional surface area, the heat transfer increases yielding respectively to the establishment of the thermal boundary layer, reducing the corresponding thermal entrance length.

Concluding Remarks

Friction factor product $f\,\mathrm{Re}$ and mean Nusselt number $\overline{\mathrm{Nu}}$ of the thermally developed flow, increase as fin height H increases, till the critical values $H=0.85$ and $H=0.73$ respectively. The mean Nusselt number of the thermally developing flow increases, as fin heigh H increases, too.

The ratio $\overline{\mathrm{Nu}}/f\,\mathrm{Re}$, interesting in engineering applications, takes the maximum value at fin height $H=0.73$. At this fin height, the maximum heat transfer with respect to the local value of the friction factor.

The thermal entrance length Lth increases as fin height varies from $H=0$ to $H=0.45$ and decreases steeply from $H=0.45$ to 0.73.

Nomenclature

Cp = heat capacity of the fluid
D_h = hydraulic diameter of square duct without fins, $(=4E/\Pi=2\alpha)$
E = cross section area
f = friction factor
H' = fin height (Fig. 1)
H = fin height, dimensionless, $(=H'/\alpha)$
h = heat transfer coefficient
k = heat conduction coefficient of the fluid
Lth = thermal entrance length
Nu = local Nusselt number, $(=hD_h/k)$
$\overline{\mathrm{Nu}}$ = local mean Nusselt number, Eq. (10)
P = fluid pressure (dimensioned)
Pr = Prandtl number, $(=\mu Cp/k)$
Re = Reynolds number, $(=\rho w_m D_h/\mu)$
$\underline{s}$ = axial coordinate (dimensioned)
$\overline{s}$ = dimensionless axial coordinate, $(=s/2\alpha\,\mathrm{Re}\,\mathrm{Pr})$
t' = time (dimensioned)
t = dimensionless time, $(=t'\mu/\rho\alpha^2)$
$\underline{T}$ = temperature of the fluid (dimensioned)
$\overline{T}$ = dimensionless temperature, $(=T-Tw/To-Tw)$
Tw = wall temperature (dimensioned)
$\overline{Tw}$ = dimensionless wall temperature, $(=0)$
To = inlet temperature (dimensioned)
$\overline{To}$ = dimensionless inlet temperature, $(=1)$
$\overline{Tm}$ = dimensionless bulk fluid temperature, Eq. (9)
$\underline{w}$ = axial velocity (dimensioned)
$\overline{w}$ = dimensionless axial velocity, $(=-\mu w/\alpha^2(dP/ds))$
$\underline{w_m}$ = mean axial velocity, (dimensioned)
$\overline{w_m}$ = dimensionless mean axial velocity, Eq. (3)
$\underline{x}$ = coordinate, dimensioned (Fig. 1)
$\overline{x}$ = dimensionless coordinate, $(=x/\alpha)$
$\underline{y}$ = coordinate, dimensioned (Fig. 1)
$\overline{y}$ = dimensionless coordinate, $(=y/\alpha)$

Greek Symbols

2α = length of the edge of the cross section (Fig. 1)
ε = parameter, Eq. (11)
μ = fluid viscosity
ρ = fluid density
Π = perimeter of the square cross section

References

[1] Nandakumar, K., and Masliyah, J. A., 1975, "Fully Developed Viscous Flow in Internally Finned Tubes," Chem. Eng. J., **10**, pp. 113–120.
[2] Soliman, H. M., and Feingold, A., 1977, "Analysis of Fully Developed Laminar Flow in Longitudinal Internally Finned Tubes," Chem. Eng. J., **14**, pp. 119–128.
[3] Soliman, H. M., Chau, T. S., and Trupp, A. C., 1980, "Analysis of Laminar Heat Transfer in Internally Finned Tubes with Uniform Outside Wall Temperature," ASME J. Heat Transfer, **102**, pp. 598–604.
[4] Masliyah, J. H., and Nandakumar, K., 1976, "Heat Transfer in Internally Finned Tubes," ASME J. Heat Transfer, **98**, pp. 257–261.
[5] Hu, H., and Chang, Y. P., 1973, "Optimization of Finned Tubes for Heat Transfer in Laminar Flow," ASME J. Heat Transfer, **95**, pp. 332–338.
[6] Rustum, I. M., and Soliman, H. M., 1988, "Numerical Analysis Of Laminar Forced Convection in the Entrance Region of Tubes with Longitudinal Internal Fins," ASME J. Heat Transfer, **110**, pp. 310–313.
[7] Prakash, C., and Liu, Ye-Di., 1985, "Analysis of Laminar Flow and Heat Transfer in the Entrance Region of an Internally Finned Circular Duct," ASME J. Heat Transfer, **107**, pp. 84–91.
[8] Prakash, C., and Patankar, S. V., 1981, "Combined Free and Forced Convection in Vertical Tubes With Radial Internal Fins," ASME J. Heat Transfer, **103**, pp. 566–572.
[9] Dong, Z. F., and Ebadian, M. A., 1992, "Convective and Radiative Heat Transfer in the Entrance Region of an Elliptic Duct with Fins," Numer. Heat Transfer, **21**, pp. 91–107.
[10] Dong, Z. F., and Ebadian, M. A., 1991, "A Numerical Analysis of Thermally Developing Flow in Elliptic Ducts with Internal Fins," Int. J. Heat Mass Transf., **12**, No. 2, pp. 166–172.
[11] Rohsenow, W. M., Hartnett, J. P., and Cho, Y. I., 1998, *Handbook of Heat Transfer*, Mc Graw Hill, New York.
[12] Aggarwala, B. D., and Gangal, M. K., 1976, "Heat Transfer in Rectangular Ducts with Fins from Opposite Walls," ZAMM, **56**, pp. 253–266.
[13] Gangal, M. K., and Aggarwala, B. D., 1977, "Combined Free and Forced Laminar Convection in Internally Finned Square Ducts," ZAMP, **28**, pp. 85–96.

Geometry Effects on Turbulent Flow and Heat Transfer in Internally Finned Tubes

Xiaoyue Liu
Mem. ASME,
Mechanical Engineer,
GE Corporate Research and Development Center,
1 Research Circle,
Niskayuna, NY 12309
e-mail: LiuXi@crd.ge.com

Michael K. Jensen
Fellow ASME,
Professor,
Department of Mechanical,
Aerospace and Nuclear Engineering,
Rensselaer Polytechnic Institute,
Troy, NY 12180-3590
e-mail: JenseM@rpi.edu

A parametric study has been performed on turbulent flow and heat transfer in internally finned tubes. For a rectangular fin profile, the effects of fin number N, fin width s, fin height H, and helix angle γ were numerically investigated for the conditions of $N=10\sim40$, $H=0.03\sim0.1$, $s=0.05\sim0.22$, $\gamma=10\,deg\sim40\,deg$, and $Re=40{,}000$. In addition, the performance of three fin profiles—rectangle, triangle, and round crest—with the same fin heights, width, and helix angles were compared for Reynolds numbers between 10,000 and 70,000. Rectangular and triangular fins behave similarly; for some geometric conditions the round crest fin has lower friction factors and Nusselt numbers (17 and 10 percent, respectively) than the rectangular fin. However, when the number of fins is large, the round crest fin can have larger friction factors (about 16 percent). Damping of turbulence energy in the interfin region is credited for the reversal of the typical trends.
[DOI: 10.1115/1.1409267]

Introduction

Internally finned tubes are one of the most widely used passive heat transfer enhancement techniques, especially in the chemical process and petroleum industries. Finned tubes are used to reduce the size of a heat exchanger required for a specified heat duty, increase the heat duty of an existing heat exchanger, reduce the approach temperature difference needed for a given heat duty, and reduce the pumping power.

Internally finned tubes perform differently depending on whether the flow is laminar or turbulent. For laminar flow and heat transfer, a comprehensive experimental and numerical investigation has been performed for variable fluid properties, mixed convection, and entrance flows in a variety of geometries by Shome and Jensen [1,2]. The current research focuses on turbulent flow and heat transfer.

The majority of early investigations (see Bergles et al. [3] for a complete listing, and Liu [4] for a review) on turbulent heat transfer and pressure drop for flows in internally finned tubes were experimental. These studies examined the overall performance in terms of circumferentially averaged friction factors and heat transfer coefficients, and examined the effects of three gross parameters: number of fins N, fin height H, and helix angle γ (e.g., Carnavos [5,6], and Jensen and Vlakancic [7]). Rectangular fins were implicitly assumed in all the studies. Because of the wide range of fin geometries and Reynolds numbers covered in their experiments, Jensen and Vlankancic [7] suggested different governing processes between ''tall fin'' and ''micro-fin'' tubes. In addition, a fourth parameter, fin width s, was shown to have a strong influence on the results. Fin profile has not been studied in any of the experimental investigations.

Experimental data for turbulent flow fields and local heat transfer coefficients in internally finned tubes are very limited (Liu and Jensen [8]). Existing turbulent flow field data are on longitudinally finned tubes with tall fin heights and small numbers of fins (Trupp et al. [9] and Edwards et al. [10]). While these data are useful, the tubes tested are not representative of what is used in industry.

Numerical investigations of fully developed turbulent flow and heat transfer in internally finned tubes are limited, too. While Liu and Jensen [8] investigated spiral rectangular fins, Patankar et al. [11], Said and Trupp [12], and Edwards and Jensen [13] used longitudinal rectangular fins and incorporated other simplifying assumption. Liu and Jensen [8] used an unstructured finite-volume method with a two-layer turbulence model to capture the near-wall turbulence in two spirally finned tubes. The circumferentially averaged friction factors and Nusselt numbers compared well with the experimental data of Jensen and Vlakancic [7]. The numerical schemes, turbulence models, grid independence, and periodically fully developed boundary conditions were carefully validated so that they could be used for further parametric studies.

Comparisons between different internally finned tubes to determine the effect of one of the gross tube parameters are fraught with problems. In experiments, many geometric parameters, but not all, can be held constant, thus resulting in uncertainties in comparisons and evaluations. Other parameters, such as fin width, have been studied only slightly.

Hence, the first objective is to explore the effect of four geometric parameters (number of fins, fin height, fin width, and helix angle, as shown in Fig. 1) for rectangular fins with fully developed turbulent flow and heat transfer in internally finned tubes using realistic flow conditions. To cover wide ranges of the four parameters and Reynolds numbers would be prohibitively expensive in terms of time and cost. The results of previous numerical and experimental studies indicate Nusselt numbers and friction factors generally are linear function of Reynolds number, except for micro-finned tubes at low Reynolds numbers ($\leqslant$10,000). Based on industrial practice, a representative Reynolds number of 40,000 and geometric parameters of $10\leqslant N\leqslant40$, $0.03\leqslant H\leqslant0.1$, $0.05\leqslant s\leqslant0.22$, and $10\leqslant\gamma\leqslant40$ deg were studied. Angles greater than 45 deg could not be investigated because of limitations in numerical accuracy and stability.

Investigators have speculated that fin profile must have some influence on performance. Examination of actual fins shows a variety of profiles. However, to the authors' knowledge, no research has addressed fin profile effects. To investigate fully the effect of fin profile in addition to the geometric combinations would be a very daunting task, and to experimentally investigate fin profile effects would be very difficult without any theoretical guidance. Therefore, the second objective is a limited numerical investigation on the effects of fin profiles on friction factors and Nusselt numbers and to speculate on governing mechanisms.

Three different fin profiles with different number of fins and fin height were used: rectangular, triangular, and round crest, as shown in Fig. 2 and Table 1. All different fin profiles in the same

Contributed by the Heat Transfer Division for publication in the JOURNAL OF HEAT TRANSFER. Manuscript received by the Heat Transfer Division December 15, 2000; revision received May 20, 2001. Associate Editor: R. L. Mahajan.

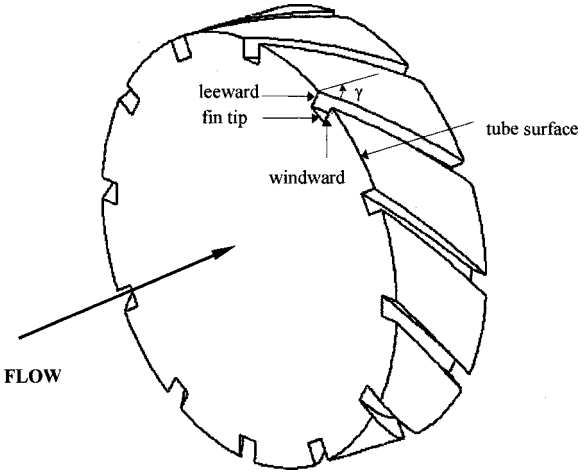

Fig. 1 The geometry of an internally finned tube

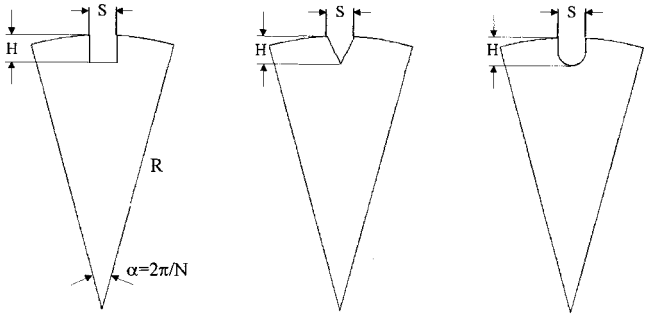

Fig. 2 Three fin profiles

Table 1 Parameters for different groups of fin profiles

Group	N	H	γ	S
1	14	0.1	30^0	0.083
2	30	0.1	30^0	0.083
3	36	0.06	25^0	0.1

group maintained the same fin height, base fin width, number of fins, and helix angle, so that the geometric difference was only the fin profile.

Numerical Analysis

Taking advantage of the typically large tube length-to-diameter ratio, entrance effects are ignored. Thus, the emphasis is on capturing the "periodically fully developed" flow characteristics and related heat transfer performance.

Computational Geometry Model. Internally finned tubes (see Fig. 1) have a rotational repeatedness (Kelkar et al. [14]) about the tube axis in the cross-section of the tube, i.e., the cross-section geometry does not change if rotated around the center axis by an angle $\alpha = 2\pi/N$. Thus, only one fin needs to be included in the computational domain. Because the helical fins are formed by spiral extrusion along the tube axis, geometric periodicity also exists in the longitudinal direction. The helix angle is defined as $\gamma = \arctan(2\pi R/NL_{\text{pitch}})$, where L_{pitch} is one pitch (i.e., the longitudinal distance between two fins), and two cross-sections separated by this distance have exactly the same local geometry dimensions and global spatial locations. The unit computational cell has this length (see Fig. 3).

For variables in Cartesian coordinates, the periodicity between boundaries $B3$ and $B4$ is rotational, but the periodicity between boundaries $B1$ and $B2$ is a mixed type of translation and rotation

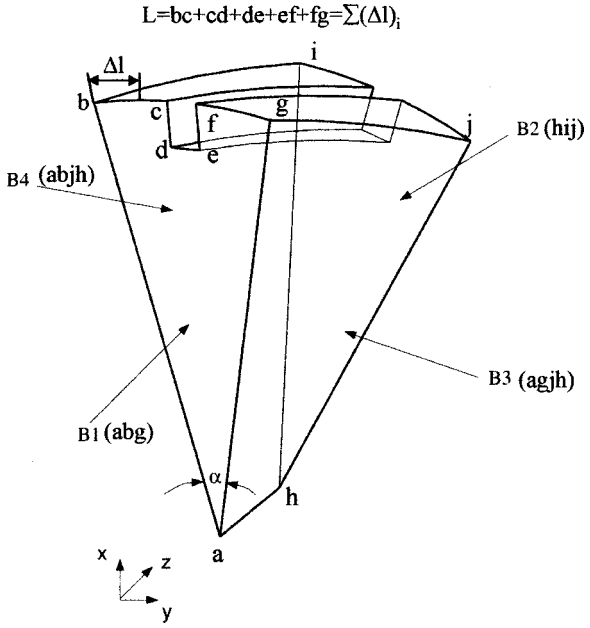

Fig. 3 A computational model of an internally finned tube

because they are translated along the tube axis by one pitch and also rotated about the tube axis by an angle of α.

Boundary Conditions. Periodic boundary conditions must be applied to the appropriate interfaces of the representative unit cell. For velocity vectors on rotationally periodic boundaries, the velocity components aligned with the axial direction remain the same, and the circumferential velocities in one module must be rotated with respect to the velocity field in a neighboring module. In translationally periodic boundaries, the velocities at the interfaces are exactly the same.

These relationships may be mathematically formulated as follows:

$$u_{B1} = u_{B2}\cos\alpha - v_{B2}\sin\alpha;$$

$$v_{B1} = u_{B2}\sin\alpha - v_{B2}\cos\alpha; \quad w_{B1} = w_{B2}$$

$$\phi_{B1} = \phi_{B2}; \quad u_{B4} = u_{B3}\cos\alpha - v_{B3}\sin\alpha;$$

$$v_{B4} = u_{B4}\sin\alpha - v_{B4}\cos\alpha$$

$$w_{B4} = w_{B3}; \quad p_{B4} = p_{B3}; \quad \phi_{B4} = \phi_{B3}, \tag{1}$$

where u, v, w, are the three velocity components in Cartesian coordinates, p is the pressure, and ϕ is a scalar variable such as turbulent kinetic energy or turbulence dissipation rate.

For fully developed flow, a periodic pressure boundary condition is applied by scaling the pressure in the momentum equations with $p' = p - \beta z$, and $\beta = (p_{B2} - p_{B1})/L_{\text{pitch}}$. β is then put into the source terms of the momentum equations as the driving force of the pipe flow.

For the experimental conditions of Jensen and Vlakancic [7], the fin efficiency was estimated by the method of Kern and Kraus [15] to be about 100 percent. Hence, a constant wall temperature boundary condition was used. However, similar to the pressure distribution, the primitive temperature field is not periodic in the longitudinal direction; the fluid temperature approaches the wall temperature as the fluid flows through the tube. Once the flow is far away from the tube inlet, the temperature difference between the fluid's bulk-mean temperature and the wall temperature decays exponentially to zero, so that (Patankar et al. [16]):

$$\frac{T(x,y,z)|_{B1}-T_w}{T_{b_{B1}}-T_w}=\frac{T(x,y,z)|_{B2}-T_w}{T_{b_{B2}}-T_w}, \tag{2}$$

where T_w is the wall temperature, and T_{bz} is the local bulk-mean temperature. Equation (2) defines a ''periodically thermally developed''module for a particular duct flow with periodically varying geometries in the main flow stream direction. The above equation dictates that the shapes of the non-dimensionalized temperature profiles on the periodic boundaries $B1$ and $B2$ are the same, and periodic boundary conditions are implemented by introducing a non-dimensionalized temperature:

$$\theta=\frac{T(x,y,z)-T_w}{T_{b_z}-T_w}. \tag{3}$$

So that

$$\theta(x,y)|_{B1}=\theta(x,y)|_{B2}. \tag{4}$$

Low Reynolds Number *k*-ε Model. The high-Reynolds number turbulence model is only applicable to fully turbulent flows, where the molecular viscous effect is not significant. The present operating conditions are in the relatively low Re region, and the characteristic length scale of the fins are comparable to the length scale of the viscous sublayer. Thus, the flow is split into a fully turbulent core region and a near-wall region. A high Re number turbulence model is applied to the fully turbulent core region and a one-equation turbulence model specially designed for capturing near-wall turbulence characteristics is applied in the near-wall region. The two-layer low-Reynolds number turbulence model proposed by Norris and Reynolds [17] is adopted in this study.

The turbulent kinetic energy equation is as follows:

$$\frac{\partial \rho u_i k}{\partial x_i}-\frac{\partial}{\partial x_j}\left(\frac{\mu_t}{\sigma_k}\frac{\partial k}{\partial x_j}\right)=P_k-\rho\varepsilon. \tag{5}$$

In the Norris and Reynolds model:

$$\varepsilon=\frac{k^{3/2}}{l_\varepsilon}\left(1+\frac{C_\varepsilon}{\mathrm{Re}_y}\right);\quad \mu_t=C_\mu \rho f_\mu \frac{k^2}{\varepsilon};\quad l_\varepsilon=C_\mu^{-3/4}\kappa y;$$
$$f_\mu=1-\exp\left(-\frac{\mathrm{Re}_y}{A_\mu}\right). \tag{6}$$

The above model reflects the correct length scale variation in the near-wall region and satisfies the requirement of $\varepsilon=\varepsilon_{\mathrm{wall}}$ as $y\to 0$. The values of constants in above turbulence model are as follows (see STAR-CD manual [18] and Liu [4]):

$$\sigma_k=1.0;\quad C_\varepsilon=5.3;\quad C_\mu=0.09;\quad \kappa=0.42;\quad A_\mu=50.5. \tag{7}$$

Results and Discussions

Comparison of Numerical Results With Experimental Data. As shown in an earlier paper (Liu and Jensen [8]), the CFD code STAR-CD [17] was used to simulate the spirally finned tubes, and the results were benchmarked against the experimental data of Jensen and Vlakancic [7] for validating mesh independence, computational convergence, and the turbulence model. During the numerical validation process, two or three periods were used for confirming the longitudinal periodicity of the computational model.

The comparison of friction factors is shown in Fig. 4(*a*) for tube Fin1, which is a ''micro-fin'' tube with $N=30$, $H=0.03$ and $\gamma=30$ deg. The friction factors matched the experimental data well. Although the predicted friction factors were all underestimated, they had the same variation in curvature as the experimental data. The maximum deviation between the two sets of results was about 10 percent. The Nu comparison between the computational and experimental data is presented in Fig. 4(*b*). Nu was favorably predicted with a 6 percent maximum difference between the experimental and computational results.

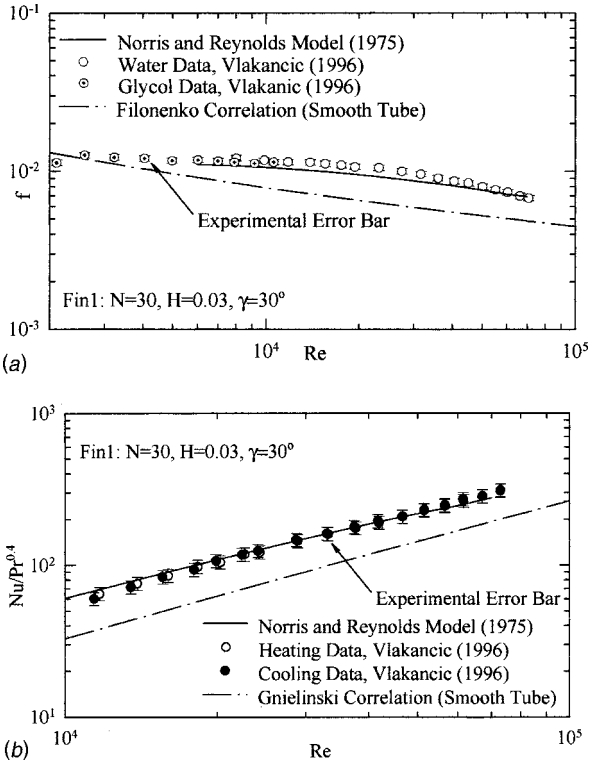

Fig. 4 (*a*) The comparison of the predicted friction factors with experimental data for Fin 1; and (*b*) the comparison of the predicted Nusselt numbers with experimental data for Fin 1.

A similar comparison was carried out with $N=8$, $H=0.1$ and $\gamma=30$ deg. Both friction factors and Nusselt numbers matched Vlakancic's data well, with maximum deviations of 6 percent and 17 percent, respectively. The largest Nusselt number deviation between the experimental and computed data occurred at Re $=70{,}000$, which may be caused by the isotropic turbulence model, which is not able to capture the anisotropic turbulence. Note that the friction factor and Nusselt number are all based on the nominal diameter of the tube for convenience of performance comparisons.

The experimental errors in the measurement system are also presented in the above figures, which are typically about ± 4 percent but higher at larger Re. The analysis of experimental uncertainties can be found in Vlakancic [19]. Note that on all figures, the smooth tube heat transfer coefficient is calculated with the Gnielinski correlation [20].

Parametric Study of the Geometric Effects of Rectangular Fins

Effect of the Number of Fins. The variation in friction factors and Nusselt numbers with the helix angle and the number of fins is presented in Figs. 5(*a*) and 5(*b*), respectively. Both quantities increase with an increase in the number of fins and helix angle. The fin plays an important role in delivering heat transfer from the solid walls to the flowing fluid, especially at the sharp corner on the fin's windward side. More fins mean that there are more sharp corners producing wall shear stresses, pressure resistance, and also heat transfer, so that both friction factors and Nusselt numbers are increased. However, when the number of fins becomes large, the friction factors and Nusselt numbers are suppressed. This will be discussed below.

The heat transfer area increase versus the increase in the number of fins and helix angle is presented in Table 2. Comparison of the heat transfer area variation with the Nusselt number change

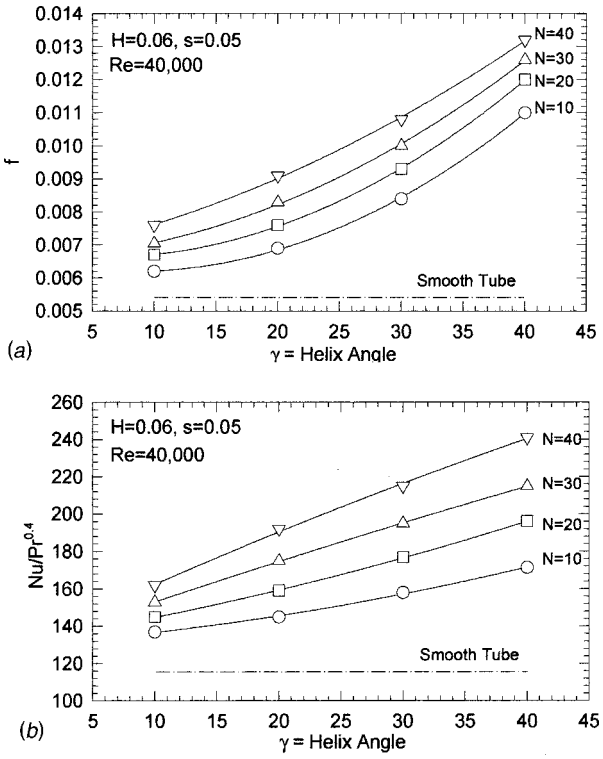

Fig. 5 (*a*) The effect of helix angle and number of fins on friction factors; and (*b*) the effect of helix angle and number of fins on Nusselt numbers.

indicates the Nusselt number increases by 36 percent from $N=10$ to 40 for a 30 deg helix angle with a corresponding heat transfer area increase of 50 percent. This means that the heat transfer per unit area for $N=40$ is smaller than that for $N=10$, though the tube with $N=40$ delivers more overall heat transfer. The physical reason for this phenomenon is that stronger viscous effects in the narrower interfin passage suppress heat transfer from the fin root and tube surface.

Effect of the Helix Angle. The variation of friction factors with the helix angle is shown in Fig. 5(*a*). The Reynolds number, fin height, and fin width are the same as for the previous comparisons, and the number of fins ranges from $N=10$ to $N=40$. For $N=10$ and with the helix angle increasing from 10 deg to 40 deg, the friction factor increases 77 percent. A similar increase is experienced with $N=40$. The variation in the friction factor with helix angle is basically independent of the number of fins. The detailed flow field shows that the circumferential velocities increase with helix angle. These velocities are generated by the incoming axial flow impinging on the solid walls of the fin. A larger helix angle causes more windward-side solid wall area to be exposed to the incoming flow, so that stronger flow impingement causes higher wall shear stresses and pressure resistance. As the helix angle becomes larger, the pressure resistance also increases.

The helix angle effects on the Nusselt numbers are presented in Fig. 5(*b*). For instance, with $N=30$, the Nusselt number increases 41 percent with a helix angle increase from 10 deg to 40 deg. As discussed before, a larger helix angle makes the windward side of the fin more inclined to the incoming flow, so that stronger interactions between the fin and the fluid flow are generated, and heat transfer is enhanced.

Comparing the heat transfer area variation (Table 2) with the Nusselt number change, the Nusselt number increases by 41 percent with $\gamma=10$ deg to 40 deg and $N=30$, but the corresponding heat transfer area increase is only 12 percent. This means that the heat transfer per unit area at $\gamma=40$ deg is much larger than that at $\gamma=10$ deg. On the other hand, for a helix angle of 30 deg, varying N from 10 to 40 resulted in a 36 percent increase in Nusselt number, but at the expense of a 50 percent increase in heat transfer area.

Effect of Fin Height. For $N=30$, the variations in the friction factors and Nusselt numbers with fin height increase are presented in Figs. 6(*a*) and 6(*b*), respectively. The general trend is that both friction factors and Nusselt numbers increase with the increase of fin height. However, the friction factors and Nusselt numbers do not increase greatly with fin height increase if the helix angle remains small (<20 deg). When the helix angle is greater than 20 deg, the fin height variation causes a dramatic increase. A large helix angle is the determinant for strong interactions between the fin and fluid flow. Hence, as the fin becomes taller, more heat transfer area is added, and the interaction between the fin tip and the fluid flow is strengthened.

Combining information from Table 3 and Fig. 6(*b*), for $\gamma=30$ deg, a 50 percent Nusselt number increase is gained with a 59 percent heat transfer area increase. The heat transfer rate per unit area for the tube with $H=0.03$ is approximately the same as that for $H=0.10$. Increasing the fin height for this geometry does not dramatically change the fluid flow and heat transfer characteristics. Rather, the heat transfer is enhanced by the heat transfer area increase.

Typical Local Distributions of Friction Factors and Nusselt Numbers. The circumferentially local friction factors along the local coordinate of the fin and tube are presented in Fig. 7(*a*) for Re=40,000 for the tube with $N=30$, $H=0.06$, $s=0.05$, and $\gamma=30$ deg. The total wall resistance of spirally finned tubes is composed of the axial components of the wall shear stresses and the

Table 2 Heat transfer area increase with $H=0.06$ and $s=0.05$

Heat Transfer Area Increase (A_{fin}/A_{smooth})	N=10	N=20	N=30	N=40
γ=10°	1.19	1.38	1.57	1.76
γ=20°	1.20	1.40	1.60	1.80
γ=30°	1.22	1.44	1.66	1.88
γ=40°	1.25	1.5	1.75	2.00

Table 3 Heat transfer area increase with $N=30$ and $s=0.05$

Heat Transfer Area Increase (A_{fin}/A_{smooth})	H=0.03	H=0.06	H=0.08	H=0.10
γ=10°	1.27	1.54	1.72	1.90
γ=20°	1.30	1.60	1.81	1.99
γ=30°	1.33	1.66	1.87	2.11
γ=40°	1.39	1.78	2.05	2.56

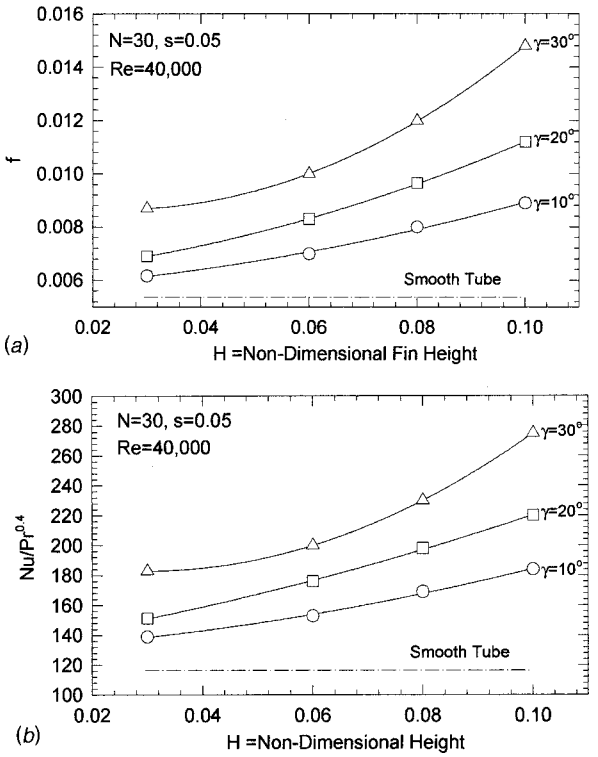

Fig. 6 (*a*) The effect of fin height on friction factors ($N=30$); and (*b*) the effect of fin height on Nusselt numbers ($N=30$).

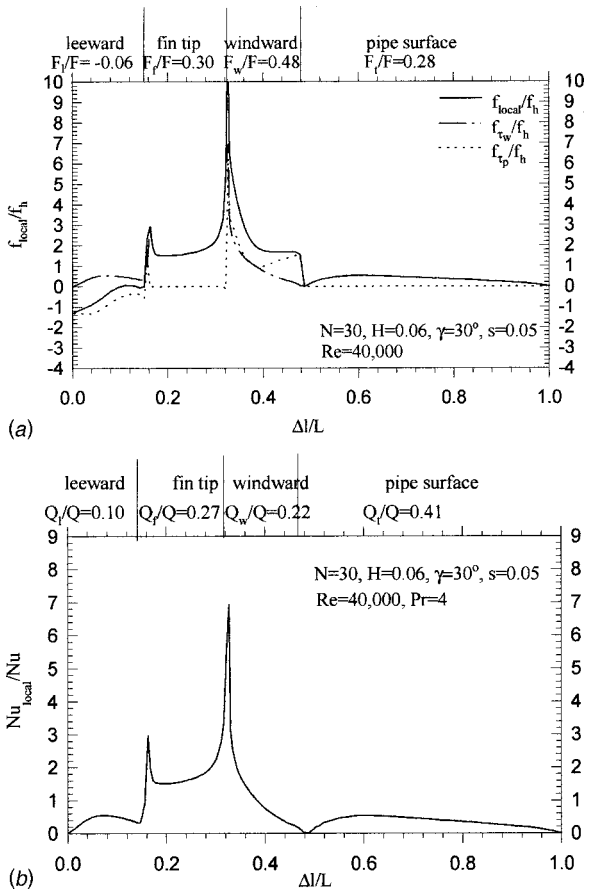

Fig. 7 (*a*) The local friction factor distribution for a rectangular fin ($N=36$, $H=0.06$, $\gamma=25$ deg, and $s=0.1$); and (*b*) the local Nusselt number distribution for a rectangular fin ($N=36$, $H=0.06$, $\gamma=25$ deg, and $s=0.1$).

form drag caused by pressure forces on the solid walls. Therefore, three local friction factors are used to represent the effects of the local wall shear stresses, pressure resistance, and total resistance, which are normalized with the average friction factor based on the hydraulic diameter. (Hydraulic diameter is used here so that integration of the non-dimensionalized local distribution equals unity.) The local coordinate was divided into the fin's leeward section, the fin's tip section, the fin's windward section, and the base tube surface, as shown in Fig. 1. The contribution from each section of the solid wall to the total flow resistance forces, F (which is the integration of local axial shear stresses and pressure forces on these solid walls) is given at the top of the figure. During the data reduction process, the local resistance forces were integrated to obtain the circumferentially friction factor. This friction factor compared well with that deduced from the pressure drop. (Refined grids were used at the fin tip corners to investigate the spikes. While the magnitude of the ''peaks'' did vary, their effect on the integrated average f and Nu was negligible. The singularity in the geometry of the corners may have produced these spikes and, thus, may be a numerical artifact.)

Figure 7(*a*) shows that the wall resistance has a more uniform distribution on the fin tip and tube surface than on the leeward and windward sides. The wall shear forces on the fin tip and tube surface contributed about 28 percent of the total resistance force at Re=40,000. The resistance on the fin's leeward side was much smaller compared with the windward side. The windward side caused much of the resistance both from wall shear stresses and pressure resistance, especially in the high Re number region.

The local Nu number distribution for the same tube and the percentage of the total heat transfer, Q, delivered by each section of the solid wall are presented in Fig. 7(*b*). The pipe surface contributed about 41 percent of the total heat transfer. The fin's leeward side contributed the least. Similar to the wall resistance distribution, the Nusselt number distribution is more uniform on the fin tip and tube surface than on the leeward and windward sides. The local Nu number reached its highest value at the fin's sharp, upper corner, which is explained by the flow pattern: the flow impinges on the sharp corner thus promoting heat transfer. With a decrease of Re number, the fin tip section delivered more heat transfer, and the heat transfer through the pipe surface decreased. The reason is that the turbulence level in the interfin region decreases as Re decreases and the thermal resistance caused by the viscous layer increase. Hence, the relative proportion of the heat transfer through the fin tip surface increases.

Effect of Fin Width. The effect of fin width on friction factors and Nusselt numbers are presented in Figs. 8(*a*) and 8(*b*), for the condition with $N=36$, $H=0.06$, $\gamma=25$ deg, and Re=40,000. For $N=36$, the friction factors and Nusselt numbers decrease with an increase of fin width. For the second tube with $N=22$, the friction factors and Nusselt numbers increase with an increase in fin width in the beginning, then peak and fall with a further increase in fin width. The striking feature of the above results is that the fin width has a totally different effect on the friction factors and Nusselt numbers for different numbers of fins.

Comparing the numerical results and the experimental data of Jensen and Vlakancic [7] (Figs. 8(*a*) and 8(*b*)), it can be seen that the numerical results match with the experimental data very well. For $N=22$, the large fin width promotes the heat transfer and friction factors, which compensates for the effects of fewer fins. For $N=36$, the smaller interfin region suppresses the heat transfer and friction factors, which cancels out the effects of the larger number of fins. Eventually, the two internally finned tubes with different fin numbers have almost the same friction factors and Nusselt numbers.

The turbulent kinetic energy, which is useful in assessing flow

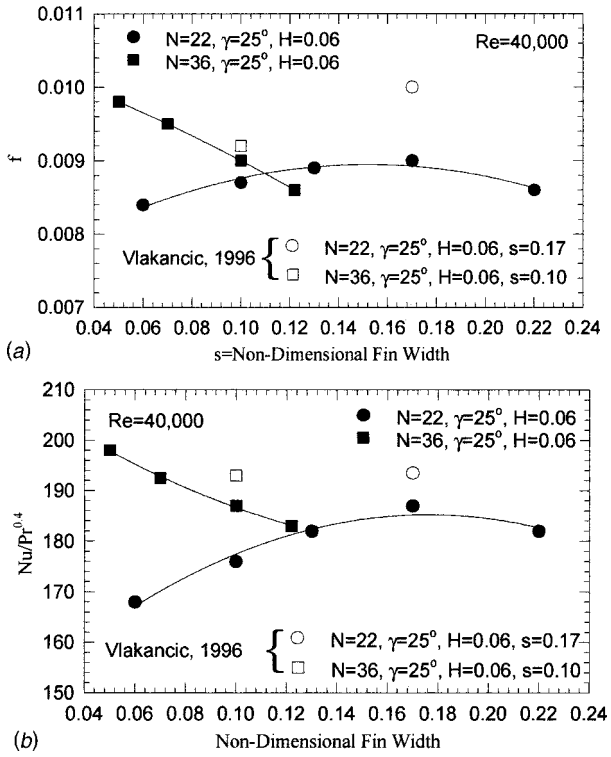

Fig. 8 (*a*) The comparison of fin width effect on friction factor with different number of fins; and (*b*) the comparison of fin width effect on Nusselt number with different number of fins.

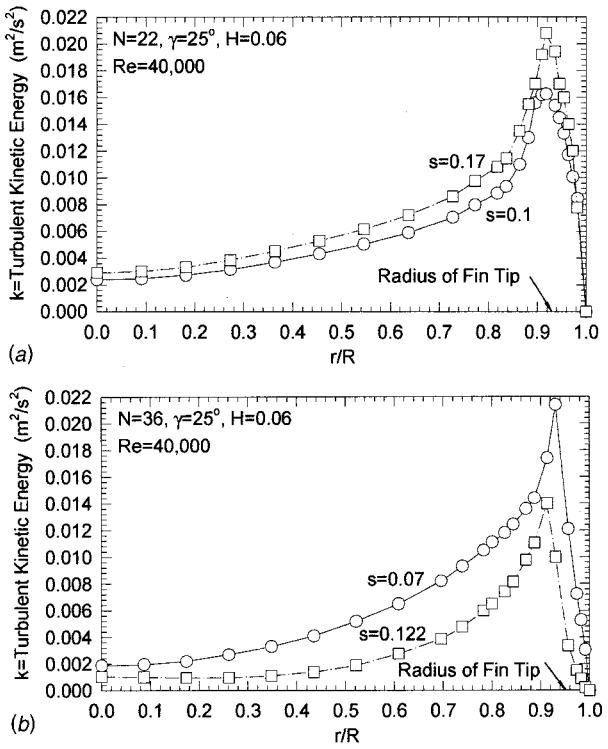

Fig. 9 (*a*) The turbulent kinetic energy on the interfin bisector for (*N*=22, *H*=0.06, and γ=25 deg); and (*b*) the turbulent kinetic energy on the interfin bisector for (*N*=36, *H*=0.06, and γ=25 deg).

and heat transfer behavior, on the interfin bisector is presented in Fig. 9(*a*) for different non-dimensional fin widths for the tube with $N=22$, $H=0.06$, $\gamma=25$ deg, and Re=40,000. As can be seen, the turbulent kinetic energy increases with an increase in the non-dimensional fin width, which means that more turbulent kinetic energy is generated by the solid walls because of the decreased interfin region, especially near the fin-tip region. The strengthened turbulent kinetic energy enhances heat transfer from the near-wall region to the flow core region. However, the turbulence also costs pumping power, so that friction factors are increased.

For the tube with $N=36$, $H=0.06$, $\gamma=25$ deg, the turbulent kinetic energy on the interfin bisector is presented in Fig. 9(*b*). In contrast to the previous tube, the turbulent kinetic energy decreases with an increase in non-dimensional fin width, which means that less turbulent kinetic energy is generated by the solid walls because of the decreased interfin region, especially near the fin-tip region. Thus, both friction factor and Nusselt number decrease.

The Effect of Fin Profile for $N=30$, $H=0.1$, $\gamma=30$ deg, and $s=0.083$. Friction factor comparisons among for the three different fin profiles are presented in Fig. 10(*a*). The friction factors in the tube with the round crest are the lowest; the rectangular and triangular fins have similar behavior, with the largest difference between the round crest and rectangular fin being as high as 15.5 percent at Re=70,000. The trend in the Nusselt numbers is similar to that of the friction factors, as shown in Fig. 10(*b*), but the Nusselt number difference has a maximum of about 10.4 percent at Re=70,000. Comparable runs were made with $N=14$ with the other three parameters the same as above (see Liu [4] for details). The trends in the data were similar. However, the largest variation in the friction factor was only 9.9 percent; for the Nusselt number, the largest variation was 5 percent.

Normalized circumferentially local friction factor and Nusselt number distributions are presented in Figs. 11(*a*) and 11(*b*) respectively, for the round crest fin profile. (The rectangular and

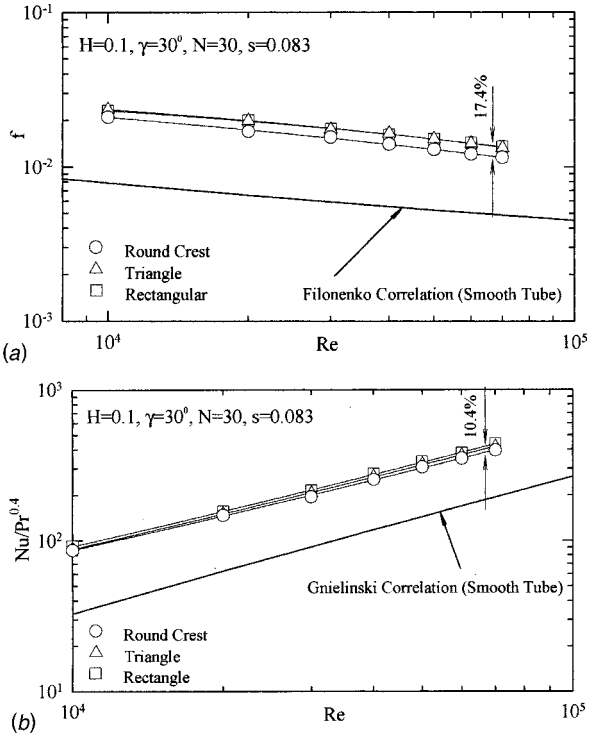

Fig. 10 (*a*) The friction factor comparison for different fin profiles (*N*=30, *H*=0.10, γ=30 deg, and *s*=0.083); and (*b*) the Nusselt number comparison for different fin profiles (*N*=30, *H*=0.10, γ=30 deg, and *s*=0.083).

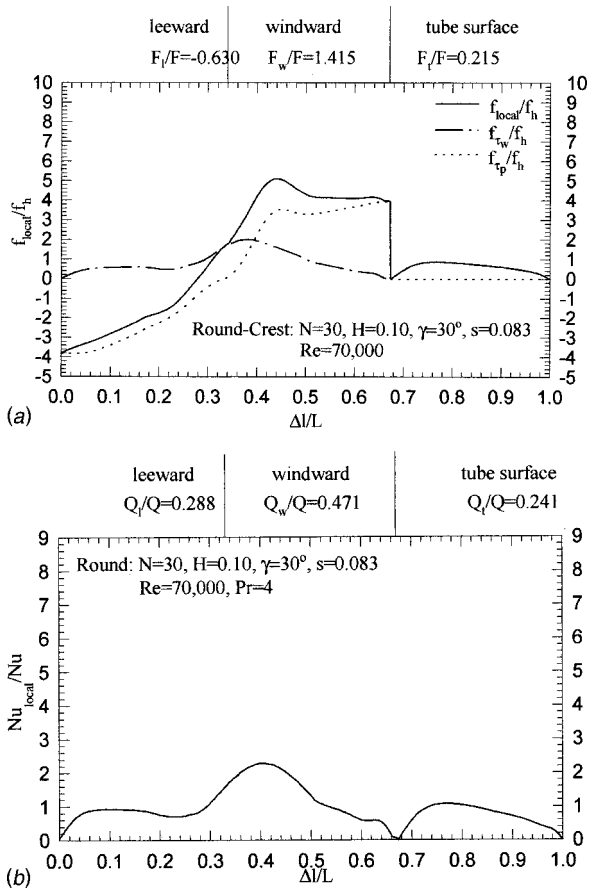

Fig. 11 (*a*) **The local friction factor distribution for the round crest fin profile; and** (*b*) **the local Nusselt number distribution for the round-crest fin profile.**

triangular fin profiles are similar to these presented in Fig. 11.) At the top of each figure, the contribution to the overall friction factor and Nusselt number is given of each part of the fin/tube surface. For all three fins, the windward side of the fin contributed most to the overall friction factor; the base tube contributed little. A similar trend can be observed with the Nusselt number. The peak values of the local shear resistance and Nusselt numbers for the rectangular fin are at the sharp corner at the tip of the windward side. For the triangular fin, the peak values are also near the sharp fin tip in the windward side. For the round-crest fin, the highest values of friction factors and Nusselt numbers are much lower than those in the rectangular and triangular fin profiles. The sharp corners produce more turbulence than the smooth surface on the round crest, thus enhancing flow resistance and heat transfer.

Table 4 presents the ratio of overall Nusselt number and friction factor compared to a corresponding smooth tube, fraction of total heat transfer and flow resistance through a single fin, fraction of pressure resistance in total flow resistance (form drag), and heat transfer area increase. The fin surface delivered more than 75 percent of total the heat transfer and flow resistance for each of the three fin profiles. However, the rectangular and triangle fin profiles produced more heat transfer and flow resistance than the round-crest fin profile. The round-crest fin profile reduced the impingement interaction between the solid wall and fluid flow by adding a more streamlined surface on the fin tip, so that both shear resistance and pressure resistance were dramatically decreased.

Note that the proportion of the total friction due to the pressure resistance is smaller with $N=30$ than that for $N=14$ for all of the fin profiles. For the rectangular, triangular, and round crest fins for $N=14$, the value of F_{press}/F are, respectively, 0.345, 0.338, and 0.318. Apparently, this is because a larger number of fins reduce the interfin region, so that the impingement area is much more restricted for each fin. Usually, the higher the fraction of pressure resistance in the total resistance, the lower is the efficiency index, $(\text{Nu}/\text{Nu}_{\text{smooth}})/(f/f_{\text{smooth}})$. This is shown by the data in Table 4.

The Effect of the Fin Profile for N=36, H=0.06, γ=25 deg, and s=0.1. For a shorter fin ($H=0.06$) and slightly different N, γ, and s than before, the friction factors and Nusselt numbers for triangular fins are very similar to those of a rectangular fin; hence, only rectangular and round-crest fin profiles are discussed below. Friction factors are presented in Fig. 12(*a*), Nusselt numbers are shown in Fig. 12(*b*). At high Reynolds numbers, the difference in friction factors between the two fins is very small. At Re $=10{,}000$, there is about a 15.5 percent difference. The most surprising result is that the round-crest fin friction factors are higher than those of the rectangular fin profile, a result which is totally different from the previous results. For the Nusselt numbers almost no difference was noted between the two fins. Again, this is considerably different that the previous results.

The general trends for the local friction factors and Nusselt numbers for the two fin profiles are similar to those discussed in the previous section. However, the contribution from each section of the solid walls to the overall Nusselt numbers and friction factors is quite different. These values are summarized in Table 5 for Re=70,000 and Table 6 for Re=10,000

Table 5 shows that the increase in friction factor and Nusselt number compared to a smooth tube is smaller than that of the corresponding tubes discussed in Table 4. This is caused by the lower fin height, smaller interfin region, and helix angle. The rectangular and round-crest fin profiles produced the same heat transfer and total flow resistance, although their heat transfer areas were very different. This contradicts the previous conclusion that the sharp corners and impingement effects on rectangular and triangular fins results in enhanced heat transfer and flow resistance. However, the geometric difference here is that the interfin region was made very small by the large fin width and number of fins.

Based on the discussion in the fin width effects in the paper of Liu and Jensen [8] for rectangular fins, the effects of the small

Table 4 The effect of heat transfer and friction for group 2 fin profiles

Re=70,000	Rectangle	Triangle	Round
Fraction of Total Heat Transfer Through Fins	0.826	0.812	0.759
Fraction of Total Resistance Caused By Fins	0.867	0.860	0.785
A_{fin}/A_{smooth}	2.100	1.740	1.900
Nu/Nu_{smooth}	2.260	2.210	2.050
$(Nu/Nu_{smooth})/(A_{fin}/A_{smooth})$	1.080	1.250	1.080
f/f_{smooth}	2.780	2.740	2.370
F_{press}/F	0.259	0.253	0.228
$(Nu/Nu_{smooth})/(f/f_{smooth})$	0.810	0.810	0.870

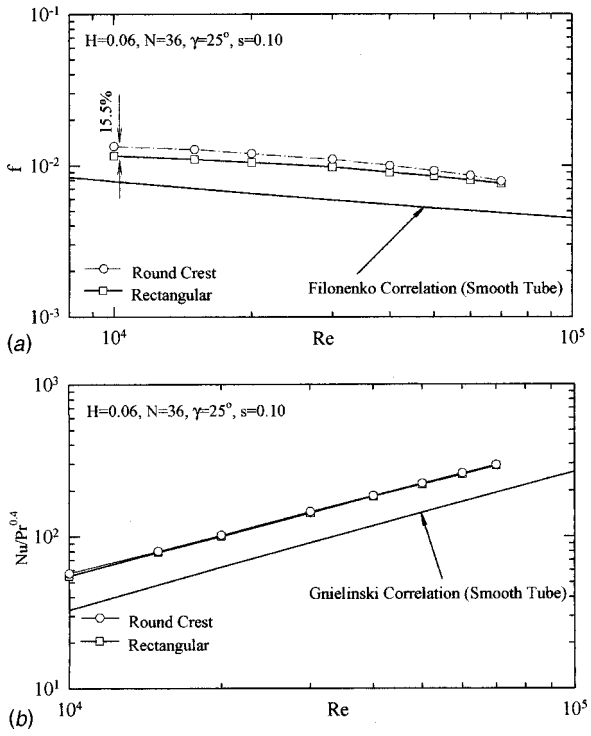

Fig. 12 (*a*) The friction factor comparison for different fin profiles (*N*=36, *H*=0.06, γ=25 deg, and *s*=0.1); and (*b*) the Nusselt number comparison for different fin profiles (*N*=36, *H*=0.06, γ=25 deg, and *s*=0.1).

interfin region cancels out the impingement interaction between the solid walls and fluid flow. Especially in the fin-root area, the viscous effects on both sides of the fin walls and the tube surface make this region almost a "dead" area, so that impingement on the fin tip has a very weak effect on this region.

For the round-crest fin, the interfin passage is enlarged through rounding out the fin tip. Although the interaction between a smooth surface and fluid flow is weaker than that of a sharp corner, the enlarged interfin passage with the round crest is able to pump more turbulence into the fin root region, so that more heat transfer occurs with a larger friction factor at the same time. This explains why the Nusselt numbers and friction factors are almost the same at Re=70,000.

At Re=10,000, viscous effects are higher than those at high Reynolds numbers, especially near the fin root in the interfin region. As shown in Table 6, the fin surface delivered more than 90 percent of the heat transfer and flow resistance for both rectangular and round fin profiles. Similar to Re=70,000, the surface of the rectangular fin delivered the same amount of heat transfer as that of the round fin. The situation of friction factors was a little different. The surface of the rectangular fin produced 97.7 percent of total flow resistance and the surface of the round fin contributed 93.3 percent of total flow resistance. Considering that the overall friction factor of the tube with the round-crest fin profile was much higher than that of the tube with the rectangular fin profile, the surface of round fin actually produced more flow resistance than the rectangular fin profile.

As shown in Table 6, the pressure resistance caused by the round fin-surface is dramatically larger than that of the rectangular fin. The reason is that the fluid flow becomes more sensitive to the interfin area change at a lower Reynolds number because the viscous sublayer is very thick at this condition. For the rectangular fin profile, the pressure resistance was only 6 percent of the total resistance because strong viscous effects in the narrow interfin passage almost eliminated the pressure resistance. In the round-crest fin tube, the impingement effects were enhanced by the enlarged interfin passage, so that the pressure resistance was dramatically increased. This explains why the overall friction factor of the tube with round-crest fin profile is much higher than that of the tube with rectangular fin profile.

Table 5 The effect of heat transfer and friction for group 3 fin profiles

Re=70,000	Rectangle	Round
Fraction of Total Heat Transfer Through Fins	0.821	0.807
Fraction of Total Resistance Caused By Fins	0.874	0.867
A_{fin}/A_{smooth}	1.760	1.500
Nu/Nu_{smooth}	1.500	1.520
$(Nu/Nu_{smooth})/(A_{fin}/A_{smooth})$	0.860	1.010
f/f_{smooth}	1.560	1.630
F_{press}/F	0.160	0.170
$(Nu/Nu_{smooth})/(f/f_{smooth})$	0.962	0.933

Table 6 The effect of heat transfer and friction for fin profile group 3

Re=10,000	Rectangle	Round
Fraction of Total Heat Transfer Through Fins	0.910	0.888
Fraction of Total Resistance Caused By Fins	0.977	0.933
A_{fin}/A_{smooth}	1.760	1.500
Nu/Nu_{smooth}	1.450	1.510
$(Nu/Nu_{smooth})/(A_{fin}/A_{smooth})$	0.820	1.000
f/f_{smooth}	1.470	1.700
F_{press}/F	0.060	0.110
$(Nu/Nu_{smooth})/(f/f_{smooth})$	0.990	0.890

Conclusions

A comprehensive numerical study on the effect of rectangular fins on Nusselt numbers and friction factors in internally finned tubes was conducted over a wide range of geometric conditions. Based upon the results obtained, the following conclusions can be drawn for rectangular fins:

1 Nusselt numbers and friction factors increase with an increase of the number of fins (if the interfin region is not too small) and helix angle. Larger helix angles generate stronger circumferential velocities, which enhance fluid mixing between the solid walls and the core flow.

2 Increased fin height produces larger Nusselt numbers and friction factors, but the increase is moderate at smaller helix angles ($\gamma < 20$ deg). When $\gamma > 20$ deg, both heat transfer and pressure drop increased greatly within the same fin-height variation range.

3 Adding fins and increasing fin width may increase or decrease heat transfer and friction factor. Variations in the interfin region turbulence level determine the increase or decrease.

The impact of fin profile on friction factors and Nusselt numbers has been investigated. For rectangular, triangular, and round-crest fins, fin profile does have a significant impact on the Nusselt number and friction factor. By examining the local distributions, the physical mechanisms were explored for the friction factor and Nusselt number differences caused by different fin profiles. The following conclusions can be drawn for fin profile effects:

1 Rectangular and triangular fin profiles have similar friction factors and Nusselt numbers. Friction factors and Nusselt numbers for round-crest fins are lower than those of rectangular and triangular fin profiles if the interfin region remains large.

2 The strong interaction between the sharp corners on the windward side of the rectangular fin tip and the fluid flow generated more turbulence than with the round-crest fin profile; this interaction then promoted stronger heat transfer through the whole fin surface and generated larger flow resistance. However, the sharp-corner effects were diminished when the interfin passage is small.

3 With a larger number of shorter fins, the rectangular and triangular fin profiles behaved similarly, with only small differences at high Reynolds numbers. For Re=10,000, the round-crest fin friction factor was about 15.5 percent higher than that of a rectangular fin. For the rectangular fin profile, the narrow interfin region diminished impingement effects caused by the sharp corner. For the round-crest fin, rounding out the fin tip enlarged the interfin region, so that the interaction between the fin and fluid flow was greatly enhanced. Thus, while the rectangular and round-crest fin tubes had the same friction factors and Nusselt numbers at high Reynolds numbers, at low Re number, the friction factor of the round-crest fin was much higher than that of a rectangular fin.

Acknowledgment

The National Science Foundation funded this research under grant number CTS-9412596. This assistance was greatly appreciated.

Nomenclature

A_{smooth} = the wall area of a smooth tube [m^2]
A_{fin} = the total heat transfer area of an internally-finned tube [m^2]
c_p = specific heat at constant pressure [J/kgK]
d_i = inner, nominal diameter of tube [m]
e = fin height [m]
f, f_h = fanning friction factor based on nominal or hydraulic diameter
f_μ = damping function for turbulent viscosity
f_{τ_w} = local friction factor based on axial wall shear stresses ($=\tau_w/0.5\rho w_t^2$)
f_{τ_p} = local friction factor based on pressure resistance ($=\tau_p/0.5\rho w_t^2$)
f_{local} = total local friction factor ($=f_{\tau_w}+f_{\tau_p}$)
F_f, F_l = axial flow resistance through the tip side, leeward side, windward side,
F_w, F_t, F = tube surface of a fin, and the total wall area [N]
F_{press} = total axial pressure resistance on the total wall area [N]
h, h_{local} = heat transfer coefficient, based on nominal or local heat transfer area [W/m^2K]
H = non-dimensional fin height ($=2e/d_i$)
k = thermal conductivity [W/mK]; Turbulent kinetic energy [m^2/s^2]
$\Delta l/L$ = non-dimensional circumferential local wall coordinate (see Fig. 3)
l_ε = turbulence length scale [m]
L_{pitch} = one pitch length (the axial distance when a fin spirally rotates by a helix angle) [m]
$\dot{m}$ = mass flow rate [kg/s]
N = number of fins
Nu = Nusselt number based on nominal tube diameter ($=hd_i/k$)
Nu_{local} = local Nusselt number based on nominal tube diameter ($=h_{\text{local}}d_i/k$)
p = pressure [Pa]
P_k = turbulence production
Pr = Prandtl number ($=\mu c_p/k$)
Q_f, Q_l = heat transfer through the tip side, leeward side, windward side,
Q_w, Q_t, Q = tube surface of a fin, and the total wall area [W]
R = tube radius [m]
Re = Reynolds number based on nominal tube diameter ($=w_t d_i/v$)
Re_y = turbulent Reynolds number ($=k^{0.5}y/v$)
s = fin width [m]
T = temperature [K]
u, v, w = velocity components in x, y, z directions in Cartesian coordinates
u_τ = friction velocity [m/s]
w_t = mean axial flow velocity based on tube nominal diameter [m/s]
y^+ = non-dimensional wall distance ($=yu_\tau/v$)

Greek Symbols

α = circumferential angle between two fins
β = the ratio of pressure drop to tube length
C_μ, C_ε = constants in turbulence model
κ, σ_k = constants in turbulence model
Δp = pressure drop [Pa]
ΔT_{lm} = log-mean temperature difference [K]
γ = fin helix angle [degrees]
μ = dynamic viscosity [Pa-s]
μ_t = turbulent Viscosity [Pa-s]
ν = kinematic viscosity [$m^2\ s^{-1}$]
ρ = fluid density [kg/m^3]
τ_w = axial wall shear stress [N/m^2]
τ_p = axial wall pressure resistance [N/m^2]

Subscripts

b = bulk
exp = experimental
h = hydraulic
lm = log-mean
min = minimum value
smooth = smooth tube

References

[1] Shome, B., and Jensen, M. K., 1996, ''Experimental Investigation of Variable Property/Mixed Convection Laminar Flow in Internally-Finned Tubes,'' Journal of Enhanced Heat Transfer, **4**, pp. 53–70.

[2] Shome, B., and Jensen, M. K., 1996, ''Numerical Investigation of Variable Property/Mixed Convection Laminar Flow in Internally-Finned Tubes,'' Journal of Enhanced Heat Transfer, **4**, pp. 35–51.

[3] Bergles, A. E., Jensen, M. K., and Shome, B., 1995, ''Bibliography on Enhancement of Convective Heat and Mass Transfer,'' Heat Transfer Lab. Report-23, Rensselaer Polytechnic Institute, Troy, New York.

[4] Liu, X., 1998, ''Investigation of Turbulent Flow and Heat Transfer in Internally Finned Tubes,'' Ph.D. thesis, Rensselaer Polytechnic Institute, Troy, New York.

[5] Carnavos, T. C., 1979, ''Cooling Air in Turbulent Flow with Internally Finned Tubes,'' Heat Transfer Eng., **1**, No. 2, pp. 41–46.

[6] Carnavos, T. C., 1980, ''Heat Transfer Performance of Internally Finned Tubes in Turbulent Flow,'' Heat Transfer Eng., **1**, No. 4, pp. 32–37.

[7] Jensen, M. K., and Vlakancic, A., 1999, ''Experimental Investigation of Turbulent Heat Transfer and Fluid Flow in Internally Finned Tubes,'' Int. J. Heat Mass Transf., **42**, pp. 1343–1351.

[8] Liu, X., and Jensen, M. K., 1999, ''Numerical Investigation of Turbulent Flow and Heat Transfer in Internally Finned Tubes,'' Journal of Enhanced Heat Transfer, **6**, pp. 105–119.

[9] Trupp, A. C., Lau, A. C. Y., Said, M. N. A., and Soliman, H. M., 1981, ''Turbulent Flow Characteristics in an Internally Finned Tube,'' Advances in Heat Transfer-1981, ASME, HTD-18, pp. 11–19.

[10] Edwards, D. P., Hirsa, A., and Jensen, M. K., 1996, ''Turbulent Air Flow in Longitudinally Finned Tubes,'' ASME J. Fluids Eng., **118**, pp. 506–513.

[11] Patankar, S. V., Ivanovic, M., and Sparrow, E. M., 1979, ''Analysis of Turbulent Flow and Heat Transfer in Internally Finned Tubes and Annuli,'' ASME J. Heat Transfer, , **101**, pp. 29–37.

[12] Said, M. N. A., and Trupp, A. C., 1984, ''Predictions of Turbulent Flow and Heat Transfer in Internally Finned Tubes,'' Chem. Eng. Commun., **31**, pp. 65–99.

[13] Edwards, D. P., and Jensen, M. K., 1994, ''An Investigation of Turbulent Flow and Heat Transfer in Longitudinally Finned Tubes,'' Heat Transfer Lab. Report HTL-18, Rensselaer Polytechnic Institute, Troy, New York.

[14] Kelkar, K. M., 1997, ''Numerical Method for The Computation of Flow in Irregular Domains That Exhibit Geometric Periodicity Using Nonstaggered Grids,'' Numer. Heat Transfer, Part B, **31**, pp. 1–21.

[15] Kern, D. Q., and Kraus, A. D., 1972, *Extended Surface Heat Transfer*, McGraw-Hill Book Company, New York.

[16] Patankar, S. V., Liu, C. H., and Sparrow, E. M., 1977, ''Fully Developed Flow and Heat Transfer in Ducts Having Streamwise-Periodic Variations of Cross-Sectional Area,'' ASME J. Heat Trasfer, , **99**, pp. 180–186.

[17] Norris, L. H., and Reynolds, W. C., 1975, ''Turbulent Channel Flow With a Moving Wavy Boundary,'' Report. FM-10, Department of Mechanical Engineering, Stanford University, CA.

[18] *STAR-CD Manuals*, 1998, Computational Dynamics, Co., London, U.K.

[19] Vlakancic, A., 1996, ''Experimental Investigation of Internally Finned Tube Geometries on Turbulent Heat Transfer and Fluid Flow,'' M.S. thesis, Rensselaer Polytechnic Institute, Troy, New York.

[20] Gnielinski, V., 1976, ''New Equations for Heat and Mass Transfer in Turbulent Pipe and Channel Flow,'' Int. Chem. Eng., **16**, pp. 359–368.

New Theory for Forced Convection Through Porous Media by Fluids With Temperature-Dependent Viscosity

Arunn Narasimhan

José L. Lage
e-mail: jll@seas.smu.edu

Laboratory for Porous Materials Applications,
Mechanical Engineering Department,
Southern Methodist University,
Dallas, TX 75275-0337, USA

Donald A. Nield
Department of Engineering Science,
University of Auckland,
Private Bag 92019,
Auckland, New Zealand

A theoretical analysis is performed to predict the effects of a fluid with temperature-dependent viscosity flowing through an isoflux-bounded porous medium channel. For validation purposes, the thermo-hydraulic behavior of this system is obtained also by solving numerically the differential balance equations. The conventional procedure for predicting the numerical pressure-drop along the channel by using the global Hazen-Dupuit-Darcy (HDD) model (also known as the Forchheimer-extended Darcy model), with a representative viscosity for the channel calculated at maximum or minimum fluid temperatures, is shown to fail drastically. Alternatively, new predictive theoretical global pressure-drop equations are obtained using the differential form of the HDD model, and validated against the numerical results. Heat transfer results from the new theory, in the form of Nusselt numbers, are compared with earlier results for Darcy flow models (with and without viscosity variation), and validated by using the numerical results. Limitations of the new theory are highlighted and discussed. [DOI: 10.1115/1.1409268]

Keywords: Analytical, Forced Convection, Heat Transfer, Porous Media, Viscous

Introduction

Recent texts on porous media that devote chapters on forced convection [1,2], general reviews on forced convection [3,4], and reviews specific to the use of permeable material to enhance forced convection [5], reveal the almost universal invocation of the uniform viscosity assumption in analyzing forced convection through porous media.

While strong interest in channel forced convection of clear fluids with temperature-dependent viscosity has generated several studies (e.g., [6,7]), not much attention has been given to the porous media counterpart of the problem. This is particularly surprising when considering the potential heat transfer enhancement of using permeable media in convection heat transfer.

Driven by the several contemporary engineering applications, from cooling of electronics [8,9] to porous journal bearings [10–12], the fundamental analysis of convection through porous media by fluids with temperature-dependent viscosity is a necessary foundation in support of new designs and the optimization of existing ones.

Ling and Dybbs [13] presented a pioneering theoretical investigation of the temperature-dependent fluid viscosity influence on the forced convection through a semi-infinite porous medium bounded by an isothermal flat plate. The fluid viscosity was modeled as an inverse linear function of the fluid temperature, the flow model followed the Darcy equation, and the results showed a very strong influence of temperature-dependent viscosity on the heat transfer from the flat plate.

Nield et al. [14] have presented a theoretical analysis of a similar configuration (parallel-plates channel, with isoflux heated surfaces, and fully developed velocity profile), also invoking the Darcy equation. Their analysis also showed an increase in the heat transfer coefficient along the channel, as a result of the temperature-dependent viscosity.

The simplified approach in [13,14], by invoking the Darcy equation (viscous-drag effect only), however, limits the scope of their analysis for neglecting the form-drag effects imposed by a porous medium. Hence, their results and main conclusions are restricted to cases in which the form-drag effect of the porous medium is minimal (such as for tube-bundle-like porous media), or for cases in which the fluid temperature does not change much along the flow direction (i.e., the plate temperature should not be very different from the fluid inlet temperature, or the channel heat flux should not be too high).

Numerical simulations considering the convection through a parallel-plates porous channel, and including the form-drag effects, was presented recently by Narasimhan and Lage [15]. In this work, the authors show the limitations of the global Hazen-Dupuit-Darcy (HDD) model (popularly known as the Forchheimer-extended Darcy model) in accurately predicting the pressure-drop along the channel, suggesting a modification to account for the temperature-dependent viscous effects. They also showed that the HDD model is inappropriate for neglecting indirect effects of temperature-dependent viscosity on the form-drag term of the model, a term originally believed to be viscosity-independent.

The objective of the present study is to establish a new theory for predicting the global pressure-drop and the heat transfer coefficient of a fluid, with temperature-dependent viscosity, convecting through a heated porous medium channel. The importance of the present theory is fundamental for studying the effects of variations in a constitutive property. It is also vital for the design engineer to anticipate the thermo-hydraulic behavior of similar systems enhanced with porous media and running fluids with temperature dependent viscosity (observe that most fluids, including water, have viscosity strongly dependent on temperature).

Physical Model and Theoretical Analysis

Consider the forced convection of a fluid with temperature-dependent viscosity $\mu(T)$ through a low-permeability, high form-coefficient porous medium sandwiched between two parallel isoflux surfaces, spaced by a distance $2H$, as shown in Fig. 1. The

Contributed by the Heat Transfer Division for publication in the JOURNAL OF HEAT TRANSFER. Manuscript received by the Heat Transfer Division September 29, 2000; revision received May 20, 2001. Associate Editor: J. Georgiadis.

channel has length L, and the fluid enters the channel with uniform temperature T_0, and uniform longitudinal speed U_0.

The differential mass, momentum and energy transport equations are, respectively,

$$\nabla \cdot \mathbf{u} = 0 \tag{1}$$

$$0 = -\nabla p - \left[\frac{\mu(T)}{K_0}\right]\mathbf{u} - \rho C_0 |\mathbf{u}|\mathbf{u} \tag{2}$$

$$\rho c_p \mathbf{u} \cdot \nabla T = k_e \nabla^2 T. \tag{3}$$

Quantities are defined in the nomenclature. The subscript "0" on the porous medium properties K and C reminds us that these quantities are obtained under isothermal condition. In this case, the fluid viscosity is uniform throughout the channel, $\mu(T) = \mu(T_{\text{in}}) = \mu_{\text{in}}$. Notice also the absence of the convective inertia and Brinkman terms in the momentum equation, Eq. (2), in accordance with the low permeability (K_0) and high form-coefficient (C_0) porous medium assumption made previously.

Assume now that the flow is fully developed, i.e., $\partial u/\partial x = 0$. When combined with the continuity equation, Eq. (1), and the impermeable boundary condition at the channel surface, we obtain $v = 0$. Therefore, the momentum equation, Eq. (2), written with $G = -\partial p/\partial x$, becomes

$$C_0 \rho K_0 u^2 + \mu(T) u - G K_0 = 0. \tag{4}$$

The energy equation, Eq. (3), with the assumption of negligible longitudinal conduction (or high Péclet number), reduces to,

$$\frac{\partial^2 T}{\partial y^2} = \frac{\rho c_p}{k_e} u \frac{\partial T}{\partial x}. \tag{5}$$

For fully developed flow, $\partial T/\partial x = dT_b/dx$. Invoking the first law of Thermodynamics, Eq. (5) can be rewritten as

$$\frac{\partial^2 T}{\partial y^2} = \left(\frac{u}{U}\right)\frac{q''}{k_e H}. \tag{6}$$

Keep in mind to solve Eq. (6) we need to determine the ratio u/U, where U is the cross-section averaged fluid speed. The quadratic equation given by Eq. (4) when solved for u will result in a positive root, which will be a function of $\mu(T)$ with a solution resembling

$$u = F(\mu(T)). \tag{7}$$

The temperature dependency of the dynamic viscosity of the fluid can be approximated as a second-order Taylor's series expansion enabling us to express the RHS of Eq. (7) as,

$$F(\mu(T)) = F(\mu_r) + F'(\mu_r)(\mu - \mu_r) + \frac{1}{2}F''(\mu_r)(\mu - \mu_r)^2, \tag{8}$$

where μ_r is the reference viscosity value, evaluated at $T = T_r$. Expanding the individual terms in Eq. (8) as functions of temperature, we get

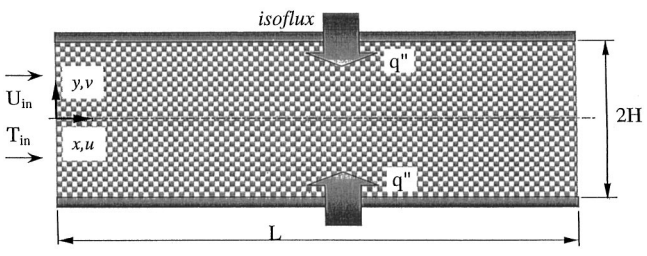

Fig. 1 Schematic of the flow channel considered for investigation

$$F(\mu(T)) = F(\mu_r) + F'(\mu_r)\mu_r'(T - T_r) + \frac{1}{2}[F'(\mu_r)\mu_r'' + F''(\mu_r)\mu_r'^2](T - T_r)^2. \tag{9}$$

By substituting for $F(\mu(T))$ in Eq. (7), we can get progressively, the zero, first, and second-order solutions for u when we use, respectively, the first, the first and second, or all the terms of Eq. (9).

The zero-order result, i.e., for $F(\mu(T)) = F(\mu_r)$, Eq. (8), corresponds to the uniform viscosity case where $u = U_0$. Hence, from Eq. (4),

$$G = \frac{\mu_r}{K_0} U_0 + C_0 \rho U_0^2. \tag{10}$$

Moreover, the energy equation, Eq. (5), can be rewritten as

$$\frac{\partial^2 T}{\partial y^2} = \frac{1}{H k_e}\left(\rho U_0 H c_p \frac{\partial T}{\partial x}\right). \tag{11}$$

Now, using the first law of Thermodynamics

$$\rho U_0 H c_p \frac{dT_b}{dx} = k_e q'', \tag{12}$$

where the fluid bulk-temperature is defined as

$$T_b = \frac{1}{UH}\int_0^H u T dy \tag{13}$$

and with $\partial T/\partial x = dT_b/dx$, one can show that the RHS term in parentheses of Eq. (11) equals $k_e q''$. Therefore, integrating Eq. (11) in y, with $\partial T/\partial y = 0$ at $y = 0$ and $T = T_w$ at $y = H$ as boundary conditions, we get the zero-order temperature distribution

$$T_0 = T_w - \frac{q'' H}{2k_e}\left[1 - \left(\frac{y}{H}\right)^2\right]. \tag{14}$$

So, upon substitution for T in Eq. (13), the fluid bulk-temperature becomes,

$$T_b = T_w - \frac{q'' H}{3k_e} \tag{15}$$

and, the local Nusselt number, defined for isoflux parallel-plate channel ([2], p. 62) as

$$\text{Nu} = \frac{2Hq''}{k_e(T_w - T_b)} \tag{16}$$

turns out to be equal to 6. This value remains unchanged along the channel for fluids with constant and uniform viscosity.

Now, to determine the first-order solution we need to find a suitable expression for $(T - T_r)$ in the second term of Eq. (8). Implicit in the way Eq. (9) is written, is the assumption that the reference temperature T_r is always higher than T. Therefore, a natural candidate for T_r is the wall temperature T_w. Using the zero-order solution for T, Eq. (14), and T_w for T_r, in Eq. (9), allows us to evaluate u in Eq. (7) as

$$u_1 = a_1 + \frac{a_2 N}{2}\left[1 - \left(\frac{y}{H}\right)^2\right], \tag{17}$$

where a_1, a_2, and N are defined as

$$a_1 = \frac{GK_0}{2\mu_w}\left[\frac{-1 + \sqrt{1 + 4\zeta}}{\zeta}\right]$$

$$a_2 = \frac{GK_0}{2\mu_w \zeta}\left[1 - \frac{1}{\sqrt{1 + 4\zeta}}\right] \quad N = \frac{q'' H}{k_e}\frac{1}{\mu_w}\left(\frac{d\mu}{dT}\right)_{T_w} \tag{18}$$

with

$$\zeta = \frac{\rho C_0 K_0^2 G}{\mu_w^2}. \tag{19}$$

It is then possible to integrate Eq. (17) along y, to find the cross-section averaged fluid speed,

$$U_1 = a_1 + \frac{a_2 N}{3}. \tag{20}$$

Using Eqs. (17) and (20) in Eq. (6), we find the first-order temperature distribution as

$$T_1 = T_w - \frac{q''H}{k_e}\left\{\frac{1}{2}\left(1-\frac{y^2}{H^2}\right) + \frac{a_2 N}{a_1}\left[\frac{1}{12}\left(1-\frac{y^2}{H^2}\right) - \frac{1}{24}\left(1-\frac{y^4}{H^4}\right)\right]\right\}. \tag{21}$$

Upon similar use of Eq. (21), we get from Eq. (7) the second-order solutions as

$$u_2 = a_1 + \frac{a_2 N}{2}\left[1-\left(\frac{y}{H}\right)^2\right] + \left[\frac{a_2^2 N^2}{24 a_1} + \frac{1}{8}(a_3 N^2 - a_2 M)\right] \times \left[1-\left(\frac{y}{H}\right)^2\right]^2 \tag{22}$$

$$U_2 = a_1 + \frac{a_2 N}{3} + \frac{a_2^2 N^2}{45 a_1} - \frac{a_2 M}{15} + \frac{a_3 N^2}{15} \tag{23}$$

$$T_2 = T_w - \frac{a_1}{U_2}\Omega_1(y) - \frac{a_1 q'' H}{U_2 k_e}\left[\frac{1}{24}\left(\frac{a_2 N}{a_1}\right)^2 - \frac{a_2 M}{8 a_1} + \frac{a_3 N^2}{8 a_1}\right]\Omega_2(y), \tag{24}$$

where the Ω_1 and Ω_2 of Eq. (24) are

$$\Omega_1(y) = T_w - \frac{q''H}{k_e}\left\{\frac{1}{2}\left(1-\frac{y^2}{H^2}\right) + \frac{a_2 N}{a_1}\left[\frac{1}{4}\left(1-\frac{y^2}{H^2}\right) - \frac{1}{24}\left(1-\frac{y^4}{H^4}\right)\right]\right\}$$

$$\Omega_2(y) = \left[\frac{1}{2}\left(1-\frac{y^2}{H^2}\right) - \frac{1}{6}\left(1-\frac{y^4}{H^4}\right) + \frac{1}{30}\left(1-\frac{y^6}{H^6}\right)\right] \tag{25}$$

and a_3 and M are defined as

$$a_3 = \frac{2GK_0}{\mu_w (1+4\zeta)^{3/2}} \quad M = \left(\frac{q''H}{k_e}\right)^2 \frac{1}{\mu_w}\left[\frac{d^2\mu}{dT^2}\right]_{T_w}. \tag{26}$$

The corresponding first and second-order Nusselt numbers, upon using Eq. (13), are given, respectively, by

$$\mathrm{Nu}_1 = 6\left[1-\frac{2a_2 N}{15 a_1}\right] \tag{27}$$

and

$$\mathrm{Nu}_2 = \mathrm{Nu}_1 + 6\left[\frac{68 a_2^2 N^2}{1575 a_1^2} + \frac{4}{105 a_1}(a_2 M - a_3 N^2)\right]. \tag{28}$$

Finally, to complete the solution, one must find a proper value for the wall temperature T_w for calculating the viscosity and its derivatives in Eqs. (18), (19), and (26). Accounting for the fact that the chosen T_w must be higher than the maximum fluid temperature anywhere in the channel, we must use the wall-temperature at $x=L$, $T_w(L)=T_{\max}$. This temperature can be found by integrating Eq. (12) along x (from 0 to L) and combining the result with Eq. (15) (for $x=L$), that is

$$T_w(L) = q''\left(\frac{1}{\rho c_p U H} + \frac{H}{3k_e}\right) + T_0 \tag{29}$$

Observe that the accuracy of the zero-order approximation of $F(\mu(T))$, from Eq. (8), is inversely proportional to $\mu_r'(T-T_r)$, and of the first-order approximation inversely proportional to $[\mu_r'(T-T_r)]^2/2$ and $[\mu_r''(T-T_r)^2]/2$. Two requirements can be written then, using Eq. (14), as

$$\frac{q''H}{2k_e}\frac{1}{\mu_w}\left|\frac{d\mu}{dT}\right|_{T_w} = \frac{|N|}{2} \ll 1 \quad \frac{1}{2}\left(\frac{q''H}{2k_e}\right)^2 \frac{1}{\mu_w}\left[\frac{d^2\mu}{dT^2}\right]_{T_w} = \frac{M}{8} \ll 1. \tag{30}$$

The first requirement, when valid, indicates that the zero-order approximation is accurate. The second requirement, together with the square of the first, when valid, indicates that the first-order approximation is accurate.

Validation

Notice when the form-drag coefficient C_0 is negligible then $\zeta \to 0$. In this case, from Eq. (18), $a_1 = a_2 \to GK_0/\mu_w$ and the first-order solutions of Eqs. (20) and (27) reduce to

$$U = \left(\frac{\Delta P}{L}\right)\frac{K_0}{\mu(T_{\max})}\left[1+\frac{N}{3}\right] \tag{31}$$

$$\mathrm{Nu} = 6\left(1-\frac{2}{15}N\right). \tag{32}$$

These results are identical to the results reported in [14], who developed a similar predictive theory for a fluid with temperature-dependent viscosity, but starting with the linear Darcy flow regime, i.e., Eq. (4) replaced by $u=[K_0/\mu(T)]G$.

Observe that N, Eq. (18), is a negative number for fluids with viscosity decreasing with increasing temperature. Equation (31) predicts a higher cross-section averaged longitudinal fluid speed than the Darcy model with uniform viscosity evaluated at T_{in}, for which $U=K_0\Delta P/(L\mu_{\mathrm{in}})$, because T_{in} is the minimum fluid temperature along the channel.

In order to validate the theoretical analysis further, numerical simulations were performed for the configuration of Fig. 1, using Eqs. (1)–(3). Details of the numerical procedure (tested for grid independence and numerical accuracy) can be found in [15]. Important specific parameters are: the distance between the plates $2H=10$ cm, the length of the heated section $L=1$ m, dimensional inlet fluid velocity U_{in} from 10^{-2} m/s to 10^{-1} m/s, and the heat flux q'' from 0.01 to 0.10 MW/m^2. These values were chosen to highlight the effect of temperature-dependent viscosity on the thermo-hydraulic behavior of the system under temperature-dependent viscosity.

The numerical simulations consider further the fluid as being Poly-α-olefins (PAOs), low molecular weight, branched, synthetically produced, saturated hydrocarbons that have lubrication properties superior to that of naturally occurring mineral oil. This has led to the wide-spread use of PAOs in a variety of applications, ranging from industrial lubrication to high grade synthetic motor oil basestock to cooling military avionics [14,16–18].

Fluids (such as PAOs, motor-oils, synthetic lubricants etc.) whose viscosity are dependent on temperature are modeled using different relations [19,20] involving power, logarithmic [16] or exponential functions [21], yielding better accuracy over different temperature ranges. The dynamic viscosity of PAOs can be modeled from the data in [22] as

$$\mu(T) = 0.1628\, T^{-1.0868} \tag{33}$$

valid for $5°\mathrm{C} \leq T \leq 170°\mathrm{C}$. Within the same temperature range, the variations of density, specific heat and thermal conductivity of PAO are negligible.

Obviously, results of the theoretical analysis presented here are not restricted by this fluid selection, as the theory in principle is valid for any functional dependence of viscosity on temperature.

The inlet temperature T_{in} of the PAO is chosen as 21°C, yielding $\mu_{\text{in}}=5.95\times10^{-3}$ kg/ms, $\rho=768.5$ kg/m^3, $c_p=1971.35$ J/kg°C, and $k_f=0.1424$ W/m°C. Our hypothetical porous matrix has $\phi=0.58$, $K_0=4.1\times10^{-10}$ m^2 and $C_0=1.2\times10^5$ m^{-1}. These values are representative of practical values obtained from isothermal (non-heating) experiments utilizing an aluminum foam having $k_s=170$ W/m°C, as reported in [18].

Results and Discussion

Figure 2 shows a comparison between the theoretical predictions and the results from the numerical simulations for $q''=0.01$ MW/m^2 (the lowest heat flux considered). The simplest theoretical predictions are obtained first from the HDD model,

$$\frac{\Delta P}{L}=\frac{\mu(T_r)}{K_0}U+C_0\rho U^2 \tag{34}$$

assuming the following:

$$(1)\quad \mu(T_r)=\mu_r=\mu(T_{\text{in}})=\mu(T_{\min})$$

$$(2)\quad \mu(T_r)=\mu_r=\mu(T_w(L))=\mu(T_{\max})$$

These two options are plotted in Fig. 2. They are, respectively, the lower-bound and upper-bound limits for the fluid speed U, with a fixed pressure-drop $\Delta P/L$ along the channel, because they are calculated using the minimum, T_{in}, and maximum, $T_w(L)$, temperatures attained by the fluid along the channel. Any other temperature chosen, *viz.* simple average between the inlet and exit bulk temperatures of the fluid, log-mean difference of the same, or a longitudinal average of the bulk temperatures for the entire channel, will fall between these two limits [15].

Observe that the result from the HDD model using a viscosity evaluated at the minimum (inlet) temperature, is independent of the heat flux (thereby, of variation in temperature inside the channel) thus representing both no-heating and uniform viscosity situations.

The analyses carried out on the unidirectional, differential HDD model, Eq. (4), as presented in this paper, leads to a theory that improves on the lower-bound velocity results predicted by Eq. (34). From Fig. 2, we can observe that the first and second-order solutions, Eqs. (20) and (23), predict velocities that compare extremely well with the numerical results.

Also plotted in the same figure is the theoretical prediction of the linear model, from Eq. (31). Observe that the predicted pressure-drop, for a given fluid speed, is smaller than the pressure-drop predicted from Eq. (20) and (23). This is expected from a model that does not include the form-drag effects.

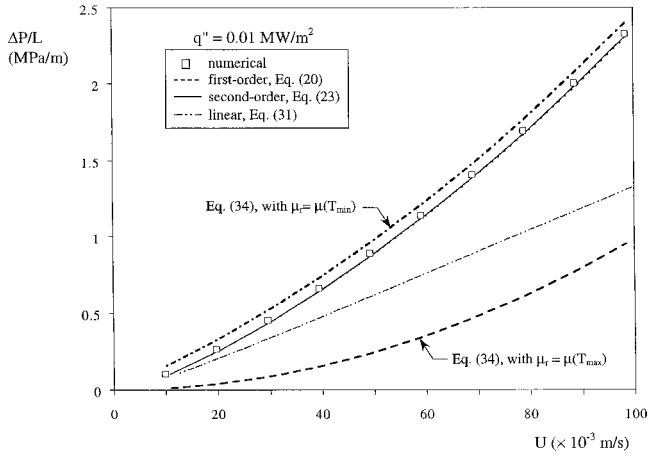

Fig. 2 Theoretical and numerical pressure-drop versus fluid-speed results for $q''=0.01$ MW/m^2

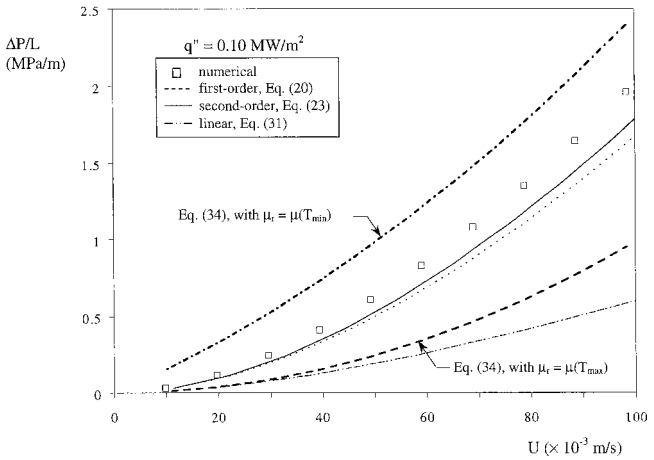

Fig. 3 Theoretical and numerical pressure-drop versus fluid-speed results for $q''=0.10$ MW/m^2

Figure 3 presents similar results, but for $q''=0.10$ MW/m^2 (maximum heat flux). A careful comparison of Figs. 2 and 3 indicates that the curve obtained from Eq. (34) with $\mu(T_r)=\mu(T_{\max})$ is unchanged when the heat flux increases. This is somewhat surprising because $T_{\max}$ certainly changes (increases) with the heat flux. The results indicate, however, that the fluid temperature is irrelevant to the fluid-speed versus pressure-drop relation Eq. (34), and this happens only when the viscous-drag effect is negligible as compared with the form-drag effect (which is viscosity independent). Our conclusion is that $T_{\max}$, even for the low heat flux considered in Fig. 2, is already high enough to yield a negligible viscous-drag. In this regard, the curves for $\mu(T_r)=\mu(T_{\max})$ from Eq. (34), presented in Figs. 2 and 3, are indeed the lower-bound curves for pressure-drop versus fluid-speed, when the form-drag effect is accounted for.

When the form-drag effect is ignored, as in the linear model based on the Darcy equation, Eq. (31), the decrease in pressure-drop with heat flux has no limit. See in Fig. 3 how the curve from Eq. (31) lies below the curve obtained by Eq. (34) with $\mu(T_r)=\mu(T_{\max})$. This is analogous to the Hagen-Poiseuille flow configuration, or to flow through a porous medium with zero form-factor C_0.

In contrast to Fig. 2, the agreement between first-order, second-order, and numerical results is not so good in Fig. 3. We can now see the improvement in going from first-order to second-order analysis. The deviation between first-order results and the numerical results is either because of the inaccuracy of the first-order truncation or from the fully developed flow assumption.

To establish the accuracy of the first-order approximation, we must consider the square of $|N|/2$ and $M/8$, Eq. (30). Within the fluid velocity ranges considered here, Fig. 4 shows $|N|/2$ and $M/8$ approaching unity for increasing heat flux, thereby invalidating the criterion. This observation corroborates the discrepancy between first- and second-order results of Fig. 3 (when the heat flux is high). In a similar fashion, examining the accuracy of the second-order approximation in Fig. 3, we require the terms of a third-order approximation, which are proportional to $(|N|/2)^3$ and $(M|N|/16)$, to be very small. The results of Fig. 4 satisfy this. Thereby, it seems that the discrepancy between second-order and numerical results stems from the fully developed flow assumption.

Figure 5 shows the local velocity variation $u(y)$ predicted by the linear model ([14], developed from Eq. (4) with $C_0=0$), and the second-order HDD model, Eq. (22), results for $q''=0.01$, 0.05, and 0.10 MW/m^2, respectively. Also shown is the velocity profile for the no-heating case ($q''=0$), labeled $\mu=\mu_{\text{in}}$. All curves are

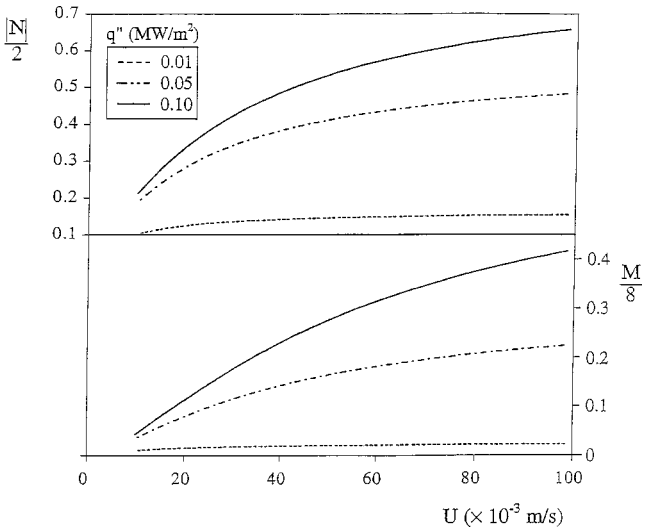

Fig. 4 Verification of the two criteria for accurate zero-order (top) and first-order (bottom) approximation results, Eq. (30)

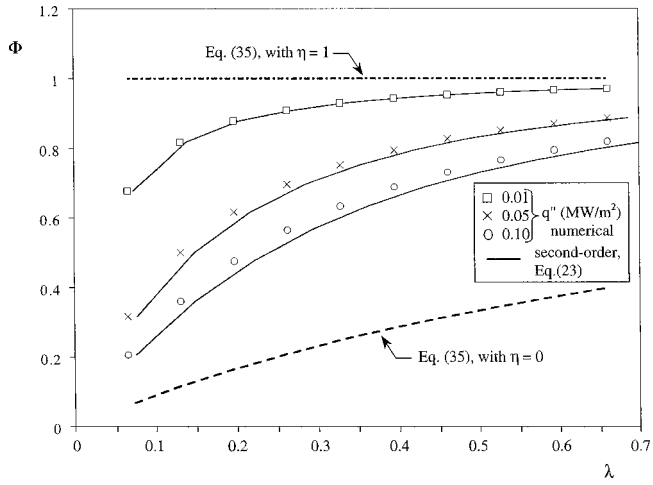

Fig. 6 Summary of longitudinal pressure-drop obtained by second-order HDD theory, Eq. (23), with numerical results for several heat fluxes

obtained with the same pressure-drop G, equivalent to $U=9.84\times10^{-2}$ m/s when the channel is not heated. Increased fluid speed is expected when heating the channel.

Considering the fact that the linear model neglects the influence of the form-drag term, the fluid velocity profile is expected to follow the temperature profile, having a maximum velocity at the wall (where viscosity is minimum because the temperature is maximum) and decreasing progressively towards the axis of the channel. This is clearly depicted in Fig. 5.

The second-order HDD model result for $q''=0.01$ MW/m^2, however, indicates a slug-flow profile, with a reduction in the fluid speed (as compared to the linear fluid speed) caused by the form-drag effect. This makes the curvature of the velocity profile (as predicted by the linear Darcy theory) to flatten near the walls, as indicated in Fig. 5.

When the heat flux is increased, the second-order HDD model results indicate a pronounced velocity increase of the fluid near the channel surface. This aspect shows the influence of viscosity variation on the viscous-drag. The variation in viscosity reduces the viscous-drag to a greater extent near the wall, where the reduction in viscosity (because of the higher temperature) is more dramatic. This is captured perfectly by the second-order HDD theory, as evident from Fig. 5.

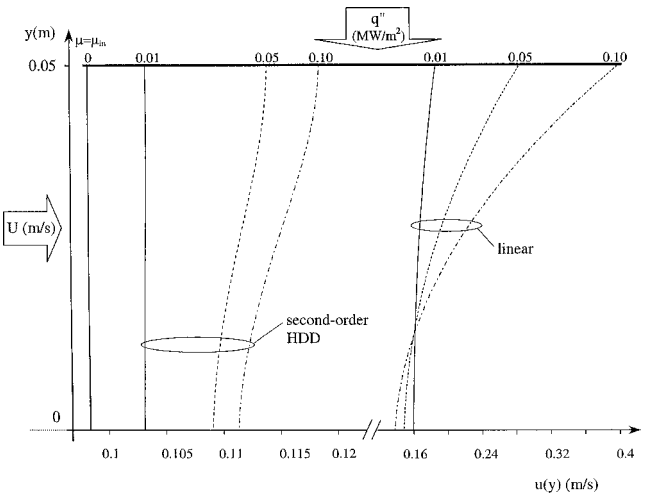

Fig. 5 Velocity profiles $u(y)$ from second-order HDD theory (left side profiles) and linear theory (right side profiles) for several heat fluxes

The hydrodynamic effect of varying the surface heat flux q'' is presented in Fig. 6, using the non-dimensional parameters

$$\lambda=\frac{D_C}{D_\mu}=\left(\frac{\rho C_0 K_0}{\mu_{\text{in}}}\right)U_{\text{in}} \quad \Phi=\frac{(\Delta P/L)}{(D_C+D_\mu)}, \tag{35}$$

where $D_C=\rho C_0 U_{\text{in}}^2$ represents the global form-drag and $D_\mu=\mu_{\text{in}}U_{\text{in}}/K_0$ represents the global viscous-drag (with viscosity evaluated at the inlet fluid temperature). Observe that by using these two nondimensional variables, the HDD model Eq. (34) can be rewritten as

$$\Phi=\left(\frac{\eta}{\lambda+1}\right)+\left(\frac{\lambda}{\lambda+1}\right), \tag{36}$$

where $\eta=\mu(T_r)/\mu_{\text{in}}$.

Notice in Eq. (35), the scale chosen for non-dimensionalizing the pressure-drop, namely $(D_\mu+D_C)$, clearly highlights the viscosity variation effect as it compares the pressure-drop got by considering viscosity variation to that for uniform viscosity (recall from Eq. (34) that $(D_\mu+D_C)$ equals $\Delta P/L$ for the case of a fluid flowing with uniform viscosity equal to μ_{in}).

From Fig. 6, it is evident that the second-order HDD theory predicts extremely well the effect of viscosity on the global longitudinal pressure-drop versus fluid-speed relation. Even for high heat fluxes (when the accuracy of the theory is known to deteriorate because of the considerable variation of temperature along the channel), the predicted results from the theory still compare surprisingly well with the numerical results.

Next, we explore how the viscosity variation affects the heat transfer in the channel. Temperature profiles, similar in style and corresponding to the second-order velocity profiles in Fig. 5, are shown in Fig. 7, obtained from Eq. (24). For the flow of a fluid with decreasing viscosity for increasing temperature, we deduced from Fig. 5, that increasing the heat flux increases the local velocity near the wall relative to that at the axis. This results in an increase in the curvature of the temperature profile near the wall and a corresponding decrease towards the axis, resulting in a net flattening of the entire profile, as shown in Fig. 7.

In Fig. 8, a comparison between the temperature profile obtained from the linear model of [14] and the profile predicted by the second-order HDD model is presented.

Nusselt numbers from the linear model, Eq. (32), and from the second-order HDD model Eq. (28), are compared in Fig. 9. Also

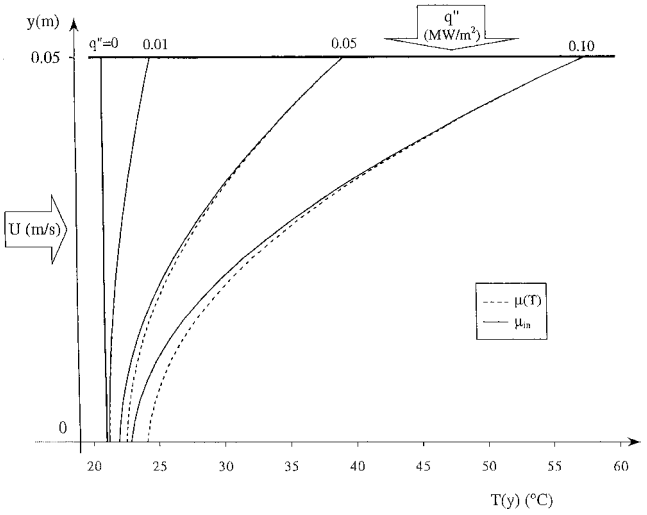

Fig. 7 Comparison of temperature profiles from second-order HDD theory, Eq. (24), with those of uniform viscosity case, for several heat fluxes

shown in the figure is the curve Nu=6, for the case of a fluid with uniform viscosity μ_{in}. Recall that the fluid bulk-temperature and the reference (maximum wall) temperature, on which Eqs. (28) and (32) are based, are both functions of the fluid speed.

From Fig. 9, the linear model, Eq. (32), yields a Nusselt number that increases with the fluid speed (represented by λ) and the heat flux. This is a consequence of the increased fluid bulk-temperature estimated by this model as the fluid speed and/or the heat flux increase. Remember that the predicted velocity distribution parallels the temperature distribution. Therefore, the high fluid temperature adjacent to the heated surface has more significance in the computation of the bulk-temperature than the low temperature near the center of the channel.

The Nusselt number predicted by the linear model, Eq. (32), is higher than the Nusselt number predicted by the second-order HDD model, Eq. (28). This is a direct consequence of the inclusion, by the second model, of the form-drag effect, which leads to a smaller fluid speed. Moreover, according to the profiles of Fig. 8, the temperature values predicted by the second-order HDD model are smaller than the values predicted by the linear model.

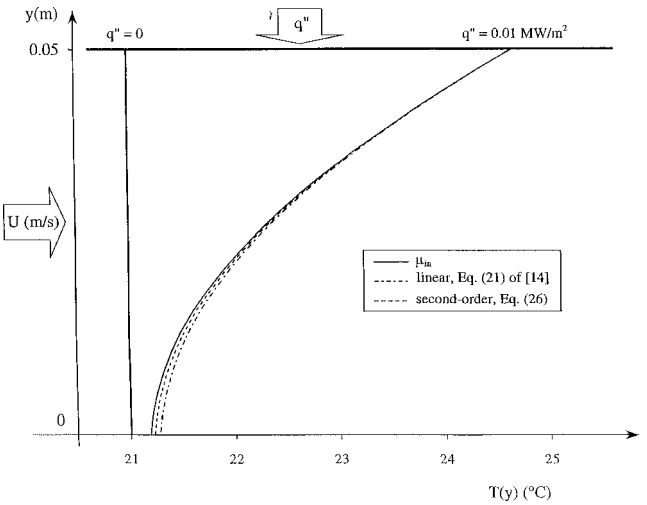

Fig. 8 Temperature profiles from second-order HDD theory and linear theory for $U_{\max}=9.84\times10^{-2}$ m/s, and $q''=0.01$ MW/m²

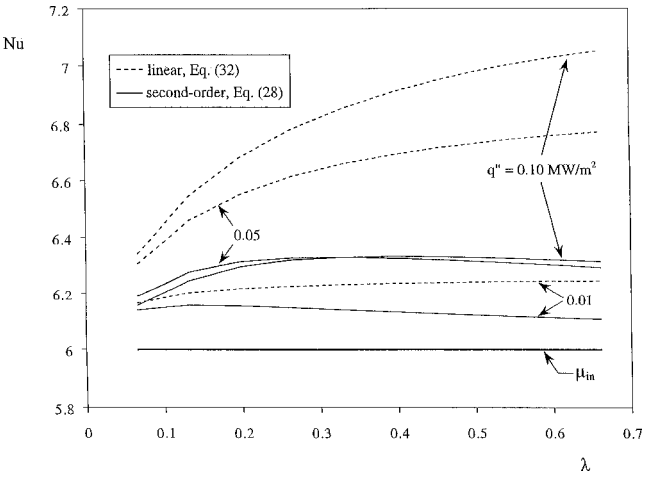

Fig. 9 Comparison of Nusselt numbers obtained by the two theories as a function of λ, for several heat fluxes, q'' (MW/m²)

Therefore, the fluid bulk-temperature found using the second-order HDD model is smaller than that of the linear model.

As the fluid speed increases, and consequentially the viscous-drag decreases in importance as compared with the form-drag, one would expect the Nu number to evolve towards Nu=6. This curious aspect, of a decreasing Nu as the fluid speed increases, is also captured well by the results from the second-order model, Eq. (28), shown in Fig. 9.

Even for fully developed flow assumption, the theory presented here predicts a Nu dependent on the fluid speed still invariant in x. However, a real situation with undeveloped flow has local Nusselt number varying in *x*. This fact makes the comparison between these two Nusselt numbers less effective and cumbersome, as the comparison in principle should be done for all fluid speeds considered. An instructive alternative is to consider a variant Nusselt number, namely

$$\text{Nu}_L=\frac{2Hq''}{k_e[\overline{T}_w-T_{\text{in}}]} \tag{37}$$

and relating it to the previous Nusselt number through

$$\text{Nu}_L=\frac{1}{\left(\dfrac{1}{\text{Nu}}+\dfrac{\gamma}{\lambda\,\text{Pr}_e}\right)}. \tag{38}$$

In Eqs. (37) and (38), $\overline{T}_w$ is the surface averaged wall temperature of the channel, $\gamma=LK_0C_0(2H)^2$ and $\text{Pr}_e=\mu_{\text{in}}c_p/k_e$.

Equation (38), obtained by integrating Eq. (16) in *x*, and relating the resulting channel-averaged T_b to T_{in} via the first law, Eq. (12), subsumes the *x*-dependency of Nu, therefore making the comparison with results from developing flow configurations straightforward.

The results plotted in Fig. 10 demonstrate that the theoretical results are very accurate for λ smaller than 0.3. Observe that Nu_L is relatively insensitive to the inclusion of the form-drag effect (linear or second-order HDD) as opposed to what happens in the pressure-drop versus fluid speed, Fig. 2. Moreover, the results of Fig. 10 demonstrate that the fully developed assumption behind the second-order HDD model affects the accuracy of the thermal results much more than it affects the accuracy of the hydraulic results.

Summary and Conclusions

A new theory for predicting the thermo-hydraulic effect on fully-developed convection by a fluid with temperature-dependent viscosity flowing through a porous medium channel is presented.

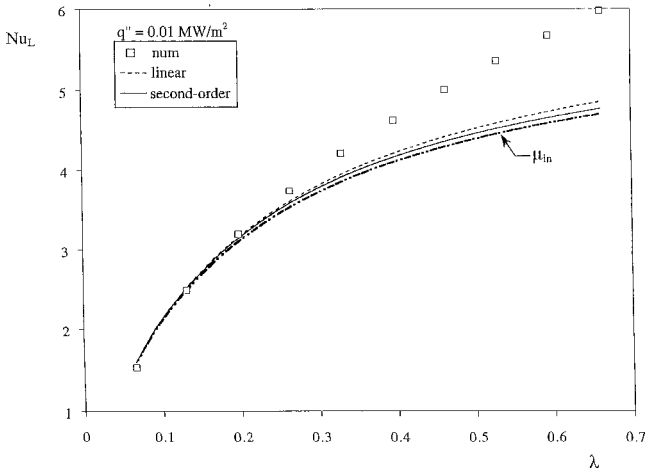

Fig. 10 Comparison of Nu_L, Eq. (38), obtained from theoretical results with numerical results

The theory incorporates the form-drag effect of the porous medium by invoking the differential representation of the Hazen-Dupuit-Darcy (HDD) equation. Zero, first, and second-order approximations are obtained for the transversal fluid speed and temperature, as well as for the global fluid-speed versus pressure-drop relation and Nusselt number.

The HDD model predictions are shown to be limited in accuracy by the truncation-error and by the assumption of fully developed flow. There might be practical situations in which the development length is very long for scalar transport in a porous medium (e.g., low effective thermal diffusivity). Criteria for evaluating the second-order truncation error are presented and evaluated.

The theoretical predictions are compared with results from a simpler linear (Darcy) model and with numerical results simulating the operation of a realistic porous medium enhanced cold-plate, running poly-alpha-olefin, designed for cooling military avionics. The comparisons show that the second-order HDD model predictions agree well with the hydraulic simulation results as opposed to the linear model and is physically consistent.

A new Nusselt number is introduced to compare the heat transfer results of the second order HDD theory (in the form of local Nusselt number that depends on fluid speed) with real-life situations. The comparison shows that the fully developed assumption behind the second-order HDD model affects the accuracy of the thermal results much more than it affects the accuracy of the hydraulic results.

Nomenclature

C = form coefficient, m^{-1}
D = specific drag, Pa m^{-1}
H = half-channel spacing, m
K = permeability, m^2
L = channel length, m
p = macroscopic pressure, Pa
P = global (cross-section averaged) pressure, Pa
Pr_e = effective Prandtl number
u = x-component, seepage macroscopic velocity, m s^{-1}
U = global (cross-section averaged) longitudinal velocity, m s^{-1}
$\mathbf{u}$ = seepage macroscopic velocity vector
v = y-component, seepage macroscopic velocity, m s^{-1}

Greek Symbols

ϕ = porosity
η = viscosity ratio, Eq. (36)
λ = form- and viscous-drag ratio, Eq. (35)
Φ = dimensionless pressure-drop, Eq. (35)

Subscripts

b = bulk
e = effective
f = fluid
r = reference
w = wall
in = inlet
μ = viscous

References

[1] Kaviany, M., 1991, *Principles of Heat Transfer in Porous Media*, Springer-Verlag, NY.
[2] Nield, D. A., and Bejan, A., 1999, *Convection in Porous Media*, 2nd ed., Springer-Verlag, NY.
[3] Lauriat, G., and Vafai, K., 1991, "Forced Convective Flow and Heat Transfer Through a Porous Medium Exposed to a Flat Plate or a Channel," *Convective Heat and Mass Transfer in Porous Media*, S. Kakaç et al., eds., Kluwer, Dordrecht, pp. 289–327.
[4] Lauriat, G., and Ghafir, R., 2000, "Forced Convective Heat Transfer in Porous Medium," *Handbook of Porous Media*, K. Vafai, ed., Marcel-Dekker, NY, pp. 201–268.
[5] Lage, J. L., and Narasimhan, A., 2000, "Porous Media Enhanced Forced Convection: Fundamentals and Applications," *Handbook of Porous Media*, K. Vafai, ed., Marcel-Dekker, NY, pp. 357–394.
[6] Xie, C., and Hartnett, J. P., 1992, "Influence of Variable Viscosity of Mineral Oil on Laminar Heat Transfer in a 2:1 Rectangular Duct," Int. J. Heat Mass Transf., **35**, pp. 641–648.
[7] Shin, S., Cho, Y. I., Gringrich, W. K., and Shyy, W., 1993, "Numerical Study of Laminar Heat Transfer With Temperature Dependent Fluid Viscosity in a 2:1 Rectangular Duct," Int. J. Heat Mass Transf., **36**, pp. 4365–4373.
[8] Lage, J. L., Weinert, A. K., Price, D. C., and Weber, R. M., 1996, "Numerical Study of a Low Permeability Microporous Heat Sink for Cooling Phased-Array Radar Systems," Int. J. Heat Mass Transf., **39**, pp. 3633–3647.
[9] Antohe, B. V., Lage, J. L., Price, D. C., and Weber, R. M., 1997, "Experimental Determination of Permeability and Inertia Coefficients of Mechanically Compressed Aluminum Porous Matrices," ASME J. Fluids Eng., **119**, pp. 404–412.
[10] Anjani, K., and Rao, N. S., 1994, "Stability of a Rigid Rotor in Turbulent Hybrid Porous Journal Bearings," Tribol. Int., **27**, pp. 299–305.
[11] Kumar, A., 1998, "Conical Whirl Instability of Turbulent Flow Hybrid Porous Journal Bearings," Tribol. Int., **31**, pp. 235–243.
[12] Lin, J. R., and Hwang, C. C., 1994, "Static and Dynamic Characteristics of Long Porous Journal Bearings: Use of the Brinkman-Extended Darcy Model," J. Phys. D, **27**, pp. 634–643.
[13] Ling, J. X., and Dybbs, A., 1992, "The Effect of Variable Viscosity on Forced Convection over a Flat Plate Submersed in a Porous Medium," ASME J. Heat Transfer, **114**, pp. 1063–1065.
[14] Nield, D. A., Porneala, D. C., and Lage, J. L., 1999, "A Theoretical Study, With Experimental Verification of the Viscosity Effect on the Forced Convection Through a Porous Medium Channel," ASME J. Heat Transfer, **121**, pp. 500–503.
[15] Narasimhan, A., and Lage, J. L., 2001, "Modified Hazen-Dupuit-Darcy Model for Forced Convection of a Fluid With Temperature-Dependent Viscosity," ASME J. Heat Transfer, **123**, pp. 31–38.
[16] Kioupis, L. I., and Maginn, E. J., 1999, "Molecular Simulation of Poly-α-olefin Synthetic Lubricants: Impact of Molecular Architecture on Performance Properties," J. Phys. Chem. B, **103**, pp. 10781–10790.
[17] Lage, J. L., Price, D. C., Weber, R. M., Schwartz, G. J., and McDaniel, J., 1999, *Improved Cold Plate Design for Thermal Management of Phased Array Radar Systems*, US Patent Office, Patent no. 5960861.
[18] Lage, J. L., Antohe, B. V., and Nield, D. A., 1997, "Two Types of Nonlinear Pressure-Drop Versus Flow-Rate Relation Observed for Saturated Porous Media," ASME J. Fluids Eng., **119**, pp. 700–706.
[19] White, F. M., 1991, *Viscous Fluid Flow*, 2nd ed., McGraw Hill, NY.
[20] Darby, R., 1996, *Chemical Engineering Fluid Mechanics*, Marcel-Dekker, NY.
[21] Maginn, E. J., 1999, private communications.
[22] Chevron, 1981, *Synfluid Synthetic Fluids*, Physical Property Data.

On the Thermal Interaction Between an Isothermal Cylinder and Its Isothermal Enclosure for Cylinder Rayleigh Numbers of Order 10^4

D. T. Newport
e-mail: david.newport@ul.ie

T. M. Dalton

M. R. D. Davies

PEI Technologies: Stokes Research Institute,
Dept. Mechanical & Aeronautical Engineering,
University of Limerick,
Limerick, Ireland

M. Whelan

C. Forno

Institute for Systems, Informatics
& Safety, Joint Research Center,
European Commission,
Ispra, Italy

An experimental investigation is made of the thermal interaction between a horizontal isothermal cylinder centrally located in a water-cooled isothermal cubical enclosure. The study is restricted to laminar flow and cylinder Rayleigh numbers of order 10^4. The application of interest is the cooling of electronic systems. This field is currently lacking in techniques that can measure the complex fluid phenomena encountered in real systems. The paper therefore begins with an experimental review of interferometry to assess its applicability as a potential solution to this need. Based on this review, a real time Digital Moiré Subtraction interferometer is used to measure temperature profiles, and local Nusselt number distributions in two regions of interest: the plume impingement on the ceiling of the enclosure, and the upper corner region of the enclosure. A Mach-Zehnder interferometer is used for the cylinder Nusselt number distribution. Results are compared both qualitatively and quantitatively with a numerical simulation run on a commercial CFD package widely used for electronic system temperature predictions. The paper gives considerable insight into the nature of the enclosure heat transfer and an indication of the accuracy of a widely used predictive code. [DOI: 10.1115/1.1389467]

Keywords: Enclosure Flows, Heat Transfer, Interferometry, Measurement Techniques, Natural Convection

Introduction

The transfer of heat from heated bodies in an enclosed environment is of considerable practical importance, particularly in the field of electronics cooling. There have been numerous investigations in the literature. Warrington and Powe [1] presented a Nusselt number correlation for spheres, cylinders and cubes in an isothermal cubical enclosure and review the literature to that date. They note the predominance of experimental investigations and a lack of applicability of numerical investigations. Numerical predictions have become more prevalent since the mid-eighties: Shaw et al. [2] carried out a numerical investigation into free convection from isolated thermal sources on an adiabatic surface located in a square enclosure. Ghaddar [3] presented a numerical prediction for heat transfer from a cylinder in a large air-filled rectangular enclosure. Dalton and Davies [4] compared numerical and experimental plume velocities and temperatures for a horizontal cylinder in an isothermal cubical enclosure. Keyhani and Dalton [5] obtained good comparison between experimental and numerical data for the Nusselt number from horizontal rod bundles in a rectangular enclosure. Liu et al. [6] numerically examined the coupled conduction convection problem for a cylinder in an enclosure and determined the majority of the heat transfer to occur through the bottom half of the cylinder. Purely experimental investigations also continued, such as Koizuimi and Hosokawa [7] who studied the effect of the enclosure on heat transfer about a horizontal isothermal cylinder in a cubical enclosure. They identify three flow regimes, steady, unsteady and oscillatory, dependent on a cylinder to enclosure aspect ratio. Cesini et al. [8] performed a holographic investigation into the influence of Rayleigh number and geometry on the heat transfer from a horizontal cylinder in a cubical enclosure.

Experimental difficulties arise in obtaining flow field information when more complex three-dimensional systems are considered, leading to a dependence on numerical investigations. Some numerical investigations are not compared to experimental data, such as Lasance [9], and Shaw et al. [2], presumably owing to the difficulties associated with experimentation. Those that do attempt a comparison very often compare parameters such as the overall Nusselt number, or temperatures at discrete locations, which does not necessarily validate the full field. There is therefore a requirement for a measuring technique to provide data in complex free convection flows.

Optical techniques coupled with developments in tomography appear to offer the best means of developing such a technique. Their advantage is that non-intrusive full field information is obtained, rather than at discrete points. The paper begins with a critical review of interferometry to examine the suitability of interferometric techniques for development as a three-dimensional measurement method.

Working on the findings of the review, an optical investigation is made into one of the simplest of geometries, the horizontal isothermal cylinder in the center of an isothermal cubical enclosure, where the cylinder is sufficiently long for the flow to be considered two dimensional. Attention is focused on three areas of interest: the region about the cylinder, the plume impingement on the roof of the enclosure, and the upper corner region of the enclosure, to gain an understanding of the heat transfer process to the enclosure. Because the particular application of interest is the cooling of electronic components, the cylinder and enclosure length scales are typical of those found in such applica-

Contributed by the Heat Transfer Division for publication in the JOURNAL OF HEAT TRANSFER. Manuscript received by the Heat Transfer Division January 31, 2000; revision received March 8, 2001. Associate Editor: R. W. Douglass.

tions. A CFD comparison is made using Flotherm which is a commercial package widely used in electronic system temperature prediction.

Experimental Review of Interferometry

As stated earlier, optical techniques offer a non-intrusive means of obtaining full field temperature measurements, are particularly useful in gaining an insight into the physics of the flow, and for comparison with CFD predictions. This review is restricted to two dimensional measurements, but the work could be extended to three dimensions by using tomographic techniques. The purpose of this review is to examine the applicability of interferometry for qualitative and quantitative measurement of temperature fields in enclosure free convection. Of particular interest is the ability to measure low gradient regions accurately, to have a large field of view, and to be able to measure in real-time. Ostrach [10] noted how enclosure free convection is particularly complex due to the interaction between the boundary layers and the regions external to them, which have small temperature gradients. It is therefore important that such regions can be studied without fringe errors. Such errors occur when fringes due to optical inhomogenities are interpretated as being caused by the measurand. A large field of view is also important to provide a systems level perspective. Finally, it is desirable to have a real-time system so that unsteady and transient flows, which are often encountered in enclosure free convection, can be studied.

In the review, two interferometers are considered, the Michelson and Mach-Zehnder, and three optical techniques are employed: Infinite Fringe Mode, Digital Phase Stepping and Digital Moiré Subtraction. First a brief introduction to the operating principles of interferometry is provided.

An interferometer essentially comprises of a collimated coherent light beam which is split into two or more beams and then re-combined. Changes in the optical path length along a beam, or arm, result in the formation of an interference pattern in the re-combined beam. The change in optical path length can be related to numerous physical quantities. This investigation is concerned solely with temperature.

For a two dimensional system, the change in path length is related to the refractive index of the phase object via,

$$\Delta\Phi = \int_0^L (n - n_0)\,dz = N\lambda. \tag{1}$$

For the case where the change in refractive index is due to a change in density of the phase object, as in free convection, the Gladstone-Dale equation,

$$n - n_0 = K(\rho - \rho_0), \tag{2}$$

relates the two. Integrating (1), and combining with (2) gives,

$$\rho_N - \rho_0 = \frac{N\lambda}{KL}. \tag{3}$$

The perfect gas law,

$$p = \rho RT, \tag{4}$$

may be used to determine the fringe temperatures, provided changes in density due to pressure are negligible to those due to temperature. This is a reasonable assumption for free convection and low Mach number forced flows. The above simple analysis assumed that the refractive index did not vary in the z-direction. If a variation is present in the z-direction, the average of that change is taken in the integration. The analysis can be extended to three dimensions by incorporating tomographic algorithms. This requires a minimum of two beam traverses of the measurement volume at different angles, and consequently increases the level of complexity of the interferometric arrangement. It should be noted however that many three-dimensional heat transfer problems do not lend themselves readily to tomographic evaluation due to the obstruction caused by solid heated elements.

The Michelson Interferometer. Developed in 1881, the Michelson Interferometer has found application in the investigation of the structures of spectrum lines, the definition of the meter in terms of light wavelengths, the testing of optical components, the investigation of weak spectra using Fourier Transform Spectrometry, and most famously in the Michelson-Morley ether experiment. In recent years, the interferometer has found application in space, locating stars of similar size to the sun, and Jupiter sized planets. Barton et al. [11] recently developed a fibre optic Michelson interferometer for measuring pressure and temperature. However, there is little evidence in the literature of the Michelson interferometer being used for the measurement of free convection temperature fields, despite widespread use of the very similar Mach-Zehnder interferometer.

Figure 1 shows a schematic of the setup used. Experimental details are given in the next section. A collimated coherent light source is passed through a beam-splitter which divides the beam into a reference and a measurement beam. Each beam is reflected back along the path travelled by mirrors, and then recombined at the beam-splitter and focused to a CCD camera connected to a PC and video recorder. The advantages of the Michelson interferometer include its relatively straightforward alignment, and a minimum of optical components, thereby reducing the cost. As with other interferometer configurations, it is susceptible to vibration and must be mounted on an optical table. Such tables are commercially available although satisfactory isolation can be obtained using a heavy table mounted on tyres.

Figure 2 shows an interferogram of the horizontal isothermal cylinder at $Ra = 7.1 \times 10^3$, corresponding to a temperature difference of 11.5°C. The Michelson interferometer is twice as sensitive than the similar Mach-Zehnder interferometer, which can be see by comparing the number of fringes present in Figs. 2 and 5. Figure 5 is taken at a higher temperature difference, but has less fringes than Fig. 2. This is because the measurement beam, having passed through the test section, is reflected back along it, before being recombined with the reference beam. Although a good sensitivity is desirable for measurements involving small temperature differences, a disadvantage of the double-pass nature is the poor focus on either the fringes or the heated body. In Fig. 2 the cylinder is in poor focus. This is because the fringes are localized on the apparent position of intersection of the two mirrors, which

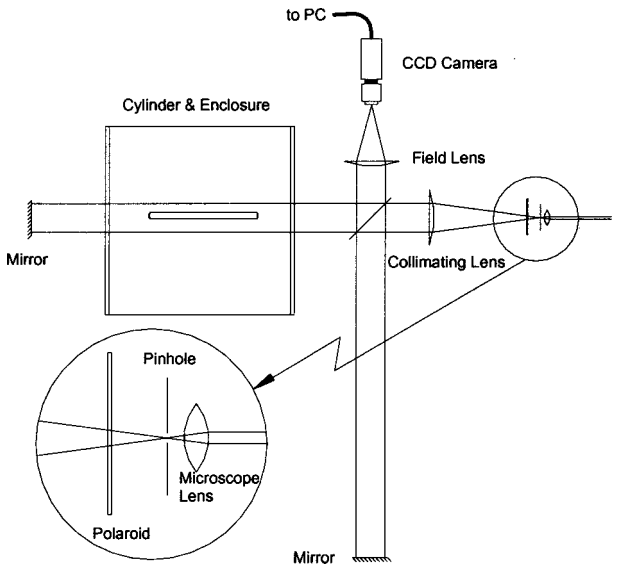

Fig. 1 Schematic of the Michelson interometer

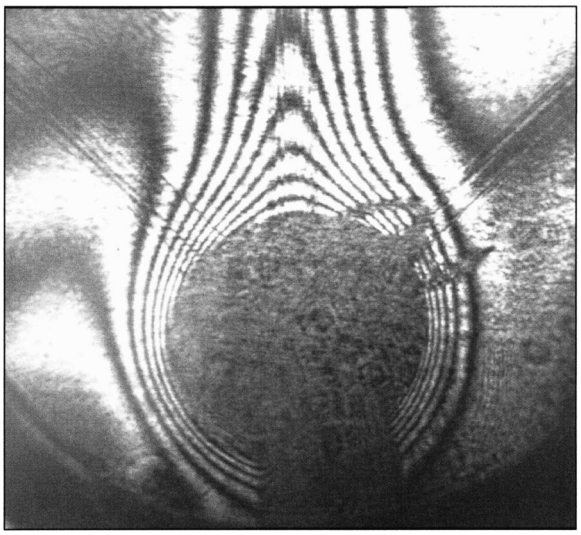

Fig. 2 Sample interferogram of a horizontal isothermal cylinder at Ra=7.1×10^3

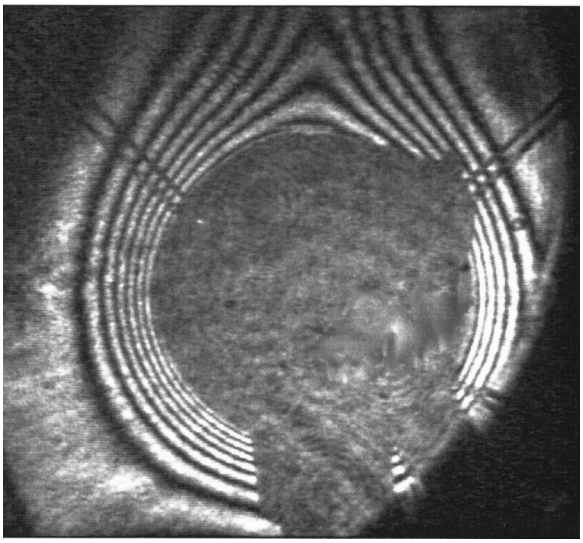

Fig. 5 Mach-Zehnder interferogram of a horizontal cylinder at Ra=1.04×10^4

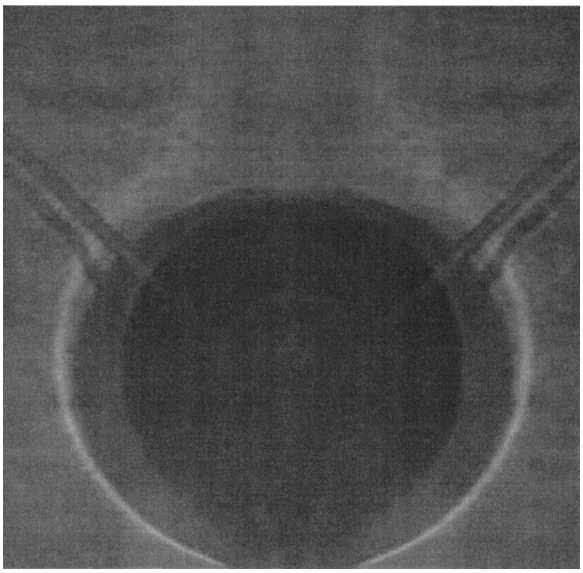

Fig. 3 Refraction effects in the Michelson interferometer

differs from that of the cylinder. Thus it is not possible to focus on the fringes and cylinder simultaneously. This is of particular consequence in determining the fringe locations.

Another disadvantage of the Michelson interferometer arising from the double-pass is its susceptibility to refraction, which occurs when a light ray traveling along the length of the heated body is deflected by the refractive index field. Figure 3 shows refraction in a Michelson interferometer along a 20 mm diameter, 300 mm long heated horizontal cylinder due to a temperature difference of 50°C. The reference beam of the interferometer has been blocked off for clarity. The distance of the white band from the cylinder surface indicates the extent to which the light passing alongside the cylinder has been deflected. In this example, the deflection is approximately 20 percent of the cylinder diameter. A consequence of this is that the temperatures within this band cannot be measured, even though such temperatures are very often the objective of the investigation in heat transfer applications.

The Mach-Zehnder Interferometer. The Mach-Zehnder interferometer, developed independently by Mach and Zehnder in 1891, has found widespread application in the measurement of

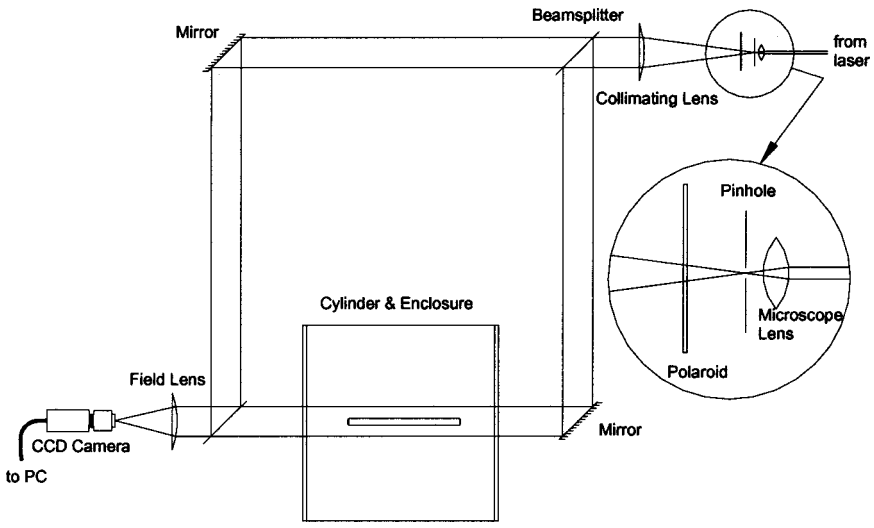

Fig. 4 Schematic of Mach-Zehnder interferometer

free convection temperature fields, with a considerable body of work amassed in the literature over the years. A review is not carried out here due to space restrictions, but the interested reader may wish to refer to Hauf and Grigull [12], Goldstein [13], or Merzkirch [14].

Figure 4 shows a schematic of the interferometer configuration used. The main difference to Fig. 1 is that the measurement beam passes through the test section only once. It is considerably more difficult to align than the Michelson, but it is possible to focus on the heated object and fringes simultaneously.

Figure 5 shows an interferogram of a horizontal cylinder at $Ra = 1.04 \times 10^4$, corresponding to a temperature difference of 18.9°C. The reduced sensitivity is apparent by the number of fringes compared to Fig. 2, again due to the measurement beam passing through the test region only once. This also renders the Mach-Zehnder less sensitive than the Michelson to refraction effects. Note also the better focus on the fringes and cylinder.

Infinite Fringe Mode. Both interferometer configurations were run in the infinite fringe mode, where the fringes correspond directly to isotherms in the flow field. However, high quality and therefore expensive optical equipment is required to eliminate fringe errors due to wave-front distortion as the light passes through the optics of the interferometer. The lower left region of Fig. 2 shows an example. The error is inversely proportional to the number of fringes present. In regions of small temperature gradients, in which one or two fringes may be present, this error can be significant. The size of an interferometer operating in infinite fringe mode is severely restricted by the cost of the optical equipment which exhibit an exponential dependence on size. Thus interferometers with large fields of view are not economically viable.

Digital Phase Stepping. Digital phase stepping interferometry (DPSI), provides a means of obtaining full field information in the form of a coloured contour plot, and offers an excellent means of comparing experimental data to CFD predictions. Phase Stepping involves shifting an interferogram over a number of steps, and employing an algorithm which determines the phase at each pixel, and results in a contour plot of the phase distribution, which may be directly correlated to the temperature of the system. Creath [15] provides a detailed discussion of the theory.

In this investigation the phase stepping was performed by mounting one of the mirrors on a piezo-electric driver. The piezo-driver was calibrated and controlled using a custom-built software package from the Joint Research Center, which also extracted the phase information from the process.

Figure 6 shows an example of the contour plot obtained from phase stepping a horizontal isothermal cylinder, at $Ra = 1.21 \times 10^4$, with temperatures ranging from 26.1°C (blue) to 47.0°C (red). The result is very poor, particularly in the region of the plume. This can be attributed to an oscillation of the plume, which was observed to oscillate at approximately 1 Hz. The frequency response of the phase stepping process is considerably less than this, therefore the interferogram could not be phased stepped sufficiently fast. It took approximately five seconds in the present investigation to obtain the images based on a three step algorithm. Thus to avail of DPSI, the measured field must be steady, or have oscillations with frequencies very much lower than the response of the stepping driver.

Digital Moiré Subtraction. A Moiré pattern can be produced in an interferometer by tilting one of the mirrors to give wedge fringes, and subtracting the undisturbed pattern from the disturbed pattern. Alternatively, the disturbed and undisturbed interferograms may be superposed. The resulting Moiré interferogram is free from fringe errors due to poor quality optics. This facilitates the development of large cheap interferometers and allows regions of small temperature gradients to be studied.

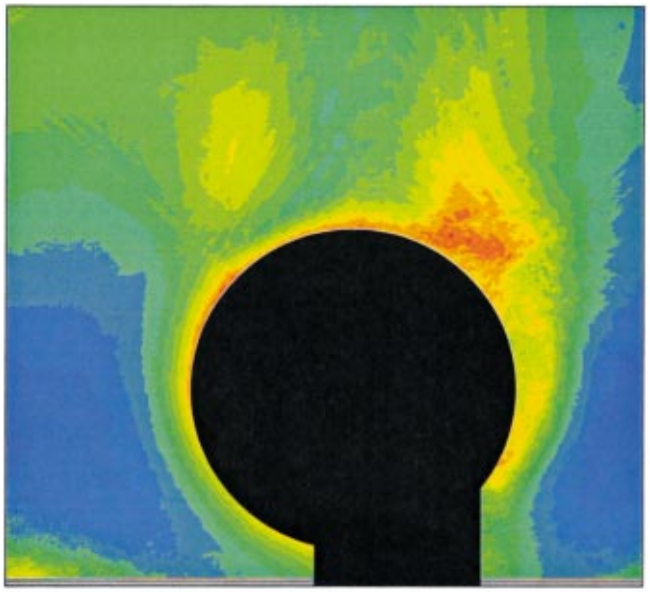

Fig. 6 Phase-stepped horizontal cylinder

Goldstein [13] superposed a disturbed interferogram over an undisturbed for a vertical flat plate in free convection. Yokozeki and Mihara [16] developed an almost real-time method employing a standard video system. A novel aspect of the present work is that a real-time digital Moiré subtraction technique, developed by Forno and Whelan [17], is applied to free convection temperature measurement. This allows regions of small temperature gradients to be investigated without fringe errors due to poor quality optics.

Figure 7(*c*) shows an example of the resulting Moiré pattern of a plume from a horizontal cylinder impinging on the upper surface of the cylinder enclosure, obtained by subtracting (*b*) from (*a*). The subtraction was performed in real-time using an Electronic Speckle Pattern Interferometry (ESPI) software package and a Mach-Zehnder interferometer arrangement. A disadvantage is that there is a reduction in the quality of the fringes. The quality of the fringes is a dependent on the number of fringes used to produce the Moiré pattern. It is hoped to develop a system in which the Moire pattern fringes will be sufficiently fine as not to be discernible to the eye, and thereby lead to fringes of similar quality to those that can be obtained with Infinite Fringe Mode.

Experimentation

Having experimentally reviewed different interferometric techniques, an optical investigation was carried out into the thermal interaction between an isothermal cylinder and its isothermal cubical enclosure. Details of this investigation are now presented.

A 20 mm diameter 300 mm long aluminum cylinder was suspended in the center of a 470 mm sided water cooled cubical aluminum enclosure. Optical access was gained by replacing two sides of the enclosure with glass panels, as shown in Fig. 8. The cylinder was heated with two N&P 300 W 9.5 mm diameter 150 mm long cartridge heaters. The cylinder and enclosure temperatures were measured using welded tip T-type thermocouples, connected to a Stanford Research Systems SR630 16 Channel Thermocouple Reader, with built-in electronic reference temperature. The thermocouples and reader were calibrated using a Lauda RM6 Calibration Fluid Bath accurate to 0.07°C over a −32°C to 152°C range.

Attention focused on three areas of interest: the region about the cylinder, the region of the plume impingement on the upper interior surface of the enclosure, and the upper corner region of the enclosure. On the basis of the preceding section, it was decided to employ a Mach-Zehnder interferometer in the Infinite

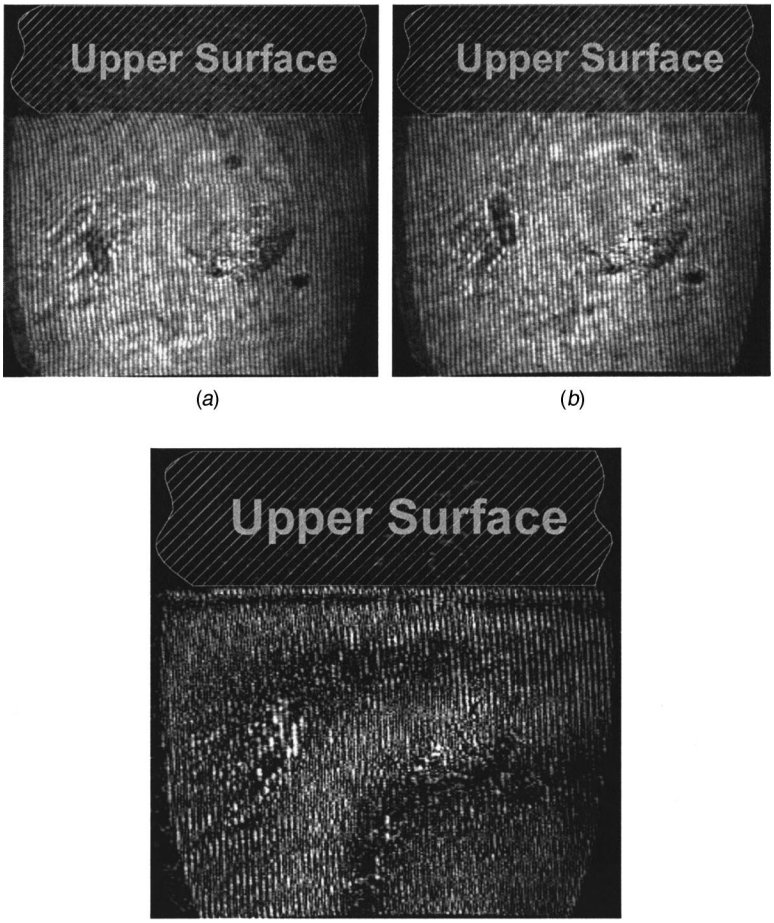

Fig. 7 Obtaining a Moiré interferogram for a plume impinging on the upper interior surface of an enclosure: (*a*) disturbed pattern; (*b*) initial pattern; and (*c*) plume impinging on upper surface of enclosure.

Fringe Mode to examine the region about the cylinder. For the corner and plume impingement regions a Mach-Zehnder interferometer with Digital Moiré Subtraction was preferable because of the small temperature gradients expected in these regions.

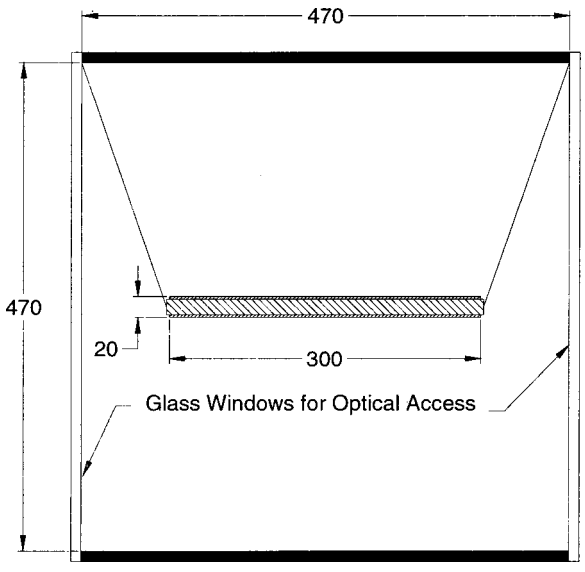

Fig. 8 Detail of geometry used in experimentation

A schematic of the interferometer is shown in Fig. 4. Light from a 60mW Helium-Neon laser was collimated and spatially filtered. The mirrors and beam-splitters were 51 mm in diameter. To prevent vibrations, all experimentation was carried out on a Newport MST series optical bench with Newport XL-A pneumatic isolation. A Pulnix CCD camera connected to a PC and video recorder was used to acquire the interferograms. Custom built software from the Joint Research Center was used to perform the Digital Moiré Subtraction in real time. The system was considered steady-state when the cylinder temperature varied by less than 0.1°C within half an hour. Typically, this was of the order of three hours. Unsteady flows were recorded on video and sampled using Matrox Intellicam v 2.0.

Fringe locations were determined digitally using Adobe Photoshop v. 4.0. Fringe temperatures were calculated relative to a reference fringe, whose temperature was measured with a T-type thermocouple calibrated to 0.1°C. Data was taken for four Rayleigh numbers, varied with the cylinder to enclosure temperature difference. Air was used as the working fluid. Local Nusselt number measurements were made at 30 deg intervals about one side of the cylinder, as the fringe pattern appeared symmetrical about a vertical plane through the cylinder, subject to observed 10 deg oscillations in the lateral displacement of the fringes at the upper cylinder stagnation point. The local Nusselt number was derived from the measured temperature distribution. Time averaged local Nusselt numbers were also measured in the impingement and corner regions.

Table 1 Experimentally measured temperature boundary conditions applied in each of the four numerical models

Model	T_{cyl} (°C)	T_e (°C)	Ra
I	37.2	26.0	6.80×10^3
II	44.0	26.1	1.04×10^4
III	62.6	28.1	1.66×10^4
IV	77.2	28.3	2.18×10^4

Numerical Model

The model was created and solved using Flotherm version 2.1, from Flomerics. Flotherm employs a finite volume method, described by Patankar [18] and Ferziger and Peric [19], which has first order accurate upwinding for the convective terms, second order for the diffusive terms, and a transient integration of first order. Because the solver uses a Cartesian co-ordinate system, it is not possible to create a curved surface in the model. Dalton and Davies [4], who compared plume measurements from a horizontal isothermal cylinder to the corresponding Flotherm version 1.4 prediction, constructed their cylinder out of cubical elements called cuboids, and prisms. Prisms require a heat transfer coefficient, which was unknown and therefore set to zero. This would usually result in zero heat transfer and a trivial solution. However, grid cells intersected the prism and were in contact with the interior cuboid surfaces, facilitating heat transfer. Flomerics [20] discuss this. Curved surfaces can be constructed in Flotherm version 2.1, but must be adiabatic, and are therefore of little use for the present geometry. In the present work it was decided to construct the cylinder out of cuboids, with an area factor applied to the *x* and *y* directions. A close-up of the model of the cylinder is shown in Figure 10, which illustrates the construction of the cylinder.

Grid cell aspect ratios were kept below twenty, as recommended by Flomerics [21]. Four models were run with temperature boundary conditions measured from the experimental investigation, shown in Table 1.

Figure 9 shows the grid arrangement used in the models. A two dimensional grid of 11,172 grid cells was used. The grid density was increased in the region near the cylinder, the plume region,

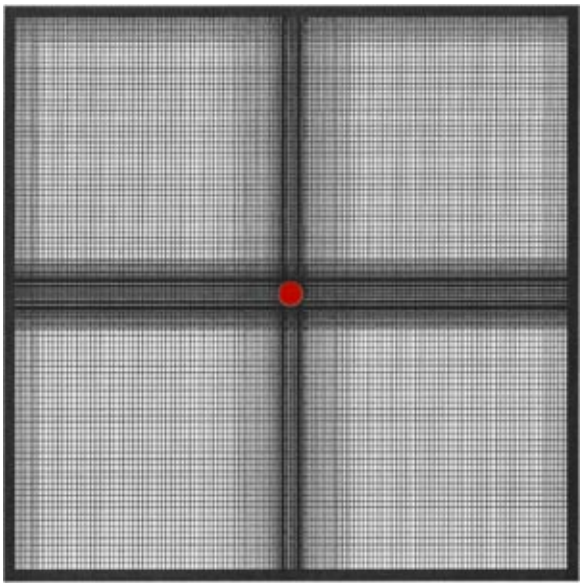

Fig. 9 Geometry and solver grid of numerical model

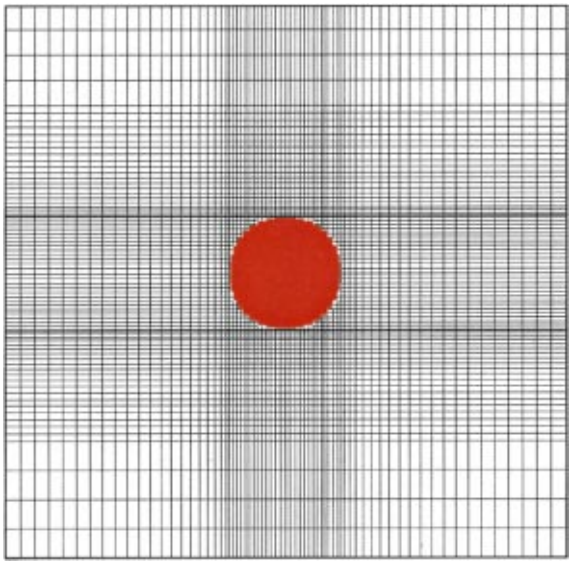

Fig. 10 Example of gridding about the cylinder. Shows the cuboid construction of the cylinder.

and the enclosure ceiling and side-walls. To check for grid independence, the number of grid cells was increased to 18,480 and 30,076, and the frequency and amplitude of the oscillation of the temperature and *x* velocity component was monitored at a point midway between the cylinder and the enclosure ceiling.

The flow was modelled as Boussinesq, with the thermophysical properties evaluated at the film temperature. Bejan [22] cites the universal Grashof number for transition as being of order 10^9. The local Grashof number in the plume is of this order, therefore an unsteady laminar model was employed. Experimental observations of the temperature field in the region of the plume impingement on the ceiling of the enclosure verified that the flow was unsteady, but not turbulent in this region. The solution was run for a transient time of 240 seconds in steps of 0.33 s, and data was time averaged over a twenty second period after this. Monitor points in the solution domain were used to verify that the flow was developed by the 240 s. Times to convergence were typically eight hours on a Pentium II 350 MHz PC with 256 MB RAM operating on a Windows NT platform.

Because Flotherm does not calculate local Nusselt numbers directly, these were calculated from the temperature field near the surface of interest. The temperature profile is theoretically linear near the wall, therefore the local Nusselt number can be determined from

$$\mathrm{Nu} = \frac{D}{(T_{\mathrm{cyl}} - T_e)} \left(\frac{T - \mathrm{Te}}{\Delta} \right), \tag{5}$$

where Δ is a small distance from the surface.

Results and Discussion

In this section, results of the optical and numerical investigations are presented, compared and discussed.

Figure 11 shows a comparison of the optical and numerical isotherms about the cylinder. The agreement is excellent, except in the lower left hand region of the interferogrames where a fringe localisation error is present. This is because of a difference in the optical path lengths travelled by the reference and measurement beams, due to the quality of the optical components used in the investigation. The error is seen to diminish as the number of

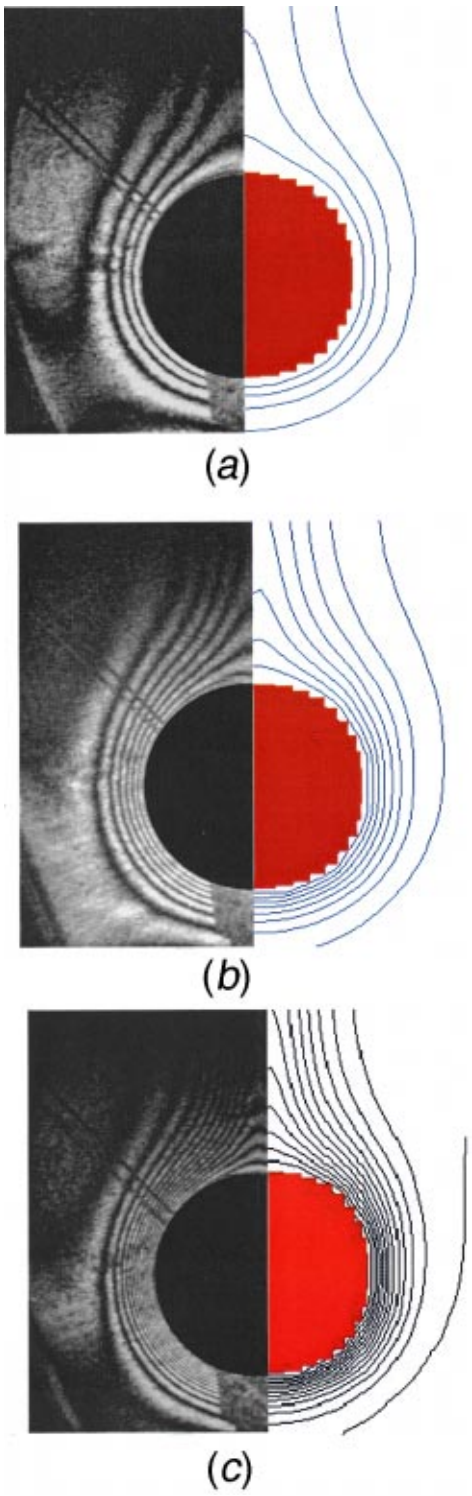

Fig. 11 Comparison of optical and numerical isotherms: (*a*) Ra=6.80×10^3; (*b*) Ra=1.04×10^4; and (*c*) Ra=1.66×10^4.

fringes increase. An asymmetry is discernible, particularly in Fig. 11(*c*), which is attributed to the plume oscillation. As noted earlier, this unsteady nature of the plume prevented Digital Phase Stepping. Data is not presented for a Grashof number of 2.18×10^4, owing to the large number of fringes present in the interferogram which makes visual comparison difficult.

Figure 12 shows a comparison of the dimensionless temperature profile, measured from the interferograms shown in Fig. 11, with data from the literature for the horizontal cylinder in an extensive atmosphere. The angle θ is measured from the lower cylinder stagnation point. Because the plume was observed to oscillate and is laterally displaced in some of the interferogrames, the profiles plotted at $\theta=180$ deg were taken at the plume centreline. For $\theta=90$ deg, very good agreement is obtained with the literature. However for $\theta=180$ deg, at the cylinder upper stagnation point, there is considerable scatter. At Ra$=1.04\times10^4$, the present data deviates up to a maximum of 25 percent from the numerical prediction of Kuehn and Goldstein [23], and up to 20 percent from the numerical benchmark solution obtained by Saitoh et al. [24]. Saitoh et al. suggest experimental error as an explanation for the discrepancies in the plume region, but fail to offer any evidence to support this claim. Kuehn and Goldstein [23] also took measurements with a Mach-Zehnder interferometer, and attributed the discrepancies in their data at $\theta=180$ deg to end effects.

Before continuing, it is worthwhile to consider the accuracy of the present interferometric temperature measurements, which depends on three parameters: the accuracy of the thermocouple used to calibrate the reference fringe, the accuracy in the placement of that thermocouple at the center of the fringe, and end effects. The thermocouple was calibrated to within 0.1°C. At worst, it is placed at the edge of the reference fringe, which would introduce an error of 1/4 of a fringe shift. This corresponds to a temperature change of 0.6°C. Therefore, at worst, the present data has an uncertainty of 0.7°C. End effects are minimized through a large ratio of cylinder length to diameter, but this increases the sensitivity of the interferometer and thereby the number of fringes. To compromise between both, the cylinder had a length to diameter aspect ratio of 15, compared to 5.7 for Kuehn and Goldstein [23]. A check on the accuracy of the measurements can be made by comparing the surface temperature of the cylinder extrapolated from the measured temperature distribution to the values measured by the two thermocouples located on the cylinder surface. Because refraction effects begin to manifest at the two higher Rayleigh numbers investigated, evident from the blurring of the cylinder outline, it is better to consider the two lower Rayleigh numbers where refraction effects were insignificant. For a Rayleigh number of 6.80×10^3, an extrapolated surface temperature of 38.6°C was obtained, compared to values of 38.6°C and 38.7°C measured by the two thermocouples. For a Rayleigh number of 1.04×10^4, an extrapolated surface temperature of 46.1°C was obtained, compared to the thermocouple values of 46.2°C and 46.5°C. This agreement also indicates that end effects were insignificant in the experiment.

The accuracy of the measurements is further supported by the excellent agreement between the experimental and numerical isotherms. Therefore, the discrepancies in the data from the present investigation in Fig. 12 cannot be explained through experimental uncertainty. If the enclosure was influencing the results, the scatter should also be present at $\theta=90$ deg, where the agreement is very good. Given the scatter also evident in the literature, it is more likely that the correlating parameters are invalid, owing to the breakdown of boundary layer assumptions in the plume region.

Figure 13 shows the numerical local Nusselt number distribution over the cylinder and enclosure inner surface at four Rayleigh numbers compared to the optical measurements taken about the cylinder, the plume impingment on the enclosure ceiling and an upper corner of the enclosure. The agreement about the cylinder in excellent, as would be expected from Fig. 11.

The local Nusselt number is greatest at the lower cylinder stagnation point, and gradually decays in magnitude along the cylinder surface. A rapid decrease occurs above an angle of 150 deg, measured from the lower stagnation point, where the two symmetric boundary layers merge to form the plume. Thus most of the heat from the cylinder passes through the lower half of the cylinder and is convected upwards into the plume. The decrease in the local cylinder Nusselt number in the plume region is caused by the insulation provided by the separation of the boundary layers to

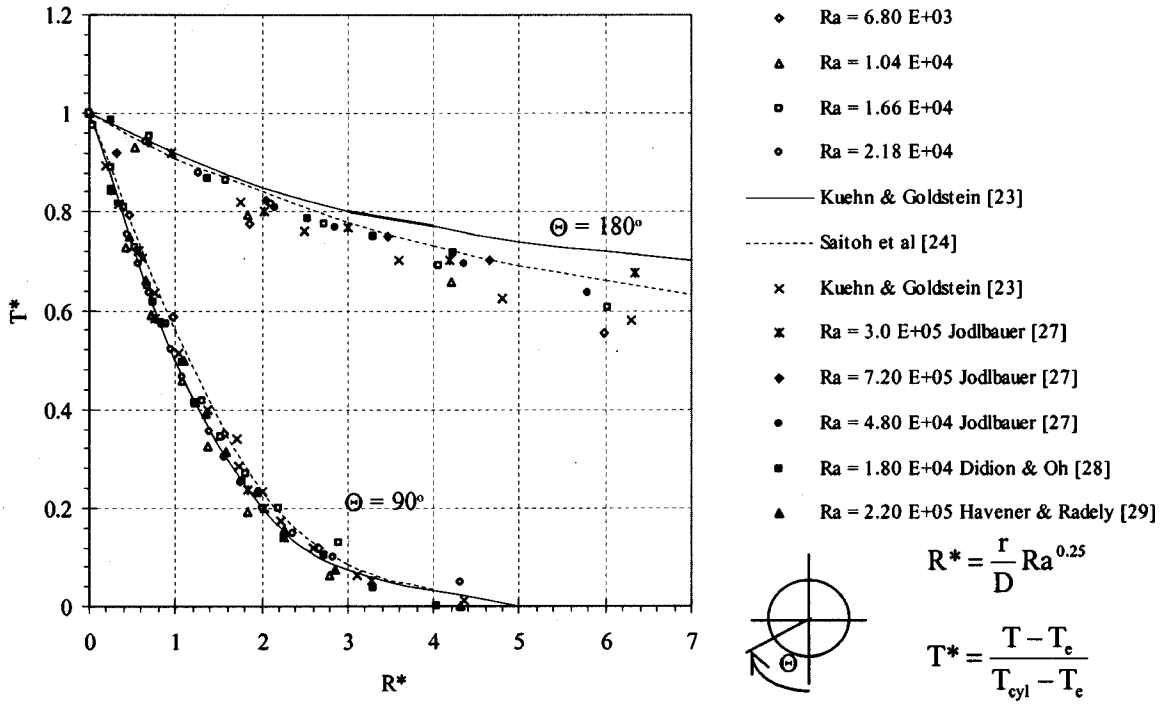

Fig. 12 Comparison of non-dimensional temperature distribution with the literature

form the plume in that region. The large thickness of the boundary layer in the plume region offers the most likely explanation for the scatter present at $\theta=180$ deg in Fig. 12.

Having been convected into the plume, most of the heat from the cylinder is transferred to the enclosure in region of the plume impingement on the ceiling, with a peak in the heat transfer coefficient at the stagnation point on the ceiling. The remaining heat is removed through the cooling of the fluid as it moves along the enclosure ceiling, with a minor peak in the heat transfer where the remaining momentum of the fluid is lost in another region of impingement immediately below the upper corners of the enclosure.

The Nusselt number distribution along the upper interior enclosure surface exhibits a bell shaped profile, similar to the profile for a jet impinging on a flat plate for large nozzle to plate spacings, described by Incropera and De Witt [25]. The numerical profiles are symmetric about the enclosure center-line. However, the measured plume impingement is displaced slightly to the left of the center-line. Dalton and Davies [4] showed that the plume is sensitive to its geometric position within the enclosure. Changing the lateral and vertical displacement of the cylinder by 1 percent resulted in changes in the temperature and lateral displacement of the plume. In the present experiment, the cylinder was centred to within 1 mm of the enclosure centreline. The cylinder was centred exactly in the numerical model, hence the zero lateral displacement of the peak impingement Nusselt number.

For Rayleigh numbers of 6.80×10^3 and 1.04×10^4, good agreement is obtained with numerical and optical results. However, at the two higher Rayleigh numbers, the agreement is not so good. The peak Nusselt number is 15 percent and 20 percent lower than the numerical prediction for each of the Rayleigh numbers of 1.66×10^4 and 2.18×10^4 respectively. The increasing discrepancy with increasing Rayleigh number is attributed to the three dimensional nature of the plume impinging on the enclosure ceiling. The *z*-component in the impingement area would result in a lower integrated average temperature, as measured by an interferometer, and thus lead to a lower measured local Nusselt number. The *z*-component would diminish in the *x*-direction as the flow moves along the the ceiling of the enclosure. This is supported by the excellent agreement between experiment and prediction in the corner region, where the flow can be regarded as two dimensional.

The corner region is essentially stagnant with little heat transfer taking place. Immediately below the corner region, where the flow reattaches, there is a peak in the Nusselt number, of similar magnitude as the Nuselt number obtained six cylinder diameters from the impingment centreline, followed by a gradual reduction as the fluid is cooled whilst it flows down the enclosure side wall. The peak indicates that the fluid has not fully lost its momentum by the time it has moved along the enclosure ceiling. No fringes were present in the corner region for the two lower Rayleigh numbers, indicating that the fluid had sufficiently cooled beforehand. Dalton [26] provides a detailed discussion of the recirculation in an isothermal and non-isothermal enclosure, and describes how the fluid, when not sufficiently cooled at the top of the enclosure, rolls into a vortex which mixes the air and cools it, leading to a recirculation.

The heat transfer at system level can be described as a combination of forced and natural convection. Although the heat transfer about the cylinder is free convection, the impingement region is in forced convection. Because the momentum of the fluid is largely lost by the ceiling corner, the downward flow over the enclosure wall is induced by free convection. Describing the heat transfer at cylinder and enclosure level as mixed convection highlights the complexity of enclosed free convection flow.

A heat balance shows that the ratio of the mean cylinder and enclosure Nusselt numbers equals the ratio of the enclosure to cylinder thermal areas. That is,

$$\frac{\mathrm{Nu}_{\mathrm{cyl}}}{\mathrm{Nu}_e}=\frac{A_e}{A_{\mathrm{cyl}}}, \tag{6}$$

where the Nusselt numbers are averaged over the entire surface area. Equation 6 is proposed as a check for numerical predictions. For $\mathrm{Ra}=1.04\times10^4$, values of 22.4 and 22.9 are obtained for the left and right hand sides of Eq. 6 respectively, or a difference of 2 percent. The method is perfectly general. For instance, to find the mean internal Nusselt number for a room, heated by a free con-

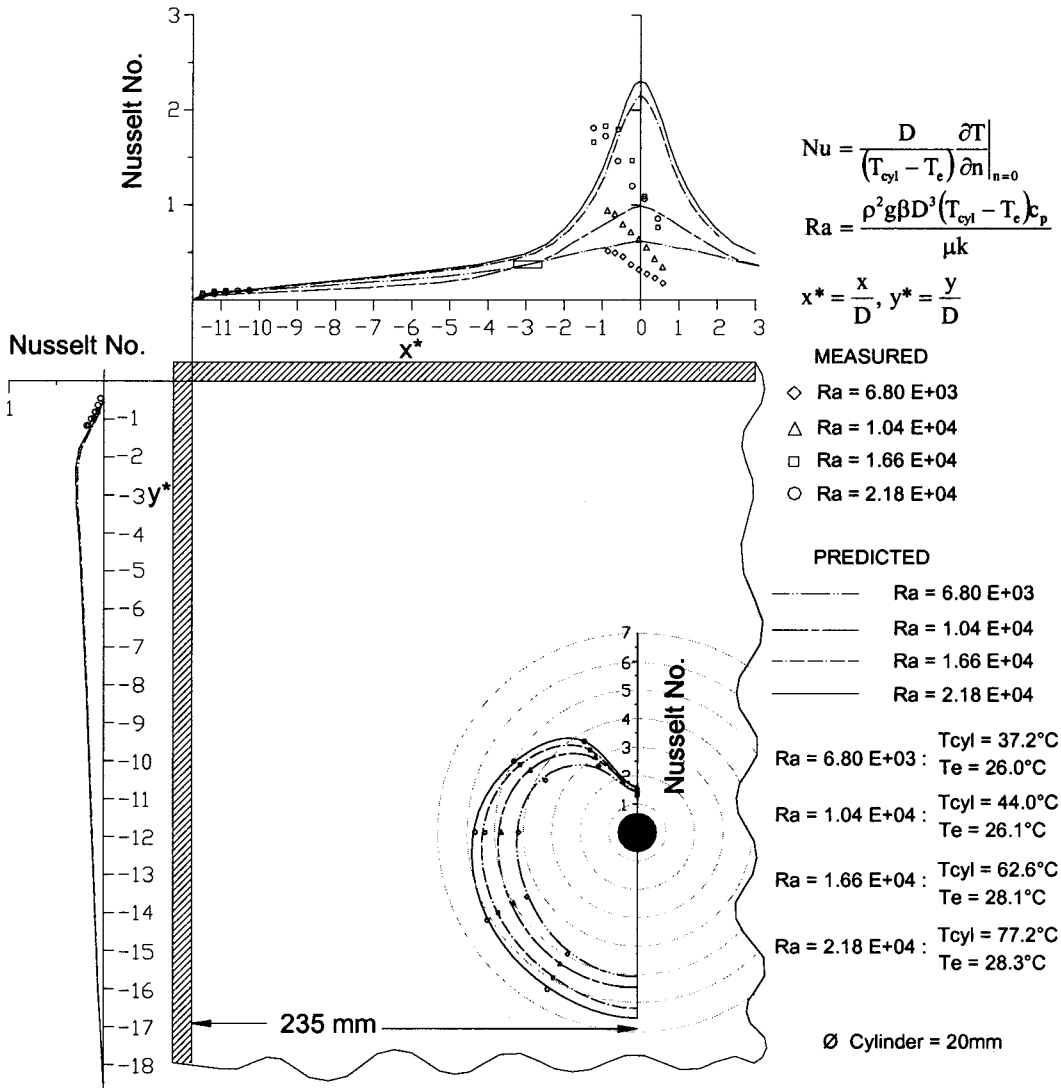

Fig. 13 Measured and predicted Nusselt number distribution at four different Rayleigh numbers, over the cylinder, shown as a polar plot, and over the inner surface of the enclosure, shown as a linear plot

vection heater, it is only necessary to know the mean Nusselt number of the heater, which is usually well known, and the area ratio of the heater to the internal walls and ceiling. The case derived is for isothermal surfaces.

Consider a system similar to that shown in Fig. 13, but in which the enclosure does influence the cylinder Nusselt number. On the basis of the local Nusselt distribution presented in Fig. 13, it would seem worthwhile recommending to replace the sharp corner of the ceiling and side-wall with a fillet radius. This would reduce the loss in momentum in the corner. At sufficiently high temperatures, the fluid may still possess momentum by the time it reaches the cylinder. The cylinder heat transfer would then be by mixed convection, and enhanced.

For the measurements presented in this paper, the boundary conditions were well defined and readily measured. Consequently, Flotherm was able to accurately predict the temperature fields in the enclosure. The largest discrepancies arose in the region of the plume impingement on the ceiling of the enclosure, where three dimensional effects were present, but had been modelled as two dimensional. Although a more expeditious solution could probably have been obtained through a steady turbulent simulation, the ambiguities introduced by attempting to define the turbulent viscosity are eliminated in the unsteady laminar approach.

Conclusions

• Although the Michelson interferometer is twice as sensitive as the corresponding Mach-Zehnder arrangement, problems with focusing cause it to be less useful than the Mach-Zehnder.

• Real-time Digital Moiré Subtraction has been successfully applied to the measurement of unsteady enclosure free convection.

• Comparison between the numerical and measured temperature field about the isothermal horizontal cylinder is excellent.

• Discrepancies in the peak numerical and optical Nusselt numbers in the plume impingement region is attributed to the three dimensional nature of the flow.

• Scaling based on $Ra^{0.25}$ breaks down in the region where the flow separates from the cylinder surface to form the plume.

• Enclosures with sharp corners create stagnant regions in the flow and result in a decrease in the enclosure Nusselt number.

• A simple ratio of areas can be used to calculate the mean Nusselt number for any shaped enclosure with a heated body located inside it, knowing the mean Nusselt number of the heated object, provided the surfaces are isothermal.

Acknowledgments

The authors gratefully acknowledge the support of PEI Technologies, the Joint Research Center of the European Commission, Flomerics (UK), and the technical staff of the University of Limerick.

Nomenclature

A = area, m^2
D = cylinder diameter, m
K = Gladstone-Dale constant, m^3/kg
L = length, m
N = fringe number
R = gas constant, J/kg K
T = temperature, °C
c_p = specific heat capacity, J/kgK
g = gravitational acceleration, m/s^2
h = heat transfer coefficient, W/m^2K
k = conductivity, W/mK
n = refractive index
p = pressure, N/m^2
r = radial distance from cylinder, m
x, y, z = Cartesian coordinates
β = volume coefficient of expansion, K^{-1}
Δ = distance, m
$\Delta\Phi$ = change in phase angle
θ = angle, deg
μ = dynamic viscosity, Ns/m^2
λ = wavelength, m
ρ = density, kg/m^3

Subscripts

cyl = cylinder
e = enclosure

Dimensionless Parameters

Nu = hD/k; Gr = $\rho^2 g\beta(T_{cyl}-T_e)D^3/\mu^2$; Pr = $\mu c_p/k$;
Ra = GrPr; $x^* = x/D$; $y^* = y/D$; $R^* = \mathrm{rRa}^{0.25}/D$

References

[1] Warrington, R. O., and Powe, R. E., 1985, ''The Transfer of Heat by Natural Convection Between Heated Bodies and Their Enclosures,'' Int. J. Heat Mass Transf., **28**, No. 2, pp. 319–330.
[2] Shaw, C., Chen, C., and Cleaver, J. W., 1988, ''The Effects of Thermal Sources on Natural Convection in an Enclosure,'' International Journal of Fluid and Heat Flow, **9**, No. 3, pp. 296–301.
[3] Ghaddar, N. K., 1992, ''Natural Convection Heat Transfer Between a Uniformly Heated Cylindrical Element and Its Rectangular Enclosure,'' Int. J. Heat Mass Transf., **35**, No. 10, pp. 2327–2334.
[4] Dalton, T. M., and Davies M. R. D., 1996, ''An Experimental and Numerical Investigation of Natural Convection Plumes Above a Horizontal Cylinder in an Isothermal Enclosure,'' HTD-Vol. 329, *National Heat Transfer Conference*, **7**, pp. 3–10.
[5] Keyhani, M., and Dalton, T., 1996, ''Natural Convection Heat Transfer in Horizontal Rod-Bundle Enclosures,'' Transactions of the ASME: Journal of Heat Transfer , **118**, pp. 598–605.
[6] Liu, N. Y., Phan-Thien, and Kemp, R., 1996, ''Coupled Conduction-Convection Problem for a Cylinder in an Enclosure,'' Computational Mechanics, **18**, pp. 429–443.
[7] Koizumi, H., and Hosokawa, I., 1996, ''Chaotic Behavior and Heat Transfer Performance of the Natural Convection Around a Hot Horizontal Cylinder Affected by a Flat Ceiling,'' Int. J. Heat Mass Transf., **39**, No. 5, pp. 1081–1091.
[8] Cessini, G., Paroncini, M., Cortella, G., and Manzan, M., 1999, ''Natural Convection From a Horozontal Cylinder in a Rectangular Cavity,'' Int. J. Heat Mass Transf., **42**, pp. 1801–1811.
[9] Lasance, C. I. M., 1993, ''Thermal Management of Air-Cooled Electronic Systems: New Challenges for Research,'' *Proceedings of EUROTHERM Seminar 29*, June, 14–16, Delft, Netherlands, pp. 3–24.
[10] Ostrach, S., 1988, ''Natural Convection in Enclosures,'' Journal of Heat Transfer, **110**, pp. 1175–1189.
[11] Barton, J. S., Kilpatrick, J. M., MacPherson, W. N., Jones, J. D. C., Chana, K. S., Anderson, J. S., Buttsworth, D. R., and Jones, T. V., 1998, ''Unsteady Temperature and Pressure Measurement Using Optical Fibre Aerodynamic Probes,'' *Proceedings of the 14th Bi-Annual Symposium on Measuring Techniques in Transonic and Supersonic Flow in Cascades and Turbomachines*, Limerick, Ireland.
[12] Hauf, W., and Grigull, U., 1970, ''Optical Methods in Heat Transfer,'' Adv. Heat Transfer, **6**, pp. 133–366.
[13] Goldstein, R. J., 1983, *Fluid Mechanics Measurements*, Hemisphere, Washington.
[14] Merzkirch, W., 1987, *Flow Visualisation*, 2nd ed., Academic Press, San Diego, CA, pp. 158–206.
[15] Creath, K., 1994, *Phase-Shifting Holographic Interferometry, for Holographic Interferometry*, edited by P. K. Rastogi, Springer-Verlag, Berlin, pp. 109–148.
[16] Yokozeki, S., and Mihara, S., 1979, ''Moire Interferometry,'' Journal of Applied Optics, **18**, No. 8, pp. 1275–1280.
[17] Forno, C., and Whelan, M., 1999, ''Digital Moire Subtraction Applied to Interferometers as a Means of Improving Accuracy and Extending Field of View for Engineering and Optical Measurement,'' Proceedings of the SPIE conference on Interferometry 99, Pultusk, Poland, pp. 49–57.
[18] Patankar, S. V., 1980, *Numerical Heat Transfer and Fluid Flow*, Hemisphere, Bristol, PA.
[19] Ferziger, J. H., and Peric, M., 1997, *Computational Methods for Fluid Dynamics*, 2nd ed., Springer-Verlag, Heidelberg, Berlin.
[20] *Natural Convection Flow Around a Heated Cylinder in a Cool Walled Enclosure*, 1997, Flomerics Ltd., PMR-1999, Confidential Report.
[21] Flotherm v. 2.1: Introductory course, 1998, Flomerics Ltd., Flomerics, UK.
[22] Bejan, A., 1993, *Heat Transfer*, 1st ed., Wiley, New York, pp. 335–397.
[23] Kuehn, T. H., and Goldstein, R. J., 1980, ''Numerical Solution to the Navier-Stokes Equations for Laminar Natural Convection About a Horizontal Isothermal Circular Cylinder,'' Int. J. Heat Mass Transf., **23**, pp. 971–979.
[24] Saitoh, T., Sajiki, T., and Maruhara, K., 1993, ''Benchmark Solutions to Natural Convection Heat Transfer Problem Around a Horizontal Circular Cylinder,'' Int. J. Heat Mass Transf., **36**, No. 5, pp. 1251–1259.
[25] Incropera, F. P., and De Witt, D. P., 1990, *Fundamentals of Heat and Mass Transfer*, 3rd Edition, Wiley Inc., New York, pp. 431–438.
[26] Dalton, T., 1997, ''On Enclosure Natural Convection for Electronic Cooling Applications,'' Ph.D. thesis, University of Limerick, Limerick, Ireland.
[27] Jodlbauer, K., 1933, ''Das Temperatur- und Geschwindigkeitsfeld um ein geheitzes Rohr bei Freier Konvektion,'' *Forschung Verein Deutsche Ingenieure*, **4**, pp. 158–172.
[28] Didion, D. A., and Oh, Y. H., 1966, ''A Quantitative Grid-Schlieren Method for Temperature Measurement in a Free Convection Field,'' Technical Report No. 1, The Catholic University of America, Washington.
[29] Havener, G., and Radlay, R. J., 1972, ''Quantitative Measurements Using Dual Hologram Interferometry,'' Aerospace Research Laboratories Report 72-0085.

Interaction Effects Between Surface Radiation and Turbulent Natural Convection in Square and Rectangular Enclosures

K. Velusamy
Scientific Officer,
Thermal Hydraulics Section,
Indira Gandhi Centre for Atomic Research,
Kalpakkam-603 102, India

T. Sundararajan
Professor,
Department of Mechanical Engineering,
Indian Institute of Technology,
Madras-600 036, India

K. N. Seetharamu
Professor,
School of Mechanical Engineering,
Universiti Sains Malaysia,
(KCP) 31750 Tronoh, Malaysia

The interaction effects of surface radiation with turbulent natural convection of a transparent medium in rectangular enclosures have been numerically analyzed, covering a wide range of Rayleigh number from 10^9 to 10^{12} and aspect ratio from 1 to 200. The vertical walls of the enclosure are isothermal and maintained at different temperatures. The adiabatic top and bottom walls of the enclosure have been modelled for the limiting cases of negligible or perfect conduction along their lengths. The interaction with surface radiation results in larger velocity magnitudes and turbulence levels in the vertical as well as horizontal boundary layers, leading to an increase in the convective heat transfer by ~25 percent. Due to the asymmetrical coupling of radiation, the augmentation of convective Nusselt number of the cold wall is larger than that of the hot wall. In tall enclosures, the convective Nusselt number exhibits three distinct regimes with respect to aspect ratio, viz. the slow growth regime, the accelerated growth regime and the invariant (or saturated) regime. The augmentation of convective Nusselt number for perfectly conducting horizontal walls is found to be of similar nature to that in the case with radiation interaction. [DOI: 10.1115/1.1409259]

Keywords: Conjugate, Enclosure Flows, Heat Transfer, Natural Convection, Radiation, Turbulence

1 Introduction

Natural convection in rectangular enclosures is encountered in many engineering applications such as heating and cooling of rooms, solar collectors, cooling of electronic equipment, cooling of various sub-systems of a nuclear reactor etc. The problem of laminar natural convection in a square enclosure has been extensively studied in literature for various boundary conditions. Bench mark numerical solutions for natural convection in a square enclosure with two isothermal and two adiabatic walls have been obtained by de Vahl Davis and Jones [1]. While these benchmark solutions have helped numerical analysts in validating their codes, there were discrepancies between the benchmark solutions and experimental measurements, with the measured values of Nusselt number being less (see [2,3]). The reason for such discrepancies has been traced to the presence of surface radiation in transparent media such as air. Moreover, it is very difficult to achieve adiabatic conditions on the top and bottom walls in an experiment, when the fluid medium in the enclosure is a gas. Even for near-ideal conditions of insulation, heat conduction within the adiabatic walls alters the flow and temperature fields in the fluid and hence the net heat transfer rate. Also the adiabatic walls contribute to the net heat transfer, by absorbing radiative heat from the hot wall and supplying it to the fluid convectively. In practical applications, the sizes of the enclosures are large so that the natural convective flow is turbulent and the temperature conditions are such that the radiative heat transfer is significant. In this paper, we present a comprehensive model for conjugate analysis, which includes heat conduction through the enclosure walls, surface radiation interaction between them and turbulent natural convection in the transparent fluid medium.

Excellent reviews of laminar natural convection in enclosures have been presented by Ostrach [4] and Hoogendoorn [5]. Many experimental and numerical analyses have been carried out to understand turbulent natural convection in enclosures also. Some of the experimental studies on turbulent natural convection are that of Elsherbiny et al. [6], Cheesewright and Ziai [7], Cheesewright et al. [8], Olson et al. [9] and Shewen et al. [10] for air filled enclosures, and Ozoe et al. [11] and Giel and Schmidt [12] for water filled enclosures. The measured data for moderate aspect ratio enclosures indicate distinct boundary layers on the vertical walls, which are significantly different from those on isolated plates, and a uniform vertical temperature gradient in the core fluid. In the turbulent regime, the Nusselt number is found to increase with aspect ratio, while the contrary is seen in the laminar regime. Some of the important numerical studies on turbulent natural convection are that of Ozoe et al. [11], Giel and Schmidt [12], Markatos and Pericleous [13], Fusegi and Farouk [14], Henkes [15], Henkes and Hoogendoorn [16], Gan [17] and Xu et al. [18]. These numerical studies demonstrate the capabilities of various turbulence models to predict turbulent natural convective flow in enclosures.

Most of the above referred literature pertains to turbulent natural convection without radiation interaction. However, in many practical situations, the temperature levels of the enclosure walls are high enough for the radiative heat transfer to be significant. Surface to surface radiation through a transparent medium modifies the temperature distribution of the adiabatic top and bottom walls, which in turn, affect the stratification in the enclosure and hence the convective heat transfer. Hence, the objectives of the present study are (i) to find the influence of surface radiation on turbulent natural convection of a transparent medium in differentially heated square and tall vertical enclosures, and (ii) to systematically analyze the effects of emissivity, mean temperature and temperature difference on the convective and radiative Nusselt numbers of the hot and cold walls.

Contributed by the Heat Transfer Division for publication in the JOURNAL OF HEAT TRANSFER. Manuscript received by the Heat Transfer Division May 10, 2000; revision received April 10, 2001. Associate Editor: R. D. Skocypec.

2 Mathematical Formulation

Consider a two dimensional vertical rectangular enclosure of height H and width W as shown in Fig. 1. The left wall is heated and the right wall is cooled, while the outer surfaces of the top and bottom walls are maintained adiabatic. The inner surfaces of these walls participate in heat transfer via conduction in the lengthwise direction, surface absorption/emission of radiation and natural convective heat exchange with the fluid medium. The turbulent flow in the enclosure is described by the time averaged Reynolds equations with Boussinesq approximation for buoyancy. To predict the turbulent stresses and fluxes, the standard k-ε model is adopted due to its simplicity and successful application in similar problems [5]. The Reynolds-averaged N-S equations along with the equations for k and ε in Cartesian coordinates are given by

$$\frac{\partial}{\partial x}(\rho u)+\frac{\partial}{\partial y}(\rho v)=0 \tag{1}$$

$$\frac{\partial}{\partial x}(\rho uu)+\frac{\partial}{\partial y}(\rho vu)=-\frac{\partial p}{\partial x}+\frac{\partial}{\partial x}\left[2\mu_{\text{eff}}\frac{\partial u}{\partial x}\right]+\frac{\partial}{\partial y}\left[\mu_{\text{eff}}\left(\frac{\partial u}{\partial y}+\frac{\partial v}{\partial x}\right)\right] \tag{2}$$

$$\frac{\partial}{\partial x}(\rho uv)+\frac{\partial}{\partial y}(\rho vv)=-\frac{\partial p}{\partial y}+\frac{\partial}{\partial x}\left[\mu_{\text{eff}}\left(\frac{\partial v}{\partial x}+\frac{\partial u}{\partial y}\right)\right]+\frac{\partial}{\partial y}\left[2\mu_{\text{eff}}\frac{\partial v}{\partial y}\right]+\rho\beta g(T-T_o) \tag{3}$$

$$\frac{\partial}{\partial x}(\rho uC_PT)+\frac{\partial}{\partial y}(\rho vC_PT)=\frac{\partial}{\partial x}\left[K_{\text{eff}}\frac{\partial T}{\partial x}\right]+\frac{\partial}{\partial y}\left[K_{\text{eff}}\frac{\partial T}{\partial y}\right] \tag{4}$$

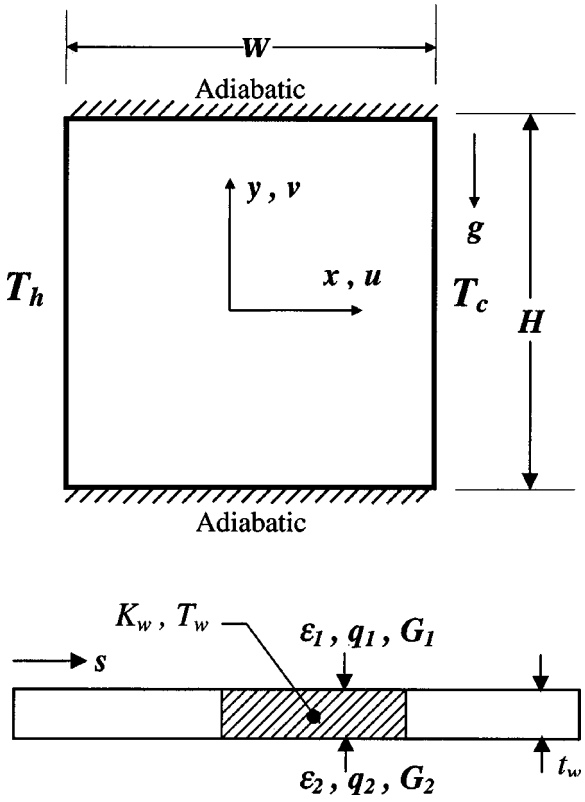

Fig. 1 Schematic of the enclosure and heat balance for an elemental wall segment

$$\frac{\partial}{\partial x}(\rho uk)+\frac{\partial}{\partial y}(\rho vk)=\frac{\partial}{\partial x}\left[\left(\mu+\frac{\mu_t}{\sigma_k}\right)\frac{\partial k}{\partial x}\right]+\frac{\partial}{\partial y}\left[\left(\mu+\frac{\mu_t}{\sigma_k}\right)\frac{\partial k}{\partial y}\right]+P_k+G_k-\varepsilon \tag{5}$$

$$\frac{\partial}{\partial x}(\rho u\varepsilon)+\frac{\partial}{\partial y}(\rho v\varepsilon)=\frac{\partial}{\partial x}\left[\left(\mu+\frac{\mu_t}{\sigma_\varepsilon}\right)\frac{\partial \varepsilon}{\partial x}\right]+\frac{\partial}{\partial y}\left[\left(\mu+\frac{\mu_t}{\sigma_\varepsilon}\right)\frac{\partial \varepsilon}{\partial y}\right]+[C_{\varepsilon 1}(P_k+C_{\varepsilon 3}G_k)-C_{\varepsilon 2}\varepsilon]\frac{\varepsilon}{k}, \tag{6}$$

where

$$P_k=\mu_t\left[2\left(\frac{\partial u}{\partial x}\right)^2+2\left(\frac{\partial v}{\partial y}\right)^2+\left(\frac{\partial u}{\partial y}+\frac{\partial v}{\partial x}\right)^2\right]$$

$$G_k=-\frac{\mu_t}{\sigma_T}g\beta\frac{\partial T}{\partial y};\quad \mu_{\text{eff}}=\mu+\mu_t;\quad \mu_t=C_\mu\frac{\rho k^2}{\varepsilon}$$

$$\text{and}\quad K_{\text{eff}}=K+\frac{\mu_t c_p}{\sigma_T}.$$

As recommended by Markatos and Pericleous [13], the various constants pertaining to the turbulence model have been selected as $C_\mu=0.09$, $C_{\varepsilon 1}=1.44$, $C_{\varepsilon 2}=1.92$, $\sigma_T=1.0$, $\sigma_k=1.0$, and $\sigma_\varepsilon=1.3$. In literature, there is no consensus on the right choice of $C_{\varepsilon 3}$ and following Henkes [15], it is taken as $\tanh(v/u)$. No wall functions are used and sufficiently fine grids are employed in the inner layer to enable integration up to the walls [15]. Equations (1)–(6) are subject to the following boundary conditions: $u=0$, $v=0$, $k=0$, and $\varepsilon=\propto$ (for the numerical implementation, it has been set as 10^{20}) on all the walls. The left and right walls are isothermal at T_h and T_c, respectively, while the temperature variation along the adiabatic top and bottom walls can be determined including the effects of surface radiation, convection and conduction in the lengthwise direction. Here, assuming the walls to be sufficiently thin, the temperature variation in the thickness direction is neglected. The generalized energy balance equation over an elemental wall segment having diffuse gray surfaces, shown in Fig. 1, can be expressed as

$$K_w t_w\frac{\partial^2 T_w}{\partial s^2}+q_1+q_2+\varepsilon_1 G_1+\varepsilon_2 G_2=(\varepsilon_1+\varepsilon_2)\sigma T_w^4, \tag{7}$$

where K_w, t_w, and T_w are the thermal conductivity, thickness and temperature of the wall, s is the length measured along wall, ε is the hemispherical emissivity of wall surface, G is the irradiation falling on wall surface and subscripts 1 and 2 refer to conditions on external and internal surfaces of the wall. Convective heat flux, q_1, is evaluated from ambient fluid temperature, heat transfer coefficient, and T_w. For a wall which is made adiabatic externally, we can set $q_1=\varepsilon_1=0$. Convective heat flux, q_2, is evaluated from $q_2=K(T-T_w)/\Delta n$, where K and T are thermal conductivity and local temperature of fluid in the enclosure and Δn is the normal distance of the first fluid node from wall surface. The irradiation is related to radiosity (B), through the relation

$$B_i=\varepsilon_i\sigma T_{wi}^4+(1-\varepsilon_i)G_i, \tag{8}$$

where subscript i is the index of the elemental segments forming the enclosure. Substituting for G in terms of B and using the inverse relationship, we get

$$G_i=\sum_{j=1}^{N}B_jF_{i-j}\quad\text{and}\quad\sum_{j=1}^{N}\left[\frac{\delta_{ij}-(1-\varepsilon_i)F_{i-j}}{\varepsilon_i}\right]B_j=\sigma T_i^4, \tag{9}$$

where, F_{i-j} is the shape factor from segment i to segment j, δ_{ij} is the Kronecker delta and N is the total number of radiating segments. Equation (7) forms a set of tridiagonal algebraic equations on discretisation, for the nodal temperatures of each wall, which need to be solved in conjunction with the Eqs. (8) and (9). It is also connected to Eqs. (1)–(6) through the wall temperatures T_w.

Thus, the interfacial requirements are the continuity of temperature and heat flux between adjacent media. Equations (1)–(6) are numerically solved by the SIMPLE algorithm on a staggered grid [19]. Fine grids are considered within the boundary layers where the flow and temperature variations are sharp and relatively coarse grids are found sufficient in the core region. The grid close to the isothermal walls is stretched by tanh function in the horizontal direction and the grid adjacent to the adiabatic walls is stretched in the vertical direction by a sine function [15]. The smallest non-dimensional grid size used close to the wall varies from $\sim 5\times10^{-5}$ (for 42×42 grid) to 3×10^{-5} (for 62×62 grid).

3 Validation

For the purpose of validation, the problem of turbulent natural convection of air without radiation interaction in a square enclosure has been solved for Rayleigh number values 10^9 to 10^{12}. This problem has been analyzed numerically by Markatos and Pericleous [13] and Henkes [15]. Table 1 compares the present predictions of average Nusselt number with these published results. Also presented in the same table are the results obtained from the experimental correlation proposed by Elsherbiny et al. [6], based on large aspect ratio enclosures in air for Rayleigh numbers up to 10^7. It is seen that the present predictions are closer to the data based on experimental correlation than the other numerical results. The maximum deviation between the present predictions and the experimental correlation is about ±9 percent. Between the two reported numerical results, the present one compares better with that of Henkes [15] with a maximum deviation (at high Rayleigh number) of <10 percent. A plausible reason for the above trend could be that Markatos and Pericleous [13] used wall functions, whereas in the predictions of the present work and that of Henkes [15] no wall function is used. The present predictions are consistently lower than those of Henkes [15], probably due to the fact that the value of σ_T employed in the present analysis is 1.0 as against the value of 0.9 used by Henkes [15].

As another validation, the problem of turbulent natural convection of air in an enclosure with aspect ratio (AR) of 5 at a height based Rayleigh number (Ra) of 5.32×10^{10} is analyzed. King [20] and Cheesewright et al. [8] have provided experimental data for this problem whereas Henkes and Hoogendoorn [16] have provided a reference solution for $AR=1$, using the numerical results of 10 groups of researchers. The local distribution of Nusselt number and mid-height values of vertical velocity are compared in Figs. 2(a–b) for $AR=5$, with the experimental data [20]. The present value of Nusselt number compares reasonably with the reference solution [16] as well as with the hot wall experimental data [20]. But the experimental cold wall Nusselt number is lower than the numerical values as well as the measured hot wall data. A plausible reason for this deviation could be the heat loss encountered in the experiment through the top wall (see, [16]). The mid-height vertical velocity within the boundary layer is in very good agreement with the reference solution [16] and the experimental data [8]. Similarly, the present results of friction factor (C_f) and turbulent shear stress ($u'v'$) for $AR=1$ are also found to compare well with the reference solution [16] and experimental data [20,8], as shown in Table 2.

Table 1 Comparison of average Nusselt numbers for turbulent natural convective flow without radiation for square enclosures

Ra	Present	Elsherbiny et al. [6] $Nu_f = 0.062 x Ra^{1/3}$ (Experiment)	Markatos and Pericleous [13] $Nu_f = 0.082 x Ra^{1/3}$ (Numerical)	Henkes [15] (Numerical)
10^9	57.97	62	74.96	58.51
10^{10}	130.14	133.57	159.89	137.5
10^{11}	296.33	287.78	341.05	320.96
10^{12}	675.75	620	727.47	744.68

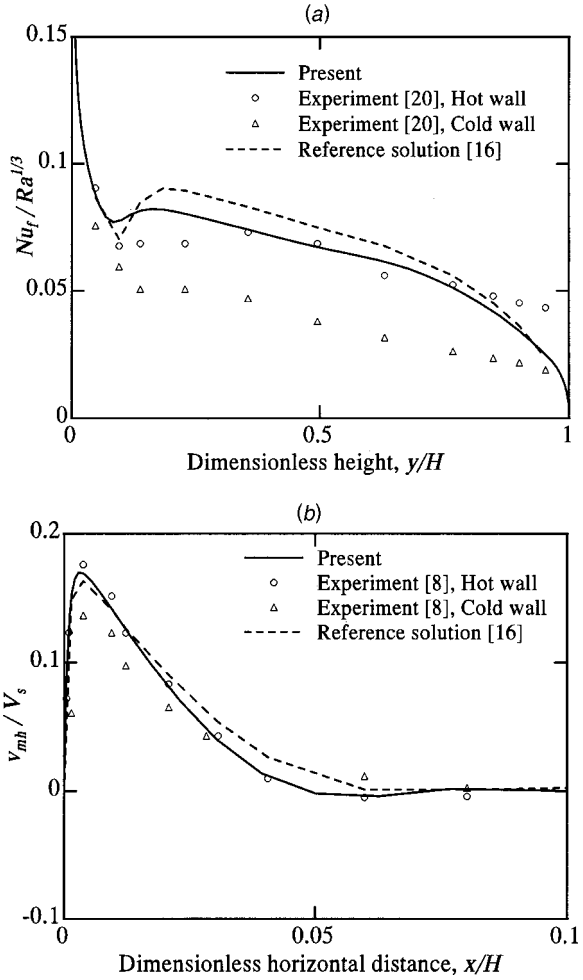

Fig. 2 Comparison of present solutions with reference solution and experimental data for Ra$=5.32\times10^{10}$, Ra$_w=4.26\times10^8$, and $AR=5$; (*a*) Nusselt number, and (*b*) mid-height vertical velocity.

Figure 3 compares the distribution of mid-width air temperature for $AR=6$ and Ra$=7.12\times10^{10}$, with experimental data of Ref. [7] and the reference solution. The present results compare reasonably with the experimental data, as much as the reference solution does. The experimental data do not exhibit the diagonal symmetry demanded by boundary conditions. In order to verify whether heat loss is the reason for the discrepancy between the theory and

Table 2 Comparison of present solution with reference solution and experiments for Ra$=5.32\times10^{10}$

Quantity	Present solution for $AR=1$	Reference numerical solution [16] for $AR=1$	Experimental results [8,20] for $AR=5$	Experimental results [22] for flat plate
Average Nu_f	237.94	256	154-210	173
Nu_f at $y=H/2$	249.57	261	133-241	173
C_f at $y=H/2$	234.76	237	160-189	180
V_{max}/V_s at $y=H/2$	0.1698	0.167	0.144-0.190	0.176
x/H for V_{max}	0.00291	0.00323	0.0026-0.0045	-
$(H/\Delta T)(\partial T/\partial y)$ at the centre of the enclosure	0.530	0.539	0.48	0.
$(u'v')_{max}/V_s^2$ at $y=H/2$	0.0006768	0.000771	0.00044-0.0008	0.000517

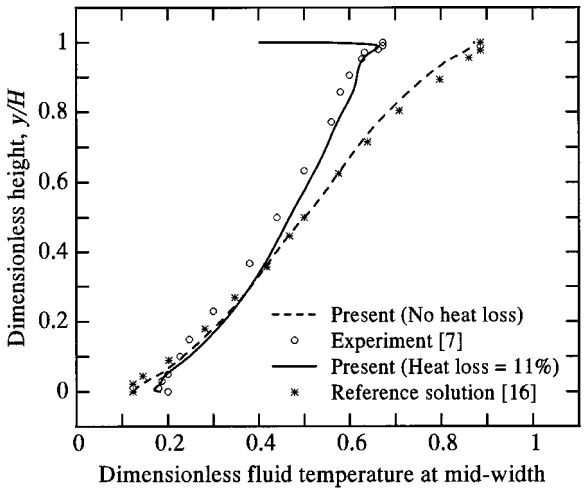

Fig. 3 Predicted fluid temperature variation at mid-width in an enclosure of $AR=6$ for $Ra=7.12\times10^{10}$: comparison with experimental data and reference solution.

experiment [7], the flow in enclosure of $AR=6$ was simulated considering heat loss through the top wall. The wall was taken as being made up of stainless steel of 5 mm thickness. The external surface of top wall was exposed to an ambient at 298 K with various values of heat transfer coefficient, while the external surface of bottom wall was taken as adiabatic. It can be seen in Fig. 3, that as the top wall heat loss is increased up to ~11 percent of the heat transfer from the hot wall, the numerical data moves closer to the measured values.

4 Grid Sensitivity and Uncertainty Analyses

For assessing the sensitivity of the predictions on the grids employed, the case of turbulent natural convection of air in a square enclosure at $Ra=10^{11}$ with emissivity of the surfaces equal to 0.9, was analyzed with two different grid patterns viz. 42×42 and 62×62. The smallest step size in the latter grid is almost half of that in the former. The distribution of local Nusselt number on the hot wall is compared in Fig. 4, for both the grid patterns. It is seen that the results of both the grids are quite close, with a maximum deviation in the average value of ~1 percent. Similar comparisons of mid-height vertical velocity and temperature, and mid-width horizontal velocity and temperature were also carried out and found to be as good as the comparison presented in Fig. 4. Hence, for almost all the results to be discussed further (except in the case of very tall enclosures), the grid pattern of 42×42 has been adopted. As shown in Fig. 4, for tall enclosures (say, $AR=20$), the number of grids in the vertical direction needs to be increased to at least 82 for accurate solution.

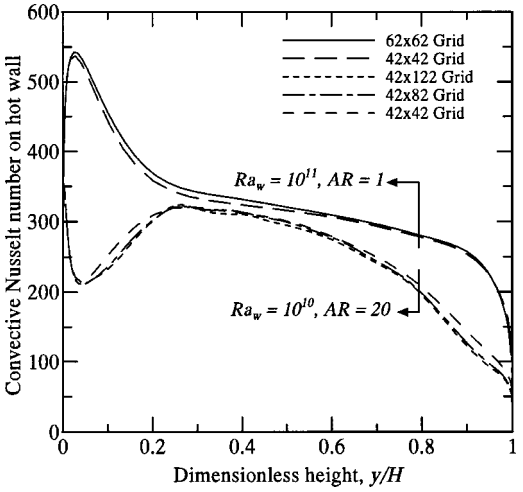

Fig. 4 Effect of grid size on hot wall Nusselt number in square and tall enclosures for $\Delta T=50$ K, $T_o=323$ K, and $\varepsilon=0.9$

The error in the present numerical analysis consists of two parts viz. (i) discretisation error due to the finite mesh size employed, and (ii) uncertainty in the k-ε turbulence model employed for predicting turbulent natural convection flow. A quantity of engineering interest is the Nusselt number (Nu_f) that is a derived quantity. The average values of Nu_f predicted on two non-uniform grid patterns 42×42 and 62×62 having the smallest non-dimensional grid sizes as 4.79×10^{-5} and 2.94×10^{-5} are 326 and 331, respectively. Extrapolating from these, the value of Nu_f, for a grid size of zero is 339. Hence, the error due to discretisation is -3.8 percent. On comparing the present predictions of Nu_f with that obtained from the correlation of Elsherbiny et al. [6], the value of Nu_f has an error of -6.5 percent at the smallest Rayleigh number of 10^9 and $+9$ percent at the largest Rayleigh number of 10^{12}. When the hot wall Nu_f is compared with the experiments of King [20], the numerically predicted Nu_f has an error of $+13$ percent. Hence, the error introduced by turbulence modeling could be taken as $+13$ percent to -6.5 percent.

5 Results and Discussion

The study has been carried out over the range of parameters, $Ra=10^9-10^{12}$, $\varepsilon=0-0.9$, $T_o=223-423$ K, $\Delta T=10-250$ K, and $AR=1-200$, with air as the fluid. For the top and bottom walls, the limiting values of negligible conduction (NCW) and perfect conduction (PCW) along the wall have been considered. For NCW, thickness and conductivity of the walls are taken to be 10^{-6} units while for PCW, these values are taken to be 1 and 10^4 units respectively. When conduction along the top and bottom walls is quite strong, a linear temperature profile results in them if they are in contact with the isothermal vertical walls, as seen from Eq. (7). Solutions are obtained by considering convection-radiation coupling as well as by neglecting this coupling. In the latter case, convective and radiative heat transfers are estimated totally independent of each other.

5.1 Flow and Heat Transfer Features for Square Enclosures. The flow distributions in the enclosure for emissivity values of 0 and 0.9 are shown in Figs. 5(*a*) and 5(*b*), respectively. The corresponding temperature distributions are shown in Figs. 6(*a*) and 6(*b*). As seen in Fig. 5(*a*), for pure natural convection ($\varepsilon=0$), distinct thin vertical boundary layers are formed adjacent to the isothermal walls. These boundary layers grow in a manner similar to natural convection boundary layer over a vertical plate kept in an infinite ambient. There is a strong thermal stratification in the enclosure with a non-dimensional temperature difference of the order of 0.7 between the top and bottom walls (Fig. 6(*a*)). The hot wall boundary layer is observed to grow monotonically up to ~3/4th height and thin down as the height increases further. Above the mid-height, some downward flow is seen outside the hot wall boundary layer (Fig. 5(*a*)). It appears that the fast moving hot boundary layer flow lifts up a part of the cold core fluid by viscous shear. The lifted core fluid experiences adverse buoyancy as it travels upwards due to stable stratification prevailing in the enclosure and eventually descends as a reverse flow. Similar observations hold for cold wall boundary layer also. Thus, stable stratification tends to retard convective circulation in the enclosure. It is worth mentioning here about the experiments of Fu and Ostrach [21], in which the authors found that by heating the top wall and cooling the bottom wall, convection could be suppressed to a considerable extent. From Figs. 5(*b*) and 6(*b*), it is clear that radiation modifies the flow and temperature fields substantially. The core of the enclosure is nearly stagnant and the natural convective flow is channalised close to the bounding walls, forming

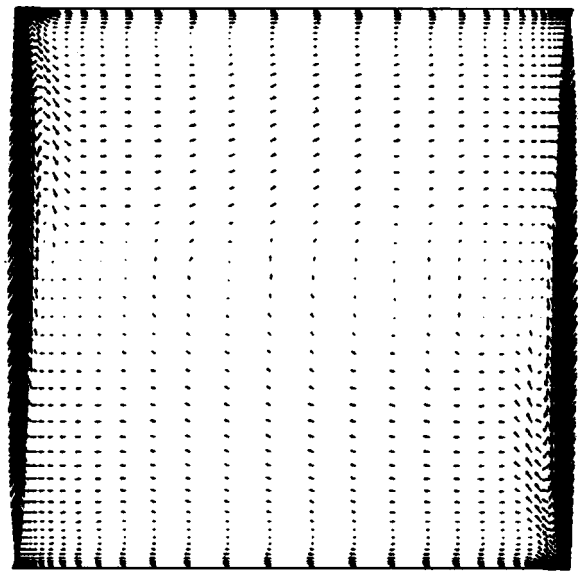

(*a*)

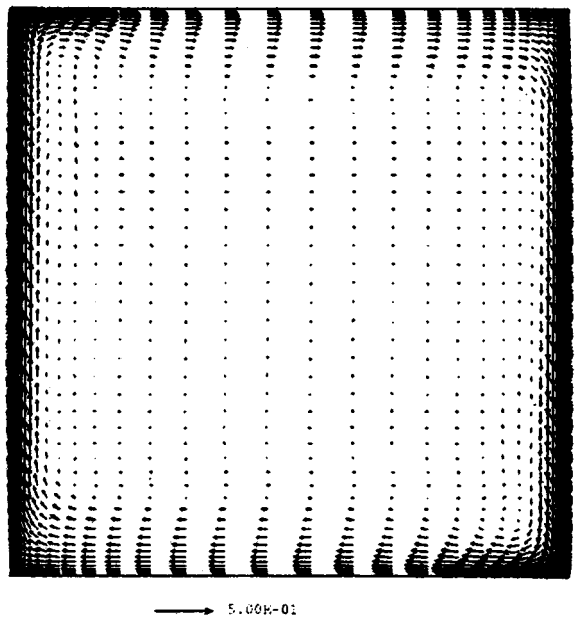

(*b*)

Fig. 5 (*a*) Velocity field in a square enclosure during pure natural convection (in m/s), (Ra=10^{11}, ε=0); (*b*) velocity field in a square enclosure during natural convection–radiation interaction (in m/s), (Ra=10^{11}, ε=0.9, T_o=323 K, ΔT=50 K).

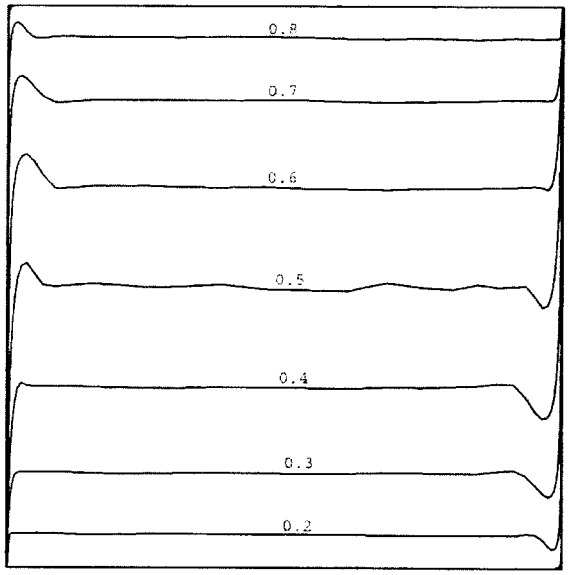

(*a*)

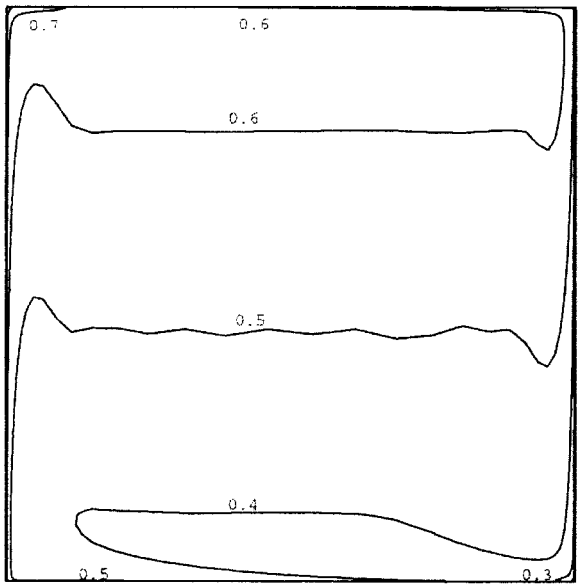

(*b*)

Fig. 6 (*a*) Temperature field in a square enclosure during pure natural convection, $[(T-T_c)/\Delta T]$, (Ra=10^{11}, ε=0); (*b*) temperature field in a square enclosure during natural convection—radiation interaction, $[(T-T_c)/\Delta T]$; (Ra=10^{11}, ε=0.9, T_o=323 K, ΔT=50 K).

distinct vertical as well as horizontal boundary layers. The magnitude of circulation velocity is larger compared to that of the non-radiative case. A glance at the temperature contours suggests that there is unstable stratification close to the top and bottom walls (i.e., hot fluid below cold fluid). Within the core there is stable stratification but it is milder than that in non-radiative enclosure. Because of this, the reverse flows adjacent to the hot and cold wall boundary layers are absent.

For the non-radiative case (ε=0) at a Rayleigh number of 10^{11}, the maximum predicted value of turbulent kinetic energy (k_{max}) is of the order of 10^{-2} m^2/s^2 and this occurs in regions close to the upper part of the hot wall and lower part of the cold wall. In fact, except in small pockets close to these walls, the value of k is less than 10^{-4} m^2/s^2 near the adiabatic walls and in the core portion of the fluid. In contrast, for the case of ε=0.9, k is of the order of 10^{-2} m^2/s^2 for the whole length of the hot and cold walls and it is in the range of 10^{-3} m^2/s^2 in the boundary layers of the adiabatic walls also. These predictions indicate that turbulence effects are significant in limited zones close to the hot and cold walls for the non-radiative case while they are significant in the entire boundary layer regions of all the four walls when radiation interaction occurs. For ε=0, the value of k_{max} at mid-height, non-dimensionalized with respect to the maximum vertical velocity at the same height was found to be 0.204 in the present calculation and it matches almost exactly with the value of 0.211 reported by Henkes [15]. The experimental value of Tsuji and Nagano [22] for

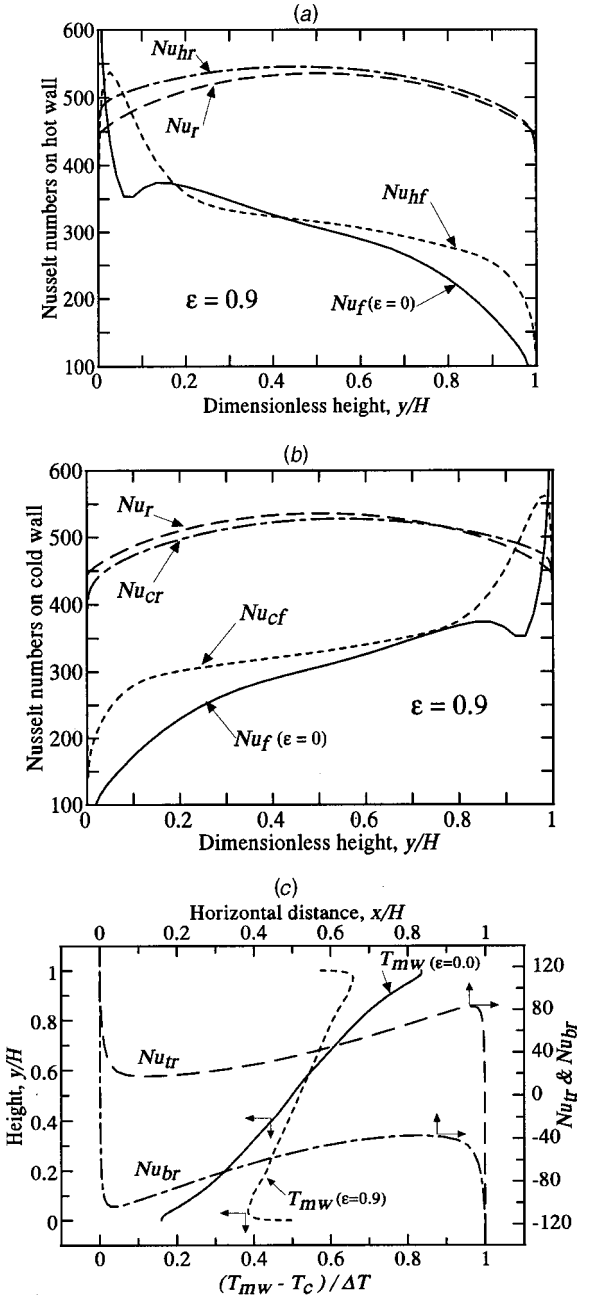

Fig. 7 Influence of radiation on Nusselt numbers and fluid temperature; (*a*) hot wall Nusselt numbers; (*b*) cold wall Nusselt numbers, and (*c*) top and bottom wall Nusselt numbers and mid-width fluid temperature for Ra=10^{11}, $AR=1$, $T_o=323$ K, and $\Delta T=50$ K: Nu_r—radiative Nusselt number without flow; Nu_f—convective Nusselt number without radiation, Nu_{hr}, Nu_{cr}, Nu_{tr}, and, Nu_{br}—radiative Nusselt numbers with coupling; Nu_{hf} and Nu_{cf}—convective Nusselt numbers with coupling.

a vertical plate in air is also 0.211. These comparisons of predicted and measured k values validate the turbulence model used in the present calculations.

The Nusselt number (Nu) on the walls is calculated from $Nu=qW/(K\Delta T)$, where $q=-K(\partial T/\partial n)_{\text{wall}}$ for convective contribution and $q=[\varepsilon/(1-\varepsilon)](\sigma T_w^4-B)$ for radiative contribution. The distributions of local Nusselt numbers on the hot wall for the cases of pure convection ($\varepsilon=0$) and with convection-radiation interaction ($\varepsilon=0.9$) are shown in Fig. 7(*a*). For the sake of comparison, the radiative Nusselt number (Nu_r) variation, in the absence of flow is also included. For the case of pure convection, it is seen that the convective Nusselt number (Nu_f) decreases from a very large value at the bottom of the wall to a minimum at around $y/H=0.08$, and then registers a mild increase with distance. The value of Ra_y at this point is $\sim 5\times 10^7$ which matches closely with the Rayleigh number for laminar to turbulent flow transition, predicted by Henkes [15] for a square enclosure. Beyond the transition zone, Nusselt number decreases gradually with distance, due to the growth of the turbulent boundary layer. With radiation interaction, the convective Nusselt number (Nu_{hf} or Nu_{cf}) is more than the pure convective value in general, due to higher flow velocity magnitudes and turbulence levels. This is contrary to the trend seen in the case of laminar natural convection [2,3]. As regards the radiative Nusselt number distributions, it is observed that the pure radiation profile is symmetric about mid-height as demanded by the boundary conditions. With interaction, however, the radiative Nusselt number of the hot wall (Nu_{hr}) increases marginally at lower elevations where the local view factor between hot wall and the relatively cold bottom wall is higher. From the Nusselt number distributions on the cold wall, shown in Fig. 7(*b*), it can be seen that the convective Nusselt number with radiation interaction is larger (by $\sim$16 percent) than the pure convection case. Evidently, the augmentation in the cold wall convective Nusselt number is more than that for the hot wall with radiation-convection interaction.

The fluid temperature variation along the mid-width of the enclosure (T_{mw}) and local Nusselt number distributions along the horizontal walls are shown in Fig. 7(*c*). Only the radiative Nusselt numbers (Nu_{tr} and Nu_{br}) have been plotted since the convective Nusselt number values will be the negative of the respective radiation based values, because of the imposed adiabatic NCW condition. Under the influence of radiation, the fluid temperature profile indicates that the top wall pre-cools the fluid thereby reducing convective heat transport to the cold wall. The heat flux absorbed by the top wall is re-emitted to other walls as radiation. The bottom wall similarly receives heat by radiation and returns it by convection. Such pre-heating by the bottom wall reduces the temperature difference between the hot wall and the boundary layer fluid. The radiative Nusselt number on the top wall (Nu_{tr}) increases as one moves towards the cold wall due to larger local view factor between the two heat exchanging surfaces, requiring a similar increase in convective heat transfer within the fluid. For similar reasons, the magnitude of Nusselt number on the bottom wall (Nu_{br}) is larger as one moves towards the hot wall.

In the absence of convection, the top and bottom wall temperatures should be identical and the mean temperature should be equal to the equilibrium temperature T_{eq} given by $((T_h^4+T_c^4)/2)^{1/4}$. It is clear that the equilibrium temperature is closer to T_h than to T_c. Therefore, the effective temperature difference between the fluid and the top wall is less than that between the fluid and the bottom wall. This is the reason for the top wall convective heat flux being lower than the bottom wall flux when radiation interaction is present. For similar reasons, the cold wall convective Nusselt number is larger than the hot wall convective Nusselt number. To satisfy the heat balance, the radiative Nusselt number to the cold wall is less than that from the hot wall. The overall heat balance between all the wall surfaces was found to be exact (within a tolerance of <0.1 percent) as a cross check on the predicted results.

In Fig. 8, the variation of average convective Nusselt number during pure convection (Nu_f) is shown as a function of Rayleigh number. The relation, $Nu_f=0.03662\times Ra^{0.3555}$ represents the numerically predicted data within 1 percent. The hot and cold wall convective Nusselt numbers with radiation ($\varepsilon=0.9$) are represented by the relations, $Nu_{hf}=0.0594\times Ra^{0.3406}$ and $Nu_{cf}=0.0654\times Ra^{0.3388}$, respectively, and it is evident that the average convective Nusselt numbers increase due to radiation interaction. The percentage of augmentation of convective Nusselt number is larger at lower Rayleigh number. For example, the augmentation

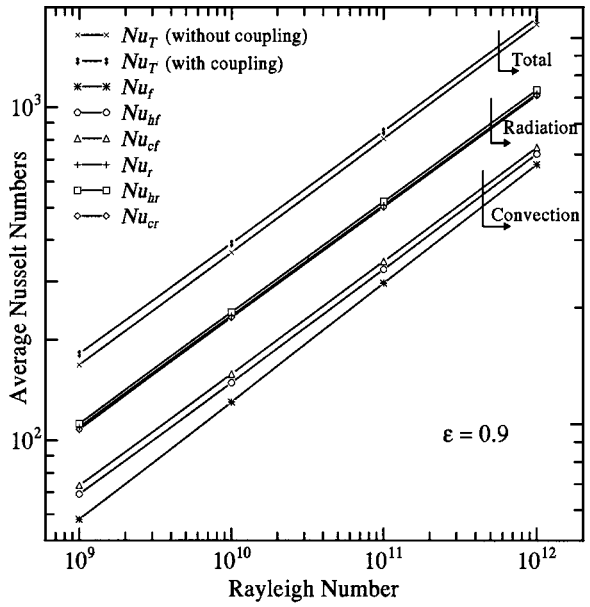

Fig. 8 Variation of convective, radiative and total Nusselt numbers with Rayleigh number for $AR=1$, $T_o=323$ K, $\varepsilon=0.9$, and $\Delta T=50$ K

in Nu_{cf} at $Ra=10^9$ is 26.4 percent as against an augmentation of 12.6 percent at $Ra=10^{12}$. The variations of radiative Nusselt number with Rayleigh number for pure enclosure radiation (Nu_r) and with convection interaction (Nu_{hr} and Nu_{cr}) are also shown in Fig. 8, for a fixed set of T_o, ΔT, and ε. The hot and cold wall radiative Nusselt numbers are only slightly higher and lower than the pure radiative value, because the temperatures of the enclosure walls are very close to the pure radiative value for large values of emissivity such as 0.9. The radiative Nusselt number is proportional to $Ra^{1/3}$, because the width W varies as $Ra^{1/3}$ when T_o, ΔT, and ε are fixed. The variations of total Nusselt number (Nu_T) which is the addition of convective and radiative contributions, obtained by coupled or decoupled analyses are also shown in the figure. They are represented by the relations, $Nu_T=0.17\times Ra^{0.3365}$ and $Nu_T=0.142\times Ra^{0.3414}$ respectively with an error <0.7 percent. The decoupled analysis thus under predicts the heat transfer rate.

5.2 Effects of Emissivity and Wall Temperature Values on Heat Transfer for Square Enclosures. The effects of parameters such as emissivity, mean temperature $T_o(=(T_h+T_c)/2)$ and temperature difference ΔT on the convective, radiative and total Nusselt numbers are highlighted in Table 3. For the sake of comparison, the results corresponding to coupled (convection-radiation interaction case) and decoupled analyses are listed. It is evident that convection-radiation interaction is quite significant at lower Rayleigh numbers. The convective Nusselt numbers slightly increase with emissivity, but the relative contribution of convection to the total heat transfer decreases due to steeper increase of the radiative Nusselt numbers. The temperature difference ΔT has an independent influence apart from its role as a part of Rayleigh number. It is known that the non-dimensional equilibrium temperature of the top and bottom walls increases and moves towards $2^{-1/4}$ as the temperature difference increases. (The maximum value is attained when $T_c=0$.) As a result of this, the cold wall convective Nusselt number increases and hot wall convective Nusselt number reduces due to changes in the temperature difference between the fluid and the wall. In fact, the hot wall convective Nusselt number can be even lower than pure natural convective value if ΔT is sufficiently large. It can be shown that for a fixed value of Ra,Nu_r varies as $(\Delta T)^{-1/3}$. The total Nusselt number also decreases, mainly due to the reduction of radiative contribution at higher values of ΔT. Radiation is seen to play a significant role as compared to natural convection heat transfer, even at low mean temperature values such as -50°C. As expected, Nu_r increases in proportion to T_o^3.

5.3 Effect of Wall Conduction for a Square Enclosure. In order to see the influence of conduction along the length of the top and bottom walls, these walls are considered to be perfectly conducting (PCW) and making contact with the vertical walls on either end. The temperature profiles of these walls will be linear with one end at T_h and other end at T_c. The local hot wall Nusselt number for a fixed set of T_o, ΔT, and Ra is shown in Fig. 9 for the case of PCW. Also shown in the same figure are the convective Nusselt numbers for pure convection and convection-radiation interaction situations for negligibly conducting top and bottom walls (NCW). It is seen that the influence of strong wall conduction on convective Nusselt number is similar to that of surface radiation. Unlike for the case with radiation, however, the influence of wall conduction is symmetric and the convective Nusselt number for the hot and cold walls are augmented uniformly (not shown in figure) as against the selective influence of radiation.

5.4 Results for Tall Enclosures. In practical applications, it is necessary to know the influence of surface radiation on turbulent natural convection in tall enclosures with aspect ratio (AR)

Table 3 Augmentation in total Nusselt number due to convection-radiation coupling for square enclosures

Fixed Parameters	Variable Parameter	Without Coupling			With Coupling					Augmentation in Nu_T with coupling
		Nu_f	Nu_r	Nu_T	Nu_{hf}	Nu_{cf}	Nu_{hr}	Nu_{cr}	Nu_T	
$\varepsilon=0.9$, $T_o=323$ K, $\Delta T=50$ K	$Ra=10^9$	57.96	109.86	167.82	69.04	73.32	112.39	108.11	181.43	8.1%
	$Ra=10^{11}$	296.43	509.87	806.30	326.03	344.57	523.06	504.52	849.09	5.3%
	$Ra=10^{12}$	675.64	1098.6	1774.2	726.07	760.74	1128.2	1093.5	1854.3	4.5%
$Ra=10^9$, $T_o=323$ K $\Delta T=50$ K	$\varepsilon=0.3$	57.96	30.16	88.12	68.87	70.87	31.10	29.10	99.97	13.4%
	$\varepsilon=0.6$	57.96	66.14	124.10	69.04	72.35	67.77	64.46	136.81	10.2%
$Ra=10^{11}$, $T_o=323$ K $\Delta T=50$ K	$\varepsilon=0.3$	296.43	140.00	436.43	320.32	329.28	144.52	135.56	464.84	6.5%
	$\varepsilon=0.6$	296.43	306.97	603.40	323.20	337.82	315.18	300.56	638.38	5.8%
$\varepsilon=0.9$, $Ra=10^{11}$, $T_o=323$ K	$\Delta T=10$ K	296.43	866.93	1163.36	334.90	339.34	873.58	869.14	1208.5	3.9%
	$\Delta T=250$ K	296.43	340.82	637.25	295.26	363.38	377.36	309.24	672.62	5.6%
$\varepsilon=0.9$, $Ra=10^{11}$, $\Delta T=50$ K	$T_o=223$ K	296.43	168.90	465.33	321.29	335.02	177.95	164.22	499.24	7.3%
	$T_o=423$ K	296.43	1142.44	1438.87	328.09	347.21	1156.4	1137.3	1484.5	3.2%

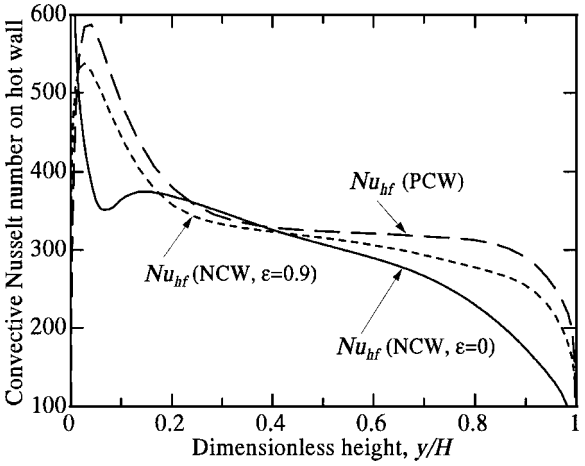

Fig. 9 Influence of top and bottom wall conduction on hot wall Nusselt number for Ra=10^{11}, AR=1, T_o=323 K, and ΔT=50 K

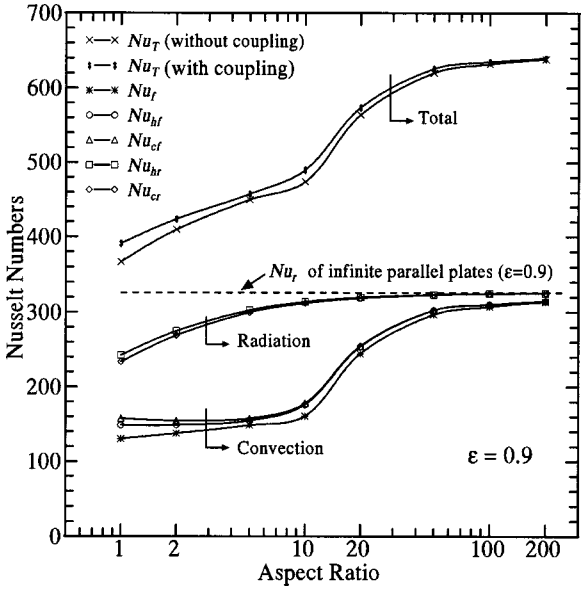

Fig. 11 Variation of Nusselt numbers in tall vertical enclosures for $Ra_w=10^{10}$, $\varepsilon=0.9$, T_o=323 K, and ΔT=50 K

>1. For this purpose, a wide range of AR values up to 200 for two values of width based Rayleigh number (Ra_w), 10^9 and 10^{10} with $T_o=323$ K and $\Delta T=50$ K are analyzed. For $AR=100$ and $Ra_w=5.4\times10^5$, the mid-height variations of vertical velocity and temperature are compared against the numerical results of Xu et al. [18] and the DNS results of Versteegh and Nieuwstadt [23], in Fig. 10. The present results compare very well with these published results validating the present model.

The dependence of average Nusselt numbers on aspect ratio, estimated from coupled and decoupled analyses are shown in Fig. 11 for $Ra_w=10^{10}$. It is seen that the pure turbulent convective Nusselt number (Nu_f) increases with aspect ratio, in line with the experimental observations of Shewen et al. [10]. This is contrary to the variation of Nu_f for laminar natural convection [24], where it reduces with increase in aspect ratio. It is also seen that Nu_f exhibits three distinct regimes viz. (i) slow growth regime up to critical aspect ratio, (ii) accelerated growth regime between critical and saturation aspect ratios, and (iii) invariant regime, beyond the saturation aspect ratio. These features are closely linked to the growth of turbulent boundary layers on the hot and cold walls. In the case of saturation aspect ratio, the flow is fully developed for most of the height (with merged boundary layers), having variation only in the horizontal direction. The radiative Nusselt numbers uniformly increase and approach the parallel plate value given by, $Nu_r=(\varepsilon\sigma(T_h^4-T_c^4)W)/((2-\varepsilon)K(T_h-T_c))$, as the aspect ratio increases. The influence of surface radiation on the convective Nusselt number decreases as the aspect ratio increases because the areas of the top and bottom walls that modify the flow distribution in the enclosure become insignificant as compared to the areas of the vertical walls. Thus, the convective-radiative coupling becomes weaker as the aspect ratio increases and in tall enclosures, the total Nusselt number can be obtained by a decoupled analysis.

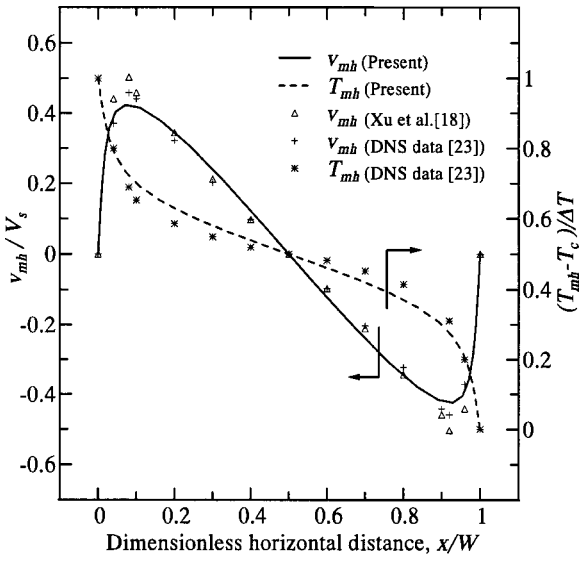

Fig. 10 Comparison of present results with published results for $Ra_w=5.4\times10^5$, AR=100, ε=0, T_o=323 K, and ΔT=50 K

6 Conclusions

The problem of turbulent natural convection in a transparent fluid medium and its interaction with surface radiation has been analyzed for rectangular enclosures. The following major conclusions are drawn from the numerical simulation.

1 Surface radiation enhances the velocity and turbulence levels in the boundary layers along the enclosure walls, thereby resulting in higher convective heat transfer. Due to the asymmetrical influence of radiation, the augmentation of convective Nusselt number for the cold wall is larger than that for the hot wall.

2 The contribution of radiative heat transfer is significant even at temperatures as low as 0°C. Also, the temperature difference between the hot and cold walls needs to be treated as an independent parameter, for the flow with radiation interaction, in addition to other governing non-dimensional parameters. The convective augmentation is significant even at low emissivity values such as 0.1, but it reduces as the Rayleigh number increases.

3 In tall enclosures, the average Nusselt number variation exhibits three distinct regimes, viz. slow growth, accelerated growth and invariant regime. This behavior can be attributed to the interaction phenomena between the boundary layers of the vertical walls.

4 The influence of perfectly conducting top and bottom walls on the turbulent natural convective flow is found to be similar to that of radiation interaction. Hence, the convective Nusselt number is enhanced when the adiabatic walls conduct heat along their length.

Nomenclature

AR = aspect ratio of the enclosure
B = radiosity
C_P = specific heat of the fluid
F_{i-j} = view factor from element i to j
g = acceleration due to gravity
H = height of the enclosure
G = irradiation
k = turbulent kinetic energy
K = thermal conductivity of the fluid
Nu = Nusselt number
p = pressure
Ra = Rayleigh number, $(\beta g \Delta T H^3)/(\upsilon \alpha)$
T = temperature of the fluid
u,v = horizontal and vertical velocity components
V_s = buoyant velocity scale, $(\beta g \Delta T W)^{1/2}$
$u'v'$ = turbulent stress
W = width of the enclosure
x, y = horizontal and vertical coordinates

Greek

α = thermal diffusivity of the fluid
β = coefficient of volumetric expansion
ΔT = temperature difference between the hot and cold vertical walls
ε = dissipation rate of k; hemispherical emissivity of the enclosure surfaces
μ = viscosity
ρ = mean density of the fluid
σ = Stefan-Boltzmann constant
$\sigma_k, \sigma_T, \sigma_\varepsilon$ = turbulent Prandtl numbers of k, T and ε

Subscripts

b = values corresponding to bottom wall
c = values corresponding to cold wall
f = values related to convection
h = values corresponding to hot wall
max = maximum values
mh = values at mid-height of the enclosure
mw = values at mid-width of the enclosure
r = values related to radiation
t = values corresponding to top wall; turbulent
T = total contribution of convection and radiation

References

[1] De Vahl Davis, G., and Jones, I. P., 1983, ''Natural Convection in a Square Cavity—A Comparison Exercise,'' Int. J. Numer. Methods Fluids, **3**, pp. 227–248.
[2] Balaji, C., and Venkateshan, S. P., 1993, ''Interaction of Surface Radiation with Free Convection in a Square Cavity,'' Int. J. Heat Fluid Flow, **14**, pp. 260–267.
[3] Akiyama, M., and Chong, Q. P., 1997, ''Numerical Analysis of Natural Convection with Surface Radiation in a Square Enclosure,'' Numer. Heat Transfer, Part A, **31**, pp. 419–433.
[4] Ostrach, S., 1988, ''Natural Convection in Enclosures,'' ASME J. Heat Transfer, **110**, pp. 1175–1190.
[5] Hoogendoorn, C. J., 1986, ''Natural Convection in Enclosures'' *Proc. 8th Int. Heat Transfer Conf.*, Vol. 1, Hemisphere Publishing Corp. Washington, DC, pp. 111–120.
[6] Elsherbiny, S. M., Raithby, G. D., and Hollands, K. G. T., 1982, ''Heat Transfer by Natural Convection Across Vertical and Inclined Air Layers,'' ASME J. Heat Transfer, **104**, pp. 96–102.
[7] Cheesewright, R., and Ziai, S., 1986, ''Distributions of Temperature and Local Heat-Transfer Rate in Turbulent Natural Convection in a Large Rectangular Cavity,'' *Proc. 8th Int. Heat Transfer Conf.*, Hemisphere Publishing Corp. DC, pp. 1465–1470.
[8] Cheesewright, R., King, K. J., and Ziai, S., 1986, ''Experimental Data for the Validation of Computer Codes for the Prediction of Two-Dimensional Buoyant Cavity Flows,'' Proc. ASME Meeting HTD, Vol. 60, pp. 75–81.
[9] Olson, D. A., Glicksman, L. R., and Ferm, H. M., 1990, ''Steady State Natural Convection in Empty and Partitioned Enclosures at High Rayleigh Numbers,'' ASME J. Heat Transfer, **112**, pp. 640–647.
[10] Shewen, K., Hollands, K. G. T., and Raithby, G. D., 1996, ''Heat Transfer by Natural Convection Across Vertical Air Cavity of Large Aspect Ratio,'' ASME J. Heat Transfer, **118**, pp. 993–995.
[11] Ozoe, H., Mouri, A., Ohmuro, M., Churchill, S. W., and Lior, N., 1985, ''Numerical Calculations of Laminar and Turbulent Natural Convection in Water in Rectangular Channels Heated and Cooled Isothermally on the Opposing Vertical Walls,'' Int. J. Heat Mass Transf., **28**, pp. 125–139.
[12] Giel, P. W., and Schmidt, F. W., 1990, ''A Comparison of Turbulence Modeling Predictions to Experimental Measurements for High Rayleigh Number Natural Convection in Enclosures,'' Proc. 9th Int. Heat Transfer Conf., Jerusalem, Israel, Hemisphere Publishing Corp., Vol. 2, pp. 175–180.
[13] Markatos, N. C., and Pericleous, K. A., 1984, ''Laminar and Turbulent Natural Convection in an Enclosed Cavity,'' Int. J. Heat Mass Transf., **27**, pp. 755–772.
[14] Fusegi, T., and Farouk, B., 1989, ''Laminar and Turbulent Natural Convection-Radiation Interactions in a Square Enclosure Filled with a Non-gray Gas,'' Numer. Heat Transfer, Part A, **15**, pp. 303–322.
[15] Henkes, R. A. W. M., 1990, ''Natural Convection Boundary Layers,'' Ph.D. thesis, Delft University of Technology, The Netherlands.
[16] Henkes, R. A. W. M., and Hoogendoorn, C. J., 1995, ''Comparison Exercise for Computations of Turbulent Natural Convection in Enclosures, '' Numer. Heat Transfer, Part B, **28**, pp. 59–78.
[17] Gan, G., 1998, ''Prediction of Turbulent Buoyant Flow Using an RNG-k-ε Model,'' Numer. Heat Transfer, Part A, **33**, pp. 169–189.
[18] Xu, W., Chen, Q., and Nieuwstadt, F. T. M., 1998, ''A New Turbulence Model for Near-Wall Natural Convection,'' Int. J. Heat Mass Transf., **41**, pp. 3161–3176.
[19] Patankar, S. V., 1980, *Numerical Heat Transfer and Fluid Flow*, Hemisphere, New York.
[20] King, K. J., 1989, ''Turbulent Natural Convection in Rectangular Air Cavities,'' Ph.D. thesis, Queen Mary College, London, U.K.
[21] Fu, B. I., and Ostrach, S., 1981, ''The Effects of Stabilising Thermal Gradients on Natural Convection Flows in a Square Enclosure,'' in *Natural Convection 20th ASME/AIChE Natl. Heat Transfer Conf.*, Wisconsin, HTD-Vol. 16, pp. 91–104.
[22] Tsuji, T., and Nagano, Y., 1989, ''Velocity and Temperature Measurements in a Natural Convection Along a Vertical Flat Plate,'' Exp. Therm. Fluid Sci., **2**, pp. 208–215.
[23] Versteegh, T. A. M., and Nieuwstadt, F. T. M., 1999, ''A Direct Numerical Simulation of Natural Convection Between Two Infinite Vertical Differentially Heated Walls: Scaling Laws and Wall Functions,'' Int. J. Heat Mass Transf. **42**, pp. 3673–3693.
[24] Venkateshan, S. P., and Balaji, C., 1995, ''Interaction of Surface Radiation and Free Convection in Open and Closed Cavities,'' *Proc. 2nd ISHMT-ASME Heat and Mass Transfer Conf.*, REC-Surathkal, India, pp. 91–101.

A Theoretical Model to Predict Pool Boiling CHF Incorporating Effects of Contact Angle and Orientation

Satish G. Kandlikar
Fellow ASME
Mechanical Engineering Department,
Rochester Institute of Technology,
Rochester, NY 14623
e-mail: sgkeme@rit.edu

A theoretical model is developed to describe the hydrodynamic behavior of the vapor-liquid interface of a bubble at the heater surface leading to the initiation of critical heat flux (CHF) condition. The momentum flux resulting from evaporation at the bubble base is identified to be an important parameter. A model based on theoretical considerations is developed for upward-facing surfaces with orientations of 0 deg (horizontal) to 90 deg (vertical). It includes the surface-liquid interaction effects through the dynamic receding contact angle. The CHF in pool boiling for water, refrigerants and cryogenic liquids is correctly predicted by the model, and the parametric trends of CHF with dynamic receding contact angle and subcooling are also well represented. [DOI: 10.1115/1.1409265]

Keywords: Boiling, Heat Transfer, Modeling, Phase Change

Introduction

Critical heat flux (CHF) represents the limit of the safe operating condition of a system or a component employing boiling heat transfer under constant heat flux boundary condition. Loss of liquid contact with the heating surface at CHF leads to a significant reduction in the heat dissipation rate. In pool boiling application, such as in electronics equipment cooling, the drastic reduction in boiling heat flux after CHF may lead to devastating results. Therefore, a fundamental understanding of the mechanisms responsible for the initiation of this condition continues to be of great importance. The current work models this phenomenon by including the non-hydrodynamic aspect of surface-liquid interaction through the dynamic receding contact angle. The model is tested with a number of data sets available in literature.

Previous Work

Historical Perspective. As early as 1888, Lang [1] recognized through his experiments on high pressure water data that as the wall temperature increased beyond a certain point, the heat flux decreased dramatically. However, it was Nukiyama [2] who realized that the maximum boiling rate might occur at relatively modest temperature differences. An excellent summary of historical developments in this area was presented by Drew and Mueller [3].

Many researchers have considered various aspects of CHF. Some of the important milestones include Lang [1], Nukiyama [2], Bonilla and Perry [4], Cichelli and Bonilla [5], Kutateladze [6,7] Rohsenow and Griffith [8], Zuber [9], Costello and Frea [10], Gaertner [11,12], Katto and Yokoya [13], Lienhard and Dhir [14], Haramura and Katto [15], Liaw and Dhir [16], Ramilison and Lienhard [17], Elkassabgi and Lienhard [18], and Dhir and Liaw [19]. A brief overview of some of these and a few other important investigations is given in the following section. (The list provided here is not intended to be comprehensive, and the author is aware that he may have made some inadvertent omissions.)

Previous Models and Correlations. Although a number of early investigators reported the critical heat flux phenomenon, Bonilla and Perry [4] proposed the concept of flooding in obtaining a correlation from the experimental data. Using the column flooding theory, they derived four dimensionless groups. The basic concept seemed to work, but the approach was not pursued further. Cichelli and Bonilla [5] correlated their experimental data for organic liquids with q''_C/p_C plotted against reduced pressure, p/p_C. Although their organic liquid data matched reasonably well, the predictions were considerably lower than the experimental data for water by Addoms [20].

Kutateladze [6,7] proposed that the meaning of bubble generation and departure were lost near the critical heat flux condition, and it was essentially a hydrodynamic phenomenon with the destruction of stability of two-phase flow existing close to the heating surface. Critical condition is reached when the velocity in the vapor phase reaches a critical value. Following a dimensional analysis, he proposed the following correlation.

$$\frac{q''_C}{h_{lg}\rho_{lg}^{0.5}[\sigma g(\rho_l-\rho_g)]^{1/4}}=K \tag{1}$$

The value of K was found to be 0.16 from the experimental data.

Borishanskii [21] modeled the problem by considering the two-phase boundary in which liquid stream flowing coaxially with gas experiences instability. His work lead to the following equation for K in Kutateladze's equation, Eq. (1).

$$K=0.13+4\left\{\frac{\rho_l\sigma^{3/2}}{\mu^2[g(\rho_l-\rho_g)]^{1/2}}\right\}^{-0.4} \tag{2}$$

Although viscosity appears in Eq. (2), its overall effect is quite small on CHF.

Rohsenow and Griffith [8] postulated that increased packing of the heating surface with bubbles at higher heat fluxes inhibited the flow of liquid to the heating surface. Plotting $q''_C/(h_{lg}\rho_g)$ versus $(\rho_l-\rho_g)/\rho_g$, they proposed the following correlation for CHF.

$$\frac{q''_C}{h_{lg}\rho_g}=C\left(\frac{g}{g_s}\right)^{1/4}\left[\frac{\rho_l-\rho_g}{\rho_g}\right]^{0.6}. \tag{3}$$

The equation is dimensional with $C=0.012$ m/s, g is the local gravitational acceleration, and g_s corresponds to the standard g value.

Zuber [9] further formalized the concept by considering the formation of vapor jets above nucleating bubbles and flow of liq-

Contributed by the Heat Transfer Division for publication in the JOURNAL OF HEAT TRANSFER. Manuscript received by the Heat Transfer Division March 9, 2000; revision received April 23, 2001. Associate Editor: V. P. Carey.

uid between the jets toward the heating surface. As the heat flux increases, the vapor velocity increases causing vapor and liquid to compete for the same space; a condition for instability is thus created.

Zuber [9] also postulated that vapor patches form and collapse on the heater surface as CHF is approached. According to Zuber, "In collapsing, . . . [as] the vapor-liquid interface of a patch approaches the heated surface, large rates of evaporation occur and the interface is pushed violently back." Zuber considered the dynamic effects of vapor jets to be important and proposed that the Taylor and Helmholtz instabilities are responsible for the CHF condition. Using the stability criterion of a vapor sheet, they obtained an equation similar to that of Kutatelazde [7], but the value of constant K ranged from 0.157 to 0.138. Simplifying the analysis further, Zuber proposed a value of $K=0.131$.

Chang [22] considered the forces acting on the bubble and postulated that the CHF condition was attained when the Weber number (incorporating the velocity of liquid relative to the rising bubble) reached a critical value. The vapor continues to leave the heater surface until the critical velocity is reached, at which time some of the vapor is carried back to the heater surface. The analysis resulted in the following equation for vertical surfaces.

$$q''_C=0.098\rho_g^{1/2}h_{lg}[\sigma g(\rho_l-\rho_g)]^{1/4} \quad (4)$$

For horizontal surfaces, he introduced a ratio $q''_{C,H}/q''_{C,V}=0.75$, thereby changing the leading constant to 0.13 in Eq. (4) for horizontal surfaces.

Moissis and Berenson [23] developed a model based on the interaction of the continuous vapor columns with each other. The maximum heat flux is then determined by introducing Taylor-Helmholtz instability for the counterflow of vapor flow in columns and liquid flow between them.

Haramura and Katto [15] refined an earlier model proposed by Katto and Yokoya [13] in which the heat transfer was related to the formation and evaporation of a macrolayer under a bubble. The presence of such macrolayer was reported by Kirby and Westwater [24] and Yu and Mesler [25]. Small vapor jets are formed in this macrolayer, and Kelvin-Rayleigh instability results in lateral coalescence of vapor stems. Using this approach, Haramura and Katto extended Zuber's [9] analysis and arrived at the same equation, Eq. (1), derived by Kutalteladze.

Lienhard and Dhir [14] critically evaluated the assumptions made in the Zuber's [9] theory and modified the vapor velocity condition at which instability would set in. Consequently, they showed that Zuber's equation would underpredict the CHF by 14 percent. Lienhard and Dhir modified Zuber's theory to include the effect of size and geometry. They also noted the increase in the number of jets as CHF was approached. This aspect was further studied by Dhir and Liaw [19] for horizontal flat surfaces, and a detailed formulation was presented.

Van Outwerkerk [26] studied the stability of pool and film boiling mechanisms using high speed photographs of n-Heptane boiling on a glass surface coated with transparent heater film. Dry patches were observed at heat fluxes 20 percent below CHF. Although the fraction or sizes of dry patches did not change, there was a sudden transition to CHF from one of the patches. Simultaneous existence of nucleate and film boiling on two adjacent sections was observed on a thin wire which was partially removed and then immersed back into the liquid. The reason behind the transition mechanism was discussed.

Effect of contact angle was studied by very few investigators. Kirishenko and Cherniakov [27] developed the following correlation with contact angle as a parameter.

$$q''_C=0.171h_{fg}\sqrt{\rho_g}[\sigma g(\rho_l-\rho_g)]^{1/4}\frac{(1+0.324\cdot 10^{-3}\beta^2)^{1/4}}{\sqrt{0.018\beta}} \quad (5)$$

Diesselhorst et al. [28] noted that this equation yielded much higher values of CHF for larger contact angles. This correlation was found to be quite inaccurate in representing the effects of contact angle for water. The correlation however exhibited the correct trend of decreasing heat flux with increasing contact angles.

Unal et al. [29] considered the existence of dry patches to lead the way toward CHF condition. The temperature reached at the center of the dry patch was considered to be an important parameter responsible for the rewetting behavior of the surface. Sadasivan et al. [30] presented a good overview highlighting the need for new experiments to aid in the understanding of the CHF phenomenon.

Parametric Effects. Although CHF was identified as a hydrodynamic phenomenon, a number of researchers recognized the important role played by the surface characteristics. Tachibana et al. [31] studied the effect of heater thermal properties and found that CHF increased as (*a*) the thermal conductivity increased, and (*b*) as the heat capacity per unit surface area increased. However, thermal diffusivity, which is the ratio of thermal conductivity to the thermal mass, did not correlate well with CHF. For thin stainless steel heaters below 0.8 mm in thickness, the CHF was found to be lower than that for thick heaters (>0.8 mm thick). They also noted that the presence of aluminum oxide coating increased CHF, attributed to its affinity to water (wettability). More recently, Golobič and Bergles [32] presented a detailed literature survey on the effect of thermal properties on CHF for ribbon heaters. They developed a criterion for the asymptotic value of heater thickness for ribbon heaters beyond which the thickness effect on CHF was quite small. They recommended similar work for other geometries.

Contact angle is a key parameter affecting the bubble-wall interaction. Its effect on CHF was recognized by many investigators. An interesting set of experiments was performed by Costello and Frea [10] with submerged cylinders heated only on the top half. The heated surface was coated with mineral deposits resulting from boiling in tap water. The heat flux and duration of boiling was carefully regulated to achieve different levels of deposit thickness. The treated cylinders were then used with distilled water and the burnout heat fluxes were measured. They found that the presence of deposits on the heater surface resulted in over 50 percent increase in CHF in some cases over the freshly prepared clean cylinders. This non-hydrodynamic effect was not predicted by any of the existing correlations. Costello and Frea noted that, for cylindrical heaters, this effect was not as pronounced due to inadequate supply of liquid to the larger heated surface.

The effect of orientation is studied by many investigators. The horizontal and vertical geometries are of most practical interest. Howard and Mudawar [33] studied the effect of heater orientation in great detail and present three regions: upward-facing (0–60 deg), near vertical (60 to 165 deg), and downward facing (>165 deg). One of the factors that affect the CHF is the size of the heater, especially for near vertical and downward facing surfaces. The surfaces studied by Howard and Mudawar included heaters of different shapes with dimensions varying from 3 mm to 300 mm.

Gaertner [12] conducted some highly illustrative experiments confirming the results reported by Costello and Frea [10]. Gaertner coated the inside bottom of a 3-inch diameter container with a thin non-wetting (close to 180 deg contact angle) fluorocarbon film, similar to Teflon. The container was then filled with distilled water and heated at the bottom. As the heater temperature increased, boiling was initiated, but the bubbles did not depart from the heater surface. Instead, they coalesced and covered the entire bottom surface with a film of vapor resulting in extremely low values of CHF. Another experiment demonstrated that the presence of grease in the system caused a gradual reduction in CHF as the heater surface was progressively coated with a non-wetting film of grease. Although the surface roughness itself was not directly responsible to any changes in CHF, if the contact angle changed as a result, the CHF was lowered. The experiments confirm that a low contact angle (highly wetting liquid) will result in

a higher value of CHF, while a high contact angle, such as a non-wetting surface, will result in drastic reduction in CHF (also confirmed by Costello and Frea).

Hydrodynamic and Non-Hydrodynamic Considerations in the Development of the Present Model. The supply of liquid to and removal of vapor from a heated surface play a major role in reaching the CHF condition. If we consider an experiment in which a growing bubble is completely confined within side walls, the CHF will be reached immediately upon nucleation as the liquid is unable to reach the heater surface. This type of CHF is observed in microgravity environment with smooth heaters where a large stationary bubble envelops the heater surface.

On the other hand, the photographs by Elkassabgi and Lienhard [18] just prior to the CHF show that, for saturated liquids, bubbles coalesce to form large vapor masses a short distance away from the heater surface. In subcooled pool boiling, bubbles are discrete, presenting little resistance to liquid flow toward the heater surface near CHF. In addition, the dependence on surface effects expressed through the contact angle (as reported by many investigators, including Gaertner, [11] and Costello and Frea, [10]), suggests that the mechanisms leading to CHF are more intimately connected to the events occurring in the immediate vicinity of the heater surface.

The theoretical models available in literature do not incorporate the effect of contact angle. Its effect is considered indirectly through the changes in bubble size and number of nucleation sites in some of these models. In the present work, a theoretical model is presented which directly incorporates the effect of dynamic receding contact angle on CHF. The model is tested with data sets available in literature for different fluids.

Development of the Model. Departing from the earlier models on hydrodynamic instability, Chang [22] considered the force balance on a bubble in deriving the condition leading to CHF. The model of Haramura and Katto [15] also focuses on the bubble behavior by considering the presence of a thin macrolayer underneath a bubble. The strong effect of contact angle on CHF suggests that the interface conditions at the bubble base play an important role.

Figure 1(*a*) shows a bubble attached to a horizontal heating surface. The excess pressure inside the bubble under a quasi-static equilibrium state is able to sustain the necessary curvature of the interface at the departure condition. At low heat fluxes, the bubble would depart at certain size as governed by the forces due to inertia, pressure and buoyancy. Now consider the left half of the bubble and the forces acting on it in the direction parallel to the heating surface. The surface tension forces $F_{S,1}$ and $F_{S,2}$ act at the bubble base and the top surface of the bubble respectively. The hydraulic pressure gradient (buoyancy) due to gravity is plotted as excess pressure due to hydrostatic head with the reference plane being at the top of the bubbles surface. It results in a triangular (excess) pressure distribution with F_G as the resultant force. The evaporation occurring on sides of the bubble causes the vapor to leave the interface at a higher velocity due to the difference in specific volumes. At high evaporation rates near CHF, the force due to the change in momentum, F_M, due to evaporation becomes larger than the sum of the gravitational and surface tension forces holding the bubble in place. This causes the liquid-vapor interface (side walls of the bubble) to move rapidly along the heater surface leading to the CHF condition. A detailed force balance is performed below to obtain the heat flux value at this condition (CHF). The present model is valid for upward-facing surfaces between horizontal and vertical orientations. For higher angles of orientations, the flow hydrodynamics and heater size effects become very important and need to be included in the model development.

The diameter D_b corresponds to the departure condition at which the force balance is performed. Although the forces at the bubble interface act in the radial direction, the movement of the interface can be analyzed in a two-dimensional plane shown in Fig. 1(*a*). Surface tension forces act at the base and the top portion of the bubble. For a unit length in the direction normal to the plane, the forces $F_{S,1}$ and $F_{S,2}$ are given by

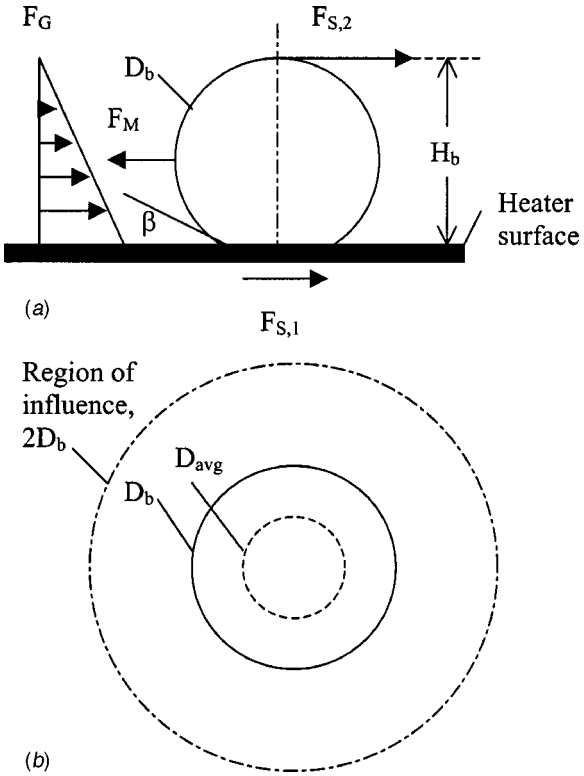

Fig. 1 (*a*) Forces due to surface tension, gravity and momentum acting on a bubble parallel to the theater surface; (*b*) sketch showing region of influence, departure bubble diameter, and average bubble size

$$F_{S,1}=\sigma\cos\beta \tag{6}$$

and

$$F_{S,2}=\sigma, \tag{7}$$

where σ is surface tension, N/m, and β is the dynamic receding contact angle of the liquid-vapor interface with the solid heater surface.

The evaporation at the interface results in a force due to the change in momentum as vapor leaves the interface. For momentum analysis, the interface is represented as a plane with bubble height H_b and a unit width normal to plane of Fig. 1(*a*). Expressing the heat flux due to evaporation per unit area of the interface as q_I'', the resulting force due to the momentum change is given by the product of the evaporation mass flow rate and the vapor velocity relative to the interface.

$$F_M=\frac{q_I''H_b\cdot 1}{h_{fg}}\frac{q_I''}{h_{fg}}\frac{1}{\rho_g}=\left(\frac{q_I''}{h_{fg}}\right)^2\frac{1}{\rho_g}H_b \tag{8}$$

The bubble height H_b is related to the bubble diameter D_b through the contact angle β as follows:

$$H_b=\frac{D_b}{2}(1+\cos\beta). \tag{9}$$

The heat flux at the interface q_I'' is an average value during the growth of the bubble since its inception. It is derived from the heat flux on the heater surface q'' by approximating the interface as a cylinder with diameter $D_{\text{avg}}/2$ and height $H_{\text{avg}}=(D_{\text{avg}}/2)(1$

$+\cos\beta$). The diameter D_{avg} corresponds to the average diameter as the bubble grows. As a first approximation, it is taken as $D_{avg}=D_b/2$. Heat is removed by the bubble from an influence area considered to be a circle with diameter $2D_b$ as shown in Fig. 1(*b*), following the assumption made by Han and Griffith [34]. The heat flux on the heater surface is obtained by comparing the heat transfer rates over the influence area and over the interface area of the average bubble of diameter D_{avg}.

$$q''=\frac{q''_I(D_{avg}/2)(1+\cos\beta)\cdot(\pi D_{avg}/2)}{(\pi/4)(2D_b)^2}=\frac{(1+\cos\beta)}{16}q''_I \tag{10}$$

The force due to gravity on the bubble interface acting in the direction parallel to the heater surface results from the triangular pressure distribution as shown in Fig. 1(*a*). In general, for a heater surface inclined at an angle ϕ to the horizontal ($\phi=0$ deg for a horizontal upward facing surface, $\phi=90$ deg for a vertical surface), the component of the force parallel to the heater surface due to the hydrostatic head on a surface of height H_b and unit width is given by

$$F_G=\frac{1}{2}g(\rho_l-\rho_g)H_b\cdot H_b\cdot 1\cdot\cos\phi. \tag{11}$$

The critical heat flux or CHF occurs when the force due to the momentum change (F_M) pulling the bubble interface into the liquid along the heated surface exceeds the sum of the forces holding the bubble, $F_{S,1}$, $F_{S,2}$, and F_G. The bubble then expands along the heater surface and blankets it. At the inception of the CHF condition, the force balance yields

$$F_M=F_{S,1}+F_{S,2}+F_G. \tag{12}$$

Substituting Eqs. (6), (7), (8), and (11) into Eq. (12) and introducing Eq. (10), the heat flux at the heater surface, which corresponds to the CHF condition, $q''=q''_C$, is obtained.

$$q''_C=h_{fg}\rho_g^{1/2}\left(\frac{1+\cos\beta}{16}\right)\left[\frac{\sigma(1+\cos\beta)}{H_b}+(\rho_l-\rho_g)g\frac{H_b}{2}\cos\phi\right]^{1/2} \tag{13}$$

Substituting for H_b from Eq. (9), Eq. (13) becomes

$$q''_C=h_{fg}\rho_g^{1/2}\left(\frac{1+\cos\beta}{16}\right)\left[\frac{2\sigma}{D_b}+(\rho_l-\rho_g)g\frac{D_b}{4}(1+\cos\beta)\cos\phi\right]^{1/2}. \tag{14}$$

The diameter D_b is obtained by assuming it to be half the wavelength of the Taylor instability of a vapor film over the heater surface. The critical wavelength for initiating this instability, derived earlier by Kelvin (referenced in Lamb [35]) and later used by Zuber [9] in the development of his hydrodynamic theory, is given by

$$\lambda_T=C_1 2\pi\left[\frac{\sigma}{g(\rho_l-\rho_g)}\right]^{1/2}. \tag{15}$$

The value of C_1 ranges from 1 to $\sqrt{3}$. Using a value of 1 and substituting $D_b=\lambda_T/2$, with λ_T from Eq. (15), Eq. (14) takes the following form:

$$q''_C=h_{fg}\rho_g^{1/2}\left(\frac{1+\cos\beta}{16}\right)\left[\frac{2}{\pi}+\frac{\pi}{4}(1+\cos\beta)\cos\phi\right]^{1/2}\times[\sigma g(\rho_l-\rho_g)]^{1/4}. \tag{16}$$

Equation (16) predicts the CHF for saturated pool boiling of pure liquids. It includes the hydrodynamic as well as non-hydrodynamic (heater surface interaction) effects and the orientation of the heater surface. Since the liquid would start to recede at the onset of CHF, the dynamic receding contact angle is used in Eq. (16). A high speed photographic study is being conducted in the author's lab to determine the contact angle at CHF from the exact shape of the interface.

Effect of Subcooling

The effect of subcooling has been investigated by Kutateladze and Schneiderman [36] who observed a linear relationship between the degree of subcooling and CHF for water, iso-octane and ethyl alcohol over a graphite rod heater at various pressures. They proposed a model that considered the enhancement due to recirculation of subcooled liquid over the heater surface. Ivey and Morris [37] modified the Kutateladze and Shneiderman model by assuming that a portion of subcooled liquid first heats up to saturation point before evaporation occurs. Ivey and Morris conducted experiments with water boiling on horizontal wires, 1.22–2.67 mm diameter, and found a linear relationship with degree of subcooling. Zuber on the other hand considered transient heat conduction to the subcooled liquid to be responsible for the increase in CHF. Duke and Schrock [38] conducted experiments with a horizontal heater surface and found that the pool boiling curve shifted to a lower wall superheat region, and the wall superheat at CHF also decreased as liquid subcooling increased. A linear relationship of CHF with subcooling was obtained by Jakob and Fritz [39] as reported by Rohsenow [40].

Elkassabgi and Lienhard [18] conducted experiments with subcooled pool boiling with R-113, acetne, methanol, and isopropanol and identified three regions depending on the level of subcooling. In region I at low subcooling levels, CHF increased linearly, while at very large subcooling in region III, CHF was insensitive to changes in subcooling. Region II represented transition between I and III.

It is proposed that the heat transfer mechanism leading to CHF involves heat transfer to the subcooled liquid. The heat transfer rate at the CHF condition is therefore related directly to the wall to bulk temperature difference. An increase in subcooling of the bulk liquid increases the transient conduction to the liquid. This approach is expected to represent Region I as defined by Elkassabgi and Lienhard. The CHF under subcooled condition is then given by

$$q''_{C,SUB}=q''_{C,SAT}\left(1+\frac{\Delta T_{SUB}}{\Delta T_{SAT}}\right)_{SUB}. \tag{17}$$

However, as seen from the results of Duke and Schrock [38], the wall superheat at the CHF condition decreases with increasing subcooling. In Eq. (17) therefore, the actual wall superheat under subcooled conditions should be used. At this time there is no accurate model available for predicting the wall superheat (or the heat transfer coefficient under subcooled condition) at the CHF; the actual experimental data will therefore be used in verifying this model.

Results

The CHF model as given by Eq. (16) for saturated pool boiling, and Eqs. (16) and (17) in conjunction with the wall superheat data at CHF for subcooled pool boiling, is compared with the experimental data available in literature. Kutateladze correlation (Eq. 1) was chosen in this comparison since other correlations, such as Zuber's, differ only in the value of the leading constant K (which is 0.16 in Kutateladze correlation, and 0.131 in Zuber's correlation). Both these earlier correlations do not include the contact angle as a parameter. Correlations such as Eq. (5) yield extremely high values of CHF especially for water.

Table 1 shows the details of the data sets and the results of the comparison with the Kutateladze correlation and the present model. It can be seen that the model predictions are quite good and are consistently better than the Kutateladze predictions.

The current model requires the knowledge of the dynamic receding contact angle for a given liquid-solid system. A majority of

Table 1 Details of the experimental data and comparison with Kutateladze correlation and present model

Author (Year)	Liquid	Pressure (kPa)	Heater Size & Orientation	Contact Angle (Degrees)	Kutateladze Correlation mean error %	Present Model mean error (%)
Liaw and Dhir [16]	Saturated Water	98.07	Flat, 6.3cm wide X 10.3cm High, Copper, Vertical	14, 27, 38, 69, 90, 107	88.07	21.59
Ramilison and Leienhard [17]	R-113	98.07	Flat Circular, 6.35cm dia, 1.524 cm thick, Copper, Horizontal	30, 40, 50	11.54	8.36
Deev et al. [42]	Helium	Reduced p– 0.4-0.95	Flat, 30×30mm, Copper Horizontal & Vertical	—	29.65	8.64
Bewilogua et al. [43]	Helium, Nitrogen, Hydrogen	Reduced p-- 0.05-0.95	Flat Circular, Copper, Horizontal & Vertical A= 2.9 cm^2 for N_2 and H_2 A=4.5 cm^2 for He	—	Nitrogen: 9.32 Hydrogen: 6.71 Helium: 12.9	Nitrogen: 13.2, Hydrogen: 7.41, Helium: 20.66
Abuaf and Staub [44]	R-113	5.49~98.07	Flat Circular, Copper, 5.9cm dia, Horizontal	—	34.49	24.26
Lienhard and Dhir [14]	Distilled Water	14.48~42.74	Flat Circular, 6.35cm dia, Copper, Horiaontal	—	88.78	0.54
Bonilla and Perry [4]	Water	15.7~98	Flat Circular, Copper, 3.58in diameter Horizontal	—	46.60	7.90
Sakurai and shiotsu [45]	Water	98.07	Cylinder, 0.12cm dia, Platinum 10cm length, Horizontal and Vertical	—	33.94	10.72

data sets, with the exception of those, which specifically investigated the contact angle effect, does not report the contact angle. In view of this, following assumptions are made regarding the dynamic receding contact angle:

- water/copper system—$\beta = 45$ deg
- water/chromium coated surface—$\beta = 65$ deg
- cryogenic liquids/copper—$\beta = 20$ deg (no information is available on contact angles for cryogenic liquids)
- R-113/copper—$\beta = 5$ deg

An experimental work reporting the dynamic receding contact angles for water droplets impinging on hot surfaces is presented by Kandlikar and Steinke [41]. They observed that for a smooth copper surface near saturation temperature of water, the dynamic receding contact angle is considerably lower than the dynamic advancing contact angle.

For this combination, they measured the dynamic receding contact angle to be between 45–80 deg for a copper surface depending on the surface roughness and temperature. In the CHF experiments, it is therefore recommended that the dynamic receding contact angles be measured using the impinging droplet technique preferably in a vapor atmosphere.

A small variation of 10 deg in estimating the dynamic receding contact angle below 60 deg results in less than 5–7 percent difference in the CHF predictions for all liquids investigated. However, changes in dynamic receding contact angles beyond 60 degrees have a significant effect of the CHF.

One of the major motivations behind the current work is to include the effect of dynamic receding contact angle, which is known to influence the CHF. Liaw and Dhir [16] specifically investigated this effect by changing the equilibrium contact angle with different surface finish on the same heater. Figure 2 shows the results of the comparison. Although the differences at the two extremes are somewhat higher, it should be recognized that as the contact angle increases, the CHF value decreases dramatically as demonstrated by Gaertner [11]. Present model correctly depicts this trend. Kutateladze model does not include the contact angle as a parameter and is seen to significantly overpredict the results at higher contact angles. The discrepancy between the present model and the data at higher values of contact angles is suspected because of the use of equilibrium contact angles as reported by Liaw and Dhir. The dynamic receding contact angles are always lower than the equilibrium contact angles. Using somewhat lower contact angle values further improves the agreement with the present model.

Similar results are obtained from the comparison with the R-113 data by Ramilison and Lienhard [17] as shown in Fig. 3. However only a small range of contact angles was investigated. The results of Kutateladze model are close to the data in this case.

Deev et al. [42] and Bewilogua et al. [43] conducted experiments with cryogenic liquids—nitrogen, hydrogen and helium. Deev et al. conducted experiments with helium on horizontal and vertical plates. Figures 4 and 5 show the results of comparison

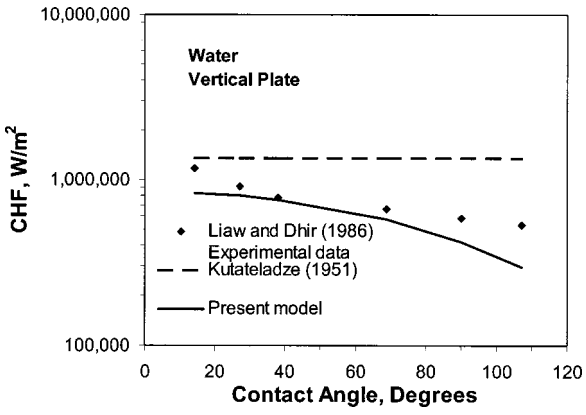

Fig. 2 Effect of contact angle on CHF for water boiling on a vertical plate; comparison of present model and Kutateladze correlation with Liaw and Dhir [16] data

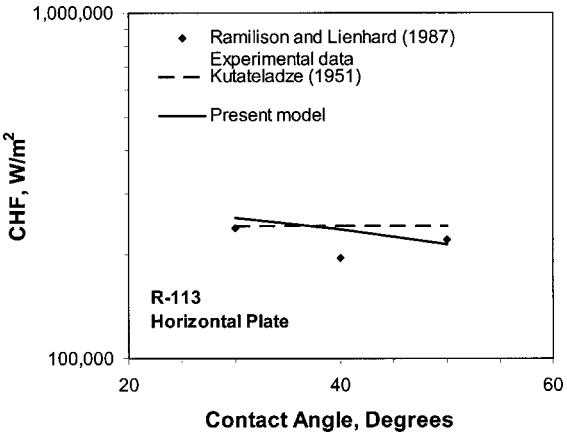

Fig. 3 Effect of contact angle on CHF for R-113 boiling on a horizontal plate; comparison of present model and Kutateladze correlation with Ramilison and Lienhard [17] data

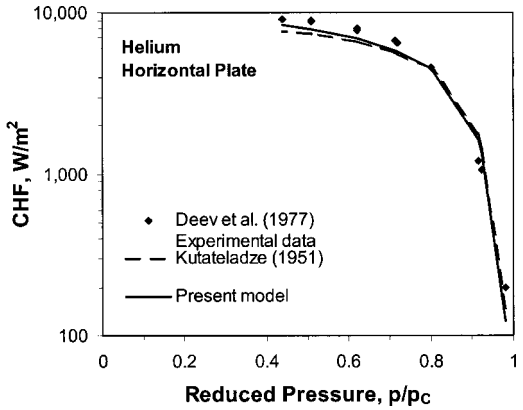

Fig. 4 Variation of CHF with pressure for helium boiling on a horizontal plate; comparison of present model (using contact angle of 20 deg) and Kutateladze correlation with Deev et al. [42] data

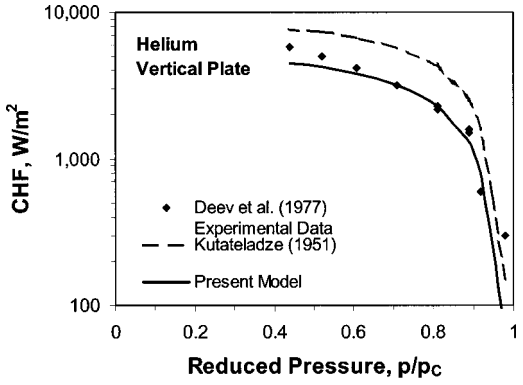

Fig. 5 Variation of CHF with pressure for helium boiling on a vertical plate; comparison of present model (using contact angle of 20 degrees) and Kutateladze correlation with Deev et al. [42] data

with the present model. The agreements between the data and both the present model and Kutateladze model are good for the horizontal plate, while only the present model is able to represent the vertical plate data well. Similar observations can be made with the nitrogen, hydrogen, and helium data of Bewilogua et al. from Figs. 6–9. Their vertical plate data is somewhat scattered between the Kutateladze and the present model predictions.

Figure 10 shows the results of comparison with R-113 data by Abuaf and Staub [44]. The agreement in the mid and high-pressure ranges is good, but significant differences are noted at low pressures with both the present model and the Kutateladze correlation. Further investigation is warranted before the cause for this behavior can be explained.

Figure 11 shows the data obtained by Lienhard and Dhir [14].

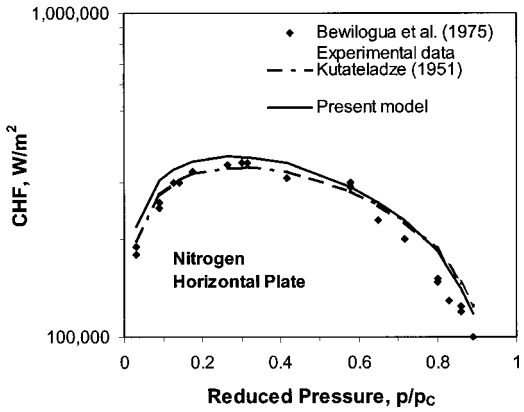

Fig. 6 Variation of CHF with pressure for nitrogen boiling on a horizontal plate; comparison of present model (using contact angle of 20 deg) and Kutateladze correlation with Bewilogua et al. [43] data

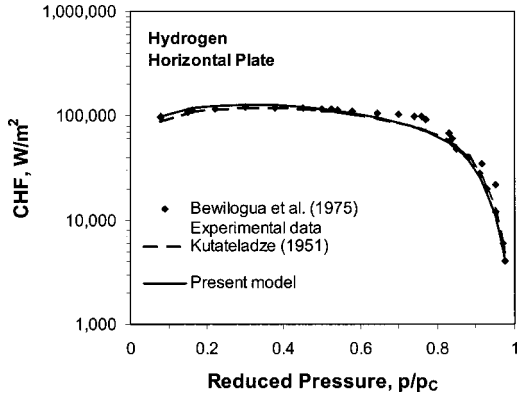

Fig. 7 Variation of CHF with pressure for hydrogen boiling on a horizontal plate; comparison of present model (using contact angle of 20 deg) and Kutateladze correlation with Bewilogua et al. [43] data

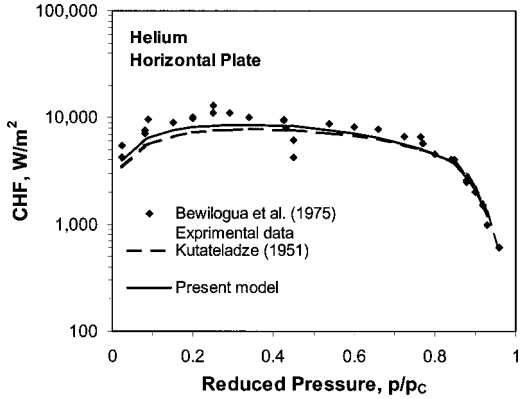

Fig. 8 Variation of CHF with pressure for helium boiling on a horizontal plate; comparison of present model (using contact angle of 20 deg) and Kutateladze correlation with Bewilogua et al. [43] data

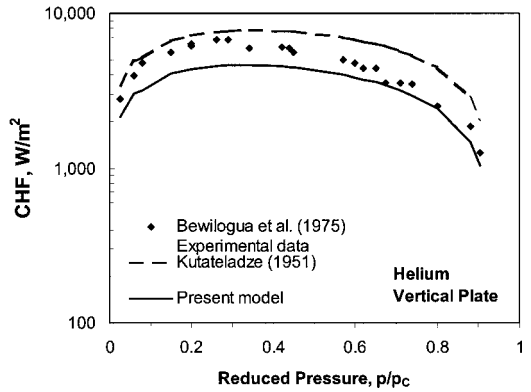

Fig. 9 Variation of CHF with pressure for helium boiling on a vertical plate; comparison of present model (using contact angle of 20 deg) and Kutateladze correlation with Bewilogua et al. [43] data

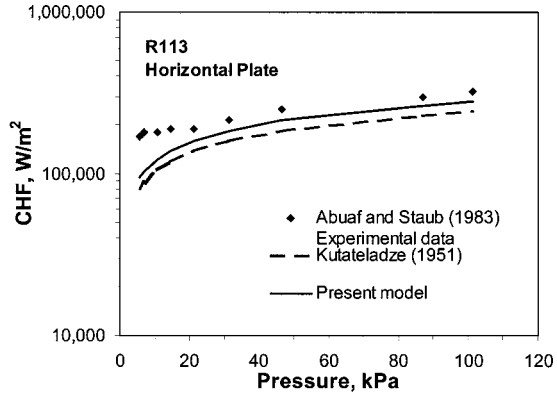

Fig. 10 Variation of CHF with pressure for R-113 boiling on a horizontal plate; comparison of present model (using contact angle of 5 deg) and Kutateladze correlation with Abuaf and Staub [44] data

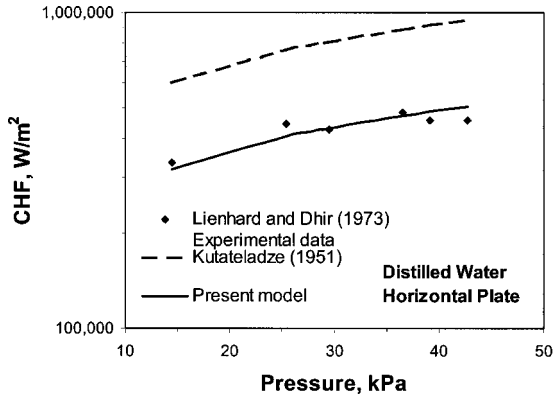

Fig. 11 Variation of CHF with pressure for distilled water boiling on a horizontal plate; comparison of present model (using contact angle of 45 deg) and Kutateladze correlation with Lienhard and Dhir [14] data

For this case, the Kutateladze correlation considerably overpredicts the results. Changing the leading constant from 0.16 to 0.085 makes it overlap with the present model predictions, which are excellent. Similar observations can be made from Fig. 12 comparing the data by Bonilla and Perry [4]. In this case, the Kutateladze correlation again overpredicts the results. Changing the leading constant to 0.11 improves the agreement in the high pressure region, but it still overpredicts the CHF in the low pressure region. The present model, on the other hand, is in excellent agreement with the data except for the lowest pressure data point.

One of the reasons why the present correlation and the Kutateladze correlation both yield almost the same results for cryogens is because the predictions from the present model for a contact angle of 20 degrees for cryogens are almost same as those from Kutateladze correlation. The product of the terms in the two parenthesis on the right hand side of Eq. (16) represents the constant K in Kutateladze correlation ($K=0.16$ in Kutateladze correlation). The variation of the corresponding term in the present model with the dynamic receding contact angle is shown in Table 2. It can be seen that for the assumed dynamic receding contact angle value of 20 deg for cryogens, this term is 0.178, which is very close to the Kutateladze constant $K=0.16$.

The effect of subcooling is shown in Fig. 13. Here, the data of Sakurai and Shiotu [45] is used in the comparison. The data is for cylindrical heating surface. Although the present model is applicable only for flat surfaces, this comparison is shown to verify the trends predicted by the present model. The values for wall superheat at CHF are available from the data. The agreement with the present model for the horizontal plate is within ten percent, except for the data point at the highest subcooling of 40°C. For the vertical plate, the model underpredicts by about 18 percent, but the trend is well represented. The data exhibits a trend that is contrary to that observed by Elkassabgi [46] and Elkassabgi and Lienhard [18]. Their data tends to level off as subcooling increases, whereas Sakurai and Shiotsu data seems to increase rapidly at higher de-

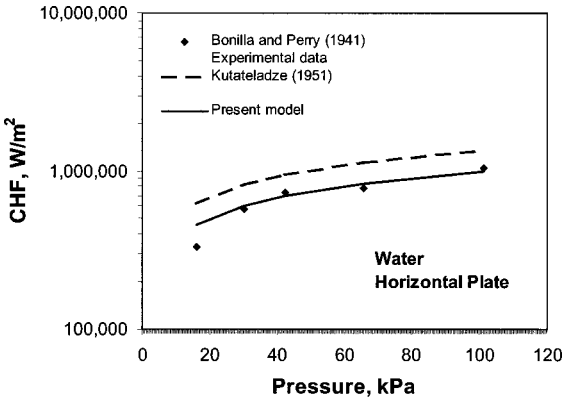

Fig. 12 Variation of CHF with pressure for water boiling on a horizontal plate; comparison of present model (using contact angle of 65 deg, chromium surface) and Kutateladze correlation with Bonilla and Perry [4] data

Table 2 Variation of Equivalent *K* factor (product of the two bracketed terms in Eq. (16)) using the present model, for a horizontal surface

Contact angle, degrees	Equivalent K from Eq. (16)
0	0.186
20	0.178
45	0.150
60	0.126
90	0.0745
120	0.0317
150	0.0072
180	0

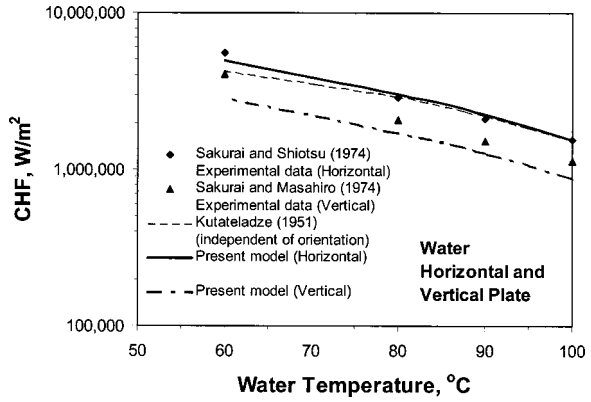

Fig. 13 Variation of CHF with pressure for water boiling on horizontal and vertical plates; comparison of present model (using contact angle of 45 deg) and Kutateladze correlation with Sakurai and Shiotsu [45] data

gree of subcooling. Although the agreement between the data and the model is quite good, extension of the present model to cylindrical geometry is recommended as future work.

A word on the accuracy of contact angle measurement is in order. The contact angles used in the correlation are obtained by previous investigators from the static measurements. The dynamic value of the receding contact angle under evaporating film condition is different than that obtained from static observations. Since the difference between the dynamic receding contact angle and the static receding contact angle is small as shown by Kandlikar and Steinke [41], the use of static receding contact angle is recommended when the dynamic values are not available.

Conclusions

The following conclusions are made from the present study:

1 After reviewing the existing models for pool boiling CHF, a need for including contact angle, surface orientation, and subcooling effects in modeling is identified.

2 A theoretical model to predict the CHF in saturated pool boiling is developed. The force parallel to the heater surface resulting from the evaporation at the liquid-vapor interface of a bubble near the heater surface is identified to be an important factor. As this force due to exiting vapor momentum exceeds the retaining forces due to gravity and surface tension, the vapor in the bubble spreads along the heater surface, blankets it, and initiates the CHF condition. The receding contact angle plays an important role in arriving at the CHF condition.

3 The model predicts the experimental data for water, refrigerants, and cryogenic liquids well as seen from Table 1. The model is valid for orientations from 0 deg (horizontal surface) to 90 deg (vertical surface).

4 The model correctly predicts the effect of dynamic receding contact angle and subcooling on CHF for low values of subcooling.

5 Further work is suggested to develop a model to predict the wall superheat at CHF under highly subcooled pool boiling conditions.

Acknowledgments

The author gratefully acknowledges Shurong Tian for her assistance in comparing the present model with the experimental data.

Nomenclature

C = constant in Eq. (3), m/s
D_b = bubble diameter at departure, m
D_{avg} = average diameter of a bubble during growth period, m
F_G = force due to gravity, parallel to the heater surface, N
F_M = force due to change in momentum due to evaporation, parallel to the heater surface, N
$F_{S,1}$ = force due to surface tension at the bubble base, parallel to the heater surface, N
$F_{S,2}$ = force due to surface tension at the top of the bubble, parallel to the heater surface, N
g = gravitational acceleration, m/s^2
g_s = standard acceleration due to gravity, m/s^2
h_{fg}, h_{lg} = latent heat of vaporization, J/kg
K = constant in Kutateladze correlation, eq. (1)
p = pressure, Pa
p_C = critical pressure, Pa
q'' = heat flux, W/m^2
q''_C = critical heat flux, W/m^2
q''_I = heat flux at the interface, W/m^2

Greek Symbols

β = dynamic receding contact angle, degrees
ϕ = heater surface angle with horizontal, degrees
λ_T = critical wavelength for Taylor instability, m
μ = viscosity, Pa s
ρ = density, kg/m^3
σ = surface tension, N/m

Subscripts

avg = average
b = departure bubble condition
C = critical heat flux condition
g = vapor
I = interface
l = liquid
lg = latent quantity

References

[1] Lang, C., 1888, *Transactions of Institute of Engineers and Shipbuilders*, Scotland, Vol. 32, pp. 279–295.
[2] Nukiyama, S., 1966, "The Maximum and Minimum Values of the Heat Q Transmitted from Metal to Boiling Water under Atmospheric Pressure," Int. J. Heat Mass Transf., **9**, pp. 1419–1433.
[3] Drew, T. B., and Mueller, A. C., 1937, "Boiling," Transactions of AlChE, **33**, pp. 449–471.
[4] Bonilla, C. F., and Perry, C. W., 1941, "Heat Transmission to Boiling Binary Liquid Mixtures," Transactions of American Society of Chemical Engineers, **37**, pp. 685–705.
[5] Cichelli, M. T., and Bonilla, C. F., 1945, "Heat Transfer to Liquids Boiling Under Pressure," Transactions of American Society of Chemical Engineers, **41**, pp. 755–787.
[6] Kutateladze, S. S., **1948**, "On the Transition to Film Boiling under Natural Convection," Kotloturbostroenie, No. 3, pp. 10–12.
[7] Kutateladze, S. S., 1951, "A Hydrodynamic Theory of Changes in a Boiling Process Under Free Convection," *Izvestia Akademia Nauk, S.S.S.R., Otdelenie Tekhnicheski Nauk*, No. 4, pp. 529.
[8] Rohsenow, W. M., and Griffith, P., 1956, "Correlation of Maximum Heat Transfer Data for Boiling of Saturated Liquids," Chem. Eng. Prog., **52**, pp. 47.
[9] Zuber, N., 1959, "Hydrodynamic Aspects of Boiling Heat Transfer," Ph.D. thesis, Research Laboratory, Los Angeles and Ramo-Wooldridge Corporation, University of California, Los Angeles, CA.
[10] Costello, C. P., and Frea, W. J., 1963, "A Salient Non-Hydrodynamic Effect on Pool Boiling Burnout of Small Semi-Cylindrical Heaters," AIChE Chemical Engineering Progress Symposium Series, **61**, No. 57, pp. 258–268.
[11] Gaertner, R. F., 1963, "Effect of Heater Surface Chemistry on the Level of Burnout Heat Flux in Pool Boiling," *Technical Information Series*, No. 63-RL-3449C, General Electric Research Laboratory, Schenectady, New York.
[12] Gaertner, R. F., 1965, "Photographic Study of Nucleate Pool Boiling on a Horizontal Surface," ASME J. Heat Transfer, **87**, pp. 17–29.
[13] Katto, Y., and Yokoya, S., 1968, "Principal Mechanism of Boiling Crisis in Pool Boiling," Int. J. Heat Mass Transf., **11**, pp. 993–1002.
[14] Lienhard, J. H., and Dhir, V. K., 1973, "Extended Hydrodynamic Theory of the Peak and Minimum Pool Boiling Heat Fluxes," NASA CR-2270, Contract No. NGL 18-001-035.
[15] Haramura, Y., and Katto, Y., 1983, "New Hydrodynamic Model of Critical Heat Flux Applicable Widely to both Pool and Forced Convection Boiling on

Submerged Bodies in Saturated Liquids,'' Int. J. Heat Mass Transf., **26**, pp. 379–399.
[16] Liaw, S. P., and Dhir, V. K., ''Effect of Surface Wettability on Transition Boiling Heat Transfer from a Vertical Surface,'' *Proceedings of the Eighth International Heat Transfer Conference*, San Francisco, CA., Vol. 4, pp. 2031–2036.
[17] Ramilison, J. M., and Lienhard, J. H., 1987, ''Transition Boiling Heat Transfer and the Film Transition Regime,'' ASME J. Heat Transfer, **109**, pp. 746–752.
[18] Elkassabgi, Y., and Lienhard, J. H., 1988, ''Influence of Subcooling on Burnout of Horizontal Cylindrical Heaters,'' ASME J. Heat Transfer, **110**, pp. 479–486.
[19] Dhir, V. K., and Liaw, S. P., 1989, ''Framework for a Unified Model for Nucleate and Transition Pool Boiling,'' ASME J. Heat Transfer, **111**, pp. 3739–3746.
[20] Addoms, J. N., 1948, ''Heat Transfer at High Rates to Water Boiling Outside Cylinders,'' Sc.D. thesis in Chemical Engineering, Massachusetts Institute of Technology, Cambridge, MA.
[21] Borishanskii, V. M., 1955, ''On the Problem of Generalizing Experimental Data on the Cessation of Bubble Boiling in Large Volume of Liquids,'' Ts. K.I.T., **28**, Moscow.
[22] Chang, Y. P., 1961, ''An Analysis of the Critical Conditions and Burnout in Boiling Heat Transfer,'' USAEC Rep. TID-14004, Washington, DC.
[23] Moissis, R., and Berenson, P. J., 1963, ''On the Hydrodynamic Transitions in Nucleate Boiling,'' ASME J. Heat Transfer, **85**, pp. 221–229.
[24] Kirby, D. B., and Westwater, J. W., 1965, ''Bubble and Vapor Behavior on a Heated Horizontal Plate During Pool Boiling Near Burnout,'' Chem. Eng. Prog., Symp. Ser., **61**, No. 57, pp. 238–248.
[25] Yu, C. L., and Mesler, R. B., 1977, ''Study of Nucleate Boiling Near the Peak Heat Flux Through Measurement of Transient Surface Temperature,'' Int. J. Heat Mass Transf., **20**, pp. 827–840.
[26] Van Outwerkerk, H. J., 1971, ''Burnout in Pool Boiling The Stability of Boiling Mechanisms,'' Int. J. Heat Mass Transf., **15**, pp. 25–34.
[27] Kirishenko, Yu. A., and Cherniakov, P. S., 1973, ''Determination of the First Critical Thermal Heat Flux on Flat Heaters,'' J. Eng. Phys., **20**, pp. 699–702.
[28] Diesselhorst, T., Grigull, U., and Hahne, E., 1977, ''Hydrodynamic and Surface Effects on the Peak Heat Flux in Pool Boiling,'' in *Heat Transfer in Boiling*, E. Hahne, and U. Grigull, eds., Hemisphere Publishing Corporation, Washington.
[29] Unal, C., Daw, V., and Nelson, R. A., 1992, ''Unifying the Controlling Mechanisms for the Critical Heat Flux and Quenching: The Ability of Liquid to Contact the Hot Surface,'' ASME J. Heat Transfer, **114**, pp. 972–982.
[30] Sadasivan, P., Unal, C., and Nelson, R., 1995, ''Perspective: Issues in CHF Modeling—The Need for New Experiments,'' ASME J. Heat Transfer, **117**, pp. 558–567.
[31] Tachibana, F., Akiyama, M., and Kawamura, H., 1967, ''Non-Hydrodynamic Aspects of Pool Boiling Burnout,'' J. Nucl. Sci. Technol., **4**, No. 3, pp. 121–130.
[32] Golobič, I., and Bergles, A. E., 1997, ''Effects of Heater-Side Factors on the Saturated Pool Boiling Critical Heat Flux,'' *Experimental Thermal and Fluid Science 1997*, Elsevier Science Inc., New York, NY, pp. 43–51.
[33] Howard, A. H., and Mudawar, I., 1999, ''Orientation Effects on Pool Boiling Critical Heat Flux (CHF) and Modeling of CHF for Near-Vertical Surfaces,'' Int. J. Heat Mass Transf., **42**, pp. 1665–1688.
[34] Han, C. Y., and Griffith, P., 1965, ''The Mechanism of Heat Transfer in Nucleate Pool Boiling, Part I, Bubble Initiation, Growth and Departure,'' Int. J. Heat Mass Transf., **8**, No. 6, pp. 887–904.
[35] Lamb, H., 1957, *Hydrodynamics*, Dover Publication, New York, NY.
[36] Kutateladze, S. S., and Schneiderman, L. L., 1953, ''Experimental Study of Influence of Temperature of Liquid on Change in the Rate of Boiling,'' USAEC Report, AECtr. 3405, pp. 95–100.
[37] Ivey, H. J., and Morris, D. J., 1962, ''On the Relevance of Vapor-Liquid Exchange Mechanisms for Subcooled Boiling Heat Transfer at High Pressure,'' U.K. Rep. AEEW-R-137, Winfrith.
[38] Duke, E. E., and Schrock, V. E., 1961, *Fluid Mechanics Heat Transfer Institute*, pp. 130–145.
[39] Jakob, M., and Fritz, W., 1931, *Forsch. Gabiete Ing*., Vol. 2, pp. 75.
[40] Rohsenow, W. M., ''Boiling,'' chap. 12, in *Handbook of Heat Transfer Fundamentals*, W. M. Rohsenow, J. P. Hartnett, and E. N. Ganic, eds., pp. 12.1–12.94.
[41] Kandlikar, S. G., and Steinke, M. E., 2001, ''Contact Angle of Droplets During Spread and Recoil After Impinging on a Heated Surface,'' Trans IChemE, **79**, Part A, pp. 491–498.
[42] Deev, V. I., Keilin, V. E., Kondratenko, I. A., and Petrovichev, V. I., 1977, ''Nucleate and Film Pool Boiling Heat Transfer to Saturated Liquid Helium,'' Cryogenics, **17**, No. 10, pp. 557–562.
[43] Bewilogua, L., Bewilogua, L., and Vinzelberg, H., 1975, ''Heat Transfer in Cryogenic Liquids under Pressure,'' Cryogenics, **15**, No. 3, pp. 121–125.
[44] Abuaf, N., and Staub, F. W., 1983, ''Low Pressure Pool Boiling and Critical Heat Flux Limits for R-113,'' AIChE Symp. Ser., **79**, No. 225, pp. 35–40.
[45] Sakurai, A., and Shiotsu, M., 1974, ''Temperature-Controlled Pool-Boiling Heat Transfer,'' *Proceedings of the Fifth International Heat Transfer Conference*, Vol. 4, B3.1, pp. 81–85.
[46] Elkassabgi, Y., 1986, ''The Peak Boiling Heat Flux from Horizontal Cylinders in Subcooled Liquids,'' Ph.D. dissertation, Mechanical Engineering Department, University of Houston, Houston, TX.

Highly Subcooled Boiling in Crossflow

LiDong Huang[1]

Larry C. Witte

Heat Transfer and Phase Change Laboratory,
Department of Mechanical Engineering,
University of Houston,
Houston, TX 77204-4792

Experiments were carried out to determine the influence of fluid flow and liquid subcooling on flow boiling heat transfer of Freon-113 across horizontal tubes. The data cover wide ranges of velocity (1.5 to 6.9 m/s) and extremely high levels of liquid subcooling (29 to 100°C) at pressures ranging from 122 to 509 kPa. Thin-walled cylindrical electric resistance heaters made of Hastelloy-C with diameter of 6.35 mm were used. The azimuthal wall temperature distributions were measured with five thermocouples around the heaters. The data were compared with Chen's two-mechanism model with modification for subcooled flow boiling. A new nucleate boiling suppression factor for cross flow was developed. The improved model could predict the present data and Yilmaz and Westwater's (1980) data well with a mean error ratio of 1.02 and standard deviation of 0.17. [DOI: 10.1115/1.1413762]

Keywords: Boiling, Heat Transfer, Tubes

1 Introduction

Research in the area of subcooled flow boiling was started in the early 1940s (McAdams et al. [1], Davidson et al. [2]). More research was carried out on flow boiling with water under subcooling conditions (Krieth and Summerfield [3], Jens and Lottes [4], Bergles and Rohsenow [5]). All of the previous investigations were conducted with flow in tubes or annuli.

Yilmaz and Westwater [6] measured boiling heat transfer to Freon-113 at near atmospheric pressure outside a 6.4 mm diameter horizontal steam-heated copper tube. They tested pool boiling and forced flow vertically upward at velocities of 2.4, 4.0, and 6.8 m/s. Their data showed that flow velocity improved boiling heat flux; i.e., the boiling curves shifted up with increasing velocity, and the peak heat flux increased very noticeably as the flow velocity was increased. In their experiments, the Freon-113 was 4 to 5°C below the saturation temperature.

More recently, Huang [7], Huang and Witte [8,9] conducted experimental investigations on the effect of fluid flow and liquid subcooling on boiling heat transfer. Their data showed that fluid flow and liquid subcooling significantly affect boiling heat transfer, including nucleate boiling, film boiling, and critical heat fluxes.

In the present study, experiments were carried out to determine the influence of fluid flow and liquid subcooling on flow boiling heat transfer across horizontal tubes. Chen's two-mechanism model was used to compare with the data by modifying the model for subcooled conditions. A complete method was developed to predict subcooled flow boiling heat transfer coefficients during cross flow.

2 Flow Boiling Models

The first correlational model for flow boiling coefficients was proposed by Rohsenow [10] as a simple addition of the nucleate and convective heat fluxes. Rohsenow [10] assumed that nucleate flow boiling heat flux could be obtained by adding nucleate pool boiling heat flux to single-phase forced convection heat flux. The method requires the knowledge of pool boiling-curves; however, for forced flow nucleate boiling, heat flux goes well past the critical values for pool boiling.

Bjorge et al. [11] modified Rohsenow's simple superposition model to account for subcooled to high quality ranges using single-phase and two-phase convection correlations, a pool boiling correlation, and an incipient boiling criterion. The model requires the prediction of wall superheat at the incipient boiling point, which is not available for many fluids and geometries.

Chen [12] formulated the first cohesive flow boiling method. He introduced a nucleate boiling suppression factor to account for diminished contribution of nucleate boiling, as convective boiling effects were increasing with higher-vapor fraction. The two-mechanism model, which is now very popular, has the following form for saturated flow boiling,

$$q_{fb} = q_{nb} + q_{cv} . \tag{1}$$

The nucleate boiling heat flux is calculated by

$$q_{nb} = S h_{nbp} \Delta T_s , \tag{2}$$

where S is a nucleate boiling suppression factor.

Chen used Forster and Zuber's [13] pool boiling correlation to predict the pool nucleate boiling heat transfer coefficient, h_{nbp}. The convective heat flux is calculated by

$$q_{cv} = F h_l \Delta T_s , \tag{3}$$

where F is a two-phase convective enhancement factor. This model assumes that parallel heat transfer mechanisms exist. For saturated flow boiling, the same temperature driving force, ΔT_s, is applied to both nucleate boiling and convective evaporation. Therefore, the flow boiling heat transfer coefficient can be calculated by

$$h_{fb} = \frac{q_{fb}}{\Delta T_s} = S h_{nbp} + F h_l . \tag{4}$$

Chen's suppression factor S was related to an effective Reynolds number for a two-phase fluid, Re_{tp}, which he defined as

$$\mathrm{Re}_{tp} = \mathrm{Re}_l F^{1.25}. \tag{5}$$

Webb and Gupte [14] gave a critical assessment of three types of models (the superposition, asymptotic, and enhancement models) used to calculate heat transfer coefficients of saturated flow boiling in tubes and across tube banks. By comparing the three types of models, they suggested an asymptotic model for application to tubes and tube banks. In their paper, they fitted Chen's curves for S and F into the following correlations:

[1]Current address: Heat Transfer Research, Inc., 150 Venture Dr., College Station, TX 77845.

Contributed by the Heat Transfer Division for publication in the JOURNAL OF HEAT TRANSFER. Manuscript received by the Heat Transfer Division August 28, 2000; revision received May 4, 2001. Associate Editor: V. P. Carey.

$$S=\frac{1}{1+2.53\times10^{-6}\,\mathrm{Re}_{tp}^{1.17}} \tag{6}$$

$$F=1+1.8X_H^{-0.79}. \tag{7}$$

Bennett et al. [15] improved Chen's suppression factor correlation by defining a bubble growth region within the thermal boundary layer. By using an exponential temperature profile to approximate thermal boundary layer within the bubble growth region, they derived an expression for nucleate boiling suppression factor as

$$S=\frac{k_l}{h_{cv}X_0}(1-e^{-(k_l/h_{cv}X_0)}), \tag{8}$$

where

$$h_{cv}=Fh_l. \tag{9}$$

They used their nitrogen and methane forced convective data for intube flow to correlate the size of the bubble growth region as

$$X_0=0.041\sqrt{\frac{\sigma}{g(\rho_l-\rho_v)}}. \tag{10}$$

Equation (10) has the same form as the departure diameter used by Stephan and Abdelsalam [16] for correlating pool nucleate boiling heat transfer data (see Eq. (16)) except that the contact angle, β, was left out and it predicts a much lower value than Equation (16). The S factor proposed by Bennett et al. [15] was intended to be applicable to both intube flow and flow across tube bundles.

We can extend Chen's two-mechanism model to subcooled flow boiling by assuming that the wall superheat (ΔT_s) only applies to nucleate boiling and the temperature difference between the wall and the fluid temperature (ΔT) applies to forced convection. Therefore, Eq. (1) becomes

$$q_{fb}=Sh_{nbp}\Delta T_s+Fh_l\Delta T, \tag{11}$$

where

$$\Delta T=\Delta T_s+\Delta T_{\mathrm{sub}}. \tag{12}$$

Dividing Eq. (11) by Eq. (12) gives the flow boiling heat transfer coefficient, based on temperature driving force, ΔT,

$$h_{fb}=\frac{q_{fb}}{\Delta T}=Sh_{nbp}\frac{\Delta T_s}{\Delta T}+Fh_l. \tag{13}$$

Different correlations are available for calculating the nucleate pool boiling heat transfer coefficient, h_{nbp}, in Eqs. (4) and (13). Chen used Forster and Zuber's [13] correlation to develop a nucleate boiling suppression factor for flow boiling. In the present study, we use Stephan and Abdelsalam's [16] pool boiling correlation for refrigerants, which is

$$\mathrm{Nu}=\frac{h_{nbp}d}{k_l}=207X_q^{0.745}\left(\frac{\rho_v}{\rho_l}\right)^{0.581}\mathrm{Pr}_l^{0.533}, \tag{14}$$

where

$$X_q=\frac{q_{nb}d}{k_lT_s}, \tag{15}$$

and d is equilibrium break-off diameter or departure diameter of bubbles and defined as

$$d=0.146\beta\sqrt{\frac{2\sigma}{g(\rho_l-\rho_v)}}, \tag{16}$$

with contact angle $\beta=35$ deg for refrigerants [16].

By using Stephan and Abdelsalam's correlation to predict nucleate boiling coefficients for subcooled flow boiling, we assume that the correlation could be extrapolated beyond the critical heat flux for pool boiling. Huang and Witte's [9] $q_{\max}$ data for subcooled flow boiling showed that $q_{\max}$ for subcooled flow boiling was much higher than that for saturated pool boiling. They reached a $q_{\max}$ for flow velocity at 4.8 m/s and liquid subcooling of 100°C at pressure of 500 kPa about 8.5 times as predicted by Zuber's pool critical heat flux equation.

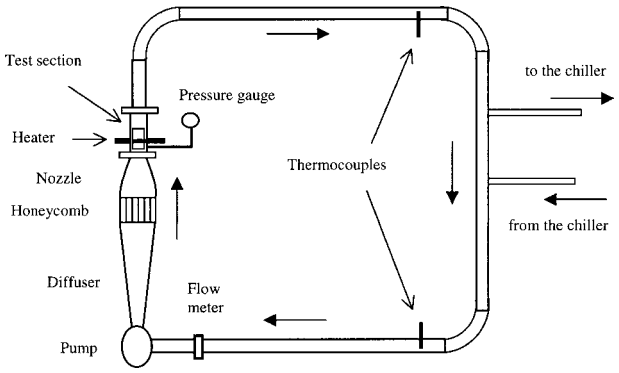

Fig. 1 Experimental setup

3 Experimental Setup

Figure 1 shows the experimental setup for the current investigation. A variable speed centrifugal pump was used to circulate the working fluid in a closed loop. The fluid passed through an expansion section, a honeycomb straightening section with screens on both ends, and a reducing nozzle to get a uniformly distributed, fully developed low-turbulence flow before it entered the test section. A Dieterich Standard Diamond II 4-in. annular flow sensor was used to measure flow rates in the test section. The liquid in the closed loop was cooled by a water-cooled Filtrine POC-500 WC chiller with 16 kW cooling capacity. The liquid in the loop could be cooled to a temperature below 0°C. Therefore, liquid subcooling as high as 100°C for Freon-113 could be reached for higher pressure runs (up to 510 kPa).

The test section, as shown in Fig. 2, was made of aluminum with a cross-section of 63.5 mm by 63.5 mm. Two Plexiglas windows were installed at opposite sides of the test section for observation during the experiments. The heater was mounted horizontally across the test section. Thin-walled Hastelloy-C tubes, of 6.35 mm outside diameter and 0.254 mm wall thickness, were used as electric resistance heaters, inside which sintered lava cylinders were inserted as a heat insulator and rigid body for mounting thermocouples. The lava cylinder was grooved axially around the cylinder wall 45 deg apart, starting from the lower stagnation point, to position the thermocouples. Five 38 gage chromel-alumel with 0.5 mm-dia Inconel 600 sheathed thermocouples were cemented in the grooves using Omega CC high-temperature cement. To establish good thermal contact between the thermocouples and the heater wall, the lava insert was fitted snugly inside the heater tube after a thin coat of high temperature cement was applied. The

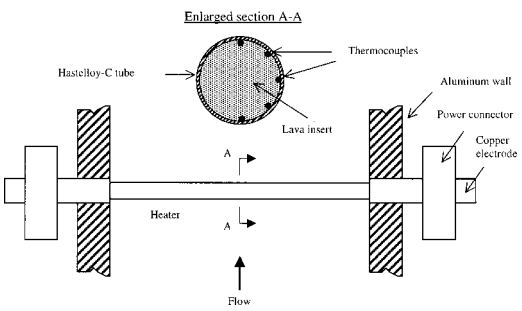

Fig. 2 Test section and heater configuration

Table 1 Experimental Uncertainties

Measured and reduced parameter	Uncertainty range
Heat flux	± 3.3%
Wall temperature	± 1.5 °C or ± 1% whichever is greater
Fluid saturation temperature	± 2.2 °C
Bulk temperature	± 1.1 °C
Fluid velocity	± 3%
System pressure	± 7 kPa

thermocouples were located at the axial center on the heater to measure the azimuthal wall temperature distribution. Power was supplied to the heater from a Gulf Electroquip dc motor-generator set capable of providing up to 1500 amps at 45 volts of dc power.

4 Experimental Data

For every flow boiling run, the heater surface was polished and cleaned with heavy-duty detergent, and then rinsed with water before it was carefully installed in the test section. The heater surface was smooth and lustrous. Boiling curve was obtained for each operating condition with flow rate, system pressure, fluid temperature set at desired values, by gradually increasing power supply to the heater, starting from single-phase forced convection to nucleate boiling until critical heat flux was reached. Heat flux was calculated based on the area in contact with Freon-113 and the measured power dissipation in the heater, less a small end-loss correction that was determined from temperature measurements outside the test section. Table 1 lists the experimental uncertainties estimated using the Kline-McClintock method.

The forced convection data, which agree very well with Churchill and Bernstein's correlation as shown in Figs. 3, 7, and 8, were used to verify the reliability of the experimental apparatus and its instrumentation. Churchill and Bernstein [17] generated the following correlation for liquids flowing across a single circular cylinder,

$$\mathrm{Nu}_l=\frac{h_l D}{k_l}=0.3+\frac{0.62\,\mathrm{Re}_l^{1/2}\mathrm{Pr}^{1/3}}{[1+(0.4/\mathrm{Pr})^{2/3}]^{1/4}}\left[1+\left(\frac{\mathrm{Re}_l}{282{,}000}\right)^{1/2}\right]\left(\frac{\mu_w}{\mu_f}\right)^{0.17}. \quad (17)$$

We found that Equation (17) could predict our forced convection data better if a wall temperature correction term (the viscosity ratio term) was added. Equation (17) was also used to calculate the forced convection coefficient, h_l, for the two-mechanism model.

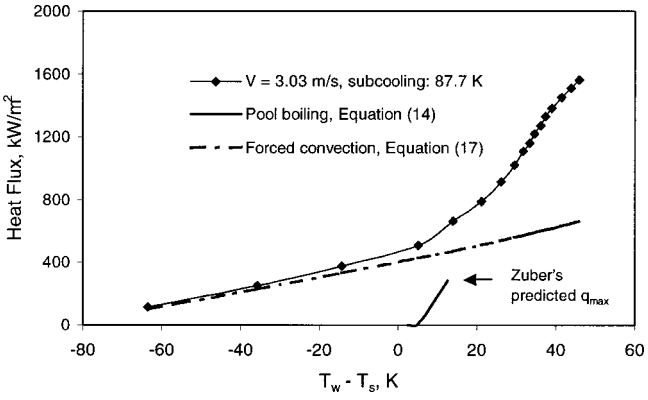

Fig. 3 Illustration of experimental subcooled flow boiling curve for Freon-113 with velocity of 3.03 m/s and liquid subcooling of 87.7°C at inlet pressure of 348.4 kPa

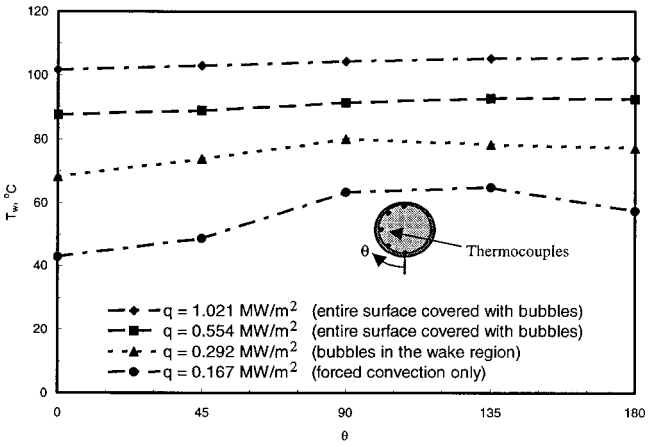

Fig. 4 Wall temperature distributions in forced convection and nucleate boiling regimes: $V=1.53$ m/s, $\Delta T_{sub}=59.4$°C, $p=153.7$ kPa

Very high heat fluxes were reached in this investigation because of high flow rate and liquid subcooling. Figure 3 shows an example of q-ΔT_s relationship for velocity of 3.03 m/s and liquid subcooling of 87.7°C at inlet pressure of 348.4 kPa. The critical heat flux for this condition is about 5.5 times that predicted by Zuber's correlation for saturated pool boiling. It is also interesting to see that the extrapolation of pool boiling curve by Stephan and Abdelsalam [16], Equation (14), would roughly predict the nucleate boiling portion of subcooled flow boiling if extended beyond Zuber's critical heat flux.

Figure 4 shows wall temperature distributions around the heater for different heat transfer mechanisms and heat fluxes. The bottom line in Fig. 4 is the wall temperature profile for forced convection. Although the wall temperature was 3.2°C and 4.7°C higher than the saturation temperature (60°C) at operating pressure (153.7 kPa) at the locations of $\theta=90$ deg and 135 deg, respectively, no bubbles were observed. The wall temperature variation around the heater was relatively high, 21.8°C. The wall temperature at the front stagnation point ($\theta=0$ deg) was the lowest, corresponding to the highest heat transfer coefficient. The heat transfer coefficient decreased as θ increased to about 90 deg. The heat transfer coefficient increased at the upper stagnation point ($\theta=180$ deg) caused by the turbulence in the wake of the heater. This tendency is consistent with the traditional local measurements of heat transfer around a cylinder in a normal crossflow with a laminar boundary layer on the front of the cylinder ($\mathrm{Re}_l=2.4\times10^4$ for the conditions in Fig. 4).

For the second line from the bottom in Fig. 4, bubbles were observed on the wake side of the heater. However, no bubbles were seen on the front of the cylinder. The temperature profile became flat on the wake side while the heat transfer behavior remains essentially the same as forced convection on the front. The area covered with nucleation sites increased with increasing heat flux and wall temperature profiles became flatter. The top two temperature profiles show the conditions with the entire cylinder covered with tiny bubbles. The bubbles were very small with the size ranging from 0.4 mm or less. As nucleate boiling became dominant, the heat transfer coefficient is more uniform around the heater with very small wall temperature differences (within 3.6°C for the top two profiles in Fig. 4).

A total of seventeen boiling curves were collected with Freon-113, covering wide ranges of fluid velocities (1.5 to 6.9 m/s) and liquid subcooling (29 to 100°C) at pressure ranging from 122 to 509 k Pa.

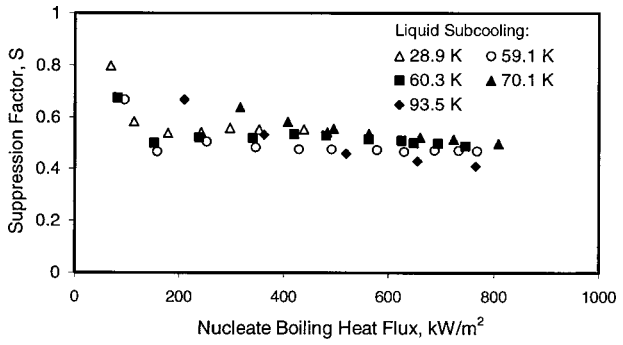

Fig. 5 Relationship of S with q_{nb} for velocity of 2.85 m/s

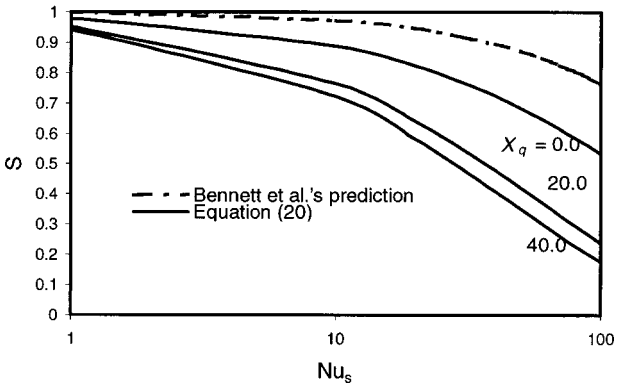

Fig. 6 Suppression factor predicted by Equation (20)

5 A New Suppression Factor For Crossflow

The nucleate boiling suppression factor accounts for the suppression of nucleate boiling observed in many flow boiling processes. Nucleate boiling suppression occurs when the thickness of the thermal boundary layer near a heated surface decreases caused by the increase of the flow over the heated surface. This effect causes wall superheat to decrease, often exposing the heated surface to colder fluid that suppresses the number of active nucleation sites. This process can completely shut down nucleate boiling mechanism as convective boiling heat transfer begins to dominate the flow boiling process. Liquid subcooling also has a cooling effect on the heated wall, which could reduce the nucleation site density.

Figure 5 shows the relationship of measured suppression factor with nucleate boiling heat flux for velocity of 2.85 m/s with liquid subcooling ranging from 28.9 to 93.5°C. The suppression factor and nucleate boiling heat flux were calculated by

$$S = \frac{q_{\text{meas}} - F h_l \Delta T}{h_{nbp} \Delta T_s}, \tag{18}$$

$$q_{nb} = q_{\text{meas}} - F h_l \Delta T. \tag{19}$$

In Eqs. (18) and (19), the forced convection coefficient, h_l, was calculated with Eq. (17), while the pool nucleate boiling coefficient, h_{nbp}, was calculated using Eq. (14) with nucleate boiling heat flux from Eq. (19). The two-phase enhancement factor, F, was set equal to unity in Eqs. (18) and (19) for our subcooled flow boiling data.

From Fig. 5, one can see that the suppression factor decreases as nucleate boiling heat flux increases. No strong effect of liquid subcooling on the nucleate boiling suppression factor is shown in Fig. 5 with liquid subcooling varying from 28.9 to 93.5°C. Actually, the convection heat flux increases as liquid subcooling increases because it raises the temperature driving force, ΔT, for forced convection. In turn, it reduces the nucleate boiling contribution. The data are more scattered at low nucleate heat flux because they are near the incipience of nucleate boiling.

Since the suppression factor calculated from Eq. (18) is not a strong function of liquid subcooling, we correlate it only as a function of forced convection coefficient and nucleate boiling heat flux. In the development of the S correlation, we also included Yilmaz and Westwater's [1] Freon-113 data. The following is the newly-developed nucleate boiling suppression factor,

$$S = e^{-0.0221 \text{Nu}_s^{0.727} X_q^{0.275}}, \tag{20}$$

where

$$\text{Nu}_s = \frac{h_{cv} d}{k_l} \tag{21}$$

is the Nusselt number for the suppression factor, which is the same non-dimensional group used by Bennett et al. [15] except the cylinder diameter d is used as the length scale instead of X_o, the size of the bubble growth region. A heat flux term defined by Eq. (15), X_q, was required if a pool boiling correlation was used and extrapolated beyond the pool boiling critical heat flux.

Figure 6 shows the prediction of Eq. (20). The suppression factor decreases with increasing of forced convection and nucleate boiling heat flux. Gungor and Winterton [18,19] also included heat flux in their F and S correlation for flow boiling in horizontal and vertical tubes, which also indicated lower suppression factor for higher heat flux. We included Bennett et al.'s [15] prediction in Fig. 6 by converting X_o in Eq. (8) to d defined by Eq. (16). Bennett et al.'s correlation, generated from their nitrogen and methane forced convective data for intube flow, over-predicted our suppression factor for cross flow. The over-prediction could be caused by the lack of a contact angle in the definition of X_o.

6 Comparison With Data

Figure 7 shows the effect of velocity on boiling curves, comparing data with the two-mechanism subcooled flow boiling model, Eq. (11), using the newly-developed suppression factor. The boiling curve moves up as velocity increases for the same liquid subcooling (59.7°C). The model can predict the data very well as shown in Fig. 7. Stephan and Abdelsalam's [16] pool boiling prediction is also shown in Fig. 7 with heat flux limited by Zuber's pool boiling maximum heat flux. For the conditions in Fig. 7, the fully developed flow boiling curves can not be exactly extrapolated from the pool boiling curve by Stephan and Abdelsalam [16].

Figure 8 shows the boiling curves for different pressures and subcoolings for a velocity of 2.85 m/s, comparing data with the model prediction. Yilmaz and Westwater's [1] data for velocity of 2.4 m/s (close to 2.85 m/s) are also included in the comparison. The comparison shows that the model can also predict data for

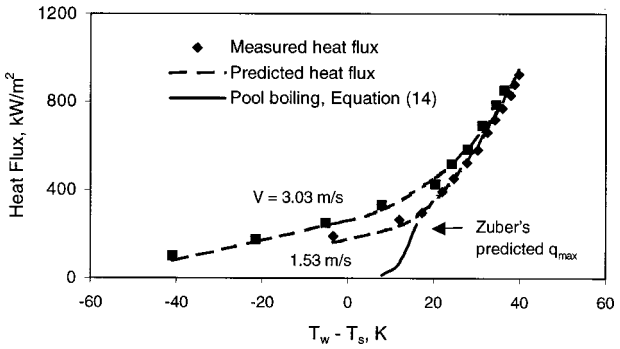

Fig. 7 Comparison of data for two different velocities with subcooling of 59.7 °C to model prediction

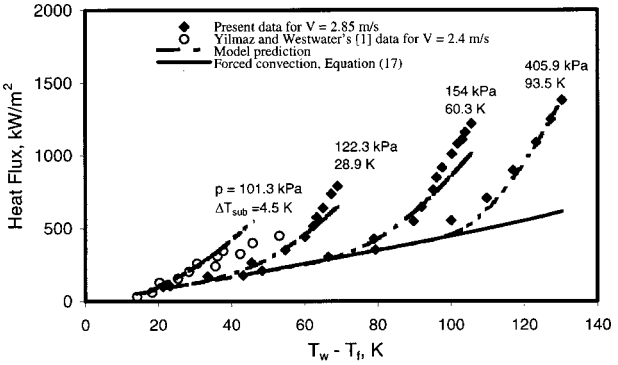

Fig. 8 Comparison of data for different pressure and subcoolings to model prediction

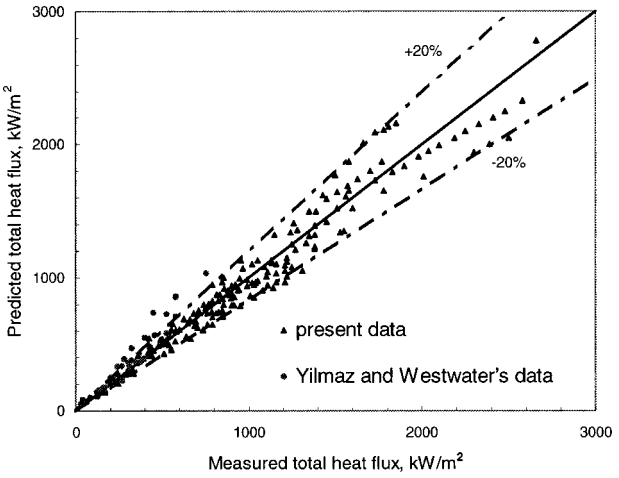

Fig. 9 Comparison of measured heat flux with predicted heat flux

different pressure and subcoolings fairly well, without any subcooling correction to the suppression factor of Eq. (20).

Figure 9 compares all of the present data and Yilmaz and Westwater's data of subcooled flow boiling across a horizontal tube with the prediction of the two-mechanism model, Eq. (11). A total of twenty boiling curves were included in the comparison with velocity ranging from 1.53 to 6.9 m/s and liquid subcooling from 4.5 to 100°C in pressure from 101 to 509 kPa. The model can predict all subcooled flow boiling data well, as shown in Fig. 9, with a mean ratio of predicted heat flux over measured heat flux to 1.02 and standard deviation of 0.17. The discrepancy between the prediction and Yilmaz and Westwater's data at high heat fluxes is probably due to the fact that the critical heat flux is being approached.

7 Conclusion

1 Extensive data of subcooled flow boiling across horizontal tubes were taken using Freon-113. The data cover wide ranges of velocity (1.5 to 6.9 m/s) and liquid subcooling (29 to 100°C) at pressure ranging from 122 to 509 kPa. A total of seventeen boiling curves were collected on horizontal tubes with diameter of 6.35 mm.

2 A new nucleate boiling suppression factor, Eq. (20), was developed based on the present data and Yilmaz and Westwater's [1] data. It was found that it was not necessary to have a separate subcooling term in the suppression factor. The subcooling contribution is included in the convection heat flux term in Equation (11) by increasing the temperature driving force or the temperature difference ratio term in Eq. (13).

3 The modified Chen's two-mechanism model for subcooled flow boiling was used to compare with the data. The model with the newly-developed suppression factor could predict the present data and Yilmaz and Westwater's [1] data very well.

Nomenclature

d = equilibrium break-off diameter, Eq. (16), m
D = tube diameter, m
F = two-phase convection enhancement factor
h_{cv} = convection heat transfer coefficient, W/m^2 K
h_{fb} = flow boiling heat transfer coefficient, W/m^2 K
h_l = heat transfer coefficient for liquid-phase flowing alone, W/m^2 K
h_{nbp} = pool nucleate boiling heat transfer coefficient, W/m^2 K
k_l = liquid heat conductivity, W/m K
Nu = Nusselt number
Nu_d = Nusselt number for suppression factor, as defined by Eq. (21)
Nu_l = liquid Nusselt number
Pr = Prandtl number
Pr_l = liquid Prandtl number
q_{cv} = convection heat flux, W/m^2
q_{fb} = flow boiling heat flux, W/m^2
$q_{\max}$ = maximum boiling heat flux, W/m^2
q_{meas} = measured total flow boiling heat flux, W/m^2
q_{nb} = nucleate boiling heat flux, W/m^2
Re_l = Reynolds number for liquid flowing alone, $G(1-y)D/\mu_l$
Re_{tp} = two-phase Reynolds number
S = nucleate boiling suppression factor
T_f = fluid bulk temperature, K
T_s = saturation temperature, K
T_w = wall temperature, K
X_o = the size of bubble growth region, as defined by Equation (10)
X_q = dimensionless heat flux as defined by Equation (15)
X_{tt} = Martinelli parameter
β = contact angle, degree
ΔT = overall temperature difference, $T_w - T_f$, K
ΔT_s = wall superheat, $T_w - T_s$, K
ΔT_{sub} = liquid subcooling, $T_s - T_f$, K
μ_f = fluid viscosity, kg/m s
μ_w = fluid viscosity at wall temperature, kg/m s
θ = angle measured from the front stagnation point, degree
ρ_l = liquid density, kg/m^3
ρ_v = vapor density, kg/m^3
σ = surface tension, N/m

References

[1] McAdams, W. H., Woods, W. K., and Bryan, R. L., 1941, "Vaporization Inside Horizontal Tubes," Trans. ASME, **63**, No. 6, pp. 545–552.

[2] Davidson, W. F., Hardie, P. H., Humphreys, C. G. R., Markson, A. A., Mumford, A. R., and Raverse, T., 1943, "Studies of Heat Transmission Through Boiler Tubing at Pressure From 500 to 3000 Pounds," Trans. ASME, **65**, No. 6, pp. 553–591.

[3] Krieth, F., and Summerfield, M., 1949, "Heat Transfer to Water at High Flux Densities With and Without Surface Boiling," Trans. ASME, **71**, No. 7, pp. 805–815.

[4] Jens, W. H., and Lottes, P. A., 1951, "Analysis of Heat Transfer, Burnout, Pressure Drop, and Density Data for High Pressure Water," USAEC Rep. ANL-4627, Argonne Natl. Lab., Argonne, IL.

[5] Bergles, A. E., and Rohsenow, W. M., 1963, "The Determination of Forced Convection Surface Boiling Heat Transfer," *6th National Heat Transfer Conference of the ASME-AIChE*, Boston, MA.

[6] Yilmaz, S., and Westwater, J. W., 1980, "Effect of Velocity on Heat Transfer to Boiling Freon-113," ASME J. Heat Transfer, **102**, pp. 26–31.

[7] Huang, L., 1994, ''Subcooled Flow Boiling Across Horizontal Cylinders,'' Ph.D. dissertation, University of Houston, Houston, TX.
[8] Huang, L., and Witte, L. C., 1995, ''Forced Convective Film Boiling Heat Transfer around Horizontal Cylinders in Highly Subcooled Freon-113,'' *Proceedings of the 4th ASME/JSME Thermal Engineering Joint Conference*, Vol. 2, pp. 315–322.
[9] Huang, L., and Witte, L. C., 1996, ''An Experimental Investigation of the Effects of Subcooling and Velocity on Boiling of Freon-113,'' ASME J. Heat Transfer, **118**, pp. 436–441.
[10] Rohsenow, W. M., 1952, ''A Method of Correlating Heat Transfer Data for Surface Boiling of Liquids,'' Trans. ASME, **74**, pp. 969–976.
[11] Bjorge, R. W., Hall, G. R., and Rohsenow, W. M., 1982, ''Correlation of Forced Convection Boiling Heat Transfer Data,'' Int. J. Heat Mass Transf., **25**, No. 6, pp. 753–757.
[12] Chen, J. C., 1966, ''Correlation for Boiling Heat Transfer to Saturated Fluids in Convective Flow,'' I&EC Process Des. Dev., **5**, No. 3, pp. 322–329.
[13] Forster, H. K., and Zuber, N., 1955, ''Dynamics of Vapor Bubbles and Boiling Heat Transfer,'' AIChE J., **1**, No. 4, pp. 531–535.
[14] Webb, R. L., and Gupte, N. S., 1992, ''A Critical Review of Correlations for Convective Vaporization in Tubes and Tube Banks,'' Heat Transfer Eng., **13**, No. 3, pp. 58–81.
[15] Bennett, D. L., Davis, M. W., and Hertzer, B. L., 1980, ''The Suppression of Saturated Nucleate Boiling by Forced Convective Flow,'' AIChE Symp. Ser., **76**, No. 199, pp. 91–103.
[16] Stephan, K., and Abdelsalam, M., 1980, ''Heat Transfer Correlations for Natural Convective Boiling,'' Int. J. Heat Mass Transf., **23**, pp. 73–87.
[17] Churchill, S. W., and Bernstein, M., 1977, ''A Correlating Equation for Forced Convection From Gases and Liquids to a Circular Cylinder in Crossflow,'' ASME J. Heat Transfer, **99**, pp. 300–306.
[18] Gungor, K. E., and Winterton, R. H. S., 1986, ''A General Correlation for Flow Boiling in Tubes and Annuli,'' Int. J. Heat Mass Transf., **29**, No. 3, pp. 351–358.
[19] Gungor, K. E., and Winterton, R. H. S., 1987, ''Simplified General Correlation for Saturated Flow Boiling and Comparisons of Correlation with Data,'' Chem. Eng. Res. Des., **65**, pp. 146–156.

X. Li
Research Assistant
Department of Mechanical Engineering,
Clemson University,
Clemson, SC 29634-0921
e-mail: xianchl@clemson.edu

J. L. Gaddis
Professor
Mem. ASME
Department of Mechanical Engineering,
Clemson University,
Clemson, SC 29634-0921
e-mail: leo.gaddis@ces.clemson.edu

T. Wang
Professor
Mem. ASME
Energy Conversion and Conservation Center,
University of New Orleans,
New Orleans, Louisiana 70148-2220
e-mail: twang@uno.edu

Modeling of Heat Transfer in a Mist/Steam Impinging Jet

The addition of mist to a flow of steam or gas offers enhanced cooling for many applications, including cooling of gas turbine blades. The enhancement mechanisms include effects of mixing of mist with the gas phase and effects of evaporation of the droplets. An impinging mist flow is attractive for study because the impact velocity is relatively high and predictable. Water droplets, less than 15 μm diameter and at concentrations below 10 percent, are considered. The heat transfer is assumed to be the superposition of three components: heat flow to the steam, heat flow to the dispersed mist, and heat flow to the impinging droplets. The latter is modeled as heat flow to a spherical cap for a time dependent on the droplet size, surface tension, impact velocity and surface temperature. The model is used to interpret experimental results for steam invested with water mist in a confined slot jet. The model results follow the experimental data closely.
[DOI: 10.1115/1.1409262]

Keywords: Augumentation, Droplet, Evaporation, Heat Transfer, Impingement, Modeling

Introduction

The addition of mist to a flow of steam or gas offers enhanced cooling for many applications, including cooling of gas turbine blades [1–3]. The mechanisms of heat transfer enhancement include effects of mist momentum on the gas phase and effects of evaporation of the droplets, both directly and via the gas. Increased specific heat and lower bulk temperature are also typical features of a mist flow. In a mist/steam jet impingement flow, the interaction of the droplets and the target wall becomes pronounced because of the relatively high impact velocity and well defined because the velocity is relatively predictable.

While single-phase jet impingement cooling has been studied extensively, few studies have been found on mist jet impingement. Goodyer and Waterston [1] considered mist/air impingement for turbine blade cooling at surface temperatures above 600°C. They suggested that the heat transfer was dominated by partial contact between the droplets and the target surface, during which the droplets vaporized at least partially. A vapor cushion and the elastic deformation of the droplets were responsible for rejecting the droplets. Addition of 6 percent water was found to improve the stagnation point heat transfer by 100 percent, diminishing away from the stagnation point. Droplet size was found to have little effect for $30\ \mu\text{m} < d_{32} < 200\ \mu\text{m}$.

Takagi and Ogasawara [4] studied mist/air heat and mass transfer in a vertical rectangular tube heated on one side. They identified wet-type heat transfer at relatively low temperatures and post-dryout type at higher temperatures. In the wet region the heat transfer coefficient increased with increased heat flux. In the post-dryout region the heat transfer coefficient increased with droplet concentration and flow velocity and with decreased droplet size. Mastanaiah and Ganic [5] confirmed that the heat transfer coefficient decreased with increased wall temperature.

Yoshida et al. [6] focused on the effect on turbulent structure with a suspension of 50 μm glass beads. In the impinging jet region, the gas velocity was found to decrease due to the rebound of beads, accompanied by an increase in the normal direction velocity fluctuations. In the wall-jet region the effect was slight. The Nusselt number was found to increase by a factor of 2.7 for mass flow ratios (solid/gas) of 0.8.

Guo et al. [2] studied the mist/steam flow and heat transfer in a straight tube under highly superheated wall temperatures. It was found that the heat transfer performance of steam could be significantly improved by adding mist into the main flow. An average enhancement of 100 percent with the highest local heat transfer enhancement of 200 percent was achieved with less than 5 percent mist. In an experimental study with a horizontal 180 deg tube bend Guo et al. [3] found both the outer wall and the inner wall of the test section exhibited a significant and similar heat transfer enhancement. The overall cooling enhancement of the mist/steam flow increased as the main steam flow increased, but decreased as the wall heat flux increased.

To explore the mechanism of mist heat transfer, interaction of droplets with the wall has been studied extensively. Wachters et al. [7] considered the impact of droplets about 60 μm impacting a heated surface in the range of 5 m/s. Impinging droplets could only maintain the spheroidal state with relatively high surface temperatures. The required temperature depended on thermal properties and roughness of the surface as well as the Weber number of the droplets. In the spheroidal state very low rates of heat flow were observed.

To obtain fundamental information concerning the heat transfer processes in spray cooling, Pederson [8] studied the dynamic behavior and heat transfer characteristics of individual water droplets impinging upon a heated surface. The droplet diameters ranged from 200 to 400 μm, and the approach velocities ranged from 2 to 8 m/s. The wall temperature ranged from saturation temperature to 1000°C. Photographs of the impingement process showed that even the small droplets studied broke up upon impingement at moderate approach velocities. The heat transfer data showed that approach velocity was the dominant variable affecting droplet heat transfer and that surface temperature had little effect on heat transfer in the non-wetting regime. The droplet deformation and break-up behavior for droplets 200 μm in diameter did not appear significantly different from that for larger droplets. He also found that, for any given parameters in the non-wetting regime, a minimum velocity could exist below which the droplets deformed consistently without break-up.

Contributed by the Heat Transfer Division for publication in the JOURNAL OF HEAT TRANSFER. Manuscript received by the Heat Transfer Division June 7, 2000; revision received April 23, 2001. Associate Editor: V. P. Carey.

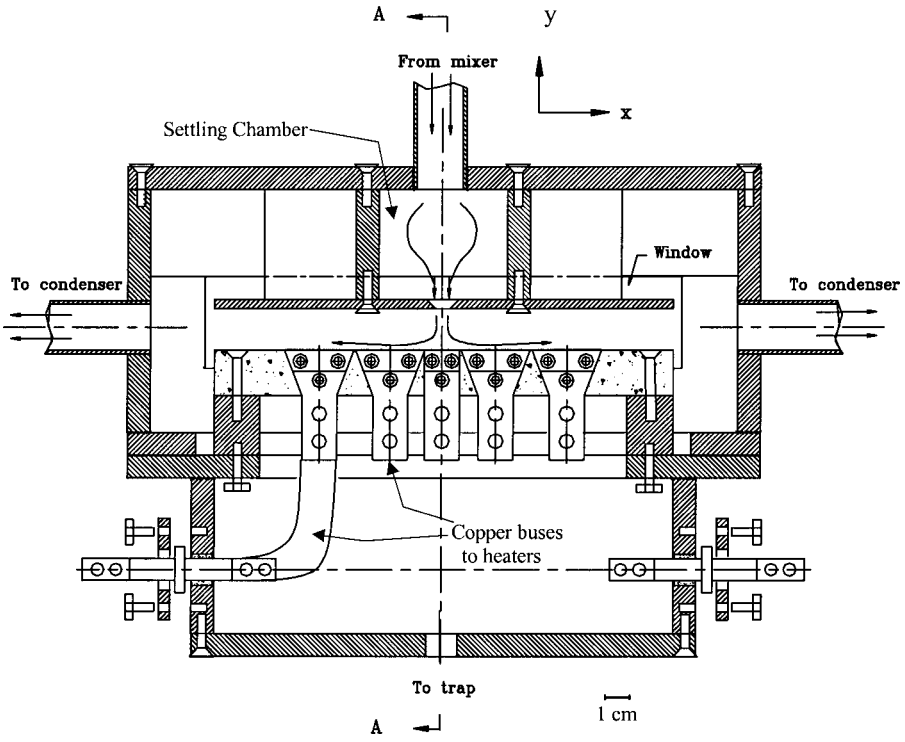

Fig. 1 Schematic diagram of test section

Chandra and Avedisian [9,10] presented photographs of heptane droplets impacting a heated surface. The relatively large (>1 mm) droplets at We=43 showed sensitivity to the surface temperature. At low temperature the droplets spread and evaporated while at higher temperature nucleate boiling was evident. Above the Leidenfrost temperature the droplets rebounded without any evidence of wetting.

Buyevich and Mankevich [11,12] modeled the impacted particles as liquid discs separated by a vapor layer whose thickness is that of the wall roughness. The liquid mass flux was assumed small enough to prevent formation of a liquid film on the heated surface. Based on the energy conservation of the droplet as well as the flow and heat conduction of the vapor interlayer between the droplet and wall, a critical impact velocity was identified to determine whether a droplet rebounds or is captured. Depending on their approach velocity, the impinging droplets are either reflected almost elastically or captured by the heated surface and completely vaporized within a sufficiently short time. They applied the model to dilute mist impingement with reported agreement with experiment.

Fujimoto and Hatta [13] studied deformation and rebound of a water droplet on a high-temperature wall. For Weber numbers of 10 to 60, they computed the distortions of the droplet as it flattened, contracted, and rebounded. They used a simple heat transfer model to confirm that surface tension dominates vapor production in the rebounding process. Hatta et al. [14] gave correlations of contact time and contact area of the droplet with Weber number.

Li et al. [15] presented an experimental study for 1.1 bar steam invested with water mist in a confined slot jet. Figure 1 is a schematic of the test article having a slot of width 7.5 mm located in a flat injection plate. The jet impacted a target wall of length 250 mm spaced 22.5 mm from the injection plate. The flow section had a width of 100 mm and Pyrex walls allowed vision of the heated surface. The droplet velocity and size distribution was obtained by a phase Doppler particle analyzer (PDPA). The experimental results are typified by Fig. 2. In the first panel the depression of temperature caused by mist is shown. Using the measured heat flux of Joulean heating in the wall divided by the wall to saturation temperature difference, the heat transfer coefficient of the second panel is produced. Panel three shows the enhancement, defined as the ratio of heat transfer coefficients with and without mist at the same Reynolds number. The cooling effect is signifi-

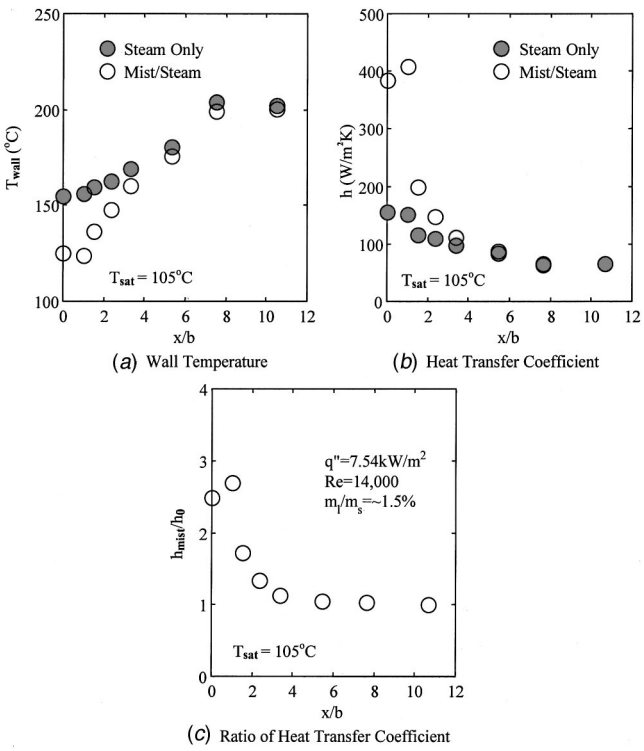

Fig. 2 A typical heat transfer result of mist/steam jet impingement (q''=7.54 kW/m^2, Re=14000, and m_l/m_s=~1.5 percent)

cant near the stagnation point and decreases to a negligible amount at 6 jet widths downstream. Up to 200 percent heat transfer enhancement at the stagnation point was achieved by injecting only ~1.5 percent by mass of mist. Direct observation through the Pyrex wall showed a dry heated surface in the experiment conditions, though no observations were made capable of disclosing the behavior of individual droplets in brief contact. The purpose of this communication is to model the processes of the experiment and trends with heat flux, mist concentration, and vapor velocity, based on Li et al. [15].

Basic Assumptions and Model

In mist/steam jet impingement, the droplets will not only influence the flow and temperature fields of the steam but also may interact directly with the target wall. In the experiment [15], water droplets, less than 15 μm diameter and at concentrations below 5 percent, impacted a heated surface with wall superheat below 60°C at a velocity up to 12 m/s. To model the heat transfer of the mist/steam impinging jet under these conditions, the following assumptions and approximations are made in this study:

- The wall is sufficiently heated to prevent accumulation of liquid.
- The interaction between droplets is ignored, since the average spacing between droplets is large.
- Because the droplet is small, no breakup is considered.
- The droplet is at the saturation temperature before entering the thermal boundary layer.
- The droplet has a less important effect on the velocity boundary layer than on the thermal boundary layer.

Under these assumptions, the heat transfer of mist/steam jet impingement is divided into three different parts: heat transfer from the target wall to the steam flow, heat transfer from the target wall to droplets and heat transfer between the steam and droplets. No radiative heat transfer is considered since the wall temperature is not very high in the current study and it is estimated to be less than 2 percent of the total heat transfer.

Heat Transfer From the Target Wall to the Steam. Heat transfer due to the steam is modeled as heat convection of a single-phase steam flow. Because of the disturbance by droplets on the boundary layer, this portion is subject to modification of the heat transfer coefficient of steam-only jet impingement flow. A detailed analysis of this effect must involve the effect of droplets on the flow field and the turbulence characteristics. The heat transfer enhancement through the effect of droplets on the flow has been assumed to be of secondary importance. Experimental study by Yoshida et al. [6] found 170 percent enhancement by adding 80 percent by mass glass beads of diameter 50 μm to the airflow. Considering the effect of the particles includes boundary layer disturbance as well as other cooling effects, the enhancement of the single-phase heat transfer due to droplets on the flow is projected to be less than 4 percent with a mist mass ratio of 2 percent.

Heat Transfer From the Target Wall to Droplets. Although many studies have been conducted on the interaction of the droplet with the bounding wall, few of these studies can be used to model the heat transfer from the target wall to droplets in the present study because of the different ranges of droplet size and flow parameters. Unlike spray cooling, where the droplet momentum is supplied by a device, small mist droplets may not be able to hit the wall because of the drag force in the present study. Based on trajectory analysis, it is believed that larger droplets will hit the wall if the approach velocity is high enough. Though neglected in trajectory analysis herein, the droplets are subject to the lift "force" of Ganic and Rosenhow [16] due to the momentum imbalance of asymmetric evaporation. A droplet in a temperature gradient near a heated wall is heated faster on the wall side. The difference in evaporation rate results in a lifting effect estimated to be of minor consequence for the conditions of this study.

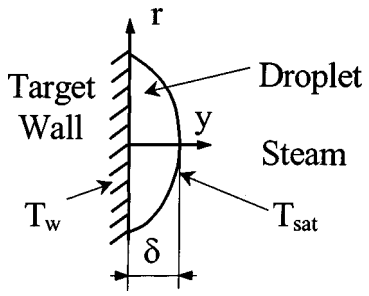

Fig. 3 Modeling of heat transfer from wall to droplet

The commercial code, FLUENT [17], a solver for the complete Navier Stokes equations using finite volume schemes, has been used to predict the trajectory of droplets including the determination of the impact velocity onto the heated surface. Complete details are included in Li [18] and only salient features are included here. The domain of Fig. 1 supplied with appropriate boundary conditions in the entrance and exit regions was subdivided to yield grid-independent results. The turbulent flow was modeled in several ways, with the k-ε model found to yield substantial agreement with the heat transfer results in single-phase steam flow. This computational model was combined with the dispersed-phase option of the program wherein droplets seeded in the entrance region of the flow were tracked and allowed both to affect the vapor flow and to evaporate in transit through the superheated layer. The droplets in the flow react with the fluid according to drag on a sphere at the slip velocity between the droplet and the fluid, usually very near the low velocity Stokes Flow asymptote.

Direct Contact Heat Transfer. According to Buyevich and Mankevich [11] (B&M model), the droplet will depart from the wall if the impact velocity is below a critical velocity, and stick if above. The critical velocity given by the B&M model is only about 0.6 m/s for $d=10\,\mu$m, $\Delta=0.5\,\mu$m and $T_w-T_{sat}=30$°C. This means that for the conditions of the current study most of the droplets will stick to the wall. According to the B&M model a sticking droplet will stay on the wall until evaporated completely. If most of the particles stick to the wall and evaporate completely the enhancement of heat transfer will be much higher than observed. Therefore the B&M model is found to be inadequate for this study.

The actual interaction between the droplets and wall is very complicated; it includes a continuous deformation of the droplet and is affected by droplet size and surface conditions. In this study, the heat transfer from wall to droplet is modeled simply by transient heat conduction to a spherical cap with a contact angle of 60 deg based on Gould [19] and Neumann et al. [20]. The corresponding height and base diameter of the cap are 0.464 and 1.608 times the original droplet diameter, respectively. Figure 3 shows the basic model ($\delta=0.464d$). The configuration of the flattened droplet is assumed fixed until conditions for rebound are established.

Quasi-steady heat flow to a droplet has been considered by many authors including Sadhal and Martin [21] and Sadhal and Plesset [22]. Under some conditions exact solutions may be obtained. In the current work there is a need to include the transient warming of the droplet, as brief contact is anticipated. Since it is difficult to obtain an analytical solution, this problem is solved numerically by using FLUENT [17], with a non-uniform grid (r, y) of 50×50. Assuming a small fraction of the droplet evaporates before rebounding, a fixed-geometry (no allowance for the decrease of mass in evaporation) transient solution is sought with a uniform initial temperature of T_{sat}, the cap surface maintained at T_{sat}, and the base (wall) suddenly raised to T_w. Figure 4(a) shows the non-dimensional results for the total base heat flow Q

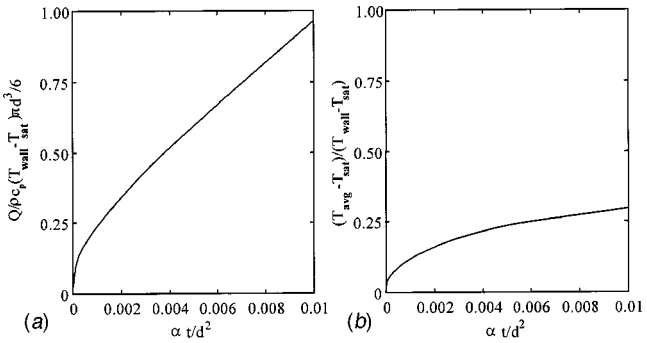

Fig. 4 Heat transfer process between droplet and wall by direct conduction (*Q* is the heat conduction from the target wall to the droplet): (*a*) total wall heat; and (*b*) superheat of droplet.

in terms of $\alpha t/d^2$. During contact the droplet is superheated in the amount given in Fig. 4(*b*). The heat entering the base and not residing in the droplet as superheat is conducted to the surface and is evaporated. There is no reference to the heat of vaporization because this quantity is not converted to a mass flow. The surface of the liquid maintained at the saturation temperature implies that the evaporative heat flux is included in the computation. For a temperature difference ($T_w - T_{sat}$) of 30°C, the heat conduction in 1.2 μs evaporates 5 percent of a 5 μm droplet. Because the fraction of droplet evaporated is small, the assumption of constant domain size and shape yields a fast, yet reasonable result.

Residence Time on Target Surface. Once a droplet hits the wall, whether it rebounds from the wall depends on the wall temperature and impact velocity. The heat conduction model above cannot give the essential condition for rebounding. To complete this model, the residence time of the droplet on the wall must be determined. It is conceivable that the droplets may wet the surface and stick on the heated wall until a vapor layer forms from nucleation at the base. Upon formation of this layer the droplet would return to its spheroidal shape and depart. A concept in pool boiling has a waiting time during which the region near the wall becomes superheated to the point where nucleation becomes spontaneous. Based on nucleation in a small cavity on the heated surface, Mikic and Rohsenow [23] studied the waiting time and provided the following simple estimate:

$$t_w = \frac{1}{\pi\alpha}\left\{\frac{(T_w - T_{sat})r_c}{T_w - T_{sat}(1 + 2\sigma/\rho_g H_{fg} r_c)}\right\}^2. \quad (1)$$

Here r_c is the radius of the nucleation cavity. This equation gives a waiting time of about 11 μs with $r_c = 2$ μm and $T_w - T_{sat} = 30$°C. The principal attractive feature of this concept is that the waiting time decreases slightly as the wall temperature increases. Because this waiting time depends strongly on the value of r_c that is difficult to determine, this model cannot be applied confidently for the present study. Besides, this model does not account for the effects of the droplet size and impact velocity.

Although the impact velocity was considered, the scale of the residence time given by Hatta et al. [14] did not include any wall temperature effect. The reason may be that their experiment was conducted at a very high wall temperature (above the Leidenfrost temperature). If the wall temperature is low, the free-slip boundary condition used in their study cannot be used any more. This basis for time scale will give a constant cooling enhancement for all wall temperatures, which is not the case from experiments. The Hatta model is expected to be valid as the temperature rises; it should from a lower bound for the contact time.

For our selected model it is assumed that the droplet will deform into the lens shape of Fig. 3 and remain on the wall momentarily without wetting gaining superheat according to the transient process of heat conduction discussed already. A vapor layer will form in response to the superheat until it reaches a sufficient pressure to repel the droplet. We reason that the pressure must overcome surface deformation (expressed through σ/d) and supply an exit velocity (pressure expressed through We σ/d) proportional to the entering velocity of impact. The temperature required to provide this pressure is that associated by the slope of the liquid-vapor saturation curve, wherein the required pressure is translated to a required superheat. Finally the superheat is linearly related to the product of wall superheat and the residence time. Expressed non-dimensionally, there results

$$\frac{\alpha t_r}{d^2} = \frac{c}{T_w - T_{sat}}\left.\frac{dT}{dP}\right|_{sat}\left[\frac{\sigma}{d}(1 + \mathrm{We}/8)\right]. \quad (2)$$

Here the constant, c, which depends on the geometry selected for the heat conduction model, is found by trial and error to be about 4.8×10^{-2} to agree with the experiment. The effect of impact velocity is not strong if the Weber number is small. This residence time is actually an effective value because it simplifies the deformation process of the droplet on the wall. The residence time of a 10 μm droplet with a Weber number of 1 and a temperature difference of 30°C is 1.7 μs. This model is expected to fail at high wall temperature where the residence time goes to zero. In this case, however, it is believed that the droplet will still contact the wall for at least the lower bound established by the deformation process.

Heat Transfer Between the Droplet and Steam. Heat transfer between the droplets and steam can be modeled by considering droplets as a distributed heat sink. The droplets evaporate into the superheated steam inside the thermal boundary layer and act to quench the boundary layer. Based on the superposition concept the temperature of mist/steam flow is divided into two parts, $T = T_1 + T_2$. $T_1(x,y)$ is the temperature of steam-only flow and $T_2(y)$ is the temperature depression caused by the mist.

The two-dimensional energy equation with a distributed heat sink is given as

$$\rho c_p u\frac{\partial T}{\partial x} + \rho c_p v\frac{\partial T}{\partial y} = k_s\frac{\partial^2 T}{\partial x^2} + k_s\frac{\partial^2 T}{\partial y^2} - k_s\beta^2(T - T_{sat}). \quad (3)$$

The last term is a heat sink per unit volume to a distributed surface at temperature T_{sat}. The coefficient, β, is equal to $(12c_{mist}\rho_s d_{10}/\rho_1 d_{30}^3)^{0.5}$ and c_{mist} is the mist concentration. $k_s\beta^2$ is the hA of the droplets per unit volume with $hd/k_s = 2$ and $k_s\beta^2(T - T_{sat})$ is the heat sink per volume. $hd/k_s = 2$ is chosen for slip Re$\ll$1 for most droplets in the current study.

The equation for T_1 can be written as

$$\rho c_p u\frac{\partial T_1}{\partial x} + \rho c_p v\frac{\partial T_1}{\partial y} = k_s\frac{\partial T_1}{\partial x^2} + k_s\frac{\partial^2 T_1}{\partial y^2}. \quad (4)$$

For the current study, the boundary conditions for T_1 include $\partial T_1/\partial x = 0$ at $x = 0$ and $x = L/2$ and for y

$$T_1 = T_w \text{ at } y = 0 \quad (5a)$$

$$T_1 = T_{sat} \text{ at } y \to \infty. \quad (5b)$$

Solution for Eq. (4) subject to (5) together with flow descriptions will produce a result for pure steam. In this work no solution is presented; rather the result is known from experiment to produce $h_0(x) = q''/(T_w - T_{sat})$. In [15] the experimental result is shown to agree substantially with other investigations. In lieu of an analytical solution, the following near-wall temperature distribution is assumed.

$$T_1 = (T_w - T_{sat})e^{-yh_0/k_s} + T_{sat}, \quad (6)$$

where h_0 is the heat transfer coefficient obtained from experimental study. T_w and h_0 depend on x.

Considering T_2 is a function of y only, the equation for T_2 can be simplified as

$$k_s\frac{d^2T_2}{dy^2}-\rho c_p v\frac{dT_2}{dy}-k_s\beta^2(T_1+T_2-T_{sat})=0. \quad (7)$$

The boundary conditions for Eq. (7) are

$$T_2=0 \text{ at } y=0 \text{ and } y\to\infty. \quad (8)$$

This equation is first solved without considering the second term and the result for $\beta\neq h_0/k_s$ can be given as

$$T_2=\frac{\beta^2(T_w-T_{sat})}{\beta^2-(h_0/k_s)^2}(e^{-\beta y}-e^{-yh_0/k_s}). \quad (9)$$

Therefore, the heat transfer augmentation due to mist, h_2, defined as $-k_s(dT_2/dy)|_{y=0}/(T_w-T_{sat})$, can be given by

$$\frac{h_2}{h_0}=\frac{(\beta k_s/h_0)^2}{\beta k_s/h_0+1}. \quad (10)$$

Assume that $h_0=100\,\text{W/m}^2\text{K}$, $c_{mist}=2$ percent and $d_{10}/d_{30}^3=10^{10}\,\text{m}^{-2}$, a value of $h_2/h_0=0.069$ is obtained. A value for c_{mist} of 10 percent will give a value of 0.269 for h_2/h_0.

The effect of the second term, $\rho_s c_p v dT_2/dy$ can be evaluated using Eq. (9). The velocity, v, leaving the boundary layer is estimated to be only about 0.25 mm/s by integrating the vapor generated from droplet evaporation. For the conditions of the example, this results in a value of the second term about 1 percent of the sink term and is neglected. The solution for T_2 given by Eq. (9) is accepted as an approximation.

The liquid concentration near the target wall might be different from the average concentration because the droplets cross the streamlines. However, migration of the droplets away from the wall occurs due to the lift forces and turbulent dispersion makes the mist concentration more uniform and close to the average value. Therefore, the quenching effect of the mist is estimated with the average concentration. Surveys by PDPA support this assumption.

Model Validation

The average heat transfer within $x/b<1$ is considered. As an example, a distribution of droplet size from the experimental study is given in Fig. 5(*a*) at the jet exit for Re=14,000 and $m_l/m_s=1.5$ percent. This size distribution, obtained by PDPA measurement entering the test section, gives the average diameters of $d_{10}=4.7\,\mu$m and $d_{30}=6.4\,\mu$m. By using FLUENT [17], the droplet distribution impacting the wall is given in Fig. 5(*b*). For the case cited, it is predicted that droplets less than 5 μm will not impact the wall, which means there is no direct heat conduction from the wall to droplets. The heat transfer to small droplets is mainly through the steam. Though not shown there is divergence of the pathlines resulting in diminished droplet flux at the stagnation point. The impact velocity varies with droplet size and injection location and for the case cited it ranges up to 12 m/s.

Table 1 lists five different cases to be predicted. Case 1 is the case shown in Fig. 2. The predicted results are given in Table 2. The input to the analytical model includes h_0, T_w, T_{sat}, m_l/m_s, as well as the droplet size distribution by PDPA. In Table 2, $q_1''=h_0(T_w-T_{sat})$ is the single-phase heat transfer from wall to steam, q_2'' using Eq. (10) is the quenching effect of the mist; and q_3'' is the direct heat conduction during the contact time of Eq. (2) from wall to droplet. It can be seen that the predicted results and the experimental data have good agreement, especially when considering the experimental uncertainty. The relative size of the various contributions is shown clearly in Table 2 and q''_{exp}/q_1'' is the heat transfer enhancement ratio, h_{mist}/h_0. The q_3'' component dominates q_2''. Both q_2'' and q_3'' become important in proportion to mist concentration.

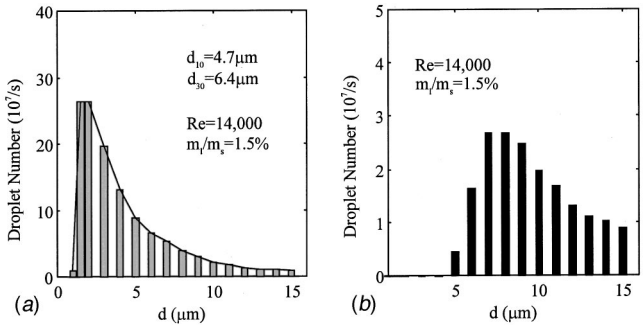

Fig. 5 Droplet distribution and number at jet exit and on target wall: (*a*) at jet exit; and (*b*) impacting on target wall ($x/b<1$).

Table 1 Experimental cases

Case	Re	h_0 (W/m^{2}K)	T_w (°C)	T_{jet} (°C)	m_l/m_s (%)	q″ (W/m^2)	h/h_0
1	14,000	150	125	105	1.5	7,540	2.5
2	22,500	210	130	105	1.75	20,900	4.0
3	22,500	210	165	105	0.75	20,900	1.7
4	7,500	105	138	103	3.5	7,540	2.1
5	14,000	153	154	105	1.5	13,400	1.8

Table 2 Results of the model

Case	Prediction Results (W/m^2)				q''_{exp} (W/m^2)	Error (%)
	q_1''	q_2''	q_3''	q''_{total}		
1	3,000	131	4,143	7,274	7,540	-3.5
2	5,250	143	15,196	20,589	20,900	-1.5
3	12,600	149	8,504	21,253	20,900	1.7
4	3,675	627	2,746	7,048	7,540	-6.5
5	7,497	317	5,691	13,505	13,400	0.8

Prediction of Parametric Effects

The general aim of the prediction is to determine the heat transfer due to droplet injection, given wall temperature, Reynolds number, liquid concentration and droplet distribution. Firstly, the analytical model discussed above requires the droplet size distribution. Secondly, the impinging velocity and deposition rate on the heated surface must be known. These can be evaluated respectively by empirical equations or obtained by numerical simulation. Thirdly, determine the heat removal from the target wall directly by the droplets. Lastly, add the heat transfer by the two other components and obtain the total heat transfer.

The current analytical model can successfully predict the effect of various parameters observed in the experiment. When the wall temperature increases, the heat transfer from wall to steam and from steam to droplets will increase proportionally with the temperature difference. However, the heat transfer due to the direct conduction from wall to droplets will change little (compare cases 1 and 5) because the residence time becomes short. Therefore, the ratio of heat transfer coefficients will decrease, which has been observed in experimental studies. Figure 6 shows the predicted result of the wall temperature effect, given the mist concentration and impact velocity for 10 μm droplets and a single-phase heat transfer coefficient of 150 W/m^2-K. As shown in this figure, the droplet impact velocity is an important variable affecting droplet heat transfer, a trend in agreement with the experiment by Pederson [9]. Figure 7 shows the comparison of the model result and the experimental data. Here the droplet size distribution measured

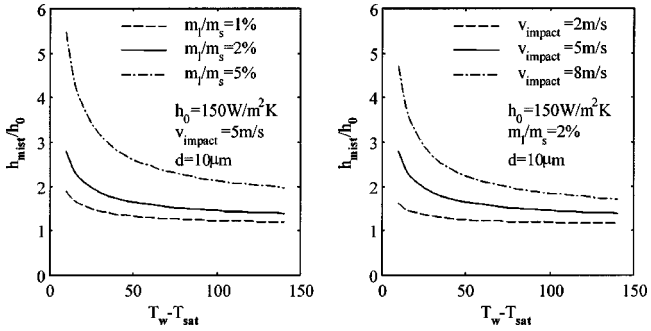

Fig. 6 Predicted effect of the wall temperature on mist/steam heat transfer at different mist concentrations and droplet impact velocities

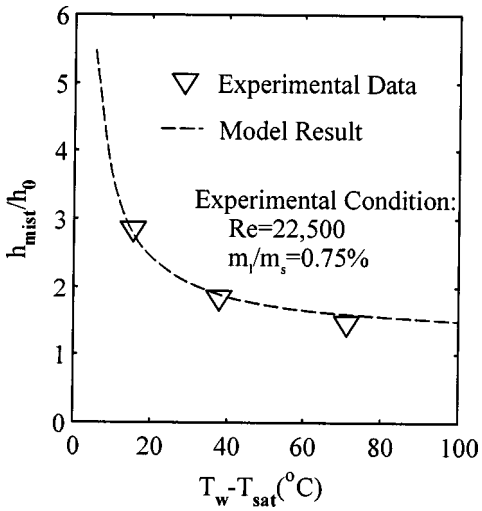

Fig. 7 Comparison of the predicted result by the model and experimental data

from experiment is used; impact density and velocity have been predicted by FLUENT's dispersed flow feature. The agreement is substantial.

Figure 8 shows the predicted trend of enhancement with mist concentration, given the wall temperature, droplet size and impact velocity. The same single-phase heat transfer coefficient as in Fig. 6 is used. The enhancement of heat transfer is proportional to the mist concentration. With a fixed value of impact velocity, smaller droplets provide greater enhancement. However, this result cannot be used simplistically because the impact velocity of a droplet

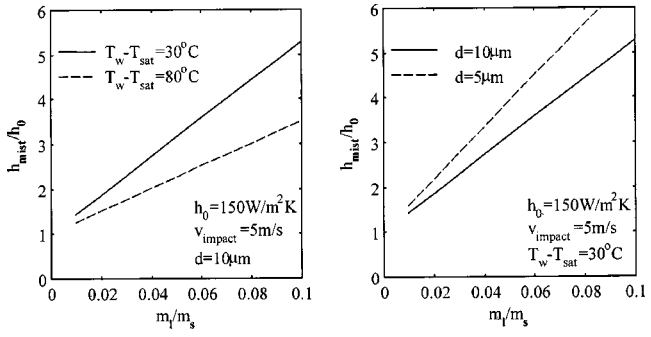

Fig. 8 Predicted effect of the mist concentration on mist/steam heat transfer at different wall temperatures and droplet diameter

depends on the jet velocity as well as the droplet size. Small droplets always have a small impact velocity if they have enough momentum to reach the wall.

Given wall temperature and mist concentration, if the jet velocity increases, the heat transfer from wall to steam will increase but the heat transfer from steam to droplet will decrease due to the thinner boundary layer (see Eq. (10)). The heat transfer from wall to droplet will increase as more droplets hit the wall at higher impact velocity. As a result, the overall heat transfer enhancement increases when the jet velocity increases. This tendency is verified by experiment.

Conclusions

A model for mist/steam jet cooling has been developed and presented which considers the total heat flow to be comprised of three components. A single-phase-like heat flow and a boundary layer quenching effect account for heat flow leaving the surface through the steam. To this is added a heat flow occurring in brief contacts with impacting droplets.

Heat conduction from the wall to droplets is found to be the dominant enhancement mechanism. The quenching effect of droplets in the steam flow becomes important when the mist concentration is high. The heat transfer to small droplets is mainly through the steam while larger droplets hit and cool the heated wall by direct heat conduction.

Because the enhancement increases at lower wall temperature, the contact time for direct conduction varies inversely with wall superheat. A contact time correlation is proposed which, with a simple conduction model, accounts for the observed heat transfer within the experimental uncertainty. The model depends on size distribution, impact velocity and density for droplets, requiring a dispersed-phase trajectory model.

All mechanisms of cooling are proportional to mist concentration. The effect of vapor velocity is mildly positive on the enhancement. The effect of droplet size has both positive and negative components and the model has implied predictions but these are not known from experiment.

Acknowledgments

The authors would like to thank Graver Separations (Wilmington, DE) for donating the steam filters for the experiment. We also want to thank Mee Industries Inc. (El Monte, CA) for donating the pressure atomizers and the high pressure pump. We appreciate the help from Dr. T. Guo in setting up the test facility. This research was sponsored by the U.S. Department of Energy under the contract DOE/AGTSR 95-01-SR-034, and was managed by Dr. N. Holcombe at the Federal Energy Technology Center and by Dr. Larry Golan at the South Carolina Institute for Energy Studies.

Nomenclature

A = area (m^2)
b = jet width (7.5 mm)
c = mass concentration
c_p = specific heat capacity (J/kg-K)
d = diameter of droplet (μm)
d_{10} = arithmetic mean diameter (μm)
d_{30} = volume mean diameter (μm)
d_{32} = Sauter mean diameter (μm)
H_{fg} = latent heat (J/kg)
h = heat transfer coefficient$=q''/(T_w-T_{sat}$ (W/m^2-K)
h_{mist} = heat transfer coefficient of mist (W/m^2-K)
h_0 = steam-alone heat transfer coefficient (W/m^2-K)
k = heat conductivity (W/m-K)
m = mass flow rate (kg/s)
P = pressure (N/m^2)
Q = heat conduction$=\int_0^t q''Adt(J)$
q'' = heat flux (W/m^2)
Re = Reynolds number ($\rho_s v_j 2b/\mu_s$)

r = coordinate in the radial direction (m)
T = temperature (K)
t = time (s)
t_r = residence time (s)
y, v = velocity components in x, y directions (m/s)
v_j = jet velocity (m/s)
We = Weber number ($\rho v^2 d/\sigma$)
x = coordinate along the target wall (m)
y = coordinate perpendicular to the target wall (m)
α = thermal diffusivity (m^2/s)
β = variable defined in Eq. (3)
Δ = thickness of vapor layer (m)
δ = height of spherical cap (m)
μ = dynamic viscosity (kg/m-s)
ρ = density (kg/m^3)
σ = surface tension (N/m)

Subscripts

l = liquid phase
s = steam
sat = saturated
w = wall

References

[1] Goodyer, M. J., and Waterston, R. M., 1973, ''Mist-Cooled Turbines,'' *Conf. of Heat and Fluid Flow in Steam and Gas Turbine Plant*, Proc. of Institution of Mechanical Engineers, pp. 166–174.
[2] Guo, T., Wang, T., and Gaddis, J. L., 2000, ''Mist/Steam Cooling in a Heated Horizontal Tube Part I: Experimental System and Part II: Results and Modeling,'' ASME J. Turbomach., **122**, pp. 360–374.
[3] Guo, T., Wang, T., and Gaddis, J. L., 2000, ''Mist/Steam Cooling in a 180-Degree Tube,'' ASME J. Heat Transfer, **122**, No. 4, pp. 749–756.
[4] Takagi, T., and Ogasawara, M., 1974, ''Some Characteristics of Heat and Mass Transfer in Binary Mist Flow,'' *Proc. of 5th Int. Heat Transfer Conf.*, Tokyo, Japan Society of Mechanical Engineers, pp. 350–354.
[5] Mastanaiah, K., and Ganic, E. N., 1981, ''Heat Transfer in Two-Component Dispersed Flow,'' ASME J. Heat Transfer, **103**, pp. 300–306.
[6] Yoshida, H., Suenaga, K., and Echigo, R., 1988, ''Turbulence Structure and Heat Transfer of A Two-Dimensional Impinging Jet with Gas-Solid Suspensions,'' NHTC, **2**, pp. 461–467.
[7] Wachters, L. H. J., Smulders, L., Vermeulen, J. R., and Kleiweg, H. C., 1966, ''The Heat Transfer from A Hot Wall to Impinging Mist Droplets in The Spheroidal State,'' Chem. Eng. Sci., **2**, pp. 1231–1238.
[8] Pederson, C. O., 1970, ''An Experimental Study of the Dynamic Behavior and Heat Transfer Characteristics of Water Droplet Impinging upon a Heated Surface,'' Int. J. Heat Mass Transf., **13**, pp. 369–381.
[9] Chandra, S., and Avedisian, C. T., 1992, ''Observations of Droplet Impingement on a Ceramic Porous Surface,'' Int. J. Heat Mass Transf., **35**, No. 10, pp. 2377–2388.
[10] Chandra, S., and Avedisian, C. T., 1991, ''On the Collision of a Droplet With a Solid Surface,'' Proc. R. Soc. London, Ser. A, **432**, pp. 13–41.
[11] Buyevich, Yu. A., and Mankevich, V. N., 1995, ''Interaction of Dilute Mist Flow with a Hot Body,'' Int. J. Heat Mass Transf., **38**, pp. 731–744.
[12] Buyevich, Yu. A., and Mankevich, V. N., 1996, ''Cooling of a Superheated Surface with a Jet Mist Flow,'' Int. J. Heat Mass Transf., **39**, pp. 2353–2362.
[13] Fujimoto, H., and Hatta, N., 1996, ''Deformation and Rebounding Processes of a Water Droplet Impinging on a Flat Surface above Leidenfrost Temperature,'' ASME J. Fluids Eng., **118**, pp. 142–149.
[14] Hatta, N., Fujimoto, H., Kinoshita, K., and Takuda, H., 1997, ''Experimental Study of Deformation Mechanism of a Water Droplet Impinging on Hot Metallic Surfaces above Leidenfrost Temperature,'' ASME J. Fluids Eng., **119**, pp. 692–199.
[15] Li, X., Gaddis, J. L., and Wang, T., 2001, ''Mist/Steam Heat Transfer in Confined Slot Jet Impingement,'' ASME J. Turbomach., **123**, No. 1, pp. 161–167.
[16] Ganic, E. N., and Rosenhow, W. M., 1977, ''Dispersed Flow Heat Transfer,'' Int. J. Heat Mass Transf., **20**, pp. 885–866.
[17] Fluent, 1997, FLUENT 4.4 User's Guide, I–III, Fluent Inc.
[18] Li, X., 1999, ''Cooling by a Mist/Steam Jet,'' Ph.D. dissertation, Dept. of Mechanical Engineering, Clemson University, SC.
[19] Gould, R. F., 1964, *Contact Angle, Wettability and Adhesion*, American Chemistry Society, DC.
[20] Neumann, A. W., and Spelt, J. K., 1996, *Applied Surface Thermodynamics*, Marcel Dekker, Inc., NY.
[21] Sadhal, S. S., and Martin, W. W., 1977, ''Heat Transfer Through Drop Condensate Using Differential Inequalities,'' Int. J. Heat Mass Transf., **20**, No. 12, pp. 1401–1407.
[22] Sadhal, S. S., and Plesset, M. S., 1979, ''Effect of Solid Properties and Contact Angle in Dropwise Condensation and Evaporation,'' ASME J. Heat Transfer, **101**, No. 1, pp. 48–54.
[23] Mikic, B. B., and Rohsenow, W. M., 1969, ''Bubble Growth Rates in Non-Uniform Temperature Field,'' Prog. Heat Mass Transfer, **2**, pp. 283–292.

Characterization of Particulate From Fires Burning Silicone Fluids

Yudaya Sivathanu
En'Urga Inc.,
West Lafayette, IN 47906

Anthony Hamins

George Mulholland

Takashi Kashiwagi

National Institute of Standards and Technology,
Gaithersburg, MD 20899

Robert Buch
Dow Corning Corporation,
Auburn, MI 48611

The optical properties of particulate emitted from fires burning two distinct polydimethylsiloxane fluids (D_4 and M_2 or MM, where $D=(CH_3)_2SiO$ and $M=(CH_3)_3SiO_2$) were obtained using a transmission cell-reciprocal nephelometer in conjunction with gravimetric sampling. The specific absorption coefficient of particulate ash from fires burning D_4 and MM is significantly lower than that of particulate soot from an acetylene (hydrocarbon) flame. Scattering is the dominant part of extinction in fires burning the silicone fluids. This is very different from extinction by soot particles in hydrocarbon fires, where absorption is approximately five times greater than scattering. Temperatures and particulate volume fractions along the axis of a silicone fire (D_4) were measured using multi-wavelength absorption/emission spectroscopy. The structure of the D_4 flames is markedly different from hydrocarbon flames. The temperatures and particulate volume fractions very close to the burner surface are much higher than in comparably sized hydrocarbon flames. [DOI: 10.1115/1.1389057]

Keywords: Combustion, Fire, Heat Transfer, Particulate, Radiation

Introduction

Fires fueled by silicones exhibit low heat release rates and fire severity [1,2]. The low heat release rates make them suitable for various industrial products such as transformer fluids, fire-barrier foam and thermal ablatives [3]. Also, silane and other silicon based fuels are being investigated for sub-micron particle synthesis [4,5]. In semiconductor industries, silane and its chlorides are used to deposit thin dielectric films on substrates using thermal or plasma dissociation of the vapor. A better understanding of the structure and properties of silicone fueled fires is needed for improved fire safety as well as to exploit their potential for particulate synthesis.

The burning velocity [6], chemical kinetics [7], and combustion hazards [8] associated with silicones have been studied in recent years. In addition, combustion models have been proposed for polydimethylsiloxanes [9]. The radiative emission fraction and ash composition of pool fires burning silicone fluids have been studied by Buch et al. [3]. The ash is composed of varying amounts of carbon depending on the initial fuel structure [3].

The measured radiative heat loss fraction to the surroundings for silicone pool fires with diameters from 0.1 m to 0.4 m is comparable to those of hydrocarbon flames [3]. In addition, longer chain length silicon fluids have lower radiative heat loss compared to the short chain silicones. The main reason for this behavior could be the lower silica ash volume fractions associated with the long-chain silicone fluids. However, there are very few studies that provide information on the ash volume fraction or the temperature distributions within siloxane flames.

In flames containing particles, obtaining temperature information using either conventional techniques such as thermocouples or laser based techniques such as Raman Scattering is not easily accomplished. Temperature and soot volume fraction information in hydrocarbon based fuels have been routinely obtained using intrusive emission/absorption pyrometry [10,11]. The crucial information required to obtain temperature and ash-volume fraction from siloxane flames is the specific absorption coefficients of the particulate.

Light scattering/extinction measurements in silane flames show that the particle diameters are rather large, varying from 50 nm to 200 nm [5]. Information, however, on the refractive indices, which are needed to obtain specific absorption coefficients are not available. In addition, Zachariah [5] performed measurements at one wavelength, while two wavelength pyrometry requires absorption coefficients at two wavelengths. Refractive indices and specific extinction coefficients in the infrared wavelengths (from 2 μm to 40 μm) for silica aerogel are available [12]. However, obtaining absorption coefficients from these measurements is not possible without knowing the scattering to extinction ratio. In addition, there is no information available in the literature on the absorption coefficients in the near infrared region of the ash formed during the burning of siloxane flames.

The objective of this study was to obtain the absorption coefficients of silicate ash in the near infrared region, and to utilize this information to obtain the temperature and ash volume fraction in a siloxane pool fire.

Experimental Methods

The specific absorption coefficients of the particulate volume fraction (referred to here as the ash volume fraction) were measured using a transmission cell reciprocal nephelometer in conjunction with gravimetric sampling. The schematic diagram of the instrument is shown in Fig. 1. This new measurement method was recently quantified and represents a unique capability for simultaneous measurements of the specific extinction and single scattering albedo with low uncertainty [13]. The nephelometer is similar to the one used by Patterson et al. [14] and Mulholland and Bryner [15]. The exhaust gas from a 5 cm diameter siloxane pool flame was mixed with diluting nitrogen and passed through a transmission cell. The specific absorption and extinction coefficients for particulate from fires burning two polydimethylsiloxane fluids (D_4 and *MM*) were obtained where $D_4=((CH_3)_2SiO)_4$ and $MM=((CH_3)_3SiO_2)_2$. The optical cell was oriented vertically and no significant deposition of particulate onto the glass walls of the nephelometer occurred.

The extinction (I/I_o) of a He-Ne laser was measured using a detector. The light scattered by the particles along the optical path was also measured using a wide angle cosine sensor, whose reponsivity varies as the cosine of the angle between the incident

Contributed by the Heat Transfer Division for publication in the JOURNAL OF HEAT TRANSFER. Manuscript received by the Heat Transfer Division February 6, 2000; revision received November 3, 2000. Associate Editor: Y. Sivathanu.

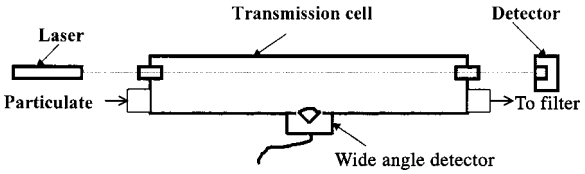

Fig. 1 Schematic diagram of the transmission cell reciprocal nephelometer

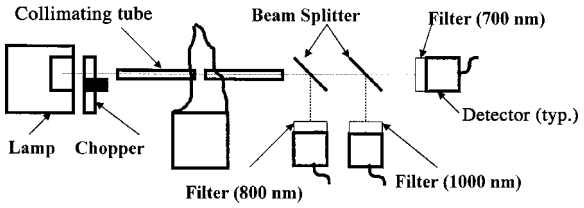

Fig. 2 Experimental arrangement used for multi-wavelength transmittance measurements

radiation and the normal. The mass flux of particles through the transmission cell was obtained by collecting and weighing the particulate on a filter.

The spectral mass specific extinction coefficient ($\kappa_{\lambda,m}$) of ash particles is given by

$$\kappa_{\lambda,m}=\frac{\ln(\tau_\lambda)}{mL}=\frac{\ln(I_\lambda/I_{\lambda_o})}{mL}, \tag{1}$$

where τ_λ is the spectral transmittance, L is the length of the transmission cell, and m is the mass concentration of particulate. The extinction coefficient is composed of two parts, the absorption coefficient ($a_{\lambda,m}$) and total scattering coefficient ($\sigma_{\lambda,m}$). The total scattering coefficient is given by

$$\sigma_{\lambda,m}=\int_0^{2\pi}\int_0^{\pi}\sigma_\lambda(\theta,\phi)\sin\theta d\theta d\phi, \tag{2}$$

where θ is the scattering angle defined by the direction of propagation of the incident beam and direction of the scatter beam, ϕ is the azimuthal angle varying from 0 to 2π for a fixed θ, and $\sigma(\theta,\phi)$ is the scattering function. The total scattering coefficient was obtained by calibration with the non-absorbing aerosol dioctylphthalate (DOP) for which the scattering and extinction coefficients are equal. From the light extinction measurement, the calibration factors for the light scattering measurements was obtained [15]. A combined expanded measurement uncertainty of approximately 6 percent is expected for the absorption and scattering coefficients based on a detailed analysis using the transmission cell nephelometer [15,16]. All uncertainties reported in this paper represent the combined standard uncertainty with a coverage factor of 2 equal to two times the value of the standard deviation [17]. Uncertainty due to laser drift in the transmittance measurement was less than 1 percent.

The above procedure provides an estimate of the extinction coefficient ($\kappa_{\lambda,m}$) and the absorption coefficient ($a_{\lambda,m}$) at 632 nm for the silicate ash. The temperature (T) and the volume fraction of the ash particulate in a 10 cm diameter pool fire burning siloxane was measured using three-wavelength absorption/emission probe measurements, similar to the techniques described by Sivathanu et al. [10] and Choi et al. [18]. Utilizing the measured emission intensity at two wavelengths (700 nm and 800 nm), the temperature of the ash particulate can be obtained as

$$T=\frac{hc}{k}\left(\frac{1}{\lambda_1}-\frac{1}{\lambda_2}\right)\Bigg/\ln\left\{\left(\frac{\varepsilon_{\lambda1}\lambda_2^5}{\varepsilon_{\lambda2}\lambda_1^5}\right)\left(\frac{I_{\lambda2}}{I_{\lambda1}}\right)\right\}, \tag{3}$$

where ε_λ is the specific emission coefficient, which for an arbitrary volume in thermodynamic equilibrium (and in the absence of self absorption within the volume) is equivalent to the absorption coefficient, a_λ [19]. I_λ is the measured spectral radiation intensity at wavelength, λ, h and k are the Planck and Boltzmann constants respectively, and c is the speed of light in vacuum. To obtain the temperature using Eq. (3) an estimate of the ratio $a_{\lambda1}/a_{\lambda2}$ (or equivalently, $\varepsilon_{\lambda1}/\varepsilon_{\lambda2}$) is needed. However, the transmission cell nephelometer provides an absorption coefficient only at one wavelength. Therefore, the ratio $a_{\lambda1}/a_{\lambda2}$ was obtained as described below.

Multi-wavelength transmittance measurements were conducted above a burning (pre-vaporized) stream of D_4 exiting from a 5 mm diameter heated tube. Figure 2 is a schematic drawing of the experimental configuration. The radiation emitted by a mercury arc lamp was collimated through a stainless steel tube, and frequency modulated using a mechanical chopper. The radiation traversed a 10 mm path in the flame, and was then split into three parts using two beam splitters. The parts were incident on three photo-detectors, which had narrow band pass filter (full-width half-maximum of 10 nm) in front of them centered at 700 nm, 800 nm, and 1000 nm. The detected signal was phase-locked using a lock-in amplifier to eliminate the emission due to radiation from the flame. The data was stored at 100 Hz using an A/D converter and a personal computer.

The conditional mean of extinction at 800 nm and 1000 nm, conditioned on the extinction at 700 nm was calculated from the measurements. The ratio of the natural logarithm of the extinction was used along with Eq. (1) to obtain the modeled spectral dependence of κ_λ as

$$\frac{\ln(\tau_{\lambda2})}{\ln(\tau_{\lambda1})}=\frac{\kappa_{\lambda2}}{\kappa_{\lambda1}}\cong\left(\frac{\lambda_1}{\lambda_2}\right)^m. \tag{4}$$

The ratio of specific absorption (emission) coefficients was assumed to have the same wavelength dependence as the extinction coefficient. This ratio was subsequently used in the two wavelength emission measurements along with Eq. (4) to obtain the local temperature [10]. The local ash volume fraction (f_v) in the D_4 pool was obtained from HeNe laser light extinction measurements

$$f_v=\frac{-\ln(\tau)}{\kappa_{\lambda,m}L\rho}, \tag{5}$$

where ρ is the density of particulate, and L is the length of the probe volume. The density of silica ash (taken to be equal to that of bulk amorphous silica) was taken to equal 2200 Kg/m^3 based on the study by Zeng et al. [12].

Particulate was collected using iso-kinetic sampling for subsequent analysis using TEM. Samples were collected in the flame ($\sim$10 cm above the fuel surface on the central axis), above the flame in the plume ($\sim$20 cm above the fuel surface on the central axis), and in the liquid fuel bed from a 10 cm diameter steadily burning pool fire of D_4. Samples collected in the fuel were dispersed in methanol and subjected to sonic treatment for 10 min. The dispersion was dropped onto a carbon coated Cu grid for TEM analysis. Samples collected in the flame were not subjected to a liquid medium or sonic treatment. Samples were also sent to testing laboratories for elemental analysis.

Results and Discussion

A sample TEM photograph of silica ash collected in the plume of a 10 cm diameter D_4 flame is shown in Fig. 3. The primary particles have fused together to form clusters of various sizes. Only a few primary particles are seen. Figure 3 shows that the primary particles vary in sizes ranging from 20 nm to 300 nm. Large primary particles were typical of particulate collected throughout the fire including within the flame, above the flame in the plume, and in the liquid fuel bed. The largest primary particle sizes were approximately 500 nm for samples collected from the

Fig. 3 TEM data obtained in the plume of a 10 cm diameter D_4 fire

liquid fuel. This is a much wider distribution of primary particle sizes than observed in soot particles. Clusters of primary particles of approximately 100 nm to 200 nm form the bulk of the particulate ash. The clusters are linked to form aggregates of sizes ranging from 1 μm to 3 μm. The cluster and aggregate sizes and shapes are similar to those observed in soot particles, although the primary particles are generally much larger.

Table I shows the specific extinction and absorption coefficients and the uncertainty obtained from measurements using the transmission cell nephelometer for D_4, *MM*, and Acetylene. The specific extinction coefficient ($\kappa_{\lambda,m}$) of the silicate ash from D_4 and *MM* is approximately 5 and 2.5 times smaller than that of soot particles from acetylene flames. In addition, the scattering albedo (the ratio of the scattering to extinction coefficient, $\sigma_\lambda/\kappa_\lambda$) of the silicate ash is also shown in Table 1 and is approximately four times larger than that of the hydrocarbon soot particles. This may be due to the small imaginary component of the refractive index of silica compared to that of soot. Therefore, scattering has a major role in the radiative transfer in silicone fluid fires compared

Table 1 Specific extinction, absorption, and scattering coefficients and their uncertainties obtained from the transmission cell nephelometer

Fuel	$\kappa_{\lambda,m}$ (m^2/g)	$a_{\lambda,m}$ (m^2/g)	$\sigma_{\lambda,m}$ (m^2/g)	$\sigma_\lambda/\kappa_\lambda$
D_4	1.7 ± 8 %	0.18 ± 6 %	1.52 ± 6 %	0.90 ± 10 %
MM	3.0 ± 8 %	0.89 ± 6 %	2.11 ± 6 %	0.71 ± 10 %
Acetylene	7.6 ± 4 %	5.89 ± 4 %	1.71 ± 4 %	0.22 ± 6 %

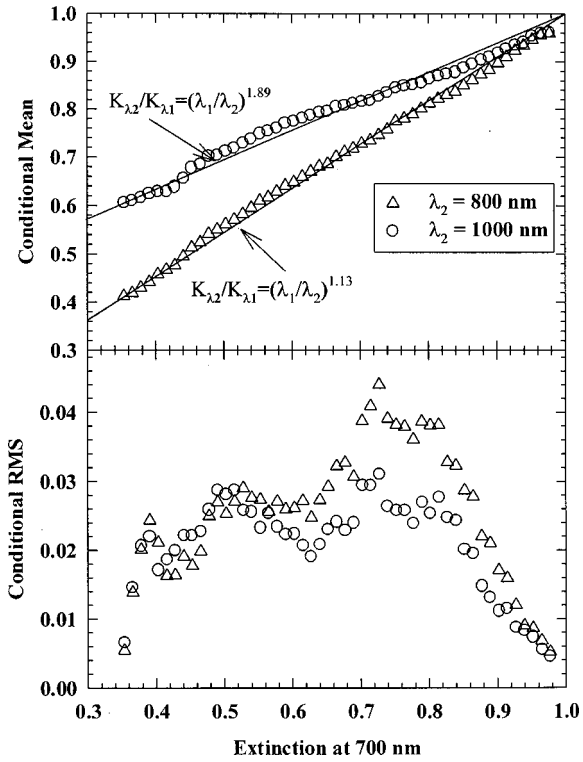

Fig. 4 Conditional mean and RMS of spectral extinction

to their relatively minor role in hydrocarbon fires. For hydrocarbon fires, there is some controversy on the variation of refractive indices with the C/H ratio of the fuel [20,21], however, the maximum variation for the extinction or the absorption coefficient is approximately 30 percent. For the fires burning silicone fluids, the variation of extinction and absorption coefficients with C/Si ratio is very high. The specific absorption coefficient ($a_{\lambda,m}$) of *MM*, which has an initial C/Si ratio (by mass) of 1.29 is 0.18 (±6 percent) m^2/g, whereas that of D_4 (initial C/Si ratio of 0.86) is 0.89 (±6 percent) m^2/g. Elemental analysis of actual particulate sample collected from the D_4 plume and from the D_4 fuel bed yielded a C/Si mass ratio of 0.24 (±26 percent) and 0.23 (±19 percent), respectively [22,23]. The fact that the value of the C/Si ratio for samples taken above the flame (in the plume) and samples from the fuel bed were nearly identical suggests that the C/Si ratio does not vary significantly throughout the flame. Particulate samples from the *MM* flame would presumably yield somewhat higher values of the C/Si ratio. Therefore, to model the radiative transfer in flames burning silicone fluids, the specific absorption and extinction coefficients have to be measured for each individual fuel. The specific extinction coefficient of 7.6 (±4 percent) m^2/g for the acetylene soot is much higher than the value obtained by Dalzell and Sarofim [24], but is within 2 percent of the value reported recently by Zhu et al. [16].

The second set of measurements conducted for this study involved multi-wavelength extinction measurements performed on a 100 mm diameter pool fire burning D_4. Simultaneous extinction measurements at 700 nm, 800 nm, and 1000 nm were conducted using the experimental arrangement shown in Fig. 2. The radiative fraction from this pool fire is approximately 30 percent [3]. The measurements were obtained at a height of 5 cm above the burner.

The conditional mean and the conditional RMS of extinction at 800 nm and 1000 nm, conditioned on the extinction at 700 nm are shown in the top and bottom panel of Fig. 4. The mean extinction at 800 nm and at 1000 nm increases linearly with the extinction at 700 nm. The conditional RMS of extinction at 800 nm and 1000 nm is less than 7 percent of the mean. Therefore, the measure-

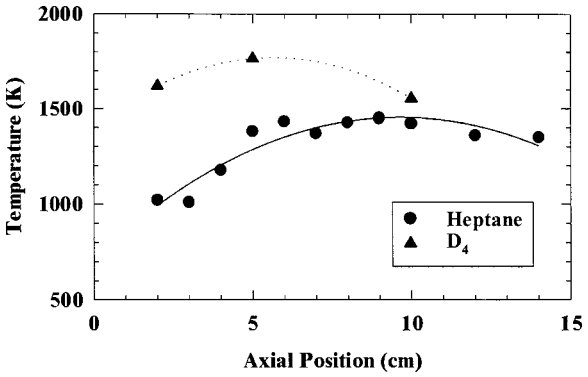

Fig. 5 Mean temperatures along the centerline as a function of distance above a 10 cm diameter D_4 pool fire. Measurements from a 10 cm heptane pool fire are also shown [18].

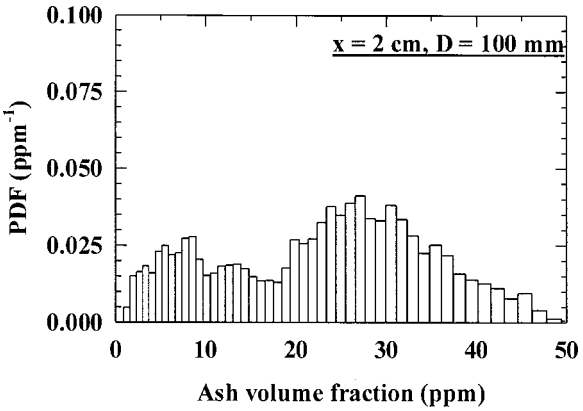

Fig. 7 PDF of ash volume fraction at an axial location 2 cm above the 10 cm diameter pool fire burning D_4

ments can be used to obtain a reasonable estimate of the spectral dependence of the extinction coefficients, using Eq. (4). Results obtained using a linear regression fit to the data and Eq. (4) are shown in Fig. 4. The spectral extinction coefficient varies inversely to the 1.13 power of the ratio of wavelengths between 700 nm and 800 nm. This information was used in Eq. (3) to obtain the local temperatures in the D_4 pool fire.

The mean temperatures along the axis of a D_4 pool fire are shown in Fig. 5. The measurements were obtained at three axial locations. For comparison, the mean temperatures along the axis of a heptane pool fire [18] are also shown in Fig. 5. The pool diameter in both cases was 100 mm. The mean temperatures at an axial location of 2 cm are approximately 1620 K ($\pm$100 K) and 1020 K ($\pm$50 K) for the D_4 and heptane pool fires respectively. This difference is in contrast to the similarity in the calculated adiabatic flame temperature determined using the NASA Chemical Equilibrium Code [25] for the D_4 and heptane flames, which equals 2370 K and 2290 K, respectively. The heptane pool fire has a fuel rich zone close to the burner, leading to lower temperatures. The structure of the heptane pool fire is similar to a laminar diffusion flame. On the other hand, the mean temperature close to the surface of the D_4 pool fire is much higher, and the temperature profile resembles that of a partially premixed flame. This effect could be due the fuel-bound oxygen present in D_4 participating in chemical reactions close to the fuel surface. Visual photographs show that the heptane pool fire bulges outwards, while the D_4 pool fire necks inwards. This structure is similar to alcohol pool fires, which also have fuel bound oxygen. Radial profiles in the siloxane flame are expected to show steep gradients only near the flame edge.

The time-averaged particulate volume fractions as a function of location on the axis of the D_4 pool fire are shown in Fig. 6. For comparison, measurements from a 10 cm heptane pool fire are also shown [18]. At an axial location 2 cm above the burner, the mean soot volume fraction is less than 0.1 ppm (or $\mu L/L$) for the heptane pool fire. On the other hand, the mean ash volume fraction at 2 cm above the burner is 26 ppm for the D_4 pool fire. The mean soot volume fraction increases from a value less than 0.1 ppm ($\pm$10 percent) at an axial location of 2 cm to approximately 0.5 ppm ($\pm$10 percent) at an axial location of 12 cm for the heptane pool fire. This is the expected soot structure for a diffusion flame. However, the ash volume fraction decreases from approximately 26 ppm at 2 cm, to 15 ppm at 10 cm for the D_4 pool fire. The existence of high levels of particulate volume fractions and high levels of temperatures close to the surface explains the similarity in the radiative heat loss fractions of silicone and hydrocarbon based pool fires, despite the very low emissivity of silicate ash in comparison to soot. Both the temperature and soot volume fraction profiles confirm that a flame burning siloxane has a very different structure as compared to a flame burning a hydrocarbon fuel.

The probability density function (PDF) of ash volume fraction at a height of 2 cm above the burner for the D_4 pool fire is shown in Fig. 7. The ash volume fractions at 2 cm above the burner range from 2 ppm to 50 ppm, with a mean value of 22 ppm, and a RMS value of 11 ppm. This indicates that the flow is turbulent very close to the burner surface. This behavior is different from hydrocarbon pool fires, where the PDF of soot volume fraction close to the burner surface typically shows a lognormal distribution [26].

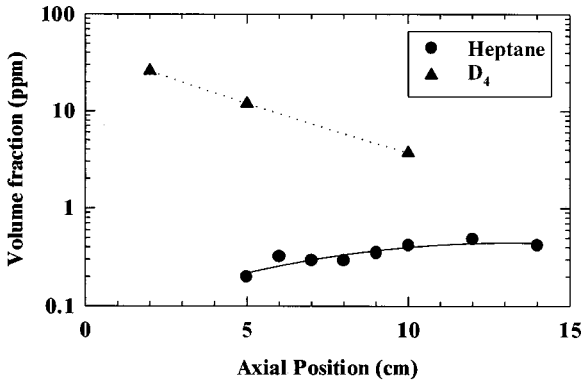

Fig. 6 Mean particulate volume fractions along the centerline as a function of distance above a 10 cm diameter D_4 pool fire. Measurements from a 10 cm heptane pool fire are also shown [18].

Conclusions

The major conclusions of the present study are:

1 The specific absorption coefficient of ash generated from flames burning D_4 is 30 times smaller than that of soot generated from flames burning acetylene.

2 The specific absorption and extinction coefficients of the ash from fires burning silicone fluids increase significantly with increasing C/Si ratio of the fuel.

3 Scattering in fires burning silicone fluids is the dominant mechanism for light extinction.

4 The structure of fires burning silicone fluids are different from those burning hydrocarbons in that higher temperatures and particulate concentrations are observed very close to the burner surface. The higher particulate concentrations and higher tempera-

tures in fires burning silicone fluids lead to the same radiative heat loss fractions (as hydrocarbon flames) despite the lower emission coefficient of silicate ash.

Acknowledgment

Dr. Yudaya Sivathanu was supported by contract number 43NANB616113 from the NIST Statistical Engineering Division, with Dr. Charles Hagwood serving as the Technical Contract Officer.

Nomenclature

a_λ, m = mass specific spectral absorption coefficient
c = speed of light
h = Planck's constant
I_λ = spectral radiation intensity
k = Boltzmann's constant
T = temperature
L = radiation path length
m = mass concentration of particulate

Greek

ε_λ = spectral emissivity
κ_λ, m = mass specific spectral extinction coefficient
λ = wavelength
σ_λ, m = mass specific spectral scattering coefficient
θ = polar angle
ϕ = azimuthal angle
ρ = particulate density
τ_λ = spectral transmittance

References

[1] Kanakia, M., 1979, ''Characterization of Transformer Fluid Pool Fires by Heat Release Rate Calorimetry,'' *4th International Conference on Fire Safety*, San Francisco, CA.
[2] Buch, R. R., 1991, ''Rate of Heat Release and Related Fire Parameters for Silicones,'' Fire Saf. J., **17**, pp. 1–12.
[3] Buch, R., Hamins, A., Konishi, K., Mattingly, D., and Kashiwagi, T., 1997, ''Radiative Emission Fraction of Pool Fires Burning Silicone Fluids,'' Combust. Flame, **108**, pp. 118–126.
[4] Ulrich, G. D., and Subramanian, N. S., 1977, ''Particle Growth in Flames III. Coalescence as a Rate-Controlling Process,'' Combust. Sci. Technol., **17**, pp. 119–126.
[5] Zachariah, M. R., Chin, D., and Semerjian, H. G., 1989, ''Silica Particle Synthesis in a Counterflow Diffusion Flame Reactor,'' Combust. Flame, **78**, pp. 287–298.
[6] Tokuhashi, K., Horiguchi, S., Urano, Y., and Kondo, S., 1990, ''Premixed Disilane-Oxygen-Nitrogen Flames,'' Combust. Flame, **81**, pp. 317–324.
[7] Allendrof, M. D., Melius, C. F., Ho, P., and Zachariah, M. R., 1995, ''Theoretical Study of the Thermochemistry of Molecules in the Si-O-H System,'' J. Phys. Chem., **99**, pp. 15285–15293.
[8] Britton, L. G., 1989, ''Combustion Hazards of Silane and Its Chlorides,'' Paper 12b, *Loss Prevention Symposium*, AIChE Spring National Meeting and Petrochemical EXPO'89, Houston, TX.
[9] Lipowitz, J., 1976, ''Flammability Properties of Poly(dimethylsiloxane). 1. A Model for Combustion,'' J. Fire Flam., **7**, pp. 482–503.
[10] Sivathanu, Y. R., Gore, J. P., and Dollinar, J., 1991, ''Transient Scalar Properties of Strongly Radiating Jet Flames,'' Combust. Sci. Technol., **76**, pp. 45–66.
[11] Sivathanu, Y. R., and Gore, J. P., 1992, ''Transient Structure and Radiation Properties of Strongly Radiating Buoyant Flames,'' ASME J. Heat Transfer, **114**, pp. 659–665.
[12] Zeng, J. S. Q., Greif, R., Stevens, P., Ayers, M., and Hunt, A., 1996, ''Effective Optical Constants *n* and *k* and Extinction Coefficient of Silica Aerogels,'' J. Mater. Res., **11**, pp. 687–693.
[13] Mulholland, G. W., and Choi, M. Y., 1998, ''Measurement of the Mass Specific Extinction Coefficient for Acetylene and Ethene Smoke Using the Large Agglomerate Optics Facility,'' *Twenty-Seventh Symposium (Int.) on Combustion*, The Combustion Institute, pp. 1515–1522.
[14] Patterson, E. M., Duckworth, R. M., Wyman, C. M., Powell, E. A., and Gooch, J. W., 1991, ''Measurement of Optical Properties of Smoke Emission from Plastics, Hydrocarbons and other Urban Fuels for Nuclear Winter Studies,'' Atmos. Environ., **25**, pp. 2539–2552.
[15] Mulholland, G. W., and Bryner, N. P., 1994, ''Radiometric Model of the Transmission Cell-Reciprocal Nephelometer,'' Atmos. Environ., **28**, pp. 873–887.
[16] Zhu, J., Choi, M. Y., and Mulholland, G. W., 2000, ''Soot Scattering in the Visible and Near-Infrared Spectrum,'' *Twenty-Eigth Symposium (Int.) on Combustion*, The Combustion Institute, pp. 439–446.
[17] International Organization of Standardization 1993, *Guide to the Expression of Uncertainty in Measurement*, Geneve, Switzerland.
[18] Choi, M. Y., Hamins, A., Rushmeier, H., and Kashiwagi, T., 1994, ''Simultaneous Optical Measurement of Soot Volume Fraction, Temperature and CO_2 in a Heptane Pool Fire,'' *Twenty-Fifth Symposium (Int.) on Combustion*, The Combustion Institute, pp. 1471–1480.
[19] Siegel, R., and Howell, J. R., 1992, *Thermal Radiation Heat Transfer*, Hemisphere Publishing Corporation, Washington, DC.
[20] Sivathanu, Y. R., Gore, J. P., Jenssen, J., and Senser, D. W., 1993, ''A Study of In-situ Specific Absorption Coefficients of Soot Particles in Laminar Flat Flames,'' ASME J. Heat Transfer, **115**, pp. 653–658.
[21] Habib, Z. G., and Vervisch, P., 1988, ''On the Refractive Index of Soot at Flame Temperature,'' Combust. Sci. Technol., **59**, pp. 261–274.
[22] Galbraith Laboratory, 1995, ''Report of Elemental Analysis for Carbon and Hydrogen.''
[23] Dow Corning Corp., 1995, ''Report of Elemental Analysis for Silicon.''
[24] Dalzell, W. H., and Sarofim, A. F., 1969, ''Optical Constants of Soot and their Application to Heat Flux Calculations,'' ASME J. Heat Transfer, **91**, pp. 100–104.
[25] Gordon, S., and McBride, B., 1976, ''Computer Program for the Calculation of Complex Chemical Equilibrium Compositions, Rocket Performance, Incident and Reflected Shocks, and Chapman-Jouget Detonations,'' NASA Special Publication, No. SP-273.
[26] Sivathanu, Y. R., 1990, ''Soot and Radiation Properties of Buoyant Turbulent Diffusion Flames,'' Ph.D. thesis, University of Michigan, Ann Arbor, MI.

Q.-S.Chen
Mem. ASME
e-mail: qschen@pml.eng.sunysb.edu

H. Zhang
Mem. ASME
e-mail: hzhang@pml.eng.sunysb.edu

V. Prasad
Leading Professor,
Fellow ASME,
e-mail: prasad@pml.eng.sunysb.edu
Tel: 631-632-8350
Fax: 631-632-8205

Department of Mechanical Engineering,
State University of New York at Stony Brook,
Stony Brook, NY 11794-2300

C. M. Balkas
e-mail: cbalkas@sterling-semiconductor.com

N. K.Yushin
e-mail: nyushin@sterling-semiconductor.com
Sterling Semiconductor, Inc.,
Sterling, VA 20166

Modeling of Heat Transfer and Kinetics of Physical Vapor Transport Growth of Silicon Carbide Crystals

Wide-bandgap silicon carbide (SiC) substrates are needed for fabrication of electronic and optoelectronic devices and circuits that can function under high-temperature, high-power, high-frequency conditions. The bulk growth of SiC single crystal by physical vapor transport (PVT), modified Lely method involves sublimation of a SiC powder charge, mass transfer through an inert gas environment, and condensation on a seed. Temperature distribution in the growth system and growth rate profile on the crystal surface are critical to the quality and size of the grown SiC single crystal. Modeling of SiC growth is considered important for the design of efficient systems and reduction of defect density and micropipes in as-grown crystals. A comprehensive process model for SiC bulk growth has been developed that incorporates the calculations of radio frequency (RF) heating, heat and mass transfer and growth kinetics. The effects of current in the induction coil as well as that of coil position on thermal field and growth rate have been studied in detail. The growth rate has an Arrhenius-type dependence on deposition surface temperature and a linear dependence on the temperature gradient in the growth chamber.
[DOI: 10.1115/1.1409263]

Keywords: Silicon Carbide, Physical Vapor Transport, Process Modeling, Heat Transfer, Radiation, Growth Kinetics

1 Introduction

Silicon carbide substrates are needed for electronic and optoelectronic devices involving high temperature, intense radiation, high frequency and high power. Commercially available SiC single crystals that are used to produce these substrates, range from 25 to 75 mm in diameter; experimental growth of 100 mm diameter SiC crystals has also been reported recently. The quality of these crystals, although improving, remains an important issue. Of particular concern are the micropipes (wormholes) and defect density [1] that occur during the deposition of SiC inside a sealed enclosure, at temperatures above 2300 K and pressures below 2.66×10^4 Pa, by a physical vapor transport technique using the modified Lely-method [2,3]. The process involves sublimation of SiC from a hot powder source, transport of vapor through an inert gas environment, and condensation on a seed that is colder than the source. The deposition continues until a bulk crystal of reasonable size is grown.

A typical SiC growth system consists of an RF copper coil, quartz tube, graphite susceptor, graphite insulation, crucible, and some other components (Fig. 1(*a*)). The graphite crucible is filled with a SiC powder charge, and a SiC seed is placed on the bottom of the lid of the crucible as shown in Fig. 1(*a*). The seed is cooled by heat loss through a hole in the upper portion of the graphite insulation. The SiC charge is heated by using RF induction heating that is generated by passing a radio-frequency current, e.g., 10 kHz and 1200 A, through the coil. The time-harmonic electromagnetic field induces eddy currents in the graphite susceptor that has a high electrical conductivity, and heat is generated. Generally, the electromagnetic wave is suscepted in a thin (skin) depth of few millimeters, and the heat generated there is transferred by conduction and radiation to the inside of the crucible and then by conduction, radiation and (weak) convection to the SiC charge and other part of the inner region.

The growth process consists of several steps [4,5]: (*a*) vacuum degassing stage—a low gas pressure (10^{-3} Pa) and an evacuation temperature ($1073\,\mathrm{K}<T<1273\,\mathrm{K}$) are applied to reduce the background nitrogen contamination; (*b*) preheating stage—temperature is gradually increased in high-purity argon environment (about 10^5 Pa) to the growth temperature and stabilized to achieve an optimum ΔT between the source and the seed; (*c*) growth stage—a programmed pressure reduction is used to achieve low-defect nucleation and uniform epitaxy on the oriented seed crystal (argon pressure is decreased to $10<p<2.66\times10^4$ Pa) [6], and boule growth begins; (*d*) cooling stage—the temperature is gradually reduced after the growth is completed. The difference of temperature between the charge and the seed during the growth stage depends on the system configuration, and is considered critical to the crystal quality. According to Lilov [7], SiC dissociates completely into liquid silicon and solid carbon at $T>3150$ K, and, therefore, the growth temperature must lie below 3150 K. Various growth systems used by the industry employ different growth temperatures depending on the temperature gradient in the growth chamber, and a lower growth temperature is usually associated with a higher temperature gradient and a lower pressure of the inert gas. Basically, different companies have developed different recipes (combination of induction coil location, temperature differential measured by two pyrometers as shown in Fig. 1(*b*), and the gas pressure) for the growth based on trial and error experiments and post-process crystal characterization.

The thermal distribution inside the growth system is determined by a complex interaction among the radiation, conduction and convection heat transfer in different material phases (gas, solids and porous media). Although convection may be weak in smaller growth systems, it may become important in larger systems, e.g., for 100 mm diameter boule. Mass transfer from the source to the

Contributed by the Heat Transfer Division for publication in the JOURNAL OF HEAT TRANSFER. Manuscript received by the Heat Transfer Division January 16, 2001; revision received April 9, 2001. Associate Editor: R. L. Mahajan.

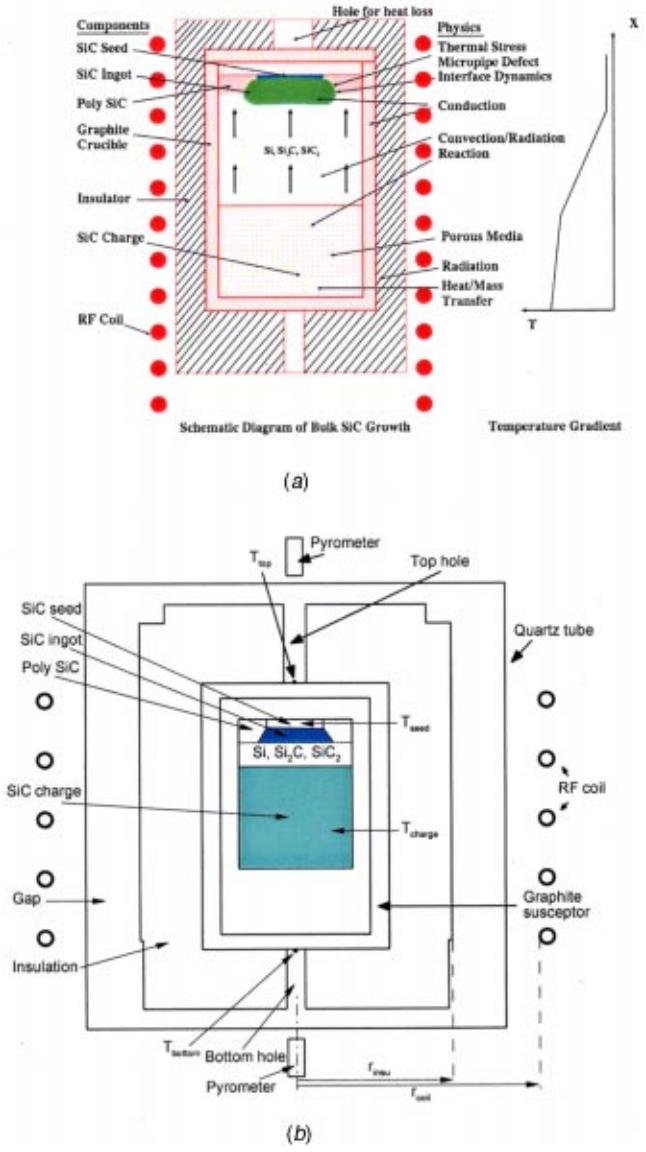

Fig. 1 (*a*) Schematic of a RF heated furnace for PVT growth of single SiC crystals and key physical phenomena associated with the process; and (*b*) geometry of a SiC growth system with 5 turns of coil

seed crystal is highly sensitive to temperature distribution, which is determined by diffusion, Stefan flow, buoyancy force and radiation. The rate of growth at the interface depends on the interplay between the surface kinetics and mass transport. Chemical reaction also plays an important role.

Several different configurations of SiC growth systems using modified Lely method have appeared over years. Tairov and Tsvetkov [8,9] were the first to use the seeded method to produce SiC single crystals. In their experiments, single-crystalline platelets of SiC with {0001} faces were used as seeds. A charge of polycrystalline silicon carbide synthesized from silicon and carbide of semiconductor purity was used as the source of vapor and was placed either around a thin walled graphite cylinder or inside it. They also obtained good results by inserting the charge into a crucible that was made of a solid graphite cylindrical block by boring a hole. The ingots were grown in the temperature range of 2073 to 2873 K at partial argon pressures of 0.013 to 10^5 Pa. They calculated that the amount of silicon carbide grown per unit mass of the graphite heater evaporated is increased 4.5 times when the growth temperature is reduced from 3000 to 2000 K. They subsequently produced ingots of 8 mm diameter and 8 mm long at about 2073 K in 0.013 to 0.13 Pa vacuum; the axial temperature gradient amounts to about 30 deg/cm with the growth rate up to 1.6–2 mm/h.

Barrett et al. [4] grew a single crystal of 20×25 mm area from a Lely grown platelet of 5×8 mm area at reduced pressures of 266 Pa with a temperature gradient of 20–35 K/cm, the temperature measured by a pyrometer within a cavity, which was extended to within 5 mm of the SiC seed, ranged from 2000–2100 K. Later, Barrett et al. [5] grew a 40 mm diameter single crystal boule using a 25 mm wafer seed in a 40 mm diameter growth cavity at a pressure of 2666 Pa and a source to seed ΔT of about 100 K. The average growth rate was observed to be 0.9 mm/h over a 58 h period. This group of researchers of Hobgood et al. [10] also grew 6H-polytype SiC single crystals with diameters up to 50 mm and lengths up to 75 mm, at growth rates of 0.25 to 1 mm/h, argon pressure of 2666 Pa, and seed temperature of 2373–2473 K. Augustine et al. [11] also succeeded in growing 50 mm diameter silicon carbide crystals using the argon pressure up to 4000 Pa, and the growth temperature up to 2398 K. Tsvetkov et al. [12] produced boules of 50–75 mm diameter with the background gas pressure ranging from 13,333 Pa to less than 133 Pa. Powell et al. [13] expanded the single crystal area in a boule up to 50 mm diameter with the aid of modeling software. A detailed review of the growth techniques and characterization of SiC crystals has been presented recently by Dhanaraj et al. [14].

Modeling has been used by several groups of researchers to develop basic understanding of physical phenomena and improve the SiC growth process. Hofmann et al. [15,16] modeled the temperature distributions for growth temperature of 2473 K and system pressure of up to 3500 Pa. Pons et al. [2,3] calculated both the electromagnetic field and temperature distribution, and found that the calculated temperatures for the seed and powder surface, 2920 K and 3020 K, were much higher than the external temperatures measured at the top and bottom of the crucible, 2390 K and 2500 K, while the maximum temperature of the insulation foam on its periphery was about 1000 K. They have reported the total pressure around 4000 Pa and the growth rate of 1.55 mm/h. Müller et al. [17] also calculated the temperature distribution in the inductively heated SiC growth reactors with the temperature of 2373–2673 K, found that the temperature in the powder was highly non-uniform, and predicted a radial temperature variation of 30–50 K along the powder surface.

Ma et al. [18] performed an order-of-magnitude analysis of various process parameters, and used a one-dimensional network model and two-dimensional finite-volume model to predict the temperature distribution in a 75 mm growth system. Chen et al. [19] proposed a kinetics model for SiC vapor growth, predicted growth rate as a function of temperature, temperature gradient and inert gas pressure, and obtained growth rate profiles across the seed surface from the temperature distribution in a 75 mm growth system. A detailed discussion on process physics and modeling of SiC growth can be found in Chen et al. [20].

In spite of several publications on SiC growth simulations, many aspects of this process remain unclear and cannot be predicted using the existing models. First of all, the models reported thus far cannot accurately predict the growth rate. Secondly, there is a remarkable controversy with respect to the possibility of growth at elevated inert gas pressures. Some experiments indicate that the growth can be performed at high pressures, such as at 26666 Pa (200 Torr) [6] or even at 1 atm [8], but the published models predict suppression of growth with an increase in the inert gas pressure. It is therefore important to develop a model that can describe the SiC growth as a function of inert gas pressure (without a restriction of low pressure). It should be noted that majority of experimental studies consider only low-pressure growth; however, it is desirable to examine the growth phenomena at high

pressures. Thirdly, all previous model calculations are valid for only specific growth chamber designs and do not present general effects of the governing parameters.

The primary goal of the present work is therefore to develop a coupled, high-resolution transport model to predict the electromagnetic field due to RF heating, heat and mass transfer in the growth system and rate of growth based on growth kinetics and chemical reactions. The model proposed here can be used for both the low-pressure and high-pressure growths to investigate the effects of current and coil position on temperature distribution and growth rate profile. Simulations have been performed for a range of parameters to study the effects of gas pressure.

2 Mathematical Model

2.1 Heat Transfer Scale Analysis. It is important to first examine the strength of various parameters in a SiC growth system. One way to perform such analysis is to consider the operational conditions of a typical system, e.g., $p=0.001$ Pa and $T=1073-1273$ K during the degassing stage, $p=10^5$ Pa and $T=2600-3100$ K during the preheating stage, as well as $p=100-26{,}666$ Pa and $T=2100-2900$ K during the growth stage. Considering the argon gas as an ideal gas, its density can be estimated from $\rho=pM/RT$, the Prandtl number from

$$\mathrm{Pr}=\frac{\mu c_p}{k}, \tag{1}$$

and Grashof number from

$$\mathrm{Gr}=\frac{\rho^2 g\beta D_c^3 \Delta T}{\mu^2}=\frac{\rho^2 g D_c^3}{\mu^2}\frac{\Delta T}{T}, \tag{2}$$

where D_c is the diameter of the crucible, and the isobaric expansion coefficient of an ideal gas

$$\beta=-\frac{1}{\rho}\frac{\partial \rho}{\partial T}=\frac{1}{T}.$$

Under the process conditions of gas pressure of 3×10^4 Pa, growth temperature of 2900 K and temperature difference of 30 K, the Prandtl number is obtained as 0.66 while the Grashof number is estimated to be between 3 and 24 for the crucible with an inner diameter of 50–100 mm (for the growth of 25–75 mm diameter crystals, current industry standard). It is evident that the heat transfer by buoyancy flow in the present industrial growth system can be considered negligible. The buoyancy effect, however, may become important if the chamber diameter or height increases by even a factor of two since the thermal conditions in the growth chamber can induce complex buoyant flows, combining both Bénard convection and vertical boundary layer flows.

If the leakage and diffusion are neglected, the advective velocity of SiC vapor flow can be estimated from

$$U=\rho_{\mathrm{SiC}} G_{\mathrm{SiC}} A_{\mathrm{SiC}}/\alpha\rho_{\mathrm{gas}} A_{\mathrm{gas}}, \tag{3}$$

where α is sticking coefficient, and A_{SiC} is the growth area. This leads to the mass Péclet number

$$\mathrm{Pe}=UL/D, \tag{4}$$

where the diffusion coefficient can be obtained from $D=D_0(T/T_0)^n(p_0/p)$ [21], with $D_0=5\times10^{-6}\sim2\times10^{-4}$ m^2/s, $n=1.8$, $T_0=273$ K, and $p_0=1$ atm. D_0 is chosen as 5×10^{-6} m^2/s for low temperature SiC growth, and 1×10^{-5} m^2/s for high temperature SiC growth [19,20]. Using $D_0=1\times10^{-5}$ m^2/s and $L=50$ mm, the advective velocity, diffusion coefficient, density and Péclet number are obtained as shown in Table 1 for two operating conditions, one with a low growth temperature and low gas pressure, and another with a high growth temperature and high gas pressure.

Table 1 Advective flow parameters for two different operating conditions

	U (m/s)	D (m^2/s)	ρ (kg/m^3)	α	Pe
2600 K, 2666 Pa	0.178	2.16×10^{-2}	4.92×10^{-3}	1	0.41
2900 K, 26666 Pa	0.0199	3.98×10^{-4}	4.41×10^{-2}	1	2.5

The enthalpy released during the deposition, the heat transfer by Stefan flow (advective mass transport) and the radiative heat transfer can be estimated using the following simple equations,

$$Q_{\mathrm{latent}}=\rho_{\mathrm{SiC}} G_{\mathrm{SiC}} A_{\mathrm{SiC}} \Delta H_{vs}, \tag{5a}$$

$$Q_{\mathrm{Stefan}}=\rho_{\mathrm{SiC}} G_{\mathrm{SiC}} A_{\mathrm{SiC}} c_p \Delta T, \tag{5b}$$

$$Q_{\mathrm{radi}}=\varepsilon A_{\mathrm{SiC}}\sigma(T_{\mathrm{charge}}^4-T_{\mathrm{seed}}^4). \tag{5c}$$

For a set of typical values, such as the growth rate of $G_{\mathrm{SiC}}=1$ mm/h, a diameter of 50 mm, $\Delta T=30$ K, $\varepsilon=0.8$, and $T_{\mathrm{seed}}=2900$ K, Q_{latent}, Q_{Stefan} and Q_{radi} are estimated as 0.01 W and 0.1 W, and 1000 W, respectively. Therefore, it is reasonable to neglect the enthalpy change due to condensation and heat transfer by Stefan flow, at least for the global study of temperature field. It should, however, be noted that the Stefan flow is important for mass transfer and growth rate, and a small change in temperature gradient near the deposition surface can change the growth kinetics significantly. These effects can be considered by developing a hybrid numerical model (fine resolution near the interface). Being the first comprehensive study of the problem, these secondary effects are not considered here, and may be analyzed in the future.

2.2 Electromagnetic Field. The electromagnetic field produced by RF induction heating can be calculated using the Maxwell's equations and the generated power in the graphite susceptor can be predicted by employing the principles of eddy current. For low frequency ($f<1$ MHz), the Maxwell's equations can be simplified using the quasi-steady state approximations. Assuming that the current in the coil is time-harmonic, the magnetic flux density can be expressed as the curl of a magnetic vector potential, $\mathbf{B}=\nabla\times\mathbf{A}$. The Maxwell equations can then be written in terms of the vector potential, $\mathbf{A}$ [22,23],

$$\nabla\times\left(\frac{1}{\mu_m}\nabla\times\mathbf{A}\right)+\varepsilon_m\frac{\partial^2\mathbf{A}}{\partial t^2}+\sigma_c\frac{\partial\mathbf{A}}{\partial t}=\mathbf{J}_{\mathrm{coil}}, \tag{6}$$

where μ_m is the magnetic permeability, ε_m is the permittivity, σ_c is the electrical conductivity, and $\mathbf{J}_{\mathrm{coil}}$ is the current density in the coil. If the coil and the electromagnetic field are assumed axisymmetric, both the magnetic potential vector, $\mathbf{A}$, and the current density, $\mathbf{J}_{\mathrm{coil}}$, will have only one angular component with an exponential form, such as,

$$\mathbf{A}=\begin{Bmatrix}0\\ A_0e^{i\omega t}+cc\\ 0\end{Bmatrix},\quad \mathbf{J}_{\mathrm{coil}}=\begin{Bmatrix}0\\ J_0e^{i\omega t}+cc\\ 0\end{Bmatrix}, \tag{7}$$

where i is the complex unit, ω is the angular frequency, and cc denotes the complex conjugate. The final equation for vector potential, A_0, is obtained by substituting Eq. (7) into Eq. (6) [24],

$$\left(\frac{\partial^2}{\partial r^2}+\frac{1}{r}\frac{\partial}{\partial r}-\frac{1}{r^2}+\frac{\partial^2}{\partial z^2}\right)\left(\frac{A_0}{\mu_m}\right)+\varepsilon_m\omega^2A_0-i\omega\sigma_cA_0=-J_0. \tag{8}$$

The second term in the left side of the above equation is negligible. The following boundary conditions can be used to solve the above equation,

$$A_0=0,\quad \text{at } r=0,\ \text{and } (r^2+z^2)\to\infty, \tag{9}$$

which are based on the conditions that magnetic flux density, $\mathbf{B}$, is axi-symmetric, and the computational domain is sufficiently large.

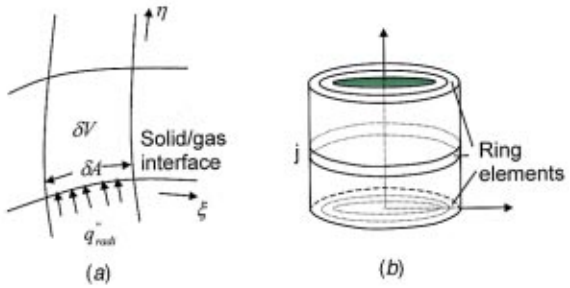

Fig. 2 (*a*) Heat flux on the radiation surface and curvilinear grid system; and (*b*) schematic of ring elements on radiative surfaces. The ring elements coincide with the finite volume grids for conduction calculation.

After solving Eq. (8) for the vector potential, A_0, the generated heat power in the graphite susceptor can be obtained using the principles of eddy current [25],

$$q'''_{\text{eddy}} = \frac{1}{2}\sigma_c \omega^2 A_0 A_0^* , \tag{10}$$

where* denotes the complex conjugate.

2.3 Energy Transport Equation. Once the eddy currents provide the distribution of volumetric heat generation in the graphite susceptor (within a skin depth of few millimeters), the temperature distribution in the growth system can be calculated using a conduction-radiation model,

$$(\rho c_p)_{\text{eff}} \frac{\partial T}{\partial t} = \nabla \cdot (k_{\text{eff}} \nabla T) + q'''_{\text{eddy}} - (q''_{\text{radi}} + q''_{\text{insu}})\, \delta A / \delta V, \tag{11}$$

where q''_{radi} is the radiative heat flux normal to the radiation surface. A brief description of the formulation for q''_{radi} is presented in section (2.4). In equation (11), $(\rho c_p)_{\text{eff}}$ and k_{eff} are local effective heat capacity and conductivity, respectively, and will change from one location to another depending on the material (see Eqs. 30 and 31). In Eq. (11), q''_{insu} is the radiative heat flux on the outer surfaces of insulation,

$$q''_{\text{insu}} = \varepsilon_{\text{eff}} \sigma (T^4 - T_\infty^4), \tag{12}$$

where ε_{eff} is the effective emissivity. For surfaces exposed to the ambient air, the effective emissivity can be chosen as that of the material, $\varepsilon_{\text{eff}} = \varepsilon_{\text{insu}}$. On the other hand, for surfaces exposed to the copper coil, the effective emissivity can be taken as, $\varepsilon_{\text{eff}} = 1/(1/\varepsilon_{\text{insu}} + r_{\text{insu}}/r_{\text{coil}}(1/\varepsilon_{\text{coil}} - 1))$, so that the reflection of energy by the inner surface of the copper coil can be included in the formulation. Here, r_{insu} and r_{coil} are the radii of the outer surface of insulation and inner surface of coil (as shown in Fig. 1(*b*)).

Radiative heat flux q''_{radi} and q''_{insu} are obtained at the grid points of the corresponding radiation surface using the curvilinear non-orthogonal finite volume method. The radiative heat flux q''_{radi} and q''_{insu} are converted to source terms in the energy equation in order to use a single domain technique. Here, δA is the area of a finite-volume face within the radiation surface, and δV is the finite volume adjacent to the radiation surface (see Fig. 2(*a*)).

To solve Eq. (11) one needs to consider realistic boundary conditions. The computational domain for the temperature is set as inside the quartz tube (Fig. 1(*b*)), and the temperature on the quartz tube is set as 293 K (quartz tube is water cooled). From the reported growth striations in SiC crystal marked by an interface demarcation technique [26], it is evident that the system behaves almost symmetric, hence at the central axis,

$$\frac{\partial T}{\partial r} = 0, \quad \text{at } r = 0 \tag{13}$$

is a good approximation. However, if the system becomes large (for large diameter growth) such that convective effects cannot be neglected, the insulation materials and graphite properties are not homogeneous, and/or the power supply fluctuates, then the three-dimensional effects will have to be considered.

2.4 Radiative Heat Transfer. A radiation model based on the method of discrete exchange factors is employed here to calculate the radiative heat transfer in the growth chamber as well as within the top and bottom holes [27,28]. It is assumed that the radiation surfaces are gray, diffusely emitting and reflecting, and opaque. The radiation surfaces are broken into a number of rings each with uniform properties (see Fig. 2(*b*)), the rings coincide with the grids using the curvilinear non-orthogonal finite volume method [29,30], and the view factors between each pair of rings are calculated [28,31]. The absorptivity α_j is assumed to be equal to the emissivity ε_j in each ring. The integral equations for radiative heat transfer is then obtained as [32],

$$\frac{q''_{\text{rad}\,j}}{\varepsilon_j} - \sum_{k=1}^{N} F_{j,k} \frac{1-\varepsilon_k}{\varepsilon_k} q''_{\text{radi}\,k} = \sigma T_j^4 - \sum_{k=1}^{N} F_{j,k} \sigma T_k^4, \tag{14}$$

where $F_{j,k}$ is the view factor from ring j to ring k. The above equations can be solved numerically by writing,

$$(A_{jk}) \cdot (q''_{\text{radi}\,k}) = (B_{jk}) \cdot (\sigma T_k^4), \tag{15}$$

where $A_{jk} = \delta_{jk}/\varepsilon_k - F_{j,k}(1-\varepsilon_k)/\varepsilon_k$, $B_{jk} = \delta_{jk} - F_{j,k}$, and $\delta_{j,k}$ is the Kronecker's delta. The radiative heat flux in Eq. (15) can be written in the tensor form as:

$$q''_{\text{radi}\,j} = (\mathbf{A}^{-1} \cdot \mathbf{B})_{jk} \cdot (\sigma T_k^4). \tag{16}$$

Once $q''_{\text{radi}\,j}$ is calculated from Eq. (16) it can be converted into the heat source in each finite-volume for solving the energy Eq. (11).

2.5 Growth Kinetics. Mass spectrometric investigations conducted by Drowart and Maria [33] have shown that the basic components of evaporation of SiC are Si, Si_2C, SiC_2, and SiC. The fraction of other components of evaporation, Si_2, C, C_2, C_3, in the vapor is insignificant and can be neglected. The following reactions are considered probable for the sublimation process [7]:

$$\text{SiC}_{(s)} \Leftrightarrow \text{Si}_{(l)} + \text{C}_{(s)} \quad K_1 = a_{\text{Si}} \tag{17}$$

$$\text{SiC}_{(s)} \Leftrightarrow \text{Si}_{(g)} + \text{C}_{(s)} \quad K_2 = P_{\text{Si}} \tag{18}$$

$$2\,\text{SiC}_{(s)} \Leftrightarrow \text{Si}_2\text{C}_{(g)} + \text{C}_{(s)} \quad K_3 = P_{\text{Si}_2\text{C}} \tag{19}$$

$$2\,\text{SiC}_{(s)} \Leftrightarrow \text{SiC}_{2(g)} + \text{Si}_{(l,g)} \quad K_4 = P_{\text{SiC}_2} P_{\text{S}} \tag{20}$$

$$\text{SiC}_{(s)} \Leftrightarrow \text{SiC}_{(g)} \quad K_5 = P_{\text{SiC}} \tag{21}$$

Because of the lack of carbon species near the seed and since SiC vapor pressure is very small [7], only reaction (20) is considered important for the deposition process. The equilibrium constant for this reaction can be calculated from the equation of equilibrium:

$$K = \exp(-\Delta G_T^0 / RT) \tag{22}$$

The change in isobaric-isothermal Gibbs-function ΔG_T^0 in Eq. (22) can be obtained from,

$$\Delta G_T^0 = \sum_{\text{prod}} v_i (\Delta h_{f,298}^0 + h_T - h_{298} - T s_T^0) - \sum_{\text{reac}} v_i (\Delta h_{f,298}^0 + h_T - h_{298} - T s_T^0), \tag{23}$$

where $\Delta h_{f,298}^0$ is the heat of formation, v_i is the stoichiometric coefficient, and h_T is the enthalpy of the reacting species.

The thermodynamic analysis [7] shows that the vapor becomes silicon rich at temperatures below 2546 K, and SiC_2 rich at temperatures above 2900 K. The rate-determining species, *A*, is therefore chosen as SiC_2 at $T<2546$ K, as Si at $T>2900$ K, and either of the two for $2546\,\mathrm{K}<T<2900\,\mathrm{K}$. Introducing z' coordinate, which is set as 0 at the charge, and L at the seed, the vapor pressures of various species can be calculated as a function of z'. In the present model, we assume that the species transport rate near the seed is proportional to the supersaturation of the rate-determining species *A* [34],

$$J_A=\chi_A(p_A(L)-p_A^*(L)), \tag{24}$$

where p_A^* is the equilibrium vapor pressure of gaseous *A*, and $\chi_A=1/\sqrt{2\pi M_A RT}$. The SiC_2 and Si vapors are assumed to have an identical transport rate, i.e., $J_{SiC_2}=J_{Si}$, which yields the growth rate of SiC crystal as,

$$G_{SiC}=\frac{2M_{SiC}}{\rho_{SiC}}\chi_A[p_A(L)-p_A^*(L)]. \tag{25}$$

The factor 2 on the right side of the above equation is needed since one SiC_2 molecule and one Si molecule form 2 SiC molecules.

Assuming the advective velocities of the species SiC_2 and Si to be the same, the distribution of the vapor pressure can be obtained by one-dimensional mass transfer equation for Stefan flow as [21],

$$p_{SiC}(z')+p_{Si}(z')=p-[p-p_{SiC_2}(0)-p_{Si}(0)]\exp(\mathrm{Pe}\cdot z'/L). \tag{26}$$

The advective velocity, *U*, in Pe can be expressed as a function of the transport rate of SiC_2 and Si as,

$$U=J_{SiC}RT/p=2\chi_A(p_A(L)-p_A^*(L))RT/p. \tag{27}$$

From the above equation, we obtain,

$$p_A(L)=p_A^*(L)+Up/2\chi_A RT. \tag{28}$$

Assuming SiC_2 and Si to have the same vapor pressure gradient in the growth chamber, Eq. (26) reduces to,

$$U=D/L\,\ln((p-2p_A(L))/(p-2p_A(0)). \tag{29}$$

Again if we assume that the vapor pressure at the source is the same as the equilibrium vapor pressure, so $p_A(0)=p_A^*(0)$, U and $P_A(L)$ can be obtained using Eq. (28) and (29) in an iterative fashion. First by setting U as 0, $P_A(L)$ is obtained from (28), then the advective velocity U is obtained by substituting (28) in (29). Consequently, the growth rate is obtained from Eq. (25). In solving the above equations, the equilibrium vapor pressures of species Si, SiC, Si_2C, and SiC_2 are taken from Lilov [7]. The growth rate can then be obtained once the source temperature, $T(0)$, seed temperature, $T(L)$, distance between the source and seed, L, and system pressure, p, is known. The two-dimensional effect of temperature distribution on growth rate is accounted by using the seed temperature $T(L)$ as a function of radial coordinate, *r*, as obtained from Eq. (11). The source temperature $T(0)$ is the maximum temperature in the charge.

2.6 Properties of Various Components. Electrical and thermal properties of various components (i.e., graphite susceptor, graphite insulation, crucible and SiC charge) in the growth system are functions of temperature, and their values are taken at a temperature interval of 250 K. Table 2 lists values of electrical resistivity and thermal conductivity at temperatures in the range of 773–3273 K. The source material is usually chemically acid-treated abrasive SiC powder, and its average grain size is considered as, $d_p=125\,\mu$m [6]. During the growth, the main species, Si, SiC_2, Si_2C, SiC, evaporate from the SiC charge, and graphitization of the charge occurs. The charge can be considered as a porous medium with porosity, ε_p, and effective specific heat,

Table 2 Material properties of various components

Components	Electrical resistivity (Ωm) (773 - 3273 K)	Thermal conductivity (W/m/K) (773 - 3273 K)
Graphite	0.8×10^{-5}-1×10^{-5}	50-20
Insulation	~0.001	0.1-3
SiC crystal	1-0.001	100-50
SiC charge	1-0.001	20-5
Argon	-	0.03-0.05

$$(\rho c_p)_{\mathrm{eff}}=(1-\varepsilon_p)(\rho c_p)_{\mathrm{SiC}}+\varepsilon_p(\rho c_p)_{\mathrm{gas}}. \tag{30}$$

The heat transfer inside the charge consists of both radiative and conductive components. A suitable expression for effective thermal conductivity for SiC charge must account for these components, for example [35],

$$k_{\mathrm{eff}}=(1-\varepsilon_p)k_{\mathrm{SiC}}+\varepsilon_p\left(k_{\mathrm{gas}}+\frac{8}{3}\varepsilon 4\sigma T^3 d_p\right), \tag{31}$$

where d_p is the mean powder diameter. The porosity, ε_p, can lie anywhere between 0.35 and 0.5, and is chosen as 0.4 for present calculations. However, it is not difficult to measure ε_p.

2.7 Numerical Method. The magnetic potential Eq. (8), heat generation Eq. (10), energy Eq. (11) and integrated radiative heat transfer Eq. (16), are solved using an in-house developed finite volume algorithm [22,23,29,30]. Conservation Eq. (8) and (11) can be written in the following general form:

$$\frac{\partial}{\partial t}(rc\phi)=\frac{\partial}{\partial x}\left(r\Gamma\frac{\partial\phi}{\partial x}\right)+\frac{\partial}{\partial r}\left(r\Gamma\frac{\partial\phi}{\partial r}\right)+r(S_C+S_P\phi), \tag{32}$$

where ϕ is the generalized variable, Γ is the diffusion coefficient, and S_C is the volumetric source. The coefficients are defined as, $c=0$, $\Gamma=1/\mu_m$, $S_C=J_0$, and $S_p=\varepsilon_m\omega^2-i\omega\sigma_c-1/r^2(1/\mu_m)$ for magnetic vector potential equation ($\phi=A_0$); $c=(\rho c_p)_{\mathrm{eff}}$, $\Gamma=k_{\mathrm{eff}}$, $S_C=q'''_{\mathrm{eddy}}-(q''_{\mathrm{radi}}+q''_{\mathrm{insu}})\delta A/\delta V$, and $S_p=0$ for energy equation ($\phi=T$).

The grid used for this task is a structured trapezoidal mesh. For a typical primary point *P*, the conservation equation in a generalized coordinate system (ξ,η) can be written as,

$$\frac{(rc\phi\mathrm{Ja}-r^0c^0\phi^0\mathrm{Ja}^0)_P\Delta\xi\Delta\eta}{\Delta t}+r\{(\alpha_\xi J_\xi)_e-(\alpha_\xi J_\xi)_w\}\Delta\eta$$
$$+r\{(\alpha_\eta J_\eta)_n-(\alpha_\eta J_\eta)_s\}\Delta\xi=\{r(S_C+S_P\phi)\mathrm{Ja}+rS_\phi\}\Delta\xi\Delta\eta, \tag{33}$$

where the curvature source term S_ϕ arises from the non-orthogonal grid, and is given by $S_\phi=\{(\beta_\xi J_\eta)_e-(\beta_\xi J_\eta)_w\}\Delta\eta+\{(\beta_\eta J_\xi)_n-(\beta_\eta J_\xi)_s\}\Delta\xi$. α_ξ and β_ξ are the primary area and the secondary area over the control-volume face, *e*, which is represented by $\xi=$const. (see Fig. 3(*a*)), e.g., $\vec{J}\cdot\vec{e^\xi}h_\eta=\alpha_\xi J_\xi-\beta_\xi J_\eta$, where $\vec{e^\xi}$ is the contravariant base vector, and h_η is the scale factor. So, $\alpha_\xi=h_\xi h_\eta^2/\mathrm{Ja}$, $\beta_\xi=h_\xi h_\eta^2(\vec{e}_\xi\cdot\vec{e}_\eta)/\mathrm{Ja}$.

The discretization equation for ϕ for the control volume surrounding point *P* can be written as,

$$a_P\phi_P=a_E\phi_E+a_W\phi_W+a_N\phi_N+a_S\phi_S+b, \tag{34}$$

where $a_P=a_E+a_W+a_N+a_S+\{rc\mathrm{Ja}/\Delta t-rS_P\mathrm{Ja}\}\Delta\xi\Delta\eta$, $b=\{r^0c^0\mathrm{Ja}^0/\Delta t\phi_P^0+rS_C\mathrm{Ja}+rS_\phi\}\Delta\xi\Delta\eta$.

The magnetic potential solver is validated by solving the magnetic flux density around a loop, which is supplied with a current, *I*. The theoretical value of the magnetic flux density at the center of a current-carrying loop is $B=\mu_m I/(2R_{\mathrm{coil}})$, where R_{coil} is the radius of the loop [24]. The radius of the loop and the current are chosen as $R_{\mathrm{coil}}=0.02$ m and $I=10A$, respectively, and the radius

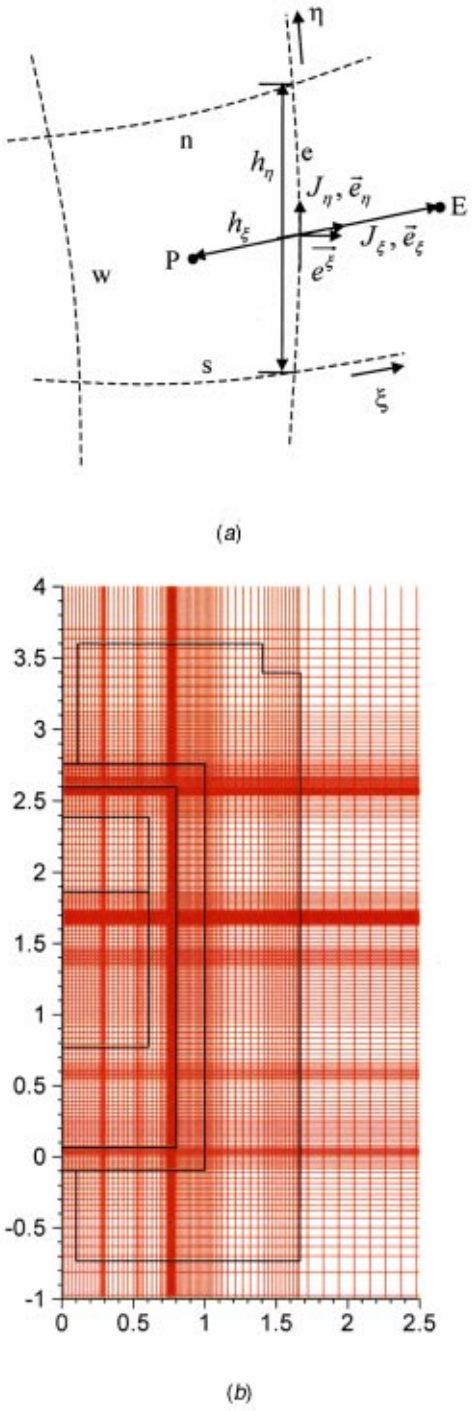

Fig. 3 (*a*) **Curvilinear finite-volume grids; and** (*b*) **computational grids for finite volume method. Grids are highly clustered in the regions of large temperature gradients.**

of the coil is chosen as 10^{-5} m in the calculation. The computed magnetic flux density at the center of the loop is shown in Table 3 using a grid of 57×57. The predicted results agree well with the theoretical ones, and the computational error is within 1 percent (see Table 3).

The grid dependence is also checked by comparing the results using a grid of 198×147 with the ones using a grid of 394 ×292. A 75 mm SiC growth system is considered here and the temperature on the top of the crucible is kept at 2400 K, and the pressure as 26,666 Pa. From Table 4, it can be seen that the computed results of temperature vary within 1 percent while the growth rate varies within 4 percent, since the growth rate is an exponential function of the inverse temperature. Further comparison between the numerical predictions and experimental data can be found in Roy et al. [36] where predicted temperatures agree extremely well with the measured temperatures in the silicon tube growth system.

Table 3 Comparison of present results with theoretical values

	Theory	Grid (57×57)
Magnetic flux density (T)	3.141	3.144

Table 4 Comparison between results in a 75 mm system using different grids

Grid	Power (W)	T_{max} (K)	Growth rate (mm/h)
198x147	7996	3079	1.16
394x292	8057	3082	1.20

A grid of 198×147 is used for the present calculations as shown in Fig. 3(*b*). Since the electrical and thermal conductivities of the graphite susceptor strongly depend on the temperature, the power generated in the graphite susceptor changes significantly with time, so a time step of 2*s* is chosen for transient calculations. The ambient temperature, T_∞, is set as 293 K. The emissivity of graphite material is taken as, $\varepsilon = 0.8$. The radiant exchange between the outer surface of the insulation and the inner surface of the coil has been considered, and the outer surface of the insulation and the inner surface of the coil are assumed diffuse with emissivities of 0.8 and 0.3 for materials of graphite and copper, respectively.

3 Results and Discussions

A 3 in. SiC growth system is considered here with 5 turns of coil and a frequency of 10 kHz. Calculations are performed to examine the effect of transient vis-à-vis steady state conditions in the growth system for a current of 1200 A. The effect of seed surface temperature, temperature difference, $T_{bottom} - T_{top}$ and gas pressure on growth rate is studied for a range of parameters. Finally, the effect of RF heating coil on temperature distribution and growth rate is examined.

3.1 Typical Magnetic Potential and Temperature Distributions. To calculate the electromagnetic field, the computational domain is set sufficiently large, e.g., $-20R_s < z < 20R_s$ and $r < 20R_s$, with the radius of the outer surface of the susceptor $R_s = 0.07$ m. The magnetic potential is always diminished at a far distance of $20R_s$ from the coil. Typical contours of magnetic vector potential for 5 turns of coil, a current of 1200 A and a frequency of 10 kHz are shown in Fig. 4. The contour lines are concentrated along the outer portion of the graphite susceptor, and the contour of $(A_0)_{real} = 1 \times 10^{-5}$ Wb/m bends in the bottom and top portion of the susceptor and passes through the outer portion of the cylindrical susceptor. The graphite susceptor with a high conductivity functions as a shield, so that a large amount of energy is generated by eddy currents in the susceptor within a small skin depth, allowing very little energy generated in the parts inside the susceptor (like the crucible, crystal, and charge).

Figure 5 shows the profiles of the generated heat power in the graphite susceptor and the SiC charge along the radial direction at different heights: $z = 0$, 1.3 R_s and 2.6 R_s. As can be seen, the heat power is mainly generated in the outer portion of the graphite susceptor. The line for $z = 1.3\ R_s$ has a gap (inert gas) between the SiC charge and the susceptor and coincides with the other two in the susceptor. The generated heat power in the SiC charge at $z = 1.3\ R_s$ is negligible compared to that generated in the graphite susceptor at $z = 0$ and 2.6 R_s (Fig. 5). The generated heat in the

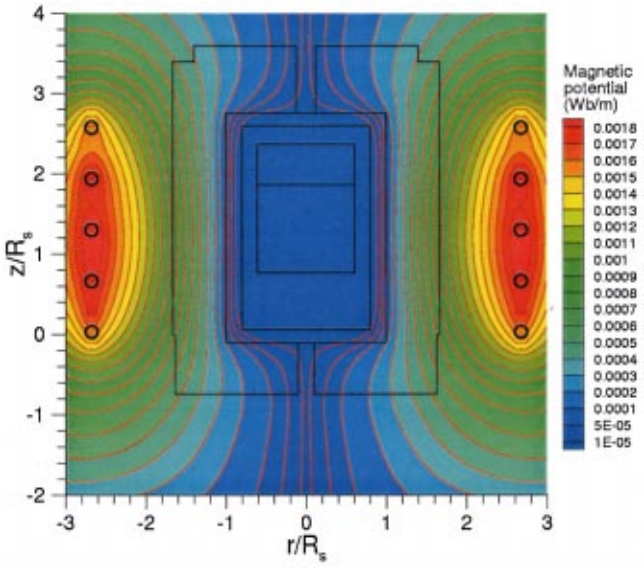

Fig. 4 Contours of magnetic potential, $(A_0)_{real}$, in the growth system for a current of 1200 *A* and a frequency of 10 kHz

graphite susceptor at $z=0$ and 2.6 R_s decreases exponentially in the radial direction from the outer surface of the graphite susceptor to the center of the chamber (Fig. 5).

The temperature distribution is obtained for the same case at a system pressure of 26,666 Pa. As shown in Fig. 6, the maximum temperature exists in the graphite susceptor, and always at the level of the geometric center of the induction coil. In the charge, the temperature is greater in the middle portion near the crucible wall than in the bottom and top regions, and it will sublime there first. The positive temperature difference between the SiC charge and the seed allows the sublimation of SiC in the charge and deposition of SiC on the seed.

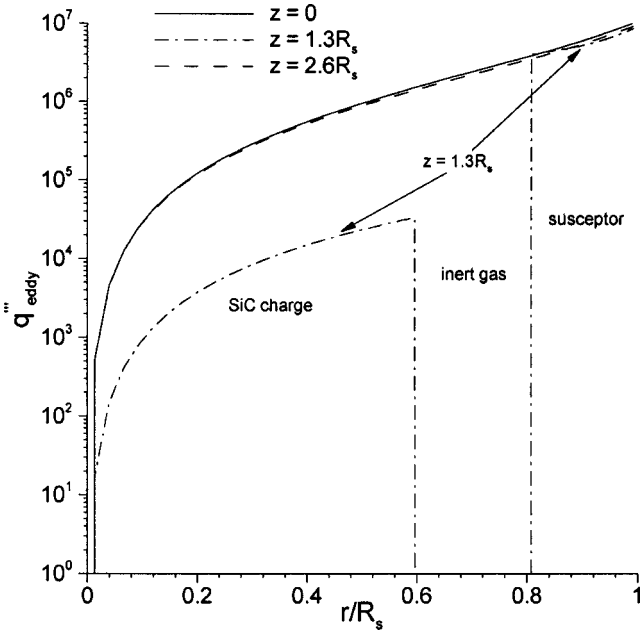

Fig. 5 Generated heat power, q'''_{eddy}, along the radial direction at different heights $z=0$, 1.3 R_s, and 2.6 R_s. The profile at $z=1.3$ R_s has an inert gas gap between the powder charge and the susceptor.

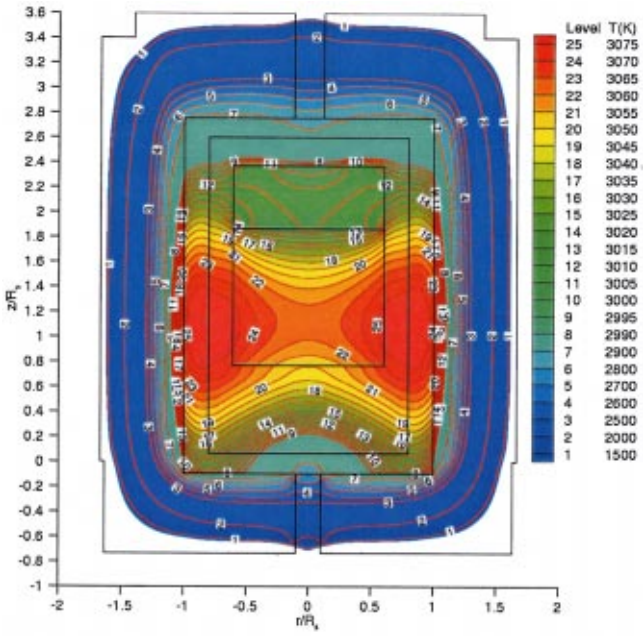

Fig. 6 Temperature distribution for a current of 1200 *A* with argon pressure of 26,666 Pa

A positive radial temperature gradient is also formed at the seed surface, which ensures an outward growth of the crystal [37]. As can be seen in Fig. 6, the temperature has a lower value at the center of the seed because of the cooling effect produced by the top hole. The temperature increases along the radial direction on the seed surface, reaches a high value before the inner wall of the growth chamber. A proper radial temperature gradient at the seed must be achieved to ensure a convex shape of the crystal interface and keep the thermal stresses and consequently the dislocation and micropipe density in the crystal low. The lower temperature at the center of the seed ensures an outward growth in the radial direction, because of higher supersaturation of the vapor species at the center of the seed than that near the edge of the seed. In Fig. 6, the temperature variation along the seed surface is less than 10 K ensuring a low thermal stress in the crystal, while the temperature difference between the charge and the seed is about 80 K to ensure a high growth rate. The temperature variation in the SiC charge (about 60 K) is much higher than that in the upper portion of the growth chamber (about 30 K).

3.2 Transient Heating Process. The temperature ramp up in the growth system is simulated here to investigate the time-dependent behavior of the temperature distribution. The temperature ramp up includes two stages: degassing stage during which the pressure is reduced to vacuum for removing the residual nitrogen contamination in the porous graphite parts, and preheating stage during which the pressure is increased to one atmosphere. The convective heat transfer between the insulation and the quartz is still considered less important than the radiative heat transfer. The initial furnace temperature is set at 293 K. The current is fixed at 1200 A with a frequency of 10 kHz. Figure 7(*a*) shows the temperature profiles along the radial direction at $z=2.3\,R_s$, at times $t=0.5$, 1, 2, 3, 4, and 5 *h*. During the first half hour of heating, the peak temperature increases rapidly, e.g., from 293 K to 1500 K. The degassing stage takes place before temperature reaches 1073–1273 K [5]. After 4 hours of heating, the temperature change becomes minimal.

Figure 7(*b*) shows the temperature profiles along the axial direction at $r=0$, at times $t=0.5$, 1, 2, 3, 4, and 5 *h*. As can be seen from the curve of $t=0.5h$ in Fig. 7(*b*), there is a dip in temperature in the SiC charge indicating that the SiC charge has a large

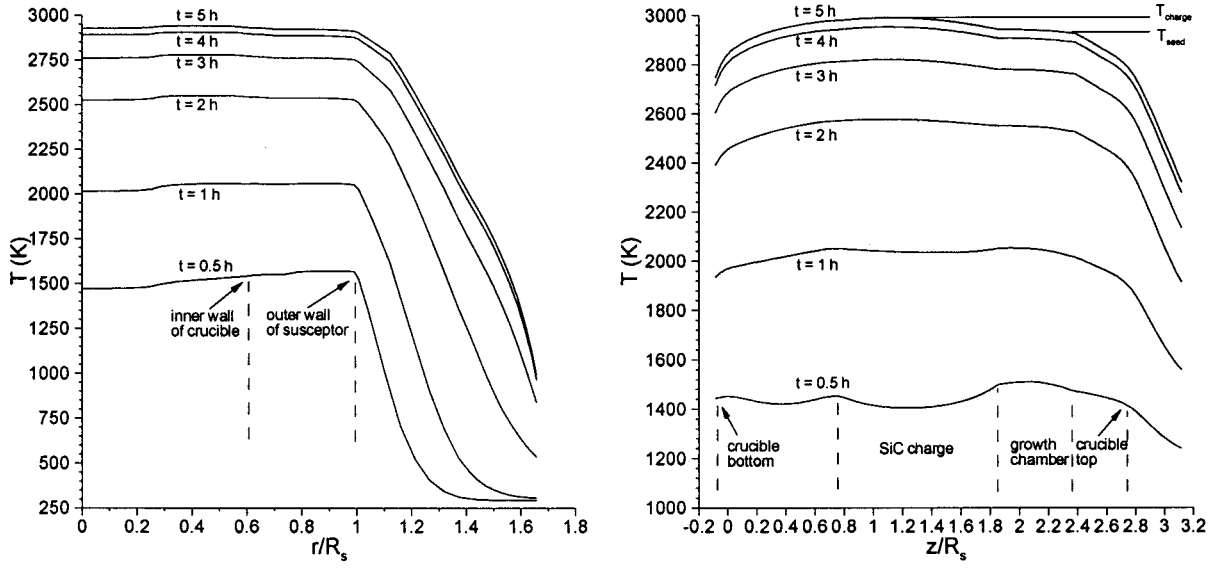

Fig. 7 Temperature profiles along (*a*) radial direction at $z=2.3\ R_s$, and (*b*) axial direction at $r=0$, when $t=0.5$, 1, 2, 3, 4 and 5 *h*. The current is maintained at 1200 *A* with a frequency of 10 kHz and pressure of 10^{-3} Pa for $t<0.5\ h$ and 10^5 Pa for $t>0.5\ h$.

thermal time constant. It takes another hour before the dip in temperature in the SiC charge disappears. Desirable temperature and temperature gradient conditions are achieved at $t=4h$, e.g., the temperature in the SiC charge is larger than that on the seed, $T_{\text{charge}}>T_{\text{seed}}$.

The evolution of the temperature in the SiC charge, T_{charge}, temperature on the seed, T_{seed}, and temperature on the bottom of the crucible, T_{bottom}, with time is shown in Fig. 8. The temperature difference between the SiC charge and the seed is not discernable before the temperature in the SiC charge reaches 1500 K in the degassing stage, and it gradually increases with time in the preheating stage. The temperatures stabilize after 4 hours of heating. The growth stage begins after the temperatures and temperature gradients stabilize [5]. In the growth stage, the growth rate and quality of the grown crystal are related to the temperature on the seed, T_{seed}, the temperature in the SiC charge, T_{charge}, and the inert gas pressure. This preconditioning of system is critical for the growth of SiC crystals.

3.3 Effect of Inert Gas Pressure on the Growth Rate. The predicted growth rate along the seed surface for the case of $I=1200$ A is shown in Fig. 9 for a better understanding of the role of the growth temperature and inert gas pressure. As can be seen, the growth rate increases when the inert gas pressure is reduced from 53,333 Pa to 26,666 Pa. The growth rate decreases along the

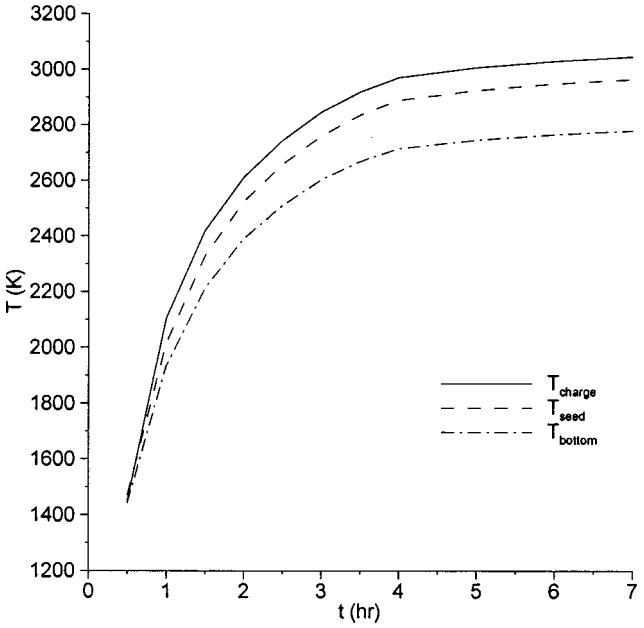

Fig. 8 Evolution of temperatures of the charge and the seed and T_{bottom} with time during the heating process as in Fig. 7

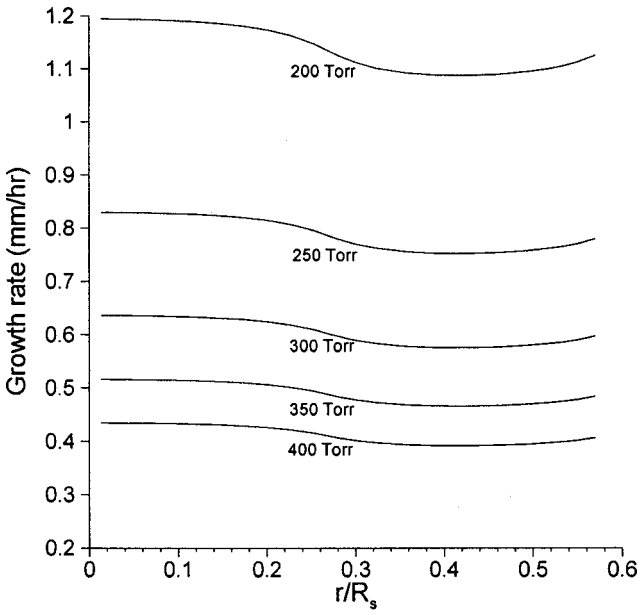

Fig. 9 Predicted growth rate along the seed surface for different inert gas pressures for the conditions as in Fig. 6

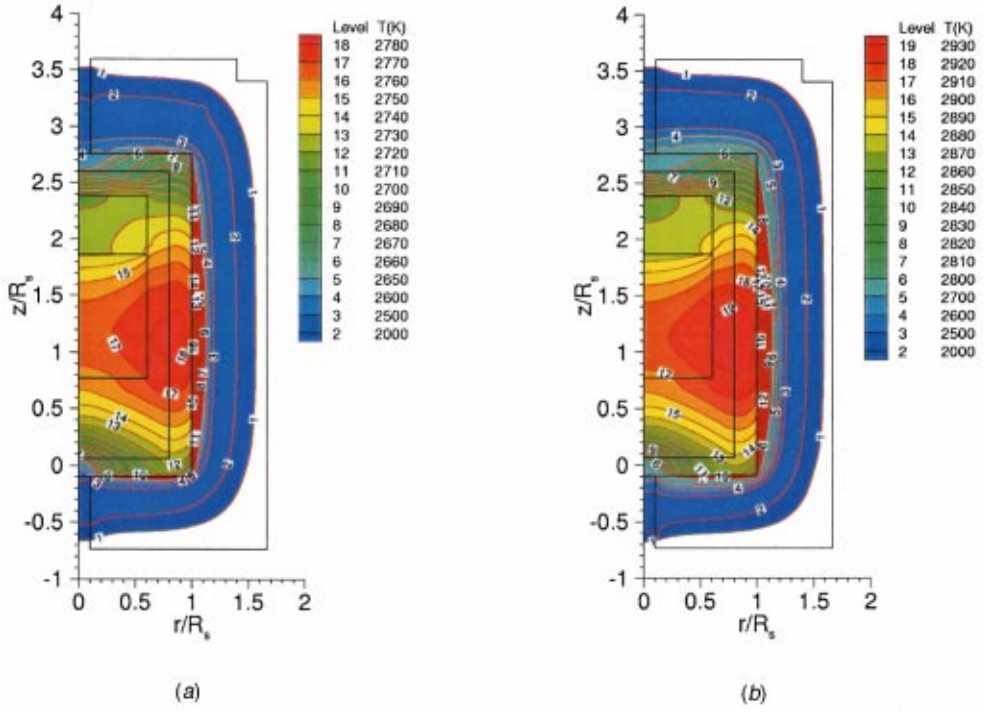

Fig. 10 Temperature distributions for different currents, (*a*) *I*=1000 *A*, and (*b*) *I*=1100 *A*

radial direction to ensure an outward growth, while the growth temperature along the seed surface increases. It is evident from Figs. 6 and 9 that a lower growth temperature at the seed surface ensures a higher growth rate for a constant charge temperature.

3.4 Effect of Temperature on the Growth Rate. Calculations have been performed to obtain temperature distribution for several values of current, e.g., 1000 A, 1100 A and 1200 A. Figure 10 shows the temperature distributions for currents of 1000 A and 1100 A with 26,666 Pa argon pressure. The temperature differences between the charge and the seed, $T_{\text{charge}}-T_{\text{seed}}$, are about 66 K, 72 K and 81 K, and T_{seed} are 2712 K, 2858 K, and 2995 K for $I=1000$ A, 1100 A and 1200 A, respectively. The magnitude of the temperature at any given location increases with the current. As reported by Tairov and Tsvetkov [9], a high temperature, between 2900 and 3000 K, is required for crystal growth by the Lely's method. However, the growth temperature for the modified Lely method ranges from 1800 K to 2900 K. The growth temperature depends on the temperature gradient that is related to the design of the system. For systems with large temperature gradients, the growth temperatures are lower, 2100–2800 K [4,5,8,9,15,16,17], while the growth temperature ranges from 2700 K to 2900 K for system that have a small temperature gradient [2,3]. The temperature distribution for the case of $I=1200$ A corresponds to an upper limit for the given coil position and other components of the system. For a low growth temperature, the required inert gas pressure is lower than that required for the high temperature growth, and the temperature gradient is larger [19,20]. The temperature gradient inside the growth chamber is determined by the hotzone design and coil position.

The predicted growth rate versus the inverse of temperature on the seed, T_{seed}, and the inverse of temperature on the bottom of the crucible, T_{bottom}, is shown in Fig. 11 for a system pressure of 26,666 Pa together with the experimental data of Balkas et al. [38]. The growth rate curve has an Arrhenius-type dependence on T_{seed} and T_{bottom}. Since it is very difficult to measure the temperatures inside the crucible, the temperatures on top of the crucible or on the bottom are measured by using two pyrometers through the holes bored into the insulation. The experimental data by Balkas et al. [38] indicate that the growth rate is a linear function of ΔT and exponential function of the inverse temperature, and have the following expression,

$$Gr=A(p,S,t)\Delta T\exp(-U/RT), \tag{35}$$

where ΔT is the temperature difference between the seed and source, U is the activation energy, $A(p,S,t)$ is a constant defined

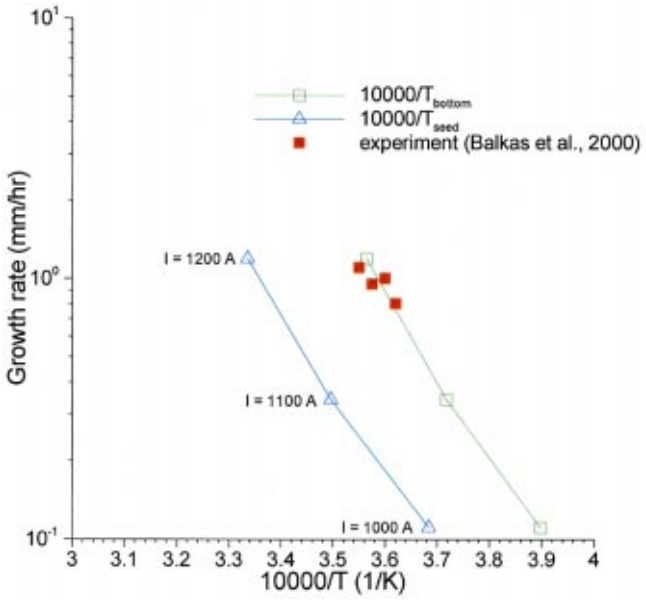

Fig. 11 Dependence of the growth rate on the temperature of the seed surface, T_{seed}, and the temperature on the bottom of the crucible, T_{bottom}. The symbols from top to bottom correspond to the currents of 1200 *A*, 1100 *A* and 1000 *A*, respectively, with argon pressure of 26,666 Pa.

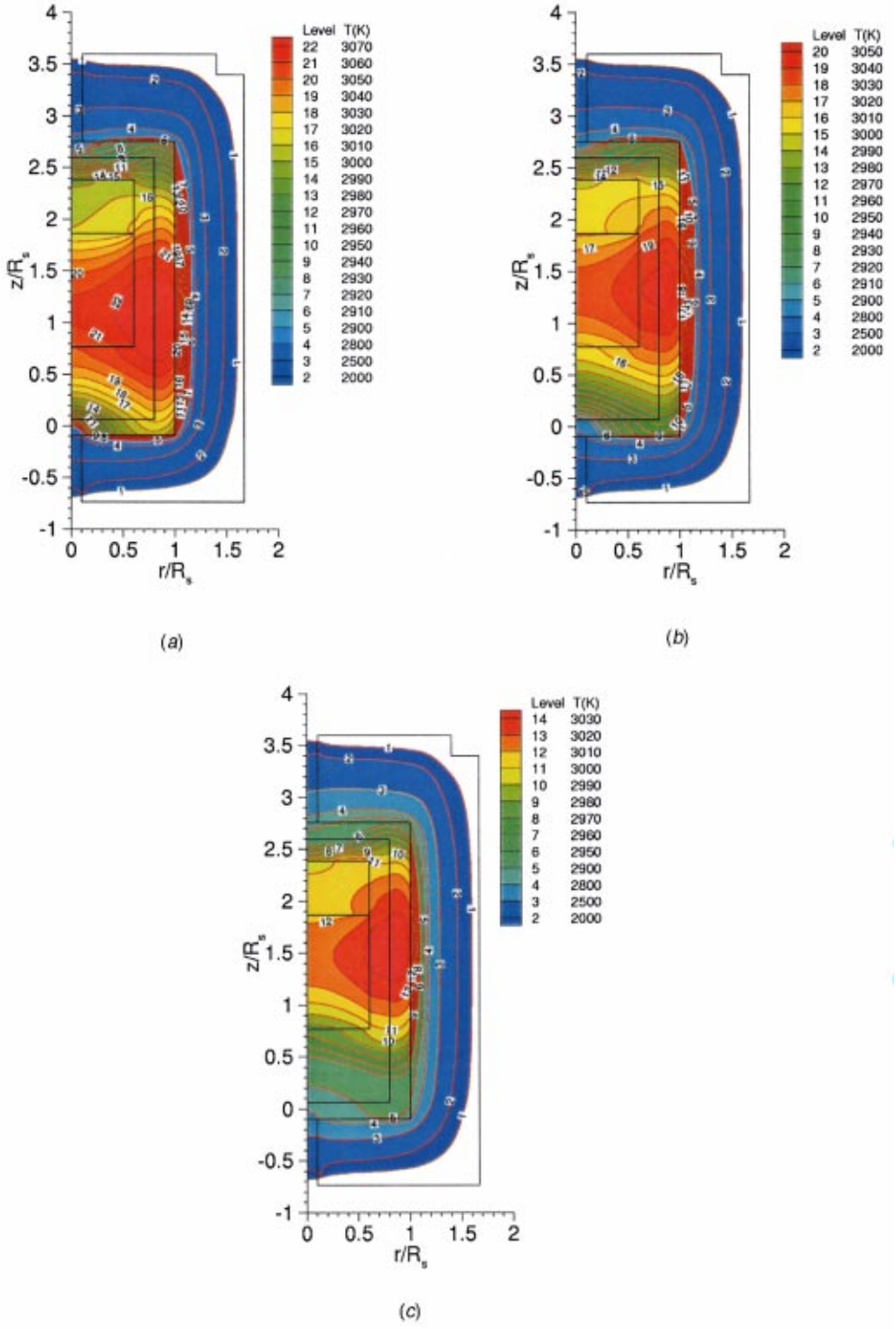

Fig. 12 Temperature distributions for different coil positions. The coil is moved upward (*a*) $z_{coil}=0$, (*b*) 0.01 m, and (*c*) 0.02 m, respectively. The coil position in (*a*) is the same as that in Fig. 6. The temperature on top of the crucible is kept at 2400 K for all the cases.

by the inert gas pressure p, the effective source surface area S and the duration of the growth run t. The temperature difference between the SiC charge and the seed, $T_{charge}-T_{seed}$, can be adjusted by moving the RF coil downward or upward.

3.5 Effect of Coil Position on Temperature Distribution and Growth Rate Profile. By moving the induction coil vertically (upward or downward), the temperature difference between the charge and the seed can be easily changed. Figure 12 presents the temperature distributions for three different positions ($z_{coil}=0$,0.01 m,0.02 m), while the temperature on top of the crucible is kept constant at 2400 K. A PID (proportional, integral and derivative) control strategy is used numerically to keep the temperature on the top of the crucible constant by changing the current. With the coil moved up, the location of the maximum temperature

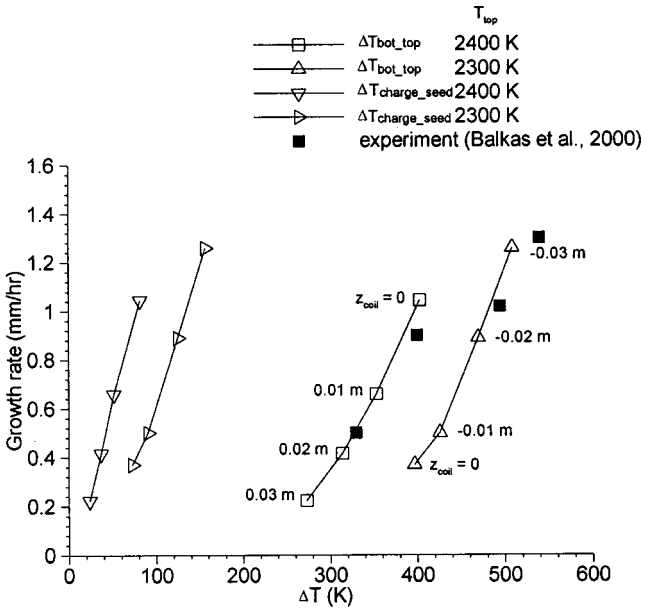

Fig. 13 Dependence of growth rate, G_{SiC}, on the temperature difference between the charge and seed, $T_{charge}-T_{seed}$, and on the temperature difference between the bottom and top of the crucible, $T_{bottom}-T_{top}$. The coil positions, z_{coil}, are denoted besides the symbols on the curve of $G_{SiC}\sim T_{bottom}-T_{top}$. The temperature on top of the crucible, T_{top}, is kept at 2400 K or 2300 K with argon pressure of 26,666 Pa.

in the charge moves up and the temperature difference between the charge and the seed decreases. In Fig. 12(*a–c*), the temperature difference between the charge and the seed, $T_{charge}-T_{seed}$, is a linear function of the coil position, z_{coil}. It should be noted that the temperature difference will not be a linear function of the coil position if the coil is moved further up. Since the growth rate depends on the temperature difference between the charge and the seed (Eq. 35), the change in the coil position significantly affects the growth rate, and can be used for control of the growth process.

The predicted growth rate versus temperature difference between the charge and the seed is shown in Fig. 13 for different coil positions when the temperature on the top of the crucible, T_{top}, is kept constant, e.g., 2400 K or 2300 K, and the pressure is maintained at 26,666 Pa. In a certain range of coil position, z_{coil}, the growth rate is almost a linear function of the coil position, z_{coil}. For example, for $T_{top}=2400$ K, the growth rate is a linear function for $0<z_{coil}<0.03$ m; while for $T_{top}=2300$ K, it is true for $-0.03\ \text{m}<z_{coil}<0$. If the coil is moved further up, the growth rate can become less than zero representing etching of the seed (not shown here).

4 Conclusions

A comprehensive process model for silicon carbide growth by modified Lely method has been developed that accounts for irregular geometry, induction heating, radiative and conductive heat transfer, and growth kinetics. The model has been successfully applied to the simulation of SiC growth. The radiant exchange between the outer surface of the insulation and the inner surface of the coil is considered. Also, the radiations inside the growth chamber, the top and bottom holes as well as in the SiC charge are modeled. The growth kinetics is incorporated to predict the growth rate that is a strong function of temperature, temperature gradient and inert gas pressure.

The temperature distribution and growth rate are predicted for a 75 mm growth system. The complex dependence of temperature distribution and growth rate on RF coil current and its position are well demonstrated by the numerical results. The growth rate has an Arrhenius-type dependence on the growth interface temperature. The temperature distribution changes significantly when the coil position changes. The portion of the charge with a maximum temperature moves up when the coil is lifted. The lower coil position corresponds to a high temperature difference between the charge and the seed, and hence a high growth rate. The computed temperature distributions and growth rate profiles provide valuable insights into the physical mechanisms of the SiC growth.

Acknowledgments

This research is sponsored by BMDO/IST and managed by ONR, N00014-98-C-0176 and by NSF award, CTS-9876198 for the second author. Acknowledgements are also due to M.H.N. Naraghi of the Department of Mechanical Engineering at Manhattan College for his help in modeling of radiative heat transfer.

Nomenclature

A_{SiC} = growth area (m^2)
$\mathbf{A}$ = magnetic vector potential (Wb/m)
$\mathbf{B}$ = magnetic flux density (T)
c_p = isobaric specific heat (J/kg·K)
d_p = mean particle diameter of the charge (m)
D_c = diameter of crucible (m)
f = frequency (Hz)
F = view factor
g = gravitational acceleration, (m/s^2)
Gr = Grashof number, $\rho^2 g\beta R^3\Delta T/\mu^2$
G_{SiC} = growth rate (m/s), dissolving rate of particles (m/s)
ΔG_T^0 = isobaric-isothermal Gibbs-function
$\Delta h_{f,298}^0$ = heat of formation
H = latent heat (J/kg)
I = current (A)
$\mathbf{J}$ = current density (A/m^2)
k = thermal conductivity, (W/m·K)
K = equilibrium constant
L = gap between the charge and seed (m)
M = molecular weight (kg/mol)
p = pressure (Pa)
Pr = Prandtl number, $\mu c_p/k$
q = heat flux (W/m^2)
q'''_{eddy} = heat power by eddy current (W/m^3)
q''_{rad} = radiative heat flux (W/m^2)
r = radial coordinate (m)
R = universal gas constant, 8.314 (J/mol·K)
R_s = radius of susceptor (m)
t = time (s)
T = temperature (K)
ΔT = temperature difference between the powder charge and seed (K)
z = axial coordinate (m)

Greek Symbols

α = absorptivity, sticking coefficient
β = volumetric expansion coefficient (1/K)
ε = emissivity
ε_m = permittivity (F/m)
ε_p = porosity
μ = viscosity (kg/m·s)
μ_m = magnetic permeability, $4\pi\times10^{-7}$ (H/m)
ρ = density (kg/m^3)
ρ_c = density of crystal (kg/m^3)
σ_c = electrical conductivity ($1/\Omega\cdot m$)
σ = Stefan-Boltzmann constant 5.670×10^{-8} ($W/m^2\cdot K^4$)
ω = angular frequency (rad/s)

Subscripts

∞ = ambient
coil = induction coil

eddy = eddy currents
eff = effective
insu = insulation material
radi = radiative
real = real part of a complex quantity
s = solid
Ste = Stefan flow related
θ = angular direction

References

[1] Glass, R. C., Henshall, D., Tsvetkov, V. F., and Carter, C. H., Jr., 1997, ''SiC Seeded Crystal Growth,'' Phys. Status Solidi B, **202**, pp. 149–162.
[2] Pons, M., Blanquet, E., Dedulle, J. M., Garcon, I., Madar, R., and Bernard, C., 1996, ''Thermodynamic Heat Transfer and Mass Transport Modeling of the Sublimation Growth of Silicon Carbide Crystals,'' J. Electrochem. Soc., **143**, No. 11, pp. 3727–3735.
[3] Pons, M., Blanquet, E., Dedulle, J. M., Madar, R., and Bernard, C., 1997, ''Different Macroscopic Approaches to the Modeling of the Sublimation Growth of SiC Single Crystals,'' Mater. Sci. Eng., B, **46**, pp. 308–312.
[4] Barrett, D. L., Seidensticker, R. G., Gaida, W., Hopkins, R. H., and Choyke, W. J., 1991, ''SiC Boule Growth by Sublimation Vapor Transport,'' J. Cryst. Growth, **109**, pp. 17–23.
[5] Barrett, D. L., McHugh, J. P., Hobgood, H. M., Hopkins, R. H., McMullin, P. G., and Clarke, R. C., 1993, ''Growth of Large SiC Single Crystals,'' J. Cryst. Growth, **128**, pp. 358–362.
[6] Sasaki, M., Nishio, Y., Nishina, S., Nakashima, S., and Harima, H., 1998, ''Defect Formation Mechanism of Bulk SiC,'' Mater. Sci. Forum, **264–268**, pp. 41–44.
[7] Lilov, S. K., 1993, ''Study of the Equilibrium Processes in the Gas Phase During Silicon Carbide Sublimation,'' Mater. Sci. Eng., B, **21**, pp. 65–69.
[8] Tairov, Yu., M., and Tsvetkov, V. F., 1978, ''Investigation of Growth Processes of Ingots of Silicon Carbide Single Crystals,'' J. Cryst. Growth, **43**, pp. 209–212.
[9] Tairov, Yu., M., and Tsvetkov, V. F., 1981, ''General Principles of Growing Large-Size Single Crystals of Various Silicon Carbide Polytypes,'' J. Cryst. Growth, **52**, pp. 146–150.
[10] Hobgood, H. M., Barrett, D. L., McHugh, J. P., Clarke, R. C., Sriram, S., Burk, A. A., Greggi, J., Brandt, C. D., Hopkins, R. H., and Choyke, W. J., 1994, ''Large Diameter 6H-SiC for Microwave Device Applications,'' J. Cryst. Growth, **137**, pp. 181–186.
[11] Augustine, G., Hobgood, H., Balakrishna, V., Dunne, G., and Hopkins, R. H., 1997, ''Physical Vapor Transport Growth and Properties of SiC Monocrystals of 4H Polytype,'' Phys. Status Solidi B, **202**, pp. 137–148.
[12] Tsvetkov, V., Glass, R., Henshall, D., Asbury, D., and Carter, C. H., Jr., 1998, ''SiC Seeded Boule Growth,'' Mater. Sci. Forum, **264–268**, pp. 3–8.
[13] Powell, A. R., Wang, S., Fechko, G., and Brandes, G. R., 1998, ''Sublimation Growth of 50 mm Diameter SiC Wafers,'' Mater. Sci. Forum, **264–268**, pp. 13–16.
[14] Dhanraj, G., Huang, X. R., Dudley, M., Prasad, V., and Ma, R.-H., 2001, ''Silicon Carbide Crystals: Part I–Growth and Characterization,'' *Crystal Growth for Modern Technology*, K. Byrappa and T. Ohachi, eds., William Andrew/Noyes Publications, NJ (in press).
[15] Hofmann, D., Heinze, M., Winnacker, A., Durst, F., Kadinski, L., Kaufmann, P., Makarov, Y., Schäfer, M., 1995, ''On the Sublimation Growth of SiC Bulk Crystals: Development of a Numerical Process Model,'' J. Cryst. Growth, **146**, pp. 214–219.
[16] Hofmann, D., Eckstein, R., Kölbl, M., Makarov, Y., Müller, St. G., Schmitt, E., Winnacker, A., Rupp, R., Stein, R., and Völkl, J., 1997, ''SiC-bulk growth by Physical-Vapor Transport and Its Global Modeling,'' J. Cryst. Growth, **174**, pp. 669–674.
[17] Müller, S. G., Eckstein, R., Hofmann, D., Kadinski, L., Kaufmann, P., Kölbl, M., and Schmitt, E., 1998, ''Modeling of the PVT-SiC Bulk Growth Process Taking into Account Global Heat Transfer, Mass Transport and Heat of Crystallization and Results on its Experimental Verification,'' Mater. Sci. Forum, **264–268**, pp. 57–60.
[18] Ma, R.-H., Chen, Q.-S., Zhang, H., Prasad, V., Balkas, C. M., and Yushin, N. K., 2000, ''Modeling of Silicon Carbide Crystal Growth by Physical Vapor Transport Method,'' J. Cryst. Growth, **211**, pp. 352–359.
[19] Chen, Q.-S., Zhang, H., Prasad, V., Balkas, C. M., Yushin, N. K., and Wang, S., 2001, ''Kinetics and Modeling of Sublimation Growth of Silicon Carbide Bulk Crystal,'' J. Cryst. Growth, **224**, pp. 101–110.
[20] Chen, Q.-S., Prasad, V. Zhang, H., and Dudley, M., 2001, ''Silicon Carbide Crystals: Part II—Process Physics and Modeling,'' *Crystal Growth for Modern Technology*, K. Byrappa and T. Ohachi, eds., William Andrew/Noyes Publications, NJ, (in press).
[21] Kaldis, E., and Piechotka, M., 1994, ''Bulk Crystal Growth by Physical Vapor Transport,'' Handbook of Crystal Growth, Vol. 2, D. T. J. Hurle, ed., pp. 615–658.
[22] Chen, Q.-S., Prasad, V., and Chatterjee, A., 1999, ''Modeling of Fluid Flow and Heat Transfer in a Hydrothermal Crystal Growth System: Use of Fluid-Superposed Porous Layer Theory,'' J. Heat Transfer , **121**, pp. 1049–1058.
[23] Chen, Q.-S., Zhang, H., Prasad, V., Balkas, C. M., and Yushin, N. K., 1999, ''A System Model for Silicon Carbide Crystal Growth by Physical Vapor Transport Method,'' ASME Proc. 33rd National Heat Transfer Conference, HTD, NHTC99-222.
[24] Kraus, J. D., and Carver, K. R., 1973, *Electromagnetics*, McGraw-Hill, New York.
[25] Bíró, O., and Preis, K., 1989, ''On the Use of the Magnetic Vector Potential in the Finite Element Analysis of Three-Dimensional Eddy Currents,'' IEEE Trans. Magn., **25**, pp. 3145–3159.
[26] Selder, M., Kadinski, L., Makarov, Yu., Durst, F., Wellmann, P., Straubinger, T., Hofmann, D., Karpov, S., and Ramm, M., 2000, ''Global Numerical Simulation of Heat and Mass Transfer for SiC Bulk Crystal Growth by PVT,'' J. Cryst. Growth, **211**, pp. 333–338.
[27] Naraghi, M. H. N., and Chung, B. T. F., 1984, ''A Stochastic Approach for Analysis of Radiative Heat Transfer in Enclosures with Non-Participating Media,'' J. Heat Transfer , **106**, pp. 690–698.
[28] Nunes, E. M., and Naraghi, M. H. N., 1998, ''Numerical Model for Radiative Heat Transfer Analysis in Arbitrarily Shaped Axisymmetric Enclosures with Gaseous Media,'' Numer. Heat Transfer, Part A, **33**, pp. 495–513.
[29] Zhang, H., Prasad, V., and Moallemi, M. K., 1996, ''Numerical Algorithm Using Multizone Adaptive Grid Generation for Multiphase Transport Processes with Moving and Free Boundaries,'' Numer. Heat Transfer, Part B, **29**, pp. 399–421.
[30] Zhang, H., and Prasad, V., 1997, ''An Advanced Numerical Scheme for Materials Process Modeling,'' Computer Modeling and Simulation in Engineering, **2**, pp. 322–343.
[31] Modest, M. F., 1988, ''Radiative Shape Factors between Differential Ring Elements on Concentric Axisymmetric Bodies,'' J. Thermophys. Heat Transfer, **2**, pp. 86–88.
[32] Siegel, R., and Howell, J. R., 1992, *Thermal Radiation Heat Transfer*, Hemisphere Publishing, Bristol, PA.
[33] Drowart, J., and De Maria, G., 1960, *Silicon Carbide*, Pergamon, Oxford, p. 16.
[34] Kaneko, T., 1993, ''Growth Kinetics of Vapor-grown SiC,'' J. Cryst. Growth, **128**, pp. 354–357.
[35] Kansa, E. J., Perlee, H. E., and Chaiken, R. F., 1977, ''Mathematical Model of Wood Pyrolysis Including Internal Forced Convection,'' Combust. Flame, **29**, pp. 311–324.
[36] Roy, A., Mackintosh, B., Kalejs, J. P., Chen, Q.-S., Zhang, H., and Prasad, V., 2000, ''A Numerical Model for Inductively Heated Cylindrical Silicon Tube Growth System,'' J. Cryst. Growth, **211**, pp. 365–371.
[37] Anikin, M., and Madar, R., 1997, ''Temperature Gradient Controlled SiC Crystal Growth,'' Mater. Sci. Eng., **B46**, pp. 278–286.
[38] Balkas, C. M., Maltsev, A. A., Roth, M. D., and Yushin, N. K., 2000, ''Role of Temperature Gradient in Bulk Crystal Growth,'' Mater. Sci. Forum, **338–342**, pp. 79–82.

Melting and Resolidification of a Substrate Caused by Molten Microdroplet Impact

D. Attinger[1]

D. Poulikakos
Fellow ASME
e-mail: Poulikakos@ltnt.iet.mavt.ethz.ch

Laboratory of Thermodynamics in Emerging Technologies,
Institute of Energy Technology,
Swiss Federal Institute of Technology (ETH),
8092 Zurich, Switzerland

This paper describes the main features and results of a numerical investigation of molten microdroplet impact and solidification on a colder flat substrate of the same material that melts due to the energy input from the impacting molten material. The numerical model is based on the axisymmetric Lagrangian Finite-Element formulation of the Navier–Stokes, energy and material transport equations. The model accounts for a host of complex thermofluidic phenomena, exemplified by surface tension effects and heat transfer with solidification in a severely deforming domain. The dependence of the molten volume on time is determined and discussed. The influence of the thermal and hydrodynamic initial conditions on the amount of substrate melting is discussed for a range of superheat, Biot number, and impact velocity. Multidimensional and convective heat transfer effects, as well as material mixing between the droplet and the substrate are found and quantified and the underlying physics is discussed. Good agreement in the main features of the maximum melting depth boundary between the present numerical results and published experiments of other investigators for larger (mm-size) droplets was obtained, and a complex mechanism was identified, showing the influence of the droplet fluid dynamics on the substrate melting and re-solidification. [DOI: 10.1115/1.1391274]

Keywords: Droplet, Manufacturing, Microstructures, Phase Change, Surface Tension

Introduction

The fluid and heat flow phenomena occurring during the impact of a molten droplet on a flat substrate of identical material that initially melts due to the energy transfer from the droplet and then resolidifies are complex. Droplet spreading is a free surface problem with large deformations in the presence of surface tension. The associated transient heat transfer and solidification processes involve convection in a deforming domain, complex fluid flow exemplified by the multidimensional motion of the phase change interface and the dynamics of the liquid phase, as well as conduction in the substrate [1,2]. In applications that will be discussed subsequently, controlled substrate melting and resolidification are desired for improved bonding purposes. This gives rise to additional interesting phenomena.

Understanding and optimizing the substrate *melting* due to the heat released by the impacting molten droplet (a phenomenon sometimes called *remelting* in the literature, assuming implicitly that the substrate is produced by previously solidified drops) is important for novel manufacturing technologies like microcasting [3] and net-form manufacturing [4]. These techniques aim at building metallic parts of a typical size of the order of 1 to 100 millimeters by targeted deposition of drops on top of each other, with a droplet size ranging from 100 μm to a few millimeters. Samples built with aluminum [4] or steel and copper [5] droplets show promise for novel cast-free and versatile manufacturing processes. The amount of remelting is a key parameter for these processes: on the one hand, in case of insufficient remelting, the quality of the material can suffer from a poor adhesion between the drops; on the other hand, in case of too much remelting, the shape of the material can be inaccurate, because a thin liquid layer is formed and remains on the top of the substrate [4].

Driven by the importance of these manufacturing technologies, some aspects of the physics involved in the substrate melting problem have been examined experimentally, analytically as well as numerically. Experimental investigations of substrate melting involving millimeter- and in particular micrometer-size droplets are quite challenging, due to the very fast fluid flow and thermal transients as well as the small length scales involved. In addition, since the materials of interest are non-transparent metals, it has been to the best of our knowledge not possible to date to investigate experimentally neither the flow inside the deforming molten region nor the phase change interface motion. Accordingly, experimental studies have been performed with rather larger millimeter-size droplets, focusing on specific aspects like heat transfer between the drop and the substrate [6], shape of solidified splats [7], maximum substrate melting depth through cross-sectioning and polishing [3,8].

Up to now, all the theoretical studies on substrate melting have either neglected or drastically simplified the fluid dynamics in the droplet without accurate justification and in order to (understandably) provide mathematical tractability. This is an approach that is certainly an acceptable first step toward understanding a complex problem.

Madejski [7] produced the first analytical model taking simultaneously strongly simplified fluid dynamics and solidification into account (without substrate melting). He assumed a simple solution for the fluid dynamics (satisfying the continuity equation), and introduced in an ad-hoc manner surface tension and viscous effects through an energy balance between the initial and final stages of the impact. He considered only conduction heat transfer. Rangel and Bian [9] added substrate melting to Madejski's approach and used a better analytical model for the fluid flow, satisfying the shear-free condition at the free surface of the liquid. They did not consider thermal contact resistance between the splat and the substrate and neglected radial conduction in the thermal energy equation.

Wang et al. [10] proposed operational maps for the melting of a substrate suddenly brought in contact with a thin layer of solidified metal experiencing no motion, focusing therefore on the solidification aspect of the problem. This situation could be comparable to substrate melting caused by drop impact, assuming that

[1]Present Address: Seyonic SA, Puits-Godet 12, 2000 Neuchâtel, Switzerland.

Contributed by the Heat Transfer Division for publication in the JOURNAL OF HEAT TRANSFER. Manuscript received by the Heat Transfer Division November 9, 2000; revision received March 20, 2001. Associate Editor: D. Zumbrunnen.

the fluid dynamics time scale is much smaller than the solidification time scales [11], which can be justifiable but only for a certain range of initial conditions [7,12–14]. The model of Wang et al. [10] simulates phase change under non-equilibrium conditions, assuming a constant heat transfer coefficient between the substrate and the splat before, during and after substrate melting (this coefficient accounts for the imperfect heat transfer between both the drop and the substrate and was studied extensively in [6]). Wang et al. [10] produced substrate melting maps identifying whether substrate melting occurs, and quantified the melting depth as a function of the superheat parameter SHP and the Biot number Bi for a given pair of materials.

At least two publications have reported comparisons between simulations and experiments, in which the substrate melting depth was evidenced by cross-sections. First, Kang et al. [8] studied the impact of a 3 mm droplet on top of a previously solidified one, at a velocity of 2.1 m/s. Their one-dimensional solidification model (with two-dimensional substrate conduction) was shown to provide a reasonable agreement with experiments with eutectic tin-lead solder, at least in the region near the center of symmetry. Observing that the occurrence of substrate melting depended on the radial location, they concluded that consideration of the radial heat conduction in the splat was important for a better modeling of substrate melting. Second, Zarzalejo et al. [3] performed experiments and calculations for steel droplets on steel, and concluded that convection heat transfer cannot be neglected for modeling the substrate melting, even in the case of large droplets.

The aim of the model presented in this paper is to take into account accurately the complex fluid flow phenomena of the substrate melting problem, in order to examine qualitatively and quantitatively their importance on the substrate melting phenomenon, particularly by considering the associated convection and free-surface driven flow. The starting point of this study is a model for droplet impact involving the full Navier–Stokes equations with free surface modeling, convective heat transfer and solidification ([15] and references therein). In this paper the model is extended to account for substrate melting and resolidification, with consideration of the interfacial contact resistance and the mixing of substrate and droplet masses. In addition, a more efficient grid generation algorithm is utilised. Detailed results are presented for the impact of microdroplets ($O(100)$ μm diameter) of eutectic tin-lead solder on a substrate of the same material, for they relate directly to net shape manufacturing by *printing* of liquid metal microdroplets. This technology constitutes a focal point of our research activities [15–18]. Numerical results are compared to existing experiments of other investigators with larger steel droplets [3].

Numerical Model

Fluid Dynamics. A mathematical model is formulated to simulate the impact of an initially spherical molten droplet on a flat substrate beginning at the instant of contact. It is based on the Navier–Stokes equations applied to an axisymmetric coordinate system shown in Fig. 1, where R, Z, and θ are the radial, axial and azimuthal dimensionless coordinates. Constant thermophysical properties are assumed for the fluid. Property variations are not important in our parametric domain. In addition, the utilization of constant properties allows the generalization of the results. The exact variation of the viscosity when the temperature approaches the melting point is not known, but is a local phenomenon at the freezing front and is not expected to affect the flow results, which are driven by the free surface and impact velocities. The governing equations are written using a Lagrangian approach [19,20], allowing an accurate tracking of the free surface. Nondimensionalization is performed with respect to the droplet initial diameter d_0, the impact velocity v_0, the liquid density ρ_l, and the initial pressure in the drop p_0. As described in [15], the dimensionless forms of the mass conservation equation and the R- and Z-momentum equations are

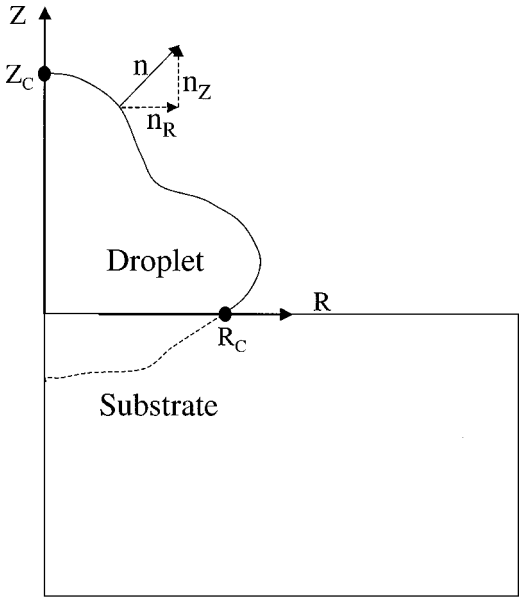

Fig. 1 Schematic of the problem of interest showing axisymmetric droplet coordinate definition and melted domain (dashed line)

$$\frac{\partial P}{\partial \tau}+\frac{1}{M^2}\left(\frac{1}{R}\frac{\partial}{\partial R}(RU)+\frac{\partial V}{\partial Z}\right)=0 \tag{1}$$

$$\frac{\partial U}{\partial \tau}-\frac{1}{R}\frac{\partial}{\partial R}(R\bar{\sigma}_{RR})-\frac{\partial \bar{\sigma}_{RZ}}{\partial Z}+\frac{\bar{\sigma}_{\theta\theta}}{R}=0 \tag{2}$$

$$\frac{\partial V}{\partial \tau}-\frac{1}{R}\frac{\partial}{\partial R}(R\bar{\sigma}_{RZ})-\frac{\partial \bar{\sigma}_{ZZ}}{\partial Z}-\frac{1}{\mathrm{Fr}}=0, \tag{3}$$

where M and Fr denote the Mach and Froude numbers, respectively. The stress components $\bar{\sigma}_{ij}$ have the usual definition for axisymmetric modeling [21] and have been cast in dimensionless form [15]. The Lagrangian velocities are given by

$$U=\frac{\partial R}{\partial \tau} \tag{4}$$

$$V=\frac{\partial Z}{\partial \tau}. \tag{5}$$

The initial and boundary conditions have the following form:

$$U=0,\ V=-1,\ P=\frac{4}{\mathrm{We}};\quad \tau=0 \tag{6}$$

$$U=0,\ \frac{\partial V}{\partial R}=0;\quad R=0 \tag{7}$$

$$U=V=0,\quad \text{phase change surface} \tag{8}$$

$$\bar{\sigma}_{RR}n_R+\bar{\sigma}_{RZ}n_Z=-2\frac{\bar{H}}{\mathrm{We}}n_R,\quad \text{free surface} \tag{9}$$

$$\bar{\sigma}_{RZ}n_r+\bar{\sigma}_{ZZ}n_Z=-2\frac{\bar{H}}{\mathrm{We}}n_Z,\quad \text{free surface,} \tag{10}$$

where n_R and n_Z are the radial and axial components of the outward unit normal to the surface (see Fig. 1), and $\bar{H}$ the dimensionless mean curvature of the free surface. Due to lack of experimental data on dynamic wetting, the wetting force at the dynamic contact angle is neglected through this analysis. This assumption is clearly justified when the impact pressure gradient in the radial

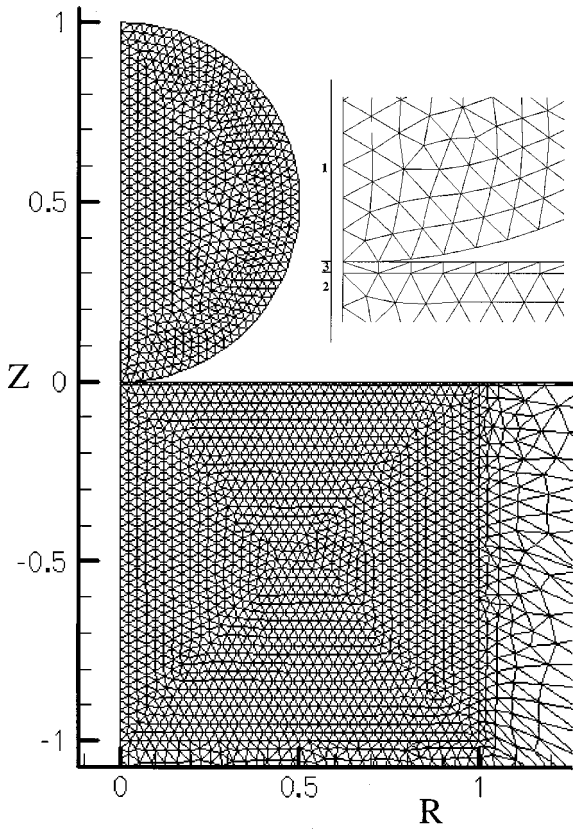

Fig. 2 Details of a typical mesh used. The first layer of the substrate has a dimensionless thickness of 0.01 and its conductivity can be tuned for simulating interfacial resistance to heat transfer. The droplet, substrate and interface domain are indicated by the symbols 1, 2, and 3.

direction is high, as well as in substrate melting cases where solidification occurs at the wetting line, as will be shown later. In general, one is justified to neglect wetting if the value of the Weber number based on the contact line velocity is greater that O(1) [1,2]. The dimensionless numbers for the fluid dynamics are defined as follows:

$$\text{Reynolds number Re} = \frac{\rho_l v_0 d_0}{\mu} \tag{11}$$

$$\text{Weber number We} = \frac{\rho_l d_0 v_0^2}{\sigma} \tag{12}$$

$$\text{Froude number Fr} = \frac{v_0^2}{d_0 g} \tag{13}$$

Heat Transfer and Phase Change. The energy equation for the droplet and substrate is also cast in Lagrangian form. The dimensionless form of this equation is:

$$C_i \frac{\partial \Theta_i}{\partial \tau} - \frac{1}{\text{Re Pr}} \left[\frac{1}{R} \frac{\partial}{\partial R} \left(K_i R \frac{\partial \Theta_i}{\partial R} \right) + \frac{\partial}{\partial Z} \left(K_i \frac{\partial \Theta_i}{\partial Z} \right) \right] = 0. \tag{14}$$

The non-dimensionalization of the heat transfer equation was carried out according to the following definitions of the dimensionless numbers:

$$\text{Pr} = \frac{\mu c_{pl}}{k_l}, \quad C_i = \frac{\rho_i c_{pi}}{\rho_l c_{pl}}, \quad K_i = \frac{k_i}{k_l}. \tag{15}$$

The index $i = 1$, 2, or 3 stands for the droplet, the substrate and the interface, respectively, as shown in Fig. 2. Initial conditions are

$$\Theta_1(R,Z,0) = 1, \quad \Theta_2(R,Z,0) = 0, \quad \Theta_3(R,Z,0) = 0, \quad \tau = 0. \tag{16}$$

Radiation heat transfer is neglected from all surfaces, and the substrate is assumed to be large enough so that the natural boundary condition (no normal heat flux) applies along the entire boundary of the computational domain. Accounting for radiation and convection between the droplet and the ambient gas has no effect on the results as shown in a previous investigation [15]. For all practical purposes, the cooling occurs through convection in the bulk fluid and conduction to the substrate.

The phase change is modeled according to the exact specific heat method [15,22], where the effect of latent heat release is introduced in the computation by a local increase of the heat capacities. This approach leads to the exact integration of the capacitance terms in the finite element formulation with linear triangular elements, and has shown very accurate energy conservation capabilities [15]. It is assumed that the phase change occurs through a sharp boundary, at equilibrium temperature, and that the densities of the solid and liquid material are the same in the fluid dynamics calculation. The Stefan number and superheat parameter SHP are defined as follows:

$$\text{Ste} = \frac{c_{pl}(T_M - T_{2,0})}{h_{ls}} \tag{17}$$

$$\text{SHP} = \frac{T_{1,0} - T_M}{T_M - T_{2,0}} \tag{18}$$

Marangoni convection was not accounted for in the model. This is justified since (*a*) the variation of the surface tension is not expected to be significant due to the fact that the initial droplet temperature is not much higher than the melting temperature, (*b*) we are dealing with a liquid metal of high thermal conductivity that does not sustain large temperature gradients, and (*c*) upon solidification and due to the release of the significant latent heat of fusion the liquid is almost isothermal as shown in previous investigations [15]. Finally, species transport (by diffusion, for example) across the freezing front of the eutectic solder has been neglected, because of the high speed of this front; the velocity of the freezing front can be up to $O(1\ \text{m/s})$.

Contact Resistance. During the spreading of a droplet on a surface, the heat transfer at the interface is reduced (due, for example, to roughness, air entrapment or surface oxidation [6]). This is particularly true before substrate melting and the ensuing merging of the two bodies. Due to lack of experimental data on the transient contact resistance to be inputed to numerical models, this interfacial resistance to heat transfer has been handled macroscopically and empirically by introducing a tunable contact heat transfer coefficient between the drop and the substrate [6], or by inserting a thin interface of massless elements between the droplet and the substrate with a lower and tunable thermal conductivity [15]. In our model, the latter approach has been used as a starting point, and extended in order to allow the heat transfer and fluid computation to be performed during the substrate melting phase in the entire molten domain. To this end, we have added mass to the elements of the thermal interface mentioned above. A low and tunable conductivity was assigned to the elements of the interface. This dimensionless interfacial conductivity K_3 ($K_3 = k_3 k_l^{-1}$) is related through the contact Biot number ($B_i = h_3 k_l^{-1} d_0$) to the interfacial heat transfer coefficient h_3 by the equation

$$K_3 = B_i L_3, \tag{19}$$

where L_3 is the dimensionless interface thickness ($L_3 = l_3 d_0^{-1}$). Our results will be expressed in terms of the contact Biot number, which is the relevant dimensionless number for interfacial conductance (inverse resistance). To account for the practical disappearance of the contact thermal resistance at a droplet/substrate interface region in which substrate melting occurs, the local con-

ductivity of an interface element is increased to the standard conductivity value of the substrate/splat material considered, when all the nodes of this element are above the melting temperature.

Mixing. During the substrate melting process, the melted substrate material participates to the fluid dynamics, which induces a mixing of the droplet and substrate material. In order to study the evolution of this mixing which can be important to the bonding quality, a mixing indicator ϕ is introduced. This indicator takes the values of 1 for splat material, and 0 for substrate material or interface material. In the absence of a chemical potential driving material diffusion between the substrate and the droplet material, the mixing equation in a Lagrangian framework is expressed as follows:

$$\frac{\partial \phi}{\partial \tau} = 0, \tag{20}$$

with the initial condition

$$\tau = 0: \quad \phi(R,Z,0) = 1, Z > 1, \quad \phi(R,Z,0) = 0, Z \leqslant 1. \tag{21}$$

In the presence of a laminar flow exhibiting no chaotic mixing, which is the case in this paper, the interface between the two bodies remains sharp. The tracking of this interface is performed by setting a specific value ($\phi = 0.5$ in the case) to every droplet node that comes in contact with the droplet/substrate interface. Tracking this specific contour value of $\phi = 0.5$ yields the location of the boundary between droplet and the substrate material in time.

Numerical Simulation Procedure

The computational domain was discretized with a mesh of triangular linear elements, and the numerical model was solved using a Galerkin Finite Element Method. A Crank-Nicholson scheme was used for the temporal integration of the energy and mass transfer equation. The fluid particle location and the energy conservation equations were coupled on the basis of a method proposed by Bach and Hassager [19]. The accuracy and capability of the methodology in dealing with the fluid dynamical complexities of the free surface of a droplet hitting a surface is amply demonstrated in Refs. [15], [18], [20], [30], [31].

The following summarizes a single time step of computation:

1 Identify the liquid domain: only the elements where at least one node temperature is higher than the melting temperature are considered for the fluid dynamics calculation.

2 Impose the fluid dynamics boundary conditions (Eqs. 6 to 10).

3 Given an initial configuration of fluid particles and flow variables, calculate the new nodal location by numerical integration of (Eqs. 4 and 5). The velocities at time τ are used as initial 'guesses' for velocities at time $\tau + \Delta\tau$.

4 Based on the current nodal locations, calculate velocity and pressure fields at $\tau + \Delta\tau$ by solving the discrete forms of the mass conservation and momentum equations (Eqs. 1 to 3).

5 Update the nodal locations by numerical integration of (Eqs. 4 and 5) after inserting the velocities at time step τ and $\tau + \Delta\tau$.

6 Iterate steps (3) and (4) until convergence is reached for the time step. Convergence is assumed when the maximum difference for each fluid particle flow variable was less than 0.1 percent from one iteration to the next.

7 Given the temperature field at time τ, solve the energy equation (Eq. 14) to obtain the overall temperature field at time $\tau + \Delta\tau$ in the whole computational domain.

8 Given the mixing field at time τ, solve the mixing equation (Eq. 20) in the entire computational domain to obtain the mixing field at time $\tau + \Delta\tau$.

Remeshing was performed every time that the element distortion attained a critical value. The element distortion is defined as the ratio of the radius of a circle passing through the three points defining an element, and the radius of a circle that circumscribes an equilateral triangle that has the same area as the element under consideration. The mesh generation was performed with a state of the art, optimized and commercially available mesh generator (Hypermesh, Altair Eng. Inc.), which has proven to be markedly more robust than the meshing generation process used in previous simulations without substrate melting [15]. Hypermesh was used in batch mode [23] since a typical run involved about sixty complete remeshing operations. After a new mesh was created, the solution variables were mapped to the new nodes via interpolation of the old mesh. The temperature and mixing variables of the nodes near the mixing front and the phase change front were adjusted after each remeshing in order to conserve accurately the shape of the mixing and phase boundaries, respectively. A detailed study has been performed to determine the temporal and spatial resolution necessary to obtain time step and grid independence, the main results of which are presented in the next section. A typical run required 22 CPU hours to complete on a PC with a 500 MHz Pentium III Processor.

Results and Discussion

Baseline Case and Parametric Variations. The main goal of the runs performed is the investigation of substrate melting in the case of molten microdroplet impact of eutectic Pb-Sn solder, as described in the introduction. In addition to featuring a sharp melting interface, this material has a relatively low melting point that will facilitate future experiments, and it is the material of choice in electronics soldering applications where larger solder amounts are deposited in one location by pileup or combination of a desired number of microdroplets [17,24,25]. A first series of runs was performed in order to investigate the sensitivity of substrate melting to the thermal parameters (SHP, Bi). The baseline case corresponds to the impact at 1.5 m s^{-1} of an 80-micron diameter solder droplet at a temperature of 210°C on a solder substrate at a temperature of 182°C (1K below the equilibrium melting temperature). These conditions are typical in solder jetting applications [15,25]. The interfacial heat transfer coefficient was set to the relatively high value of 10^7 $Wm^{-2}K^{-1}$. The thickness l_3 of the heat transfer interface was one percent of the drop diameter, i.e., 0.8 microns. The choice of an initial substrate temperature near the melting point corresponds also to conditions encountered in actual applications of micromanufacturing [4], where the frequency of droplet deposition is high in order to minimize the manufacturing time. These values were nondimensionalized according to the following thermophysical properties for Pb-Sn eutectic solder: $\sigma = 0.345$ Jm^{-2}, $\mu = 0.00262$ Pas, $\rho_l = 8218$ kgm^{-3}, $\rho_s = 8420$ kgm^{-3}, $c_{pl} = 238$ $J\,kg^{-1}\,K^{-1}$, $c_{ps} = 176$ $J\,kg^{-1}\,K^{-1}$, $k_l = 25$ $Wm^{-1}K^{-1}$, $k_S = 48$ $Wm^{-1}K^{-1}$, $h_{ls} = 42000$ J/kg, and $T_M = 183$°C. The thermal dimensionless groups, i.e., superheat parameter SHP, Stefan and the Biot numbers, assume respectively the values 9.64×10^{-1}, 5.7×10^{-3} and 32. The Weber and Reynolds numbers are 4.3 and 376, respectively.

The substrate is flat with radial and axial dimensions eight times larger than the diameter of the droplet, in order to simulate the impact on a substrate much larger than the droplet. The chosen criterion for determining the substrate size was that the system constituted by the droplet and substrate exhibit after heat transfer and solidification a mean temperature increase smaller than 10 percent of the difference between the initial substrate temperature $T_{2,0}$ and the melting temperature T_M. Around the baseline case, $T_{2,0}$, h_3, and v_0 have been varied individually in order to investigate the importance on the substrate melting of SHP (0.9, 0.931, and 0.9643), Bi (0.032, 0.32, 3.2, 32, and ∞) and impact velocity ($1-2$ ms^{-1}), respectively. In order to compare the numerical results with existing experiments for larger droplets [3]—none could be found for microdroplets—a simulation of substrate melt-

ing with mm-size steel droplets has been performed and the results of the comparison as well as interesting related findings will also be reported later in this paper.

Mesh Size and Time Step Independence. A fact of central importance to every numerical solution is the independence of the reported results on the grid size and time step. In this subsection we discuss the independence of the present results for droplet impact fluid dynamics as well as substrate melting on the temporal and spatial discretization. Our baseline case, described earlier, was selected for it is a demanding case featuring a large amount of substrate melting and large temperature gradients in the presence of which energy must be conserved.

Figure 2 shows a detail of the mesh used for the baseline case, as well as a detail of the interface elements. It has a typical number of 2654 nodes and 5113 elements, with 664 nodes and 1234 elements in the droplet. In order to limit the thermal energy losses by numerical diffusion and to keep the calculation time reasonable, the region of the mesh shown in Fig. 2 (where the largest temperature gradients appear) was meshed with a high and constant density of elements, while the mesh outside the shown region was gradually coarser. This ''baseline'' mesh was compared to a coarser and a finer mesh. The coarser mesh has a lower density of elements in the region of high temperature gradients. It has 2076 nodes and 3978 elements, with 503 nodes and 924 elements in the droplet. The finer mesh has a higher density in the region of high temperature gradients, and this fine mesh region was also extended axially and radially from respectively -1 to -2, and 1 to 2. The finer mesh has about four times the number of elements of the baseline mesh (9905 nodes and 19517 elements, with 913 nodes and 1717 elements in the droplet). We use for the baseline case a time step of $d\tau = 5\times10^{-4}$, as used for simulations of a comparable problem without substrate melting considerations [15]. Results with this time step were compared to results with one smaller ($d\tau = 2.5\times10^{-4}$) and one larger ($\tau = 1.0\times10^{-3}$) time step in order to test the effect of the temporal discretization.

Figure 3(*a*) shows the effects of the temporal and spatial discretization on the fluid dynamics, exemplified by the evolution of Z_C, the *Z*-axis contact point with the free surface of the droplet, as a function of time. A marked and undesirable phase lag in the position of Z_C appears in the simulation with the larger time step ($d\tau = 1.0\times10^{-3}$), while the four other simulations show a good agreement. Figure 3(*b*) shows the temporal evolution of the melted volume V_M (defined in the next section). It appears that the simulation with the small time step ($d\tau = 2.5\times10^{-4}$) is not adequate for predicting the remelted volume near its maximum. This result is likely due to the accumulation of numerical inaccuracies and round off errors during the larger number of calculation steps, leading to thermal energy losses. The simulation with a coarse mesh also underestimates the amount of substrate melting. We conclude from both investigations that only two configurations are suitable for the calculation, namely the baseline case ($d\tau = 5\times10^{-4}$, baseline mesh) and the fine mesh case ($d\tau = 5\times10^{-4}$, fine mesh). Since a run with the baseline case takes about 22 hours on a Windows NT 500 MHz Pentium III workstation, a run with the fine mesh case, more than 100 hours on the same machine, the baseline case is chosen for our calculations, after verifying that the total amount of thermal energy losses at the end of the computation were acceptable (within 4 percent to 5 percent).

The slight stair-stepping characteristic visible in the numerical accuracy curves of the melted volume in Fig. 3(*b*) stems from the fact that in the early stages of the spreading, where most of the substrate melting occurs, the contact area between the splat and the substrate increases by successive ''attachment'' of free surface nodes to the substrate as the droplet spreads. This induces an instantaneously sudden increase of the contact heat transfer area between drop and substrate and causes the above mentioned slight stair-stepping characteristic.

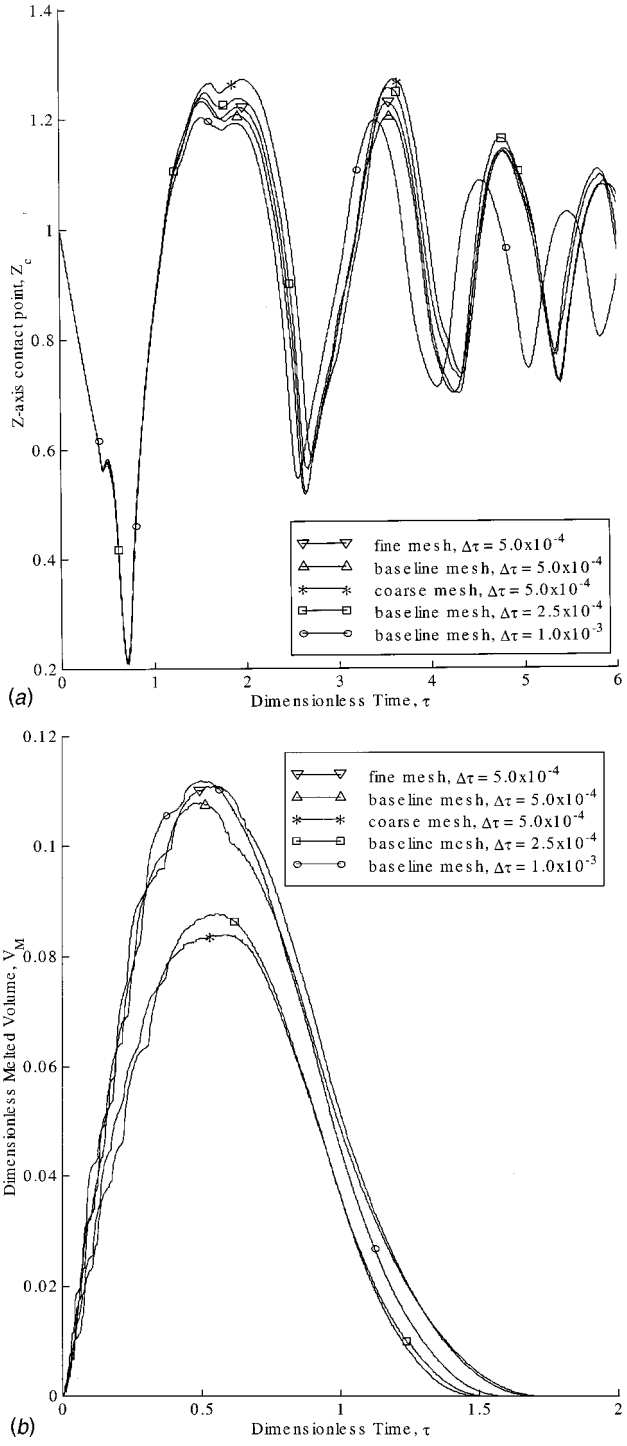

Fig. 3 (*a*) **Temporal evolution of the *Z*-axis contact point for the baseline case, for different temporal and spatial discretizations; and (*b*) temporal evolution of the melted volume V_M for the baseline case, for different temporal and spatial discretizations.**

General Description of the Substrate Melting Process. Figure 4 shows the droplet shape and phase change boundary (sepa-

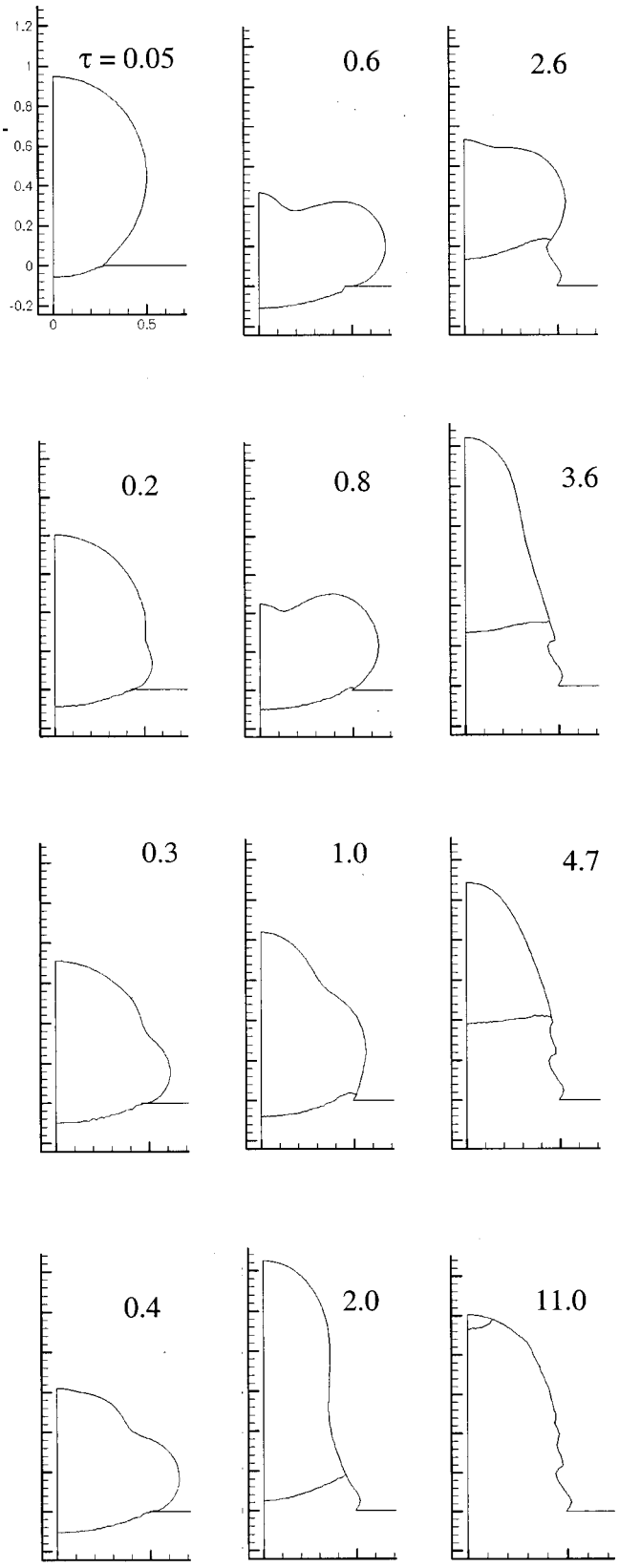

Fig. 4 Droplet shape and phase change location as a function of the dimensionless time for the baseline case

rating the liquid and solid phases) at successive instants of the substrate melting process, for the baseline case. One observes that substrate melting occurs already in the early stages of the spreading (τ=0.05) and that the melting process extends in the radial direction simultaneously with the droplet. No effects of interfacial contact resistance are visible, which would delay the melting with respect to the spreading advance. During the spreading of the droplet, a maximum substrate melting depth of about 10 percent of the initial droplet diameter is attained along the *Z*-axis, at the time τ=0.05. The simultaneous spreading and melting indicate that in the parametric domain of interest of the present study the time scales of the fluid dynamics and the substrate melting phenomenon are of the same order, and that any model uncoupling the fluid dynamic calculation from the heat transfer and solidification process would probably oversimplify the problem. Also, the motion and shape of the phase change boundary, crossing the *R*-axis at time 1.0 shows the highly two-dimensional aspects of the substrate melting and re-solidification phenomenon. For τ>1.0, the phase front progresses upward and the coupling between freezing and oscillations produces ripples on the splat surface, a mechanism found and explained in the numerical work of Waldvogel and Poulikakos [15] and verified experimentally by Attinger et al. [16]. Before closing this section, it is worth noting that the areas of the cross-sections in Fig. 4 at different times appear to be unequal (for example, the area at time 0.8 is smaller than the area at time 2.0). However, it is incorrect to conclude from this fact that mass is not conserved. Our model is axisymmetric and not two-dimensional Cartesian. As a matter of fact, the volume at time 0.8 is practically identical to the volume at time 2.0. We have calculated that the volume of the system is conserved within $\pm$0.3 percent.

Quantitative Characterization of Substrate Melting. In order to discuss features of the substrate melting phenomenon, we quantify this melting in terms of the dimensionless melted volume V_M, defined as the amount of liquid material below the $Z=0$ boundary. This parameter has been preferred to the dimensionless volume of liquid in the entire computational domain V_1, for the following reason: a value of V_M larger than zero means unequivocally that some substrate material has melted while a value of V_1 lower than unity does not mean that all the material below the $Z=0$ line has solidified, since our results show (Fig. 4, τ=1.0) that solidification can start at the periphery of the droplet while the zone near the *Z*-axis still experiences a significant amount of melting. It is also worth noting that we write ''material below the $Z=0$ boundary'', rather than ''substrate material'', since there is a significant mixing between the droplet and the substrate material, as will be shown in the next section.

Figure 5 shows the temporal evolution of V_M for three values of superheat (SHP). As expected and shown in previous studies [10], the maximum melted volume increases with SHP. It also appears that the time when this maximum is reached increases with SHP, which can be explained by the fact that the substrate melting depth increases with the SHP, the thermal diffusivity being the same for the three cases. The time for reaching the maximum substrate melting is smaller than the time between the maximum substrate melting and the instant where the entire material below $Z=0$ is solid. This is different from the symmetry of the amount of substrate melting versus time curves presented in previous one-dimensional simulations by Wang et al. [10].

The strong influence of the impact velocity v_0 on the amount of melted volume is shown in Fig. 6. The velocities ranging from 1 to 2 ms^{-1} correspond to Reynolds and Weber numbers in the interval (250.6; 501.3), respectively (1.903; 7.61). All the other parameters have been kept constant as in the baseline case. The amount of substrate melting increases clearly with the impact velocity: doubling v_0 increases the amount of substrate melting by about 60 percent. This is a clear sign of the important role of the fluid dynamics on the substrate melting process. Considering the complex flow pattern in the droplet (to be discussed later in this section), it appears that this can only be studied accurately with a modeling involving consideration of the complex fluid dynamics and free surface dynamics of droplet impact. Similarly with Fig.

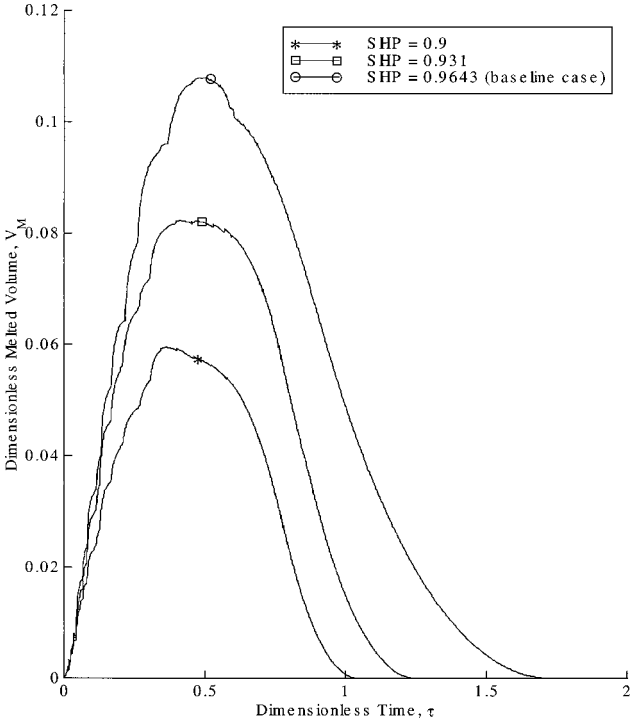

Fig. 5 Temporal evolution of the melted volume V_M for different values of the superheat parameter SHP, corresponding to initial substrate temperatures of 180, 181, and 182°C

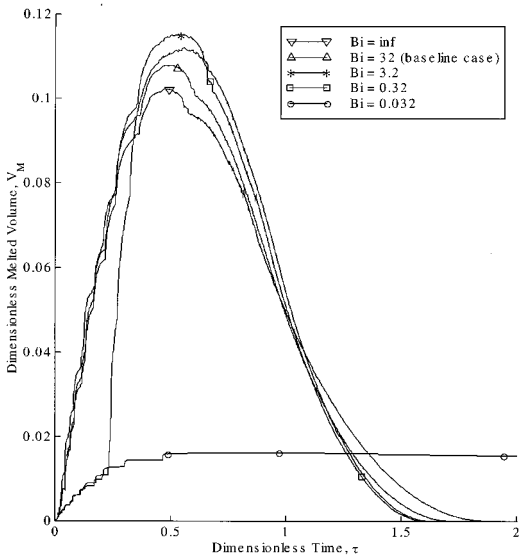

Fig. 7 Temporal evolution of the melted volume V_M for different values of the Biot number. The case with an infinite Biot number is the case without thermal contact resistance between the splat and the substrate, and the four subsequent cases correspond to interfacial heat transfer coefficient values of 10^7, 10^6, 10^5, and 10^4 $Wm^{-2}K^{-1}$.

5, it appears also that the time where the maximum substrate melting is reached increases with the melted volume.

The influence of the interfacial heat transfer, indicated by the Biot number, on the amount of substrate melting V_M is shown in Fig. 7. It appears that the substrate remelts in a comparable way for every Biot number larger than a threshold value (Bi=0.32). This is related to the feature of the interfacial heat transfer model used in this study, where a low and specific heat transfer conductivity at the interface is only assumed as long as no melting has occurred. Any simulation with a Biot number markedly larger than a threshold value, with the melting boundary advancing simultaneously with the contact line (as in Fig. 4), will therefore show qualitatively similar behavior. At the threshold value (Bi =0.32), the initiation of substrate melting is delayed somewhat compared to cases with markedly higher values of Bi, which can be explained by the fact that the interface layer resists a longer time (up to about τ=0.25) before melting. It is interesting to note that the maximum amount of substrate melting at this threshold Biot number value is comparable to the maximum amount of substrate melting at larger Biot numbers.

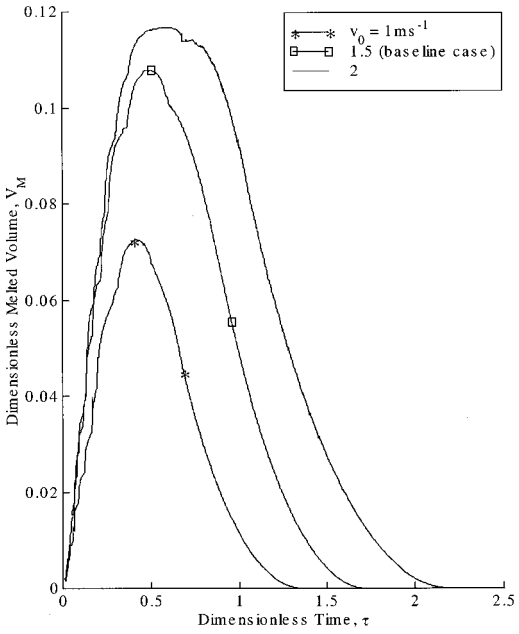

Fig. 6 Temporal evolution of the melted volume V_M for different values of the impact velocities. The velocities ranging from 1 to 2 m s^{-1} correspond to Reynolds and Weber numbers in the interval (250.6; 501.3), respectively (1.9;7.61).

When the Biot number is lowered by an order of magnitude again (Bi=0.032), V_M exhibits much lower values and assumes a different shape, signifying that the substrate melting is confined to the interfacial layer, whose low thermal conductivity value is conserved through the entire process (no substrate melting takes place below the interfacial layer). It is worth noting that Kang et al. [8] have shown that assuming an interfacial contact heat transfer coefficient h_3 of 10^6 $Wm^{-2}K^{-1}$ provided a reasonable agreement between a model of one-dimensional freezing/melting in the droplet combined with two-dimensional conduction in the substrate, and experiments with mm-size eutectic tin-lead solder droplets, but only in the region near the center of symmetry where the one-dimensional hypothesis is more likely to be valid. Assuming the same contact heat transfer coefficient for the microdroplet considered here would mean a Biot number of 3.2, larger than the threshold Biot number mentioned above. In this case, the behavior is expected to be similar to that of an infinite Biot number (no contact resistance).

Key aspects of the above effects are summarized in a substrate melting ''design'' graph, shown in Fig. 8. This graph shows the influence of the impact velocity and the superheat parameter SHP on the melted volume of substrate material V_M, assuming an infinite Biot number according to the above discussion. A series of 25 simulations has been performed (5 values of SHP and 5 values of Re), corresponding to the legend and the labeling of the *X*-axis. Figure 8 shows first a dependence of the melted volume on the

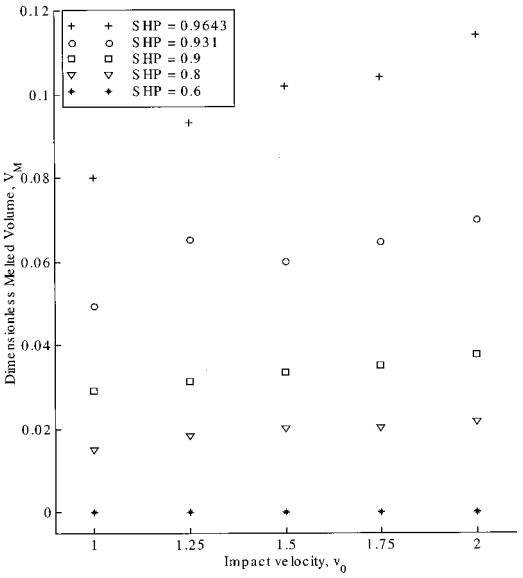

Fig. 8 Maximum melted volume V_M as a function of the impact velocity for five different superheat parameter SHP in case of an infinite Biot number

SHP (compare with Fig. 5), which allows controlling V_M in the range of one to more than ten percent in both cases. The general increase of the amount of substrate melting with the impact velocity demonstrates the importance of the fluid dynamics in particular for high superheat values. More details about the coupling between the fluid dynamics and the heat transfer are provided in the next section.

Considerations of the Mixing Between Droplet and Substrate. Mixing between the droplet and the substrate material has never been considered in substrate melting treatment up to now (to the best of our knowledge). Investigation of this phenomenon requires the consideration of the complex fluid dynamics in the entire time-dependent molten domain. All existing substrate melting studies that we are aware of either assume that the remelted substrate material does not experience any marked motion, or do not investigate the details of the motion for simplicity. The present study shows a significant and complex mixing process between the droplet and substrate material.

Figure 9 provides an insight into the mechanisms governing the mixing, identifying the time history of the boundary between the substrate and droplet material. Contrary to the phase change (see Fig. 4), the mixing is relatively moderate during the first phase of the spreading ($\tau<0.8$), while a more significant amount of material is exchanged during the subsequent recoiling phase (0.8 to 2.0). The freezing process then arrests the final shape of abovementioned boundary. The shape of the interface between substrate and droplet material shows that substrate material has been transported in the droplet in regions near the *Z*-axis ($R<0.2$) and that droplet material has been transported in the substrate in peripheral region ($R\geqslant 0.2$). Two mechanisms have been identified that contribute to this mixing process. First, during the spreading and simultaneous substrate melting, a donut-shaped shear-induced vortex is created in the melted substrate material by the radially moving droplet fluid. The corresponding streamlines are shown in detail (*a*) of Fig. 9. This vortex is important to the material mixing since it lifts up substrate material from the substrate in the droplet. The mixing is albeit weak since the large radial pressure gradient that drives the droplet flow along the substrate reduces the vertical spreading of the vortex. When recoiling occurs, the vortex breaks down, giving place to an upward flow pattern (detail (*b*) in Fig. 9), which causes most of the mixing. Obviously, the above described complex substrate melting phenomenon caused by the impact of a warm microdroplet differs markedly from the simple ''first-level'' representation of a an amount of hot material suddenly placed in contact with a substrate that melts without exhibiting any significant internal fluid dynamics [3,8–10]. Such mixing considerations are important for modeling the interfacial heat transfer coefficient at the interface between the substrate and the drop. We have shown that the initial interface at $Z=0$ is displaced and distorted during remelting. It is also worth mentioning that tracking of this mixing can be important in the case of heterogeneous substrate melting (the drop and the substrate are of dissimilar materials), not treated in the present study. In this case, the mixing fractions of both materials need to be determined over the entire computational domain in order to modify the thermal and fluid properties accordingly.

Comparison With Experiments for Larger Droplets. In substrate melting induced by microdroplets, the above study has shown that the complex coupling between fluid dynamics and heat transfer needs to be considered in its entirety, as exemplified by the dependence of the amount of substrate melting on the initial impact velocity and superheat, or by the mixing process.

Is the consideration of this coupling also important in case of substrate melting involving larger, mm size droplets? Or is it possible to uncouple the fluid dynamics from the heat transfer, with the assumption that the fluid dynamics occurs first, and only then heat transfer to the substrate? This widely used assumption [7,12–14,26] has been adopted to some extent in the work of Zarzalejo et al. [3], one of the more complete conduction-based models, where these authors compare numerical modeling with substrate melting experiments. Their findings are shown in Fig. 10(*a-b*), which is transferred here from the above-mentioned paper to illustrate the discussion. They simulated the experimental shape of the maximum depth of the phase change boundary (the darker line separating the portion of substrate material that has melted from that which has not) with a numerical model where the calculation domain experienced no deformation and no fluid dynamics, the droplet shape being identical to the final solidified shape of an experiment during the entire conduction computation. They obtained a relatively good agreement between experiments and simulation (at least for the substrate melting depth along the *Z*-axis), but this agreement was only reached after increasing in an ad-hoc manner—by a factor five—the thermal conductivity in their diffusion heat transfer model, in order to account for convection. In other words the splat thermal conductivity was selected as the one that gives good agreement with the experiments. While this approach can be deemed as reasonable for rough estimates, in case where no fluid dynamics modeling is performed, it has clearly no predictive power, since convection is accounted for a-posteriori and in terms of an estimate that yields some agreement with previously performed experiments.

Our work suggests that considering the complex coupling between fluid dynamics and heat transfer in a complete sense can be fruitful. The case reported in [3] is the impact of a 3.5 mm stainless steel (they have used the properties for SS308 in their numerical model) droplet at 2500°C on a flat homogeneous substrate at 35°C, with an impact velocity of the order of 1 m/s. We have performed several numerical simulations with our code to reproduce this case. The best agreement was obtained with the following values for the thermophysical properties of SS308 [27–29]: $\sigma=1.0\ \mathrm{Jm}^{-2}$, $\mu=0.005$ Pas, $\rho_l=7000\ \mathrm{kgm}^{-3}$, $\rho_s=7665\ \mathrm{kgm}^{-3}$, $h_{ls}=273000$ J/kg, $c_{pl}=810\ \mathrm{J\,kg}^{-1}\,\mathrm{K}^{-1}$, $c_{ps}=576\ \mathrm{J\,kg}^{-1}\,\mathrm{K}^{-1}$, $k_l=28.4\ \mathrm{Wm}^{-1}\,\mathrm{K}^{-1}$, $k_s=23\ \mathrm{Wm}^{-1}\,\mathrm{K}^{-1}$, and $T_M=1445$°C. One should keep in mind that there are variations in the values of these properties reported in the literature ([29] and references therein). These properties and the initial conditions given in [3] lead to the following dimensionless numbers: $\mathrm{Re}=5.88\times10^3$, We=27.13, Fr

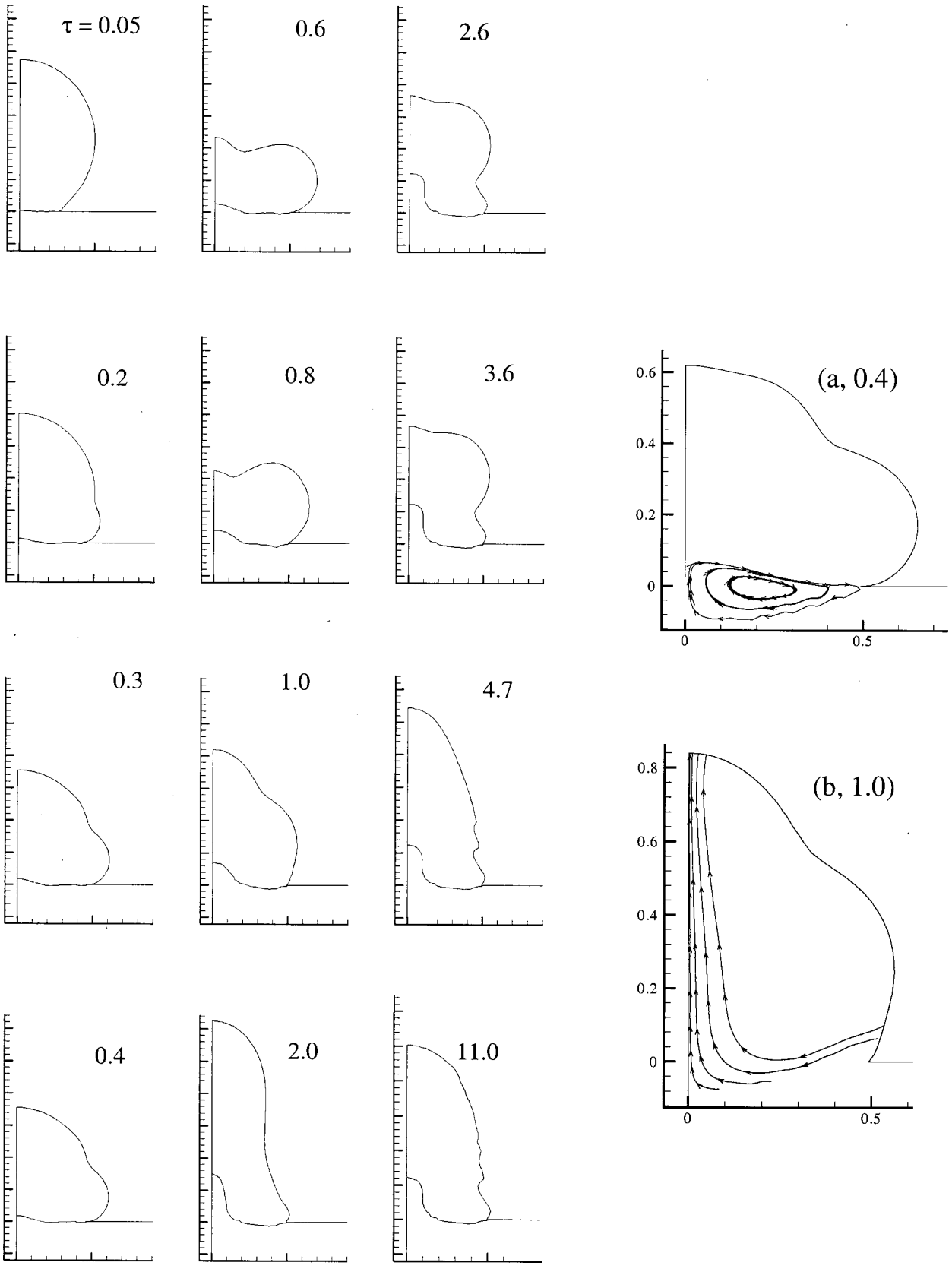

Fig. 9 Droplet shape and interface between the drop and substrate material as a function of the dimensionless time for the baseline case. Details (*a*) and (*b*) show the instantaneous flow pathlines corresponding to τ=0.4 and 1.0.

=41.93, Pr=0.14, Ste=4.21, and SHP=0.43. We assumed an infinite Biot number, in accordance with our results described in Fig. 7.

Results of our simulation can explain experimental findings such as the formation of the shoulders on the maximum depth of the phase change boundary circled in Fig. 10(*a*), impossible to explain or reproduce with diffusion models (neglecting careful modeling of convection). Figure 10(*c*,*d*) show the phase change

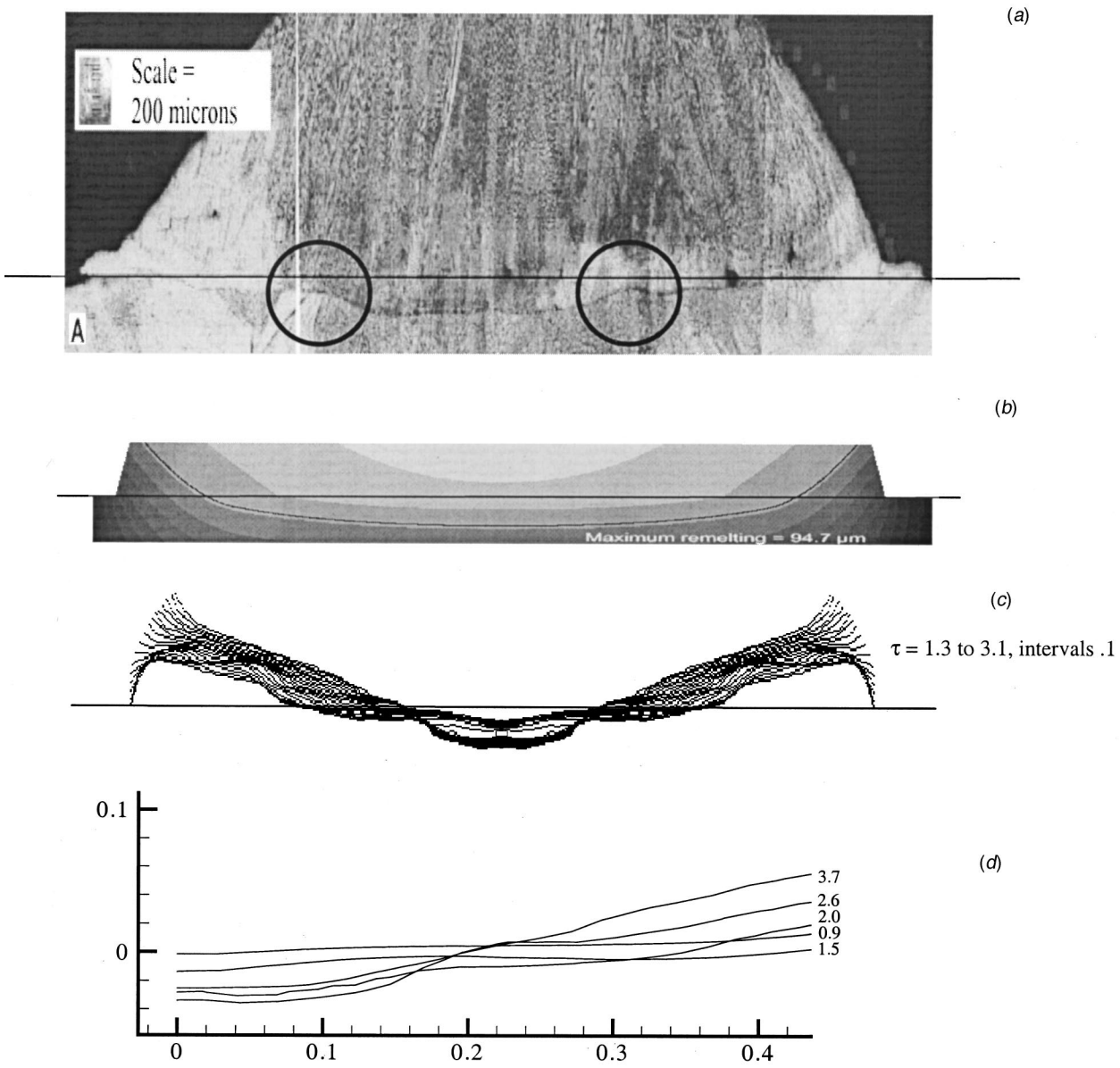

Fig. 10 Experimental cross-section of a solidified 3.5 mm steel droplet on a steel substrate [3] compared with two numerical models, (*b*, conduction model of Zarzalejo et al., [3]) and (*c*,*d* present study). The horizontal line crossing figures (*a*, *b*, and *c*) denotes the substrate surface. The maximum substrate melting location visible as a darker line in (*a*) is approximated by a heat-diffusion based model (*b*), [3]), with a heat conductivity artificially increased for convection, and by the numerical model developed in the present study (*c*,*d*). Oscillations of the phase change front around approximately $R=0.2$ explain the formation of the shoulders circled in the cross section (*a*), since the envelope of the instantaneous phase change fronts defines the maximum substrate melting location (*c*). With permission from Springer-Verlag for frames (*a*) and (*b*).

boundary obtained with the present simulations at characteristic times. Figure 10(*c*), drawn at the same scale as that of Fig. 10(*a*,*b*), contains the phase change boundary at many such characteristic times. The bottom of the phase change boundary envelope formed by the superposition of these interfaces corresponds to the maximum depth of the phase change boundary and has a shape comparable to the experimental maximum depth phase change boundary in Fig. 10(*a*), with two clearly visible shoulders. An explanation of the shoulder formation is provided in Fig. 10(*d*), where the instantaneous shape of the phase change boundary is plotted for 5 times ranging from before the termination of the spreading ($\tau=1.3$ is the time of the maximum radial extension of the free surface) to well into the recoiling phase. If the phase change boundary propagates downwards in the early times (from $\tau=0.9$ to 1.5), its evolution afterwards resembles a wave, with a nodal point at the location $R=0.2$. As a result of this wavy motion, a shoulder is formed. The physics explaining this phenomenon is related to the complex coupling between the motion of the free surface and convection heat transfer.

Figure 11 shows the free surface, the velocity field and the streamlines corresponding to Figure 10(*c*-*d*) for a host of representative times. A mass accumulation ring is formed at the splat periphery of the droplet (also observed in several earlier investigations of droplet impact [30,31]). There, the spreading is arrested by solidification at the contact line ($\tau=0.6$). The existence of this mass accumulation ring induces a local minimum of the height of the free surface (point A), and a vortex pair V1 and V2. Vortex V1 is created by the recirculation of the liquid entering and contained

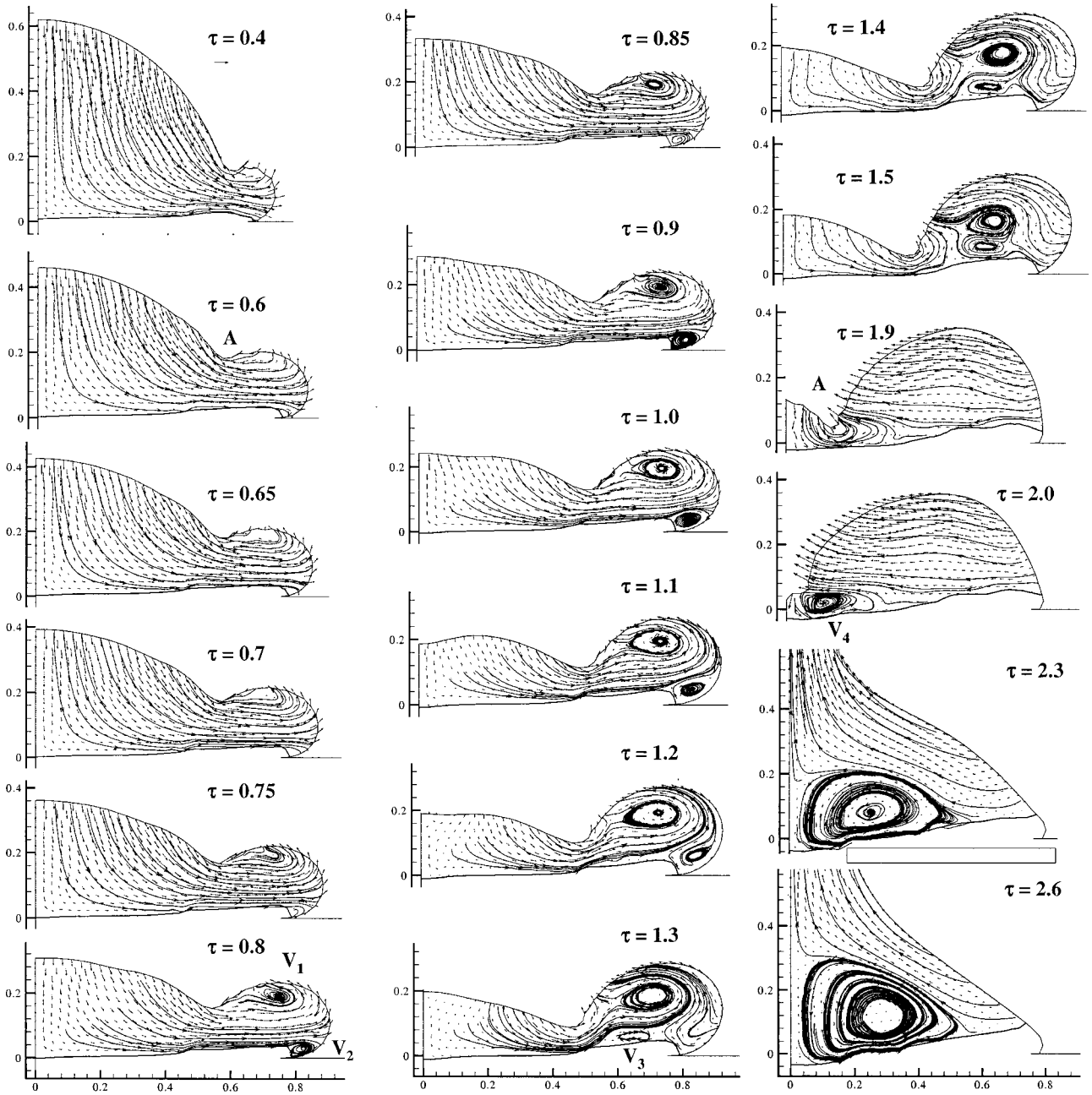

Fig. 11 Droplet shape, instantaneous velocity distribution and flow pathlines corresponding to the simulation in Fig. 10 (*c*,*d*). The dimensionless time is indicated, and the length of the horizontal arrow in the first frame corresponds to a dimensionless velocity of 1.

in the ring. This flow is directed toward the free surface of the ring and gradually initiates an inward motion of the ring free surface reminiscent of the motion and swelling of a free surface wave (times 0.9 and greater). Vortex V2 is direct consequence of the larger vortex V1, since the flow entering the mass accumulation ring is first deflected slightly upwards by the shoulder shape of the freezing front ($0.4<R<0.8$, $\tau=0.8$) and entrains then the flow in the zone where V2 is created.

The creation of V2 can be termed as a ''backward facing step effect'' due to the shape of the freezing front, underpinning one more time the importance of the fluid mechanics in the freezing process. The creation of this step is a direct consequence of the fact that when the contact line is arrested by freezing, the free surface region above it keeps moving (bulging) outward due to its own inertia (time=0.6). The resulting local downward motion of the liquid in this region retards the solidification process and creates the step configuration which in turn facilitates the formation and growth of vortex V2. During the recoiling phase ($\tau=1.2$ to 2.6), V2 breaks down and V3 is created because the ring motion displaces V1 towards the *Z*-axis, engendering a dead zone between V1 and the frozen material under V1.

The formation of vortex V3 resembles that of a vortex on the top surface of a forward facing step. Later during recoiling ($\tau=1.3$ to 1.9), the local minimum A moves toward the *Z*-axis and accelerates locally the fluid flow through the narrow channel beneath A. This increases the corresponding convection heat transfer, increasing correspondingly the melting rate below A. At the same time, the liquid of the central part of the droplet keeps moving

outward. However (τ=1.5) as it enters the mass accumulation ring, it is now partially ''blocked'' by the abovementioned vortex pair and it is forced to turn toward the free surface in the neighborhood of the local minimum A. The resulting flow structure also increases the melting rate below A.

The vortex pair V1 and V3 stretches with time and disappears (time 1.9). The valley flow region to the left and below the vortex pair region develops into vortex V4 as the recoiling free surface approaches the center of symmetry. This vortex grows further as the recoiling proceeds with the majority of the liquid moving upward (τ=2.6). This vortex increases again the convection heat transfer near the *Z*-axis. The combination of these melting rate increases (first due to the complex fluid motion under A around times 1.5 and 1.9, then to the creation of V4) explains the formation of the shoulders found experimentally on the maximum substrate melting depth and illustrates the complex coupling between free surface motion, fluid dynamics, heat transfer and phase change.

Conclusion

In this paper the main features and results of a numerical investigation of molten microdroplet impact and solidification on a colder flat substrate that can melt are described. The melted volume has been determined and presented as a function of time for various combinations of thermal and fluid dynamics parameters. The influence of the interfacial heat transfer between the splat and the substrate has been studied, and the existence of a threshold Biot number for substrate melting modeling has been demonstrated. A strong influence of the impact velocity on the amount of substrate melting underpins the importance of the fluid dynamics on the substrate melting phenomenon. Substrate melting maps have been produced, where the amount of substrate melting is expressed as a function of the impact velocity and the superheat parameter SHP. Significant material mixing between the substrate and splat has been identified and quantified and implications of this mixing have been discussed. Good agreement between the numerical results and experiments of previous investigators for larger (mm-size) droplets was obtained, and explanations for the complex shape of the maximum melting depth boundary found in these experiments were provided for the first time. In all, this study demonstrates that the complex coupling between free surface motion, fluid dynamics, material mixing and multidimensional heat transfer is of central importance to the thorough understanding of the physics of substrate melting problems involving droplet sizes in the range O(100 microns) to O(1 mm).

Acknowledgments

We acknowledge the help of our colleagues Vincent Butty and Stephan Haferl for the implementation of the commercial mesh generator Hypermesh in the numerical modeling. Financial support by the Swiss National Science Foundation (Grant No. 21-49183.96) is gratefully acknowledged.

Nomenclature

c = speed of sound (m s^{-1})
d = diameter (m)
E = energy (J)
h_3 = interfacial heat transfer coefficient ($Wm^{-2}K^{-1}$)
h_{ls} = fusion enthalpy (J kg^{-1})
H = dimensionless free surface curvature (κd_0)
l_3 = thickness of the interface layer (m)
L_3 = dimensionless thickness of the interface layer ($l_3 d_0^{-1}$)
M = Mach number ($v_0 c^{-1}$)
n = outward unit normal vector
P = dimensionless pressure ($p\rho_L^{-1} v_0^{-2}$)
r = radial coordinate (m)
R = dimensionless radial coordinate ($r d_0^{-1}$)
u = radial velocity (m s^{-1})
v = axial velocity (m s^{-1})
V = dimensionless axial velocity (vtd_0^{-1})
U = dimensionless radial velocity (utd_0^{-1})

Greek Symbols

Δ = difference
ρ = density (kg m^{-3})
ϕ = dimensionless mixing indicator
κ = mean free surface curvature (m^{-1})
Θ_i = dimensionless temperature $((T_i - T_{2,0})(T_{1,0} - T_{2,0})^{-1})$
$\overline{\sigma}$ = dimensionless stress tensor term
τ = dimensionless time ($tv_0 d_0^{-1}$)

Subscripts

0 = initial
1 = droplet
2 = substrate
3 = interface
l = liquid
M = melting point, melted
R = radial
s = solid
Z = axial

References

[1] Attinger, D., Haferl, S., Zhao, Z., and Poulikakos, D., 2000, ''Transport Phenomena in the Impact of a Molten Droplet on a Surface: Macroscopic Phenomenology and Microscopic Considerations: Part II—Heat Transfer and Solidification,'' in *Annual Review of Heat Transfer*, C. L., Tien, ed., Vol. XI, Begell House, NY, pp. 145–205.

[2] Haferl, S., Zhao, Z., Giannakouros, J., Attinger, D., and Poulikakos, D., 2000, ''Transport Phenomena in the Impact of a Molten Droplet on a Surface: Macroscopic Phenomenology and Microscopic Considerations: Part I—Fluid Dynamics,'' in *Annual Review of Heat Transfer*, C. L., Tien, ed., Vol. XI, Begell House, NY, pp. 65–143.

[3] Zarzalejo, L. J., Schmaltz, K. S., and Amon, C. H., 1999, ''Molten Droplet Solidification and Substrate Remelting in Microcasting: Part I—Numerical Modeling and Experimental Verification,'' Heat and Mass Transfer, **34**, pp. 477–485.

[4] Orme, M., Liu, Q., and Fischer, J., 2000, ''Mono-Disperse Aluminum Droplet Generation and Deposition for Net-Form Manufacturing of Structural Components,'' in *Eighth International Conference on Liquid Atomization and Spray Systems*, Pasadena, CA, USA, July 2000, pp. 200–207.

[5] Amon, C. H., Schmaltz, K. S., Merz, R., and Prinz, F. B., 1996, ''Numerical and Experimental Investigation of Interface Bonding via Substrate Remelting of an Impinging Molten Metal Droplet,'' ASME J. Heat Transfer, **118**, pp. 164–172.

[6] Wang, G. X., and Matthys, E. F., 1996, ''Experimental Investigation of Interfacial Thermal Conductance for Molten Metal Solidification on a Substrate,'' ASME J. Heat Transfer, **118**, pp. 157–163.

[7] Madejski, J., 1976, ''Solidification of Droplets on a Cold Surface,'' Int. J. Heat Mass Transf., **19**, pp. 1009–1013.

[8] Kang, B., Waldvogel, J., and Poulikakos, D., 1995, ''Remelting Phenomena in the Process of Splat Solidification,'' J. Mater. Sci., **30**, pp. 4912–4925.

[9] Rangel, R. H., and Bian, X., 1997, ''Metal-Droplet Deposition Model Including Liquid Deformation and Substrate Remelting,'' Int. J. Heat Mass Transf., **40**, pp. 2549–2564.

[10] Wang, S.-P., Wang, G.-X., and Matthys, E. F., 1998, ''Melting and Resolidification of a Substrate in Contact with a Molten Metal: Operational Maps,'' Int. J. Heat Mass Transf., **41**, No. 10, pp. 1177–1188.

[11] Jones, H., 1971, ''Cooling, Freezing and Substrate Impact of Droplets Formed by Rotary Atomization,'' J. Phys. D, **4**, pp. 1657–1660.

[12] Bennett, T., and Poulikakos, D., 1994, ''Heat Transfer Aspects of Splat-Quench Solidification: Modeling and Experiment,'' J. Mater. Sci., **29**, pp. 2025–2039.

[13] Madejski, J., 1983, ''Droplets on Impact with a Solid Surface,'' Int. J. Heat Mass Transf., **26**, pp. 1095–1098.

[14] Mcpherson, R., 1980, ''On the Formation of Thermally Sprayed Alumina Coatings,'' J. Mater. Sci., **15**, pp. 3141–3149.

[15] Waldvogel, J. M., and Poulikakos, D., 1997, ''Solidification Phenomena in Picoliter Size Solder Droplet Deposition on a Composite Substrate,'' Int. J. Heat Mass Transf., **40**, No. 2, pp. 295–309.

[16] Attinger, D., Zhao, Z., and Poulikakos, D., 2000, ''An Experimental Study of Molten Microdroplet Surface Deposition And Solidification: Transient Behavior and Wetting Angle Dynamics,'' Int. J. Heat Mass Transf., **122**, No. 3, pp. 544–556.

[17] Waldvogel, J. M., Diversiev, G., Poulikakos, D., Megaridis, C. M., Attinger, D., Xiong, B., and Wallace, D. B., 1998, ''Impact and Solidification of Molten-

Metal Droplets on Electronic Substrates,'' ASME J. Heat Transfer, **120**, p. 539.
[18] Xiong, B., Megaridis, C. M., Poulikakos, D., and Hoang, H., 1998, ''An Investigation of Key Factors Affecting Solder Microdroplet Deposition,'' ASME J. Heat Transfer, **120**, No. 1, pp. 259–270.
[19] Bach, P., and Hassager, O., 1985, ''An Algorithm for the Use of the Lagrangian Specification in Newtonian Fluid Mechanics and Applications to Free-Surface Flow,'' J. Fluid Mech., **152**, pp. 173–190.
[20] Fukai, J., Zhao, Z., Poulikakos, D., Megaridis, C. M., and Miyatake, O., 1993, ''Modeling of the Deformation of a Liquid Droplet Impinging upon a Flat Surface,'' Phys. Fluids A, **5**, pp. 2588–2599.
[21] Landau, L. D., and Lifshitz, E. M., 1959, *Fluid Mechanics, Course of Theoretical Physics*, Pergamon, Tarrytown, NY.
[22] Bushko, W., and Grosse, I. R., 1991, ''New Finite Element Method for Multidimensional Phase Change Heat Transfer Problems,'' Numer. Heat Transfer, Part B, **19**, pp. 31–48.
[23] Haferl, S., Butty, V., Poulikakos, D., Giannakouros, J., Boomsma, K., Megaridis, C. M., and Nayagam, V., 2000, ''Freezing of Molten Solder Droplets Impacting onto Flat Substrates in Microgravity,'' in *2000 International Mechanical Engineering Congress and Exhibition*, Orlando, FL.
[24] Hayes, D. J., Wallace, D. B., and Boldman, M. T., 1992, ''Picoliter Solder Droplet Dispension,'' in *ISHM Symposium 92 Proceedings*, pp. 316–321.
[25] Hayes, D. J., and Wallace, D. B., 1998, ''Solder Jet Printing: Wafer Bumping and CSP Applications,'' Chip Scale Review, **2**, No. 4, pp. 75–80.
[26] Kang, B., Zhao, Z., and Poulikakos, D., 1994, ''Solidification of Liquid Metal Droplets Impacting Sequentially on a Solid Surface,'' ASME J. Heat Transfer, **116**, pp. 436–445.
[27] Murr, L. E., 1975, *Interfacial Phenomena in Metals and Alloys*, Addison-Wesley, Reading, MA.
[28] Toh, T., 2000, personal communication, Steel Research Laboratories, Nippon Steel, Japan.
[29] Miettinen, J., 1997, ''Calculation of Solidification-Related Thermophysical Properties for Steels,'' Metall. Mater. Trans. B, **28B**, pp. 281–297.
[30] Zhao, Z., Poulikakos, D., and Fukai, J., 1996, ''Heat Transfer and Fluid Dynamics During the Collision of a Liquid Droplet on a Substrate: II-Experiments,'' Int. J. Heat Mass Transf., **39**, pp. 2791–2802.
[31] Zhao, Z., Poulikakos, D., and Fukai, J., 1996, ''Heat Transfer and Fluid Dynamics During the Collision of a Liquid Droplet on a Substrate: I-Modeling,'' Int. J. Heat Mass Transf., **39**, pp. 2771–2789.

Thermal-Fluid Phenomena Induced by Nanosecond-Pulse Heating of Materials in Water

I. Ueno[1]

M. Shoji

Department of Mechanical Engineering,
The University of Tokyo,
7-3-1-Hongo, Bunkyo-Ku, Tokyo 113-8658,
Japan

Thermal-hydraulic phenomena adjacent to the liquid metal-water and solid material-water interfaces induced by nanosecond pulsed Nd:YAG laser (wavelength: 532 nm, FWHM: ~13 ns) heating with the fluence F of $5.0\times10^{1}\sim1.0\times10^{3}$ mJ/cm^2 were experimentally investigated. By applying the high-speed photography with a frame speed up to 2.0×10^{7} fps, the aspects of the bubble formation, shock wave generation and propagation were observed. The bubble formation on the heated material's surface of about 80 nm in diameter was detected in Si-water system from the time-resolved reflection (TRR) signal by applying the pump and probe method. [DOI: 10.1115/1.1409264]

Keywords: Boiling, Heat Transfer, Shock Waves, Vaporization

1 Introduction

High-speed and high-powered heating of materials in water results in an explosive pressure generation as indicated by preceding research [1–5]. In the process of pressure generation, complicated factors in terms of thermal-hydraulic dynamics are involved as follows; abrupt heat transfer in a very narrow region due to a sharp temperature distribution, thermal expansion and phase change of heated material and ambient material. Such problems never raise in a process induced by relatively slow heating on the order of milliseconds to hundreds of microseconds. The remarkable evolution of laser technology enables us the rapid heating on the order of nanoseconds or less with higher and more stable power, which may lead higher impulsive pressure generation with precise control of the intensity. It thus becomes important and indispensable to obtain comprehensive knowledge of the thermal-hydraulic dynamics in ultrafast heating. The details of the physical processes caused by such a rapid heating, however, are not fully understood because of the strong non-equilibrium of the thermophysical state as well as the rapidity of the phenomena.

Experimental and theoretical research concerning the short-pulsed laser heating of solid materials in the air has been extensively performed and has provided profitable results for the elucidation of heat transfer in the heated materials and phase change [6–12]. The short-pulsed laser heating of materials in liquids, on the other hand, brings complexities into the induced processes such as the heat transfer between the two contacting fluids and the successive phase changes of both or volatile liquid, as well as the solid material-laser light interaction. Former research has indicated valuable knowledge concerning the rapid heating of materials in liquids; Board et al. [13] and Duffey et al. [14] evaluated the heat flux and vapor layer thickness induced by millisecond laser pulse heating. As for nanosecond laser-pulse heating, the optical measurement of nucleation and bubble growth were conducted by Yavas et al. [15]. The temperature variation on the heated surface was optically monitored by Park et al. [16] and the generated pressure was measured by use of the photo-acoustic probe-beam deflection by Park et al. [2]. Recently more precise measurements of the bubbles formed on the thin metal surface and the successive generated pressure were carried out by Yavas et al. [5] by use of a surface-plasmon probe. It is noted that such work was conducted with low energy input, resulting in a lower superheated condition of the liquid. Little information has been reported concerning the process induced by laser heating of materials in a liquid with higher energy input, which would bring higher superheating of the liquid near the heated surface and more explosive pressure generation. In addition, there exist few investigations about the rapid heating of liquid materials in an ambient liquid, that is, rapid heating in liquid-liquid system. The vaporization of the heated liquid material may contribute to the induced phenomena due to its low boiling temperature and small latent heat in that system. This paper concentrates upon the thermal-hydraulic phenomena induced by higher energy input in the systems of two contacting materials, the liquid metal-water system and the solid material-water system, which were detected with applying the high-speed photography and the pump and probe method.

2 Experiment

In this research two series of experiments concerning nanosecond-pulse heating of materials as (i) liquid metal or mercury, and (ii) solid material or silicon are carried out. Experimental apparatus is schematically shown in Fig. 1. The apparatus is basically consisted of the same components for the both series. A pulse of second harmonic Nd:YAG laser ($\lambda_{pump}=532$ nm) of 5 mm in diameter is employed as a heat source or ''pump laser'' with the fluence F of $4.0\times10^{1}\sim1.4\times10^{3}$ mJ/cm^2. The pulse width of the pump laser is approximately 13 ns in full width at half maximum (FWHM). Test material submerged in distilled water of 20°C in a cubic tank with the inner size of $100\times100\times100$ mm^3 is irradiated by a single pulse of the pump laser. A quartz window of 1 mm in thickness is placed in the path of the laser light. The direction of impingement of the pulse is perpendicular to the material's surface.

Aspects of induced phenomena are captured by a high-speed electric image converter photographic system with a frame speed of 40,000 to 20,000,000 fps. With this apparatus, eight-successive image frames are obtained in a single run. The event through the object lens is changed into electron beam on the photo-cathode. The beam irradiates the Polaroid film. The capturing of images is controlled by four couples of the electric plates; shuttering, aperture, compensating and shift plates. When the camera is triggered, two sinusoidal waves with π out of the phase are imposed upon the shutter and compensating plates. The wave upon the shutter

[1]Present address of the first author is, Department of Mechanical Engineering Faculty of Sciences & Technology, Tokyo University of Science, 2641 Yamazaki, Noda-Shi, Chiba 278-8510, Japan.

Contributed by the Heat Transfer Division for publication in the JOURNAL OF HEAT TRANSFER. Manuscript received by the Heat Transfer Division May 7, 1999; revision received April 27, 2001. Associate Editor: P. Ayyaswamy.

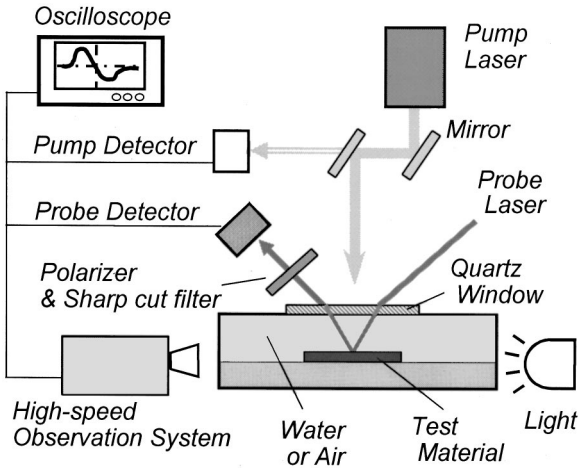

Fig. 1 Schematic layout of experimental apparatus for nanosecond-pulse heating of materials. Pressure transducer is omitted in the figure for the sake of brevity (see Fig. 2).

plates controls the frame speed and the aperture period, and another one upon the compensating plates does the vertical position of the images on the film. Two successive images up and down on the film are captured during a single period of the sine wave. The step wave upon the shift plates, which is synchronized with the sinusoidal wave, slides the next pair of images horizontally.

Generated pressure is detected by PVDF pressure transducer with the sensitivity of 14.8 mV/MPa (rise time $<$50 ns) at about 9 mm apart from the heating spot on the material surface. The description of the transducer is omitted in Fig. 1. The transducer is confirmed in advance to detect the generated pressure wave itself first and not to be influenced by the reflected pressure waves by the tank wall or by the quartz window. In order to estimate the pressure decay in propagation, the distance between the pressure transducer and the heated spot is varied. The detail description is conducted in the following section.

In the series of mercury heating, the experiments are carried out in an open tank as well as the closed one. The mercury thickness is varied from 5 mm to 20 mm in order to evaluate the thickness effect for the pressure generation and mercury surface behavior. Water layer thickness is fixed as 50 mm, which is assessed in a preliminary test to have little influence of the water surface behavior upon the fluid motion adjacent to Hg-water interface. This water-thickness effect on the mercury surface behavior was discussed by Ueno et al. [3]. The water temperature is fixed at 20°C and the water is put into the tank just before the laser impingement. It is confirmed that as the water temperature increases the water layer absorbs the passing laser light and thus the intensity of induced pressure decreases remarkably, because the solubility of mercury increases at higher water temperature.

In the series of silicon heating, on the other hand, the ''pump and probe method'' is employed as well as the high-speed photography. The *p*-polarized continuous He-Ne laser light with a different wave length from the pump laser ($\lambda_{probe}=632.8$ nm) is employed as a ''probe laser.'' The probe laser of almost 1 mm in diameter irradiates the center of the heated area by the pump laser at an fixed angle of incidence of about 10 deg, at which the reflectivity is almost the same as that at the perpendicular incident angle [15]. The intensity of the probe laser is weak enough compared with that of the pump laser, so that the influence of the probe-laser irradiation upon the induced phenomena is completely negligible. Time-resolved reflectance (TRR) signal of the probe laser is detected by a fast photo detector at a fixed angle. The detector is composed by Si PIN photo diodes (rise time $<$1 ns). In measuring the intensity of the TRR signal, a polarizer and a sharp-cut filter are placed in front of the detector for the probe laser light (''probe detector'') in order to shut off the light of the pump laser scattered on the silicon surface. The energy profile of the pump laser is measured by another photo detector (''pump detector'') fixed just behind the beam splitter. All signals are obtained by a fast digitizing oscilloscope with a sampling rate up to 2 G Sa/s.

3 Results and Discussions

3.1 Pressure Decay in Propagation. The generated impulsive pressure is detected by the PVDF pressure transducer located at about 9 mm apart from the center of the heated spot on the material surface. In order to evaluate the pressure decay in its propagating in the container, the distance *d* between the transducer and the spot center is varied as shown in Fig. 2(*a*). In varying the position, only the normal distance l_n is changed. The direction of the transducer head is aimed to the heated-spot center. A typical result of the propagation in Hg-water system is presented in Fig. 2(*b*). The intensity of the generated pressure decays exponentially as a function of the distance. The pressure-wave front propagates at an averaged speed of about 1.7×10^3 m/s. The pressure decay as well as the propagating speed is almost the same in the whole experimental conditions. One can thus estimate the pressure value at the very close region to the heated surface by extrapolation. In what follows in this paper the generated pressure is discussed in terms of the extrapolated value.

3.2 Liquid Metal Heating

3.2.1 Observation by High-Speed Camera. Figures 3(i) and (ii) show the typical high-speed photographs taken with the three different frame speeds when 10 mm thick mercury was heated with the laser fluence *F* of 1.4×10^3 mJ/cm^2 and 2.0×10^2 mJ/cm^2, respectively. The frame speed is varied as (*a*) 40,000 fps, (*b*) 1,000,000 fps, and (*c*) 4,000,000 fps. The exposure time to take the pictures in Figs. 3(*a*) and (*b*) is 150 ns and that in

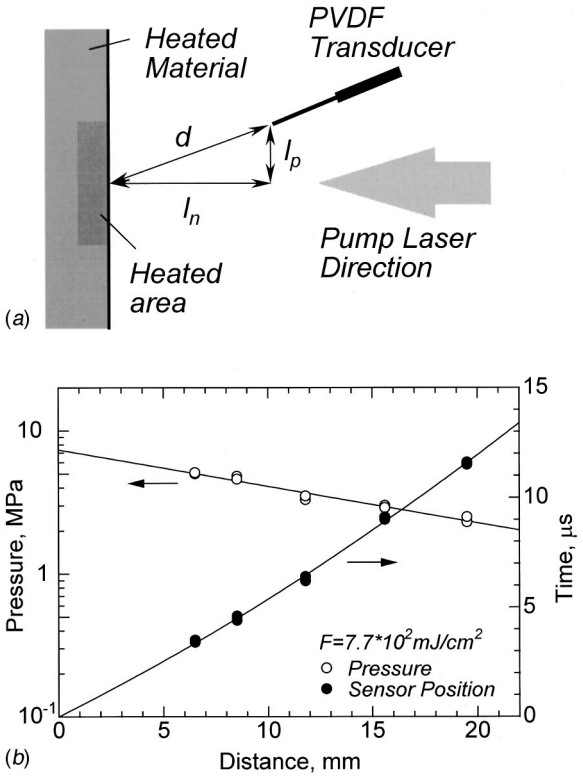

Fig. 2 (*a*) Schematic layout of PVDF pressure transducer; and (*b*) typical result of the pressure decay in propagation.

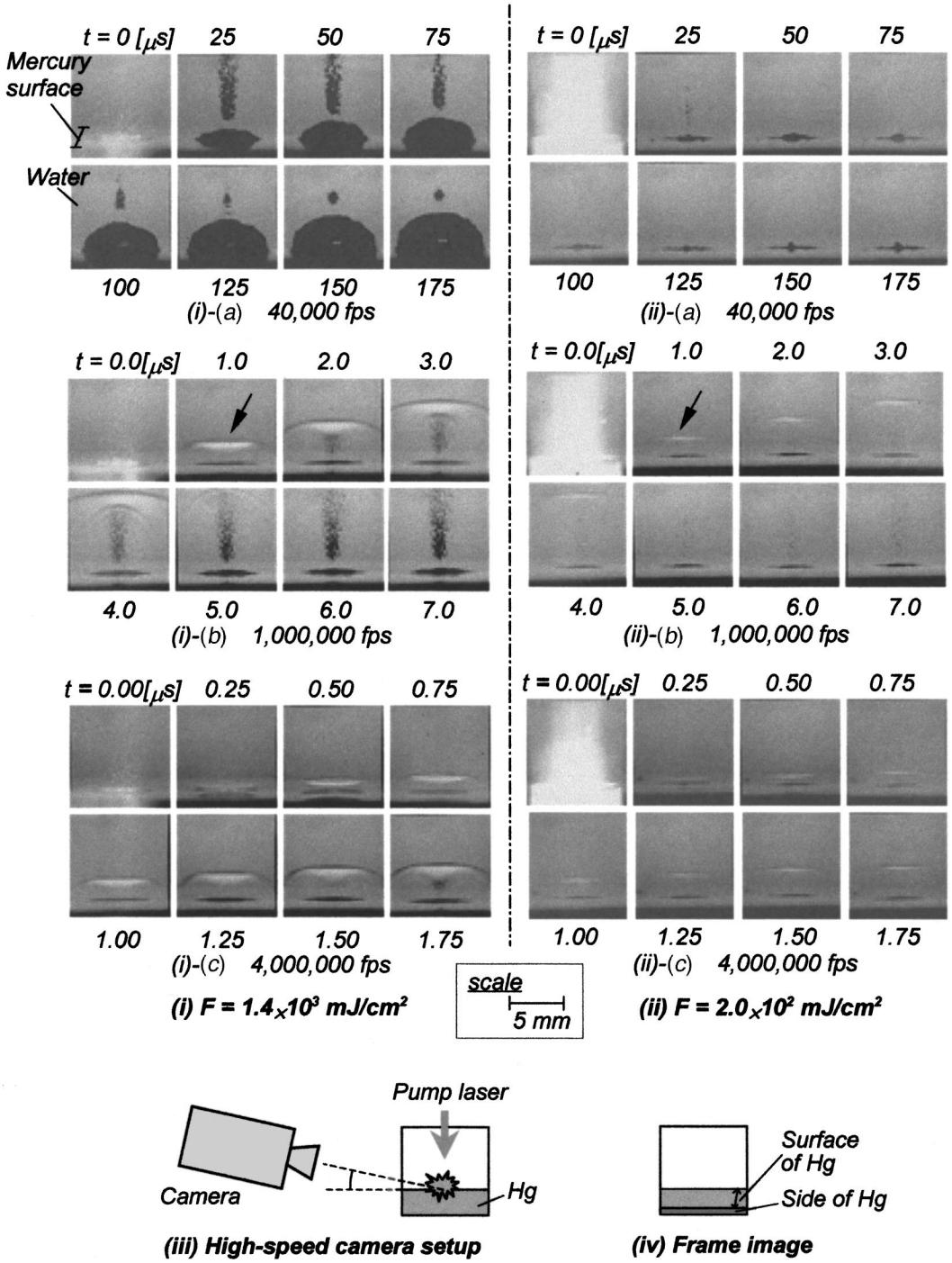

Fig. 3 Bubble formation and shock wave generation/propagation in heating with (i) $F=1.4\times10^3$ mJ/cm^2 (on the left hand side) and (ii) $F=2.0\times10^2$ mJ/cm^2 (on the right) taken with frame speeds of (*a*) 40,000 fps [exposure time: 150 ns], (*b*) 1,000,000 fps [150 ns], and (*c*) 4,000,000 fps [100 ns] in the system of $\Delta Hg=10$ mm and $\Delta H_2O=50$ mm. All photographs were taken with a little depression angle as shown schematically in (iii). (iv) The image captured in each frame.

Fig. 3(*c*) is 100 ns. The time shown above/below frame indicates the time passing since the beginning of the pump-laser irradiation at $t=0$. It is noted that the pulse length of the pump laser is of the order of ten nanoseconds so that the only first frame captures the irradiation. In the figure, in addition, (iii) the schematic layout of high-speed camera and test material and (iv) the sketch of the frame image shown in (i) and (ii) are presented. According to Figs. 3(i)-(*a*) and (ii)-(*a*), the vaporization of the mercury is observed for a relatively long time period on the heated surface. The intensity of phase change or vaporization decreases as the laser fluence F decreases. Although there exists a difference of the vaporization intensity due to the laser fluence difference, the characteristics of the induced event, that is, the shock wave generation as well as the vaporization, are of almost the same in quality as shown in Figs. 3(*a*) to (*c*). The detail descriptions of the event are conducted with the pictures in Fig. 3(i) in what follows. In the case of (i) $F=1.4\times10^3$ mJ/cm^2, the explosive bubble formation is observed following the shock wave propagation. Figure 3(*a*) con-

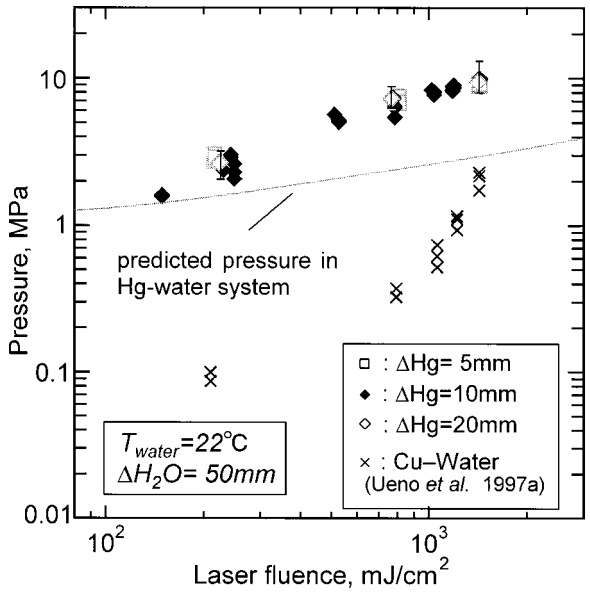

Fig. 4 Generated pressure variations upon pump laser fluence *F* in Hg-water system in different Hg layer thicknesses. Plotted values are equivalent to the extrapolated pressure values measured at the surface. Solid line in the figure indicates the prediction of the pressure generation in heating of Hg in water [17].

sists of the whole stages of the semi-sphere shaped bubble formation. The early stage of the event as shown in the first two frames in Fig. 3(*a*) is presented in Fig. 3(*b*). The shock wave appears subsequently to the laser irradiation on the mercury surface. Tiny bubbles are formed right behind the propagating shock wave. The formation of the tiny bubbles, which is also seen in Fig. 3(*a*), can be explained by considering the abrupt pressure fall behind the shock wave front. Figure 3(*c*) shows the further early stages of the shock wave propagation. The shock wave emerges just above the heated spot with almost the same shape as the spot. The wave propagates as the almost plain wave at the beginning, then the wave travels with having the curvature at the edge. The shock-wave propagation speed is estimated by the high-speed photographs and by changing the position of the pressure transducer to be 1.7×10^3 m/s. The speed has little dependence upon the laser fluence *F* in this experimental range. The description of the event after the bubble collapse on the heated surface was conducted by Ueno et al. [3].

3.2.2 Pressure Generation. The intensity of the generated explosive pressure versus the laser fluence *F* is shown in Fig. 4. The plotted pressure values are extrapolated ones, which are evaluated values, as aforementioned, equivalent to those just after the appearance on the heated surface. The figure consists of the results for the cases with different mercury-layer thickness. In addition, the figure involves the pressure values in the case that the solid copper was heated in the same system [3]. The solid line in the figure shows the prediction of the pressure generation obtained by a physical model [17] applied to the Hg-water system.

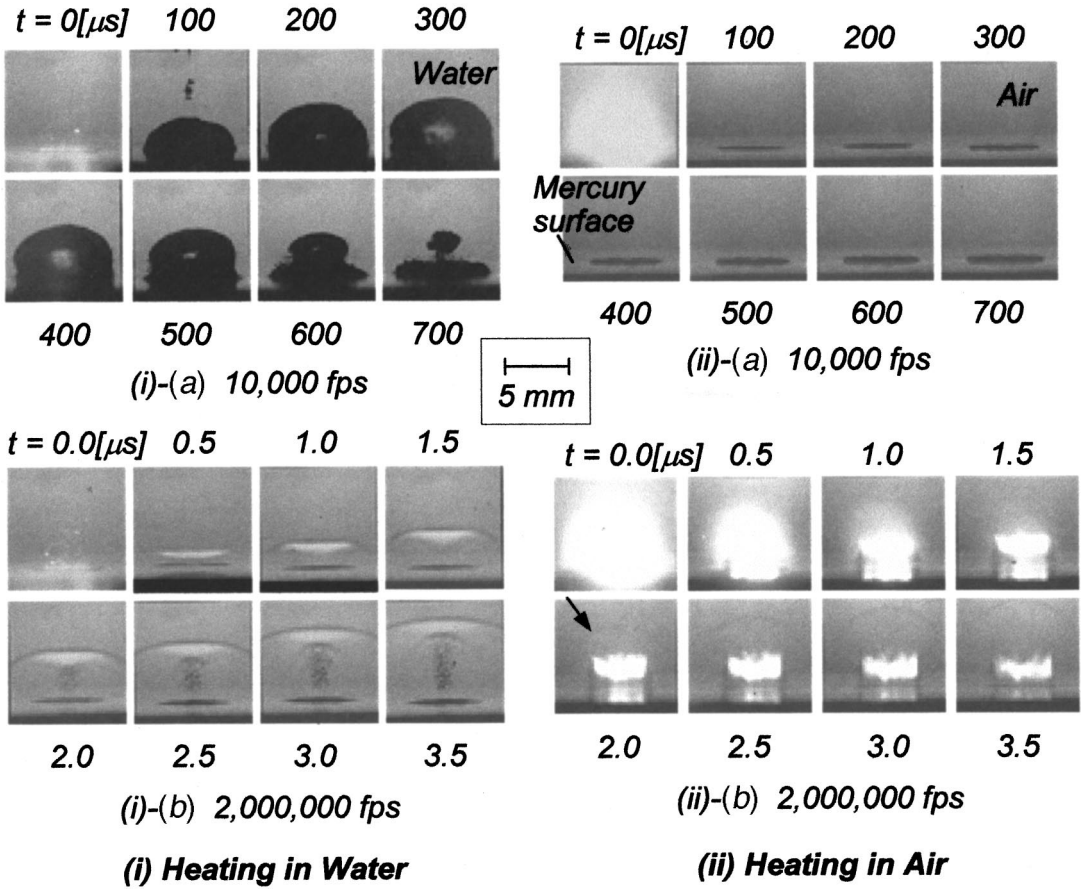

Fig. 5 Mercury surface heating (i) in the water (on the left hand side) and (ii) in the air (on the right) taken with frame speeds of (*a*) 10,000 fps [exposure time: 150 ns], and (*b*) 2,000,000 fps [150 ns]. Pump laser fluence $F=1.4\times10^3$ mJ/cm^2 for both cases.

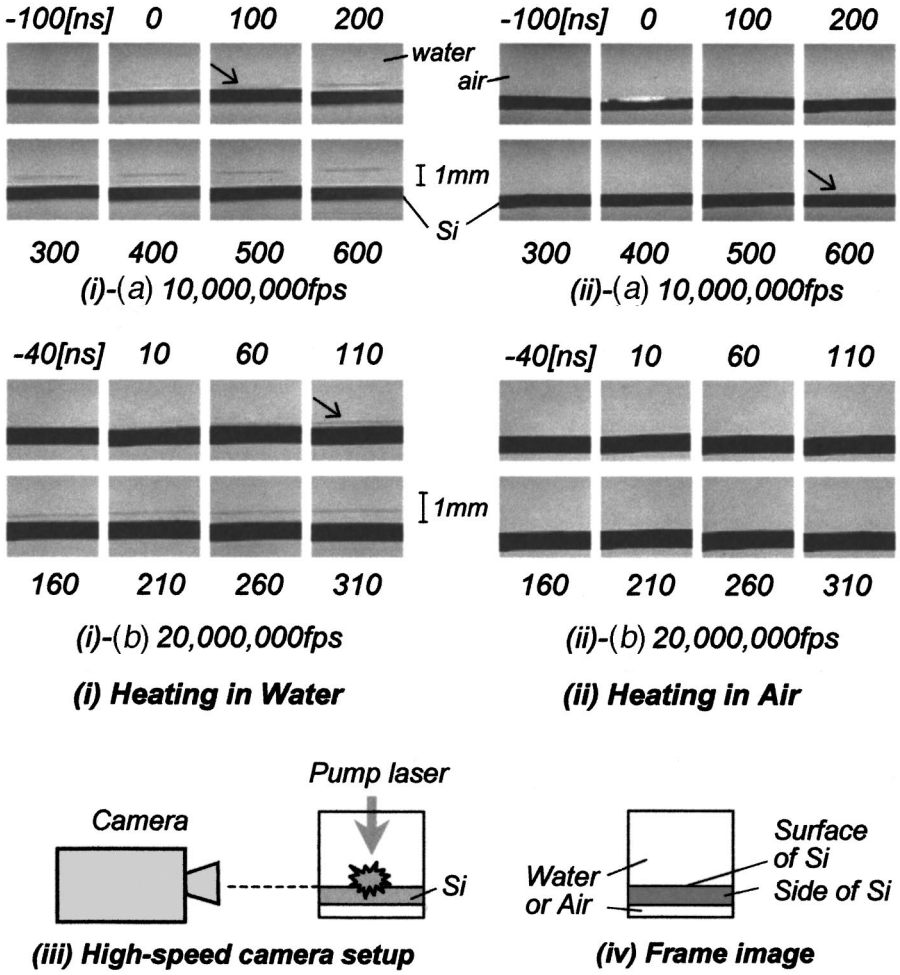

Fig. 6 Shock wave generation/propagation in heating of Si of 0.6 mm in thickness with $F=2.0\times10^2$ mJ/cm^2 (i) in the water (on the left hand side) and (ii) in the air (on the right), taken with frame speeds of (*a*) 10,000,000 fps [exposure time: 20 ns] (top), and (*b*) 20,000,000 fps [10 ns] (middle). All photographs were taken with an angle parallel to the Si surface as shown schematically in (iii). (iv) The schematic image captured in each frame.

In thismodel the abrupt vaporization is assumed to dominate the explosive pressure generation. The generated pressure by heating of materials increases as the laser fluence F increases. The thickness of the mercury layer has little influence upon the pressure generation. In spite of the large difference of the absorption coefficients $\kappa_{Hg} \ll \kappa_{Cu}$, the intensities of the events in Hg-water system are obviously stronger than in the Cu-water system.

3.2.3 Heating of Mercury in Air. Another series of experiments in which the mercury surface is irradiated in the open boat is conducted. In this system the vaporization of the metal yielded the induced phenomena as observed in the cases of heating of solid metal [18,19,7,8,20].

A mercury layer of 10 mm in thickness is placed in the same rectangular tank as the Hg-water experiments. Figure 5(ii) shows the aspects of the heating of the mercury in the air with the same laser fluence F as the case shown in Fig. 3(i) taken with the exposure time of 150 ns with the different frame speeds. In order to make a comparison, the induced events in Hg-water system with the same F taken with the same frame speeds are shown in the figure (i). It is noted again that these photographs are taken at a little depression angle and each frame image corresponds to that as shown in Fig. 3(iv). According to Fig. 5(ii)-(*a*), no certain violent fluid motion on the mercury surface for a relatively long period is observed such as the bubble formation and collapse as shown in the figure (i)-(*a*). One could observe a certain morphological change with a circular shape of almost the same size as the laser spot. Figure 5(ii)-(*b*) shows the early stage of the events. Noted again that the laser irradiation is captured only in the first frame with considering the inter-frame time, the exposure time and the laser pulse length. The light emission is observed after the irradiation above the heated spot, which lasts about several microseconds with decaying. This emission can be explained by a high-temperature plasma formation formed right above the mercury surface. The plasma absorption of the laser energy and resulting thermal plasma radiation enhance the energy delivery to the heated surface, which is more efficient than heat transfer due to the surface absorption alone [12]. The emitting body in shape of cylinder-like, is formed with almost the same diameter as the heating laser pulse. On the contrary such a light emission lasting for microseconds is not observed when the mercury is heated in the water. The water layer prevents the mercury vaporization and plasma formation. The shock wave propagation is observed, with having a larger curvature than that of in the water, above the light emitting body. The propagation speed of the shock wave is estimated to be over 1.5×10^3 m/s.

According to Fig. 3 and Fig. 5, the pressure generation in heating of the mercury in the water can be yielded by the abrupt vaporization of water and/or mercury. Although the plasma formation is not observed obviously in Hg-water system, even slight ionization of the metal vapor can trigger the plasma absorption,

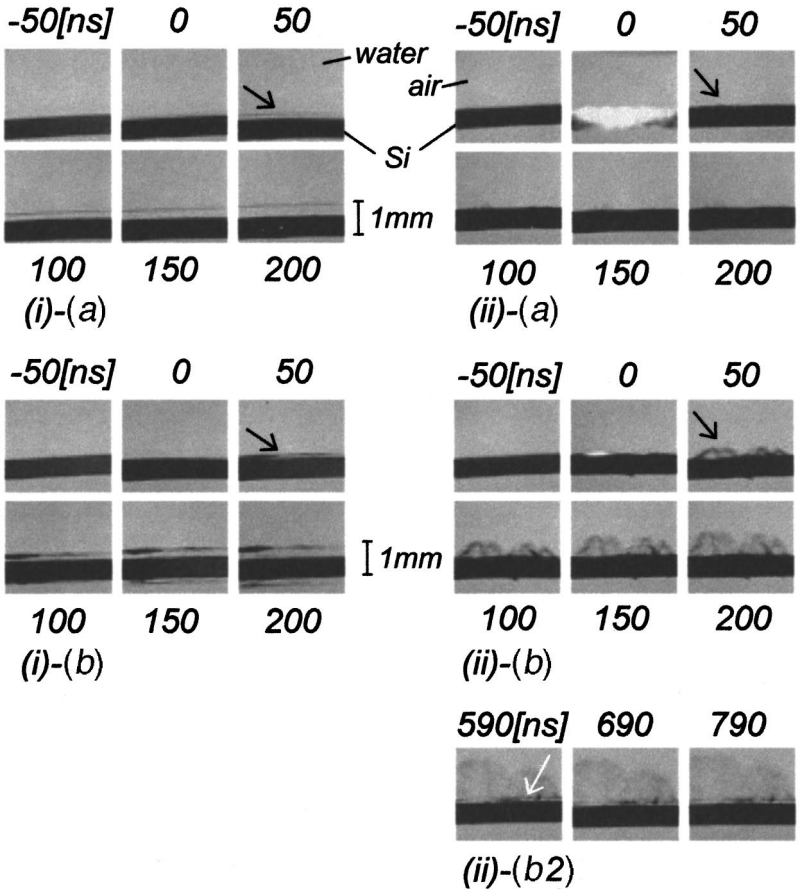

Fig. 7 Shock wave generation/propagation and Si vaporization in heating of Si (i) in the water (on the left hand side) and (ii) in the air (on the right) with the pump laser fluence $F=(a)3.8\times10^2$ mJ/cm^2 (top), and (b) 7.1×10^2 mJ/cm^2 (middle) taken with a frame speed of 20,000,000 fps [exposure time: 10 ns]. Arrows in (i)–(a) and (i)–(b) indicate the generated shock waves and those in (ii)–(a) and (ii)–(b) indicate the Si vapor, respectively. In (ii)–($b2$) the later stage of induced phenomenon in the same case of (ii)–(b) Si-air system is shown. Arrow indicates the shock wave. All photographs were taken with an angle parallel to the heated Si surface.

which would facilitate the energy transfer from the laser beam to the metal. The plasma formation in the water would play an important role for heating of the mercury in the water and for the resulting phenomena.

3.3 Solid Material Heating

3.3.1 Observation by High-Speed Camera. The description of induced events just after the irradiation of solid silicon surface is conducted in this section. The typical high-speed photographs taken with different frame speeds when 0.6 mm-thick silicon is heated with the laser fluence $F=2.0\times10^2$ mJ/cm^2 (i) in the water and (ii) in the air are shown in Fig. 6. The time shown above/below frame indicates the time passage from the beginning of laser irradiation at $t=0$. In the figure, the schematic layout of the high-speed camera and test material is presented in (iii), and the schematics of the frame image of (i) and (ii) is shown in (iv). In the Si-water system, the shock wave is generated above the heated area just after the beginning of irradiation and propagates at the speed of 1.5×10^3 m/s, almost the same as the sound speed in the water. The spatial distribution of shock-wave intensity seems uniform. In the Si-air system, on the other hand, the shock-wave front appears in view at about 600 ns and it travels at about 3×10^2 m/s, almost the same speed of sound in the air. The shock-wave intensity seems remarkably weaker than that in the Si-water system. According to these observations, the generation of the shock wave in the Si-water system is dominated by the sudden phase change of water lied on the heated surface. The contribution of the thermal expansion and vaporization of silicon is negligibly small. In this time scale, one can observe only the shock-wave generation and propagation as the resultant fluid behavior. Any convective motion of the ambient fluid is not seen. That means the compressibility and inertia prevail the concerned fluid behavior.

Figure 7 indicates the high-speed photographs capturing the phenomena in heating with (a) 3.8×10^2 mJ/cm^2 and (b) 7.1×10^2 mJ/cm^2 in the case of (i) Si-water system and (ii) Si-air system. Noted that those fluences are higher than those in the case shown in Fig. 6. The experimental layout and captured frame images correspond to those in Fig. 6. As shown in Fig. 7(i)-(a), the observed events in the Si-water system are almost the same as shown in Fig. 6(i). A plane shock-wave front appears and propagates at a speed of 1.5×10^3 m/s. In the Si-air system, (i)-(b), on the other hand, the vaporization of silicon is observed as indicated by an arrow. In increasing F, the intensity of shock wave exhibits a spatial variation in the Si-water system, which is seen in (ii)-(a). The distribution of the intensity corresponds to the silicon vaporization taken place non-uniformly as shown by the arrow in the third frame of (ii)-(b), which might be due to the spatial distribution of pump laser intensity. Figure 7(ii)-($b2$) shows the relatively

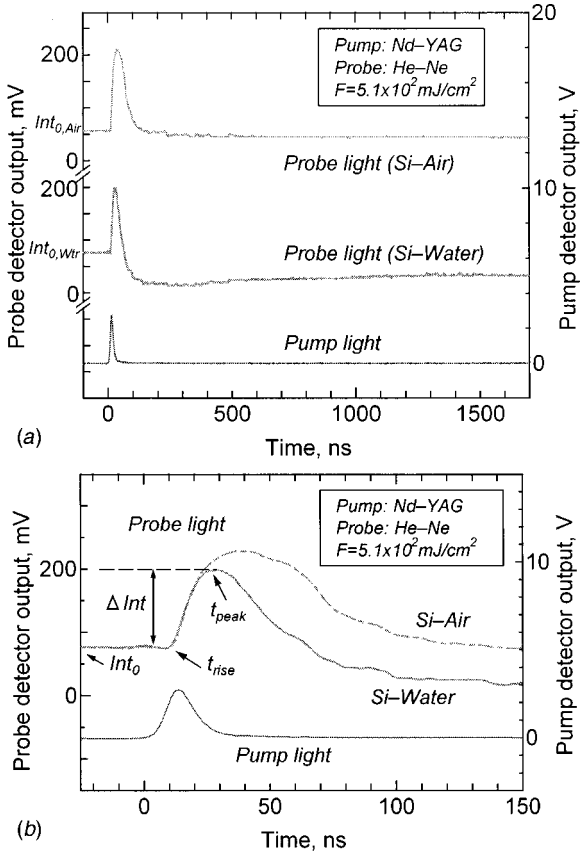

Fig. 8 (*a*) Time-resolved reflectance (TRR) signals (top and middle) of probe laser in the case of heating with $F=5.1\times10^2$ mJ/cm^2. Top curve and the middle indicate the cases of Si-air system and of Si-water system, respectively. The bottom shows the pump-laser light profile. (*b*) Detail of reflectance signals as shown in (*a*). Noted that TRR signal detected in the Si-air system is offset to coincide with the initial intensity in the Si-water system for the sake of convenience for comparison.

later stage of the events in heating of the silicon in the air. It should be noted that shock wave appears in view behind the diffusing silicon vapor, which is indicated by the white arrow. Such a kind of feature is not demonstrated in heating of the mercury in the air as indicated in Fig. 6(ii)-(*b*).

3.3.2 TRR Signal Measurements and Estimations. Estimation of the time-resolved reflectance (TRR) signals coupled with the results of high-speed observations is carried out in this section. Figure 8(*a*) shows the typical 632.8 nm TRR signals for a long time period in the case of $F=5.1\times10^2$ mJ/cm^2. Noted that qualitative features of TRR signals in this experimental range of F are almost the same. The top curve and the middle one correspond to the results in the Si-air system and in the Si-water system, respectively. The pump laser profile is shown at the bottom. The detecting time of the pump laser by the pump detector is equivalent to $t=0$. In the Si-air system, the intensity of the TRR signal increases after the irradiation and then falls to the initial value $\mathrm{Int}_{0,\mathrm{air}}$. This tendency corresponds with the result of Jellison et al. [20]. This can be translated as following; TRR-signal increase is caused by the increase of reflectivity due to the temperature rise of Si surface. After the heating period, the surface temperature decreases due to the thermal diffusion, which results in the decrease of the reflectivity towards the initial value. In this experimental range in the Si-air system the TRR intensity decreases below the Int_0 in the case of heating with the fluence $F>7\times10^2$ mJ/cm^2, which is explained that no morphological changes on the surface take place in the range of $F<7\times10^2$ mJ/cm^2. In the Si-water system, on the other hand, after the increase of the signal, the intensity falls down abruptly below the initial reflection-intensity $\mathrm{Int}_{0,\mathrm{Wtr}}$. A subsequent slow rise towards $\mathrm{Int}_{0,\mathrm{Wtr}}$ is then observed. Such a trend corresponds with the results of Yavas et al. [15]. The high-speed observation as shown in Figs. 6 and 7 reveals experimentally that this abrupt fall is not caused by either shock wave generation or silicon vapor plume above the heated surface. The probe-laser light is thus scattered by certain objects in the Si-water system. As indicated in previous work, this abrupt fall is dominated by Mie scattering owing to the water bubbles larger than $\lambda_{\mathrm{probe}}/2\pi n_{\mathrm{liq}}\equiv R_{\mathrm{Mie}}$ [14,5]. The intensity rises back to the initial value during the condensation and/or collapse of the bubbles. The bubble growth rate and the quantity of generated bubbles increase by increasing F so that the scattering period becomes longer. In the cases of $F>5.1\times10^2$ mJ/cm^2 the intensity does not rise back to $\mathrm{Int}_{0,\mathrm{Wtr}}$ but converges to the lower value. Certain morphological changes are observed on the surface after the experiments.

Figure 8(*b*) details the TRR signals at the early stage of the event in the same case as shown in Fig. 8(*a*). The TRR signal detected in the Si-air system is offset to coincide with the initial intensity in the Si-water system shown as Int_0 in the figure. A sharp rise which started at about 10 ns (shown as t_{rise} in the figure) is captured in both signals. It is noted that the onset time of intensity rising, t_{rise}, and the increasing rate of the intensity are almost coincident in both systems. At the early stage of the heating in both cases the temperature variation of Si contributes the increase of TRR intensity. The start of the intensity decrease in the Si-water system, at the time t_{peak} shown in the figure, is dominated by the scattering of the probe-laser light by the bubbles larger than $R_{\mathrm{Mie}}\approx80$ nm as aforementioned. Thus the onset time of the nucleation must lie between t_{rise} and t_{peak}, although the accurate nucleation time cannot be determined by this series of experiments with the pump and probe method.

In order to exclude certain time lags due to the measuring system involved in the detected signals, the traveling times of the pump and probe-laser lights, and the time lags involved in the photo detectors are taken into account as shown schematically in Fig. 9(*a*). Assuming that the pump laser arrived in front of the photo-detecting element of the pump detector at $t=t_0$, the traveling time of pump light between the pump detector and the Si surface is $t_A(=d_1/c)$, the traveling time of probe light between the Si surface and the probe detector is $t_B(=d_2/c)$, where d_1 and d_2 indicate the distances between the pump detector and the Si surface, and between the Si surface and the probe detector, respectively. Noted that the pump detector is located right behind the beam splitter. The time lag involved in the pump detector from the capturing of the light to the delivering of the signal to the oscilloscope is Δ_A, and the one involved in probe detector is Δ_B. In addition, a time lag between the irradiation of the pump laser and the temperature change, and between the temperature change and the optical property change are assumed as τ_1 and τ_2, respectively. The time t_{rise} when the TRR signal intensity rises is then described as $t_{\mathrm{rise}}=(\tau_1+\tau_2)+(\Delta_B-\Delta_A)+(t_A+t_B)$ as shown in the figure (*b*). The flight time of the lights (t_A+t_B) is derived by measuring the distances d_1 and d_2, and $(\Delta_B-\Delta_A)$ is estimated by the pump-laser pulse measurements with the pump and probe detectors located just behind each beam splitter. The variations of t_{rise}, t_{peak} and time-lag$\equiv(\Delta_B-\Delta_A)+(t_A+t_B)$ versus laser fluence F are indicated in Fig. 10. It can be seen that t_{rise} variation is almost equivalent to the time lag variation, which means that t_{rise} is almost equivalent to the beginning time of the pump laser irradiation of the Si surface. Therefore, the time of $(t_{\mathrm{peak}}-t_{\mathrm{rise}})$, which is also shown in the figure, can be approximately translated into the time when bubbles of the order of 80 nm in radius appear on the Si surface. An accurate evaluation of $(\tau_1+\tau_2)$ is beyond resolution in this experimental apparatus.

3.3.3 Temperature Field in Laser Heating. Now the correlation between TRR signal and the temperature variation of the irradiated surface is considered. First of all, the temperature field

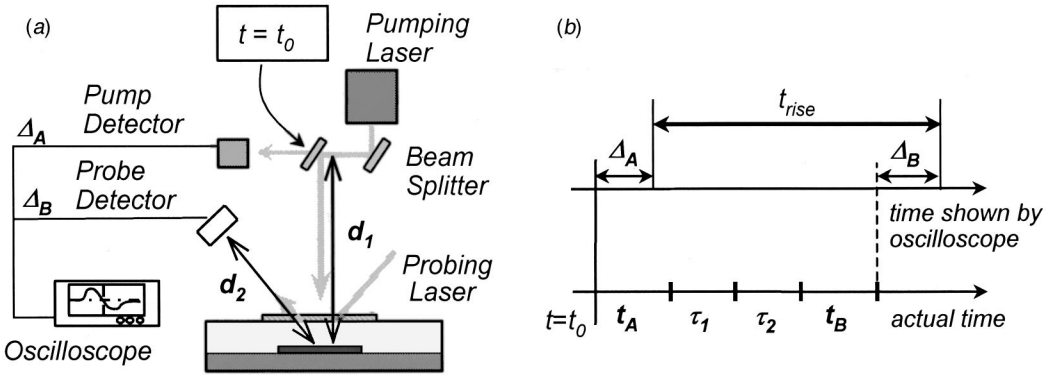

Fig. 9 (*a*) **Schematic of time lags due to the light travels along the paths of pump laser and probe laser and time lags due to photo detectors.** d_1 **and** d_2 **indicate the distances between pump detector and test material surface, and between probe detector and test material surface, respectively.** Δ_A **and** Δ_B **indicate time lags involved in pump detector and probe detector, respectively.** (*b*) **Estimation of time lags involved in the measuring system.** $t_A(=d_1/c)$ **and** $t_B(=d_2/c)$ **are equivalent to flight time along** d_1 **and** d_2**, respectively.**

induced by the laser heating must be described. At the center of the irradiated area, the heat transfer can be assumed essentially one-dimensional [15] taking the thermal penetration depth during the heating period into account. The temperature profiles in the heated material and in the ambient liquid or water are calculated by use of one-dimensional Fourier's heat conduction equations as follows assuming that the water region is transparent for second harmonic Nd:YAG laser of 532 nm in wavelength:

$$(\rho c_p)_\zeta \frac{\partial T_\zeta}{\partial t} + \frac{\partial q_\zeta}{\partial x} = \omega(t,x) \quad \text{(in heated material)}$$

$$(\rho c_p)_{\mathrm{Wtr}} \frac{\partial T_{\mathrm{Wtr}}}{\partial t} + \frac{\partial q_{\mathrm{Wtr}}}{\partial x} = 0 \quad \text{(in water)}$$

$$q_\xi = -\lambda_\xi \frac{\partial T_\xi}{\partial x},$$

where ω is the heat source term described below with the assumption that the incident pump laser light has an uniform spatial profile, subscript ζ and Wtr indicate the heated material and water, respectively. Subscript ξ shows heated material ζ or water Wtr.

The heat source term is described as following:

$$\omega(t,x) = I(t)\cdot(I-R)\kappa \exp(-\kappa x) \quad :(0 \leqslant t \leqslant t_l)$$
$$= 0 \quad :(t_l \leqslant t)$$

where $I(t)$ is the temporal intensity of incident light of the pump laser, R the reflectivity of the heated material in water, κ the absorption coefficient, and t_l the pulse duration of the pump laser.

Though the actual intensity profile can be described as a temporal Gaussian profile, it is further assumed that the laser fluence F is distributed with a triangle shape proposed by Ho et al. [11].

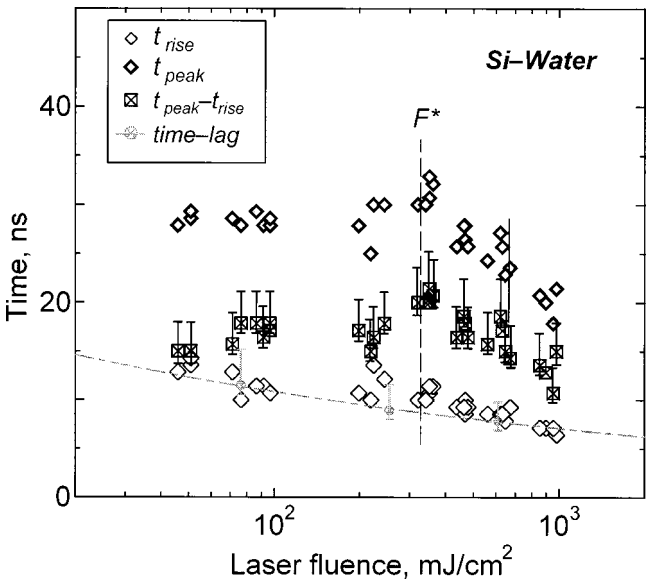

Fig. 10 Variations of t_{rise} **(time when TRR signal rises),** t_{peak} **(time when TRR signal reaches maximum),** $t_{\mathrm{peak}}-t_{\mathrm{rise}}$ **and time lag** $(\Delta_B-\Delta_A)+(t_A+t_B)$ **lied in the measuring system as shown in Fig. 9 in the Si-water system.**

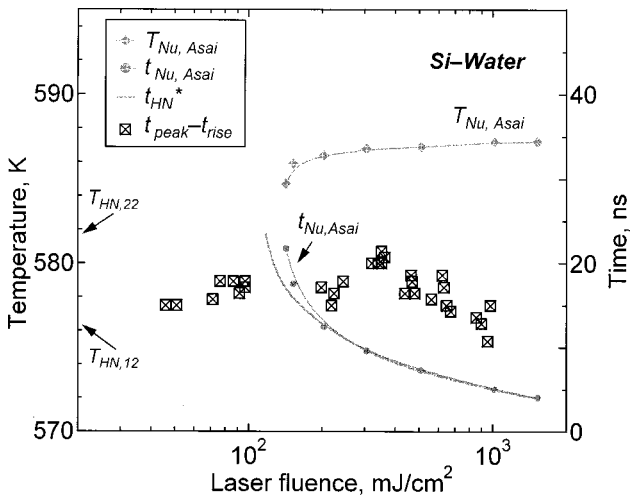

Fig. 11 Nucleation threshold temperatures $T_{\mathrm{HN,12}}$ **and** $T_{\mathrm{HN,22}}$ **obtained from the conventional thermodynamics, the theoretical nucleation temperature** $T_{\mathrm{Nu,Asai}}$ **derived from heterogeneous nucleation theory in the field with temperature distribution by Asai [23], the corresponding nucleation times** t^*_{HN} **and** $t_{\mathrm{Nu,Asai}}$ **variations in the case of Si-water system, and the measured value of** $(t_{\mathrm{peak}}-t_{\mathrm{rise}})$ **versus pump laser fluence** F**. Nucleation time** t^*_{HN} **indicates the time when Si surface temperature reaches** $T_{\mathrm{HN,12}}$ **in the one-dimensional heat conduction problem.**

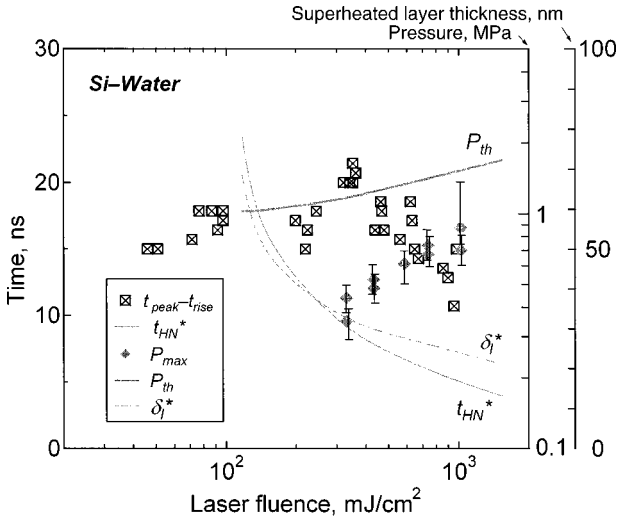

Fig. 12 Experimental results of pressure values P_{max} and the prediction of the generated pressure P_{th} obtained by applying the physical model [17] to this experimental system. Experimental results of ($t_{peak}-t_{rise}$) and the numerical result of assumed nucleation time t_{HN}^*, as shown in Fig. 10 are also shown. In addition, calculated superheated layer thickness of water δ_l^* when the surface temperature reaches T_{HN} of water is indicated.

Here the pulse duration t_l and the time when TRR intensity reaches maximum t_p are valued from the measurement as 26 ns and 10 ns, respectively. In addition, no phase change in either region is assumed. It should be noted that the authors have also estimated the temperature field by use of one-dimensional hyperbolic heat conduction equations, which has converged into the results by Fourier's law in this experimental range.

3.3.4 Criterion of Onset of Nucleation. The sudden vaporization of superheated water dominates the explosive pressure generation. The criterion of nucleation onset or nucleation temperature must be then considered. Now take thermodynamic analysis concerning the kinetics of the vapor embryo formation process into account. In the conventional homogeneous nucleation theory a certain value of the nucleation rate J is considered as a threshold to determine the nucleation temperature. The nucleation rate J is described as follows [22];

$$J=N_l\left(\frac{3\sigma_l(T)}{\pi m_l}\right)^{1/2}\exp(G(T))$$

$$G(T)=-\frac{16\pi\sigma_l(T)^3}{3k_BT(P_v(T)-P_\infty)},$$

where N_l is the number of liquid molecules per unit volume, σ_l the surface tension, m_l the mass of the one liquid molecule, k_B the Boltzmann constant, P_v the vapor pressure and P_∞ the ambient pressure. The homogeneous nucleation temperatures at two different thresholds of nucleation rate are evaluated; $T_{HN,12}$ at $J=10^{12}$ and $T_{HN,22}$ at $J=10^{22}$.

In addition, the heterogeneous nucleation theory with a sharp temperature distribution proposed by Asai [23] is applied to this experimental condition. In his theory, the nucleation temperature, presented here as $T_{Nu,Asai}$, is obtained from the correlation presented as follows:

$$\frac{S_h\lambda_{Wtr}J_{HN}(T_{Nu,Asai})}{q_w(t_{Nu,Asai})T_w(t_{Nu,Asai})\{G'(T_{Nu,Asai})\}^2}=1,$$

where S_h is the heated area, J_{HN} the nucleation rate of the homogeneous nucleation q_w the heat flux on the interface, and T_w the surface temperature.

Figure 11 indicates the nucleation threshold temperatures described above, i.e., temperatures obtained by (i) the conventional thermodynamic homogeneous nucleation theory and (ii) the Asai's theory, and their corresponding times of nucleation (N-time hereafter) when the laser-heated surface temperature reaches those thresholds. The N-time is obtained in the one-dimensional heat conduction problem applied to this experimental system. The N-times at $T_w=T_{HN,12}$ and $T_w=T_{Nu,Asai}$ are presented as t_{HN}^* and $t_{Nu,Asai}$, respectively.

In the case of $F>1\times10^2$ mJ/cm^2, the nucleation threshold temperature of the Asai's theory $T_{Nu,Asai}$ is almost constant at 586 K, which is higher than that of $T_{HN,12}$ and $T_{HN,22}$. Despite the difference of about 10 K between $T_{Nu,Asai}$ and $T_{HN,12}$, the N-times of t_{HN}^* and $t_{Nu,Asai}$ are almost coincide, especially at higher F. This means that that a slight difference of the nucleation threshold temperature up to 10 K has little influence upon the onset time of nucleation in such a rapid heating process. The experimental results of R_{Mie}-size bubble formation time ($t_{peak}-t_{rise}$) exhibit higher values than the N-times while show almost the same trend in increasing F.

In the case of $F<1\times10^2$ mJ/cm^2 in the calculation, the surface temperature of the irradiated material does not reach any nucleation threshold temperatures considered above. Noted that the nucleation threshold temperature does not exist in the Asai's theory at this range of the laser fluence. The experimental results, on the other hand, indicate that the bubbles of about 80 nm in diameter are formed on the heated surface at approximately 20 ns. The bubble formation is revealed by the fact that the TRR signal intensity falls below the initial intensity after it reaches the maximum value in this range of F. This result indicates that the nucleation takes place when the surface temperature reaches a certain temperature less than the homogeneous nucleation temperature $T_{HN,12}$.

3.3.5 Pressure Generation. Figure 12 shows the extrapolated pressure values P_{max} as a function of F. The measured pressure values in the range of $F>F_p=3\times10^2$ mJ/cm^2 are plotted in the figure. Noted that this is because the PVDF pressure transducer cannot detect such a weak pressure, and that this does not mean that any evident pressure is generated in heating with $F<F_p$. The shock wave is actually generated in the case of $F<F_p$, which is confirmed by use of the optical pressure measuring method considering the mirage effect proposed by Park et al. [2]. The generated pressure increases proportionally to the fluence. In the figure the prediction of the generated pressure value P_{th} based upon the physical model [17] applied to this experimental system is presented. In this model the explosive pressure is assumed to be generated by the abrupt vaporization of the superheated layer of the water of δ_l^* in thickness when the surface temperature reaches $T_{HN,12}$. The measured pressure exhibits lower value than the prediction, but has almost the same tendency as a function of F in the range of higher F.

The calculated superheated layer thickness of the water δ_l^* is also indicated in the figure. The superheated layer grows up to several tens of nanometer in thickness in the rapid heating. The thickness almost corresponds to the size of the bubbles scattering the probe light. It is noteworthy that the sudden vaporization of such a thin water layer dominates the explosive pressure generation.

Conclusions

In the present study, thermal-fluid phenomena adjacent to liquid metal-water and solid material-water interfaces induced by nanosecond-pulsed laser heating with the fluence F of 5.0×10^1 $\sim1.0\times10^3$ mJ/cm^2 were investigated experimentally. In the mercury-water system, the shock wave generation and the bubble

formation took place by laser heating. Instantaneous vaporization of water and/or mercury yielded the explosive pressure generation up to 10 MPa and resulting fluid motion. In the silicon-water system, the explosive bubble formation and the resultant shock wave generation were induced by the rapid heating. The variation of the time-resolved reflectance (TRR) signal indicated the heated surface temperature change and the bubble formation at the interface. The high-speed observations revealed that the abrupt fall of TRR signal was caused not by shock wave nor Si vapor above the surface, but by scattering of the light by bubbles of the order of 80 nm in radius. The vaporization of the thin superheated water region of the order of several tens of nanometer led the explosive pressure generation.

Acknowledgments

The authors would like to extend their thanks to Mr. Takao Tsuno and Mr. Yoshio Nakamura at Laboratory for High Speed Photography in the Engineering Research Institute, the University of Tokyo, for their valuable supports for applying the high-speed photography in the series of Si heating experiments. The dedicated contribution in carrying out the experiments by Mr. Koji Ito, Mr. Noriaki Ida and Mr. Yuto Takagi at the University of Tokyo is gratefully acknowledged. One of the authors, Ueno, would like to appreciate the financial support by a Grant-in-Aid for JSPS Fellows from the Ministry of Education, Science and Culture of Japan.

Nomenclature

c = speed of light
c_p = specific heat
d_l = distance between the pump detector and the Si surface
d_2 = distance between the Si surface and the probe detector
k_B = Boltzmann's constant
F = pump laser fluence
I = temporal intensity of incident light of the pump laser
Int = intensity of the TRR signal
J = nucleation rate
m_l = mass of the liquid molecule
n = refractive index
N_l = number of liquid molecules per unit volume
p = pressure
q = heat flux$\equiv -\lambda(\partial T/\partial x)$
R = reflectivity of the heated material in water
R_{Mie} = $\equiv \lambda_{\mathrm{probe}}/2\pi n_{\mathrm{liq}}$
S_h = heated area
t = time
t_A = traveling time of pump laser light between the pump detector and the Si surface
t_B = traveling time of probe laser light between the Si surface and the probe detector
t_l = pulse duration of the pump laser
t_{peak} = time when TRR intensity reaches the maximum value
t_{rise} = time when TRR intensity begins to increase
T = temperature
T_{HN} = homogeneous nucleation temperature of liquid
T_{Nu} = nucleation threshold temperature
x = coordinate in the normal to the heated material surface direction

Greeks

κ = absorption coefficient
Δ_A = time lag involved in the pump detector
Δ_B = time lag involved in the probe detector
δ_l^* = superheated layer thickness in water
λ = thermal conductivity
λ_{probe} = wavelength of the probe laser
λ_{pump} = wavelength of the pump laser
ρ = density
σ = surface tension
ω = heat source term

Subscripts

HN = homogenous nucleation
Hg = mercury region
probe = probe laser
pump = pump laser
Si = silicon region
v = vapor phase of water
w = surface
Wtr = water region
0 = initial
∞ = ambient region

References

[1] Shoji, M., et al., 1995, "Pressure Generation by Rapid Heating of a Metal Wire in Water," *Proc. A Multidisciplinary Int. Seminar on Intense Multiphase Interactions*, pp. 201–206.
[2] Park, H. K., et al., 1996, "Pressure Generation and Measurement in the Rapid Vaporization of Water on A Pulsed-Laser-Heated Surface," J. Appl. Phys., **80**, pp. 4072–4081.
[3] Ueno, I., et al., 1997, "Pressure Generation by Laser Pulse Heating of Liquid Metal in Water," *Proc. Int. Seminar on Vapor Explosions & Explosive Eruptions-AMIGO-IMI- (Sendai, Japan. May 1997)*, pp. 143–148.
[4] Ueno, I., et al., 1997, "Laser Pulse Heating of Metal Surface in Water," *Proc. 4th World Conf. on Experimental Heat Transfer, Fluid Mechanics and Thermodynamics*, Vol. 4, Brussels, Belgium, June 1997, pp. 2027–2033.
[5] Yavas, O., et al., 1997, "Bubble Nucleation and Pressure Generation During Laser Cleaning of Surfaces," Appl. Phys. A, **64**, pp. 331–339.
[6] Wood, R. F., and Geist, G. A., 1986, "Theoretical Analysis of Explosively Propagating Molten Layers in Pulsed-Laser-Irradiated *a*-Si," Phys. Rev. Lett., **57**, pp. 873–876.
[7] Aden, M., et al., 1992, "Laser-Induced Vaporization of a Metal Surface," J. Appl. Phys., J. Phys. D, **25**, pp. 57–65.
[8] Aden, M., et al., 1993, "Laser-Induced Plasma Formation During Pulsed Laser Deposition," J. Phys. D, **26**, pp. 1545–1553.
[9] Park, H. K., et al., 1993, "Transient Optical Transmission Measurement in Excimer-Laser Irradiation of Amorphous Silicon Films," ASME J. Heat Transfer, **115**, pp. 178–183.
[10] Xu, X., et al., 1995, "Transient Temperature During Pulsed Excimer Laser Heating of Thin Films Obtained by Optical Reflectivity Measurement," ASME J. Heat Transfer, **117**, pp. 17–24.
[11] Ho, J. R., et al., 1995, "Computational Study of Heat Transfer and Gas Dynamics in the Pulsed Laser Evaporation of Metals," J. Appl. Phys., **78**, pp. 4696–4709.
[12] Ho, J. R., et al., 1996, "Gas Dynamics and Radiation Heat Transfer in the Vapor Plume Produced by Pulsed Laser Irradiation of Aluminum," J. Appl. Phys., **79**, pp. 7205–7215.
[13] Board, S. J., et al., 1971, "An Experimental Study of Energy Transfer Processes Relevant to Thermal Explosions," Int. J. Heat Mass Transf., **14**, pp. 1631–1641.
[14] Duffey, R. B., et al., 1973, "Measurements of Transient Heat Fluxes and Vapor Generation Rates in Water," Int. J. Heat Mass Transf., **16**, pp. 1513–1525.
[15] Yavas, O., et al., 1994, "Optical and Acoustic Study of Nucleation and Growth of Bubbles at a Liquid-Solid Interface Induced by Nanosecond-Pulsed-Laser Heating," Appl. Phys. A, **58**, pp. 407–415.
[16] Park, H. K., et al., 1996, "Optical Probing of the Temperature Transients During Pulsed-Laser Induced Boiling of Liquids," Appl. Phys. Lett., **68**, pp. 596–598.
[17] Ueno, I., and Shoji, M., 1999, "Experimental Study of Nucleation and Pressure Generation Induced by Nanosecond Laser Pulse Heating of Metal in Water," *Proc. 5th ASME/JSME Joint Thermal Engineering Conf.*, San Diego, U.S.A. March '99, CD-ROM (AJTE99-6357).
[18] Rosen, D. I., et al., 1982, "Coupling of Pulsed 0.35-μm Laser Radiation to Aluminum Alloys," J. Appl. Phys., **53**, pp. 3190–3200.
[19] Singh, R. K., and Narayan, J., 1990, "Pulsed-Laser Evaporation Technique for Deposition of Thin Films: Physics and Theoretical Model," Phys. Rev. B, **41**, pp. 8843–8859.
[20] Yilbas, B. S., 1997, "Laser Heating Process and Experimental Validation," Int. J. Heat Mass Transf., **40**, pp. 1131–1143.
[21] Jellison, Jr., G. E. et al., 1986, "Time-Resolved Reflectivity Measurements on Silicon and Germanium Using a Pulsed Excimer KrF Laser Heating Beam," Phys. Rev. B, **34**, pp. 2407–2415.
[22] Carey, V. P., 1992, *Liquid-Vapor Phase-Change Phenomena*, Taylor & Francis, London, UK.
[23] Asai, A., 1991, "Bubble Dynamics in Boiling under High Heat Flux Pulse Heating," ASME J. Heat Transfer, **113**, pp. 973–979.

A Fractional-Diffusion Theory for Calculating Thermal Properties of Thin Films From Surface Transient Thermoreflectance Measurements

Vladimir V. Kulish
Assistant Professor,
ASME Associate Member
School of Mechanical & Production Engineering,
Nanyang Technological University,
50 Nanyang Ave., Singapore 639798

José L. Lage
Professor,
Mem. ASME
e-mail: JLL@SEAS.SMU.EDU

Pavel L. Komarov
Research Fellow,
Assoc. Mem. ASME

Peter E. Raad
Professor,
Mem. ASME

Box 750337,
Mechanical Engineering Department,
Southern Methodist University,
Dallas, TX 75275-0337

The transient thermoreflectance (TTR) method consists of measuring changes in the reflectivity of a material (thin film) under pulsed laser heating, and relating these changes to the corresponding surface temperature variations. Analytical solutions of the diffusion problem are then used to determine the thermal conductivity of the material following an iterative matching process between the solutions and the experimental results. Analytical solutions are attainable either when the material absorbs the laser energy volumetrically or when the material absorbs the laser energy at the surface. Either solution allows for the determination of only one thermal property (thermal conductivity or diffusivity), with the other one assumed to be known. A new, single, analytical solution to the transient diffusion equation with simultaneous surface and volumetric heating, found using fractional calculus, is presented in a semi-derivative form. This complete solution provides the means to determine the two thermal properties of the material (thermal conductivity and diffusivity) concomitantly. In this preliminary study, the solution component for surface heating is validated by comparison with experimental data for a gold sample using the classical thermoreflectance method. Further results, for surface and volumetric heating, are obtained and analyzed considering a GaAs sample. [DOI: 10.1115/1.1416688]

Keywords: Analytical, Heat Transfer, Laser, Measurement Techniques, Thin Films

Introduction

Obtaining analytical solutions for transient heat diffusion problems within a certain domain is complicated because of the mathematical intricacies involved in solving the differential equation governing the phenomenon (see, for instance, Özisik [1], Kakaç and Yener [2], Poulikakos [3]). Numerical simulations are often the only choice for solving the problem.

When seeking a relationship between temperature and heat flux at a particular location, say at the boundary (surface) of the domain, the diffusion equation must be solved within the entire domain first.

There are practical situations in thermal engineering in which a relationship between surface (local) temperature and heat flux would suffice. Consider for instance the experimental transient thermoreflectance (TTR) method used to determine the thermal conductivity of different materials including thin films (Xu et al. [4], Chen et al. [5], Goodson and Flik [6]). The TTR method consists of heating the surface of the material with a very short laser-pulse and then tracking the time-decay of the surface temperature (by measuring the surface reflectivity). Therefore, the time evolutions of the surface temperature and of the heat flux are known.

The thermal conductivity of the material can then be determined by matching the experimental results (i.e., the time evolution of the surface temperature) to the analytical (theoretical or numerical) solution obtained by solving the transient diffusion equation that models the laser-heating phenomenon. This approach has the following three main limitations:

1 - to find an analytical solution for the surface temperature, one is required to find a solution to the diffusion equation not only for the surface, but for the *entire domain*;

2 - analytical transient solutions, with uniform and constant properties, require the density and the specific heat of the material to be known a priori (if the objective is to find the specific heat—assuming the density is known—then the thermal conductivity must be known; in either case, only one thermophysical property can be determined, i.e., thermal conductivity or specific heat);

3 - a theoretical solution for the TTR method exists only when the laser radiation is assumed to be absorbed at the surface of the film (in which case the material is said to be *opaque*); when the laser radiation is absorbed volumetrically as it penetrates through the material (in which case the material is said to be *semi-transparent*), a numerical simulation approach is followed.

In the following sections, a relatively simple methodology for deriving a single, general, fractional equation relating surface temperature, surface heat flux, volumetric heating and thermal properties (thermal diffusivity *and* thermal conductivity) is presented. This methodology, based on *fractional calculus*, was shown by Lage and Kulish [7] to be extremely effective when applied to solving transient diffusion problems.

The general fractional equation, applied to the TTR method, is shown to alleviate the three limitations of standard analytical solutions described previously. Furthermore, it is shown that the temperature solution to this equation is dependent on two independent groups of thermal properties. Hence, both the thermal diffusivity *and* the thermal conductivity of the material under test can be determined simultaneously, extending the applicability of the TTR method.

Solutions from this new theoretical approach are validated us-

Contributed by the Heat Transfer Division for publication in the JOURNAL OF HEAT TRANSFER. Manuscript received by the Heat Transfer Division August 28, 2000; revision received May 4, 2001. Associate Editor: R. Skocypec.

ing experimental thermoreflectance measurements of a gold sample, with additional solutions obtained for the case of GaAs.

Extraordinary Diffusion Equation

Consider a one-dimensional time-dependent diffusion problem in a semi-infinite medium, with a space and time-dependent volumetric heat source or sink. The diffusion equation, assuming constant and uniform properties, is

$$\frac{\partial T(x,t)}{\partial t}-\alpha\frac{\partial^2 T(x,t)}{\partial x^2}-\frac{\dot{q}'''(x,t)}{\rho c}=0, \tag{1}$$

where $T(x,t)$ is the scalar temperature field, t is the time, α (equal to $k/\rho c_p$), k, ρ, and c_p are, respectively, the thermal diffusivity, the thermal conductivity, the density, and the specific heat of the material being heated, and $\dot{q}'''$ is the volumetric heat sink or source (heat-power per unit volume).

The system is initially at equilibrium, so $T(x,t)=T_0$ for $t\leqslant 0$, where T_0 is a constant and uniform temperature everywhere in the domain. At $x=0$ the boundary condition is one of known heat flux (either adiabatic or uniform nonzero heat flux). For a semi-infinite domain, when $x\to\infty$ the boundary condition is $T\to T_0$.

Implementing the change of variables $\xi=\alpha^{-1/2}x$, and $T^*=T-T_0$, Eq. (1) becomes

$$\frac{\partial T^*(\xi,t)}{\partial t}-\frac{\partial^2 T^*(\xi,t)}{\partial \xi^2}-\frac{\dot{q}'''(\xi,t)}{\rho c}=0, \tag{2}$$

and the initial condition is now written as $T^*(\xi,0)=0$. Taking the Laplace transform of Eq. (2), and using the initial condition $T^*(\xi,0)=0$,

$$\frac{d^2\Theta}{d\xi^2}-s\Theta+Q(\xi,s)=0, \tag{3}$$

where $\Theta(\xi,s)$ is the Laplace transform of $T^*(\xi,t)$, and $Q(\xi,s)$ is the Laplace transform of $\dot{q}'''(\xi,t)/(\rho c_p)$.

Equation (3) is an ordinary differential equation, which is known as the *forced oscillations equation*, commonly found in the field of dynamics (see Kamke [8]). The solution to this nonhomogeneous equation can be written as

$$\Theta(\xi,s)=C_1(s)\exp[\xi s^{1/2}]+C_2(s)\exp[-\xi s^{1/2}]+P(\xi,s), \tag{4}$$

where the two first terms on the right side form the general solution of the associated homogeneous equation, when $Q(\xi,s)=0$, and $P(\xi,s)$ is a particular solution.

For the solution, Eq. (4), to be bounded as $\xi\to\infty$, the parameter $C_1(s)$ must be zero, so

$$\Theta(\xi,s)=C(s)\exp[-\xi s^{1/2}]+P(\xi,s). \tag{5}$$

Hence, the constant $C(s)$ can be written as

$$C(s)=[\Theta(\xi,s)-P(\xi,s)]\exp[\xi s^{1/2}]. \tag{6}$$

On differentiating Eq. (5) with respect to ξ,

$$\frac{\partial\Theta(\xi,s)}{\partial\xi}=-C(s)s^{1/2}\exp[-\xi s^{1/2}]+\frac{\partial P(\xi,s)}{\partial\xi}. \tag{7}$$

Eliminating C in Eq. (7) using Eq. (6), one obtains

$$\frac{\partial\Theta(\xi,s)}{\partial\xi}=-s^{1/2}\Theta(\xi,s)+s^{1/2}P(\xi,s)+\frac{\partial P(\xi,s)}{\partial\xi}. \tag{8}$$

Applying the inverse Laplace transform and restoring the original variables, then

$$\frac{\partial T(x,t)}{\partial x}=\frac{1}{\alpha^{1/2}}\left[\frac{T_0}{(\pi t)^{1/2}}-\frac{\partial^{1/2}T(x,t)}{\partial t^{1/2}}+\frac{\partial^{1/2}p(x,t)}{\partial t^{1/2}}-\frac{p(x,0)}{(\pi t)^{1/2}}\right]+\frac{\partial p(x,t)}{\partial x}, \tag{9}$$

where $p(x,t)$ is the inverse Laplace transform of the function $P(x,s)$.

Invoking the Fourier law together with Eq. (9), a relationship between the heat flux $\dot{q}''$, and the temperature T in any location inside the domain, including the boundary, is obtained.

$$\dot{q}''(x,t)=\frac{k}{\alpha^{1/2}}\left[\frac{\partial^{1/2}T(x,t)}{\partial t^{1/2}}-\frac{T_0}{(\pi t)^{1/2}}-\frac{\partial^{1/2}p(x,t)}{\partial t^{1/2}}+\frac{p(x,0)}{(\pi t)^{1/2}}\right]-k\frac{\partial p(x,t)}{\partial x} \tag{10}$$

An expression for the local temperature $T(x,t)$ can be derived from Eq. (10) by the use of the fractional operator $\partial^{-1/2}(\ )/\partial t^{-1/2}$ and the fractional calculus properties (see [7])

$$\frac{\partial^h}{\partial t^h}\left(\frac{\partial^f g(t)}{\partial t^f}\right)=\frac{\partial^{h+f}g(t)}{\partial t^{h+f}};\quad \frac{\partial^f[t^n]}{\partial t^f}=\frac{\Gamma(n+1)}{\Gamma(n+1-f)}t^{n-f};\quad \frac{\partial^{-1/2}[C]}{\partial t^{-1/2}}=2C\left(\frac{t}{\pi}\right)^{1/2}. \tag{11}$$

The result is

$$T(x,t)=T_0-p(x,0)+p(x,t)+\frac{\alpha^{1/2}}{k}\frac{\partial^{-1/2}\left[\dot{q}''(x,t)+k\dfrac{\partial p}{\partial x}\right]}{\partial t^{-1/2}}. \tag{12}$$

Equations (10) and (12) depend on two distinct groups of thermal properties, namely, $(k\rho c_p)^{1/2}$ and k. Results particular to the zero volumetric heat source/sink case and to the uniform volumetric heat source/sink case can be obtained from Eqs. (10) and (12) by setting $p(x,t)=0$ and assuming $p(x,t)=p(t)$, respectively. The resulting equations are peculiar for depending on one group of thermal properties, $(k\rho c_p)^{-1/2}$. This aspect can be highlighted by re-writing the last term of Eq. (12) as

$$T(x,t)=T_0+T_f(x,t)+T_v(x,t), \tag{13}$$

where the last two terms are the individual contributions from the local heat flux and the local volumetric heat source, respectively,

$$T_f(x,t)=\frac{1}{(k\rho c_p)^{1/2}}\frac{\partial^{-1/2}[\dot{q}''(x,t)]}{\partial t^{-1/2}} \tag{14a}$$

$$T_v(x,t)=-p(x,0)+p(x,t)+\left(\frac{k}{\rho c_p}\right)^{1/2}\frac{\partial^{-1/2}\left[\dfrac{\partial p(x,t)}{\partial x}\right]}{\partial t^{-1/2}}. \tag{14b}$$

Transient Thermoreflectance Method

The TTR method comprises heating the surface of the material under test with a short laser pulse. Part of the radiation energy from the laser is reflected by the surface of the material. The remaining radiation energy is absorbed within the material during the heating process. The surface reflectivity of the material is continuously measured as it changes during the heating process. Relating the relative surface reflectivity variation to the relative surface temperature variation allows one to infer the time variation of the surface temperature from the reflectivity data.

If the heating area is much bigger than the probing area and the properties of the material are considered uniform and constant, the energy balance equation can be considered unidirectional.

The radiation power flux distribution at the surface is Gaussian in time (normal distribution), i.e., $I''(0,t)=I''_b\exp\{-[(t-b)/\sigma]^2\}$, where I''_b— the incidence radiation power flux at $t=b$ —equals $F/(\sigma\pi^{1/2})$, with F being the fluence of the laser irradiation (i.e., radiation energy E per unit of heated surface area A), and b and $(2^{-1/2}\sigma)$ represent the mean value and the standard deviation of the normal distribution, respectively.

Two alternatives exist for modeling the laser heating process. The first and most common alternative is to assume the material as opaque, in which case the material absorbs all the radiation at the surface. In this case, the volumetric (internal) heat source $\dot{q}'''$ of Eq. (1) is set equal to zero. Consequently, $T_v(0,t)=0$ and the surface temperature, from Eqs. (13) and (14), becomes

$$T_s(t)=T_0+\frac{1}{(k\rho c_p)^{1/2}}\frac{\partial^{-1/2}\dot{q}_s''(t)}{\partial t^{-1/2}}, \tag{15}$$

where the surface heat flux (the boundary condition at the surface of the material) is

$$\dot{q}_s''(t)=\frac{F(1-r)}{\sigma\pi^{1/2}}\exp\left[-\left(\frac{t-b}{\sigma}\right)^2\right], \tag{16}$$

where r is the surface reflectivity. Notice that Eq. (15) can be shown to be identical to the solution provided by Özisik [1], p. 77, Eq. (2–138), supporting the validity of the fractional solution with no source/sink term.

The second alternative, normally pursued via numerical simulations, is to consider the material semi-transparent. Hence, the boundary heat flux is set as equal to zero and the laser energy is assumed to be absorbed volumetrically within the material. The energy balance is then identical to Eq. (1) with $\dot{q}'''$, the absorbed laser radiation per unit of volume, expressed as

$$\dot{q}'''(x,t)=I_b''(1-r)\kappa\exp(-\kappa x)\exp\left[-\left(\frac{t-b}{\sigma}\right)^2\right], \tag{17}$$

where κ is the extinction or attenuation coefficient of the material. The Laplace transform of Eq. (17), after dividing it by ρc_p, and using $\xi=\alpha^{-1/2}x$, is

$$Q(\xi;s)=\frac{I_b''}{2\rho c_p}(1-r)\kappa\sigma\pi^{1/2}e^{(-\kappa\alpha^{1/2}\xi)}e^{(\sigma^2/4s^2-bs)}\times\operatorname{erfc}\left[\frac{\sigma}{2}\left(s-\frac{2b}{\sigma^2}\right)\right]. \tag{18}$$

It follows that

$$P(\xi;s)=\frac{\tilde{Q}(s)}{s-\kappa^2\alpha}\exp(-\kappa\alpha^{1/2}\xi), \tag{19}$$

where $\tilde{Q}(s)=Q(\xi;s)\exp(\kappa\alpha^{1/2}\xi)$. By applying the convolution theorem and taking into account that the inverse Laplace transform of $\tilde{Q}(s)$ is $I_b\kappa\exp\{-[(t-b)/\sigma]^2\}$, and the inverse Laplace transform of $1/(s-\kappa^2\alpha)$ is $\exp(\kappa^2\alpha t)$, we obtain

$$p(x,t)=\frac{I_b''(1-r)\kappa e^{-\kappa x}}{\rho c_p}e^{\kappa^2\alpha t}\frac{\sigma\pi^{1/2}}{2}\times e^{[-b^2/\sigma^2+K^2]}\left[\operatorname{erf}\left(\frac{t}{\sigma}+K\right)-\operatorname{erf}(K)\right], \tag{20}$$

where

$$K=\frac{\kappa^2\alpha\sigma^2-2b}{2\sigma}. \tag{21}$$

Noticing from Eq. (20) that $\partial p(x,t)/\partial x=-\kappa p(x,t)$, and

$$p(0,t)=\frac{I_b\alpha\kappa\sigma}{2\pi^{1/2}}\left[\operatorname{erf}\left(\frac{b}{\sigma}\right)\exp(\kappa^2\alpha t)-\operatorname{erf}\left(\frac{b-t}{\sigma}\right)\right] \tag{22}$$

$$\frac{\partial p(0,t)}{\partial x}=\frac{I_b\alpha\kappa^2\sigma}{2\pi^{1/2}}\left[\operatorname{erf}\left(\frac{b-t}{\sigma}\right)-\operatorname{erf}\left(\frac{b}{\sigma}\right)\exp(\kappa^2\alpha t)\right] \tag{23}$$

then, from Eq. (14*b*) with $p(0,0)=0$, we have

$$T_v(0,t)=A^*\left(-B^*+\kappa\alpha^{1/2}\frac{\partial^{-1/2}B^*}{\partial t^{-1/2}}\right), \tag{24}$$

where $A^*=I_b\alpha\kappa\sigma/(2\pi^{1/2})$, $B^*=erf(t^*)-erf(b/\sigma)\exp(\kappa^2\alpha t)$, and $t^*=(b-t)/\sigma$.

Equations (15) and (24) can be combined into a single equation (Eq. (13)) if two lasers are used to heat the sample material, and one laser has its wavelength tuned such that the laser radiation is absorbed preferentially at the surface and the other has its wavelength tuned such that the laser radiation is absorbed volumetrically. The advantage of this combination, not yet explored, is that the temperature solution becomes dependent on two independent groups of thermal properties. Hence, the thermal diffusivity *and* the thermal conductivity of the material can be found concomitantly, extending the applicability of the TTR method.

Model Validation

The model validation is accomplished by utilizing an experimental setup for the TTR measurements, shown in Fig. 1, consisting of a pulsed Nd:YAG laser radiating at 532 nm wavelength used as a heating source, with radiation energy E that can be set from 0 to 1.0 mJ.

The probing region, shown in Fig. 2, has a diameter $d=2.4\,\mu$m, about 100 times smaller than the heating region characteristic dimension of 200 μm. The heated surface area is $A=5.1\times10^{-8}$ m^2, hence the fluence F can be set from 0 to approximately 19.6 kJ/m^2. The surface temperature is monitored during approximately 100 ns, counting from the beginning of the heating process. The uniformity of the laser beam intensity was estimated as the standard deviation of the peaks and valleys magnitudes in respect to the mean value. The calculations were carried out with values obtained from a fast digital camera, which has 12 bits intensity resolution depth of the image, as shown in Fig. 3. The standard deviation of the laser beam intensity uniformity, with 95 percent confidence level, is nine percent. Therefore, the one-dimensional equation used for the heat transfer analysis seems to be justified in the present case.

An essential laser beam characteristic is the temporal distribution of the heating beam intensity on the sample surface. The experimental data indicates that a Gaussian curve, with $b=9.6$ ns, and $\sigma=4.3$ ns, fits well the time evolution of the laser radiation during one pulse. The average uncertainty of the curve fitting is less than 6 percent.

A direct comparison with experimental results using gold, which has a very large attenuation coefficient κ (i.e., it is expected to behave as an opaque material absorbing all the radiation at the surface), and with $E=0.5$ mJ, is presented in Fig. 4. A normalized temperature $\theta=T_s^*/(T_m-T_0)$, is used, where T_m is the maximum temperature value (equal to 60°C in this case) found within the time interval 0–100 ns (the experimental time range). Observe that within this temperature range the reflectivity of gold falls within a linear regime.

The uncertainty of the experimental θ results shown in Fig. 4 is estimated at six percent. This uncertainty value was derived from the standard deviation of the random fluctuations of the temperature response in respect to the mean value, with 95 percent confidence. Observe, from Eqs. (15) and (16), that the shape of the normalized curve is independent of $(k\rho c_p)$ and $F(1-r)/(\sigma\pi^{1/2})$. The agreement between the experimental results and the theoretical prediction is excellent, in that the theoretical values fall within the experimental error band. This agreement validates the fractional theoretical equation for the surface temperature, Eq. (12).

For the sake of demonstration of the applicability of the fractional solution, we consider now a GaAs bulk sample ($r=0.39$, $\rho c_p=1.73\times10^6$ J/m^{3}K, $k=52$ W/mK). Using the same laser characteristics as in the previous case, and assuming the material as opaque (i.e., all radiation energy absorbed at the surface), the theoretical results from Eq. (15) are shown in Fig. 5, in terms of the excess temperature T_s^*, considering three different laser fluences. Keep in mind that very high temperatures can induce non-

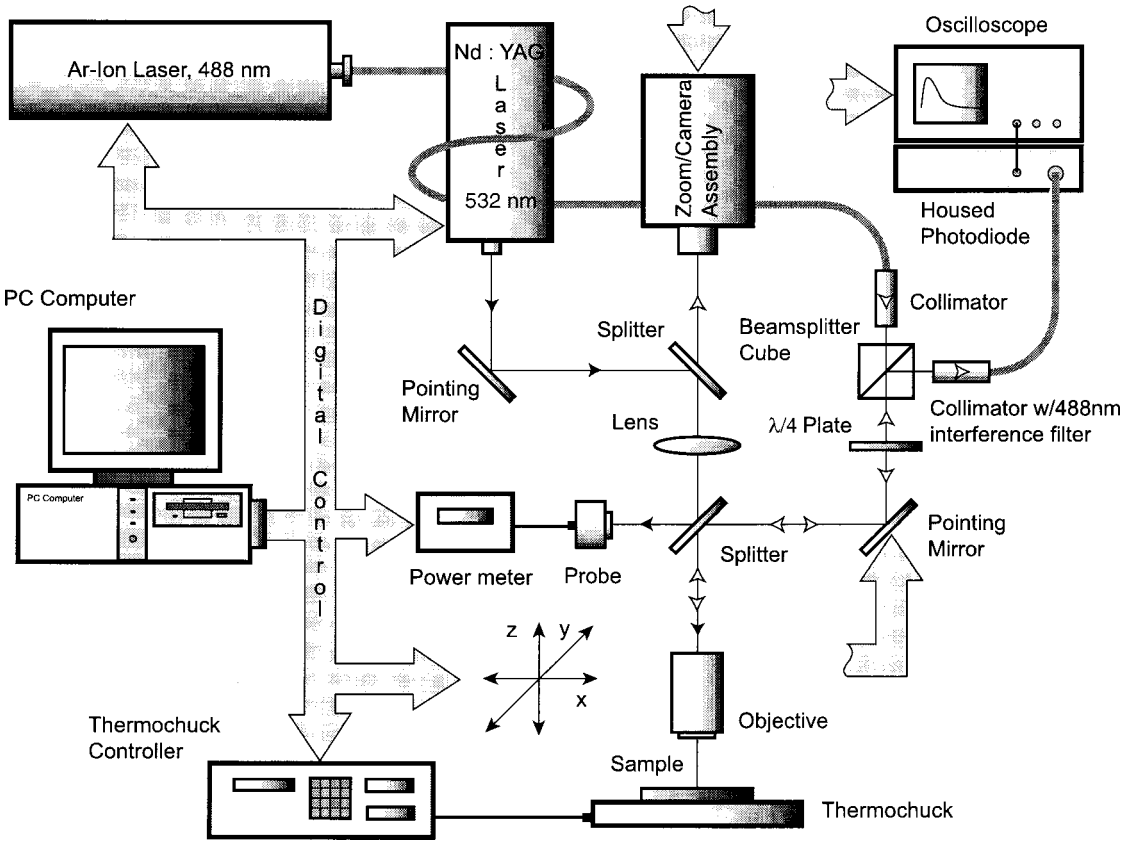

Fig. 1 Schematic of the experimental setup (http://www.seas.smu.edu/setsl)

linear effects in certain materials (e.g., properties strong dependency on temperature), and this effect is not accounted for in the present analytical solution.

Also plotted in the same graph (dashed line) is the time evolution of the normalized laser radiation, i.e., $\dot{q}''_s/\dot{q}''_m$. It is interesting to note that the delay in the temperature response of the material, in comparison to the laser energy, is independent of the fluence of the laser as indicated by the maximum temperature being attained at the same time in all cases.

We now consider the material as semi-transparent (i.e, the radiation energy is absorbed as a volumetric heat source), and solve Eq. (24) with $F=0.5\,\mathrm{mJ}$ and different values of κ. Results are shown in Fig. 6. Notice that the correct value of the attenuation coefficient for GaAs is $\kappa=7.8\times10^6\,\mathrm{m}^{-1}$.

Observe how the temperature evolution with time tends, when β increases, to the same evolution presented in Fig. 5. This tendency indicates the consistency of the model, at least as far as opaque materials (high κ) are concerned.

Also interesting is that the results from the volumetric source fractional solution diverges (T_s^* increases without bounds) when $\kappa=1.5\times10^6\,\mathrm{m}^{-1}$ or greater. This abnormal behavior, shown as the dashed-line curve in Fig. 6, is a consequence of trying to simulate, with the volumetric heat source solution, a configuration in which the laser energy is in fact concentrated at the surface of the material (because κ is too high). Again, the model seems consistent in this regard as well. (Mathematically, the diverging behavior of the analytical results for large t, when κ is high, is attributed to the exponential function in time of the term B^*, with positive coefficient $\kappa^2\alpha$, that must be calculated for determining $T_v(0,t)$ from Eq. (24).)

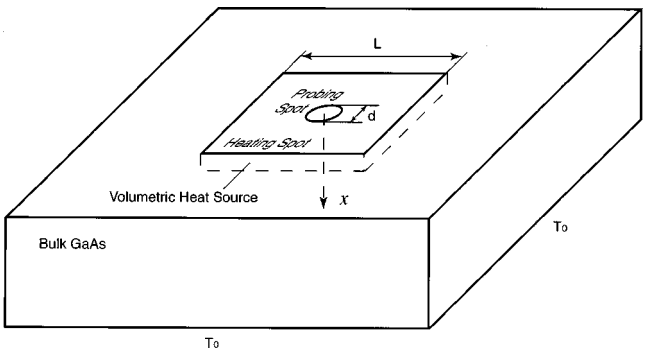

Fig. 2 Schematic of the heating and probing spot positioning on the sample

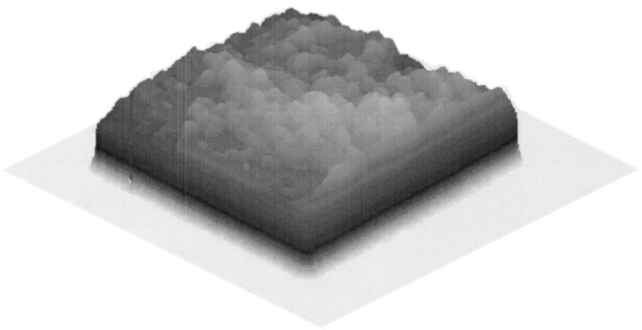

Fig. 3 Spatial intensity distribution of the heating laser

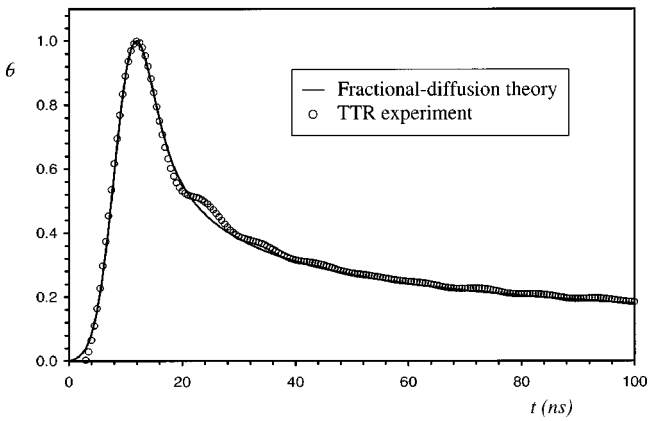

Fig. 4 Time evolution of the normalized surface temperature for opaque (gold) material

It is certainly instructive then to consider when the volumetric heat source model is preferable to the boundary heat flux model. The energy balance equation with volumetric heat source, namely

$$\frac{\partial T}{\partial t}=\alpha\frac{\partial^2 T}{\partial x^2}+\frac{\kappa F(1-r)}{\rho c_p\sigma\pi^{1/2}}e^{-\kappa x}e^{\{-[(t-b)/\sigma]^2\}} \tag{25}$$

can be scaled as

$$\frac{\Delta T}{\tau}\sim\alpha\frac{\Delta T}{\delta^2}+\frac{\kappa F(1-r)}{\rho c_p\sigma}. \tag{26}$$

When the volumetric source term scales with the diffusion term, the length scale for the heat penetration depth is

$$\delta_v\sim\left(\frac{\sigma k\Delta T}{\kappa F(1-r)}\right)^{1/2}. \tag{27}$$

When the volumetric source term is not present, the length scale for the heat penetration depth (characteristic of the surface-heating model) is

$$\delta_f\sim(\alpha t)^{1/2}. \tag{28}$$

By comparing the two previous scales, one can find a criterion for determining when the volumetric source model is expected to be accurate, namely,

$$\delta_v\geqslant\delta_f\Rightarrow\left(\frac{\sigma k\Delta T}{\kappa F(1-r)}\right)^{1/2}\geqslant(\alpha t)^{1/2}. \tag{29}$$

In terms of the radiation attenuation coefficient, the criterion reads,

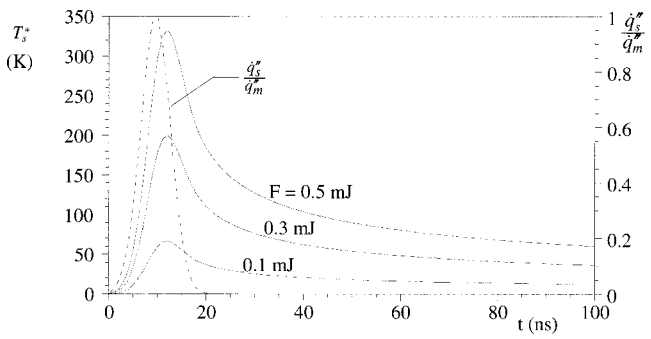

Fig. 5 Laser fluency effect on the time evolution of the excess surface temperature for opaque material: analytical results

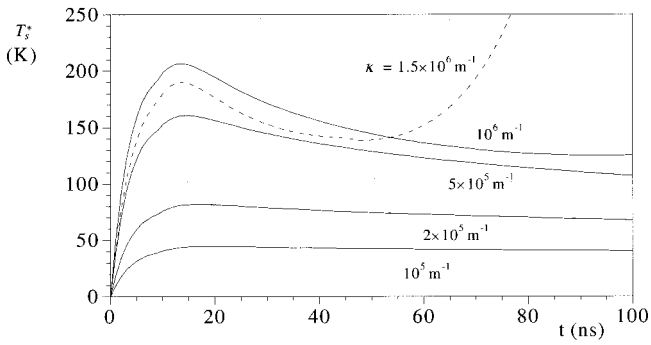

Fig. 6 Time evolution of the excess surface temperature for GaAs

$$\kappa\leqslant\frac{\sigma k\Delta T}{\alpha t F(1-r)}=\frac{\sigma\rho c_p A\Delta T}{tE(1-r)}. \tag{30}$$

If we now use the scales for the parameters involved as: $A\sim10^{-8}$ m^2, $\sigma\sim10^{-9}$ s, $k\sim10^2$ W/mK, $\Delta T\sim10^2$ K, $\alpha\sim10^{-5}$ m^2/s, $t\sim10^{-9}$ s, $E\sim10^{-4}$ J, and $(1-r)\sim1$, we can substitute the values in the inequality Eq. (30), and obtain $\kappa\leqslant10^5$ m^{-1}. Considering the value of κ for GaAs, namely 7.8×10^6 m^{-1}, we conclude from our criterion that the laser heating process of GaAs would be better modeled using the surface flux model, not the volumetric source model. This conclusion is corroborated by experiments with GaAs, for which the results are identical to the ones presented in Fig. 4.

Summary and Conclusions

A theoretical analysis, based on fractional calculus, was conducted for the solution of the unidirectional diffusion equation with time-dependent surface heat flux and with time and space-dependent volumetric heating. The analysis unveiled a novel, single, and general equation (a fractional solution) for determining the surface temperature of a material under surface heat flux and volumetric heating, with direct application to the TTR method of determining thermal properties of thin films.

Experimental results of TTR tests conducted on gold (an opaque material) validated the fractional solution for the case of laser radiation absorbed at the surface of the material.

Theoretical results were also obtained for a bulk sample of GaAs, with the laser radiation first assumed to be totally absorbed at the surface (opaque) of the sample, and then with the laser radiation assumed to be absorbed volumetrically by the sample (semi-transparent). The analytical results predicted by the fractional approach were consistent with our experimental observations, and with a new simplified criterion for determining when a material, under a certain laser radiation, is better modelled as opaque or as semi-transparent.

The general theoretical solution obtained via the fractional approach creates a new experimental possibility for the TTR method. As the single general solution, for surface heat flux and volumetric heating, is dependent on two distinct thermophysical properties, one can envision an experiment in which two lasers are used to heat up concurrently a material, instead of only one as usually done. One laser would have the frequency tuned so that the material would behave as opaque (i.e., a frequency at which the attenuation coefficient of the material is very high so that the laser energy is absorbed mainly at the surface). The other laser would have the frequency tuned such that the material absorbs the energy as a semi-transparent material (i.e., a frequency at which the attenuation coefficient of the material is very low so the laser energy would be absorbed volumetrically as it penetrates through the material). In this way, the surface temperature response of the test material would be influenced by a surface heat flux as well as

by a volumetric heating effect. Comparison with experimental results would allow the determination of both thermophysical property groups from a single measurement. This idea is yet to be explored.

Acknowledgments

Prof. Raad and Dr. Komarov acknowledge the financial support of SMU, the National Science Foundation under grants DMII-9632798 and ECS-9601570, and of Texas Instruments and Raytheon, in the form of research funding and in-kind contributions towards the establishment of the Submicron Electro-Thermal Sciences Laboratory at SMU, from where the experimental data presented in this study has been obtained. Prof. Lage is grateful for the hospitality of the Swiss Federal Institute of Technology for providing, in the Fall of 1998, a conducive environment for him to explore the new analytical ideas set forth in this study.

Nomenclature

b = mean of normal distribution, s
C, C_1, C_2 = auxiliary parameters or constants
F = laser fluence, J m^{-2}
I'' = surface radiation power flux intensity (at $x=0$), W m^{-2}
I''_b = surface radiation power flux intensity (at $t=b$), W m^{-2}
K = auxiliary parameter, Eq. (21)
p = inverse Laplace transform of P
P = particular solution
$\dot{q}''_s$ = surface heat flux (at $x=0$), Eq. (16), W m^{-2}
$\dot{q}''_m$ = maximum local heat flux, Eq. (10), W m^{-2}
Q = Laplace transform of $\dot{q}'''/\rho c_p$
r = surface reflectivity
s = Laplace transform variable
T_0 = initial temperature (at $t \leqslant 0$), K
T_f = local heat flux temperature contribution, Eq. (14*a*), K
T_v = local volumetric heat source/sink temperature contribution, Eq. (14*b*), K
T_s = surface temperature (at $x=0$), K
T^* = temperature difference, $=T-T_0$, K
T_m = maximum temperature during heating, K
T_s^* = temperature difference, $=T_s-T_0$, K
x = coordinate perpendicular to material surface, m

Greek Symbols

δ_f = penetration depth scale for surface heating, Eq. (28)
δ_v = penetration depth scale for volumetric heating, Eq. (27)
θ = nondimensional normalized temperature, $=T_s^*/(T_m-T_0)$
Θ = Laplace transform of T^*
σ = Gaussian parameter (equal to $2^{-1/2}$ times the standard deviation), s, Eq. (16)
ξ = nondimensional length

References

[1] Özisik, M. N., 1980, *Heat Conduction*, Wiley, New York.
[2] Kakaç, S., and Yener, Y., 1985, *Heat Conduction*, Hemisphere, Washington, DC.
[3] Poulikakos, D., 1994, *Conduction Heat Transfer*, Prentice Hall, New Jersey.
[4] Xu, X., Grigoropoulos, C. P., and Russo, R. E., 1995, "Transient Temperature During Pulsed Excimer Laser Heating of Thin Polysilicon Films Obtained by Optical Reflectivity Measurement," ASME J. Heat Transfer, **117**, pp. 17–24.
[5] Chen, G., Tien, C. L., Wu, X., and Smith, J. S., 1994, "Thermal Diffusivity Measurement of GaAs/AlGaAs Thin-Film Structures," ASME J. Heat Transfer, **116**, pp. 325–331.
[6] Goodson, K. E., and Flik, M. I., 1994, "Solid Layer Thermal Conductivity Measurement Techniques," Appl. Mech. Rev., **47**, pp. 101–112.
[7] Kulish, V. V., and Lage, J. L., 2000, "Fractional Diffusion Solutions for Transient Local Temperature and Heat Flux," ASME J. Heat Transfer, **122**, pp. 372–376.
[8] Kamke, E., 1959, *Differentialgleichungen: Lösungsmethoden und Lösungen*, Leipzig.

Synchronization of Vortex Shedding and Heat Transfer Enhancement Over a Heated Cylinder Oscillating With Small Amplitude in Streamwise Direction

C. Gau
e-mail: gauc@mail.ncku.edu.tw

S. X. Wu

H. S. Su

Institute of Aeronautics and Astronautics,
National Cheng Kung University,
Taiwan, R.O.C

Experiments are performed to study the flow structure and heat transfer over a heated cylinder oscillating radially with small amplitude in streamwise direction. Both flow visualization using a smoke wire in the upstream and the local heat transfer measurements based on wall temperatures around the cylinder were made. The excitation frequencies of the cylinder are selected at $F_e/F_n=0$, 0.5, 1, 1.5, 2, 2.5, and 3. The oscillation amplitude selected is less than a threshold value of $A/D=0.06$ where synchronization of vortex shedding with the cylinder excitation was not expected. However, experiments indicate that synchronization still occurs which stimulates a great interest to study its enhancement in the heat transfer. Synchronization occurred at $F_e/F_n=2$ is antisymmetric vortex formation while synchronization at $F_e/F_n=2.5$ and 3 is symmetric type. The forward motion (advancing into the cross flow) of the cylinder during one cycle of oscillation has an effect to suppress the instability and the vortex formation. This leads to the occurrence of a smaller and symmetric vortex formation and a less enhancement of heat transfer than the case of antisymmetric type ($F_e/F_n=2$). For excitations at lower frequencies ($F_e/F_n \leqslant 1.5$), all the vortex formations occurred are mostly antisymmetric. The dominant mode of the instability in the shear layer is actually the natural shedding frequency F_n of the vortex. A closer excitation frequency to $2F_n$ causes a greater enhancement in the heat transfer. During the experiments, the Reynolds numbers varies from 1600 to 3200, the dimensionless amplitude A/D from 0.048 to 0.016. [DOI: 10.1115/1.1404121]

Keywords: Enhancement, Heat Transfer, Instability, Vortex, Wakes

Introduction

Any thermal device under its normal operation will encounter some degree of vibration. The vibration may be generated from the flow itself and or other components in motion. These kinds of vibrations usually are at small amplitude and relatively high or low frequency. In practical design of a thermal system, vibrations under this small amplitude are not considered and their effects on the wall heat transfer are neglected. Previous studies [1] indicate that even a small amplitude ($A/D=0-0.064$) of cylinder vibration in the transverse direction of the flow can have a significant effect on both the vortex flow structure and the heat transfer around the cylinder. Under synchronization of vortex shedding with the cylinder oscillation at $F_e/F_n=3$, the enhancement in the overall heat transfer can reach 50 percent. Both the flow and the local heat transfer measurements provide very important information on the nature of the flow and its enhancement in the heat transfer. These findings [1] stimulate an interest to study the flow and heat transfer over cylinder oscillating in the streamwise direction of the flow. The amplitude ratio (A/D) of the cylinder oscillation selected is very small and is from 0 to 0.048.

A review of the flow structure and the heat transfer over cylinder oscillating in transverse direction of the flow has been made in the reference [1] and will be omitted here. Studies relevant to the present work are very few. For cylinder oscillating in the streamwise direction, the vortex formation processes in the back of the cylinder have been studied [2,3]. Based on the experimental data from several investigators, Griffin and Ramberg [2] obtained the lock-on regime in terms of the threshold amplitude versus the frequency ratio F_e/F_n over which the vibrations of a cylinder control the vortex shedding. The vortex structure and its formation process are significantly different from the case of cylinder oscillation in the transverse direction. Depending on the values of the frequency ratio F_e/F_n, complete synchronization of vortex shedding with the cylinder oscillation can occur either in antisymmetric or symmetric mode. At frequency ratios other than the complete synchronization frequency, there is mode competition and switching between symmetric and antisymmetric vortex formation [3]. Symmetric vortex formation and mode switching were not found for cylinder oscillating in transverse direction of the flow. However, the amplitude ratio A/D selected in their work is large enough ($A/D=0.13$) to produce control of the near wake structure over the frequency range from 1.6 F_n to 2.5 F_n. According to the experiments by Griffin and Ramberg [2], the minimum threshold amplitude (A/D) to produce synchronization of vortex shedding with the cylinder vibration is close to 0.06. To consider a practical application as mentioned previously, the amplitude ratio needs be small. In the present experiments, therefore, all the amplitude ratios A/D selected are small and are less than the minimum threshold of 0.06. Therefore, synchronization of vortex shedding with the cylinder vibration may or may not be expected

Contributed by the Heat Transfer Division for publication in the JOURNAL OF HEAT TRANSFER. Manuscript received by the Heat Transfer Division March 27, 2000; revision received November 3, 2000. Associate Editor: B. Chung.

to occur. The vortex formation processes obtained by Ongoren and Rockwell are expected to be different from the case of cylinder excitation at small amplitudes. The effects of these kinds of vortex flows on the heat transfer around the cylinder are not known.

In this work, one needs to find is there synchronization of vortex shedding with the cylinder vibration at small amplitudes and how the vortices form and affect the heat transfer around the cylinder? What can we infer for the nature of the entire flow from the local heat transfer measurements? Therefore, the present paper will provide a better understanding of the flow structure and heat transfer of air moving over a heated cylinder oscillating, at small amplitudes, in the streamwise direction of the mean flow. Flow visualization is made by smoke generation, which is facilitated approximated 10*D* upstream of the cylinder by a thin, electrically heated wire coated with oil. The temperature distributions around the cylinder wall are measured with *K*-type thermocouples and are used to reduce the heat transfer data. The variation of the flow structure and the heat transfer with the oscillating amplitudes and frequencies will be systematically discussed.

Experimental Apparatus and Procedures

The cylinder is made of 50 cm long and 0.3 cm wall thick Bakelite tube which has outside diameter of 3 cm. The purpose to select a thin Bakelite tube is first to reduce both the radial and the circumferential conduction of heat, second to reduce the vibration load of the cylinder and third to maintain a certain kind of rigidity that causes no deformation during vibration. To further reduce the circumferential conduction of heat, a 0.05 cm thick rubber tube is used to cover the cylinder. This makes the outside diameter of the cylinder to be 3.1 cm. A 0.015 mm thick stainless steel foil is used to glue on the tube. The electrodes are very small. They are fixed at the ends of tubes that are extended to the outside of the wind tunnel. After passing electric current through the foil, the cylinder surface can be heated uniformly at desired heat flux conditions. The tube ends are sealed with formed rubber for insulation. The total heat loss to the ambient, which includes the conduction loss along the cylinder wall and the radiation loss directly from the steel foil, is estimated to be less than 2 percent.

The cylinder is placed horizontally (perpendicular to the direction of the gravitational force), as shown in Fig. 1, in the test section of a wind tunnel that has a cross section of 30 cm $\times$ 30 cm. The wind tunnel can provide a uniform airflow over the cylinder with a turbulence intensity less than 0.7 percent. The freestream velocity in the wind tunnel was measured with a Pitot tube. The wall of the test section is made of Plexiglass to allow for flow visualization. A horizontal slot of 3.5 cm wide is cut on each of the sidewalls of the wind tunnel to allow the cylinder oscillating in the horizontal direction. The cylinder is holding by an aluminum frame which is connected to a cam driven by a motor at desired speed. Two ball bearings fixed on the sidewalls of the wind tunnel are used to allow the frame or the cylinder oscillating in the streamwise direction to the mean flow but prevent oscillating in the transverse direction. By using different shapes of cam and rotation speeds of the motor, a different amplitude and frequency of vibration signal (sinusoidal) can be obtained. An accelerometer is attached to the cylinder wall to acquire and monitor the amplitude of the vibration.

Flow visualization by smoke generation is facilitated by a thin, electrically heated wire coated with oil. This thin wire is inserted vertically across the cross section of the wind tunnel, as shown in Fig. 1, and is at approximately 10*D* upstream of the cylinder. Due to surface tension small amount of oil flows down slowly along the wire from an oil pan in the top of the wind tunnel and causes vaporization upon heating. To avoid turbulence generation which can dissipate the smoke rapidly, the velocity of the flow remain relatively low (Re=1600) during the flow visualization experiments. Since the wire is very thin and is at a distance far from the cylinder, it could not affect the upstream flow conditions. The streamline of the flow and its pattern can be clearly visualized as shown in the latter section.

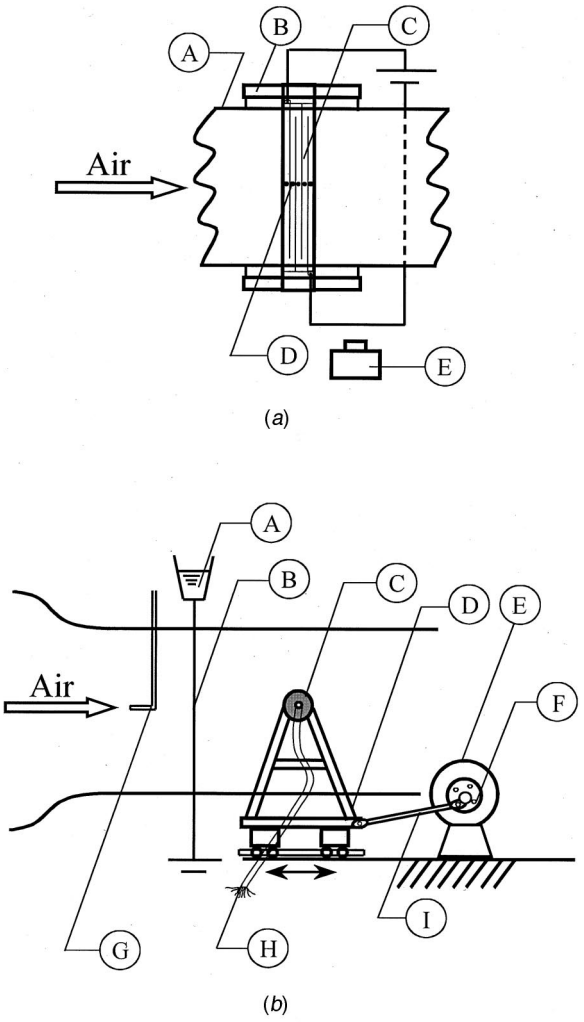

Fig. 1 Schematic diagram of the experimental setup: (*a*) *A*, wall of the wind tunnel, *B*, aluminum frame, *C*, stainless steel foil, *D*, thermocouples, *E*, camera; and (*b*) *A*, oil pan, *B*, electric resistance wire, *C*, cylinder, *D*, aluminum frame, *E*, electric step motor, *F*, rotating cam, *G*, Pitot tube, *H*, thermocouple wires, and *I*, connecting rod.

To measure the circumferential temperature distribution around the cylinder wall, a total of 30 thermocouples are inserted individually into equally spaced small holes drilled in the tube wall in order that the thermocouple junction can attach to the heated steel foil. All the thermocouple junctions are coated with epoxy to avoid electric contact with the foil. The thermocouple wires used have very small diameter $d=0.05$ mm. This can further reduce the vibration load of the cylinder. To check the axial conduction loss along the cylinder wall, some additional thermocouples are embedded in the tube wall close to the ends. All the temperature signals are acquired with a data logger and sent into a PC for data processing and plotting. Before the experiments, all the thermocouples are calibrated in a constant temperature bath to ensure a measurement accuracy of ± 0.1°C.

To ensure that the stainless steel foil is heated uniformly, the entire foil is cut into a number of long strips that are axial. The strips are smoothly glued on the tube wall. There is no waviness or overlapping of foils. Each strip is heated individually with an equal amount of *d-c* power. With the desired voltage *V* and cur-

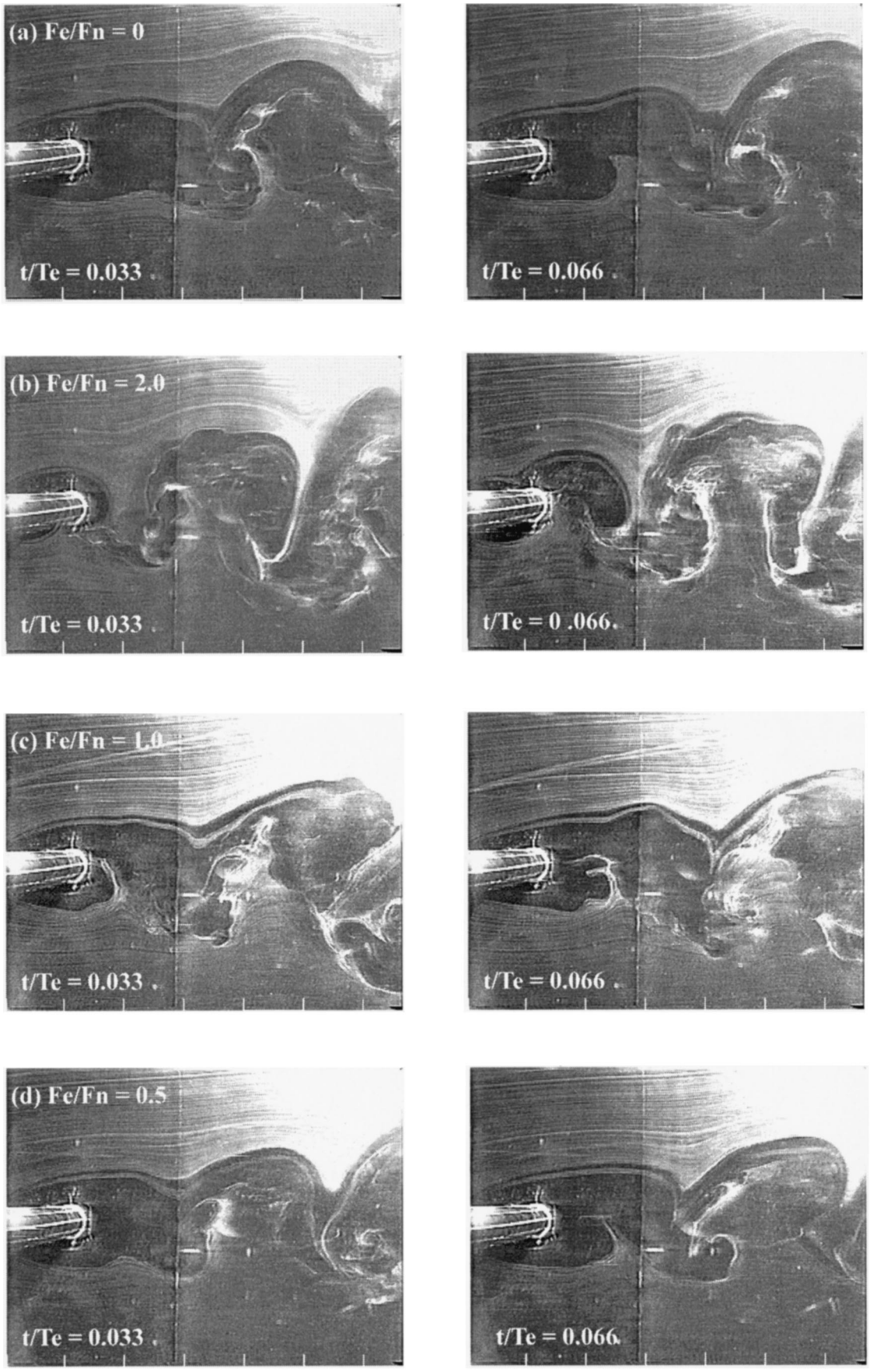

Fig. 2 Vortex structure when antisymmetric mode occurs at $t/Te=0.33$ and 0.66 for Re=1600, $A/D=0.048$ and (*a*) $F_e/F_n=0$, (*b*) $F_e/F_n=2$, (*c*) $F_e/F_n=1$, (*d*) $F_e/F_n=0.5$, and (*e* $F_e/F_n=1.5$

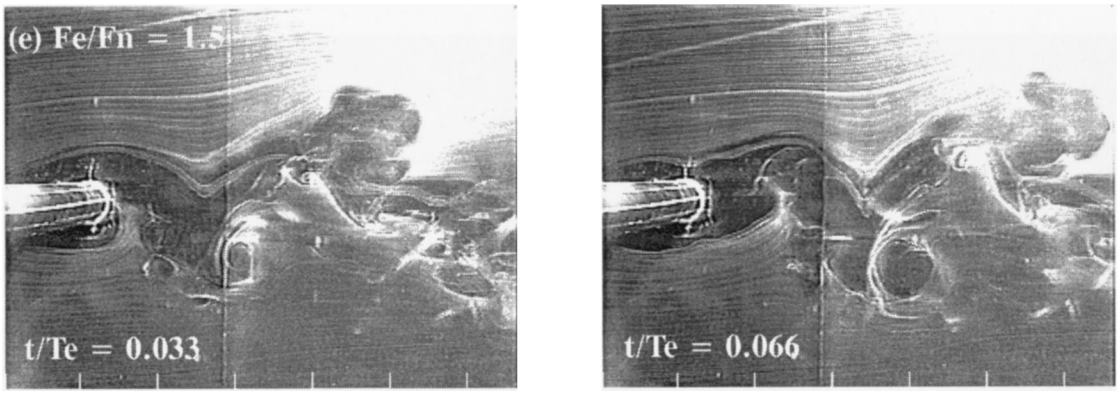

Fig. 2 (***Continued***)

rent I passing through the thin strip, the heat flux along the surface can be calculated and is equal to VI/A, where A is the area of the strip. The local heat transfer coefficient can be determined with the following equation:

$$h = q/(T_w - T_o). \tag{1}$$

The uncertainty of the experimental data obtained in the present system is determined according to the procedure outlined in the references [4,5]. It is found that the maximum uncertainty in the local Nusselt number is 3.5 percent, while the Reynolds number is 5.7 percent.

From the correlations listed in the references [6,7], the Strouhal number of the vortex shedding in the current experimental range of the Reynolds number covered was $F_n D/u_o = 0.194$. Therefore, the shedding frequency of the vortex can be calculated at a given flow speed and a known size of cylinder. The calculated shedding frequencies agree well with the ones obtained from our experimental observations. Therefore, the previous correlation was adopted to find the shedding frequencies of the vortex in the present work.

During the experiments, the excitation frequencies of the cylinder are selected at 0.5, 1, 1.5, 2, 2.5, and 3 times the natural shedding (Strouhal) frequency of the vortex. In this way, one could examine the effect of the cylinder excitation of the flow and heat transfer at subharmonic frequency $F_e/F_n = 0.5$, harmonic frequency $F_e/F_n = 1$, superharmonic frequencies $F_e/F_n = 2, 3$ and nonharmonic frequencies $F_e/F_n = 1.5, 2.5$.

Results and Discussion

Flow Visualization. In general, the current flow visualization results indicate that two different types of vortex formation can occur, somewhat like those described in the report [3], one is symmetric and the other is antisymmetric type. For symmetric type, the vortex shedding in both the upper and the lower side of the cylinder occurs and grows simultaneously, at the same time the vortex becomes synchronized with the cylinder oscillation. In other words, the threshold amplitudes for the occurrence of synchronization found by Griffin and Ramberg are at Re=100, which cannot be used for air at a higher Reynolds number. For antisymmetric type, the vortex shedding in either the upper or the lower side of the cylinder occurs and grows alternately. The occurrence of different types of vortex formation will depend on the oscillation frequency and amplitude of the cylinder. When the antisymmetric type of vortex formation occurs, the shedding frequency of the vortex does not vary at all with the oscillation frequency of the cylinder, and is maintained at the natural shedding frequency (or the Strouhal frequency) F_n of the vortex. This finding is completely different from the results of Ongoren and Rockwell [3] at a higher A/D (=0.13) where cylinder oscillation controls the vortex shedding. In some frequencies ($F_e/F_n = 1, 1.5$ and 2.5) of cylinder oscillation, the switching between symmetric and antisymmetric mode occurs. However, one found that the antisymmetric mode occurs most of the time at lower values of excitation ($F_e/F_n = 1.5$), while the symmetric mode occurs most of the time at higher values ($F_e/F_n = 2.5$). ''Most of the time'' means it occurs twenty times for approximately every twenty one cycles). At $F_e/F_n = 1$, however, switching between symmetric and antisymmetric mode occurs frequently. In the following presentation for antisymmetric mode, instead of the complete cycle, only the vortex structure at two particular instants, i.e., $t/Te = 0.33$ and 0.66, are presented and compared with each other at different excitation frequencies. For symmetric mode, the vortex structures at smaller time intervals are presented.

When the cylinder is stationary, the vortex formation process in the wake region is shown in Fig. 2(a). The formation of vortex is due to the exponential growth of small disturbances in the shear layer where the dominant mode of (fundamental) frequency is the shedding frequency F_n of the vortex. When the cylinder is oscillated at harmonic, subharmonic or superharmonic frequencies, the small disturbances can be greatly amplified, the vortex can be initiated and formed in an earlier stage. The formation length of the vortex can be shortened greatly, as shown in Fig. 2. Instead of occurring at $F_e/F_n = 1$ as in the case of cylinder oscillation in the transverse direction of the flow, complete synchronization of vortex shedding with the cylinder oscillation occurs at $F_e/F_n = 2$ where the formation length of the vortex is much shortened. By carefully examining this vortex formation process, the small bud of vortex is initiated and grows only when the cylinder is moving in the reverse direction of the flow, but not when the cylinder is moving in the forward direction. It appears that the cylinder motion in the reverse direction of the flow has the effect to amplify the small disturbance of the shear layer and cause an earlier formation of vortex, while the cylinder motion in the forward direction of the flow has the effect to suppress the small disturbance in the shear layer and may eventually completely suppress the vortex formation. Therefore, only the reverse motion of the cylinder can cause the synchronization of vortex shedding with the cylinder excitation. This explains why complete synchronization of vortex shedding with cylinder excitation does not occur at $F_e/F_n = 1$. The explanation for the occurrence of synchronization is given in Fig. 3. The circles and solid dots in Fig. 3 represent the vortex shedding in the upper and the lower side of the cylinder, respectively. They both are drawn in the positive ordinate. The sine curves in Fig. 3 represent the oscillation of the cylinder. When the sine curve touches either the circles or the solid dots, this represents the synchronization of this vortex shedding with the cylinder oscillation. At $F_e/F_n = 2$, shown in Fig. 3(b), the phase of vortex shedding is completely locked in with the phase of cylinder motion in the reverse direction of the flow. The synchronization occurs for cylinder oscillation at $2F_n$ and A/D greater than a thresh-

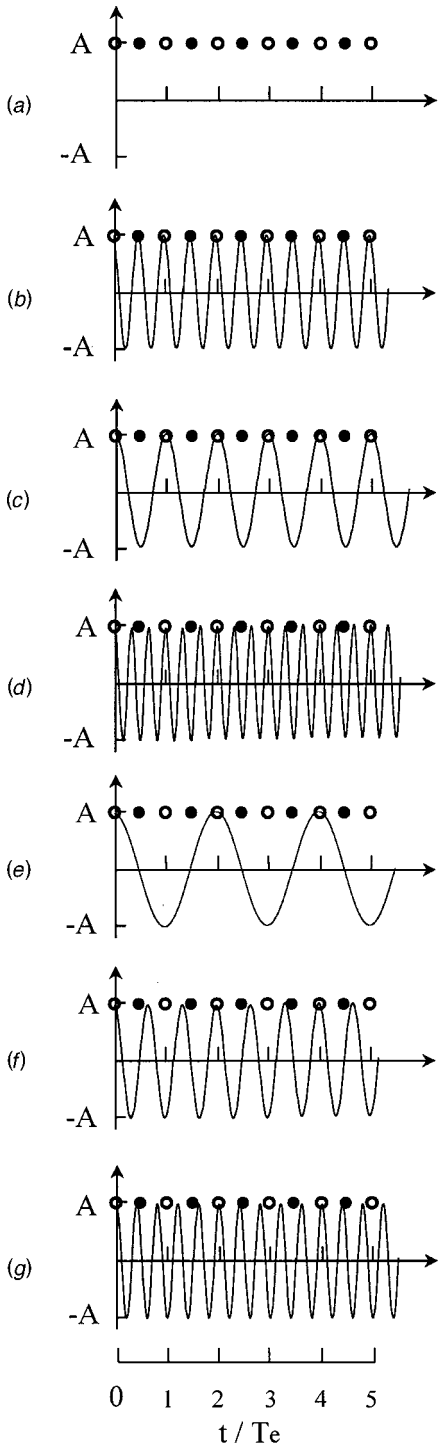

Fig. 3 Phase of vortex shedding (circles and dots) relative to phase of cylinder displacement (sin curve, A/D can be 0.048, 0.032, and 0.016) as function of time for (*a*) $F_e/F_n=0$, (*b*) $F_e/F_n=2$, (*c*) $F_e/F_n=1$, (*d*) $F_e/F_n=3$, (*e*) $F_e/F_n=0.5$, (*f*) $F_e/F_n=1.5$, and (*g*) $F_e/F_n=2.5$

old value of 0.06 has been found by others [2,3]. One can expect that the intense activity of the vortex formation in the close vicinity of cylinder can greatly enhance the heat transfer in that region.

For excitation at $F_e/F_n=1$, only one side (either on the upper or the lower side of the cylinder) of the vortex shedding can be synchronized with the cylinder oscillation, as explained in Fig. 3(*c*). When the suppression effect on one side of the vortex formation is not strong enough, antisymmetric type of vortex formation occurs, as shown in Fig. 2(*c*). The vortex is stronger and its formation length is shortened, as compared with the case when the cylinder is stationary. Therefore, a higher heat transfer due to the intense activities of the vortices can be expected. When complete suppression of vortex formation occurs in one (either the upper and the lower) side of the cylinder, the cylinder motion in the reverse direction of the flow still cause the initiation and formation of the vortex as in the other side of the cylinder and trigger the symmetric type of vortex formation, as shown in Fig. 4(*a*). The vortex shedding frequencies in both modes are identical. The switching between the two different modes are also found in other work [3]. In the present work, however, switching of the two different modes at other excitation frequencies ($F_e/F_n=1.5$ and 2.5) is not so frequent as found in the former reference. At $F_e/F_n=0.5$, mode switching does not even occur. Vortex shedding occurs only at antisymmetric mode.

For excitation at $F_e/F_n=3$, it appears that the vortex formation process should be very similar to the case at $F_e/F_n=1$, as explained in Fig. 3(*d*), except that the frequency of cylinder excitation is higher and the excitation energy input into the flow per second is higher. However, this large energy input can cause a larger amplification of the disturbance in the shear layer for the reverse motion of cylinder and a greater suppression of the disturbance for the forward motion of cylinder. Therefore, the antisymmetric mode of the vortex formation can be completely suppressed and only symmetric mode occurs, as shown in Fig. 4(*b*). The vortex formation length at $F_e/F_n=3$ is much smaller and the vortex activity is more intense than the case at $F_e/F_n=1$ when symmetric mode occurs. One can expect a much higher heat transfer enhancement than the case at $F_e/F_n=1$. However, the vortex structure formed at $F_e/F_n=3$ is much smaller than the case at $F_e/F_n=2$. Thus, a less enhancement in the heat transfer than the case at $F_e/F_n=2$ is expected.

For excitation at $F_e/F_n=0.5$, 1.5, 2.5, the synchronization of vortex shedding occurs every two of the vortex formation in either the upper or the lower side of the cylinder, as explained in Figs. 3(*e*), 3(*f*), and 3(*g*). However, the suppression of vortex shedding for cylinder motion in the forward direction of the flow also occurs every two of the vortex formation in the same side. For excitation at low frequency such as $F_e/F_n=0.5$ and 1.5, the suppression effect of the cylinder motion is not so effective that vortex shedding occurs in antisymmetric mode and its shedding frequency remains the same as the case when the cylinder is stationary. However, the vortex structure at $F_e/F_n=1.5$ is more irregular and its formation length is much smaller than the case at $F_e/F_n=0.5$, as shown in Figs. 2(*d*) and 2(*e*) due to the higher excitation energy transmitting into the shear layer during the vortex formation process, which can generate turbulent mixing with the wake flow and greatly enhance the heat transfer in the back of the cylinder.

For $F_e/F_n=2.5$, the excitation frequency is so high that the suppression effect of the cylinder motion becomes effective and makes the onset of vortex shedding in symmetric type most of the time, as shown in Fig. 4(*c*). The number of vortex formation in a given period of time can be counted. It is found that the vortex shedding frequency is equal to the cylinder oscillation frequency. That means that vortex shedding in the shear layer becomes synchronized with the cylinder oscillation. The synchronization at $F_e/F_n=2.5$ has not been found in other reports [2,3].

Heat Transfer. The current heat transfer data was validated [1,8] by comparing our data with the ones obtained from the literatures when the cylinder is stationary. The agreement was found to be very good. When the cylinder oscillates with an amplitude of $A/D=0.048$, the heat transfer can be significantly enhanced, as shown in Fig. 5. From previous flow visualization, synchronization of vortex shedding with cylinder excitation occurs at $F_e/F_n=2$, 2.5 and 3. When synchronization of cylinder oscillation with the vortex shedding occurs, the heat transfer results are much

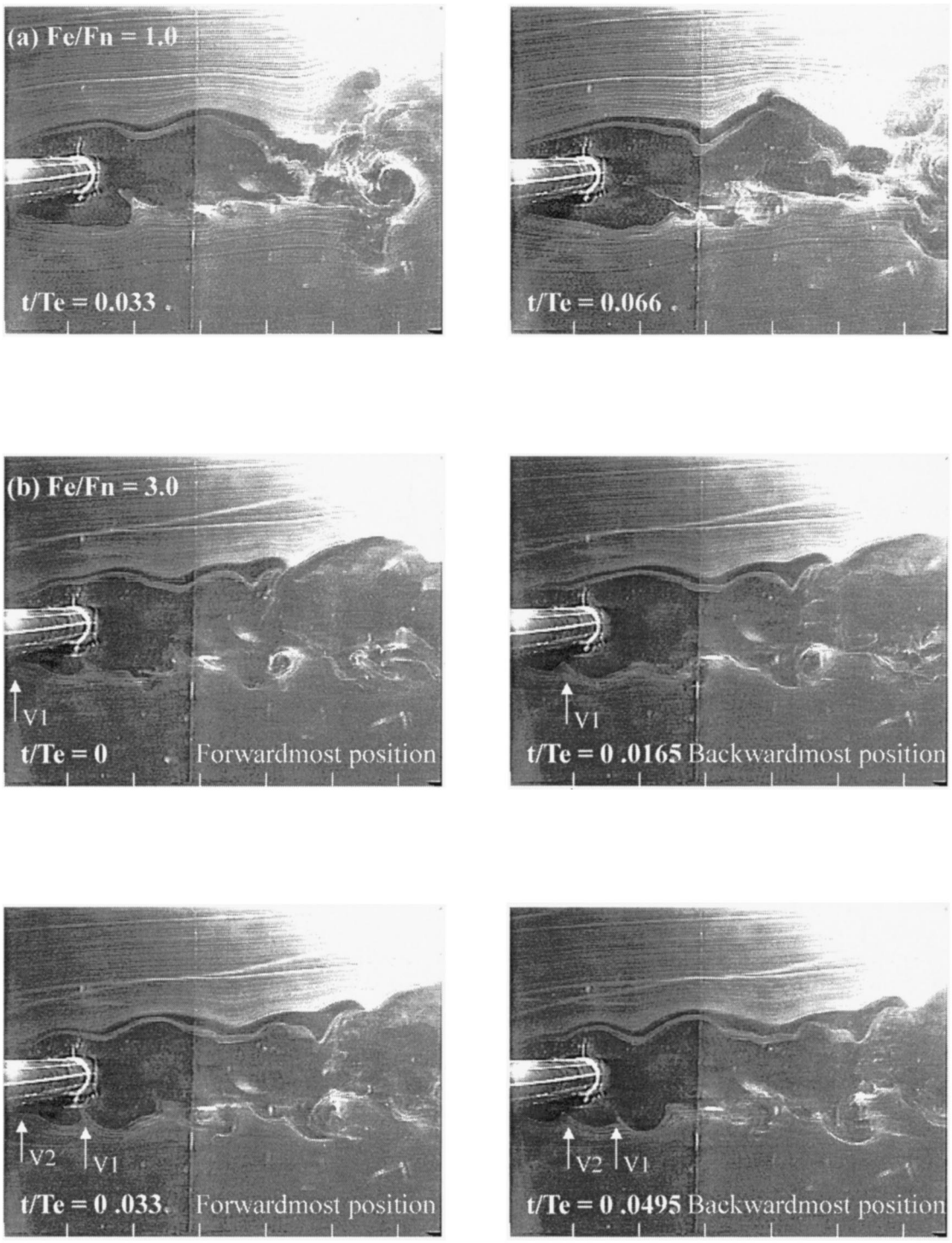

Fig. 4 Vortex structure when symmetric mode occurs with Re=1600, $A/D=0.048$ and (*a*) $F_e/F_n=1$, (*b*) $F_e/F_n=3$, and (*c*) $F_e/F_n=2.5$ (*V*1, *V*2, and *V*3 represent the vortex No. 1, vortex No. 2 and vortex No. 3, respectively

greater than the case at frequencies other than the synchronization frequencies. It has been found [1] that for cylinder oscillation in the transverse direction the heat transfer increases with the synchronization frequency due to a greater oscillation energy input to amplify the disturbance in the shear layer. However, the current results do not follow this trend, as shown in Fig. 5. It appears that the mechanism of synchronization occurred here is somewhat different from the case of cylinder oscillation in the transverse direction of the flow, except when $F_e/F_n=2$. When $F_e/F_n=2$, the oscillation frequency of the cylinder in the reverse direction is identical to and is completely synchronized with the natural shedding frequency of the vortex, i.e., the natural instability causing vortex formation in the shear layer in both the upper and the lower side of the cylinder can be fully amplified by the cylinder excitation. Therefore, synchronization of vortex shedding with the cylinder oscillation at $F_e/F_n=2$ can lead to a maximum enhancement in the heat transfer, as shown in Fig. 5. When the natural instability causing vortex formation in the shear layer in either the

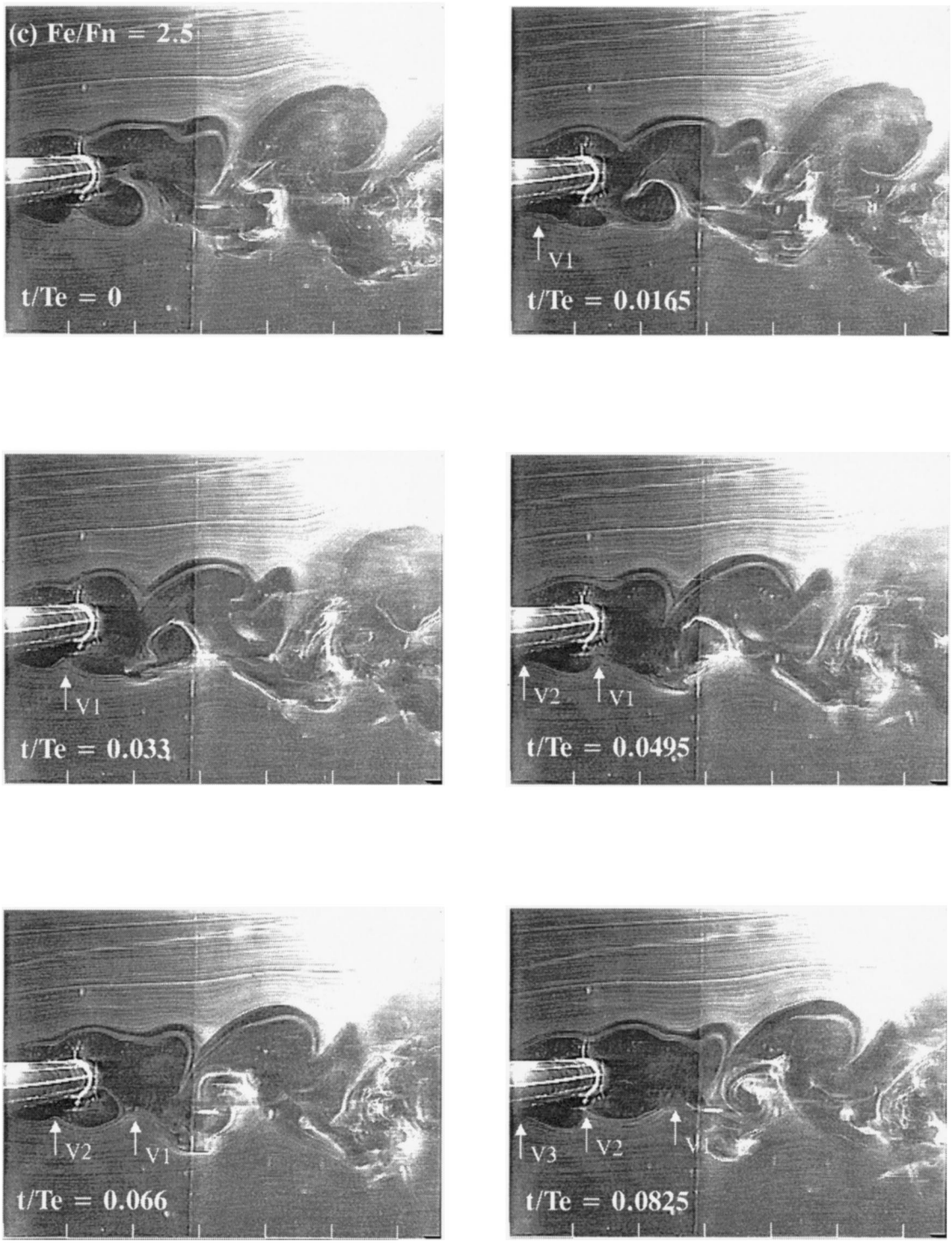

Fig. 4 (***Continued***)

upper or the lower side of cylinder is suppressed by the cylinder motion in forward direction of the flow, the backward motion of cylinder can generate instability causing synchronized vortex shedding in symmetric mode. The vortices formed are not so large which is able to have an intense activity in the near wake to enhance the heat transfer as the case at $F_e/F_n=2$. This is the case for both $F_e/F_n=2.5$ and 3. However, it appears that the suppression effect of the cylinder motion is more serious at $F_e/F_n=3$ than at $F_e/F_n=2.5$. For $F_e/F_n=2.5$, although the cylinder oscillation is synchronized with every two of the vortex initiated in one side (either the upper or the lower side) of the cylinder, as explained in Fig. 3(*g*), the phase of the vortex shedding in the other side of the cylinder is close to the phase of the cylinder displacement. This can readily cause wake capture and lead to greater enhancement of the heat transfer at $F_e/F_n=2.5$ than at $F_e/F_n=3$. In other words, as the cylinder excitation frequency is closer to $2F_n$, a greater (but still less than the case of $F_e/F_n=2$) enhancement in the heat transfer is expected to be obtained. This is also the case when the cylinder excitation frequency is less than $2F_n$.

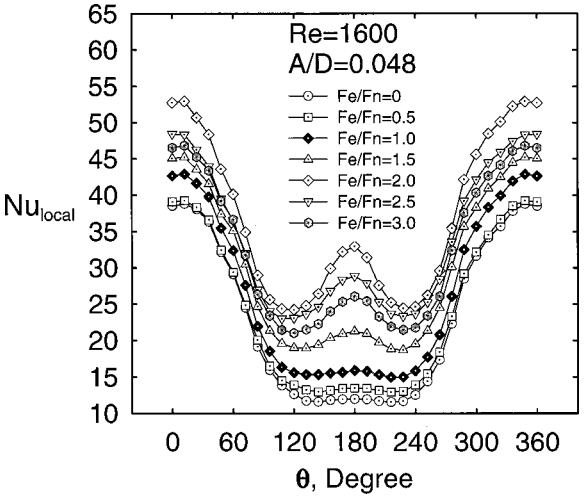

Fig. 5 The Nusselt number distributions around the cylinder at different excitation frequencies for Re=1600, $A/D=0.048$

When $F_e/F_n \leqslant 1.5$, this is the case when synchronization does not occur, the heat transfer increases with the excitation frequency, as shown in Figs. 5, 6, and 7. This is attributed to the fact that a higher frequency excitation of cylinder can provide more energy to disturb the flow, which causes an earlier formation of the vortex and a greater enhancement in the heat transfer. For $F_e/F_n=1$, synchronization of vortex shedding with the cylinder oscillation does occur only when the symmetric mode appears. When the antisymmetric mode appears, vortex shedding is not synchronized with the cylinder oscillation. Even when synchronization occurs, the vortices generated are small and the formation length is relatively large, as shown in Fig. 4(*a*). As one compares the vortex formation length at antisymmetric mode with that at symmetric mode, as shown in Fig. 2(*c*), the vortex formation length for both modes is approximately the same. In other words, synchronization occurred at $F_e/F_n=1$ does not benefit the heat transfer. The enhancement in the heat transfer for an average of both modes is not large, as shown in Fig. 5.

Note that the vortex shedding and its interaction with the wake can only enhance the heat transfer in the back of the cylinder. However, the enhancement in the heat transfer is found not only in the back but also in the front and the stagnation point of the cylinder. This phenomenon is also found for cylinder excitation in the transverse direction [1], since the intense activity of the vortices in the wake region could not possibly affect the flow in the upstream, especially in the forward stagnation point. One can readily conclude this point from flow visualization experiments. It appears that the cylinder excitations not only amplify the instability occurred in the shear layer of the near wake but also the instability occurred in the stagnation point and its downstream region. The only chance that the dominant mode of instability in these regions can be amplified simultaneously by the cylinder excitation is that the dominant modes of instability, i.e., the fundamental frequencies, in these regions are the same. Therefore, one concludes that the instability (natural) occurred in the shear layer of the near wake is actually generated far upstream in the stagnation point region. It appears that when the natural instability around the cylinder is suppressed by the forward motion of the cylinder, new instability around the cylinder is initiated by the backward motion of the cylinder. This new instability is synchronized with the cylinder oscillation and leads to symmetric vortex formation. When the frequency of the instability generated by the cylinder oscillation is closer to two times the frequency of the natural instability (i.e., the Strouhal frequency), a greater enhancement in the heat transfer is obtained.

As the Reynolds number increases, the shedding frequency of vortex increases significantly. Due to the limitation of the current experimental facility, the maximum frequency of excitation one can reach is $F_e/F_n=2.5$ for Re=1900 and $F_e/F_n=1.5$ for Re=3200. The greater enhancement in the heat transfer at $F_e/F_n=2$ and 2.5, as shown in Figs. 6(*a*) and 6(*b*), suggests that synchronization also occurs at higher Reynolds numbers. However, the percentage of the heat transfer enhancement at higher Reynolds numbers is higher than that at lower Reynolds numbers. The trends found for streamwise oscillation of cylinder reverse the trends found for transverse oscillation of cylinder [1]. This is attributed to the fact that at a higher Reynolds number the amplification of disturbance by the reverse motion of cylinder is more efficient than the amplification of disturbance by the flow itself. Therefore, one can expect that to get the same percentage of heat transfer enhancement, the excitation energy, i.e., the excitation amplitude, provided can be smaller. Note that the heat transfer at $F_e/F_n=1.5$ is still very high especially at a high Reynolds num-

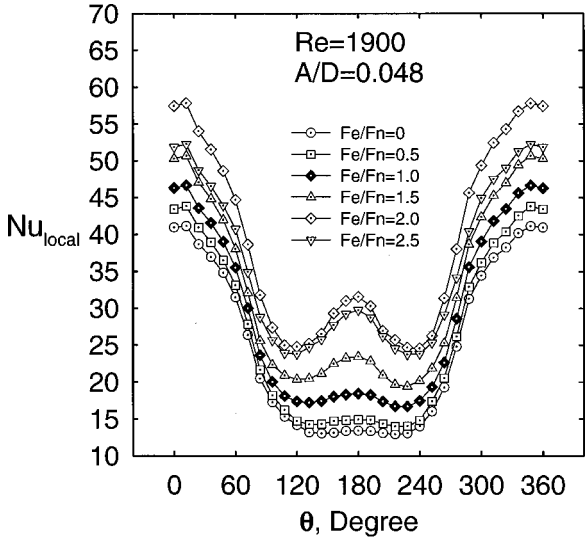

(*a*)

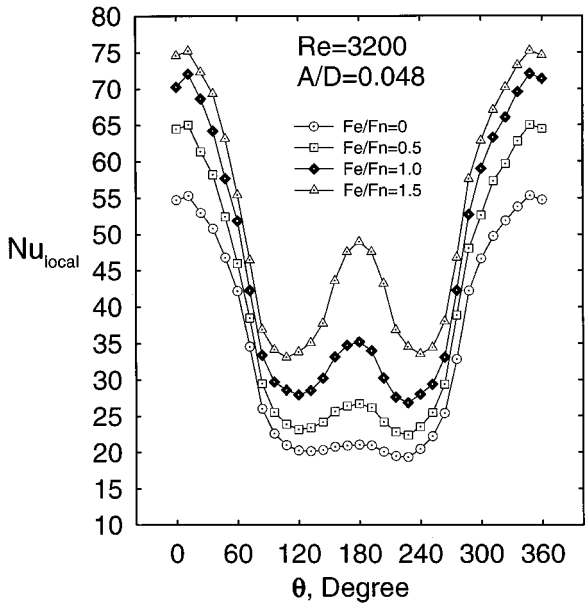

(*b*)

Fig. 6 The Nusselt number distributions around the cylinder at different excitation frequencies for $A/D=0.048$ and (*a*) Re =1900 and (*b*) Re=3200

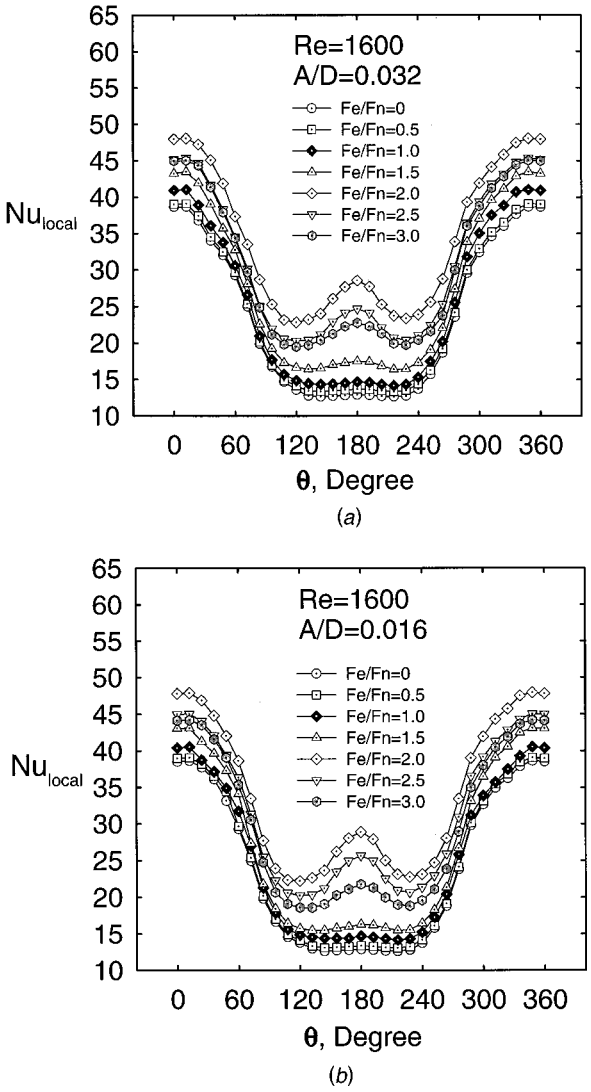

Fig. 7 The Nusselt number distributions around the cylinder at different excitation frequencies for Re=1600 and (*a*) *A*/*D* =0.032 and (*b*) *A*/*D*=0.016

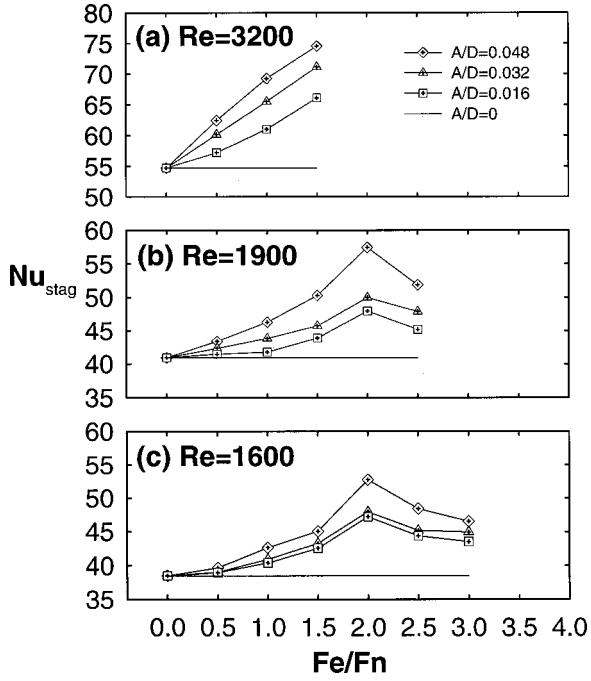

Fig. 8 The stagnation point Nusselt number for cylinder excitation at different frequencies and amplitudes with (*a*) Re =3200, (*b*) Re=1900, and (*c*) Re=1600

ber. As explained in Fig. 3(*f*), although the cylinder oscillation is synchronized with every two of the vortex initiated in one side (either the upper or the lower side) of the cylinder, the phase of vortex shedding in the other side is close to the phase of the cylinder displacement. This will cause earlier initiation and more rapid growth of the vortex, as shown in Fig. 2(*f*).

At a lower amplitude excitation of cylinder, as shown in Fig. 7(*a*) and 7(*b*), the heat transfer enhancement is reduced. This is due to the fact that the excitation energy provided to disturb or amplify the instability in the flow become small. However, the heat transfer at $F_e/F_n=2$, 2.5, and 3 is still significantly larger than at other frequencies where synchronization is not expected to occur. It appears that synchronization of vortex shedding with the cylinder oscillation still occurs at these small amplitudes. When the oscillation frequency of the cylinder is expected to completely synchronize with the natural shedding frequency of the vortex, i.e., at $F_e/F_n=2$, the enhancement in the heat transfer is the higher than the cases at $F_e/F_n=2.5$ and 3. Synchronization at these small amplitudes is not reported in the literatures [2,3]. The threshold amplitude versus the frequency ratio F_e/F_n for the control of cylinder oscillation over vortex shedding in the report by Griffin and Ramberg [2] suggests that synchronization of vortex shedding with the cylinder excitation does not occur in these small amplitudes. Therefore, the current findings do not support previous conclusions in the literature. This may be caused by the difference of the Reynolds numbers used in a different work. The Reynolds number in experiments by Griffin and Ramberg is at Re=100 and 190 which is significantly lower than the one used in the current experiments.

Similar trends as discussed previously can be observed in Fig. 8 for the stagnation point heat transfer and Fig. 9 for the average heat transfer. In the experimental ranges covered for the Reynolds number from 1600 to 3200 and A/D from 0.016 to 0.048, in general, the decrease in the Reynolds number or the decrease in the excitation amplitude of the cylinder leads to a less enhancement of heat transfer. To obtain a higher heat transfer enhancement at small amplitude oscillation, the excitation of cylinder must be synchronized with the shedding of the vortex. The simultaneous enhancement of the heat transfer at the back, the front side and the stagnation point of the cylinder at smaller amplitudes suggests again that the instability occurred in the back of the cylinder is actually initiated far upstream at the stagnation point. The instability is suppressed as the flow moves up the cylinder and accelerates, and re-amplified as the flow moves down the cylinder and decelerates. Excitation of the cylinder can amplify the instability, disturb the flow and enhance the heat transfer, especially when synchronization occurs.

Conclusions

Current experiments are performed for Re in the range from 1600 to 3200, A/D from 0 to 0.048 and F_e/F_n from 0 to 3.0. Flow visualization has provided a clear vortex structure that grows more rapidly as the dominant mode of the instability in the shear layer can be amplified by the excitation. Synchronization of the vortex shedding with the cylinder oscillation occurs not only at $F_e/F_n=2$ but also at $F_e/F_n=2.5$ and 3, which can greatly enhance the heat transfer. At $F_e/F_n=2.5$ and 3, however, due to the suppression effect by the forward motion of the cylinder, vortex formation appears in symmetric mode. Only part of the excitation energy can be used to disturb the flow. This leads to a smaller enhancement in the heat transfer than the case at F_e/F_n

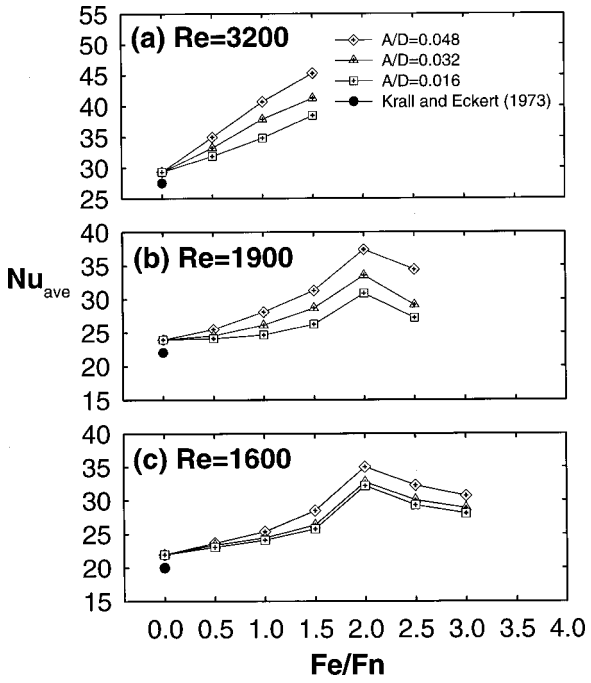

Fig. 9 The average Nusselt number for cylinder excitation at different frequencies and amplitudes with (*a*) Re=3200, (*b*) Re =1900, and (*c*) Re=1600

=2. Synchronization can also occur at very small amplitudes of excitation, which can also greatly enhance the heat transfer. This has not been found in other reports. At higher Reynolds number (Re 11600), enhancement in the heat transfer becomes greater. For $F_e/F_n \leq 1.5$, the vortex formation length decreases and the vortex becomes stronger which leads to a greater enhancement in the heat transfer as the excitation frequency of the cylinder increases. In general, the accompanying enhancement of the heat transfer in both the stagnation point and its downstream region suggests that the dominant mode of the instability occurred in the wake region is actually initiated in the stagnation point region, which is suppressed in the accelerated flow region and re-amplified in the decelerated flow region. Therefore, as the cylinder oscillation frequency is closer to twice the natural instability frequency (i.e., the Strouhal frequency) in the shear layer, a greater enhancement in the heat transfer at every point around the cylinder is obtained.

Acknowledgments

This research was sponsored by the National Science Council of Taiwan under contract No. NSC 86-2212-E-006-046.

Nomenclature

A = oscillating amplitude of cylinder
D = diameter of cylinder
F_e = oscillating frequency of cylinder
F_n = natural shedding frequency of the vortex
h = convective heat transfer coefficient
I = electric dc current
k = thermal conductivity of air
Nu = local Nusselt number, hD/k
q = heat flux
Re = Reynolds number, u_oD/ν
St = Strouhal number, F_nD/u_o
t = time
Te = the period for complete cycle of vortex formation, $1/F_n$
T = temperature
u = velocity
V = voltage

Greek Symbols

ν = kinematic viscosity
θ = angle measured from the stagnation point

Subscript

ave = refers to average
o = refers to freestream
stag = refers to stagnation
w = refers to the wall of cylinder

References

[1] Gau, C., Wu, J. M., and Liang, C. Y., 1999, ''Heat Transfer Enhancement and Vortex Flow Structure over a Heated Cylinder Oscillating in Cross-Flow Direction,'' ASME J. Heat Trasfer , **121**, No. 4, pp. 789–795.
[2] Griffin, O. M., and Ramberg, S. E., 1976, ''Vortex Shedding from a Cylinder Vibrating in Line With an Incident Uniform Flow,'' J. Fluid Mech., **75**, pp. 257–271.
[3] Ongoren, A., and Rockwell, D., 1988, ''Flow Structure form an Oscillating Cylinder, Part 2. Mode Competition in the Near Wake,'' J. Fluid Mech., **191**, pp. 225–245.
[4] Kline, S. J., and McClintock, F. A., 1953, ''Describing Uncertainties in Single-Sample Experiments,'' Mech. Eng. (Am. Soc. Mech. Eng.), **75**, pp. 3–12.
[5] Coleman, H. W., and Steele, W. G. 1999, *Experimentation and Uncertainty Analysis for Engineers*, Wiley, New York.
[6] Roshko, A., 1954, ''On the Drag and Shedding Frequency of Two-Dimensional Bluff Bodies,'' NACA Technical Note, p. 3169.
[7] Zdravkovich, M. M., 1982, ''Modulation of Vortex Shedding in the Synchronization Range,'' ASME J. Fluids Eng., **104**, pp. 513–517.
[8] Wu, S. X., 1998, ''Vortex Formation Process and Heat Transfer over a Heated Cylinder Oscillating in the Streamwise Direction of the Flow,'' M. S. thesis, National Cheng Kung University, Tainan, Taiwan, ROC.
[9] Takahashi, K., and Endoh, K., 1990, ''A New Correlation Method for the Effect of Vibration on Forced Convection Heat Transfer,'' J. Chem. Eng. Jpn., **23**, No. 1, pp. 45–55.

Characterization of the Effect of Corrugation Angles on Hydrodynamic and Heat Transfer Performance of Four-Start Spiral Tubes

X. D. Chen

X. Y. Xu
Department of Chemical and Materials Engineering,
The University of Auckland,
Private Bag 92019,
Auckland, New Zealand

S. K. Nguang
Control Engineering Group,
Department of Electrical and Electronic Engineering,
The University of Auckland,
Private Bag 92019,
Auckland, New Zealand

Arthur E. Bergles
Department of Mechanical Engineering,
Aeronautical Engineering and Mechanics,
Rensselaer Polytechnic Institute,
Troy, New York, U.S.A.

A series of four-start spirally corrugated tubes has been subjected to heat transfer and hydrodynamic testing in a double-pipe heat exchanger. The study has been focused on the non-symmetric nature of the corrugation angles along the longitudinal direction. Both friction factors and heat transfer coefficients inside the tubes have been correlated against various process parameters. It can be shown that by altering the internal non-symmetric wavy shapes of the tubes, one is able to manipulate heat transfer and friction characteristics. The experimental results have been compared with some popular correlation models developed previously for both friction and heat transfer for corrugated tubes. Considerable differences between the experimental results and the predictions made using the existing correlations have been found and the probable causes have been discussed. Performance evaluation criteria are presented using the standard constant power criterion. A neural network modeling approach has been taken so that, based on the limited data, one can generate the contour showing the effect of corrugation angle on heat transfer coefficient for geometry optimization purposes. [DOI: 10.1115/1.1409261]

Keywords: Enhancement, Heat Transfer, Heat Exchangers, Internal

Introduction

The design of high performance thermal systems is still stimulating considerable interest. The conventional heat exchangers are improved by means of a number of argumentation techniques. Many types of surface enhancements have been studied for the augmentation of forced convection heat transfer inside tubes. Sand grain tubes [1], transverse ribbed tubes [2], finned tubes [3], wire-coil-inserted tubes [4] and spirally corrugated tubes [5–9] have been extensively investigated and some of these have been used as augmentative devices for enhancing the turbulent flow heat transfer coefficient. There are a number of rather comprehensive review articles published previously on this topic, e.g., a recent one by Ravigururajan and Rabas [8].

The spirally corrugated tube is widely used in the industry and has several advantages over other modified surfaces, i.e., easier fabrication, higher enhancements (compared with the flat surface) of the heat transfer coefficient, and limited increase in friction loss. This type of tubes is not only used for the shell-side as well as for the tube-side heat transfer enhancement.

It is generally accepted that four geometric parameters are sufficient for characterizing the spirally corrugated tube, i.e., the groove pitch (P), the groove depth (H_i) (in this work this refers to the internal ridge height), the helix angle (α) and the groove shape (see Fig. 1(a) and (b)). A change in any of these parameters should affect the heat transfer and friction characteristics of the tube. The performance evaluation criteria have also been established and summarized by various authors [10–12]. There have been a number of experimental work done and correlation equations established in literature [1–9,18–20].

The effect of groove shape (or the effect of the angles in Fig. 1(c), which shows a non-symmetrical groove investigated in the current work) has not been reported in previous literature. Here the angles of interest are α' and α'' (Fig. 1(c)) which can be seen to be different from the helix angle α (Fig. 1(a)). Because of the non-symmetrical nature along the longitudinal direction, one expects quite different fluid flow patterns occurring in the grooves if the fluid is fed in at different direction into the tube, thus inducing different frictional and heat transfer characteristics. The consequence of this non-symmetric feature has been evaluated in the current work.

This paper describes the results of an experimental investigation testing the performance of nine spirally corrugated tubes with different wavy shapes of the non-symmetrical nature as mentioned above. A neural network approach has been undertaken to correlate the data and to produce the empirical formula for practical use.

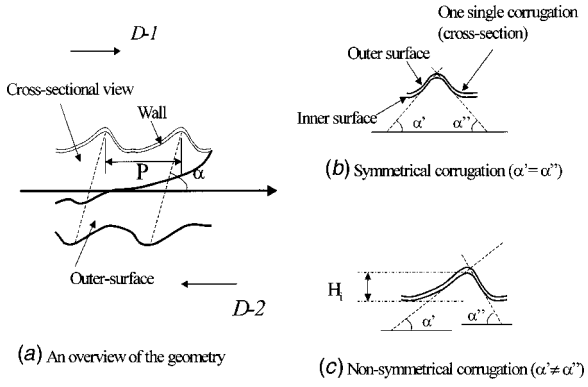

Fig. 1 Characteristic parameters of the spirally corrugated tube (the dashed lines are the outlines one would see from the outside of the tube); α is the usual helix angle.

Contributed by the Heat Transfer Division for publication in the JOURNAL OF HEAT TRANSFER. Manuscript received by the Heat Transfer Division August 29, 2000; revision received April 23, 2001. Associate Editor: B. T. F. Chung.

Experimental

Experimental Setup. The experimental work was carried out in a double-pipe heat exchanger (refer to Fig. 2) in the Department of Chemical and Materials Engineering of the University of Auckland. The experimental set-up shown in Fig. 2 consisted of a double-pipe heat exchanger, steam jacketed tank, water tank, rotameters, pumps and data acquisition unit. Tap water was used as the working liquid for both streams through the heat exchanger. The heat exchanger was degassed during each start-up period. The fluid flow was arranged in a counter-flow mode within the heat exchanger to give a large log-mean-temperature-difference (LMTD) for better measurement accuracy. Hot water was prepared in a steam-jacketed kettle. A 0.96-kW electric powered pump was used for the annulus side loop and a 0.75-kW one for the tube side. Three standard variable-area flow tubes (Fisher Controls Limited, England) were used to measure the water flow rates for both streams. A 24E rotameter was used for the tube side; a 35E rotameter for the annulus side and, another 35E for monitoring the mixing of cold water with the water to achieve the required steady state temperature.

Nine spirally corrugated copper tubes with different wavy shapes but similar corrugation heights were selected in this investigation from a large number of tubes manufactured specially for this study using a 3 wheel-head compression-extrusion facility available at Parex Industries (Auckland, NZ). Figure 3 shows a photo of the corrugated tubes. The geometric parameters are listed in Table 1. The heat exchanger was set up at the vertical direction with the flow entered the tube at the bottom end. The straight-length of the tubes was 1.015 meter. The annular diameter was 50 mm and the internal tube diameter was 19.2 mm. The inner tube was either a smooth or a spirally corrugated copper tube. A pair of brass connectors was made for connecting the tube and the pipe for easy alteration of inner tubes. Both inlet and outlet temperatures in the shell-side and the tube-side streams were measured using type-T thermocouples. Four temperature probes of 3 mm diameter were mounted directly on a miniature plug and linked through a Hewlett-Packard 61013A Digital Multimeter and a 61011A Relay Multiplexer, to a IBM 286 computer for displaying and recording the data. The temperature readings had errors within $\pm 0.2°C$. Insulation (50 mm) was applied on all the elements of the test section to minimize heat losses.

To verify the experimental set-up, a smooth copper tube, which had the same nominal diameter as the spirally corrugated tubes, was used to measure for both friction factor and heat transfer coefficients. An inverted U-tube manometer was used to measure the pressure drop along the length of the tube. Clear plastic tubes were used so that air bubbles could be visualised and eliminated.

Experimental Procedure. Pressure drops were all measured

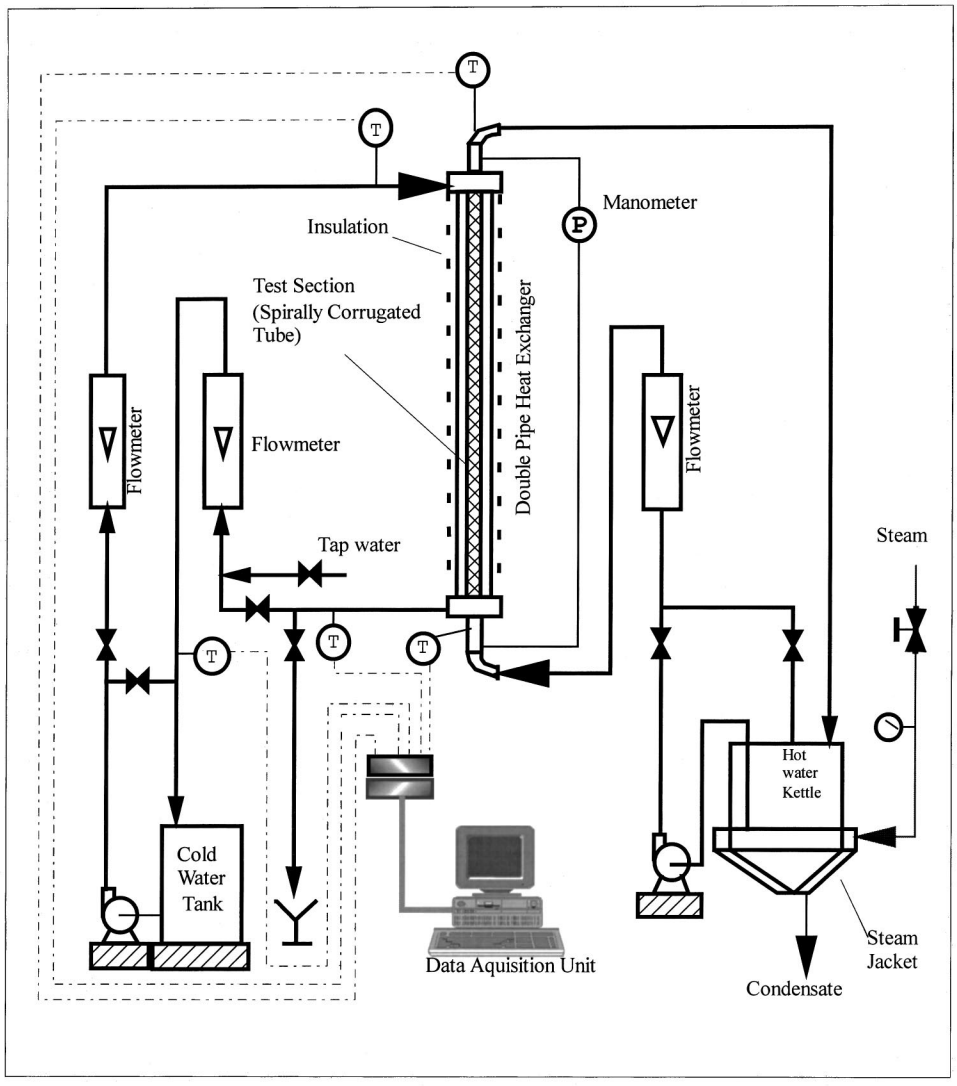

Fig. 2 Schematic diagram of the experimental setup

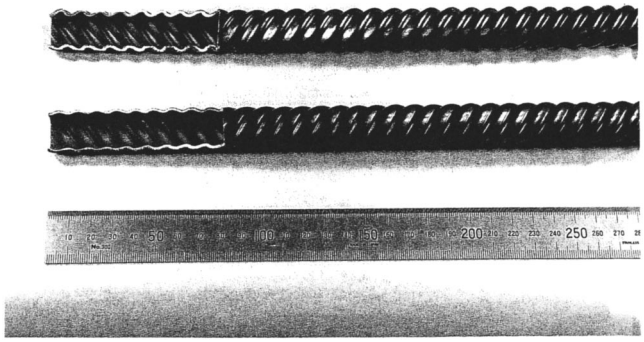

Fig. 3 Photo of spirally corrugated tubes

at room temperature and under turbulent flow regimes. A series of runs at different flow rates was carried out for each tube in the D-1 and D-2 direction (as shown in Fig. 1). The height of the water column in each side of the manometer and the corresponding flow rate and inlet and outlet water temperatures were recorded. The experimental procedure for heat transfer performance was the same for all the tubes tested in the present work. All the tests were performed after steady state was attained. The cold water was placed in the annulus and the hot water in the tube. The cold water was maintained at constant flow rate (33.0 *L*/min) for all test runs and an essentially constant temperature difference between the inlet and the outlet of the shell side was held (3±0.2°C). The average temperatures in the shell side were maintained at the level of 28–33°C. All these ensured a constant shell side heat transfer coefficient (h_o). The tube side temperature drops were in general greater than 9°C, the inlet temperatures were from 70 to 76°C and the flow rates were from 5 *L*/min to just over 15 *L*/min. In each run, once the steady-state temperatures had been reached, the temperature readings over a period of 7~10 minutes were saved and averaged for later data analysis. A heat balance of the two sides in all the runs reported here were between ±2 percent and ±5 percent. The Prandtl number ranged from ~2.3 to 2.6. The Reynolds numbers ranged from 13,000 to 41,000 and the tube side heat transfer coefficients (h_i) ranged from around 4,000 to about 12,000 ($W.m^{-2}.K^{-1}$). The heat flows from the annulus side to the tube side were in the order of 1×10^4 W.

Data Analysis

For the determination of the tube-side friction factors and convective heat transfer coefficients, the flow rates, temperatures of the inlet and outlet streams, and the pressure drops along each tube were measured. The following standard equations were used for the analyses [21].

Friction Factor. The pressure drop data were converted to Fanning friction factors using the following equation:

$$f=\frac{D_i g\Delta H}{2V^2L}. \tag{1}$$

The Fanning friction factors for both smooth and spirally corrugated tubes are related to the *Reynolds* number by the following equation, which has been widely accepted in the literature,

$$f=\frac{\beta}{\mathrm{Re}^j}. \tag{2}$$

Here, the *Reynolds* number is defined as $\mathrm{Re}=\rho VD_i/\mu$ and β is a constant, and j is the power of the Re dependence function.

For smooth tubes, the classical Blasius equation applies with $\beta_{\mathrm{smooth}}=0.079$ and $j_{\mathrm{smooth}}=0.25$ [21]. A plot of $\ln f$ versus $\ln\mathrm{Re}$ should give a straight line with a slope of $-j$ and a intercept of $\ln\beta$.

Heat Transfer Coefficient. The rate of heat transfer is determined experimentally by

$$q=\dot{m}C_p\Delta T_{\mathrm{tube}}, \tag{3}$$

where ΔT_{tube}=inlet temperature—outlet temperature. The log-mean temperature difference (LMTD) was used to determined the overall heat transfer coefficient *U*. The result for the integrated energy equation can then be written as

$$q=UA_i(LMTD). \tag{4}$$

The overall heat transfer coefficient can then be determined by substituting Eq. (3) into (4) to give

$$U=\frac{\dot{m}C_p\Delta T_{\mathrm{tube}}}{A_i(LMTD)}. \tag{5}$$

The overall heat transfer coefficient based on the inside surface area of a clean tube is influenced by three components

Table 1 Copper tube specifications used in this work

Tube Label	D_I (mm)	D_0 (mm)	H_i (mm)	P (mm)	α (deg.)	H_i/D_i	P/D_i	α/90	α'	α''	180°-($\alpha+\alpha''$)	α'/α''
no. 1	18.89	20.98	2.21	8.99	61.38	0.117	0.476	0.682	28.5	47.4	104.1	0.60
no. 2	18.85	20.99	2.20	9.01	61.34	0.117	0.478	0.682	29.7	48.6	101.7	0.61
no. 3	18.90	21.00	2.22	9.02	61.33	0.117	0.477	0.681	32.1	53.4	94.5	0.60
no. 4	18.86	20.99	2.21	9.00	61.37	0.117	0.477	0.682	31.9	58.3	89.8	0.55
no.35	18.90	20.99	2.21	8.31	63.25	0.117	0.440	0.703	32.8	54.9	92.3	0.60
no.40	18.90	21.00	2.19	8.52	62.68	0.116	0.450	0.696	31.3	53.2	95.5	0.59
no.45	18.88	20.98	2.20	8.95	61.49	0.117	0.474	0.683	28.8	51.7	99.5	0.56
no.50	18.89	20.98	2.20	9.31	60.53	0.118	0.493	0.673	27.8	51.7	100.5	0.54
no.55	18.90	20.98	2.21	9.92	58.95	0.117	0.525	0.655	26.4	50.8	102.8	0.52
smh*	18.90	20.99	0	0	0	0	0	0	0	0	0	0

*Smh: smooth

$$\frac{1}{UA_i} = \frac{1}{h_i A_i} + \frac{R_w}{A_i} + \frac{1}{h_o A_o}. \tag{6}$$

R_w is the tube wall thermal resistance, $R_w = r_i \ln(r_o/r_i)/k$. Because the wall is made of copper and is of about 1 mm thick giving a resistance in the order of 1×10^{-6} K.m^2.W^{-1}, this resistance has been assumed to be negligible when compared with the convective resistances (which are in general greater than 1×10^{-4} K.m^2.W^{-1}). Again because the tube wall is thin (about 1 mm) it has been assumed that $A_i \approx A_o$.

As mentioned in the experimental section, the heat transfer coefficient of the shell side was kept constant. The last term of Eq. (6) can then be taken as a constant, *B*. The following can then be obtained

$$\frac{1}{U} = \frac{1}{h_i} + B. \tag{7}$$

Nothing that the *Nusselt* number for the tube side can be given by

$$\mathrm{Nu} = \frac{h_i D_i}{k_w} = C \cdot \mathrm{Re}^m \mathrm{Pr}^n. \tag{8}$$

C is 0.023, $m=0.8$, and $n=0.3$ for the smooth tube [21]. The Reynolds number exponent (m) is known to vary from 0.8 for smooth tubes to a maximum of 1.17 for the roughest tubes [6,9]. Although there are other correlations which can be used to treat the data points but none of these allows a simple-effective comparison of the effect of angle in this study. While keeping $n=0.3$, the exponent (m) in Eq. (8) had been varied in the data analysis but the improvement in linearity in the correlation presented here was minimal thus this value was taken as 0.8 for all cases. As such, it was very convenient to simply use C (in Eq. 8) as the parameter for the purpose of comparison, without worrying about the parameter (m) being variable at the same time.

Following Eq. (7) and (8), we can now have

$$\frac{1}{U} = \frac{1}{C} \frac{1}{\mathrm{Re}^{0.8}\mathrm{Pr}^{0.3}\dfrac{k_w}{D_i}} + B. \tag{9}$$

A Cartesian plot of $1/U$ versus $(\mathrm{Re}^{0.8}\,\mathrm{Pr}^{0.3}(k_w/D_i))^{-1}$ should yield a straight line, giving a slope $1/C$ and an intercept B (Typical examples are given in Fig. 4; in general the results had the correlation coefficient r^2 better than 0.98.)

Performance Evaluation Criteria (PEC). Bergles et al. [10] presented their PEC for enhanced heat transfer surface in 1974, and Webb [11] extended it and established a broad range of PEC applicable to single-phase flow in tubes in 1981. A major PEC is to maximize the heat transfer rate for equal pumping power and nominal heat exchanger surface area. The criteria can be conveniently expressed by an enhancement factor h^*, which is defined as the ratio of the spirally corrugated tube side heat transfer coefficient (h_{ia}) to the smooth tube side heat transfer coefficient (h_{is}) for equal pumping power:

$$h^* = \left(\frac{h_{ia}}{h_{is}}\right)_{\text{equal pumping power}} \tag{10a}$$

The tube side heat transfer coefficient h_{ia} of each spirally corrugated tube is calculated using the equivalent flat pipe *Reynolds* numbers (Re_{eq}) [12] using the correlation established in this study. The equivalent Reynolds number for this criterion is defined as follows:

$$\mathrm{Re}_{eq} = \left(\frac{\beta}{\beta_{\text{smooth}}} \cdot \mathrm{Re}^{3-j}\right)^{1/3-j_{\text{smooth}}}, \tag{10b}$$

where, ''smooth'' denotes the values for the smooth tube.

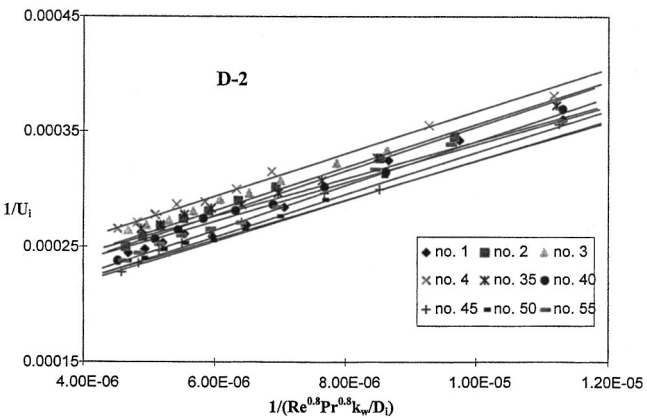

Fig. 4 Plot for obtaining the constants *C* in Eq. (8) for copper tubes at *D*-2 direction

Neural Network Analysis. The neural network analysis was undertaken to generate the contour plot showing how the correlation constant in Eq. (8), C, varies with the two angles of interest. Because the difficulty involved in making the angles that would match an ideal experimental design for statistical purposes, the non-uniform data point distribution was thought to be best characterized by the neural network approach. The neural network technique used here is based on the Radial Basis Function (RBF) Network which were first used within the neural network community in 1988 by Broomhead and Lowe [13]. These networks were originally proposed as a technique for modelling data in high-dimensional space [14]. Recently, RBF networks have been widely used for data modelling and control task. In a series of papers by Chen et al. [15–17], a variety of different learning algorithms have been used to train the RBF networks for a wide range of different modelling problems. Here, the radial basis functions have a special structure, that is,

$$f_i(X) = R(\|W_i - X\|_2), \tag{11}$$

where W_i is the n-dimensional vector denoting the center of the ith basis function, $\|\cdot\|_2$ is the common Euclidean norm, and $R(\cdot)$ is a univariate function from R^+ to R. The network output is then formed from a linear combination of these basis functions. For predicting the heat transfer coefficient (here, the coefficient C is the object representing heat transfer coefficient as mentioned above) as influenced by the angles illustrated in Fig. 1, the radial basis function that we consider is of the form

$$f_i(X) = \exp(-\|W_i - X\|_2^2 B_i), \tag{12}$$

where W_i is the n-dimensional vector and B_i is the bias. The network output is given by

$$\hat{y} = B_L + \sum_{i=1}^{k} L_i f_i(X), \tag{13}$$

where L_i and B_L are constants. There are essentially three angles one can use to describe the shape of the corrugation (refer to Fig. 1). Attempts have been made to correlate the angles with the friction factors, but this was not successful. All the three angles (α', α'' and 180 deg$-(\alpha'+\alpha'')$) were first normalized based on 180 deg. Exercises were carried out to see if each of the angles had effects on heat transfer coefficients. The network input vector is

$$X = \begin{cases} [\alpha' \quad \alpha'' \quad (\alpha'+\alpha'')]/180\,\text{deg} & \text{for } D-2 \\ [\alpha'' \quad \alpha' \quad (\alpha'+\alpha'')]/180\,\text{deg} & \text{for } D-1 \end{cases} \tag{14}$$

The network output is $y = C$.

We picked (with no preference) the following set of data for training the network: the values of all the above three angles, the values of C (see Eq. (8)) for no. 35, 40, 45, 50, and 55 were

selected for direction D-1 and nos. 1, 2, 3, and 4 were chosen for direction D-2 (refer to Tables 1 and 3). The remaining nine sets of data were used for testing the network. The MATLAB Neural Network Toolbox was used to train the network. It was found that four radial basis neurals are good enough for predicting the heat transfer coefficients. The four radial basis functions are given as follows:

$$f_i(X) = \exp(-\|W_i - X\|_2^2 B_i) \quad \text{for} \quad i = 1,2,3,4, \tag{15a}$$

where

$$W_1 = [0.3050 \;\; 0.1822 \;\; 0.4872], \; B_1 = 0.8325 \tag{15b}$$

$$W_2 = [0.1583 \;\; 0.2633 \;\; 0.4217], \; B_2 = 0.8325,$$

$$W_3 = [0.2822 \;\; 0.1467 \;\; 0.4289], \; B_3 = 0.8325,$$

$$W_4 = [0.1650 \;\; 0.2700 \;\; 0.4350], \; B_4 = 0.8325, \text{ and,}$$

$$L_1 = 33.2602, \; L_2 = 139.7302, \; L_3 = -31.3159,$$

$$L_4 = -141.5159, \; B_L = -0.0166$$

Results and Discussion

Friction Factor. The calculated friction factors of the smooth copper tube tested were found to be satisfactorily correlated by the classical Blasius equation, over the range of Reynolds number from about 10,000 to 25,000 with relative errors within ±2 percent. The same technique was applied to the spirally corrugated tubes to generate the results of f versus Re. Because the wavy shape is not symmetrical, two different flow directions showed considerable differences in both hydrodynamic and heat transfer performance. Both flow directions D-1 and D-2 (see Fig. 1) were investigated. The values for β and j for each tube (see Eq. (2)) are listed in Table 2 with r^2 values of better than 0.95.

The calculated Fanning friction factors of the smooth and all spirally corrugated tubes are plotted against Reynolds number for both flow directions in Fig. 5. The friction factors of the spirally corrugated tubes are clearly greater than that of the smooth tube under the same operation conditions. Also, it can be seen that the effect of the corrugation angle (thus the effect of flow direction) is very significant.

The pressure drop results were compared with the correlation by Ravigururajan and Bergles [18] for several internally ribbed tubes with wide ranges of H_i/D_i(0.01–0.2), P/D_i(0.1–7.0), α/90(0.3,1.0), flow parameters Re (5,000–250,000) and Pr (0.66–37.6):

$$\frac{f}{f_s} = \left\{ 1 + \left[29.1 \,\mathrm{Re}^{k_1} \left(\frac{H_i}{D_i}\right)^{k_2} \left(\frac{P}{D_i}\right)^{k_3} \left(\frac{\alpha}{90}\right)^{k_4} \times \left(1 + \frac{2.94}{n_o} \sin\psi \right) \right]^{15/16} \right\}^{16/15}, \tag{16}$$

where, f_s is Filenenko's smooth tube fraction factor which is defined as

$$f_s = (1.58 \mathrm{Ln}\,\mathrm{Re} - 3.28)^{-2} \tag{17}$$

and

Table 2 The values of j and β (Eq. (2)) for spirally corrugated tubes ($r^2 > 0.95$)

Direction	**D-1**								
Tube No	no. 1	no. 2	no. 3	no. 4	no.35	no.40	no.45	no.50	no.55
j	0.153	0.068	0.157	0.101	0.124	0.059	0.130	0.089	0.103
β	0.295	0.119	0.309	0.200	0.239	0.131	0.265	0.179	0.213
Direction	**D-2**								
Tube No	no. 1	no. 2	no. 3	no. 4	no.35	no.40	no.45	no.50	no.55
j	0.190	0.265	0.202	0.232	0.297	0.181	0.250	0.275	0.286
β	0.303	0.638	0.329	0.496	0.985	0.317	0.623	0.834	0.814

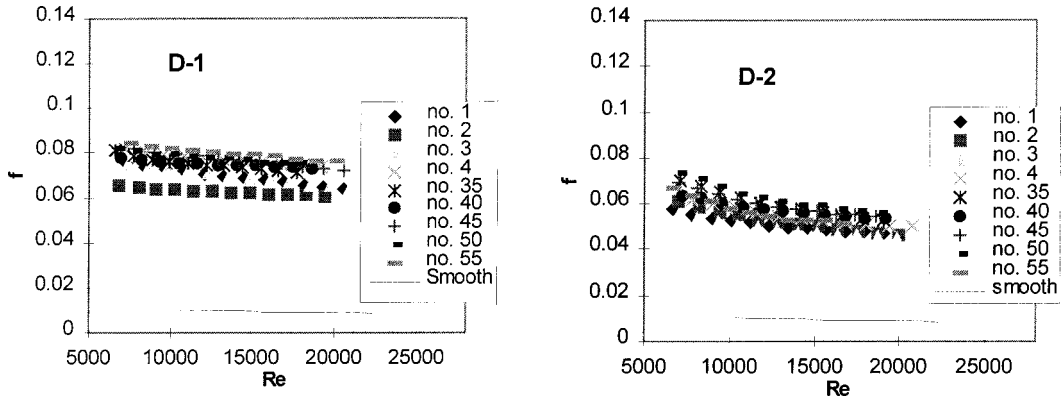

Fig. 5 Dependence of the Fanning friction factors of spirally corrugated tubes on Reynolds numbers

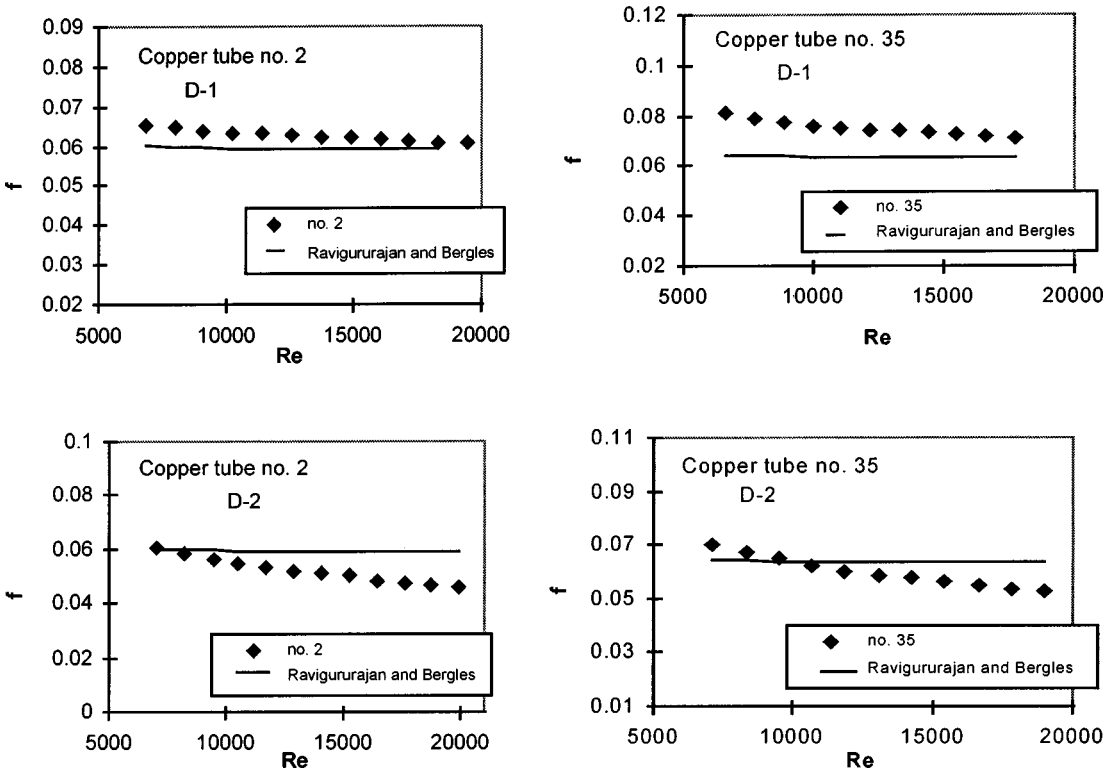

Fig. 6 Comparison of the friction factors for the tubes no. 2 and no. 35

$$k_1 = 0.67 - 0.06\frac{P}{D_i} - 0.49\frac{\alpha}{90}$$

$$k_2 = 1.37 - 0.157\frac{P}{D_i}$$

$$k_3 = -1.66\times 10^{-6}\,\mathrm{Re} - 0.33\frac{\alpha}{90} \qquad (18)$$

$$k_4 = 4.59 + 4.11\times 10^{-6}\,\mathrm{Re} - 0.15\frac{P}{D_i},$$

where, n_o is the number of sharp corners facing the flow and ψ is the profile's contact angle [18].

As an example, for the D-1 direction, the friction factor results of tube no. 2 can be shown to be close to the values predicted by this general correlation. The results of tube no. 35 are higher than the values predicted and the errors are up to some 25 percent in the Re range tested. Generally the errors are smaller for larger Reynolds numbers at D-1 direction. The correlation gives a rather flat curve but the experimental results show more significant declining trends as Reynolds number increases. Figure 6 shows the comparison results for two tubes (i.e., the no. 2 and no. 35 tubes) for both the D-1 and the D-2 directions, respectively. One can see that there are significant differences between the two flow directions.

Heat Transfer Coefficient. The experimental tube-side heat transfer coefficient for water in a smooth tube was first determined. The Dittus and Boelter equation (i.e., Eq. (8) with $m = 0.8$, $n = 0.3$, and $C = 0.023$ [21]) was used to verify the experimental set-up. The result of the constant $C_{\mathrm{smooth}} \approx 0.024$ for this smooth copper tube agrees well with the value 0.023 in the Dittus and Boelter equation. The experimental technique for the spirally corrugated tubes was the same as that used for the smooth tube. The C values (Eq. (8)) are shown in Table 3, with r^2 values that are all better than 0.98.

Examples of the calculated heat transfer coefficients plotted against Reynolds number for the D-1 and D-2 flow directions (for the same Pr and k) are presented in Fig. 7. All the tubes show a

Table 3 C values of the tubes tested ($r^2 > 0.98$)

Direction	**D-1**								
Tube No	no. 1	no. 2	no. 3	no. 4	no. 35	no. 40	no. 45	no. 50	no. 55
C	0.0471	0.0563	0.0635	0.0760	0.0682	0.0629	0.0618	0.0585	0.0552
Direction	**D-2**								
Tube No	no. 1	no. 2	no. 3	no. 4	no. 35	no. 40	no. 45	no. 50	no. 55
C	0.0532	0.0542	0.0553	0.0564	0.0587	0.0548	0.0545	0.0542	0.0540

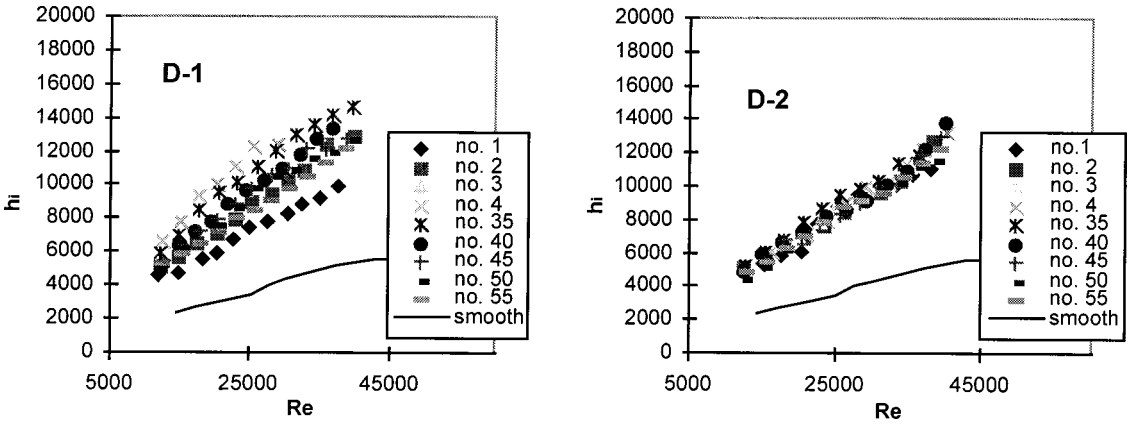

Fig. 7 Dependence of heat transfer coefficients of spirally corrugated tubes against Reynolds numbers

certain degree of heat transfer enhancement. Tube no. 4 had the highest heat transfer enhancement of 272 percent for the flow direction D-1 when compared to the smooth tube; tube no. 1 had the lowest enhancement of 206.8 percent. However, for flow direction D-2, the heat transfer enhancement ranged from 231 percent to 246 percent for all tubes. It was difficult to recognize which angle plays a more important role in heat transfer.

The heat transfer results have been compared with previously established models (i.e., the correlations from Ravigururajan and Bergles [18], Srinivasan and Christensen [19], and Wang et al. [20] which are popular correlations) (see Fig. 8). These models are listed below.

Ravigururajan and Bergles

$$\frac{\mathrm{Nu}}{\mathrm{Nu}_s}=\left\{1+\left[2.64\,\mathrm{Re}^{0.036}\left(\frac{H_i}{D_i}\right)^{0.212}\left(\frac{P}{D_i}\right)^{-0.21}\left(\frac{\alpha}{90}\right)^{0.29}\mathrm{Pr}^{0.024}\right]^7\right\}^{1/7}, \tag{19}$$

where the reference Nu_s is given as

$$\mathrm{Nu}_3=\frac{(f_s/2)\mathrm{RePr}}{1+12.7(f_s/2)(\mathrm{Pr}^{2/3}-1)}. \tag{20}$$

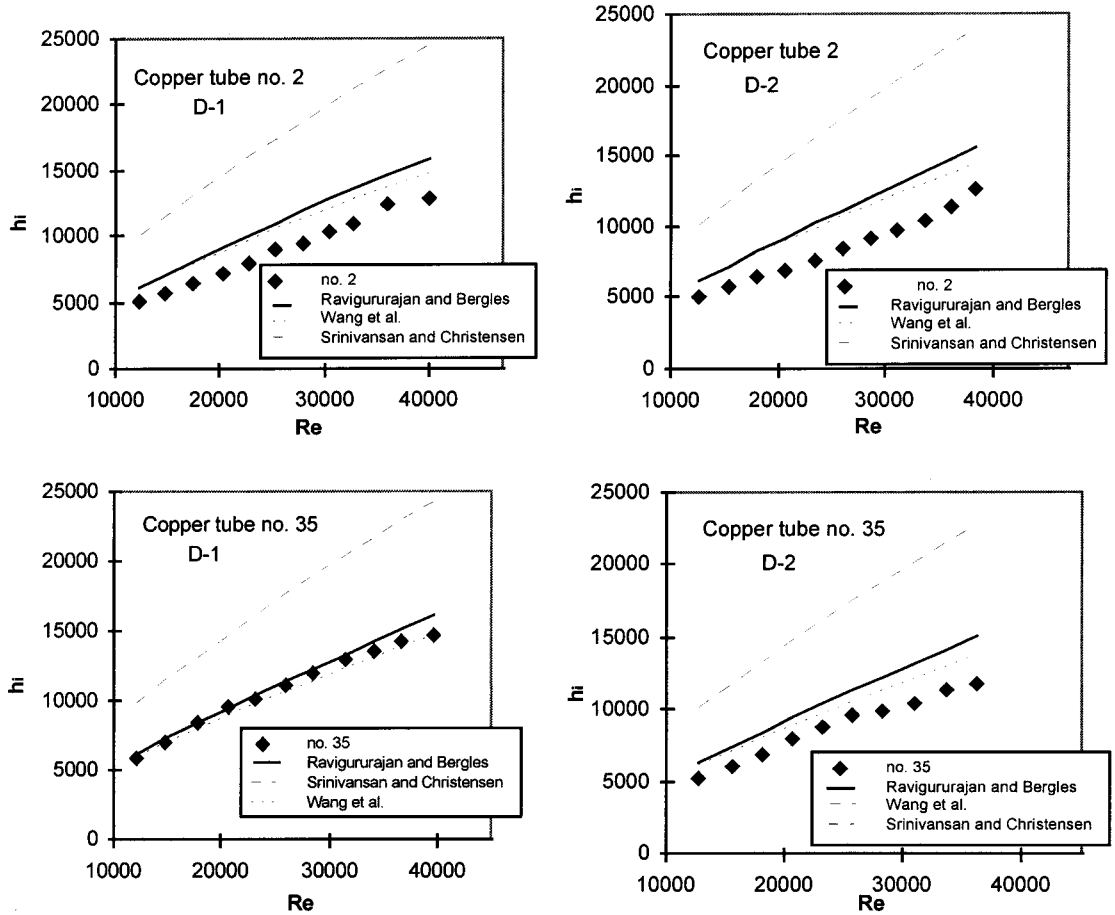

Fig. 8 Comparison of heat transfer coefficients for tubes no. 2 and no. 35

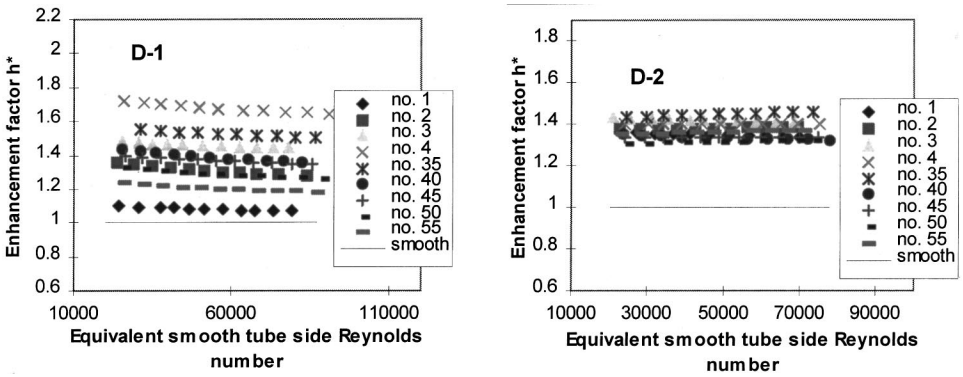

Fig. 9 Heat transfer enhancement factors for the spirally corrugated tubes

Srinivasan and Christensen

(i) for $500 \leqslant Re \leqslant 5{,}000$

$$\frac{Nu}{Pr^{0.4}} = 0.014\,Re^{0.842}\left(\frac{H_i}{D_i}\right)^{-0.067}\left(\frac{P}{D_i}\right)^{-0.293}\left(\frac{\alpha}{90}\right)^{-0.705} \tag{21}$$

(ii) for $5{,}000 \leqslant Re \leqslant 80{,}000$

$$\frac{Nu}{Pr^{0.4}} = 0.064\,Re^{0.773}\left(\frac{H_i}{D_i}\right)^{-0.242}\left(\frac{P}{D_i}\right)^{-0.108}\left(\frac{\alpha}{90}\right)^{-0.599} \tag{22}$$

Wang et al.

$$Nu = 0.178\,Re^{0.77}Pr^{0.4}\left(\frac{H_i}{D_i}\right)^{0.19}\left(\frac{P}{H_i}\right)^{-0.2} \tag{23}$$

One must notice that none of these correlations have the influence of the flow direction due to the non-symmetrical nature of the corrugation angles examined here (see Fig. 1). It was found that the experimental heat transfer coefficients agreed with the general trends predicted by the correlations of Ravigururajan and Bergles [18] and Wang et al. [20] for all tubes with differences of up to 3000 $W.(m^2.K)^{-1}$ (see Fig. 8). The results of this study did not support the correlation presented by Srinivasan et al. [14]. This may well be due to the different tube parameter range for helix angle (α/90 deg) (from 0.3 to 0.65 for the correlation of Srinivasan et al.and from 0.655 to 0.703 for this study).

Performance Evaluation. As a standard practice, the performance evaluation must be carried out with a new geometry. The enhancement factors for the tested spirally corrugated tubes were calculated by Eq. (10) and plotted against the equivalent Reynolds number [12] for constant pumping power in Fig. 9. The enhancement factors h^* were between 1.07 and 1.72 for flow direction D-1 and between 1.31 and 1.46 for D-2. Tube no. 4, which gave good heat transfer performance in the tested *Reynolds* number range, is regarded as the best of all the tubes for the D-1 flow direction; tube no. 35 gave the best performance in its D-2 flow direction.

Neural Network Modeling of the Effect of Corrugation Angle. This method was used, as it is an effective way to derive the response surface of the coefficient *C* for the current set of data. To validate the model developed based on a number of data points obtained in this study, the predicted heat transfer coefficients were plotted against the test data in Fig. 10. The maximum percentage of error is 5.6 percent, except for the first point. The effects of various angles are too complex to be correlated in an analytical manner so it was satisfying to see the neural network approach could give such good results.

Correlation of the *C* values (refer to Eq. (8)) using the neural network model for a broader range of corrugation angles is shown in Fig. 11. Good agreement between the model predictions and the experimental *C* values has been obtained. It can be shown that the

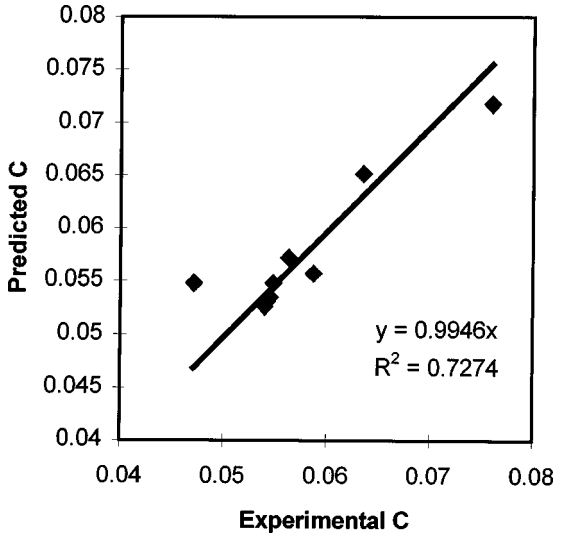

Fig. 10 Comparison between the predicted and the experimental values of *C* (refer to Eq. (8) and Table 3); the solid line indicates 100 percent agreement.

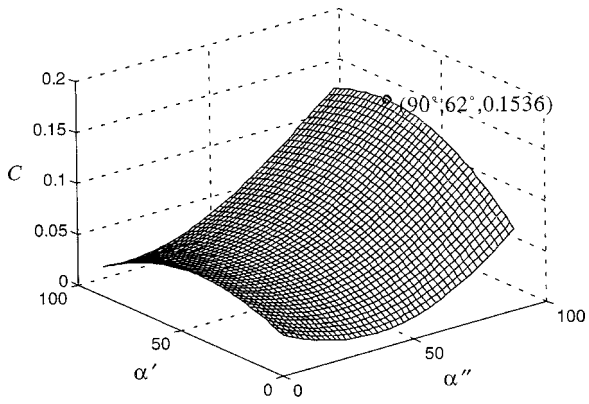

Fig. 11 Predicted *C* value as function of α' and α'' using the neural network model

highest C value, i.e., 0.1536 occurs at $\alpha'' \approx 90$ deg and $\alpha' \approx 62$ deg (corresponding to the flow direction D-1 in Fig. 1(a,c)). The empirical formula, which predicts the response surface shown in Fig. 11 is derived using (12), (13), (14), and (15b) and is given below:

$$C(\alpha',\alpha'') = -0.0166 + \exp(-2.14\times10^{-5}\cdot[(\alpha')^2+(\alpha'')^2+(\alpha'\alpha'')^2]) \cdot \begin{bmatrix} 25.8517\cdot \exp(2.14\times10^{-5}\cdot(285.2\alpha''+241\alpha')) + 115.7059\cdot \exp(2.14\times10^{-5}\cdot(208.8\alpha''+246.6\alpha')) \\ -25.709\exp(2.14\times10^{-5}\cdot(256\alpha''+207.2\alpha')) - 115.8014\cdot \exp(2.14\times10^{-5}\cdot(253.8\alpha''+216\alpha')) \end{bmatrix} \quad (24)$$

Conclusions

In this work, the effect of the corrugation angles on heat transfer and hydrodynamic performance has been investigated. The corrugation angles produce quantitative differences in heat transfer and friction loss for spirally corrugated tubes. The results can be summarized as follows:

- The friction loss was found to become greater as the angle ratio α'/α'' increased. This effect is stronger for flow direction D-1 than for D-2.
- For constant pumping power criteria, the tube no. 4 was found to be the best among all the tested tubes for the flow direction D-1 and no. 35 was the best for D-2.
- A neural network model has been used for correlating the heat transfer coefficient taking into account the effect of the corrugation angles so that the optimal angle combinations can be established.

Manipulation of the corrugation geometry, especially the angle, as this study has shown, may offer opportunities for industry to improve or tailor-make their heat exchangers for specific purposes.

Acknowledgments

The work was partially supported by the Parex Industries Ltd. (NZ) at Auckland City.

Nomenclature

A_i = inner surface area of the tube, m^2
A_o = outer surface area of the tube, m^2
B = heat transfer resistance constant (Eq. (7)), m^2.K/W
C = constant in Eq. (8)
C_p = heat capacity of water, J/Kg.K
D = tube diameter, m
D_i = inner diameter of the heat exchanger tube, m
D_0 = outer diameter of the heat exchanger tube, m
f = fanning friction factor
g = acceleration of gravity, m/s^2
H_i = internal ridge height, mm
h_i = convective heat transfer coefficient (inner tube), W/m^2.K
h^* = heat transfer enhancement factor
j = exponent in Eq. (2)
k = thermal conductivity of copper, W/m.K
k_w = thermal conductivity of water, W/m.K
m = exponent in Eq. (8)
$\dot{m}$ = mass flow rate of water, kg/s
n = exponent in Eq. (8)
Nu = Nusselt number
P = pitch of tube, mm
p = pressure, Pa
Δp = pressure drop along tested tube length, Pa
Pr = Prandtl number
q = heat flux, W
Re = Reynolds number
R_w = resistance to heat transfer through the wall of tube, m^2.K/W
ΔH = pressure drop expressed in terms of water height, m
ΔT_{tube} = temperature difference between inlet and outlet of tube side, K
LMTD = log mean temperature difference, K
U = overall heat transfer coefficient, W/m^2.K
V = velocity of water in the tube, m/s

Greek Letters

α = helix angle, deg
α' and α'' = angles representing the non-symmetrical corrugation (See Fig. 1), deg
β = constant in Eq. (2)
μ = viscosity of water, $N.s/m^2$
ρ = density of water, kg/m^3

Subscripts

a = augmented tube (spirally corrugated)
s = smooth tube
i = inner tube
o = outer tube
w = tube wall or water

References

[1] Dipprey, D. F., and Sabersky, R. H., 1963, "Heat and Momentum Transfer in Smooth and Rough Tubes at Various Prandlt Numbers," Int. J. Heat Mass Transf., **6**, pp. 329–353.
[2] Webb, R. L., Eckert, E. R. G., and Goldstein, K. J., 1971, "Heat Transfer and Friction in Tubes With Repeated Rib Roughness," Int. J. Heat Mass Transf., **14**, pp. 601–617.
[3] Watkinson, A. P., Miletti, D. L., and Tarassoff, P., 1973, "Turbulent Heat Transfer and Pressure Drop in Internal Finned Tubes," AIChE Symp. Ser., **69**, pp. 94–103.
[4] Sethumdhavan, R., and Raja Rao, M., 1983, "Turbulent Flow Heat Transfer and Fluid Friction in Helical Wire Coil Inserted Tubes," Int. J. Heat Mass Transf., **126**, pp. 1833–1845.
[5] Mehta, M. H., and Raja Rao, M., 1988, "Analysis and Correlation of Turbulent Flow Heat Transfer and Friction Coefficient in Spirally Corrugated Tubes for Steam Condenser Application," *Proceedings of 1988 Heat Transfer Conference*, ASME, HTD-96, Vol. 3, pp. 307–312.
[6] Sethumadhavan, R., and Raja Rao, M., 1986, "Turbulent Flow Friction and Heat Transfer Characteristics of Single and Multi-Start Spirally Corrugated Enhanced Tubes," J. Heat Transfer , **108**, pp. 55–61.
[7] Zimparov, V. D., Vunchanov, N. L., and Delov, L. B., 1991, "Heat Transfer and Friction Characteristics of Spirally Corrugated Tubes for Power Plant Condenser: 1—Experimental Investigation and Performance Evaluation," Int. J. Heat Mass Transf. , **34**, No. 9, pp. 2187–2197.
[8] Ravigururajan, T. S., and Rabas, T. J., 1996, "Turbulent Flow in Integrally Enhanced Tubes: Part 1—Comprehensive Review and Database Development," Heat Transfer Eng., **17**, No. 2, pp. 19–29.
[9] Kidd, G. J., 1970, "The Heat Transfer and Pressure Drop Characteristic of Gas Flow Inside Spirally Corrugated Tubes," ASME Read: Transf. J. Heat Transfer, **92**, pp. 513–519.
[10] Bergles, A. E., Blumenkrantz, A. R., and Taborek, J., 1974, "Performance Evaluation Criteria for Enhanced Heat Transfer Surfaces," *Proc. 5th Int. Heat transfer Conf.*, Vol. 2, pp. 239–243.
[11] Webb, R. L., 1981, "Performance Evaluation Criteria for Use of Enhanced Heat Transfer Surface in Heat Exchanger Design," Int. J. Heat Mass Transf., **24**, No. 4, pp. 715–726.
[12] Zimparov, V. D., and Vulchanov, N. L., 1994, "Performance Evaluation Criteria for Enhanced Heat Transfer Surfaces," Int. J. Heat Mass Transf., **37**, No. 12, pp. 1907–1816.
[13] Broomhead, D. S., and Lowe, D., 1988, "Multivariable Functional Interpolation and Adaptive Network," Complex Syst., **2**, pp. 321–355.
[14] Powell, M. J. O., 1987, "Radial Basis Functions for Multivariable Interpola-

tion: A Review,'' in *Algorithms for Approximation of Functions and Data*, J. C. Mason, M. G. Cox, eds., Oxford University Press, pp. 143–167.
[15] Chen, S., Billings, S. A., Cown, C. F. N., and Grant, P. M., 1990, ''Practical Identification of MARMAX Models Using Radial Basis Functions,'' Int. J. Control, **52**, No. 6, pp. 1357–1350.
[16] Chen, S., Billings, S. A., and Grant, P. M., 1992, ''Recursive Hybrid Algorithm for Non-Linear System Identification Using Radial Basis Function Networks,'' Int. J. Control, **55**, No. 5, pp. 1051–107.
[17] Chen, F. C., and Khalil, H. K., 1994, ''Adaptive Control of Non-Linear Systems Using Neural Networks,'' in *Advances in Intelligent Control*, C. J. Harris, ed., Chap. 7, Taylor & Francis, London.
[18] Ravigururajan, T. S., and Bergles, A. E., 1985, ''General Correlations for Pressure Drop and Heat Transfer for Single-Phase Turbulent Flow in Internally Ribbed Tubes,'' *Augmentation of Heat Transfer in Energy Systems*, ASME, HTD-Vol. 52, pp. 9–20.
[19] Srinivasan, V., and Christensen, R. N., 1992, ''Experimental Investigation of Heat Transfer and Pressure Drop Characteristic of Flow Through Spirally Fluted Tubes,'' Exp. Therm. Fluid Sci., **5**, pp. 820–827.
[20] Wang, Z., Zhou, Q., and Zhang, H., 1996, ''Heat Transfer and Pressure Drop of Air Flow in Spirally Corrugated Tubes,'' *Proceedings of the Chinese Society of Mechanical Engineering*, Vol. 16, No. 1, pp. 59–62.
[21] Incropera, F. P., and DeWitt, D. P., 1996, *Fundamentals of Heat and Mass Transfer*, 4th Ed., John Wiley & Sons, New York.

Mohammad B. Shafii

Amir Faghri
Fellow ASME

Yuwen Zhang[1]
Mem. ASME

Department of Mechanical Engineering,
University of Connecticut,
Storrs, CT 06269-3139

Thermal Modeling of Unlooped and Looped Pulsating Heat Pipes

Analytical models for both unlooped and looped Pulsating Heat Pipes (PHPs) with multiple liquid slugs and vapor plugs are presented in this study. The governing equations are solved using an explicit finite difference scheme to predict the behavior of vapor plugs and liquid slugs. The results show that the effect of gravity on the performance of top heat mode unlooped PHP is insignificant. The effects of diameter, charge ratio, and heating wall temperature on the performance of looped and unlooped PHPs are also investigated. The results also show that heat transfer in both looped and unlooped PHPs is due mainly to the exchange of sensible heat. [DOI: 10.1115/1.1409266]

Keywords: Condensation, Evaporation, Heat Transfer, Heat Pipes, Pulsating

1 Introduction

Downsizing of personal computers and advancing performance of processors has called for the development of micro and miniature heat pipes [1,2] to transport heat from chips to heat sinks. The Oscillating or Pulsating Heat Pipe (OPH or PHP) is a very promising heat transfer device [3]. In addition to its excellent heat transfer performance, it has a simple structure: in contrast with conventional heat pipes, there is no wick structure to return the condensed working fluid back to the evaporator section. The PHP is made from a long, continuous capillary tube bent into many turns. The diameter of the PHP must be sufficiently small so that vapor plugs can be formed by capillary action. The PHP is operated within 0.1–5 mm inner diameter range. If the diameter is too large, the liquid and vapor phases will tend to stratify. The PHP can operate successfully for all operation modes, including both horizontal and vertical. Due to the pulsation of the working fluid in the axial direction of the tube, heat is transported from the evaporator section to the condenser section. The heat input, which is the driving force, increases the pressure of the vapor plug in the evaporator section. In turn, this pressure increase will push the neighboring vapor plugs and liquid slugs toward the condenser, which is at a lower pressure. However, due to the continuous heating of bubbles formed by nucleate boiling, there will not be steady-state vapor pressure equilibrium for an operating PHP. There are two types of PHPs: the looped PHP, which has two open ends, connected to one another, and the unlooped PHP, which has two unconnected ends.

Active oscillations of working fluid were observed at charging ratios of 40~60 percent for a vertical looped PHP. With this charge ratio range, the circulation velocity is at maximum value which results in best heat transfer performance. It has been reported that the looped heat pipe is better than the unlooped heat pipe for heat transfer performance [4]. In an unlooped PHP, the working fluid is unable to circulate and the heat is transferred by driving force due to the oscillation. Gi et al. [5] investigated an ''O'' shaped oscillating heat pipe as it applied to the cooling of a CPU. Their results showed that the temperature of a CPU chip with a power less than 40 W rises to 90°C, which is the maximum temperature for the safe use of notebook computers. They were able to make a very small thermal resistance heat transfer system between a CPU with the power of 40 W and cooling fins. To predict the oscillatory flow characteristics, Miyazaki and Arikawa [6] proposed a theoretical model, which was strongly supported by experimental results. The visualization test showed that the oscillatory flow formed waves that traveled among the turns of PHPs. Their theoretical model could be used to estimate the pressure and displacement of oscillatory flow. Kiseev and Zolkin [7] experimentally investigated the effects of acceleration and vibration on the performance of the unlooped PHP. Acetone was used as the working fluid and the filling charge ratio was 60 percent. Their results indicated that the PHP operates successfully by various acceleration effects. There was an increase in evaporator temperature, about 30 percent by increase of the acceleration from −6g to +12g.

Dobson and Harms [8] presented simple mathematical models in which the behavior of PHPs was simulated. The mathematical model was applied to the open-ended PHP. They showed that the oscillating behavior would be different for different initial values. Wong et al. [9] proposed a theoretical model of PHPs based on a Lagrangian approach in which the flow was modeled under adiabatic conditions for the entire PHP. A sudden pressure pulse was applied to simulate local heat input into a vapor plug. They were able to show the pressure and velocity variations with time for the vapor plugs.

In the present study, a very detailed theoretical model will be developed to accurately simulate the behavior of liquid slugs and vapor plugs in both unlooped and looped PHPs. Heat transfer due to the phase change is also considered.

2 Theoretical Model

2.1 Initial Plug Distribution. When a capillary tube is partially filled, the working fluid will break into liquid slugs and vapor plugs (see Fig. 1(*a*)). Hosoda et al. [10] conducted a numerical analysis for bubble geometry in a tube and determined the maximum inner diameter that can hold a vapor plug.

$$D_{\max} = 1.84 \sqrt{\frac{\sigma}{g(\rho_l - \rho_v)}} \tag{1}$$

$D_{\max}$ is about 2.5 mm for saturated water at 300 K and thus a tube of 1.5 mm is chosen in the present study. A simple momentum equation can be solved in order to predict the length of liquid slugs. When a slug of liquid is formed in a vertical tube, gravity naturally tends to pull the liquid downward. However, as downward motion begins, the contact angles at top and bottom of the liquid plug must be receding and advancing, respectively. Figure 2(*a*) shows a control volume of a liquid slug bounded with two vapor plugs in a vertical tube. Force balance requires that

[1]Presently at Department of Mechanical Engineering, New Mexico State University, Las Cruces, NM 88003.

Contributed by the Heat Transfer Division for publication in the JOURNAL OF HEAT TRANSFER. Manuscript received by the Heat Transfer Division July 11, 2000; revision received May 30, 2001. Associate Editor: J. Georgiadis.

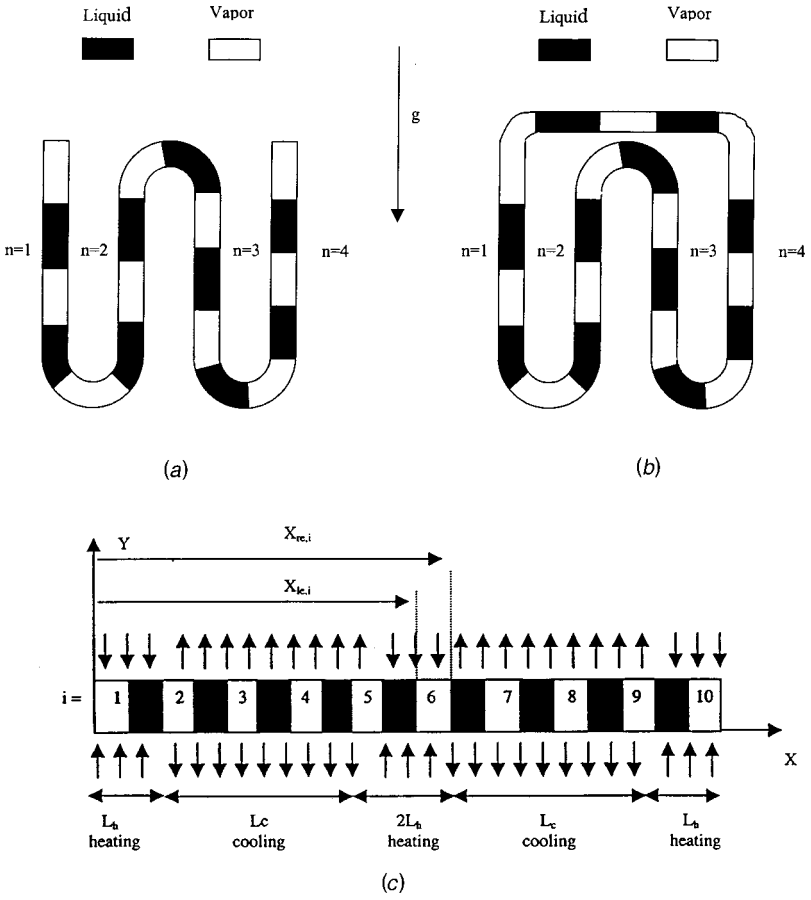

Fig. 1 Oscillating heat pipes: (*a*) unlooped PHP; (*b*) looped PHP.

$$P_{va}\pi R^2 - P_{vb}\pi R^2 + \rho_l g L_l \pi R^2 + 2\pi R_b \sigma - 2\pi R_a \sigma = 0, \quad (2)$$

$$P_{vb} - P_{va} = \rho_v g L_l . \quad (3)$$

Combining Eq. (3) into (2) results in

$$L_l = \frac{2\sigma}{R(\rho_l - \rho_v)g}(\cos\theta_{\min} - \cos\theta_{\max}). \quad (4)$$

Assuming that $\theta_{\min}$ and $\theta_{\max}$ have minimum and maximum values, one can find the length of the liquid slugs that can be supported against gravity. It should be noted that Eq. (4) is valid only when the pressure difference between the two vapor plugs has such a relation as Eq. (3). However, when the unlooped heat pipe is partially filled, it is less likely to display the relationship between pressures of vapor plugs expressed as Eq. (3). In this case instability theory of condensate film and capillary blocking in small diameter tube can be used to predict the initial length of liquid slugs. Teng et al. [11] investigated instability of the condensate film in small diameter tubes using an integro-differential approach. They mentioned that liquid bridging caused by the breakup of condensate film originates from capillary instability. This breakup of condensate film causes the formation of liquid slugs. The film instability results from surface tension and the length of the disturbance waves, which can be approximated as a function of the radius of the undisturbed inner condensate film. The most-unstable wavelength can be obtained from [11]

$$\lambda_m = \sqrt{8}\pi a, \quad (5)$$

where a is the undisturbed radius of the condensate film inner surface and is assumed to be half the size of the tube radius. The length of liquid slugs can be predicted from Eq. (5) by assuming the most-unstable wavelength to be the length of the liquid slugs. Table 1 is the summary of the experimental works on the pulsating heat pipes. The predicted lengths of the liquid slugs obtained from Eq. (4) and Eq. (5) are also included in this table.

2.2 Governing Equations. The oscillatory phenomenon in PHPs can be predicted by solving mass, momentum, and energy equations for each liquid slug and vapor plug. The schematics of unlooped and looped PHPs are shown in Fig. 1(*a*) and (*b*). The bends are not considered in the present study and the PHP is assumed to be a straight tube (see Fig. 1(*c*)). The locations and the number of heating and cooling sections represent the number of bends or turns in actual PHPs. There are three heating sections and two cooling sections on the PHP. The inner wall temperature at the heating and cooling sections of the PHP are T_h and T_c, respectively. A control volume of a liquid slug bounded with two vapor plugs is shown in Fig. 2(*b*).

To solve the problem analytically, the following assumptions are made:

1 Evaporative and condensation heat transfer coefficients are assumed to be constants.

2 The liquid is incompressible and the vapor plugs are assumed to behave as an ideal gas in the heating sections.

3 The pressure losses at the bends are not considered. This assumption is valid for the PHPs do not have many turns. When the number of turns is larger, the pressure loss at the turns may not be negligible.

The continuity equation for i^{th} liquid slug can be found from following equation:

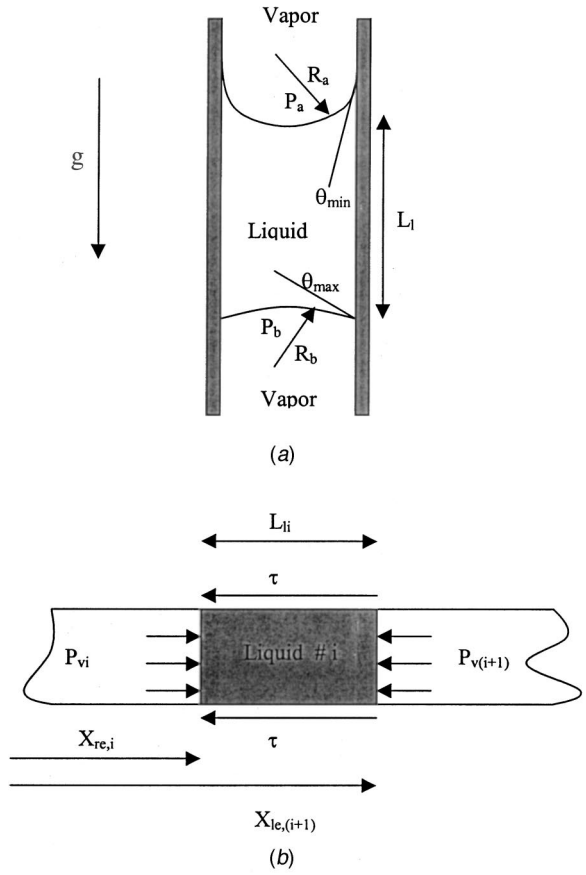

Fig. 2 (*a*) Control volume of *a* liquid slug in a vertical tube; (*b*) control volume of i^{th} liquid plug.

$$\frac{dm_{\mathrm{li}}}{dt}=\dot{m}_{\mathrm{in,li}}-\dot{m}_{\mathrm{out,li}}=\frac{1}{2}\left(\frac{dm_{\mathrm{vi}}}{dt}+\frac{dm_{v(i+1)}}{dt}\right). \tag{6}$$

This means that the change in mass of liquid slug is equal to the average changes in mass of its adjacent vapor plugs. The momentum equation for i^{th} liquid slug, assuming the PHP operates vertically, is

$$\frac{dm_{\mathrm{li}}v_{\mathrm{li}}}{dt}=(P_{\mathrm{vi}}-P_{v(i+1)})A-\pi dL_{\mathrm{li}}\tau-(-1)^n m_{\mathrm{li}}g, \tag{7}$$

where n indicates the tube number. Since it is assumed that the PHP is a straight tube, gravity has different signs at different locations. In this model, there are four parallel tubes, which are labeled from one to four (Fig. 1). The heating section is located at the top of the PHP. Gravity vector is in positive direction when a liquid slug is in the first or third tubes; therefore, the gravity term in Eq. (7) is positive. In the second or fourth tubes the gravity vector is in the opposite direction and the gravity force term in Eq. (7) is negative. τ is the shear stress acting between i^{th} liquid slug and the tube and can be determined from

$$\tau=\frac{1}{2}C_{\mathrm{li}}\rho_l v_{\mathrm{li}}^2, \tag{8}$$

where the friction coefficient can be determined by

$$C_{\mathrm{li}}=\begin{cases}\dfrac{16}{\mathrm{Re}} & \mathrm{Re}\leqslant 1180\\ 0.078\,\mathrm{Re}^{-0.2} & \mathrm{Re}>1180\end{cases}. \tag{9}$$

The continuity equation for the i^{th} vapor plug is

$$\frac{dm_{\mathrm{vi}}}{dt}=\dot{m}_{\mathrm{in,vi}}-\dot{m}_{\mathrm{out,vi}}, \tag{10}$$

where $\dot{m}_{\mathrm{in,vi}}$ is the rate of mass transferred into the vapor plug due to the evaporation and $\dot{m}_{\mathrm{out,vi}}$ is the rate of mass transferred from the vapor plug due to the condensation for i^{th} vapor plug and can be calculated by the following equations:

$$\dot{m}_{\mathrm{in,vi}}=(h_h+h_{\mathrm{vsen}})\pi dL_{\mathrm{hi}}(T_{\mathrm{vi}}-T_h)/h_{fg}, \tag{11a}$$

$$\dot{m}_{\mathrm{out,vi}}=(h_c+h_{\mathrm{vsen}})\pi dL_{ci}(T_c-T_{\mathrm{vi}})/h_{fg}. \tag{11b}$$

It is assumed that the evaporative heat transfer coefficient, h_h, is constant as long as one of the ends of the vapor plug is in the

Table 1 Summary of experimental works on pulsating heat pipe data

Investigators	Type and heat (mode of PHP)	Cross section of tubes	Number of parallel tubes	Length of each tube(cm)	Charging Ratio (%)	Working fluid	Length of Liquid slug (cm)	Length of vapor plug (cm)	D (mm)	Initial length of liquid slug required by stability (mm)	Initial liquid slug length by eq. (4) (mm)	Comments
Gi et al. [13]	Looped (Vertical bottom)	Circular	20	50	30-70	R-142b	NA	NA	2	4.4	2.66	The effect of charging ratio, operating temperature and inclination angle
Gi et al. [13]	Unlooped (Vertical bottom)	Circular	20	50	30-70	R142b	NA	NA	2	4.4	2.66	The effect of charging ratio and inclination angle
Lee et al. [4]	Looped (Vertical bottom)	Rectangular	8	22	20-80	Ethanol	NA	NA	1.5	3.33	7.48	Nucleate boiling observed, Most active oscillation at charging ratio of 40-60% and the inclination angle of 90°
Maezawa et al. [12]	Unlooped (Horizontal) (Vertical top) (Vertical bottom)	Circular	41	60	40-50	Water R-142b	NA	NA	2	4.4	14.88 2.66	Top mode operated very well. R-142b was better working fluid. Non-periodic dynamics System was governed
Miyazaki and Arikawa [6]	Looped (Vertical top)	Rectangular	50	27.3	42	R142b	21.84	32.76	NA	-	-	Analytical model was proposed for circulation of wave velocity
Miyazaki and Akachi [13]	Looped (Vertical bottom) (Horizontal)	Circular	31	20	26-70	R142b	NA	NA	1	2.22	5.32	Circulation was observed. An analytical model was proposed.
Nishio [14]	Looped (Vertical bottom)	Circular	8	39.6	20-100	Water Ethanol R-142b	NA	NA	1.8 2.4 5	Water Ethanol R 142b 4 4 4 5.33 5..33 5.33 11.1 11.1 11.1	Water Ethanol R 142b 16.53 16.53 2.96 12.4 4.67 2.22 5.95 2.24 1.06	The total temperature difference between hot and cold water in heating and cooling section varied (30-60°C)

heating section. When the two ends are out of the heating section, the liquid film in the evaporator dries out and the evaporative heat transfer is zero. The sensible heat transfer coefficient, h_{vsen}, is negligible in comparison with the evaporative heat transfer coefficient. The energy equation of a vapor plug is

$$\frac{dm_{\text{vi}}u_{\text{vi}}}{dt}=\dot{m}_{\text{in,vi}}h_{\text{in,vi}}-\dot{m}_{\text{out,vi}}h_{\text{out,vi}}-P_{\text{vi}}\frac{dV_{\text{vi}}}{dt}. \tag{12}$$

Letting $u=c_vT$ and $h=c_pT$, Eq. (12) may be rewritten as

$$m_{\text{vi}}c_v\frac{dT_{\text{vi}}}{dt}=(\dot{m}_{\text{in,vi}}-\dot{m}_{\text{out,vi}})RT_{\text{vi}}-P_{\text{vi}}A\frac{dX_{\text{vi}}}{dt}. \tag{13}$$

The pressure of the i^{th} vapor plug, P_{vi} is calculated using the ideal gas law

$$P_{\text{vi}}V_{\text{vi}}=m_{\text{vi}}RT_{\text{vi}}. \tag{14}$$

It is important to note that the pressure, calculated from Eq. (14), cannot exceed the saturation pressure corresponding to the temperature calculated from Eq. (13). When the vapor pressure, calculated by Eq. (14), is lower than the saturation pressure the vapor plug is superheated and the ideal gas law is valid. On the other hand, if the vapor pressure, calculated by Eq. (14), is higher than saturation pressure, the ideal gas law is no longer valid and the pressure is set to the saturation pressure calculated by

$$P_{\text{vi}}=P_{\text{sat}}(T_{\text{vi}}). \tag{15}$$

2.3 Heat Transfer. Heat transfer in a PHP is defined as total heat transferred from heating sections to the cooling sections. Part of heat transfer is due to evaporation and condensation of working fluid. Another part is due to heat transfer between tube wall and liquid slugs in the form of single-phase heat transfer. Evaporative and condensation heat transfer for each vapor plug can be calculated by

$$Q_{\text{in,vi}}=\dot{m}_{\text{in,vi}}h_{fg}, \tag{16a}$$

$$Q_{\text{out,vi}}=\dot{m}_{\text{out,vi}}h_{fg}. \tag{16b}$$

The single-phase heat transfer between the tube wall and liquid slugs is obtained by solving the energy equation for a liquid slug

$$\frac{1}{\alpha_l}\frac{dT_{\text{li}}}{dt}=\frac{d^2T_{\text{li}}}{dx^2}-\frac{h_{\text{lsen}}\pi D}{k_lA}(T_{\text{li}}-T_w), \tag{17}$$

with the following boundary conditions:

$$T_{\text{li}}=T_{\text{vi}} \qquad x=x_{\text{re},i}$$

$$T_{\text{li}}=T_{v(i+1)} \qquad x=x_{\text{le},(i+1)}. \tag{18}$$

Since the Reynolds number of the liquid slug varies in a wide range that covers laminar, transition, and turbulent flow, the heat transfer coefficient h_{lsen} of the liquid slug varies from time to time. For laminar regime, (Re<2200), the problem is considered as thermally developing Hagen-Poiseuille flow and the Nusselt number is

$$\text{Nu}=\frac{1}{4L_1^*}\ln\left(\frac{1}{\theta_m^*}\right), \tag{19}$$

where

$$\theta_m^*=8\sum_{n=0}^{\infty}\frac{G_n}{\lambda_n^2}\exp(-2\lambda_n^2L_1^*). \tag{20}$$

The eigenvalues, λ_n, and the constants, G_n, can be found in Ref. [12]. The dimensionless L_l^* is defined as

$$L_l^*=\frac{L_{\text{li}}/D}{\text{Re}_D\,\text{Pr}}. \tag{21}$$

In the transition and turbulent regions, the following empirical equations are used:

$$\text{Nu}=0.012(|\text{Re}|^{0.87}-280)\text{Pr}^{0.4}\left(\frac{\text{Pr}_m}{\text{Pr}_w}\right)^{0.11}\left[1+\left(\frac{D}{L_{\text{li}}}\right)^{2/3}\right]$$

$$2200<|\text{Re}|<10000 \tag{22}$$

$$\text{Nu}=0.0236|\text{Re}|^{0.8}\text{Pr}^{0.43}\left(\frac{\text{Pr}_m}{\text{Pr}_w}\right)^{0.25} \qquad |\text{Re}|>10000. \tag{23}$$

The heat transferred into and out of the liquid slug is

$$Q_{\text{in,li}}=\int_{X_{\text{re},i}}^{X_{\text{le},(i+1)}}\pi\text{Dh}_x(T_{\text{li},x}-T_w)dx \qquad T_{\text{li}}\geqslant T_w \tag{24a}$$

$$Q_{\text{out,li}}=\int_{X_{\text{re},i}}^{X_{\text{le},(i+1)}}\pi Dh_x(T_w-T_{\text{li},x})dx \qquad T_{\text{li}}\leqslant T_w, \tag{24b}$$

where $T_{\text{li},x}$ represents the temperature of the i^{th} liquid plug at location x. The total heat transferred into and out of the PHP can be calculated by

$$Q_{\text{total,in}}=\sum_{i=1}^{N}Q_{\text{in,iv}}+\sum_{i=1}^{N-1}Q_{\text{in,li}}, \tag{25a}$$

$$Q_{\text{total,out}}=\sum_{i=1}^{N}Q_{\text{out,iv}}+\sum_{i=1}^{N-1}Q_{\text{out,in}}. \tag{25b}$$

3 Numerical Procedure

The new values at time $t+dt$ can be found explicitly from the old values at time t by using the following equations:

$$m_{\text{vi}}^{\text{new}}=m_{\text{vi}}+(\dot{m}_{\text{in,vi}}-\dot{m}_{\text{out,vi}})\Delta t, \tag{26}$$

$$T_{\text{vi}}^{\text{new}}=T_{\text{vi}}+\frac{(\dot{m}_{\text{in,vi}}-\dot{m}_{\text{out,vi}})RT_{\text{vi}}\Delta t-P_{\text{vi}}A\Delta X_{\text{vi}}}{m_{\text{vi}}c_v}, \tag{27}$$

$$P_{\text{vi}}^{\text{new}}=\frac{m_{\text{vi}}RT_{\text{vi}}}{V_{\text{vi}}}, \tag{28}$$

$$m_{\text{li}}^{\text{new}}=m_{\text{li}}+\frac{1}{2}[(\dot{m}_{\text{in,vi}}-\dot{m}_{\text{out,vi}})+(\dot{m}_{\text{in},v(i+1)}-\dot{m}_{\text{out},v(i+1)})]\Delta t, \tag{29}$$

$$m_{\text{li}}^{\text{new}}v_{\text{li}}^{\text{new}}=m_{\text{li}}v_{\text{li}}+[(P_{\text{vi}}-P_{v(i+1)})A-\pi dL_{\text{li}}\tau+m_{\text{li}}g]\Delta t. \tag{30}$$

The determinations of the locations of liquid slugs and vapor plugs are different for unlooped and looped PHPs.

3.1 Unlooped PHP. The position of each vapor plug is known by the location of its ends; one can write

$$\begin{cases}X_{\text{re},i}^{\text{new}}=X_{\text{re},i}+v_{\text{li}}\Delta t\\ X_{\text{le},i}^{\text{new}}=X_{\text{le},i}+v_{l(i-1)}\Delta t,\end{cases} \tag{31}$$

$$\begin{cases}X_{\text{re},N}=L\\ X_{\text{le},l}=0,\end{cases} \tag{32}$$

where N is the number of vapor plugs. X is measured from the origin shown in Fig. 1(*b*).

$$\begin{cases}\Delta X_{\text{re},i}^{\text{new}}=X_{\text{re},i}^{\text{new}}-X_{\text{re},i}\\ \Delta X_{\text{le},i}^{\text{new}}=X_{\text{le},i}^{\text{new}}-X_{\text{le},i}\end{cases} \tag{33}$$

$$\Delta X_{\text{re},N}^{\text{new}}=0$$

$$\Delta X_{\text{le},1}^{\text{new}}=0 \tag{34}$$

$$\Delta X_{\text{vi}}^{\text{new}}=\Delta X_{\text{re},i}^{\text{new}}-\Delta X_{\text{le},i}^{\text{new}}, \tag{35}$$

where $\Delta X_{vi}^{\text{new}}$ is the change in length of the i^{th} vapor plug. $\Delta X_{\text{re},i}$ and ΔX_{2i-l} are the changes in location of the ends of the i^{th} vapor plug.

3.2 Looped PHP. The looped PHP is similar to the unlooped PHP except its two ends are connected to each other (Fig. 1(*b*)). Governing equations used for unlooped PHPs are valid for looped PHPs, except that the first and last vapor plugs (shown in Fig. 1(*b*)) are basically one vapor plug, and both of them have the same values of pressure and temperature. The position of the two ends of the vapor plugs is found from the following equations:

$$\begin{cases} X_{\mathrm{re},i}^{\mathrm{new}} = X_{\mathrm{re},i} + v_{\mathrm{re},i}\Delta t \\ X_{\mathrm{le},i}^{\mathrm{new}} = X_{\mathrm{le},i} + v_{\mathrm{le},(i-1)}\Delta t \end{cases} \tag{36}$$

$$\begin{cases} X_{\mathrm{re},i}^{\mathrm{new}} = X_{\mathrm{re},i}^{\mathrm{new}} - L & X_{\mathrm{re},i}^{\mathrm{new}} > L \\ X_{\mathrm{le},i}^{\mathrm{new}} = X_{\mathrm{le},i}^{\mathrm{new}} - L & X_{\mathrm{le},i}^{\mathrm{new}} > L \end{cases} \tag{37}$$

$$\begin{cases} X_{\mathrm{re},i}^{\mathrm{new}} = X_{\mathrm{re},i}^{\mathrm{new}} + L & X_{\mathrm{re},i}^{\mathrm{new}} < 0 \\ X_{\mathrm{le},i}^{\mathrm{new}} = X_{\mathrm{le},i}^{\mathrm{new}} + L & X_{\mathrm{le},i}^{\mathrm{new}} < 0 \end{cases} \tag{38}$$

$$\Delta X_{\mathrm{vi}}^{\mathrm{new}} = \Delta X_{\mathrm{re},i}^{\mathrm{new}} - \Delta X_{\mathrm{le},i}^{\mathrm{new}} . \tag{39}$$

The last two equations guarantee that the position of the two ends of the vapor plug remains between 0 and L. Time step independence of the numerical solution for both unlooped and looped PHP was verified by systematically varying the time step. It was found that varying the time step from 5×10^{-6} s to 10^{-8} s results in less than 0.2 percent variation in the locations of the liquid slugs. Therefore, the time step used in the numerical solution is 5×10^{-6} s.

To find the sensible heat transferred by the liquid slugs, Eq. (17) is solved using an implicit scheme [13]. A nonuniform grid was chosen to solve the energy equation of liquid slugs. The total number of grids chosen is 360, with 140 belonging to each end (2 cm) and 80 grids in the middle of each liquid slug. Doubling the number of grids does not change the solution results. Since decreasing the time step to 10^{-4} s results in 0.2 percent variation in temperature distribution along the liquid slugs, the time step used in the numerical solution is 10^{-3} s.

4 Results and Discussion

4.1 Evolution of Flow Pattern. The verification of the numerical method was performed by simulating the propagation of

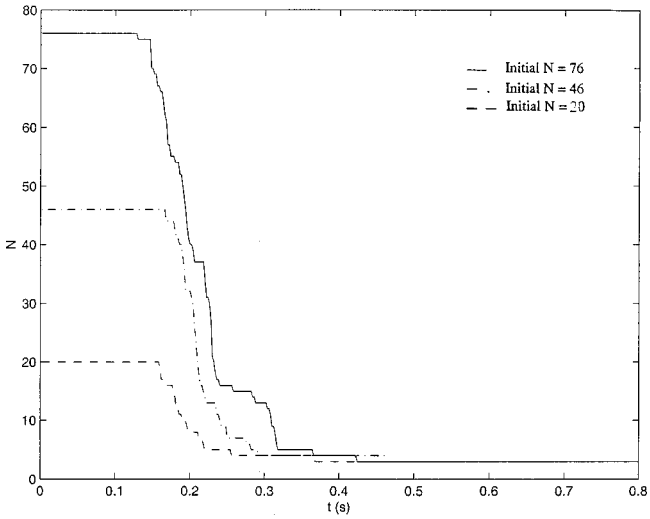

Fig. 4 The variation of the total number of vapor plugs with time

Table 2 Initial values of PHP

Initial pressure of vapor plugs	P_{vi} = 5628 pa
Initial temperature of vapor plugs	T_{vi} = 35 ^{0}C
Percentage filled	α = 61.4%
Total length	L = 1.14 m
Total number of plugs	N_p = 5
Number of bends	B = 3
Length of each vapor plug	L_{v1} =L_{v2}=0.11 m ,L_{v2}=0.22 m
Temperature of wall in cooling section	T_c = 20 ^{0}C
Temperature of wall in heating section	T_h = 120 ^{0}C
Heat transfer coefficient at heating wall	h_h = 150 W/m^2 ^{0}C
Heat transfer coefficient at cooling wall	h_c = 100 W/m^2 ^{0}C
Diameter	d = 0.0015 m
Length of heating section	L_h = 0.1m
Length of cooling section	L_c = 0.37m

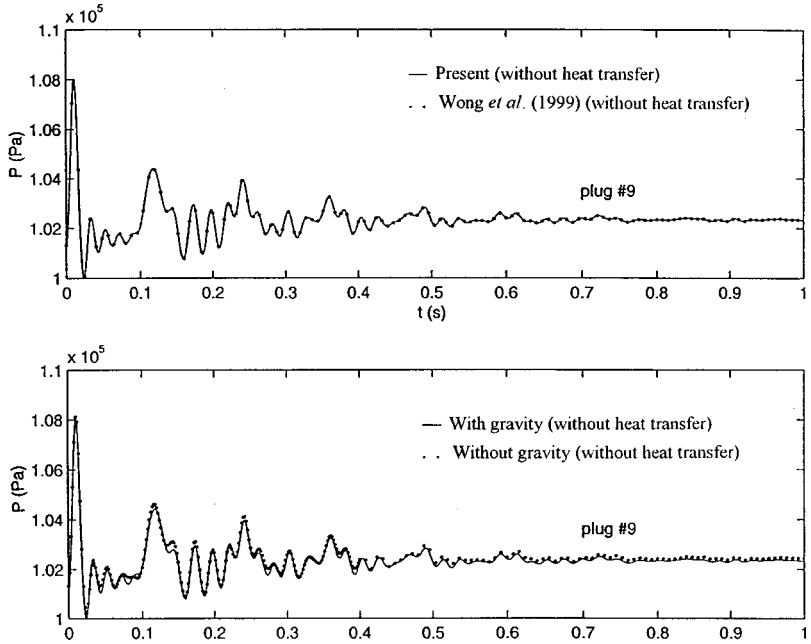

Fig. 3 Comparison of the pressure variation with time: (*a*) without gravity; (*b*) with gravity; and (*c*) comparison with a previous model.

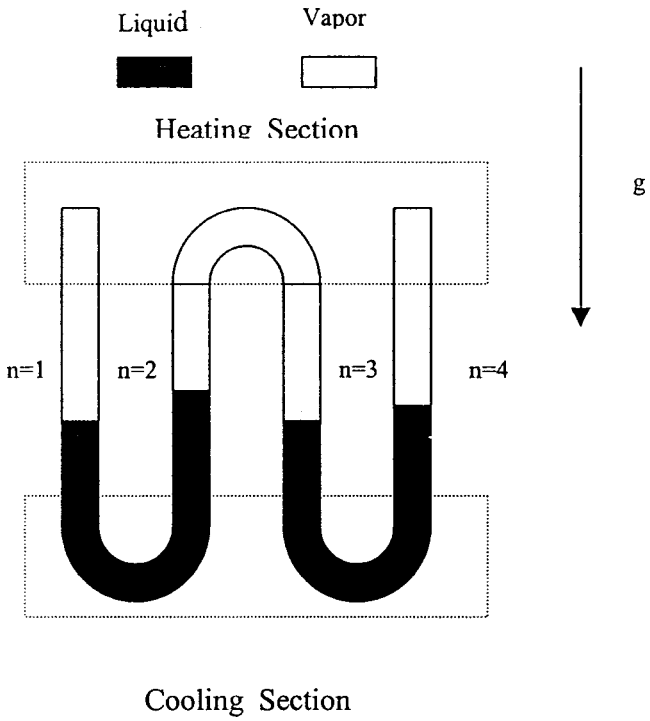

Fig. 5 Unlooped PHP including three vapor plugs

pressure waves inside a PHP [9]. The capillary heat pipe is modeled under adiabatic conditions. A sudden pressure pulse is applied to a plug at one end of the PHP to study the pressure variation with time. A total of 20 liquid slugs and vapor plugs exist in the pipe. The length of all vapor and liquid plugs was assumed to be identical. An initial pressure of 1.1 times higher than the rest is applied to the 10^{th} vapor plug. The comparison between the present result and that of Ref. [9] for the 9^{th} plug is presented in Fig. 3(*a*). It can be seen that the agreement between the present numerical results and the results of Wong et al. [9] is excellent for the case with no heat transfer. Figure 3(*b*) shows the effect of gravity on the pressure variation. It is seen that the effect of gravity on pressure variation is not significant, and therefore it can be neglected in the numerical model.

When the heating sections are heated and cooling sections are cooled, the pressure of vapor plugs located in the cooling sections is lower than that of vapor plugs in the heating sections, since the temperature is lower. This pressure difference causes the liquid slugs to move toward cooling sections and consequently the volume of vapor plugs in cooling sections decreases until the adjacent liquid slugs merge to one another and the vapor plugs diminish. Figure 4 shows the variation of the total number of vapor plugs with time when unlooped PHP is exposed to heating and cooling conditions. The parameters used in the numerical simulation are listed in Table 2 except that the total number of vapor plugs varies. The number of vapor plugs eventually reduces to three, which is equal to the number of heating sections. This means that vapor plugs exist only in heating sections, no matter how many vapor plugs are initially in the PHP (see Fig. 5). It can also be observed that when the total initial number of vapor plugs is high, the evolutionary time is high.

4.2 Unlooped PHP. The parameters used are listed in Table 2. An initial pressure of 1.2 times higher than the rest is applied to the first vapor plug. The lengths of liquid slugs are equal and can be found based on the charge ratio of the system. Therefore, the parametric study of PHP in the following section will be performed for three vapor plugs in the heating sections. Figure 6 shows the variations of pressure, temperature and positions of the two ends of the first vapor plug with respect to time. Initially, both the temperature and pressure drop to certain values, since the right end of the first vapor plug is located in the cooling section and condensation takes place. When the pressure is low enough, the adjacent liquid slug starts moving back toward the heating section, and as it moves back, the temperature of the vapor plug increases due to the compression. However, condensation is still taking place. When the right end moves into the heating section, evaporation takes place. The pressure and temperature of vapor plug keep increasing until the pressure in the vapor plug is high enough

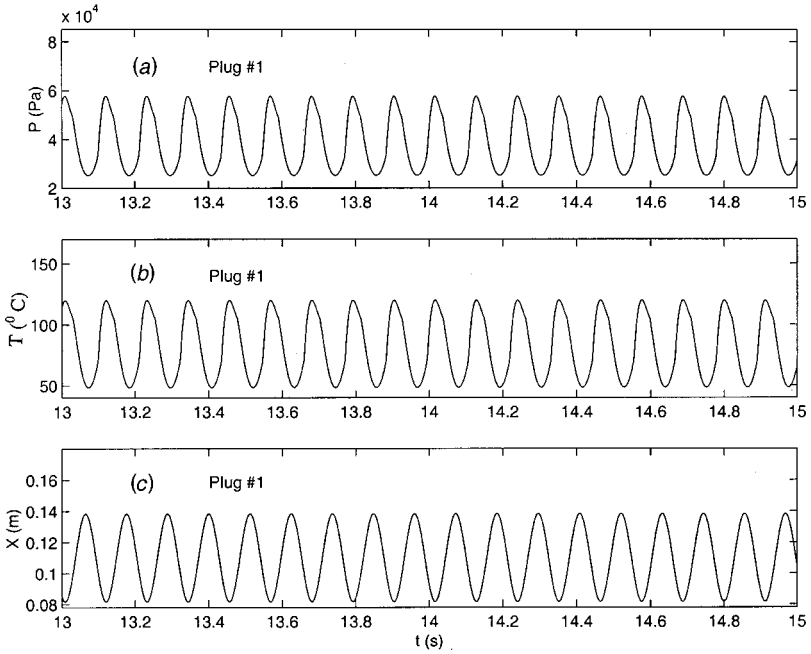

Fig. 6 Variation of pressure, temperature, and the end positions of the first plug with time (d=1.5 mm)

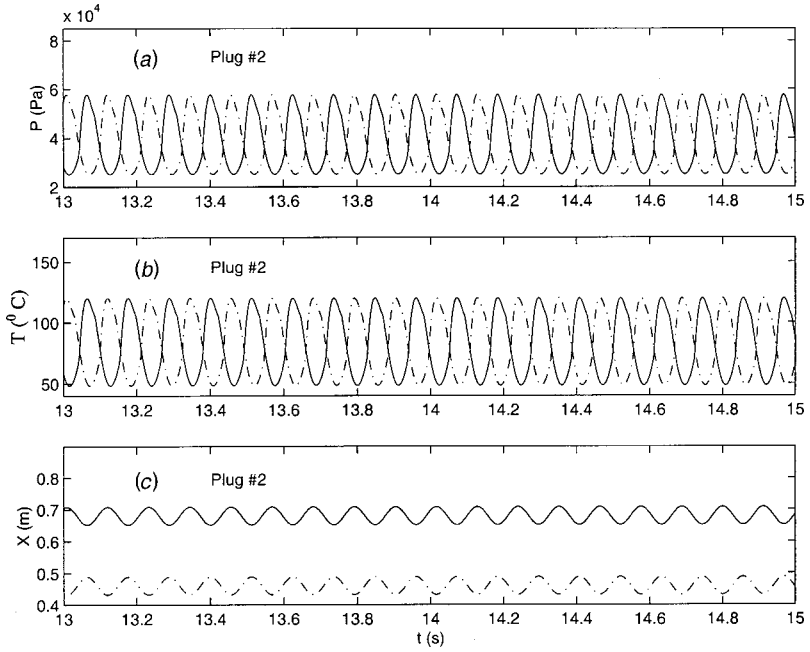

Fig. 7 Variation of pressure, temperature, and the end positions of the second plug with time ($d=1.5$ mm)

to push the adjacent liquid slug toward the cooling section. This phenomenon repeats itself and periodic oscillation occurs after almost 10 s. The temperature of the first vapor plug is maximum, or equal to the heating wall temperature, when it is completely compressed in the heating section. At this point its pressure is also maximum at 6×10^4 Pa. Since the pressure is lower than saturated pressure, the vapor plug is super heated. Fig. 6(*c*) shows the position of the two ends of the first vapor plug. Since the first vapor plug is located at the end of the PHP, the left end is always located at $x=0$ m. The right end oscillates between $x=0.08$ m and $x=0.14$ m.

Figure 7 shows the variations of pressure, temperature and positions of the two ends of the second vapor plug. Since the two ends are free to move into heating and cooling sections, the frequencies of the pressure and temperature oscillation are equal to that of the first vapor plug and the phase difference is 180 deg. Figure 7(*c*) shows the position of two ends of this vapor plug. The solid and dashed lines represent the location of the right and left ends. The distance between these two lines indicates the length of the vapor plug. The two ends always move in opposite directions and they move into either the cooling or heating sections. Figure 8 represents pressure, temperature and position of the two ends of

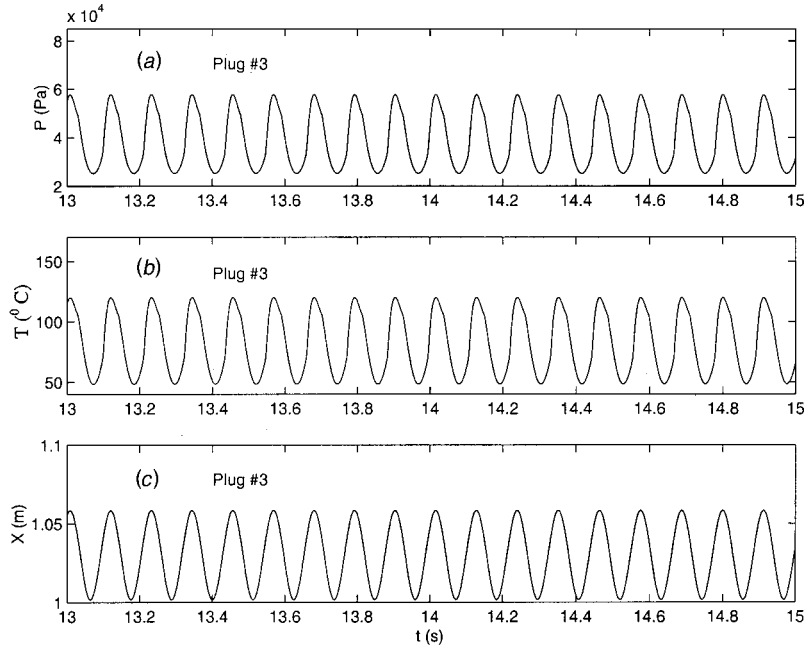

Fig. 8 Variation of pressure, temperature, and the end positions of the third plug with time ($d=1.5$ mm)

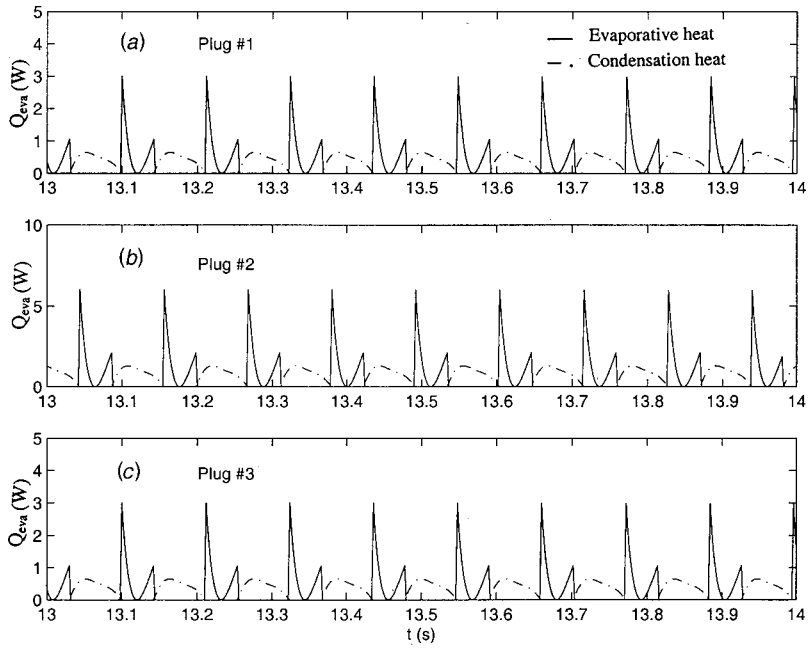

Fig. 9 The evaporative and condensation heat transfer rate

the third vapor plug variations with time. Since the system is symmetric, the oscillating trends of pressure temperature and position of the ends are the same as those of the first vapor plug and there is no phase difference between the oscillations.

The rate of evaporative and condensation heat transfer of each individual vapor plug, when periodic oscillation is obtained, is shown in Fig. 9. It can be seen from Fig. 9(*a*) that when the right end of the first vapor plug moves into the heating section, the evaporative heat transfer suddenly jumps to its maximum value. Then it starts decreasing to its minimum value as the right end continues moving inside the heating section and compresses the first vapor plug. Meanwhile, the vapor plug temperature increases due to evaporation and compression. As the vapor expands, its temperature drops and heat transfer increases until the right end moves into the cooling section where condensation occurs. Figure 9(*b*) and 9(*c*) show the same behavior for the second and third plugs.

The variation of the sensible heat transferred into and out of the liquid slugs is shown in Fig. 10. The solid line represents heat transferred into the liquid slugs from heating sections and the dashed line represents the heat rejected from the liquid slugs into the cooling systems. When the liquid slugs are completely in the cooling sections, there is no sensible heat transferred into the slugs and the heat rejected from the slugs is at its maximum. The sudden changes in the sensible heat are due to the change from laminar flow to transition flow. The maximum Reynolds number

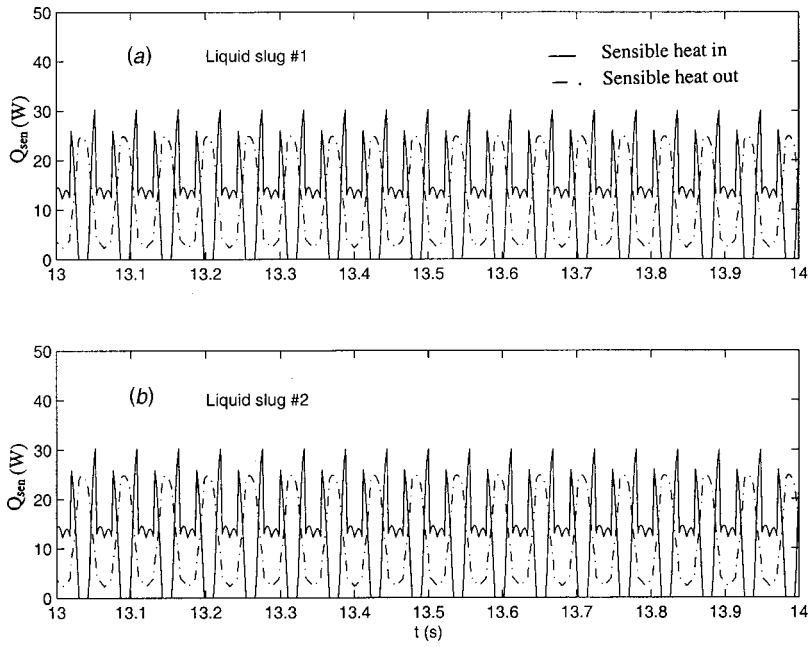

Fig. 10 Sensible heat transferred in and out of liquid slugs

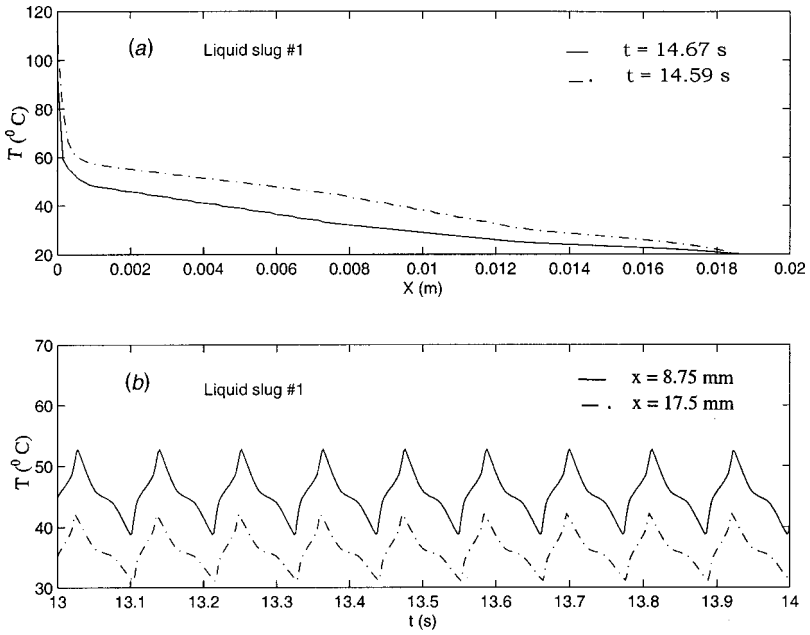

Fig. 11 Temperature of the first liquid slug: (*a*) distribution along the left end of the first liquid slug; and (*b*) variation with time.

for liquid slugs is Re=4200. Figure 11(*a*) shows temperature distribution of the left end of the first liquid slug. The distance is measured from the tip of the left end of the first liquid slug. Only 2.5 cm of the left end moves into the heating section and contributes in transferring heat. Since the middle part always remains in the cooling section, its temperature is always at the cooling wall temperature (20°C). Figure 11(*b*) shows the temperature variation of two selected points on the left end of the first liquid slug. One is 4.37 mm (solid line) and the other one is 8.75 mm (dashed line) away from the left end. The one closer to the left end has a higher temperature because it remains longer in the heating section. The total heat transferred into the PHP for this case is 24.88 W. The total sensible heat transferred is 23.84 W and this means that 95.84 percent of heat transferred into the system is due to the sensible heat. To investigate the effect of diameter on performance of the PHP, the diameter of the tube is increased to 3 mm. The other parameters and initial values are not changed. Figure 12(*a*) shows the pressure variation with time for the first vapor plug. It can be observed that the frequency of oscillation is higher than that of the small diameter tube. From Fig. 12(*b*) and 12(*c*) one can conclude that the average temperature of the first vapor plug is the same as that of the first vapor plug in the small diameter tube by

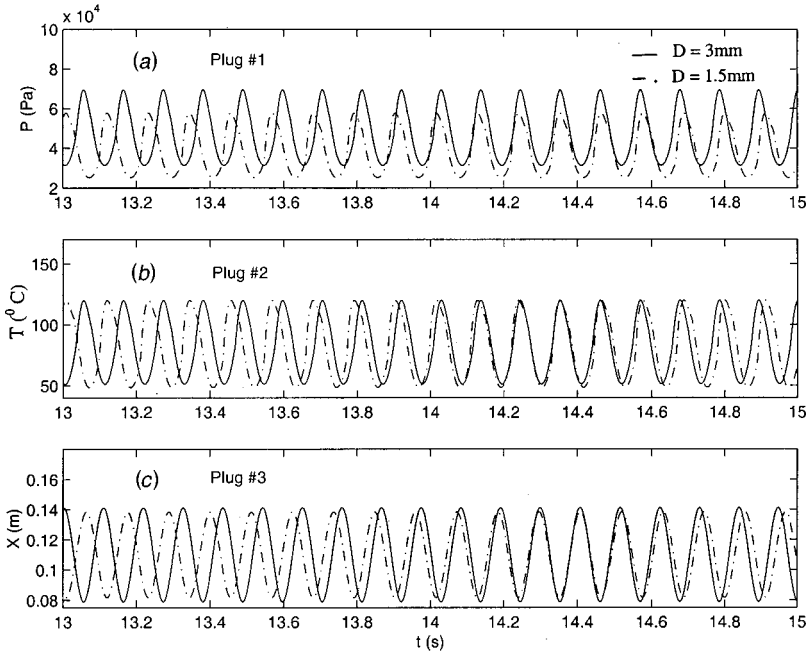

Fig. 12 Effect of the diameter of PHP on the performance of the first vapor plug

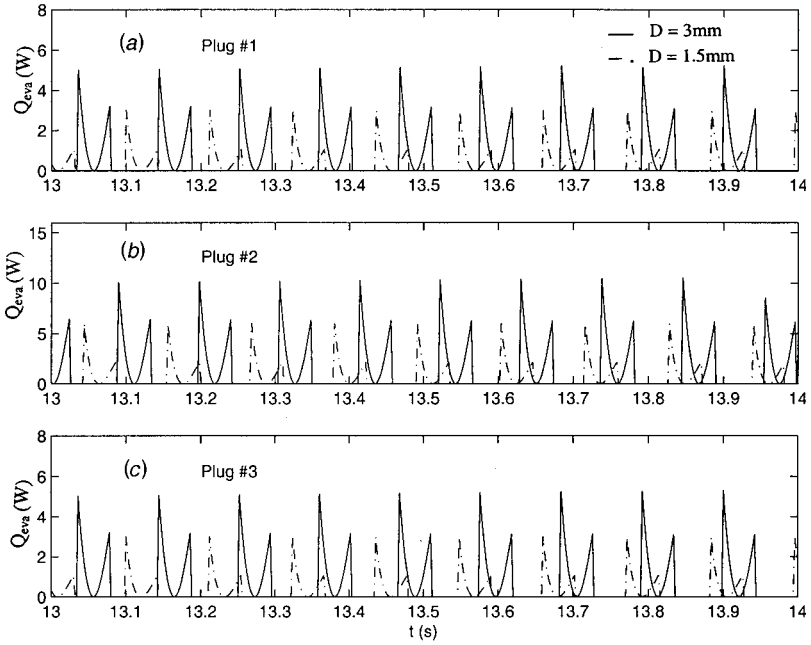

Fig. 13 Effect of PHP diameter on the total evaporative heat transfer rate

the time the right end moves into the heating section (see at $t = 14.95$ s). However, since the heating area is greater than that of the small diameter tube, the evaporative heat is higher for all vapor plugs (Fig. 13). The total heat transferred into the PHP for this case is 80.17 W. Results indicate that the contribution of the sensible heat is 97.12 percent of the total heat.

Figure 14 shows the effect of heating wall temperature on pressure, temperature and end positions of the first plug. The parameters and thermal properties are similar to what is given in Table 2, except that the wall temperature is reduced to 90°C. Decreasing the wall temperature results in the decreased magnitude of pressure and the location of the right end and it also slightly decreases the frequency of oscillation. It can be seen from Fig. 14(*b*) that the average temperature of the first vapor plug decreases when the wall temperature decreases and the temperature difference between the wall and vapor plug is lower. This results in lower evaporative heat transfer shown in Fig. 15. This figure indicates that the heat transferred into the vapor plugs decreased with decreasing the temperature difference between heating and cooling section. The total heat transferred into the PHP for this case is 8.35 W. Results indicate that the contribution of the sensible heat is 92.54 percent of the total heat transferred. From calculated results, it can be concluded that a 25 percent reduction in the tem-

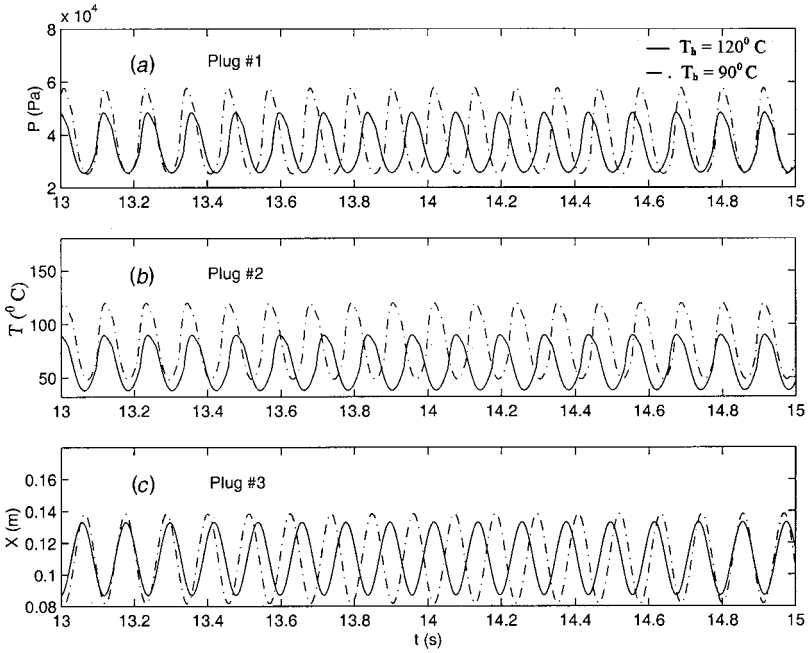

Fig. 14 Effect of the heating wall temperature on the performance of the first plug

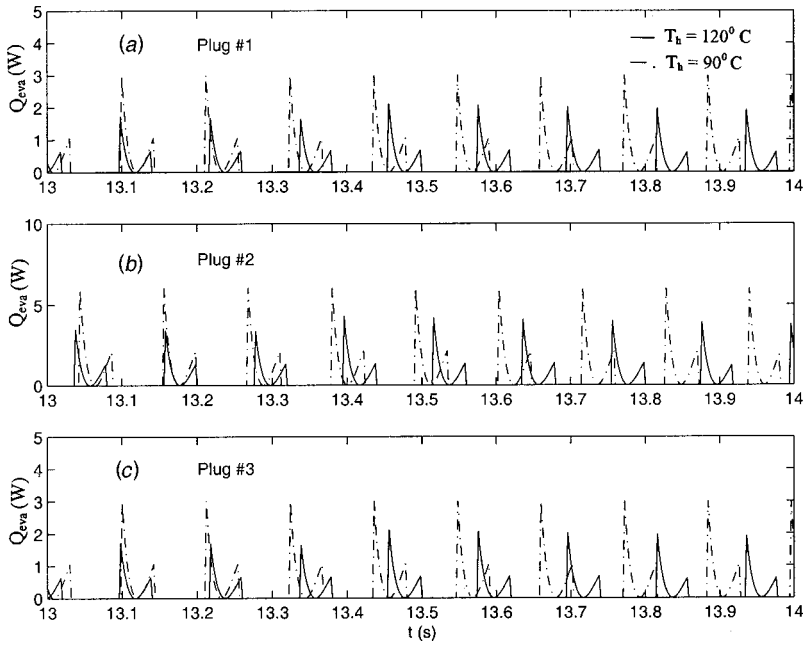

Fig. 15 Effect of the heating wall temperature on the total evaporative heat transfer rate

perature difference between heating and cooling wall sections results in almost 90 percent reduction in total heat transferred into the PHP.

The effect of charging ratio on the performance of the PHP is shown in Fig. 16. The tube diameter is 1.5 mm. The length of all liquid slugs is 0.51 m. Therefore, the first and third vapor plugs would have the length of 0.03 m and the second one would be twice as long as the other two. This yields a charge ratio of 89.4 percent in the PHP. Figure 16 indicates that oscillation cannot be obtained when the charging ratio is high. When the charging ratio is high in the PHP, the liquid slugs are long, and a higher-pressure difference is needed to move more massive liquid slugs. Since this pressure difference cannot be obtained, the temperature rises to the wall temperature. As a result, no heat will be transferred into the plugs (Fig. 17) and the PHP will not perform properly. This prediction is consistent with experimental results presented by Gi et al. [14]. Their results showed that heat transport rate decreased with increasing charge ratio for unlooped PHP. The effect of different parameters, as discussed above, on the heat transfer performance of the unlooped PHP is listed in Table 3.

4.3 Looped PHP. Miyazaki and Arikawa [6] performed visualization experiments on looped PHPs and observed that liquid slugs and vapor plugs were almost separated into two parts in the

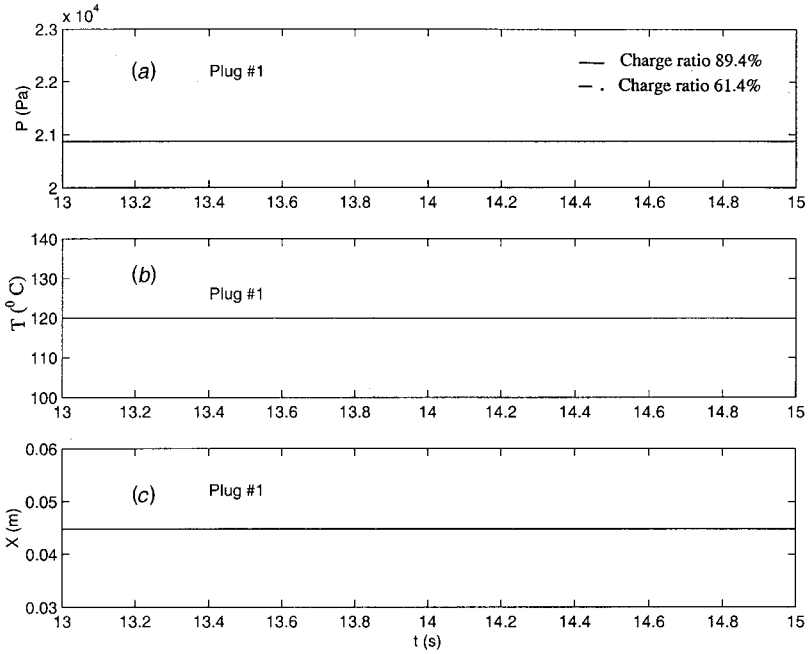

Fig. 16 Effect of the charge ratio on the performance of the first plug

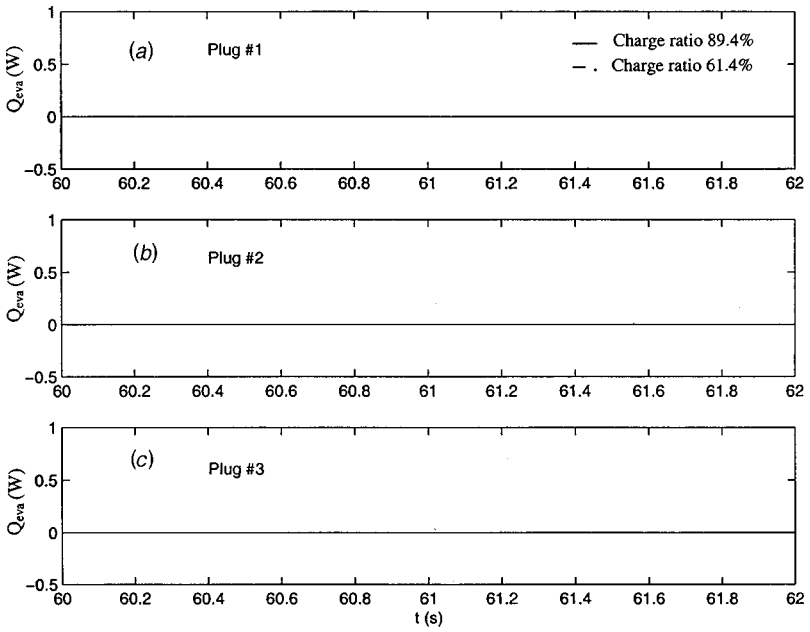

Fig. 17 Effect of the charge ratio on the total evaporative heat transfer rate

Table 3 Effect of parameters on the performance of the PHPs

Type of PHP	T_h (c)	Charge ratio %	D (mm)	Evaporative heat (W)	Sensible heat (W)	Total heat transfer (W)
Unlooped	120	61.4	1.5	1.033	23.84	24.88
	90	61.4	1.5	0.62	7.73	8.35
	120	61.4	3	2.3	77.87	80.17
	120	89.47	1.5	0	0	0
Looped	120	61.4	1.5	1.12	23.83	24.95
	90	61.4	1.5	0.6	7.74	8.36
	120	61.4	3	2.24	77.13	79.37
	120	89.47	1.5	0	0	0

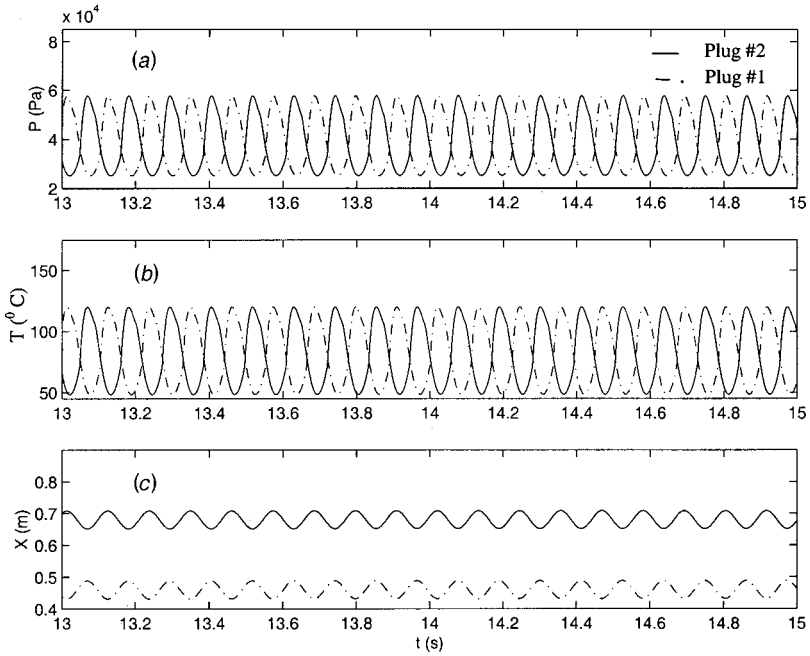

Fig. 18 Variation of pressures, temperatures, and the end positions of the first and second plugs with time for looped PHP (d=1.5 mm)

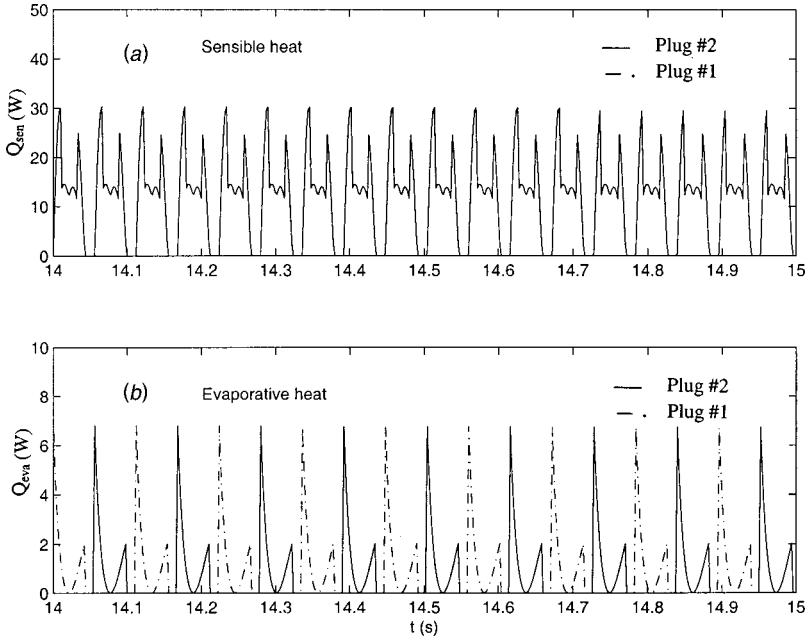

Fig. 19 Variation of heat transfer rate with time for looped PHP: (*a*) sensible heat; and (*b*) evaporative and condensation heat.

individual turns. Liquid was observed at the cooling side, forming a U-shaped column, while vapor was observed at the heating side. This means that, similar to the unlooped PHP, vapor plugs exist only in heating sections. The behavior of liquid slugs and vapor plugs in looped PHPs is also investigated. The parameters specified in Table 2 are used except that the total number of plugs is $N=4$. Also, the length of the first and second vapor plugs would be equal due to the fact that the first and the last vapor plugs are connected to make one plug. Figure 18(*a*) shows the variations of the pressure of the first and second vapor plugs with time. Figure 18(*b*) shows the variation of the temperatures. Since the system is symmetric, the phase difference between oscillation of the first and last plugs is 180 deg. Figure 18(*c*) represents the oscillation of the two ends of the second vapor plug. Figure 19(*a*) shows the sensible heat transferred into the liquid slugs. Both the first and the second slugs have the same phase and amplitude, since they move at the same velocity in opposite directions. Figure 19(*b*) shows the evaporative heat transferred into the vapor plugs. The amplitudes of the oscillation of the two plugs are equal, but there is a phase difference of 180 deg. The total heat transferred into the PHP for this case is 24.95 W. Results indicate that the contribution of the sensible heat is 95.50 percent of the total heat. The effects of changes in diameter, heating wall temperature and charge ratio on the heat transfer performance of looped PHPs are also investigated, and the summarized results are shown in Table 3. Increasing the diameter and heating wall temperature increases the total heat transfer similar to that of the unlooped PHP. It can also be observed that increasing the charge ratio to 90 percent will stop the performance of looped PHPs. Calculated results show no circulation in the system, which is consistent with the visualization of Lee et al. [4] and Miyazaki and Arikawa [6].

5 Conclusions

Thermal modeling of both unlooped and looped PHPs with multiple vapor plugs and liquid slugs is proposed, and the behaviors of liquid and vapor plugs in the PHP are investigated. The following conclusions were obtained:

1 The results show that gravity does not have significant effect on the performance of unlooped PHPs with top heat mode.

2 The total number of vapor plugs reduced to the total number of heating sections, no matter how many vapor plugs were initially in the system.

3 For both looped and unlooped PHPs, periodic oscillation is obtained under specified parameters.

4 Heat transfer in both looped and unlooped PHPs is due mainly to the exchange of sensible heat. The role of evaporation and condensation on the performance of the PHPs is mainly on the oscillation of liquid slugs.

5 By increasing the diameter of the PHP (both looped and unlooped), the total average heat transfer increases.

6 Decreasing the temperature of the heating wall sections significantly decreases the total average heat transfer. This means that the temperature difference between heating and cooling walls is significant in the total amount of heat transferred.

7 The results also showed that both looped and unlooped PHPs did not operate for higher charging ratios.

Acknowledgments

Funding for this work was provided by NASA grant NAG3-1870 and NSF grant CTS 9706706.

Nomenclature

a = undisturbed radius of inner surface of condensate film, m
A = tube cross sectional area, m^2
B = number of bends
C_l = friction coefficient
c_p = specific heat (constant pressure), J/kg K
c_v = specific heat (constant volume), J/kg K
d = diameter, m
g = gravitational acceleration, m^2/s
h = enthalpy, J/kg
h_c = heat transfer coefficient at the cooling section, W/m^2K
h_{fg} = latent heat, J/kg
h_h = evaporative heat transfer coefficient, W/m^2K
L = length, m

L_h = length of heating section, m
L_c = length of cooling section, m
m = mass, kg
$\dot{m}$ = mass flow rate, kg/s
N = total number of vapor plugs
n = number of parallel tubes
N_p = total number of plugs
P = pressure, Pa
Pr = Prandtl number
R = gas constant, J/kgK
Re = Reynolds number
t = time, s
u = internal energy, J/Kg
T = temperature, K
V_v = volume of vapor, m^3
v_1 = velocity of liquid plug, m/s
X = distance, m

Greek Symbols

α = charge ratio
α_l = thermal diffusivity of liquid, m^2/s
λ = wavelength, m
μ = dynamic viscosity, kg/ms
ρ = density, kg/m^3
τ = shear stress, N/m^2
θ_{max} = maximum contact angle
θ_{min} = minimum contact angle

Subscripts

in = inlet
li = i^{th} liquid plug
le = left end
out = outlet
re = right end
vi = i^{th} vapor plug

References

[1] Faghri, A., 1995, *Heat Pipe Science and Technology*, Taylor & Francis, Washington, DC.
[2] Faghri, A., 1999, ''Recent Advances and Challenges in Micro/Miniature Heat Pipes,'' *Proceedings of 11th International Heat Pipe Conference*, Tokyo, Japan.
[3] Akachi, H., 1994, *Looped Capillary Heat Pipe*, Japanese Patent, No. Hei6-97147.
[4] Lee, W. H., Jung, H. S., Kim, J. H., and Kim J. S., 1999, ''Flow Visualization of Oscillating Capillary Tube Heat Pipe,'' *Proceedings of 11th International Heat Pipe Conference*, Tokyo, Japan, pp. 131–136.
[5] Gi, K., Maezawa, S., Kojima, Y., and Yamazaki, N., 1999, ''CPU Cooling of Notebook PC by Oscillating Heat Pipe,'' *Proceedings of 11th International Heat Pipe Conference*, Tokyo, Japan, pp. 166–169.
[6] Miyazaki, Y., and Arikawa, M., 1999, ''Oscillatory Flow in The Oscillating Heat Pipe,'' *Proceedings of 11th International Heat Pipe Conference*, pp. 143–148, Tokyo, Japan.
[7] Kiseev, V. M., and Zolkin, K. A., 1999, ''The Influence of Acceleration on The Performance of Oscillating Heat Pipe,'' *Proceedings of 11th International Heat Pipe Conference*, Tokyo, Japan, pp. 154–158.
[8] Dobson, R. T., and Harms, T. M. 1999, ''Lumped Parameter Analysis of Closed and Open Oscillatory Heat Pipes,'' *Proceedings of 11th International Heat Pipe Conference*, Tokyo, Japan, pp. 137–142.
[9] Wong, T. N., Tong, B. Y., Lim, S. M., and Ooi, K. T., 1999, ''Theoretical Modeling of Pulsating Heat Pipe,'' *Proceedings of 11th International Heat Pipe Conference*, Tokyo, Japan, pp. 159–163.
[10] Hosoda, M., Nishio, S., and Shirakashi, R., 1999, ''Meandering Closed-Loop Heat-Transport Tube (Propagation Phenomena of Vapor Plug),'' *Proceedings of the 5th ASME/JSME Joint Thermal Engineering Conference*, March 15–19, San Diego, CA.
[11] Teng, H., Cheng, P., and Zhao, T. S., 1999, ''Instability of Condensate Film and Capillary Blocking in Small-Diameter-Thermosyphon Condensers,'' Int. J. Heat Mass Transf. **42**, pp. 3071–3083.
[12] Bejan, B., 1995, *Convection Heat Transfer*, 2nd edition, John Wiley & Sons, Inc., New York.
[13] Patankar, S. V., 1980, *Numerical Heat Transfer and Fluid Flow*, McGraw-Hill, New York.
[14] Gi, K., Sato, F., and Maezawa, S., 1999, ''Flow Visualization Experiment on Oscillating Heat Pipe,'' *Proceedings of 11th International Heat Pipe Conference*, Tokyo, Japan, pp. 149–153.

Analysis of the Thermal Stress and Strain on Arrigo Fiammingo's Artistic Window in the Cathedral of Perugia

Cinzia Buratti
Department of Industrial Engineering,
University of Perugia, Via G. Duranti 1-A/4,
06125 Perugia, Italy
e-mail: cburatti@unipg.it

Thermal stress can damage fragile materials such as glass. It is a worrisome problem if the glass is a work of art, such as the polychromatic window of Arrigo Fiammingo (1565), in the Cathedral of Perugia, the topic of this paper. The window surface, irradiated by sunlight, suffers different thermal stresses, according to the color of the glass elements. In the present paper a calculation of stresses and strains on the window is carried out, for different temperature distributions due to sunlight, by using the ANSYS 5.3 software program. Results are compared with the actual state of the fissures on the window.
[DOI: 10.1115/1.1404120]

Keywords: Finite Element, Heat Transfer, Modeling, Numerical Methods, Stress

1 Introduction

Building materials and components are often exposed to thermal stress; in the long run it could be harmful. Effects on fragile materials such as glass could be significant, because they can break if subjected to large and rapid fluctuations in temperature. High thermal stresses are connected with direct solar radiation on the surfaces, more than with micro-climatic conditions, such as air temperature. Temperature fluctuations are rapid if induced by solar radiation more so than by equilibrium with the air temperature, which is a slower process. In a day, over a material with a certain exposure, incident solar radiation varies between 10–50 W/m^2 (diffuse radiation) to 100–400 W/m^2 (total radiation). Material temperature fluctuations could change by ten or more °C; the process could affect different parts of the component at the same time and not only the same part of the material at different times. When materials or components are works of art, such as the artistic windows in the churches of the Romanesque and Gothic age, the problem is rather important. These windows play a dominant role in natural lighting and iconographical decoration. The Umbria region in Italy, in particular, has many artistic windows: in the Cathedral of Perugia, in Saint Domenico's Church, one of the biggest in Europe and the wonderful windows of the Basilica of Saint Francis in Assisi are just examples.

The Thermotechnical and Environmental Control Laboratory of the Department of Industrial Engineering at the University of Perugia has been focusing for some time now on the conservation of works of art, with special attention on the microclimate (thermal and hygrometric conditions), lighting and air quality conditions [1].

The present paper was developed in connection with the intervention that the Superintendence of Environmental, Architectural, Artistic and Historical Works of Art of Umbria carried out on the just recently restored Arrigo Fiammingo window, located on the right aisle of the Cathedral of Perugia. The glass represents ''The Sermon of Saint Bernardino''; the saint is on a podium and is preaching to people absorbed in thought. At the top of the window the monogram of Christ is surrounded by angels, which compose an ornamental motif. People are intensely and brightly colored and stand out against the architectural light background.

During restoration, a protective window was installed externally to the artistic one, in order to limit the damage that atmospheric and polluting agents could induce. This installation caused changes in the microclimate, thoroughly investigated in previous papers [2,3,4,5,6].

In the present paper, the deterioration caused by thermal stress induced on the window surface due to climatic variations and to sunlight is examined. An analysis of the temperature distribution over the artistic glass surface has been carried out by means of a calculation software program (ANSYS 5.3), in order to assess the resulting stresses, which cause fissures on the window itself. During the 1988–1993 restoration performed by the Superintendence many fissures were detected and afterward repaired. In particular the ''grisaille'' has been fixed, then the glass surface has been cleaned and the fissured tesserae have been bonded; finally putty has been made.

ANSYS 5.3 also assessed the strains and the corresponding stresses occurred in the artistic glass. Results were compared with the admissible values for stresses on the glass and with the actual situation of the glass, by surveying the present fissures and the analysis of those already repaired in the recent restoration.

2 Arrigo Fiammingo's Glass Characteristics

Arrigo Fiammingo's window is a window with one panel with maximum dimensions of 1.8×7 m (surface area: about 11 m^2). The protective glass is placed on the external countersinking part of the window, at about 18 cm from the artistic window, which has about the same dimensions. Both artistic and protective windows have northerly exposure (see Fig. 1).

The artistic window is made of polychromatic glass; the protective glass is made up of two-coupled glass sheets glued together with epoxy resin: one sheet is in conventional glass, the other is in Murano (Venice) blown glass.

The spectral coefficients of transparency and reflection for global solar radiation and for visible radiation of the two glass sheets have been measured by a spectrophotometer [6], and have been used in this work. The global coefficients of the artistic window, first used for the ventilation system design, were evaluated as the average among the values found for the different colors, weight with the respective surface area. Overall, the following were ob-

Contributed by the Heat Transfer Division for publication in the JOURNAL OF HEAT TRANSFER. Manuscript received by the Heat Transfer Division May 2, 2000; revision received February 1, 2001; Associate Editor: D. A. Kaminski.

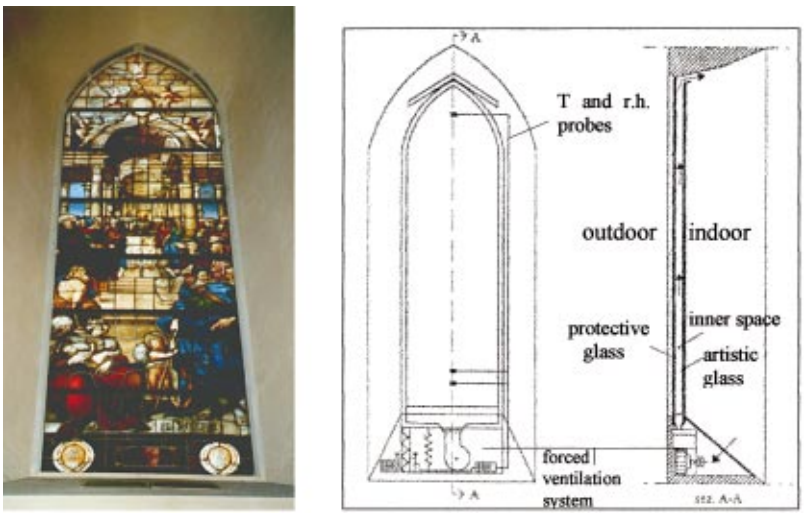

Fig. 1 Arrigo Fiammingo's window in the Cathedral of Perugia in its current state, with forced ventilation system in the space between artistic and protective glass

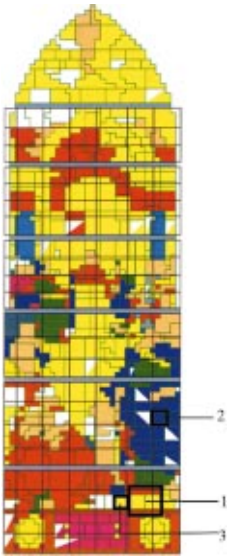

Fig. 2 Finite elements to analyze temperature, strain and stress distribution on Arrigo Fiammingo's glass; 1, 2, and 3 are the sections of the glass first examined

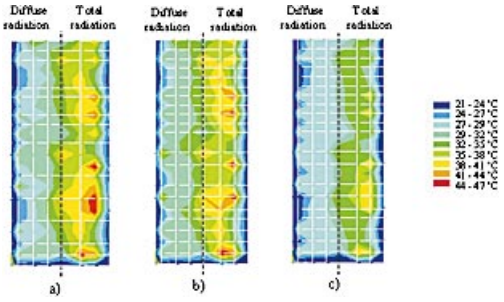

Fig. 3 Temperature distribution with direct and diffused sunlight (situation *A*): (*a*) without external protective glass; (*b*) with external protective glass and natural ventilation of the inner space; (*c*) with external protective glass and forced ventilation of the inner space.

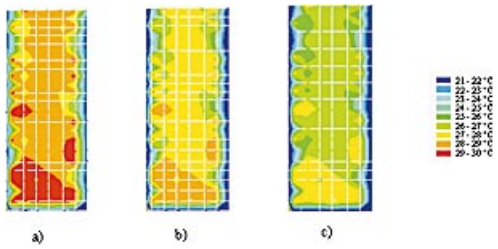

Fig. 4 Temperature distribution with only diffused sunlight (situation *B*): (*a*) without external protective glass; (*b*) with external protective glass and natural ventilation of the inner space; (*c*) with external protective glass and forced ventilation of the inner space.

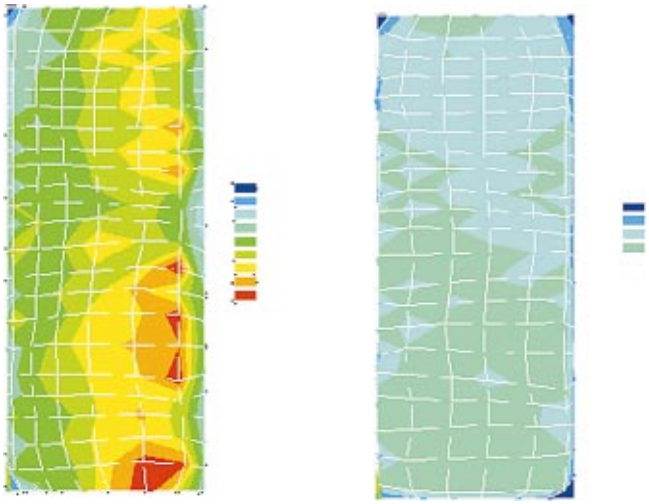

Fig. 9 Von Mises' stress trends on the glass in the situations (*A*) and (*B*), with protective glass and forced ventilation in the internal space.

tained: $t=0.03$, $r=0.10$; the corresponding absorption coefficient is $a=0.87$. The coefficients of transparency and reflection for visible radiation were $t=0.01$, $r=0.10$, and $a=0.89$. The protection glass has values $t=0.81$, $r=0.10$, and $a=0.09$; the coefficients of transparency and reflection for visible radiation were $t=0.83$, $r=0.10$, and $a=0.07$.

3 Thermal and Mechanical Properties of Different Glasses

The following thermal and mechanical properties of glass with different composition were employed in the calculation software ANSYS 5.3, to predict the fissures and the fiber cracks on Arrigo Fiammingo's window and to verify the actual fissures. In the final assessments, it must be considered that the final parameters found relate to new glass, whereas the artistic window was produced with different techniques many years ago. Its chemical composition—analyzed during the recent restoration process—revealed that it cannot be compared to a particular kind of glass, so data relating to silica glasses are considered [7]. The *coefficient of linear thermal dilation* α *of glass* varies according to the chemical composition; it is about 10^{-7}–10^{-6}°C (see Table 1).

The *thermal conductivity of glass* does not vary much with temperature (between 0 and 100°C) and composition. Some values are reported in Table 1, but, on average, it is roughly 0.1 W/m°C. The *specific heat of the glass* composed of more than 60 percent of silica does not depend on the composition and is approximately 0.8 ± 0.1 kJ/kg°C at 25°C to 1.1 ± 0.1 kJ/kg°C at 500°C. Since glass is a fragile material and a poor conductor of heat, it doesn't withstand temperature variations. The temperature difference ΔT to which the object can be subjected rapidly without suffering damage is called *resistance to rapid temperature variations* (thermal shock, [8]). It depends on the thermal and mechanical properties of the material (traction resistance, Poisson's ratio, linear thermal dilation coefficient, Young's modulus, thermal conductivity, density and specific heat):

$$\Delta T = n\left[\frac{N(1-\mu)}{\alpha E}\right]\sqrt{\frac{\lambda}{\rho\gamma}}. \tag{1}$$

The ΔT values for different glass thickness are reported in Table 2; they vary roughly in the range 35–180°C, for glass with different chemical composition and with thickness between 3 and 13 mm. Glass behaves like an elastic solid under transition temperatures; anywhere above this it becomes viscous. Its behavior in the glass transition interval is viscous-elastic. Therefore glass will not accept plastic or elastic-plastic deformation, but ruptures just as soon as it reaches its linear elastic limit. Glass follows Hooke's law and its modulus of elasticity depends on its composition, as reported in Table 3. The compressive resistance in glass is very good; traction resistance can't practically be measured due to micro-fissures which occur in the production phase. Rupture proceeds continuously once it is triggered, since it doesn't find propagation obstacles, as in critical materials (fragility). The kind of micro-fissures is purely random, therefore a sole value for mechanical resistance doesn't exist. So statistical measures are used to describe resistance distribution for a certain type of glass and Weibull's statistic distribution is used:

$$P = 1 - \exp[-(\sigma/\sigma_0)^m], \tag{2}$$

where P is the probability of rupture corresponding to the applied stress σ, σ_0 is a scalar parameter, and m is Weibull's modulus. Table 4 reports the safe loads (assessed with numerous trials) that different sized and thick sheets can withstand, with a safety factor of 2.5; they vary roughly in the range of 2–44 N/mm^2 for thickness between 3 and 12 mm and sheets with different sizes.

Table 1 Thermal properties of glass with different compositions versus temperature [8]

Glass	ρ (kg/m^3)	α_{0-300} (10^{-6}°C^{-1})	λ (W/m°C)	
			0 °C	100 ° C
Silica glass	2200	0.5	0.132	0.148
Sodium-Calcium glass	2510	9.2	0.100	0.112
Boron-Silica glass	2230	3.3	0.112	0.129
Lead glass	2860	8.9	0.083	0.096
Aluminium-Silica glass	2520	4.2	0.137	0.129

Table 2 Resistance to rapid temperature variations for flat glass sheets for different composition and thickness [8]

Glass	ΔT (°C)		
	0.0032 m	0.0064 m	0.0126 m
Sodium-Calcium glass	60	50	35
Boron-Silica glass	180	150	100
Lead glass	65	50	35
Aluminium-Silica glass	135	115	75

Table 3 Young's Modulus *E*, tangent modulus *G* and Poisson's ratio μ for some glasses [8]

Glass	E (GPa)	G (Gpa)	μ
Silica glass	73	31	0.16
Sodium-Calcium glass	72	29	0.25
Boron-Silica glass	64	27	0.20
Lead glass	61	25	0.21
Aluminium-Silica glass	88	35	0.25

Table 4 Safe loads in N/mm^2, which can bear on glass sheets of different dimensions and thickness [8]

Glass sheet dimensions (m)	Glass sheet thickness			
	0.003 m	0.007 m	0.010 m	0.012 m
1,83 x 1,83	14.6	21.0	29.8	43.9
1,12 x 3,05	13.2	19.0	27.3	39.5
1,83 x 2,43	1.7	15.6	22.4	33.2
1,83 x 3,05	8.8	12.7	18.1	26.4
2,43 x 3,05	5.9	9.3	13.7	20.0
1,83 x 4,27	5.9	8.8	13.2	19.0
3,05 x 3,05	5.3	7.3	10.7	16.1
2,43 x 4,27	4.9	6.8	9.8	14.2
3,05 x 4,27	3.9	5.4	7.8	10.7
3,05 x 6,1	2.4	3.9	5.4	7.8

4 Temperature Distribution on the Artistic Glass

The assessment of the thermal strain and stress depends on the temperature distribution of the surface of the artistic glass; it is due to the microclimate and sunlight conditions. Some situations must be chosen in which thermal stress is more significant, so to attain the most critical events for glass strain and stress. To this aim, the temperature distribution is evaluated in the most critical situations, all concerning the month of July (see also [6]). July was chosen because it is characterized by the highest temperatures of the year and the section of the glass irradiated by sunlight is at its peak. In particular, there are four hours of sunlight in the morning and one in the afternoon; in the remaining part of the day the glass is in the shade. So two situations were chosen for sunlight (total and only diffused sunlight). The values for sunlight are reported in Table 5.

The examined situations are:

Table 5 Hourly values of direct and diffused sunlight on the glass surface (W/m^2) referred to the month of July [4]

Hour	Direct radiation (W/m^2)	Diffused radiation (W/m^2)	Total radiation (W/m^2)
5	49.7	9.3	*59.0*
6	202.9	30.8	*233.7*
7	284.5	52.3	*336.8*
8	314.6	72.2	*386.8*
9	-	89.1	*89.1*
10	-	101.9	*101.9*
11	-	109.9	*109.9*
12	-	112.6	*112.6*
13	-	109.9	*109.9*
14	-	101.9	*101.9*
15	-	89.1	*89.1*
16	-	72.2	*72.2*
17	-	52.3	*52.3*
18	-	30.8	*30.8*
19	15.3	9.3	*24.6*

A. direct and diffused sunlight on half of the artistic glass and only diffused sunlight on the other half, in the three following conditions:

- external protective glass not installed
- external protective glass installed, with natural ventilation in the internal space between the glasses
- external protective glass installed with forced ventilation in the internal space between the glasses

B. only diffused sunlight over all the glass, in the same three conditions.

Cases without the protective glass are particularly significant as they show the microclimatic history of the glass, in this situation from its installation in 1565 until 1993.

The most critical situations for the glass have been included among the examined ones. The ANSYS 5.3 software, based on finite elements, has been used for calculations. Hypotheses about finite elements of the system are described in [6]. The geometrical model was first built, composed of a net of rectangular elements (finite elements, see Fig. 2). The nodes of the net were matched as much as possible with the central points of the elements, so to distinguish the behavior of the glass with different colors and different absorption coefficients. The arched top of the window was left out of the analysis because the glass is in light color and the absorption coefficients are low [6]; so low temperatures and dilatations are expected.

The temperature variation between the nodes is considered linear; internal heating in each element is considered, equal to the absorbed solar energy (as a function of the absorption coefficient of the colored glass). The solar radiation absorption properties of the colored glasses used in this work have been measured by a spectrophotometer in a previous work [6].

A heat exchange between the nodes and the internal and external air is considered, so two grids are built: their points are respectively over an internal and an external plane parallel to the glass. In the nodes of the two grids, hypotheses on air temperature have been made:

- internal air: $T=\text{constant}=T_i$
- external air: with protective glass $T=\text{constant}=T_e$; without protective glass $T=$constant for nodes at the same height; T increases from down to bottom with linear low (maximum growth equal to 2°C).

Discretization through the thickness was not considered because it is about 3 mm, so the glass dilatations in the thickness directions are negligible. The following environmental parameters have been assumed:

- adduction coefficient between air and artistic glass equal to 23.2 W/m^2°C without protective glass, equal to 8.14 W/m^2°C with protective glass and natural ventilation in the inner space, equal to 11.14 W/m^2°C with protective glass and forced ventilation in the inner space
- temperature around the glass is supposed equal to the wall and to the air inside the Cathedral temperature (about 21°C in July).

The following values of the thermophysical and mechanical properties of the glass have been chosen as input data:

- $\alpha=5\times10^{-7}$°C^{-1}
- $\lambda=0.136$ W/m°C
- $E=73$ GPa
- $G=31$ GPa
- $\mu=0.16$

The results are shown in Figs. 3 and 4. As seen in [6], in the situation *A*, the maximum temperatures are found in the right half part of the glass, where there are both direct and diffused radiation; in that section, the highest temperatures are found in the blue, red, and purple tesserae, with a higher absorption coefficient. The maximum temperatures range from 47°C when the protective glass is not installed (Fig. 3(*a*)) to 43°C with the protective glass and natural ventilation in the inner space (Fig. 3(*b*)), to 40°C with the protective glass and forced ventilation in the inner space (Fig. 3(*c*)). The minimum temperatures are found near the masonry and are around 21°C, so temperatures variations on the glass surface range, in the three conditions, from 26 to 19°C.

Figure 4 concerns situation *B*; it shows that temperature distribution depends only on the different colors of the tesserae, with higher temperatures in the darker colors of the glass (higher absorption coefficients). The maximum T value varies from 31, to 30, and to 28°C in the three mentioned conditions, with variations on the glass surface between 10 and 7°C.

On the bases of the temperature distribution on the situation *A*, corresponding to the most critical conditions for the glass, the strain and the stress were assessed; for sake of completeness, stress and strain were calculated on the situation *B* too.

5 Strain Analysis

An analysis of strain was performed considering the external protective glass and forced ventilation in the inner space, installed after restoration. Calculating the two extreme situations (this one and the one without protective glass), a maximum difference was detected for strain of 0.001 μm. So it was thought more suitable to consider the present situation, with external protective glass and forced ventilation in the inner space, considering both situations *A* and *B*, to which the window is really subjected during the month of July.

The lead pieces that surround the glass tesserae create discontinuities on the surface, because they have different thermal properties from the glass, so they behave differently when temperature varies. First, instead of analyzing the whole glass, three sections only were examined (Fig. 2). The first (1) has some colors that contains lead pieces; the second (2) and the third (3) are respectively blue and yellow (maximum and minimum absorption coefficient values), don't contain lead pieces and lead only surrounds the section.

Each section of the glass chosen was divided in finite squared elements, considering the two different materials, glass and lead, and their different properties (Fig. 5). There aren't appreciable discontinuities between the dilation of glass and lead; results (Fig. 6) show that they differ slightly even in the most critical areas. So it could be hypothesized that the two materials do not interact that much: in fact the dilatation coefficients have the same magnitude (about 10^{-6}°C^{-1}) and the presence of lead has not been considered in the analysis of the whole glass. The whole glass sheet was finally examined, neglecting the presence of lead and considering the window made up of only one material, the glass. Figs. 7(*a*) shows the trend of strain in the situation *A*; most of the dilatation is in the right hand side of the glass, where the highest temperatures due to sunrays are present. The maximum dilatation is 0.157 μm and it falls in the blue tesserae of the section under total radiation.

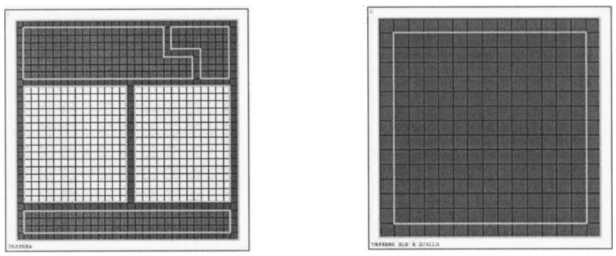

section (1) *sections (2) and (3)*

Fig. 5 Finite elements in glass sections (*1*), (*2*), (*3*)

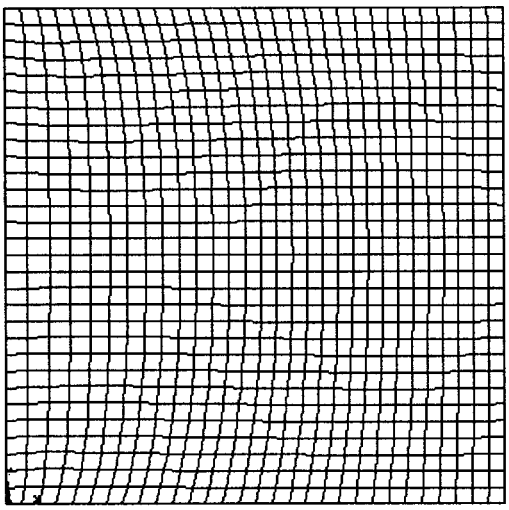

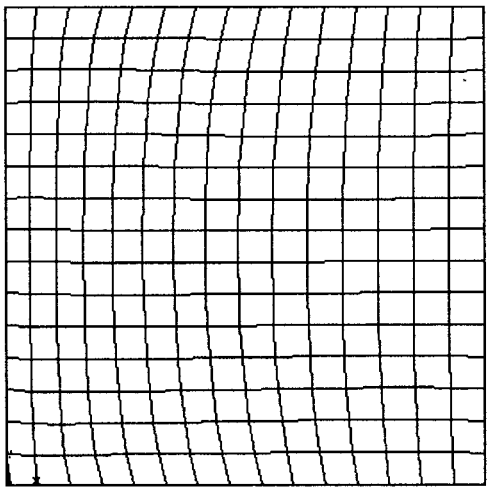

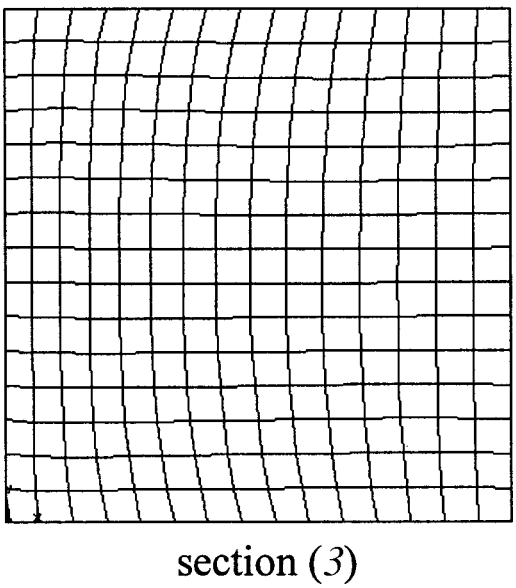

Fig. 6 Dilatation trends in glass sections (*1*), (*2*), (*3*)

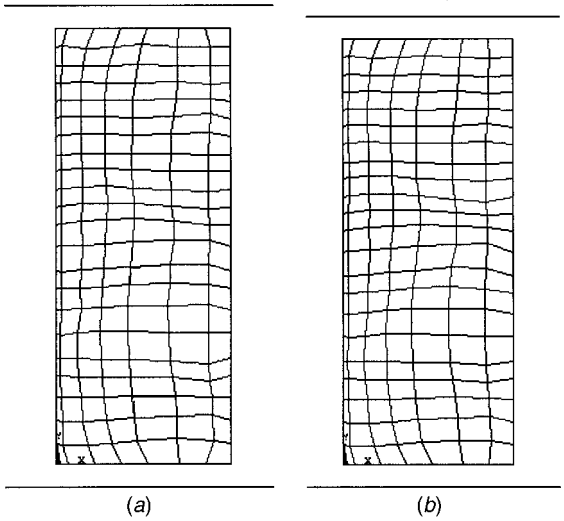

Fig. 7 Dilatation trends on the artistic glass subjected to direct and diffused sunlight (situation *A*) and to only diffused sunlight (situation *B*)

Figure 7(*b*), concerning dilatations in the situation *B*, shows that they depend only on the color of the tesserae which take on higher values in the darker colors. The maximum dilatation is about 0.042 μm, remarkably below those of the previous case (the scale in Fig. 7(*b*) is about 2.5 times the one in Fig. 7(*a*)).

A further verification about the lead influence was performed once the analysis was finished: a simulation was carried out considering the glass as if entirely made up of lead; the strain obtained was compared with those considering the window made up of only glass (see Fig. 8). The differences are negligible in all the portions of the glass sheet (about a few μm tenths in the worst conditions), thus confirming that the glass dilatation is not influenced by the surrounding lead.

6 Stress Analysis

Stress analysis was also performed, for the same reasons as in section 5, only in the conditions with external protective glass and forced ventilation in the space between the windows. We saw the maximum temperature variation from portion to portion of the glass was about 20°C. This value, although high, is lower than the limit value of the resistance to rupture variations of temperature, as indicated in Table 2. For glass sheets of 3 mm thickness the limit value is about 60°C.

The stress distribution that the temperatures induce on the glass was calculated by means of ANSYS software. The hypothesis is that the glass has fixed boundaries and it can't rotate at its edges. Stress values vary between 0.96 and 1 N/mm^2 in the situation *A* (Fig. 9(*a*)) and between 0.806 and 0.812 N/mm^2 in the situation *B* (Fig. 9(*b*)). They have been calculated in the different nodes with Von Mises method.

A comparison between calculated data and allowable stress limits has been carried out; allowable stress limits have been found in the Literature for glasses with chemical composition similar to the one of the Arrigo Fiammingo's window. The allowable stress value considered for the comparison is 2.4 N/mm^2, corresponding to a 3 mm thickness glass, with 3.05×6.10 m dimensions (see Table 4). Artistic window's thickness is 3 mm, but its dimensions are about 1.8×7 m, for a surface area smaller than the reference one. Se we operate under safe acceptable conditions.

Maximum stress values calculated, respectively, 1 and 0.81 N/mm^2 in the situations *A* and *B*, are both lower than the stress allowable limit.

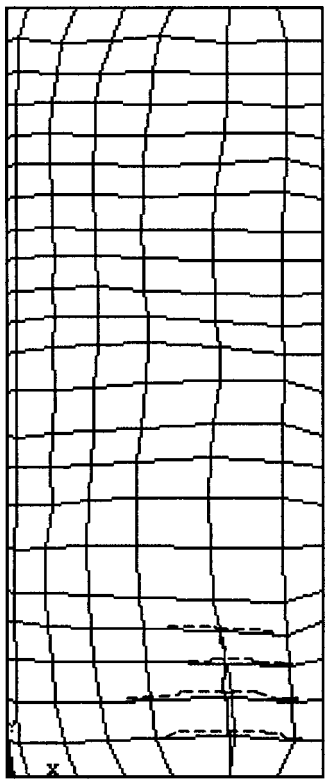

Fig. 8 Dilatation trend on the glass (situation *A*) when only lead is considered. the dashed lines show the dilatation differences of Fig. 7(*a*) (when only glass is considered).

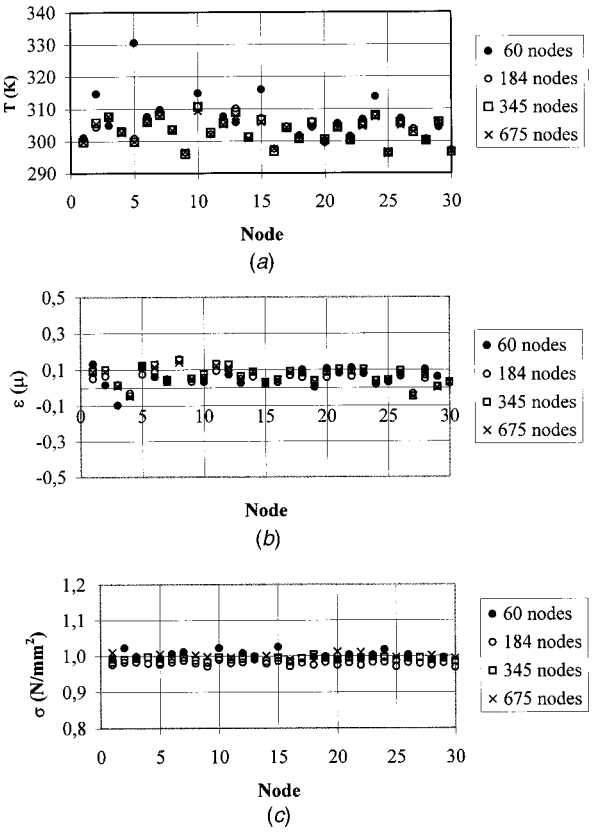

Fig. 10 Numerical accuracy: temperature (*a*), strain *b*) and stress (*c*) values in 30 significant nodes, with different mesh refinements.

7 Numerical Accuracy

In order to evaluate the numerical accuracy of the model, four different mesh refinements were considered.

1 rectangular elements, with 5×12=60 nodes
2 rectangular elements, with 8×23=184 nodes
3 rectangular elements, with 15×23=345 nodes
4 rectangular elements, with 15×45=675 nodes

The temperature, strain and stress values in the different grid refinements were calculated and a comparison between the values of these parameters in 30 significant nodes was carried out.

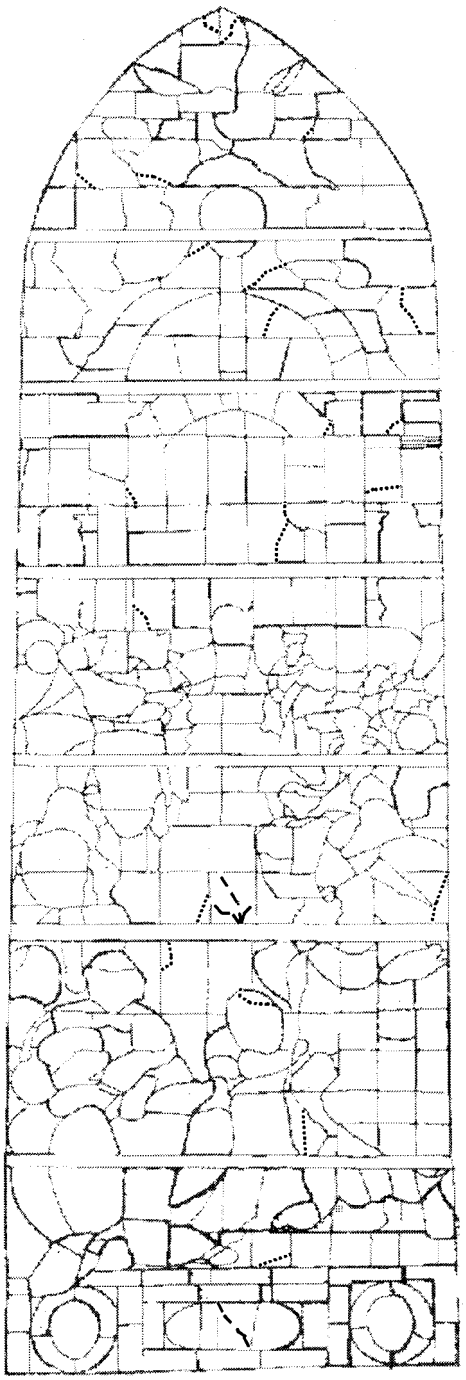

Fig. 11 Current lesions (dashed lines) and lesions repaired with added lead (dotted lines) during the 1998 restoration and before

Results are shown in Fig. 10(*a,b,c*), where temperature, strain and stress values in the 30 grid points chosen are reported, for the different mesh refinements; the mean difference between mesh 1 and 2 is significant (temperature differences are about $\pm(0-30)$°C, strain differences are about $\pm(0.05-0.08)$ μm and stress differences are about $\pm(0.02-0.04)$ N/mm^2). The mean differences between mesh refinements 2 and 3 and mesh refinements 3 and 4 are of the same entity and are less significant; they could be considered as the numerical accuracy of the model. So the mean values of the numerical accuracy are

- about $\pm$0.4°C for temperature calculations
- about $\pm$0.02 μm for strain calculations
- about $\pm$0.01 N/mm^2 for stress calculations.

The mesh refinement no. 2 is therefore the one chosen for the simulation.

8 Fissure State

A check at the Cathedral of Perugia was performed in order to detect possible fissures on the surface of Arrigo Fiammingo's glass.

Many interventions had been carried out during the 1989 restoration, when fissures were welded with lead. Strands of lead were inserted to repair and support the fragments of glass tesserae damaged throughout the years (the so-called *added lead*). Figure 11 indicates these interventions with dotted lines; dashed lines show the fissures now present on the glass. The actual fissures are in the area where the strain of the glass is highest (see Fig. 7). Therefore, even after restoration, the thermal stress could have caused the glass tesserae rupture, although the stress values are below the limits.

So in the present conditions there is a temperature, strain and stress distribution, which should not cause lesions on the surface of the artistic glass. But the investigation was conducted assuming that the glass is in perfect condition, without considering the deterioration or aging factors: these could decrease the mechanical and resistance characteristics of the glass tesserae. Other environmental factors, which can act alone or worse yet simultaneously, can speed up the process of deterioration (temperature and relative humidity of the air, air pollution, natural or artificial lighting conditions, etc.) [1,3]. This explains why some lesions on the glass were found in the area most subjected to stress and strain.

9 Conclusions

This paper illustrates the investigation of the thermal stress and strain on a particularly precious artistic glass (Arrigo Fiammingo 1565) located in the Cathedral of Perugia. Stresses are due to the microclimate created in the space between the glass examined and the external protective glass (installed during a recent restoration), but overall to sunlight.

A computer software program (ANSYS 5.3) has been employed to calculate the temperature distribution on the glass both in its present situation, with a protective glass and a ventilation system, and in the situation preceding the restoration intervention in 1988. Afterwards, on the bases of temperature distribution over the glass, dilatations and stresses were found.

The study of temperature distributions shows remarkable differences from one area to another of the glass, due to partially direct sunlight irradiation in summer months; these differences reach the maximum value of 20°C in the most critical conditions.

Finally, thermal dilatation and stress analysis show that values are below rupture limits defined for modern glass with composition similar to the window. However the results do not reflect wear and deterioration conditions that the glass has suffered in time; in spite of the restoration, they have certainly diminished thermal and mechanical characteristics of the glass. So a thorough examination of the window has revealed some lesions in areas most exposed to stress and strain.

Acknowledgments

Author wishes to thank Dr. Angelo Venneri for the precious collaboration in the simulations with ANSYS software program.

Nomenclature

a = absorption coefficient (/)
E = Young's modulus (GPa)
G = tangent modulus (GPa)
m = Weibull's modulus (/)
n = dimensional constant in relation (1)
N = traction resistance (N/mm^2)
P = fracture probability (/)
r = reflection coefficient (/)
r.h. = relative humidity (%)
t = transparency coefficient (/)
T = temperature (°C, K)
α = linear thermal dilation coefficient (°C^{-1}, K^{-1})
γ = specific heat (J/kgK)
ΔT = resistance to rapid temperature variation (°C, K)
ϵ = strain (m, μm)
λ = thermal conductivity (W/mK)
μ = Poisson ratio (/)
ρ = density (kg/m^3)
σ = stress (N/mm^2)

Subscripts

e = external
i = internal

References

[1] Asdrubali, F., and Buratti, C., 1999, "Condizioni ottimali di conservazione delle oper d'arte: rassegna bibliografica ed analisi critica," Proceedings of 54th Congresso Nazionale ATI, L'Aquila, September 1999.
[2] Buratti, C., Cotana, F., and Felli, M., 1994, "Sulla ventilazione di una vetrata artistica del Duomo di Perugia," Proceedings of 49th Congresso Nazionale ATI, Perugia, September 1994.
[3] Asdrubali, F., Buratti, C., and Cotana, F., 1999, "II sistema di ventilazione della vetrata di Arrigo Fiammingo nel Duomo di Perugia: monitoraggio delle condizioni termoigrometriche," Proceedings of 54th Congresso Nazionale ATI, L'Aquila, September 1999.
[4] Rossi, F., and Baruffa, R., 1999, "Simulazione delle Condizioni Termoigrometriche di una Vetrata della Cattedrale di Perugia," Proceedings of 54th congresso Nazionale ATI, L'Aquila, September 1999.
[5] Buratti, C., Cotana, F., and Baruffa, R., 1999, "II contributo di vetrate artistiche all'illuminazione naturale," Workshop AIDI-ENEL La civiltà della Luce, Perugia—Assisi, November 5, 1999.
[6] Cotana, F., "Impianto Sperimentale di Ventilazione e Termoregolazione per la Conservazione di una Vetrata Storico Artistica," Condizionamento dell'Aria, Riscaldamento e Refrigerazione (CDA), No. 6, June 2000, p. 641–654.
[7] UNI En 572-1, 1996, "Vetro per edilizia. Prodotti di base di vertro di silicato sodo-calcico. Definizione e proprietà geneali fisiche e meccaniche," April 1996.
[8] Colombo, 1997, Manuale dell'Ingegnere, Hoepli, Milan.
[9] Gottardi, V., 1982, Il vetro; appunti dalle lezioni di tecnologie dei materiali e chimica applicata, Patron Edition, Bologna.
[10] Perry, R. H., and Green, D., 1984, *Perry's Chemical Engineers' Handbook*, Sixth Edition, McGraw Hill.
[11] Aghemo, C., Filippi, M., and Prato, E., 1994, "Ricerca bibliografica comparata sulle condizioni termoigrometriche per la conservazione delle opere d' arte," Proceedings of 49th Congresso ATI, Perugia, September 1994.
[12] *Handbook of Fundamentals*, SI Edition, ASHRAE, Atlanta, GA 1997.
[13] Cesari, F., 1993, *Analisi di problemi termici col metodo degli elementi finiti*, Pitagora Edition, Bologna.
[14] Cianini Pierotti, M. L., 1992, *Una cittã e la sua Cattedrale. II Duomo di Perugia*, Chiesa S. Severo Edition, Perugia.
[15] Colburn, P., 1933, "A Method of Correlating Forced Convection Heat Transfer Data and a Comparison with Fluid Friction," AIChE J., **29**, 174.
[16] Corallini, A., and Bertuzzi, V., 1994, *II restauro delle vetrate*, Nardini Edition, Fiesole.
[17] Felli, M., 1993, "Soluzioni di integrazione impiantistica nel recupero: aspetti energetici," Progetto Finalizzato Edilizia, Final Report, Perugia, May 1993.
[18] Felli, M., 1999, "Lezioni di Fisica Tecnica," Vol. 1, 2 e 3, Morlacchi Edition, Perugia.
[19] Filippi, M., *Air Conditioning for Works of Art*, Bulletin irr. 97.3, March 1997.
[20] Filippi, M., 1988, "Gli impianti nei musei," Condizionamento dell'Aria, Riscaldamento e Refrigerazione (CDA), No. 8.
[21] Filippi, M., Lombardi, C., and Silvi, C., 1994, "Conservazione di beni di

interesse storico ed artistico,'' Condizionamento dell'Aria, Riscaldamento e Refrigerazione (CDA), No. 4.
[22] Filippi, M., Aghemo, C., and Alessio, E., 1997, ''Dalmicroclima per la conservazione della opere d'arte: principi e tecniche di controllo ambientale,'' Workshop AICARR *Microclima, qualità dell'aria e impianti negli ambient museali*, Firenze, February 7, 1997.
[23] Hall, M., 1987, *On Display, a Design Grammar for Museum Exhibition*, Lund Hempkries, London.
[24] Holman, J. P., 1989, *Heat Transfer*, McGraw Hill, Singapore.
[25] ICCROM, 1982, ''La conservazione nei musei. II controllo del clima. Il controllo dell'illuminazione,'' ICCROM, Roma.
[26] Isetti, C., 1997, ''Problematiche termoigrometriche relative alla conservazione di beni di interesse culturale,'' Workshop AICARR *Microclima, qualità dell'aria e impianti negli ambienti museali*, Firenze, February 7, 1997.
[27] *Annuario di Statistiche Meteorologiche*, editions from 1960 to 1990, ISTAT.
[28] Lydersen, L., 1989, *Fluid Flow and Heat Transfer*, Bath.
[29] Massa, S., and Russo, A., ''Conservazione museale,'' Edizioni per la Conservazione III No. 25/26.
[30] Osizik, M. N., 1985, *Heat Transfer*, McGraw Hill, Singapore.
[31] Raffellini, G., ''La qualità ambientale nei musei,'' Workshop AICARR *Microclima, qualità dell'aria e impianti negli ambienti museali*, Firenze, February 7, 1997.
[32] Rohsenow, W. M., Hartnett, J. P., Ganic, E. N., 1985, *Handbook of Heat Transfer Fundamentals*, McGraw Hill, New York.
[33] Sayigh, A. M., 1977, *Solar Energy Engineering*, Academic Press, New York.
[34] Turner, K., 1980, ''Museum Showcase,'' A Design Brief. British Museum, London.
[35] UNI 10829, 1999, ''Beni di interesse storico-artistico. Condizioni ambientali di conservazione. Misurazione ed analisi,'' July, 1999.

Journal of Heat Transfer

Technical Notes

This section contains shorter technical papers. These shorter papers will be subjected to the same review process as that for full papers.

Foundations of Buoyancy Driven Heat Transfer Correlations

Vedat S. Arpacı
Professor, ASME Fellow
e-mail: arpaci@umich.edu

Shu-Hsin Kao
Mem. ASME

Department of Mechanical Engineering, The University of Michigan, 2142 G. G. Brown, 2350 Hayward, Ann Arbor, MI 48109-2125

In terms of a dimensionless number, $\Pi_N \sim Ra/(1+Pr^{-1})$, introduced by Arpacı (1986, 1990, 1995) for buoyancy driven flows, Ra and Pr respectively being the usual Rayleigh and Prandtl numbers, two well-known correlations (Churchill and Chu, 1975) for natural convection next to a vertical isothermal plate are reduced in terms of $\Pi_L=Ra/(1+0.492Pr^{-1})$ to $Nu=0.67\Pi_L^{1/4}$, $10^3 \leqslant \Pi_L \leqslant 10^9$, for the laminar case, and in terms of $\Pi_T=Ra/(1+0.164Pr^{-1})$ to $Nu=0.15\Pi_T^{1/3}$, $10^9 \leqslant \Pi_T \leqslant 10^{12}$, for the turbulent case. [DOI: 10.1115/1.1392987]

Keywords: Heat Transfer, Microscale, Modeling, Natural Convection, Turbulent

Introduction

Dimensional arguments on natural convection lead for heat transfer,

$$\mathrm{Nu}=f(\mathrm{Ra},\mathrm{Pr}), \tag{1}$$

Nu, Ra, and Pr respectively being the usual Nusselt, Rayleigh and Prandtl numbers. The experimental data of the literature for $\mathrm{Pr}\geqslant 1$ are known correlating with

$$\mathrm{Nu}=f(\mathrm{Ra}), \quad \mathrm{Pr}\geqslant 1, \tag{2}$$

and, for $\mathrm{Pr}\ll 1$, with

$$\mathrm{Nu}=f(\mathrm{RaPr}), \quad \mathrm{Pr}\ll 1. \tag{3}$$

To date a dimensionless number explicitly depending on Ra and Pr,

$$\Pi_N \sim \frac{\mathrm{Ra}}{1+\mathrm{Pr}^{-1}}, \tag{4}$$

apparently remained overlooked except for the recent Arpacı [1,2,3] studies. The objective of this study is to propose, in terms of this number, correlations for laminar and turbulent natural convection from a vertical isothermal plate,

$$\mathrm{Nu}=f(\Pi_N). \tag{5}$$

Although the existence of Π_N has never been directly shown, the integral solution for the laminar natural convection near a vertical plate given by Squire [4] almost five decades ago,

$$\mathrm{Nu}=0.508\mathrm{Pr}^{1/2}(20/21+\mathrm{Pr})^{-1/4}\mathrm{Gr}^{1/4}, \tag{6}$$

can be rearranged in terms of Ra=GrPr to give

$$\mathrm{Nu}=0.508\Pi_N^{1/4}, \tag{7}$$

where

$$\Pi_N=\frac{\mathrm{Ra}}{1+0.952\mathrm{Pr}^{-1}}. \tag{8}$$

There are empirical correlations, illustrating the dependence of Nu on Pr and Ra, which can be expressed in terms of Π_N. For example, Catton [5] suggests for a vertical cavity

$$\mathrm{Nu}=0.18\left(\frac{\mathrm{Pr}}{0.2+\mathrm{Pr}}\mathrm{Ra}\right)^{0.29} \tag{9}$$

which can be arranged as

$$\mathrm{Nu}=0.18\Pi_N^{0.29} \tag{10}$$

where

$$\Pi_N=\frac{\mathrm{Ra}}{1+0.2\mathrm{Pr}^{-1}}. \tag{11}$$

There is computational literature (Bertin and Ozoe [6]) recognizing the dependence of Benard transition on the Prandtl number. This fact can readily be demonstrated by noting

$$\lim_{\mathrm{Pr}\to\infty} \Pi_N \to \mathrm{Ra}_c(\infty), \tag{12}$$

or, explicitly,

$$\mathrm{Ra}_c=\left(1+\frac{C}{\mathrm{Pr}}\right)\mathrm{Ra}_c(\infty), \tag{13}$$

where C is a constant.

Recalling the critical Rayleigh number $\mathrm{Ra}_c=10^9$ for $\mathrm{Pr}>1$, recent experimental studies (Bejan and Lage [7], Vitharana and Lykoudis [8]) dealing with buoyancy driven flows with $\mathrm{Pr}\ll 1$ suggest

$$\mathrm{Ra}_c=10^9\mathrm{Pr} \tag{14}$$

for the transition from laminar to turbulent heat transfer from vertical plates subject to an imposed heat flux. This transition can readily be explained in terms of Π_N by letting

$$(\Pi_N)_C=\left(\frac{\mathrm{Pr}}{1+\mathrm{Pr}}\right)10^9, \tag{15}$$

Contributed by the Heat Transfer Division for publication in the JOURNAL OF HEAT TRANSFER. Manuscript received by the Heat Transfer Division March 9, 2000; revision received February 12, 2001. Associate Editor: A. Bejan.

which leads to

$$\lim_{\mathrm{Pr}\to 0}(\Pi_N)_C \to 10^9 \mathrm{Pr}. \tag{16}$$

In other recent studies, Arpacı and co-workers [9,10] develop microscales for pool fires, and in terms of these scales, propose a fuel consumption model based on Π_N which now depends on flame Rayleigh and Schmidt numbers. Also, Arpacı and Kao [11,12] develop microscales for thermocapillary flow and rotating flow, introduce models in terms of these scales and correlate the experimental literature.

Laminar Convection

Because of its importance to the present study, Squire's work is briefly reviewed here following the dimensional arguments of Arpacı [1]. Let the momentum balance in terms of inertial, viscous and buoyancy forces (say F_I, F_V, and F_B) be

$$F_I + F_V \sim F_B. \tag{17}$$

On dimensional grounds,

$$V\frac{V}{\ell} + \nu\frac{V}{\delta^2} \sim g\beta\Delta T \tag{18}$$

δ being the thickness of the momentum boundary layer, ℓ a length characterizing the geometry. Also, let the thermal energy balance, in terms of enthalpy flow and conduction (say Q_H and Q_K), be

$$Q_H \sim Q_K. \tag{19}$$

On dimensional grounds, Eq. (19) leads to

$$V\frac{\theta}{\ell} \sim \alpha\frac{\theta}{\delta_\theta^2}, \tag{20}$$

δ_θ being the thickness of the thermal boundary layer, or

$$V \sim \alpha\frac{\ell}{\delta_\theta^2}. \tag{21}$$

Inserting Eq. (21) into Eq. (18), and following the Squire postulate, let

$$\delta \sim \delta_\theta. \tag{22}$$

This assumption implies a second order effect of the difference between δ and δ_θ for thermal considerations rather than suggesting equal thickness for the two boundary layers. Then, from Eqs. (18), (21), and (22),

$$\frac{\ell}{\delta_\theta^4}\left(1+\frac{\alpha}{\nu}\right) \sim \frac{g\beta\Delta T}{\nu\alpha} \tag{23}$$

or,

$$\frac{\delta_\theta}{\ell} \sim \left(1+\frac{1}{\mathrm{Pr}}\right)^{1/4}\mathrm{Ra}^{-1/4}, \tag{24}$$

or,

$$\frac{\delta_\theta}{\ell} \sim \Pi_N^{-1/4}, \tag{25}$$

and

$$\mathrm{Nu} \sim \frac{\ell}{\delta_\theta} \sim \Pi_N^{1/4}, \tag{26}$$

which is identical in form to Eq. (7). Also, the recent Arpacı [1,2] model for buoyancy driven turbulent convection leads, after neglecting the core effect, to

$$\mathrm{Nu} \sim \Pi_N^{1/3}. \tag{27}$$

The next section on turbulent convection is devoted to a review on thermal microscales of buoyant flows and to microscale foundations of Eq. (27).

Turbulent Flow

Following the usual practice, let the instantaneous velocity and temperature of a rotating turbulent flow be decomposed into a temporal mean (denoted by capital letters) and fluctuations, $\tilde{u}_i = U_i + u_i$ and $\tilde{\theta} = \Theta + \theta$, and assume U_i and Θ be statistically steady.

For a homogeneous pure shear flow (in which all averaged quantities except U_i and Θ are independent of position and in which S_{ij} and $\partial\Theta/\partial x_j$ are constant), the balance of the mean kinetic energy of velocity fluctuations reduces to

$$(-\mathcal{P}_\mathcal{B}) = \mathcal{P} + (-\epsilon), \tag{28}$$

where

$$\mathcal{P}_\mathcal{B} = -g_i\overline{u_i\theta}/\Theta_0 \tag{29}$$

is the buoyant production,

$$\mathcal{P} = -\overline{u_i u_j}S_{ij} \tag{30}$$

is the inertial production, and

$$\epsilon = -2\nu\overline{s_{ij}s_{ij}} \tag{31}$$

is the viscous dissipation of turbulent energy, and, the balance of the root mean square of temperature fluctuations reduces to

$$\mathcal{P}_\theta = \epsilon_\theta \tag{32}$$

where

$$\mathcal{P}_\theta = -\overline{u_j\theta}\frac{\partial\Theta}{\partial x_j} \tag{33}$$

is the thermal production, and

$$\epsilon_\theta = \alpha\frac{\overline{\partial\theta}}{\partial x_j}\frac{\overline{\partial\theta}}{\partial x_j} \tag{34}$$

is the thermal dissipation. Eq. (28) states that the buoyant production is partly converted into inertial production and partly into viscous dissipation.

On dimensional grounds, assuming $S_{ij} \sim u/\ell$ and $\partial\Theta/\partial x_j \sim \theta/\ell$, Eqs. (28) and (32) may be written as

$$\mathcal{P}_\mathcal{B} \sim \frac{u^3}{\ell} + \nu\frac{u^2}{\lambda^2}, \tag{35}$$

and

$$u\frac{\theta^2}{\ell} \sim \alpha\frac{\theta^2}{\lambda_\theta^2}, \tag{36}$$

where u and θ respectively denote the rms values of velocity and temperature fluctuations, ℓ is an integral scale, λ and λ_θ are the Taylor scales. Eqs. (35) and (36) imply isotropic mechanical and thermal dissipations. Note that the isotropic dissipation is usually a good approximation for any turbulent flow (Tennekes and Lumley [13]).

To proceed further, assuming the Squire postulate to be independent of flow conditions and following Eq. (22), let

$$\lambda \sim \lambda_\theta. \tag{37}$$

Then, elimination of velocity between Eqs. (35) and (36) results in a thermal Taylor scale

$$\lambda_\theta \sim \ell^{1/3}\left(1+\frac{1}{\mathrm{Pr}}\right)^{1/6}\left(\frac{\nu\alpha^2}{\mathcal{P}_\mathcal{B}}\right)^{1/6}, \quad \mathrm{Pr} \geqslant 1 \tag{38}$$

which may alternatively be written as

$$\lambda_\theta \sim \ell^{1/3}(1+\mathrm{Pr})^{1/6}\left(\frac{\alpha^3}{\mathcal{P}_\mathcal{B}}\right)^{1/6}, \quad \mathrm{Pr} \leqslant 1, \tag{39}$$

where Eq. (38) explicitly includes the limit for $\mathrm{Pr}\to\infty$ and is convenient for fluids with $\mathrm{Pr}\geqslant 1$, and Eq. (39) explicitly includes the limit for $\mathrm{Pr}\to 0$ and is convenient for fluids with $\mathrm{Pr}\leqslant 1$.

Now, consider the local (isotropic) behavior of the homogeneous flow (in a sublayer next to a wall or in a vortex tube) and let all scales (which are no longer distinguished) be replaced by an isotropic scale η_θ. Thus, Eqs. (38) and (39) are respectively reduced to a thermal Kolmogorov scale for buoyancy driven flows,

$$\eta_\theta \sim \left(1+\frac{1}{\mathrm{Pr}}\right)^{1/4}\left(\frac{\nu\alpha^2}{\mathcal{P}_\mathcal{B}}\right)^{1/4}, \quad \mathrm{Pr} \geqslant 1 \tag{40}$$

or, alternatively,

$$\eta_\theta \sim (1+\mathrm{Pr})^{1/4}\left(\frac{\alpha^3}{\mathcal{P}_\mathcal{B}}\right)^{1/4}, \quad \mathrm{Pr} \leqslant 1. \tag{41}$$

To date the relation between the small scales of turbulence and the scales used in the correlation of natural and forced convection data appears to remain unnoticed. To demonstrate this relation, return to one of the foregoing scales, say Eq. (40) and assume, on dimensional grounds,

$$\mathcal{P}_\mathcal{B} \sim g u \theta / \Theta_0. \tag{42}$$

Let Θ_0 be the temperature of the isothermal ambient. Noting

$$\Theta_0^{-1} = \beta \tag{43}$$

β being the coefficient of thermal expansion, rearrange Eq. (42) as

$$\mathcal{P}_\mathcal{B} \sim g u \beta \theta \tag{44}$$

or, with the isotropic velocity obtained from Eq. (36),

$$u \sim \alpha / \eta_\theta$$

as

$$\mathcal{P}_\mathcal{B} \sim g \alpha \beta \theta / \eta_\theta. \tag{45}$$

Insertion of Eq. (45) into Eq. (41) yields, after some rearrangement,

$$\eta_\theta \sim \left(1+\frac{1}{\mathrm{Pr}}\right)^{1/3}\left(\frac{\nu\alpha}{g\beta\theta}\right)^{1/3}. \tag{46}$$

Further, assuming the buoyant sublayer to control heat transfer, let

$$\theta \sim \Delta T \tag{47}$$

ΔT being the imposed temperature difference between the wall and ambient. Thus, Eq. (46) becomes, in terms of Eq. (47),

$$\eta_\theta \sim \left(1+\frac{1}{\mathrm{Pr}}\right)^{1/3}\left(\frac{\nu\alpha}{g\beta\Delta T}\right)^{1/3} \tag{48}$$

or, in terms of a characteristic scale for geometry, ℓ,

$$\frac{\eta_\theta}{\ell} \sim \Pi_N^{-1/3}, \tag{49}$$

or,

$$\mathrm{Nu} \sim \frac{\ell}{\eta_\theta} \sim \Pi_N^{1/3}. \tag{50}$$

In summary, the small (or micro) scales of turbulence are also the fundamental scales characterizing the heat transfer in buoyancy driven flows. The apparent difference in these scales, as demonstrated by the thermal scales proposed in this section, comes from the fact that the turbulence scale given by Eq. (40) is in terms of the buoyant (production of) energy while the equivalent heat transfer scale given by Eq. (48) is in terms of buoyancy (force). The next section is devoted to a heat transfer model for buoyancy-driven flows to be based on the scale given by Eq. (49).

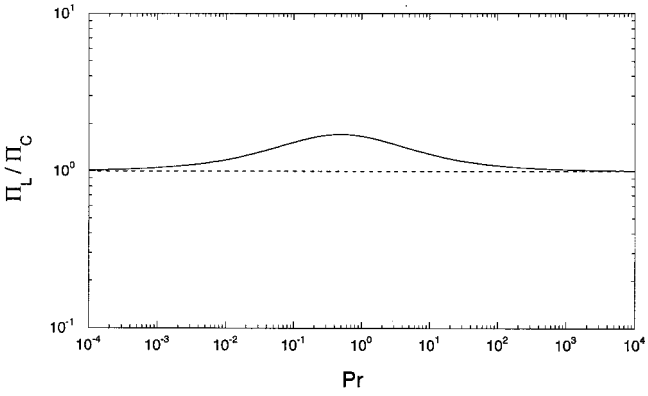

Fig. 1 The ratio of Π_L/Π_C in terms of Prandtl number

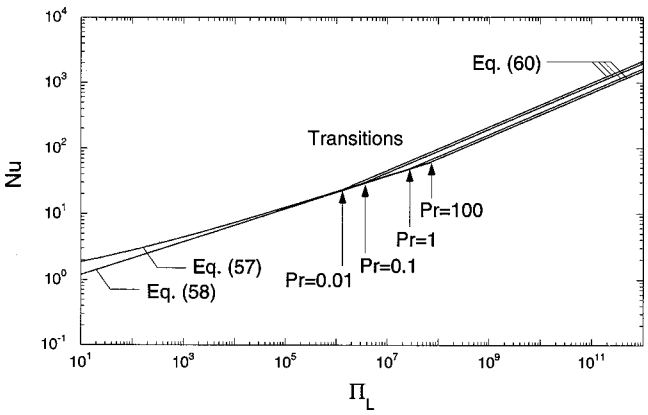

Fig. 2 Nusselt number in terms of Π_L

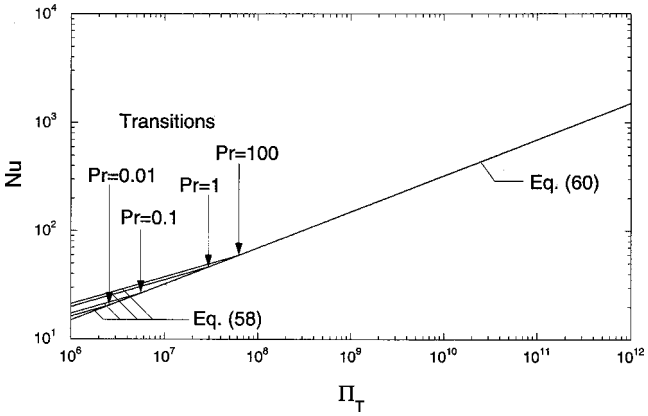

Fig. 3 Nusselt number in terms of Π_T

A Correlation

In terms of a mathematical curve best fitted to the extensive experimental data accumulated over a period of five decades on natural convection next to a vertical plate, Churchill and Chu [14] proposed the following correlation for the laminar regime of isothermal, vertical plates,

$$\mathrm{Nu} = 0.68 + \frac{0.670\mathrm{Ra}^{1/4}}{[1+(0.492/\mathrm{Pr})^{9/16}]^{4/9}}, \tag{51}$$

and one for both the laminar and turbulent regimes,

$$\mathrm{Nu}^{1/2}=0.825+\frac{0.387\mathrm{Ra}^{1/6}}{[1+(0.492/\mathrm{Pr})^{9/16}]^{8/27}}. \quad (52)$$

For both correlations, they empirically introduced a pseudo Π_C in the form of

$$\Pi_C^m=\frac{\mathrm{Ra}^m}{[1+(C/\mathrm{Pr})^s]^n}, \quad (53)$$

or

$$\Pi_C=\frac{\mathrm{Ra}}{[1+(C/\mathrm{Pr})^s]^{n/m}} \quad (54)$$

which, in terms of three exponents related by $m=n\times s$ to satisfy $\mathrm{Pr}\to 0$ limit, admittedly provides flexibility for a best mathematical fit to the experimental data. Note that

$$\lim_{\mathrm{Pr}\to 0}\Pi_C\to\Pi_N \quad \text{and} \quad \lim_{\mathrm{Pr}\to\infty}\Pi_C\to\Pi_N \quad (55)$$

and Π_C somewhat deviates from Π_N only in the interval $0.01<\mathrm{Pr}<100$ (Fig. 1). Furthermore, Π_C is not only empirical but also more complex in form than Π_N which is justified on physical grounds.

Following the dimensional arguments, a heat transfer correlation satisfying both $\mathrm{Pr}\to 0$ and $\mathrm{Pr}\to\infty$ limits (Le Fevre [15]) for laminar natural convection is shown, in terms of

$$\Pi_L=\frac{\mathrm{Ra}}{1+0.492\mathrm{Pr}^{-1}}, \quad (56)$$

to be

$$\mathrm{Nu}=0.68+0.670\Pi_L^{1/4}, \quad \Pi_L\leqslant 10^6, \quad (57)$$

and

$$\mathrm{Nu}=0.670\Pi_L^{1/4}, \quad 10^6\leqslant\Pi_L\leqslant 10^9, \quad (58)$$

and for turbulent convection is shown, in terms of

$$\Pi_T=\frac{\mathrm{Ra}}{1+0.164\mathrm{Pr}^{-1}}, \quad (59)$$

to be

$$\mathrm{Nu}=0.150\Pi_T^{1/3}, \quad 10^9\leqslant\Pi_T\leqslant 10^{12}, \quad (60)$$

satisfying $\mathrm{Pr}\to 0.024$ (McDonald and Connolly [16]) and $\mathrm{Pr}\to\infty$ (Churchill and Chu [14]). Eqs. (57), (58), and (60) are plotted in Figs. 2 and 3 in terms of Π_L and Π_T, respectively. As can be seen from these figures, transitions happen at different Π_N for different fluids. This feature can be clearly explained in terms of Π_L and Π_T, respectively, characterizing the laminar and turbulent flows.

References

[1] Arpacı, V. S., 1986, "Microscales of Turbulence and Heat Transfer Correlations," Int. J. Heat Mass Transf., **29**, pp. 1071–1078.
[2] Arpacı, V. S., 1990, "Microscales of Turbulence and Heat Transfer Correlations," Annu. Rev. Heat Transfer, **3**, pp. 195–231.
[3] Arpacı, V. S., 1995, "Buoyant Turbulent Flow Driven by Internal Energy Generation," Int. J. Heat Mass Transf., **38**, pp. 2761–2770.
[4] Squire, H. B., 1938, *Modern Developments in Fluid Dynamics*, S. Goldstein ed., Oxford University Press, Oxford.
[5] Catton, I., 1978, "Natural Convection in Enclosures," *6th Int. Heat Transfer Conf.*, Toronto, **6**, pp. 13–31.
[6] Bertin, H., and Ozoe, H., 1986, "Numerical Study of Two-dimensional Natural Convection in a Horizontal Fluid Layer Heated from Below, by Finite-Element Method: Influence of Prandtl Number," Int. J. Heat Mass Transf., **29**, pp. 439–449.
[7] Bejan, A., and Lage, J. L., 1990, "The Prandtl Number Effect on the Transition in Natural Convection along a Vertical Surface," ASME J. Heat Transfer, **112**, pp. 787–790.
[8] Vitharana, V. L., and Lykoudis, P. S., 1994, "Criteria for Predicting the Transition to Turbulence in Natural Convection along a Vertical Surface," ASME J. Heat Transfer, **116**, pp. 633–638.
[9] Arpacı, V. S., and Li, C. Y., 1995, "Turbulent Forced Diffusion Flames," Combust. Flame, **102**, pp. 170–178.
[10] Arpacı, V. S., and Selamet, A., 1991, "Microscales of Buoyancy Driven Turbulent Diffusion Flames," Combust. Flame, **86**, pp. 203–215.
[11] Arpacı, V. S., and Kao, S.-H., 1997, "Microscales of Turbulent Rotating Flows," Int. J. Heat Mass Transf., **40**, pp. 3819–3826.
[12] Arpacı, V. S., and Kao, S.-H., 1998, "Thermocapillary Driven Turbulent Heat Transfer" ASME J. Heat Transfer, **120**, pp. 214–219.
[13] Tennekes, H., and Lumley, J. L., 1972, *A First Course in Turbulence*, MIT Press, Cambridge, MA.
[14] Churchill, S. W., and Chu, H. H. S., 1975, "Correlating Equations for Laminar and Turbulent Free Convection from a Vertical Plate," Int. J. Heat Mass Transf., **18**, pp. 1323–1329.
[15] Le Fevre, E. J., 1956, "Laminar Free Convection from a Vertical Plane Surface," *Proc. 9th Int. Congress on Applied Mechanics*, Brussels, **4**, p. 168.
[16] McDonald, J. S., and Connolly, T. J., 1960, "Investigation of Natural Convection Heat Transfer in Liquid Sodium," Nucl. Sci. Eng., **8**, pp. 369–377.

Constructal Placement of High-Conductivity Inserts in a Slab: Optimal Design of "Roughness"

M. Neagu and A. Bejan
Department of Mechanical Engineering and Materials Science, Box 90300, Duke University, Durham, NC 27708-0300

This paper addresses the fundamental problem of how to facilitate the flow of heat across a conducting slab heated from one side. Available for distribution through the system is a small amount of high-conductivity material. The constructal method consists of optimizing geometrically the distribution of the high-conductivity material through the material of lower conductivity. Two-dimensional distributions (plate inserts) and three-dimensional distributions (pin inserts) are optimized based on the numerical simulation of heat conduction in a large number of possible configurations. Results are presented for the external and internal features of the optimized architectures: spacings between inserts, penetration distances, tapered inserts and constant-thickness inserts. The use of optimized pin inserts leads consistently to lower global thermal resistances than the use of plate inserts. The side of the slab that is connected to the high-conductivity intrusions is in effect a "rough" surface. This paper shows that the architecture of a rough surface can be optimized for minimum global contact resistance. Roughness can be designed.

[DOI: 10.1115/1.1392988]

Keywords: Contact Resistance, Heat Transfer, Interface, Packaging, Roughness, Constructal Design

1 Constructal Theory

Constructal theory draws attention to the possibility of explaining natural phenomena of "self-organization" on the basis of a principle of design optimization, subject to global constraints [1,2]. The initial presentation of the theory was made in terms of minimizing the resistance to heat conduction between a heat-generating volume and one point-size heat sink [3]. This fundamental problem was stimulated by electronics cooling applications at progressively smaller dimensions, where geometric optimization plays an increasingly important role [4–8]. In the volume-to-point heat flow problem, heat was generated uniformly throughout the volume. A small amount of high-conductivity ma-

Contributed by the Heat Transfer Division for publication in the JOURNAL OF HEAT TRANSFER. Manuscript received by the Heat Transfer Division November 22, 1999; revision received February 22, 2001. Associate Editor: S. Sadhal.

terial could be used in the form of thin inserts to collect the generated heat and to channel it with minimum resistance to the heat sink.

The optimization was geometric. It consisted of choosing the best thicknesses, shapes and positions for the high-conductivity inserts. This work was done at several volume scales, starting with the smallest (elemental volume) and proceeding toward larger scales (assemblies, constructs). At the end of this optimization procedure the inserts formed a tree network in which every single geometric feature was a result of the invoked design principle.

Subsequent extensions of constructal theory showed that tree networks also emerge after minimizing the resistance to fluid flow between a volume and point [1,2]. Analogous trees were derived for minimum travel time and minimum cost between an area and one point, offering in this way a theoretical basis for the occurrence of urban structure and economics and transportation networks. The implications of this principle to the physics of tree networks in physiology (e.g., lungs, vascularized tissues), geophysics (e.g., river basins, deltas, lightning), rapid solidification and social organization are summarized in a new book [1].

In this paper we return to the original engineering focus of the constructal method, which was the optimization of architecture. The engineering contribution of the method is to show that it is possible to arrive at the main features of the optimized architecture in a few steps of geometric optimization and organization (assembly, construction). Refinements of the optimized architecture can be pursued subsequently, for example, via numerical simulations of the flow in many configurations that differ only slightly from each other [9].

In the present paper we address a new fundamental problem of geometric optimization, which departs from the tree network problem in two significant respects. First, the given volume is heated on one of its surfaces, not volumetrically (e.g., Fig. 1). Second, the role of heat sink is played by an entire surface, not by a point-size heat sink. Once again, the challenge is to determine the optimal spatial distribution of the given high-conductivity material through the given volume.

With reference to Fig. 1, the objective is to minimize the global thermal resistance $(T_{\max}-T_0)/q''$, where $T_{\max}$ is the peak temperature (hot spot) that occurs along the top boundary heated by q''. The distribution of temperature on this boundary depends on the shape and distribution of the high-conductivity (k_p) inserts through the low-conductivity (k_0) medium. The resistance $(T_{\max}-T_0)/q''$ is *global* because it belongs to the entire construct: $T_{\max}$ depends on the architecture of the construct. The exact location of $T_{\max}$ is not the issue. The constraint is that the level $T_{\max}$ must not be exceeded by the temperature anywhere inside the system. Constraints of this kind rule the thermal design of electronic components and packages. The constraint analogous to $T_{\max}$ in the optimization of the architecture of mechanical supports is the maximum allowable stress [1]. *Global* objective functions are a characteristic of constructal design and optimization [1].

The global character of $T_{\max}$ and the associated thermal resistance is important especially on the background provided by the classical approach to the thermal resistance across irregular boundaries between two bodies (thermal contact resistance). The configuration of Fig. 1 may be viewed as the thermal contact between the body of conductivity k_0 and the irregular boundary formed by the T_0 base and the k_p-protuberances. The classical approach is to characterize the contact resistance in terms of the constant (temperature difference) by which the linear temperature distribution is displaced at distances (y) sufficiently far above the T_0 plane [10–12]. The linear temperature distribution drives the heat flux q''. This classical formulation has no place here, because the system is as large (L) as the protuberances. There is nothing above the $y=L$ plane. The temperature $T_{\max}$, which occurs in some places along $y=L$, is truly the highest temperature experienced by the system.

The T_0 base and the high-conductivity protrusions installed on it may be viewed as a ''rough'' surface. In this paper we show that the architecture of the rough surface can be optimized for minimum contact resistance. Roughness can be designed.

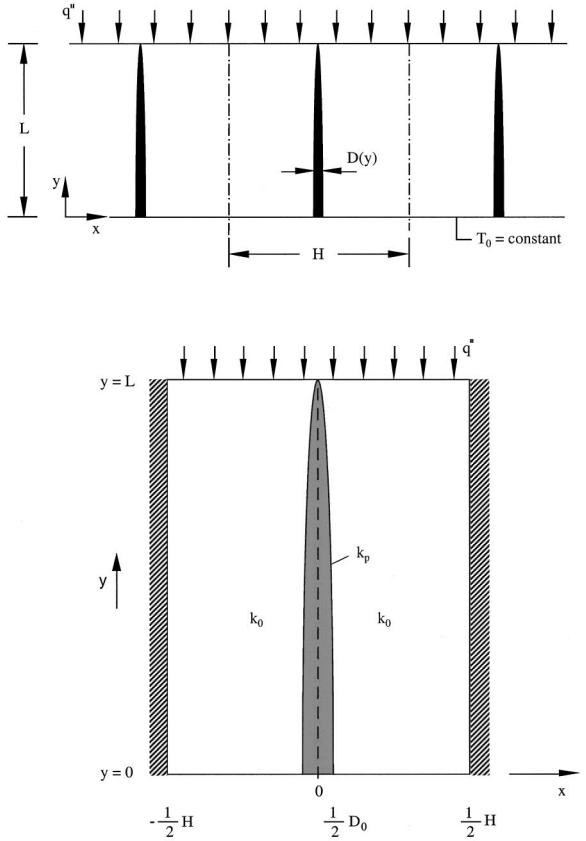

Fig. 1 Two-dimensional inserts of high conductivity for cooling a body heated from the side

2 Plate Inserts

Consider a two-dimensional body of thickness L and low thermal conductivity k_0. One side is heated with uniform heat flux (q''), and the other side is cooled isothermally to the temperature T_0. The reference design is the one where no high-conductivity inserts are used. In this case the isotherms are planes parallel to the two sides of the body, and the ''hot spot'' is the entire surface that receives the heat flux q''. The uniform temperature of the upper surface $(T_{\max})$ is related to the other parameters through the Fourier law,

$$T_{\max}=T_0+\frac{q''L}{k_0}. \tag{1}$$

When inserts of high-conductivity k_p are present, the conduction of heat is no longer unidirectional, and the hot spots are concentrated at discrete points on the upper (heated) surface. This situation is illustrated in Fig. 1, where the hot spots are the intersections of the planes of symmetry with the upper surface. In Fig. 1 the two-dimensional inserts are assumed to have the length L and the tapered profile

$$D(y)=c(L-y)^n. \tag{2}$$

The unspecified exponent n accounts for the variable shape of each insert. The leading factor c accounts for the specified volume fraction occupied by inserts. If H is the spacing between two inserts, the volume fraction of k_p material is given by

$$\phi=\frac{D_0}{H(n+1)}(\text{constant}), \tag{3}$$

where D_0 is the thickness of the insert in its base plane, $D_0 = cL^n = \phi(n+1)H$.

To calculate the hot-spot temperature T_{max}, we simulated numerically the steady-state conduction in the entire domain, and repeated the simulations for many different geometries. The lower part of Fig. 1 shows that the two-dimensional conduction domain is divided into two regions, according to the thermal conductivities k_0 and k_p. The conduction in the entire domain is ruled by the energy conservation equation

$$\frac{\partial^2 T}{\partial x^2} + \frac{\partial^2 T}{\partial y^2} = 0 \tag{4}$$

subject to the appropriate boundary conditions for the k_0 subdomain, namely, $T = T_0$ at $y = 0$, $\partial T/\partial y = -q''/k_0$ at $y = L$, $\partial T/\partial x = 0$ at $x = H/2$, and the boundary conditions for the k_p subdomain, namely, $\partial T/\partial y = -q''/k_p$ at $y = L$, and $\partial T/\partial x = 0$ at $x = 0$. Symmetry allows us to simulate heat conduction only in half of the domain allotted to a single insert, $0 \leqslant x \leqslant H/2$. The continuity of heat flux through the interface between the k_0 and k_p regions requires $k_p(\partial T/\partial m)_{x=(D/2)^-} = k_0(\partial T/\partial m)_{x=(D/2)^+}$, where m is the direction normal to the interface between the k_p and k_0 regions.

The nondimensional version of this problem statement is based on using L as length scale, and $q''L/k_0$ as temperature difference scale, cf. Eq. (1). The dimensionless variables are $(\tilde{x},\tilde{y},\tilde{H}) = (x,y,H)/L$ and $\tilde{T} = (T - T_0)/[(q''L)/k_0]$. The dimensionless counterparts of the boundary conditions are not shown. In particular, the continuity of flux at the $k_0 - k_p$ interface reveals $\tilde{k} = k_p/k_0$ as a dimensionless group that characterizes the combination of two conductive materials. The objective of the numerical work is to calculate the hot spot temperature,

$$\tilde{T}_{max} = \frac{T_{max} - T_0}{q''L/k_0} \tag{5}$$

and to minimize it. The value $\tilde{T}_{max} = 1$ corresponds to the reference case where the inserts are absent, Eq. (1). The inserts and their optimal placement will bring the value of $\tilde{T}_{max}$ below 1.

The conduction problem defined in the lower part of Fig. 1 was solved using a finite elements package [13]. We made this choice because we needed a reliable and flexible solver capable of rapid simulations in many different geometric configurations. The code used quadrilateral elements with 9 nodes, and boundary elements with 3 nodes. The solver used the Newton-Raphson iterative method and a grid with 200 nodes in each direction $(\tilde{x},\tilde{y})$. The grid was nonuniform and curvilinear, and was fitted smoothly to the boundary of the high-conductivity insert. The convergence criteria were $\|(\tilde{T}_i - \tilde{T}_{i-1})/\tilde{T}_i\| \leqslant 10^{-6}$ and $\|R_1\| \leqslant 10^{-3}$, where i, R, and $\|\cdot\|$ are the iteration number, residual vector and Euclidean norm.

The first geometric feature investigated was the shape of each plate insert, which is described by exponent n, Eq. (2). We varied n in a wide range of insert profiles, from shapes with rounded tips $(n < 1)$ to shapes with sharp tips $(n > 1)$ [14]. We found that designs with rounded tips are better, and that $\tilde{T}_{max}$ reaches its lowest value in the limit $n \to 0$. This limit represents the plate profile with constant thickness.

This is why in the remainder of the work on two-dimensional inserts we set D = constant. Figure 2 shows this choice, and a new feature in the design: the constant-thickness inserts penetrate the body only partially. Their relative length P/L, or slenderness ratio D/P, is an additional degree of freedom in the design. The other degree of freedom is the relative spacing $\tilde{H} = H/L$. The volume fraction of high-conductivity material continues to be a constraint, $\phi = DP/(HL)$.

We found numerically [14] that the global resistance can be minimized with respect to the spacing $\tilde{H}$, or the density of plate inserts, when the materials $(\tilde{k},\phi)$ and the plate slenderness ratio (D/P) are fixed. When the distribution is sparse $(\tilde{H} \gg 1)$ the resistance $\tilde{T}_{max}$ approaches 1, in accordance with Eqs. (1) and (5). The optimization was repeated for many combinations of $\tilde{k}$, ϕ, and D/P, and for each combination we located the resistance minimum, i.e., $\tilde{H}_{opt}$ and $\tilde{T}_{max,min}$.

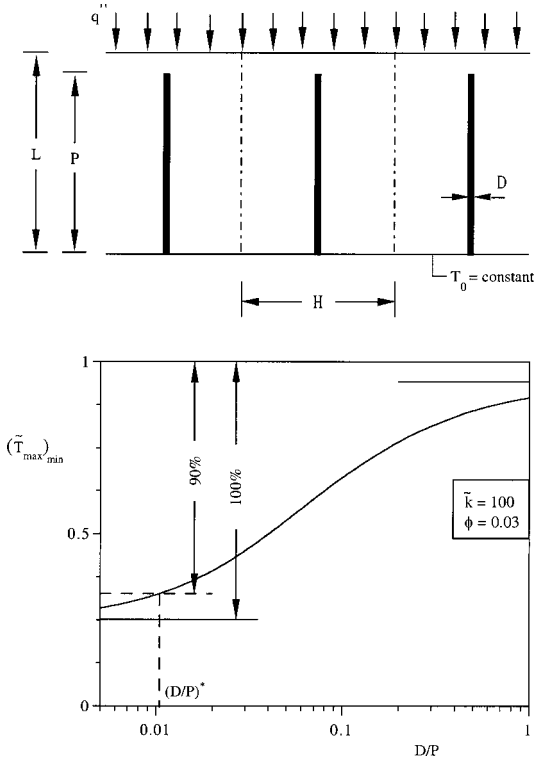

Fig. 2 Constant-thickness plate inserts that penetrate partially the heated body, and the smallest dimensions cutoff: the minimized global resistance can be reduced by making the plate inserts sufficiently slender.

The second step of the geometric optimization is presented in the lower part of Fig. 2. The global resistance minimized with respect to the spacing is now plotted versus the second free parameter, D/P. The resistance does not exhibit a minimum with respect to D/P. Instead, it decreases as the plate profile becomes more slender, and in the limit $D/P \to 0$ it reaches its lowest value. This limiting $\tilde{T}_{max,min}$ value corresponds to the effective resistance of a "laminated" composite in which very thin k_0 plates alternate with even thinner k_p plates, and where the heat transfer is unidirectional (along the plates). It can be shown that the effective resistance in this limit is $\tilde{T}^* = [1 + \phi(\tilde{k} - 1)]^{-1}$. The opposite limit corresponds to wide high-conductivity plates $(D \gg P)$ attached to the cold surface (T_0). The effective resistance of this composite is comparable to that of a two-layer sandwich (k_0, k_p) oriented perpendicularly to the heat current.

Of practical interest is the $D/P \ll 1$ range, where the minimized resistance can be decreased further by making inserts and interstices of progressively smaller dimensions. Diminishing returns are reached in this direction, and this brings up the engineering design question: What small dimensions are small enough? A similar "cutoff" question established the smallest scale (elemental volume) in the earlier work on heat networks [1–3].

In Fig. 2 we see that the minimized resistance is within 10 percent of the lowest possible value when the slenderness ratio has the value $(D/P)^*$. This ratio and the corresponding optimized ratios $(P/L)^*$ and $(H/L)^*_{opt}$ [or $\tilde{H}^*_{opt}$] are reported in Fig. 3 as functions of the composite material parameters ϕ and $\tilde{k}$. These calculations show that the plate inserts must be more slender as the volume fraction ϕ decreases, and as the conductivity of the

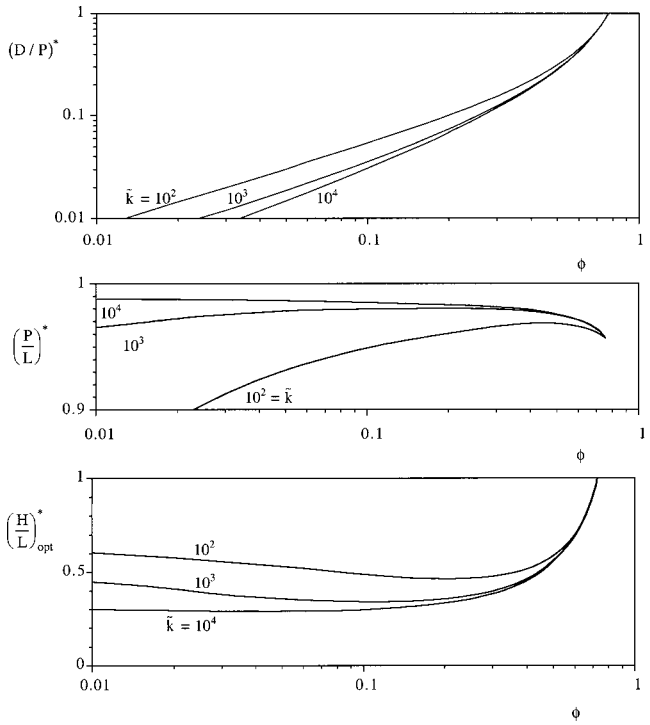

Fig. 3 Top: The smallest robustness ratio for plate inserts. Middle: The relative penetration length of plate inserts. Bottom: The relative spacing between plate inserts.

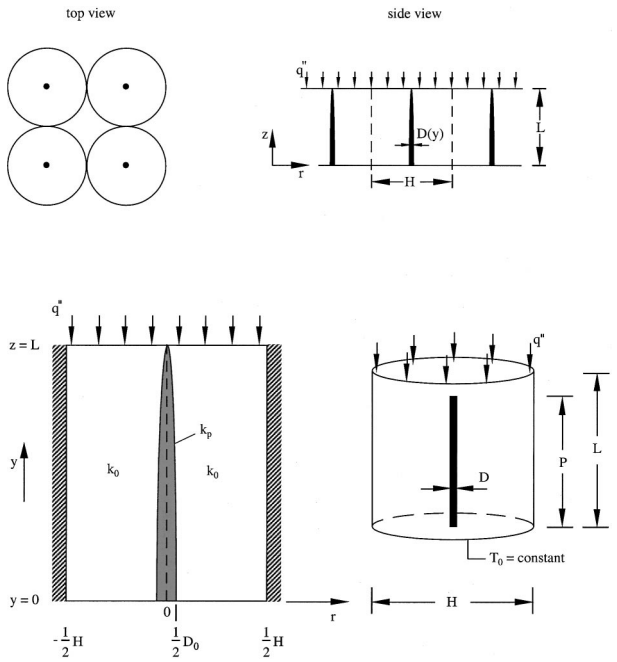

Fig. 4 Cylindrical model for the three-dimensional conduction around pin-shaped inserts of high thermal conductivity.

insert increases. The penetration depth of each insert increases as $\tilde{k}$ increases. The spacings decrease as $\tilde{k}$ increases, however, the effect of the volume fraction ϕ is considerably weaker.

3 Pin Inserts

A general trend in the geometric optimization of paths for heat and other flows is that the global resistance decreases when the high-conductivity channels are distributed "more uniformly" through the given volume. When this is done, the complexity of the structure constituted by these channels increases. We pursued this direction in the present study, and, instead of the two-dimensional flow pattern of Fig. 1, we considered the three-dimensional configuration shown in Fig. 4. The temperature field is three-dimensional because the inserts of high-conductivity material are shaped as pins. The other features of the conductive composite $(q'', T_0, k_0, k_p, L, \phi)$ are the same as in the system studied until now.

It is easier to study numerically a single insert than an entire population of inserts. This is why we adopted the simplifying model shown in the lower-left part of Fig. 4. If the spacing between adjacent inserts is H, and if the inserts are arranged in a regular array (squares, equilateral triangles), then the temperature field around a single insert is approximated adequately by the field calculated inside a cylinder of diameter H, with the insert on its axis. The cylindrical surface is adiabatic. In the array with many inserts the hot spots are expected to occur in the $y=L$ plane in the small "islands" located the farthest from the inserts. In the single cylinder model the hot-spot temperature is approximated by the temperature of the rim of diameter H situated in the $y=L$ plane.

The numerical work proceeded in the same steps as in Section 2, therefore in this section we highlight only the results and the features that are due specifically to the three-dimensionality of the flow [14]. First, we examined the effect of the pin profile, which is controlled by the exponent n in the power-law shape, Eq. (2). The volume fraction occupied by k_p material is fixed,

$$\phi = \frac{D_0^2}{H^2(2n+1)} \tag{6}$$

and controls the size of the base diameter of the pin, $D_0 = cL^n = H[\phi(2n+1)]^{1/2}$. The computational domain was divided into two regions according to the presence of the k_0 and k_p materials. The equation for steady state conduction

$$\frac{\partial^2 T}{\partial r^2} + \frac{1}{r}\frac{\partial T}{\partial r} + \frac{\partial^2 T}{\partial y^2} = 0 \tag{7}$$

was subjected to the boundary conditions for the k_0 region, namely, $T=T_0$ at $y=0$, and $\partial T/\partial y = -q''/k_0$ at $y=L$, and $\partial T/\partial r = 0$ at $r=H/2$, and the conditions around the k_p region, namely, $T=T_0$ at $y=0$, $\partial T/\partial y = -q''/k_p$ at $y=L$, and $\partial T/\partial r = 0$ at $r=0$. The condition for the continuity of heat flux at the $r=D(z)/2$ interface between the two regions reveals again the dimensionless parameter $\tilde{k} = k_p/k_0$. The dimensionless formulation of the three-dimensional conduction problem was based on the variables defined above Eq. (5). The grid, numerical method and convergence criteria were the same as in the preceding section.

The effect of the pin shape (n) is documented by Neagu [14]. The limit $n \ll 1$ is beneficial from the point of view of minimizing the global resistance. The rest of the numerical work was devoted to pins of constant diameter (D) and partial penetration distance (P), as shown in the lower-right part of Fig. 4. In this geometry the k_p-volume fraction is $\phi = D^2P/(H^2L)$. The geometry of the elemental cylinder model has two degrees of freedom, the external aspect ratio $\tilde{H} = H/L$, and the internal ratio D/P, or P/L. The global resistance has a minimum with respect to $\tilde{H}$, as shown by Neagu [14]. This minimum $(\tilde{H}_{\text{opt}}, \tilde{T}_{\text{max,min}})$ was identified and stored in all subsequent calculations.

The effect of the internal ratio D/P on $\tilde{T}_{\text{max,min}}$ is qualitatively the same as in Fig. 2. For each case we constructed the equivalent of Fig. 2, and based on convention we chose $(D/P)^*$ and $\tilde{T}^*$ as the point where $\tilde{T}_{\text{max,min}}$ is within 10 percent of its lowest value. The remaining graphs of Fig. 5 report as functions of $\tilde{k}$ and ϕ the geometrical features that allows the design to reach this level of performance. The robustness ratio $(D/P)^*$ decreases almost pro-

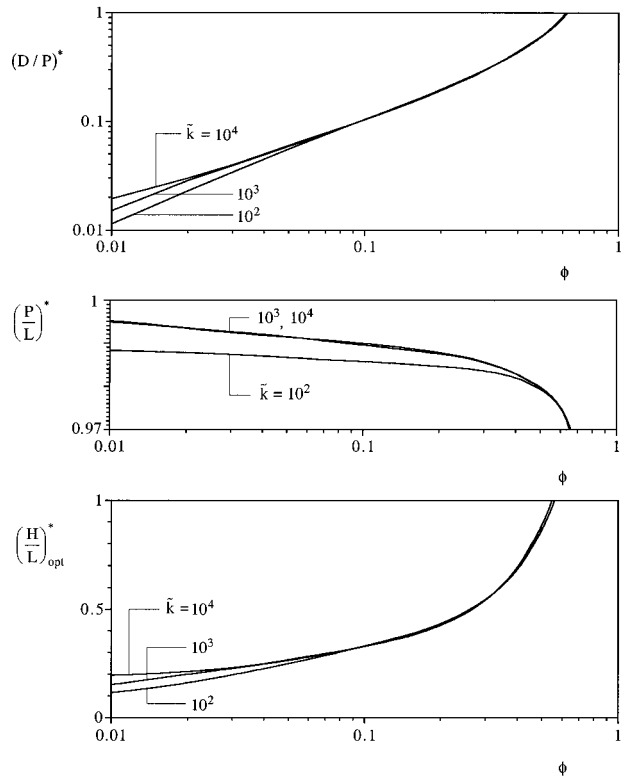

Fig. 5 Top: The smallest robustness ratio for pin inserts. Middle: The relative penetration length of pin inserts. Bottom: The minimized global thermal resistance of systems with optimized plates and pins inserts, using the same amounts and types of conducting materials $(\tilde{k}, \phi)$.

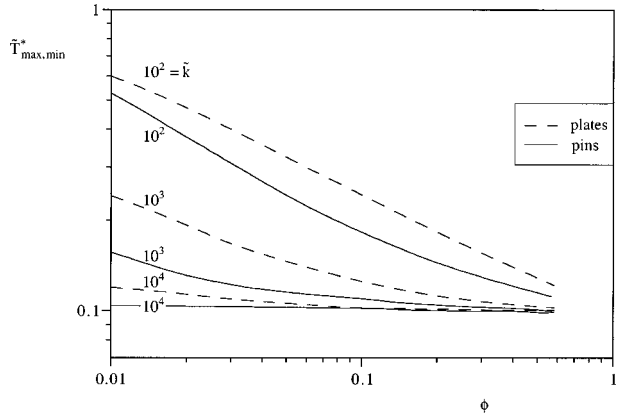

Fig. 6 The minimized global thermal resistance of systems with optimized plates and pins inserts, using the same amounts and types of conducting materials $(\tilde{k}, \phi)$

portionally with ϕ. Remarkable is that the effect of $\tilde{k}$ is insignificant, unlike in the corresponding set of results for plate inserts. Comparing Figs. 3 and 5 we see that pin inserts have considerably larger $(D/P)^*$ ratios than plate inserts for the same composite material $(\tilde{k}, \phi)$.

An alternate presentation of the internal aspect ratio is the relative penetration distance shown in Fig. 5 (middle). This can be compared with the earlier chart for plate inserts (Fig. 3) to see that the penetration length of pin inserts is larger than for plate inserts. When ϕ is of order 1 or smaller, the $(P/L)^*$ ratio of pin inserts is nearly equal to 1, meaning that the inserts extend almost completely across the system.

The external aspect ratio $\tilde{H}^*_{\text{opt}}$ [or $(H/L)^*_{\text{opt}}$] that corresponds to the 10-percent cutoff design of Fig. 5 (top) is reported in Fig. 5 (bottom). Once again, the effect of the conductivity ratio is insignificant. The slenderness ratio $(H/L)^*_{\text{opt}}$ is proportional to roughly $\phi^{0.7}$ when ϕ becomes sufficiently small. Comparing Figs. 5 (bottom) and 3 (bottom) we see that the optimal distance between pin inserts is three or four times smaller than for plate inserts.

4 Conclusions

The main conclusion of this work is that it is possible to distribute optimally in space a finite amount of high conductivity material, for the purpose of facilitating the flow of heat across a conducting body heated from the side (Figs. 1 and 4). The optimization is geometric and involves external and internal features: spacings between inserts, penetration distances, two-dimensional and three-dimensional arrangements, and shapes of inserts (constant thickness or tapered). This conclusion reinforces the main point of the constructal method of optimizing the access to flow subject to global and local constraints: the optimization can be pursued geometrically, in space. The very architecture of the system—its geometric form (shapes, structure)—is the visualization of the optimization principle.

Simple optimization results of the type developed in this paper can provide orientation to the designer, at an early stage. For example, the choice between two-dimensional and three-dimensional inserts for the same amount of high-conductivity material can be made on the basis of which geometry yields the largest reduction in global thermal resistance. The unavoidable tradeoff between further reductions and increasing manufacturing difficulties must also be considered. In the present case, the use of optimized pin inserts leads to consistently smaller global resistances, as shown by the plates vs. pins comparison presented in Fig. 6.

Acknowledgment

This work was supported by a grant from the National Science Foundation.

Nomenclature

c = factor
D = insert thickness, m
D_0 = thickness at the base of the insert, m
H = spacing between inserts, m
k_0 = low thermal conductivity, $\mathrm{W\,m^{-1}\,K^{-1}}$
k_p = high thermal conductivity, $\mathrm{W\,m^{-1}\,K^{-1}}$
k = conductivity ratio, k_p/k_0
L = thickness of conducting system, m
n = exponent
P = insert penetration length, m
q'' = imposed heat flux, $\mathrm{W\,m^{-2}\,K^{-1}}$
r = radial position, m
T = temperature, K
$T_{\max}$ = hot-spot temperature, K
T_0 = lowest temperature, K
x = transversal position, m
y = longitudinal insert position, m
z = longitudinal insert position, m

Greek Symbol

ϕ = volume fraction of high-conductivity material

Superscripts

$(\sim)$ = dimensionless notation, Eqs. (11, 12)
$(\ )^*$ = dimension at the cutoff, Figs. 5 and 12

Subscripts

max = maximum
min = minimum
opt = optimum

References

[1] Bejan, A., 2000, *Shape and Structure, from Engineering to Nature*, Cambridge University Press, Cambridge, UK.
[2] Bejan, A., 1997, *Advanced Engineering Thermodynamics*, 2nd ed. chap. 13, John Wiley and Sons, New York.
[3] Bejan, A., 1997, "Constructal-Theory Network of Conducting Paths for Cooling a Heat Generating Volume," Int. J. Heat Mass Transf., **40**, pp. 799–816.
[4] Bar-Cohen, A., and Rohsenow, W. M., 1984, "Thermally Optimum Spacing of Vertical, Natural Convection Cooled, Parallel Plates," ASME J. Heat Transfer, **106**, pp. 116–123.
[5] Peterson, G. P., and Ortega, A., 1990, "Thermal Control of Electronic Equipment and Devices," Adv. Heat Transfer, **20**, pp. 181–314.
[6] Knight, R. W., Goodling, J. S., and Hall, D. J., 1991, "Optimal Thermal Design of Forced Convection Heat Sinks—Analytical," ASME J. Electron. Packag., **113**, pp. 313–321.
[7] Anand, N. K., Kim, S. H., and Fletcher, L. S., 1992, "The Effect of Plate Spacing on Free Convection Between Heated Parallel Plates," ASME J. Heat Transfer, **114**, pp. 515–518.
[8] Kakac, S., Yüncü, H., and Hijikata, K., eds., 1994, *Cooling of Electronic Systems*, Kluwer, Dordrecht, The Netherlands.
[9] Ledezma, G. A., Bejan, A., and Errera, M. R., 1997, "Constructal Tree Networks for Heat Transfer," J. Appl. Phys., **82**, pp. 89–100.
[10] Pozrikidis, C., 1993, "Unsteady Viscous Flow Over Irregular Boundaries," J. Fluid Mech., **255**, pp. 11–34.
[11] Brady, M., and Pozrikidis, C., 1993, "Diffusive Transport Across Irregular and Fractal Walls," Proc. R. Soc. London, Ser. A, **442**, pp. 571–583.
[12] Fyrillas, M. M., and Pozrikidis, C., 2001, "Conductive Heat Transport Across Rough Surfaces and Interfaces between Two Conforming Media," Int. J. Heat Mass Transf., **44**, 1789–1801.
[13] FIDAP, *Theory Manual*, 1993, v. 7, Fluid Dynamics International, Evanston, IL.
[14] Neagu, M., 1999, "Characteristics and Optimization of Composite Systems with Heat Conduction," Ph.D. thesis, Duke University, Durham, NC.

Some Algebraically Explicit Analytical Solutions of Unsteady Nonlinear Heat Conduction

Ruixian Cai
e-mail: crx@mail.etp.ac.cn

Na Zhang
Associate Professor

Institute of Engineering Thermophysics, Chinese Academy of Sciences, P.O. Box 2706, Beijing 100080, China

The analytical solutions of nonlinear unsteady heat conduction equation are meaningful in theory. In addition, they are very useful to the computational heat conduction to check the numerical solutions and to develop numerical schemes, grid generation methods and so forth. However, very few explicit analytical solutions have been known for the unsteady nonlinear heat conduction. In order to develop the heat conduction theory, some algebraically explicit analytical solutions of nonlinear heat conduction equation have been derived in this paper, which include one-dimensional and two-dimensional unsteady heat conduction solutions with thermal conductivity, density and specific heat being functions of temperature. [DOI: 10.1115/1.1392990]

Keywords: Analytical, Conduction, Heat Transfer, Unsteady

Contributed by the Heat Transfer Division for publication in the JOURNAL OF HEAT TRANSFER. Manuscript received by the Heat Transfer Division May 17, 2000; revision received March 5, 2001. Associate Editor: C. Beckermann.

1 Introduction

Analytical solutions of constant coefficient heat conduction equations played a key role in the early development of heat conduction. However, when thermal conductivity, density and specific heat are taken into account as functions of temperature, the governing equations are nonlinear. It is difficult to find analytical solutions to such problems. The common Kirchhoff's transformation [1] is unable to completely simplify the unsteady nonlinear equations with thermal diffusivity being function of temperature as mentioned by Özisik [2]. According to the knowledge of the authors, perhaps no algebraically explicit analytical solutions of unsteady nonlinear heat conduction have been found in the open literature so far. From the viewpoint of theoretical study on unsteady heat conduction, it is valuable to find out some analytical solutions. For the same reason, the first author [3] recently provided some algebraically explicit analytical solutions of unsteady nonlinear compressible flow to develop aerodynamics.

Besides theoretical meaning, analytical solutions can also be applied to check the accuracy, convergence and effectiveness of various numerical computation methods and their differencing schemes, grid generation ways and so on. The analytical solutions are therefore very useful even for the computational heat conduction. For example, in the fluid dynamics field, several analytical solutions which can simulate the three-dimensional potential flow in turbomachine cascades were given by the first author Cai et al. [4]; these solutions have been used successfully by scientists to check their computational methods and computer codes (Cai et al. [4], Zhu and Liu [5], Xu et al. [6], Gong and Cai [7], Shen et al. [8]).

Several algebraically explicit analytical solutions of unsteady nonlinear heat conduction are derived in this paper to develop the theory of unsteady heat conduction and to serve as the benchmark solutions for numerical calculations.

It is emphasized that the main aim of this paper is to obtain some possible explicit solutions of the governing equation, the initial and boundary conditions are indeterminate before derivation and deduced from the solutions afterward. It makes the derivation procedure easier. In order to be able to derive explicit analytical solutions, another important point is that the function of the thermal conductivity and the function of the density and specific heat have to be matchable in some degree. Actually, the derivation procedure is not a general or classically mathematical one; basically it is a trial and error method with the help of inspiration, experience and fortune. Moreover, in some cases a skill is applied to solve the unsteady nonlinear equations: it is assumed that the unknown solutions $\theta(t,x,y)=T(t)+X(x)+Y(y)$.

2 Analytical Solutions of Geometrically One-Dimensional Unsteady Nonlinear Heat Conduction

The governing equation for one-dimensional unsteady heat conduction with variable coefficients is commonly given as follows:

$$\rho C_p \frac{\partial \theta}{\partial t} = \frac{\partial}{\partial x}\left(K \frac{\partial \theta}{\partial x} \right). \tag{0}$$

Generally, K, ρ, and C_p are not constant but positive.

Three solutions have been found as follows:

$$\left.\begin{array}{c} K=ke^{l\theta}, \quad \rho C_p = \text{Const.} = m \\ \theta = \ln\{C_1 m (x+C_3)^2/[2k(C_2-C_1 t)]\}/l \end{array}\right\}. \tag{1}$$

If C_1 and C_2 are positive, the permissible time value of this solution is $t<C_2/C_1$, otherwise Eq. (1) is not effective. The initial and boundary conditions can be obtained with Eq. (1) as follows: When $t=0$, $\theta=\ln[C_1 m(x+C_3)^2/(2C_2 k)]/l$; when $x=0$, $\theta=\ln\{C_1 C_3^2 m/[2k(C_2-C_1 t)]\}/l$; and when $x=1$, $\theta=\ln\{C_1 m(1+C_3)^2/[2k(C_2-C_1 t)]\}/l$.

The initial and boundary conditions of the following solutions can be derived in the same way. For a given analytical solution, its

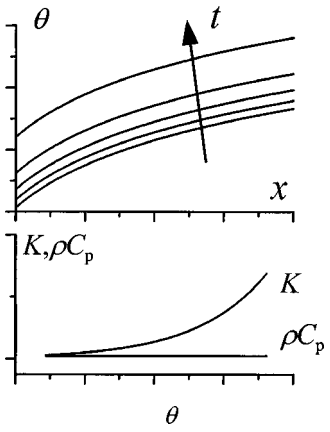

Fig. 1 The typical diagram of Eq. (1)

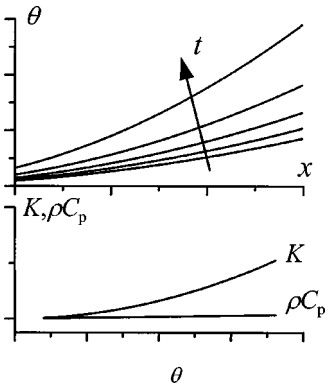

Fig. 2 The typical diagram of Eq. (2)

correctness can be easily proven by substituting it into the governing equation. It is the same for the following solutions.

The parameter variations of Eq. (1) are shown in Fig. 1.

Usually, the variation of thermal conductivity is unlikely large, then l in Eq. (1) is commonly a low number.

$$\left.\begin{array}{c} K=k\theta^{l}, \quad \rho C_p=m\theta^{n} \\ \theta=\left[\dfrac{C_1 m(n-l)(x+C_3)^2}{2k(2+n+l)(C_1 t-C_2)}\right]^{1/(l-n)} \end{array}\right\} \tag{2}$$

Commonly, $t<C_2/C_1$ is necessary except when $1/(l-n)$ is a positive even round number; l and n in Eq. (2) are low numbers.

The parameter variations of Eq. (2) are shown in Fig. 2.

$$\left.\begin{array}{c} K=ke^{l\theta}, \quad \rho=me^{j\theta}, \quad C_p=ne^{p\theta} \\ \theta=\ln\{2k(p+j+l)(t+C_2)/[(p+j-l)mn(x+C_3)^2]\}/ \\ (p+j-l) \end{array}\right\} \tag{3}$$

It is not a complicated solution even all the coefficients in the governing equation—K, ρ, and C_p—are functions of θ.

By the way, solution (1) is actually a special case of solution (3) with $p+j=0$ and $n=1$.

In addition, there are some other one-dimensional solutions which are special cases of the following two-dimensional solutions.

3 Analytical Solutions of Geometrically Two-Dimensional Unsteady Nonlinear Heat Conduction

The governing equation for two-dimensional unsteady heat conduction with variable coefficients is commonly given as follows:

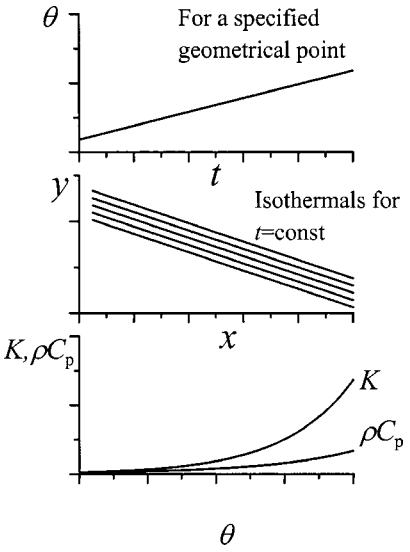

Fig. 3 The typical diagram of Eq. (4)

$$\rho C_p \frac{\partial\theta}{\partial t}=\frac{\partial}{\partial x}\left(K\frac{\partial\theta}{\partial x}\right)+\frac{\partial}{\partial y}\left(K\frac{\partial\theta}{\partial y}\right). \tag{0a}$$

Similar to Eq. (0), K, ρ, and C_p are not constant but positive.

Some algebraically explicit analytical solutions with variable K, ρ, and C_p are derived with the hint of Kirchhoff's transformation as follows:

$$\left.\begin{array}{c} K=ke^{l\theta}, \quad \rho C_p=me^{l\theta} \\ \theta=C_1 kt/m\pm(C_3/l)^{1/2}x\pm[(C_1-C_3)/l]^{1/2}y+C_2 \end{array}\right\}, \tag{4}$$

where the constants C_3/l and $[(C_1-C_3)/l]$ must be positive.

It is worth noticing that the solution is very simple—temperature is linear function of both time and geometric coordinates, although the governing equation is highly nonlinear.

The parameter variations of Eq. (4) are shown in Fig. 3.

When $C_3=C_1$, this solution degenerates into one-dimensional solution:

$$\theta=C_1 kt/m\pm\sqrt{C_1/l}\cdot x+C_2 \tag{4a}$$

The parameter variations of Eq. (4*a*) are shown in Fig. 4.

Another possible solution with $K=ke^{l\theta}$, $\rho C_p=me^{l\theta}$ can be deduced as follows:

$$\begin{aligned}\theta=C_1 kt/m&+\ln\{\cosh[\pm\sqrt{C_3 l}(x+C_2)]\}/l \\ &+\ln\{\cosh[\pm\sqrt{(C_1-C_3)l}(y+C_4)]\}/l+C_5.\end{aligned} \tag{5}$$

When $C_3=C_1$, this solution degenerates into one-dimensional solution too.

$$K=k\theta^l,\quad \rho=m\theta^l,\quad l\neq -1$$
$$\theta=\exp\left\{\frac{C_1t+C_2}{m}+\left[\frac{C_1-C_3k}{k(1+l)}\right]^{1/2}(x+C_4)+\left(\frac{C_3}{1+l}\right)^{1/2}(y+C_5)\right\}+C_6 \tag{6}$$

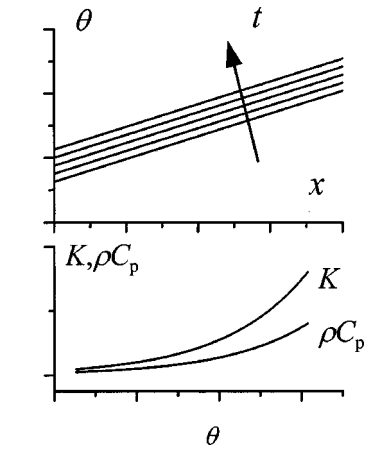

Fig. 4 The typical diagram of Eq. (4*a*)

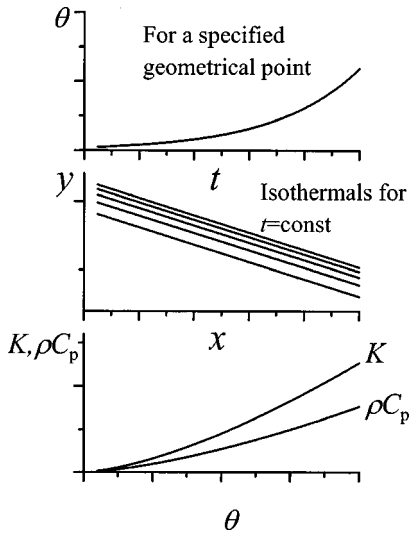

Fig. 5 The typical diagram of Eq. (6)

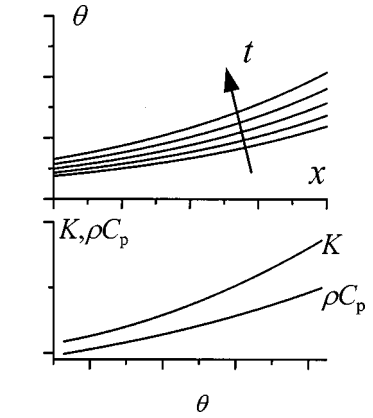

Fig. 6 The typical diagram of Eq. (6*a*)

In Eq. (6), $(C_1-C_3k)/[k(1+l)]$ and $C_3/(1+l)$ have to be positive. The parameter variations of Eq. (6) are shown in Fig. 5.

When $C_3=0$, this solution degenerates into one-dimensional solution:

$$\theta=\exp\left\{\frac{C_1t+C_2}{m}+\left[\frac{C_1}{k(1+l)}\right]^{1/2}(x+C_4)\right\}+C_6 \tag{6a}$$

The parameter variations of Eq. (6*a*) are illustrated in Fig. 6.

Although Eq. (0*a*) is a mathematical three-dimensional equation with three independent variables *t*, *x*, and *y*, but solutions (4), (5), and (6) are quite simple. Hence, they are appropriate to be basic analytical solutions for theory and benchmark solutions for computational heat conduction.

4 Summary

Some algebraically explicit analytical solutions of nonlinear unsteady heat conduction equation have been derived. According to the knowledge of the authors, no such algebraically explicit analytical solutions of nonlinear heat conduction have been published in the open literature. The abovementioned solutions will be valuable to the theory of unsteady heat conduction, especially to the computational heat transfer as the benchmark solutions to check the numerical solutions and to develop the numerical computation approaches such as the differencing schemes, grid generation methods and so forth.

The analytical solutions given in this paper are based on rectangular coordinates, the derivation based on other coordinates will be given in a forthcoming paper.

Acknowledgment

The study is supported by the National Science Foundation of China (59846006, 59925615) and NKBRSF Project of China (G2000026305).

Nomenclature

C_i = different constants
C_p = specific heat
j,k,l,m,n,p = different constants
K = thermal conductivity
t = time
u = specific internal energy
x,y = geometric coordinates
θ = temperature
ρ = density

References

[1] Kirchhoff, G., 1894, *Vorlesungen über die Theorie der Warme*, Barth, Leipzig.
[2] Özisik, M. N., 1980, *Heat Conduction*, International Textbook Co., Scranton, Pa.
[3] Cai, R., 1998, "Some Analytical Solutions of Unsteady Compressible Flow," ASME J. Fluids Eng., **120**, pp. 760–764.
[4] Cai, R., Jiang, H., and Sun, C., 1984, "Some Analytical Solutions Applicable to Verify Three-Dimensional Numerical Methods in Turbomachines," *MechE Conf. Publications C80/84*, pp. 255–263.
[5] Zhu, S., and Liu, Z., 1988, "An Investigation of Numerical Method of Three-Dimensional Flow Field in the Blade Passage of Centrifugal Pump (Compared with Analytical Solution)," Journal of Engg. Thermophysics, **9**, pp. 242–244 (in Chinese).
[6] Xu, J., Shi, J., and Ni, W., 1989, "Three Dimensional Imcompressible Flow Solution of an Axial Compressor Using Pseudostream-Functions Formulation," ASME Paper 89-GT-319.
[7] Gong, Y., and Cai, R., 1989, "3D MSLM—A new Engineering Approach to the Inverse Problem of 3D Cascade," ASME Paper 89-GT-48.
[8] Shen, M., Liu, Q., and Zhang, Z., 1996, "Calculating Three-Dimensional Transonic Flow of Turbomachine in the Generalized von Mises Coordinates," Scientia in China (Series E), **29**, pp. 325–332 (in Chinese).

Journal of Heat Transfer

Discussion

Discussion: "Fin (On a Pipe) Effectiveness: One-Dimensional and Two-Dimensional" (Look, Jr., D. C., 1999, ASME J. of Heat Transfer, 121, No. 1, pp. 227–230)

P. Razelos[1]
2 Kanigos St. Athens 10677, Greece

The author in his Introduction gives the reasons why one should consider the two-dimensional analysis and non-insulated tip. Briefly, he states the "*mathematics in the one-dimensional solution are not difficult, because of large heat transfer coefficients, the tip should no be considered insulated, and the two-dimensional solution is more difficult.*" However, the following discussion will show that the above are rather superficial statements without any scientific basis. The dimensionless variables employed by the author are not appropriate, this leads to *n* confusing results.

Given the fin geometry r_1, r_2, and L, the parameters k,h,h_e, and the temperatures T_w, T_∞, these quantities should be combined to form the dimensionless parameters that characterize the heat transfer process. In the heat transfer literature these non-dimensional parameters are

$$\text{the ratio } \beta=\frac{r_2}{r_2} \tag{1a}$$

$$\text{the } \frac{\text{conductiom}}{\text{convection}} \text{ coefficient } u^2=\frac{(r_2-r_1)^2h}{kL}=\frac{(\beta-1)^2hr_1^2}{kL}=(\beta-1)^2w^2 \tag{1b}$$

$$\text{the parameter}\left(\frac{h_e}{h}\right)\frac{hr_1}{k}=\left(\frac{h_e}{h}\right)B_r \tag{1c}$$

The parameters w^2 and B_r are usually called the surface *conduction/convection* coefficient and *surface Biot number*, respectively. B_r enters the solution through the boundary condition, author's equation, (2), which is written as

$$\xi=\beta,\ \frac{d\theta}{d\xi}+(h_e/h)B_r=0. \tag{2}$$

Similarly, in the two-dimensional solution B_r is introduced via the author's Eqs. (7*a*) and (7*b*). Using the above non-dimensional parameters the fin dimensionless temperature is

$$\theta=\theta(u,\beta,\xi,(h_e/h)B_r)=\theta(w,\beta,\xi,(h_e/h)B_r) \quad \text{one-dimensional solution} \tag{2a}$$

$$\theta=\theta(u,\beta,\xi,\nu,(h_e/h)B_r,B_r)=\theta(w,\beta,\xi,\nu,(h_e/h)B_r,B_r) \quad \text{two-dimensional solution} \tag{2b}$$

The heat dissipated by the fin is

$$Q_{\text{fin}}=Q_{\text{fin}}(u,\beta,(h_e/h)B_r)=Q_{\text{fin}}(w,\beta,(h_e/h)B_r) \quad \text{one-dimensional} \tag{3a}$$

$$Q_{\text{fin}}=Q_{\text{fin}}(u,\beta,(h_e/h)B_r,B_r)=Q_{\text{fin}}(w,\beta,(h_e/h)B_r,B_r) \quad \text{two-dimensional.} \tag{3b}$$

From the above equations one can readily derive the following fin efficiency and effectiveness:

$$\text{efficiency } \eta=\eta(u,\beta,(h_e/h)B_r)=\eta(w,\beta,(h_e/h)B_r) \tag{4}$$

$$\text{effectiveness } R=R(u,\beta,(h_e/h)B_r,B_r)=R(w,\beta,(h_e/h)B_r,Br). \tag{5}$$

Considering the tip to be insulated the above equations become

$$\eta=\eta(u,\beta) \tag{4a}$$

$$R=R(u,\beta,B_r). \tag{5a}$$

One can choose any set of parameters involving u or $w=u/(\beta-1)$, and B_r or $B_i^{1/2}=B_r/w=(\beta-1)B_r/u$. Gardner (author's reference) used Eq. (4*a*) to produce graphs of the fin's efficiency versus u for different values of β. Razelos and Imre (author's reference) and Netrakanti and Huang [1] employed w, and β to determine the optimum fin dimensions with variable thermal parameters.

The author's two-dimensional solution, of which that no reference is given, contains some confusing non-dimensional variables Γ, B_i, and the roots λ_n, that he states are determined from Eq. (6*f*), not (8*e*) that do not exist. He never noticed that the solution always contains the product $\lambda_n L$. The author should have consulted Carslaw and Jaeger [2]. The roots of equation (6*f*) are

$$\rho_n=\lambda_n L=\rho_n(B_i). \tag{6}$$

These roots and are tabulated in [2]. One key observation is the fact that the magnitude of the roots for $n>1$, irrespectively of the B_i value are

$$(n-1)\pi\leqslant\rho_n\leqslant(2(n-1)+1)\pi/2. \tag{7}$$

Moreover, the author should have followed [2] and express the $\sin(\rho_n)$ as a function of $\tan(\rho_n)=B_i/\rho_n$ to obtain the solution given by Eq. (2). It has been shown by Razelos and Georgiou (author's reference) that due to the large values of ρ_n, the predominant

[1]Prof. Emeritus City University of New York and Assoc. *Editor Heat Transfer Engineering*. E-mail: razel@ath.forthnet.gr

Contributed by the Heat Transfer Division for publication in the JOURNAL OF HEAT TRANSFER. Manuscript received by the Heat Transfer Division September 28, 2000; revision received April 16, 2001.

term in the series for $n>1$ is the first one. Therefore, the two-dimensional solution consists of only one term and is not more difficult than the one-dimensional solution. In addition, in the above reference, graphs of the effectiveness are presented for different values of u and β versus $B_i^{1/2}$, which show that two-dimensional solution actually reduces to the one-dimensional solution.

In concluding, we should point out that the author's comments such as "*large heat transfer coefficients, thin and thick fins,*" should be disregarded because all these quantities are introduced through the proper non-dimensional parameters. Also, the author's last statement "*the major difference is that the one-dimensional solution is less restrictive*" whatever that means should be ignored.

Today fin designers are using more sophisticated programs to design optimum or nearly optimum fins, taking into account variable thermal parameters. Therefore this paper does not offer any help due to an inappropriate set of dimensionless variables and the misleading statement "*Use Fin*" that appears in the Figs. 2 and 3.

References

[1] Netrakanti, M. N., and Huang, C. L. C., 1985, "Optimization of Annular Fins With Thermal Parameters by Invariant Imbedding" ASME J. Heat Transfer, **107**, pp. 966–968.

[2] Carslaw, H. S., and Jaeger, J. C., 1959, *Conduction of Heat in Solids*, Oxford at the Clarendon Press, London, p. 222.

Journal of Heat Transfer

Errata

Erratum: "An Experimental Study of Heat Transfer of a Porous Channel Subjected to Oscillating Flow" [ASME J. Heat Transfer, 123, No. 1, pp. 162–170]

H. L. Fu, K. C. Leong, X. Y. Huang, and C. Y. Liu

1. Ligament diameters for ERG A1 40 PPI and ERG RVC 45 PPI in Table 1 should read as 1.194×10^{-4} m and 1.086×10^{-4} m, respectively.
2. The magnitudes of the Reynolds number labels indicated as Re on Figs. 2–5 and Fig. 7 should be divided by 10.
3. The Reynolds number scale in the *x*-axes of Figs. 8–10 should be divided by 10.

Erratum: "A Scattering-Mediated Acoustic Mismatch Model for the Prediction of Thermal Boundary Resistance" [ASME J. Heat Transfer, 123, No. 1, pp. 105–112]

Ravi S. Prasher and Patrick E. Phelan

The paper was listed in the ***Radiative Transfer*** category in the table of contents. The paper should have been in the ***Microscale Heat Transfer*** category.

